New Trends in Science and Mathematics

Editor:
Prof. Hüsniye SAĞLIKER, Ph.D.

DUVAR

New Trends in Science and Mathematics

Editor:
Prof. Hüsniye SAĞLIKER, Ph.D.

New Trends in Science and Mathematics
Editor: Prof. Dr. Hüsniye SAĞLIKER, Ph.D.

Editor in chief: Berkan Balpetek
Cover and Page Design: Duvar Design
Printing : First Edition-December 2022
Publisher Certificate No: 49837
ISBN: 978-625-8261-56-1

853 Sokak No:13 P.10 Kemeraltı-Konak/Izmir/ Turkey
Phone: 0 232 484 88 68
www.duvaryayinlari.com
duvarkitabevi@gmail.com

Printing and Binding: REPRO BİR
Repro Bir Mat Kağ. Rek. Tas. Tic. Ltd. Şti.
İvogsan 1518. Sokak 2/30 Mat-Sit iş Merkezi Ostim
Yenimahalle/Ankara
Certificate No: 47381

TABLE OF CONTENTS

Bioindicator Aquatic Plant Organisms

Asst. Prof. Dr. Baran AŞIKKUTLU

Selçuk University
Orcid: 0000-0003-2532-5517

Introduction

Most of the Earth's surface is covered by oceans. Fresh water sources make up a small part of the total water. Human beings must protect the fresh water resources around them, as they constantly need water to live. Every field of ecology is interconnected and water science can be seen as a representative example of all environmental sciences (Moss, 2010).

Aquatic ecosystems are important areas that provide life to their environment. Researching water resources and the members of these systems, which have high importance, is a remarkable subject. The aquatic ecosystems that living beings use to maintain their lives and the organisms living there are also important in terms of showing the characteristics of their environment. Ecological stress due to the increasing population causes aquatic ecosystems to be adversely affected.

The increase in human health problems due to losses in ecosystems has increased the importance of investigating these natural ecosystems through bioindicators. All species can tolerate a limited range of chemical, physical and biological conditions, and some species can be used to assess environmental quality. Despite technological advances, it is necessary to examine the biota of natural ecosystems to understand the changes in our environment (Holt and Miller, 2011). The state of aquatic ecosystems, where environmental conditions are sensitive or considered endangered, can be evaluated in terms of different parameters through bioindicators. Monitoring of bioindicators is a bioassessment method used in many studies. Monitoring of important aquatic indicator organisms can be considered as early warning signals for adverse environmental health conditions. This approach is in the form of examining the biological and ecological changes of the parameters determined in organisms. Properly designed field studies and studies evaluating bioindicators can help identify the negative effects of environmental stress effects on human populations and thus enable applications where health assessments of aquatic organisms can be made. Slow-response bioindicators and other faster-responding biomarkers can be evaluated together and used in bioassessment studies to determine limit values for the environment, to make regulatory decisions and to evaluate ecological risk (Adams and Greely, 2000).

Definition Of Bioindicator

In the evaluation of changing conditions within an ecosystem, since it is almost impossible to determine the functions, properties and values of all components, some selected components must be evaluated in terms of giving conclusions about the ecosystem as a whole. Biological components that serve

this purpose are called bioindicators (Kushlan, 1993). Evaluation of the status of bioindicators will provide information about whether the ecosystem is in its natural state or under the influence of contamination. Bioindicators in an aquatic ecosystem can be specified as algae, macrophytes, plankton, mollusks, fish and seabirds in the water system. An ecosystem acts as an important indicator of environmental health by responding rapidly to changes occurring around it. Changes in bioindicator species can be considered as pollution indicators. Since developments in industry and agriculture will increase pollution in ecosystems, bioindicators in these ecosystems can be used as an important model to characterize environmental health (Manickavasagam et al., 2019). Bioindicators began to be widely used in the 1960s and their use has increased over the years (Holt and Miller, 2011).

If the advantages of using bioindicators are mentioned, in traditional studies, the instantaneous physical parameters of the environment have been measured directly, but throuIn addition, pollutants can be found in very low concentrations in the ecosystem and their detection requires sensitive and costly technologies.gh bioindicators, both the status of pollutants and the changes over time can be followed. On the other hand, with the help of bioindicators, it is possible to determine the biological pollutant levels of the environment. Another benefit of bioindicators is their ability to show indirect biotic effects of pollutants when physico-chemical measurements are not available. Finally, considering the large number of species and parameters to be studied, it is widely accepted by scientists that biota is the best study material for detecting the disturbance of ecosystems and the presence of a stressor. Focusing on only one type of biota to identify the problems occurring in the ecosystem can yield important results in terms of seeing the problems. When choosing a bioindicator species, attention should be paid to the fact that the species is specific to the environment, as well as organisms related to local problems and local species, because a single species may not fully represent all stressors. Some characteristics of a good bioindicator are given in Figure 1. Despite its significant benefits, the applicability of bioindicators may be limited due to changes in environmental conditions as a result of anthropogenic effects. In addition, the fact that the indicator characteristics of bioindicator species depend on scale and fail to protect species with different requirements living in a habitat can be stated as the negative aspects of these organisms. Although there are some flaws mentioned, the benefits of bioindicators outweigh these flaws. These organisms can be evaluated at scales ranging from the cellular level to the ecosystem level to determine the state of an ecosystem under investigation. Bioindicators enable us to access data of biological, physical and chemical

components caused by changes in ecosystems as a result of population related human influence and industrialization. These data allow to understand whether the studied ecosystems are biologically sustainable and to take action against existing problems (Holt and Miller, 2011).

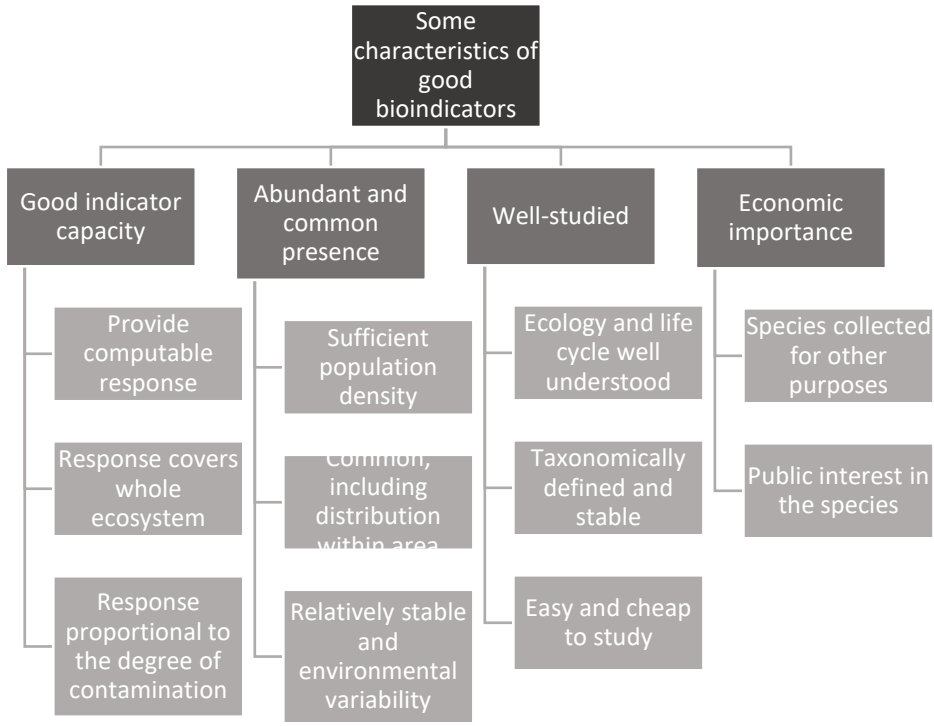

Figure 1. Some characteristics of good bioindicator (Holt and Miller, 2011).

Properties Of BioindicatorAquatic Plant Organisms

The presence or absence of plants or vegetative organisms can provide important information about the health of their environment. These creatures can act as accumulators for metals and metabolic products. Plants are highly effective organisms for predicting and diagnosing environmental stress and are being used more and more in this field. The problem of water pollution has reached remarkable dimensions as a result of increasing industrialization and urbanization. Aquatic plants are stable creatures and provide useful information about their aquatic environmental state, as they can quickly become balanced with their environment (Jain et al., 2010).

In bioindication, plants are organisms that are used to provide information about the quality of the environment, the source of the pollutant, its nature and

its intensity as a result of environmental changes, and they are living things with a high capacity to process heavy metals (Markert, 1993). With the increase in the use of agricultural chemicals, studies using plant organisms to determine the negative effects of these substances on the environment have also increased. In these studies, algae, aquatic and terrestrial macrophytes are frequently used in toxicity tests (Gadzała-Kopciuch et al., 2004). Studies have shown that aquatic plant organisms have bioindicator properties for their ecosystems (Marwood et al., 2001; Bonanno, 2011; Demirezen and Aksoy, 2006). For these reasons, and because of the importance of aquatic plant organisms to form the first step of the food chain in the ecosystems they are in, these organisms are living beings that should be examined and investigated in order to determine and follow the elemental composition of aquatic ecosystems.The taxonomic groups, species and ecological habitats of some aquatic plants are listed in Table 1.

Table 1. The taxonomic groups, species and ecological habitats of some aquatic plants. (Ansari et al. 2017)

Aquatic plant organism	**Taxonomic group**	**Species**	**Ecological habitat**
Microalgae	Cyanobacteria	*Microcystis* sp.	Free Floating
	Chlorophyta	*Scenedesmus* sp.	Free Floating
	Chlorophyta	*Chlorella* sp.	Free Floating
	Chlorophyta	*Stigeoclonium* sp.	Submerged
Macroalgae	Chlorophyta	*Chara* sp.	Rooted Submerged
	Chlorophyta	*Nitella* sp.	Rooted Submerged
	Chlorophyta	*Hydrodictyon* sp.	Free Floating
	Chlorophyta	*Cladophora* sp.	Amphibious
Macrophyte	Bryophyta	*Sphagnum acutifolia*	Amphibious
	Bryophyta	*Fontinalis* sp.	Submerged
	Pteridophyta	*Azolla filiculoides*	Free Floating
	Pteridophyta	*Salvinia* sp.	Free Floating
	Angiosperm	*Vallisneria* sp.	Rooted Submerged
	Angiosperm	*Hydrilla* sp.	Rooted Submerged
	Angiosperm	*Myriophyllum* sp.	Rooted Submerged
	Angiosperm	*Sagittaria montevidensis*	Amphibious/Emergent
	Angiosperm	*Lemna minor*	Free Floating
	Angiosperm	*Mikania periplocifolia*	Amphibious
	Angiosperm	*Utricularia sp*.	Submerged/Free
	Angiosperm	*Nymphoides indica*	Rooted/Leaves Floating

As a result of the pollution of water by human influence, differences in plant diversity or extinction of aquatic plants have been encountered in most of the world's water resources. Plant diversity in polluted aquatic ecosystems has been

evaluated as an important bioindicator in showing water quality. Numerous studies have been conducted on phytoplankton and aquatic macrophytes. Anthropogenic water pollution causes changes in species composition, reduction in overall plant diversity and loss of rare species. The deterioration in these ecosystems causes the loss of underwater vegetation and the proliferation of phytoplankton, weeds and macrophytes (Ansari et al., 2017).

In the ECOTOX database, 25% of the more than 6000 aquatic species evaluated in aquatic ecotoxicology, including animals, plants and fungi, are plant species. In these plant species, 60% of microalgae, 33% of flowering plants, 6% of macroalgae, 1.6% of ferns, 1% of mosses are included. Approximately 65% of the aquatic plant species used are composed of freshwater plant organisms, while the remaining part consists of seawater and brackish water taxa (Ceschin et al., 2021)

BioindicatorAquatic Plant Organism Types

Benthic Algae

Aquatic ecosystems generally contain many algae species. They are equally important in the ecology of aquatic ecosystems, although they are not as visually evident as other aquatic organisms such as plants and fish, mainly due to their microscopic nature. Their visibility can be noticed when they come together in dense populations, color the water and form residues on the water surface. Benthic algae associated with the substrate may be stationary in their positions or may have limited mobility with according to their substrate. The algae associated with the substrate are in dynamic equilibrium with the planktonic organisms. This balance depends on two main factors, namely the depth of the water and the water flow rate. Benthic algae are creatures that need light in their environment and can tolerate high water flow rates. Therefore, benthic algae are the dominant organisms in rivers compared to planktonic algae. Benthic algae need inorganic substrate, submerged aquatic plants or needs aquatic plants located at the edge of the water body to hold on. In lakes and rivers, stones, mud, aquatic plants are associated with inorganic and organic material at the bottom of the water column. Some benthic algae are able to move along substrate surfaces, loosely attached by gelatinous biofilms.Many algae species can show both planktonic and benthic characteristics during their lifetime.In some cases, they develop as benthic, then they become planktonic form. In other cases, algae spend most of the active photosynthetic growth phase as planktonic but spend the winter period in a metabolically inactive phase (Bellinger and Sigee, 2015).

Considering the studies on benthic algae; Ostapczuk et al., (1997) investigated the elements determined in algae and mussel samples collected from the North and Baltic Seas using CV-AAS, INAA, HG-AAS, ETAAS, ICP-AES, IDMS and Stripping Voltammetry methods. In many previous biological monitoring studies, algae and mussels have been used and according to the results obtained, it has been determined that algae and mussels do not accumulate all the elements found in their environment. Some elements such as As, Mn, Co, Ni and Ba were found to accumulate more in algae than in mussels, whereas Hg and Se elements were found to accumulate more in mussels than in algae, and significant concentration differences were not detected in other studied elements. Data obtained from long-term studies have shown that these creatures are effective in biomonitoring studies. Lavoie et al., (2004) evaluated agricultural pollution in southern Québec using benthic algae found in streams identified in 29 sites. From July to August, the algae that were grown on the artificially placed material were examined.Along with benthic algae, water analyzes and land use data were also detected.The results showed that artificial substrates and natural substrates contain similar biomass and species composition. In the study, it was concluded that the use of benthic algae as a bioindicator will contribute to physico-chemical water quality determination studies. In the study of Khalil et al., (2021), 201 algae species identified taxonomically were used in water quality evaluation according to the Palmer pollution index. According to the data obtained in the study, it was determined that there is possible organic pollution in Banjosa Lake, low organic pollution in Ali Sojal Dam and Dothan Dam, medium organic pollution in Drake Dam, and high organic pollution in Rawalakot Nullah region. By using indexes, it has been shown that the algae species as bioindicators, which are systematically identified, can be used to determine the pollution levels of the ecosystem they are in. In the study conducted by Tedeschi and Chow-Fraser (2021), algae increases in Lake Erie due to agricultural phosphorus inputs were evaluated. Instead of traditional methods, which can be costly and time-consuming, they suggested using benthic algae biomass as a bioindicator to determine the trophic status of streams where agricultural input interacts with the aquatic ecosystem.Bioanalysis was carried out using benthic algae during the two-week runoff to determine the agricultural impact in 19 streams identified in Southern Ontario. Cost-effective and low-training methods were used and it was determined that benthic algae biomass and total P concentration were significantly related, but not significantly related to soluble reactive P. They suggested that environmental agencies and landowners use this bioassay to reduce P input in the Lake Erie basin.

Planktonic Algae

In stagnant waters, planktonic algae predominate in the main water body. Their temporal changes depend on the trophic state of the lake and the concentrated algae are in the form of diatoms, colony-forming blue-green algae, and late populations of dinoflagellates in eutrophic lakes. Phytoplankton blooms during the annual cycle can be calculated based on algal biovolume, chlorophyll-a concentration and "Secchi Disk" depth (Bellinger and Sigee, 2015).Phytoplanktonic organisms tend to sink or swim because they rarely have the same density as the environment in which they live. The speed of these vertical movements is also related to the size of the organisms, and the neutrally swimming state is consistently used by these microscopic creatures (Naselli-Flores et al., 2021).In general, it can be concluded that phytoplanktonic organisms can be considered as sensors of their environmental ecosystems, thanks to their potential to generate integrated responses proportional to their lifetime (Estrada and Berdalet, 1997).

Considering the studies on planktonic algae; Díaz-Pardo et al. (1998) investigated the seasonal and annual sequential patterns of phytoplankton community at Lake Atezca, located in a mountainous region of Northeast Mexico, between 1981 and 1994. It has been found that thermal changes affect physico-chemical properties.It was determined that the nutrients increased depending on the mixture. These dynamics affected the phytoplankton community because bacillariophyceae and chlorophyceae in early stratification, dinophyceae and cyanophyceae in late stratification, and bacillariophyceae and chrysophyceae members in the mixing cycle were found to be abundant. It was determined that chlorophyceae members dominated the phytoplankton community from 1981 to 1986, and they were replaced by cyanophyceae, especially *Microcystis aeruginosa* from 1990 to 1994.According to the results, it has been determined that the lake has been showing signs of high eutrophication in recent years. Amengual-Morro et al. (2012) aimed to determine microalgae models in facultative and maturation ponds in order to obtain information about operation and maintenance studies. In the study, organic load, temperature, light penetration, dissolved oxygen and nutrient parameters were measured for phytoplankton. The study method includes the steps of main water quality parameter analysis, taxonomic determination of plankton, and abundance calculation. According to the results, it was shown that cyanobacteria members were found under low load pond conditions and chlorophyta members were found under overloaded pond conditions. With this methodology, it was concluded that phytoplankton determination and density can be used as a bioindicator that can help determine the performance of ponds and operation-maintenance tasks. Sakset and Chankaew (2013) investigated the

phytoplankton diversity of the Pak Phanag River Basin in Southern Thailand in 2006 in three different seasons and three different habitats in order to determine the water quality status and fisheries management. The parameters showed that it is suitable for inland water fishing. In the study conducted with 62 genera of phytoplankton members belonging to six divisions, the third most abundant species was *Peridinium* sp., the species most associated with velocity was *Protoperidinium* sp. and the species most associated with ammonia nitrogen was determined as*Trachelomonas* sp..The Shannon-Wiener diversity index indicated that the phytoplankton diversity was moderate and the water quality status was moderately polluted. According to the Shannon-Wiener diversity index, phytoplankton diversity and water quality status were shown to be moderately polluted. In addition, according to the AARL-PP score, it was concluded that the water quality status was at the meso-eutrophic level and moderately polluted, but still suitable for the life of aquatic organisms. Dorche et al. (2018) investigated phytoplankton and zooplankton communities as bioindicator organisms in the evaluation of water quality in Zayandehrud Dam Lake located in Isfahan Province, which is the largest lake in the center of Iran.It has been stated that the presence of genera such as Cyclotella, Dynobrion, Bosmina and Daphnia from phytoplankton and zooplankton communities in general are considered as indicators of oligotrophic lakes, and the absence of genera such as Microsystis, Brachionus and Lecane are considered important indicators of eutrophic lakes. It was determined that the phytoplankton community in the lake consisted of Bacillariophyceae, Cyanophyceae, Euglenophyceae, Dinophyceae and Chrysophyceae members. According to the data obtained in the study, it was concluded that the lake can be classified as a healthy water body.

Macroalgae

Macroalgae are the primary producer organisms that form the basis of complex aquatic food webs and are economically important organisms as several hundred thousand tons of macroalgae are harvested each year for food production and technological use (Häder and Figueroa, 1997). It is estimated that there are 1800 brown, 6200 red and 1800 green macroalgae in marine ecosystems, and although red algae are more diverse, brown algae are the largest in size (Pereira, 2021). Studies show that macroalgae are effective bioindicator organisms for trace elements. The use of macroalgae as bioindicators should be encouraged to comprehensively determine the presence of trace elements in abiotic and biotic components of coastal ecosystems (Bonanno and Orlando-Bonaca, 2018). Macroalgal bioindicator organisms are important markers for determining metal accumulation levels in coastal areas

exposed to human-induced contamination (Chalkley et al., 2019). It has been concluded that macroalgal metal concentrations are more related to sediment metal concentrations than to metal concentrations in water, and they may be usable biomonitors for sediment contamination in their aquatic ecosystem.Macroalgae in the more polluted region generally contain higher metal concentrations. However, despite varying sediment concentrations, iron, nickel and manganese concentrations were found to be similar in macroalgae, while the difference in copper, zinc, lead and chromium concentrations was found to be related concentrations in the environment.The uptake of metals also yielded different results among different species, leading to the conclusion that differing parameters such as morphology may have an effect on metal uptake and accumulation (Melville and Pulkownik, 2007).

Considering the studies on macroalgae; Ho (1990) evaluated the use of *Ulva lactuca* species collected from 24 tidal zones around Hong Kong island as indicators of Mn, Fe, Ni, Cu, Zn, Cd and Pb metal contaminations. 12 stations were selected from places that are considered to be relatively rural and clean, and the remaining 12 stations were selected from populated areas.Cd was detected in all stations with similar results.A high level of metal contamination was detected, especially in the eastern part of the port. Preliminary results showed that *Ulva lactuca* is a good indicator that can show Mn, Fe, Cu, Zn and Pb contaminations.Melville and Pulkownik (2006) investigated the distribution and abundance of macroalgae in four estuarine regions in Sydney, Australia. It has been determined that the diversity and distribution of macroalgae is affected by the amount of pollutants in the environmentand the biomass is related to the nutrient concentrations.It was determined that Rhodophyta member *Catenella nipae* decreased significantly as metal concentrations increased in all seasons studied.This species has been found to have an important potential as a bioindicator of estuarine contamination.Al-In the study of Al-Homaidan et al. (2011) used two macroalgae species taken from a stream under anthropogenic stress in the Hanifah Valley to determine heavy metal concentrations. Mn, Cu, Zn, As, Cd and Pb concentrations in the samples were determined using the ICP-OES device.Mn, Cu and As loads were detected in all samples and a high degree of contamination was detected.Zn, Cd and Pb levels were within the limits. In the study, it was concluded that *Enteromorpha intestinalis* can be used as an excellent indicator for Mn, Zn and As pollution, and *Cladophora glomerata* can be used as an excellent indicator for Cu, Cd and Pb pollution.In the study of Aşıkkutlu and Okudan (2021), elemental analyzes of two macroalgae species collected from the coastal region of Serik District of Antalya Province were carried out.About macro elements, the highest value was obtained for K and the lowest value was obtained for P element in *Cystoseira*

foeniculacea and *Gongolaria montagnei* species. About trace elements, the highest value was obtained for Fe element in *Cystoseira foeniculacea* and *Gongolaria montagnei* species, the lowest value was obtained for Mo element in *Cystoseira foeniculacea* and for Cd element in *Gongolaria montagnei*. It was determined that the data obtained in the study were similar to the data of other studies. Salo and Salovius-Laurén (2022) investigated the changes of nutrient concentrations in the coastal region of the North Baltic Sea in terms of eutrophication and macroalgae were evaluated as bioindicators to reflect nutrient concentrations.The temporal variation of P and N concentrations of *Cladophora glomerata* and *Ulva intestinalis* species was investigated. Measurements in the *U. intestinalis* speices were less reliable for current and previous water and nutrient concentrations, also *C. glomerata* was reported to be a useful species for assessing both spatial and temporal variation.

Macrophytes

Freshwater macrophytes consist of members of Charophyta, Bryophyta, Pteridophyta and Spermatophyta. Their photosynthetically active parts may be permanently submerged or submerged for several months each year, or may be found floating on the water surface (Cook et al., 1974). Macrophytes in water respond to changes in element concentrations that occur in the environment.These creatures can take nutrients from both the sediment and the water they are in. Therefore, macrophytes are suitable organisms for the comprehensive assessment of river ecosystems (Kohler and Schneider, 2003). Aquatic mosses can be used as indicators to indicate the presence or amount of a contaminant. Biomonitoring of these species is in the form of analyzes involving passive observation of native species or active biomonitoring of transplanted species for a fixed exposure time (Gecheva and Yurukova, 2014). Ferns are important, but not adequately researched, potential ecological indicators (Della and Falkenberg, 2019). Water quality assessment studies can be performed using samples of chlorophyta, bryophyta, pteridophyta and angiosperms in freshwater or marine, lentic or lotic, wetlands or coastal ecosystems (Ansari et al., 2017).

Considering the studies on macrophytes; Klumpp et al. (2002) investigated metal contamination in freshwater ecosystems in the southern parts of the state of Bahia in Brazil. Copper fungicides, which have been used in cocoa production in the region for years, have caused copper accumulation in the components of cocoa plants and are thought to cause environmental contamination. In order to determine whether anthropogenic contaminants cause water pollution and eutrophication in the Rio Cachoeira River in the region, the concentrations of copper, aluminum, chromium, nitrogen and phosphorus in

Eichhornia crassipes and *Pistia stratiotes* species, which are included in aquatic macrophytes, were examined from seven stations. Especially in *Eichhornia crassipes* roots, an increase in heavy metal levels was determined. Significant increases in nitrogen and phosphorus concentrations in plant tissues and water were detected downstream in Itabuna City.It has been determined that metal inflow and eutrophication are related to industrial and agricultural resources in the region. It has been suggested that aquatic macrophytes can be used as bioindicator species in water quality and biological monitoring, in addition to chemical water analysis. In their study, Galal and Shehata (2014) investigated *Myriophyllum spicatum* in terms of its ability to accumulate nutrients and heavy metals in polluted water resources of Egypt. For this study, 6 stations were selected at different locations. It was determined that there was no significant difference between S5-S6 measurements and S1-S6 vegetative measurements. In addition, there was no significant difference in Mn, Cd, Pb and Ni measurements in S1 and S6 sediment samples, but N, P and K measurements were significantly different. While the concentrations of heavy metals in sediment samples had the sequence Fe > Mn > Cu > Zn > Pb > Ni > Cd, in plants it was determined as Mn > Fe > Zn > Cu > Ni > Pb > Cd. In addition, the bioaccumulation factor was found to be more than one for all heavy metals except Pb, and the uptake capacity order was Ni > Mn > Cd > Fe > Zn > Cu > Pb. The high bioaccumulation factor indicates that this plant species has a high potential to accumulate heavy metals in its tissues, and as a result it can be used as a bioaccumulator for these toxic metals. In their study, Galal and Farahat (2015) evaluated the trace metal accumulation potential, phytoremediation perspective and the possibility of using it as a bioindicator in different pollution types of the *Pistia stratiotes* macrophyte species obtained from the stations determined from Lake Mariut. The water physicochemical data of Lake Mariut showed significant differences between lake basins in all variables except temperature, pH and Cd metal. In contrast to trace metals, *P. stratiotes* accumulated higher macronutrients in its leaves than in the roots. It was concluded that the growth response of this plant to different pollutants can be used as a potential bioindicator for these pollutants in water. Harguinteguy et al. (2016) evaluated the usability of *Myriophyllum aquaticum* and *Potamogeton pusillus* macrophytes collected from 10 stations from the Ctalamochita River in Argentina as indicator organisms in aquatic ecosystem biomonitoring studies to determine the accumulation of Co, Cu, Fe, Mn, Ni, Pb and Zn. It was determined that Cu and Pb values in surface water exceeded the limits determined for the protection of aquatic life determined in Argentine regulations, while Cu and Zn values exceeded the ecological scanning level limit in sediment. High accumulation of Co, Cu, Ni and Zn elements in P.

pusillus species correlated with the accumulation in sediment, and high accumulation of Co, Cu, Mn and Zn elements in *M. aquaticum* species correlated with accumulation in water. It has been stated that these macrophytes reflect the spatial changes of metals in the water and sediment of the Ctalamochita River and therefore have the potential to be used as heavy metal bioindicators of river pollution. Farias et al. (2018) determined the metal contents of arsenic, cadmium, copper, lead, selenium and zinc in 12 species including macrophytes and macroalgae in Derwent Estuary in Tasmania (Australia). Different amounts of copper, lead and zinc were detected in all species. Macrophytes accumulated the highest level of all metals. It was determined that Zn element in *Ruppia megacarpa* species, Pb element in *Zostera muelleri* species, Zn element in *Ulva australis* species accumulated in high amounts.The findings concluded that more than one species should be investigated for a detailed understanding of metal pollution throughout the estuary.

Conclusion

Aquatic ecosystems are environments that need to be constantly investigated because they are essential for living beings to survive. The investigation of ecosystems can be in the form of physical, chemical and biological evaluation of environmental parameters. Among these methods, in the biological approach, both the instantaneous state of the ecosystem and its change over time can be determined with bioindicators. Although there are many biological monitoring studies in aquatic ecosystems, the results of studies on metal pollution or nutrient discharges are remarkable. These organisms are preferred by many researchers because the results of aquatic biological indicators are remarkable in researches to determine contamination levels.The data obtained in the studies provide important information to the researchers about the determination of the contamination factors, their long-term follow-up, or what precautions should be taken against these contaminants in the environment. The data obtained from aquatic organisms are evaluated in various indexes, allowing different approaches to contamination studies. As a result, aquatic plant organisms are important biological indicators that should be investigated and evaluated periodically, which enable us to have information about environmental conditions and changes, and also allow the necessary precautions to be taken at the appropriate time.

REFERENCES

1. Adams, S. M., & Greeley, M. S. (2000). Ecotoxicological indicators of water quality: using multi-response indicators to assess the health of aquatic ecosystems. *Water, air, and soil pollution*, 123(1), 103-115.
2. Amengual-Morro, C., Niell, G. M., & Martínez-Taberner, A. (2012). Phytoplankton as bioindicator for waste stabilization ponds. *Journal of Environmental Management*, *95*, S71-S76.
3. Ansari, A. A., Shalini Saggu, S. S., Al-Ghanim, S. M., Abbas, Z. K., Gill, S. S., Khan, F. A., Dar, M. D., Naikoo, M. I. & Khan, A. A. (2017). Aquatic plant biodiversity: a biological indicator for the monitoring and assessment of water quality. In Plant biodiversity: monitoring, assessment and conservation (pp. 218-227). Wallingford UK: CABI.
4. Al-Homaidan, A. A., Al-Ghanayem, A. A., & Alkhalifa, A. H. (2011). Green algae as bioindicators of heavy metal pollution in Wadi Hanifah Stream, Riyadh, Saudi Arabia. *International Journal of Water Resources and Arid Environments*, *1*(1), 10-15.
5. Aşıkkutlu, B., & Okudan, E. Ş. (2021). Macro and Trace Element Levels of Macroalgae *Cystoseira foeniculacea* ve *Gongolaria montagnei* Species from Mediterranean Region (Antalya/Turkey). *Journal of Anatolian Environmental and Animal Sciences*, *6*(4), 757-764.
6. Bellinger, E. G., & Sigee, D. C. (2015). Freshwater algae: identification, enumeration and use as bioindicators. John Wiley & Sons.
7. Bonanno, G. (2011). Trace element accumulation and distribution in the organs of Phragmites australis (common reed) and biomonitoring applications. *Ecotoxicology and Environmental Safety*, *74*(4), 1057-1064.
8. Bonanno, G., & Orlando-Bonaca, M. (2018). Trace elements in Mediterranean seagrasses and macroalgae. A review. *Science of the total environment*, *618*, 1152-1159.
9. Ceschin, S., Bellini, A., & Scalici, M. (2021). Aquatic plants and ecotoxicological assessment in freshwater ecosystems: A review. *Environmental Science and Pollution Research*, *28*(5), 4975-4988.
10. Chalkley, R., Child, F., Al-Thaqafi, K., Dean, A. P., White, K. N., & Pittman, J. K. (2019). Macroalgae as spatial and temporal bioindicators of coastal metal pollution following remediation and diversion of acid mine drainage. *Ecotoxicology and environmental safety*, *182*, 109458
11. Cook, C. D., Gut, B. J., Rix, E. M., & Schneller, J. (1974). *Water plants of the world: a manual for the identification of the genera of freshwater macrophytes*. Springer Science & Business Media.

12. Della, A. P., & Falkenberg, D. D. B. (2019). Pteridophytes as ecological indicators: an overview. *Hoehnea*, *46*.
13. Demirezen, D., & Aksoy, A. (2006). Common hydrophytes as bioindicators of iron and manganese pollutions. *Ecological Indicators*, *6*(2), 388-393.
14. Díaz-Pardo, E., Vazquez, G., & López-López, E. (1998). The phytoplankton community as a bioindicator of health conditions of Atezca Lake, Mexico. *Aquatic Ecosystem Health & Management*, *1*(3-4), 257-266.
15. Dorche, E. E., Shahraki, M. Z., Farhadian, O., & Keivany, Y. (2018). Seasonal variations of plankton structure as bioindicators in Zayandehrud Dam Lake, Iran. *Limnological Review*, *18*(4), 157-165.
16. Estrada, M., & Berdalet, E. (1997). Phytoplankton in a turbulent world. Scientia Marina. 61 (1): 125-140.
17. Farias, D. R., Hurd, C. L., Eriksen, R. S., & Macleod, C. K. (2018). Macrophytes as bioindicators of heavy metal pollution in estuarine and coastal environments. *Marine Pollution Bulletin*, *128*, 175-184.
18. Gadzała-Kopciuch, R., Berecka, B., Bartoszewicz, J., & Buszewski, B. (2004). Some considerations about bioindicators in environmental monitoring. *Polish Journal of Environmental Studies*, *13*(5), 453-462.
19. Galal, T. M., & Farahat, E. A. (2015). The invasive macrophyte Pistia stratiotes L. as a bioindicator for water pollution in Lake Mariut, Egypt. *Environmental Monitoring and Assessment*, *187*(11), 1-10.
20. Galal, T. M., & Shehata, H. S. (2014). Evaluation of the invasive macrophyte *Myriophyllum spicatum* L. as a bioaccumulator for heavy metals in some watercourses of Egypt. *Ecological Indicators*, *41*, 209-214.
21. Gecheva, G., & Yurukova, L. (2014). Water pollutant monitoring with aquatic bryophytes: a review. *Environmental Chemistry Letters*, *12*(1), 49-61.
22. Harguinteguy, C. A., Cofré, M. N., Fernández-Cirelli, A., & Pignata, M. L. (2016). The macrophytes Potamogeton pusillus L. and Myriophyllum aquaticum (Vell.) Verdc. as potential bioindicators of a river contaminated by heavy metals. *Microchemical Journal*, *124*, 228-234.
23. Häder, D. P., & Figueroa, F. L. (1997). Photoecophysiology of marine macroalgae. *Photochemistry and Photobiology*, *66*(1), 1-14.
24. Ho, Y. B. (1990). Ulva lactuca as bioindicator of metal contamination in intertidal waters in Hong Kong. *Hydrobiologia*, *203*(1), 73-81.

25. Holt, E. A. & Miller, S. W. (2011) Bioindicators: Using Organisms to Measure Environmental Impacts. *Nature Education Knowledge*, 2(2):8
26. Jain, A., Singh, B. N., Singh, S. P., Singh, H. B., & Singh, S. (2010). Exploring biodiversity as bioindicators for water pollution. In National Conference on Biodiversity, Development and Poverty Alleviation (pp. 50-56).
27. Khalil, S., Mahnashi, M. H., Hussain, M., Zafar, N., Khan, F. S., Afzal, U., Shah, G. M., Niazi, U. M., Awais, M., & Irfan, M. (2021). Exploration and determination of algal role as Bioindicator to evaluate water quality–Probing fresh water algae. *Saudi Journal of Biological Sciences*, *28*(10), 5728-5737.
28. Klumpp, A., Bauer, K., Franz-Gerstein, C., & De Menezes, M. (2002). Variation of nutrient and metal concentrations in aquatic macrophytes along the Rio Cachoeira in Bahia (Brazil). *Environment International*, *28*(3), 165-171.
29. Kohler, A., & Schneider, S. (2003). Macrophytes as bioindicators. *Large Rivers*, *14*(1-2), 17-31.
30. Kushlan, J. A. (1993). Colonial waterbirds as bioindicators of environmental change. *Colonial waterbirds*, 223-251.
31. Lavoie, I., Vincent, W. F., Pienitz, R., & Painchaud, J. (2004). Benthic algae as bioindicators of agricultural pollution in the streams and rivers of southern Québec (Canada). *Aquatic Ecosystem Health & Management*, *7*(1), 43-58.
32. Manickavasagam, S., Sudhan, C., & Aanand, S. (2019). Bioindicators in aquatic environment and their significance. *Journal of Aquaculture in the Tropics*, 34(1/2), 73-79.
33. Markert B. (1993). Plants as biomonitors: indicators for heavy metals in the terrestrial environment. Weinheim, New York, Basel and Cambridge: VCH.
34. Marwood, C. A., Solomon, K. R., & Greenberg, B. M. (2001). Chlorophyll fluorescence as a bioindicator of effects on growth in aquatic macrophytes from mixtures of polycyclic aromatic hydrocarbons. *Environmental Toxicology and Chemistry: An International Journal*, *20*(4), 890-898.
35. Melville, F., & Pulkownik, A. (2006). Investigation of mangrove macroalgae as bioindicators of estuarine contamination. *Marine Pollution Bulletin*, *52*(10), 1260-1269.

36. Melville, F., & Pulkownik, A. (2007). Investigation of mangrove macroalgae as biomonitors of estuarine metal contamination. *Science of the Total Environment*, *387*(1-3), 301-309.
37. Moss, B. (2010). Ecology of fresh waters: a view for the twenty-first century. John Wiley & Sons,
38. Naselli-Flores, L., Zohary, T., & Padisák, J. (2021). Life in suspension and its impact on phytoplankton morphology: an homage to Colin S. Reynolds. *Hydrobiologia*, *848*(1), 7-30.
39. Ostapczuk, P., Burow, M., May, K., Mohl, C., Froning, M., Süßenbach, B., Waidmann, E., & Emons, H. (1997). Mussels and algae as bioindicators for long-term tendencies of element pollution in marine ecosystems. *Chemosphere*, *34*(9-10), 2049-2058.
40. Pereira, L. (2021). Macroalgae. *Encyclopedia*, *1*(1), 177-188.
41. Sakset, A., & Chankaew, W. (2013). Phytoplankton as a bio-indicator of water quality in the freshwater fishing area of Pak Phanang River Basin (Southern Thailand). *Chiang Mai Journal of Science*, *40*(3), 344-355.
42. Salo, T., & Salovius-Laurén, S. (2022). Green algae as bioindicators for long-term nutrient pollution along a coastal eutrophication gradient. *Ecological Indicators*, *140*, 109034.
43. Tedeschi, A. C., & Chow-Fraser, P. (2021). Periphytic algal biomass as a bioindicator of phosphorus concentrations in agricultural headwater streams of southern Ontario. *Journal of Great Lakes Research*, *47*(6), 1702-1709.

Frequency-resolved Photoconductivity in Amorphous Arsenic

Ruhi KAPLAN[1], Bengü KAPLAN[2]

[1]Prof. Dr., University of Mersin, Physics Division,
Department of Mathematics and Science Education,
Çiftlikköy Campus, 33343 Mersin, Turkey. rkaplan@mersin.edu.tr,
Orcid ID: 0000-0003-1000-2889

[2]Prof. Dr., University of Mersin, Physics Division,
Department of Mathematics and Science Education,
Çiftlikköy Campus, 33343 Mersin, Turkey. bkaplan@mersin.edu.tr,
Orcid ID: Orcid ID: 0000-0002-1334-6137

1. Introduction

Chalcogenide glasses are considered to be the subject of a great deal of interest in the study of their basic physics as well as of device technology. They are appropriate material for optical memory disk [1,2], optical elements [3,4] and optical sensors working in the infrared region [5].

The optical properties of materials are important to determine their usage in optoelectronic applications. The optical band gap is usually dependent on the defects due to additional elements. The decreasing in direct band gap with increase in thickness is attributed to the formation of some defects leading to an increase in localised states in the band gap.

A-As based thin film glasses have been found to exhibit interesting changes with composition in properties such as the local structure, density, electrical switching behaviour, conductivity activation energy, etc., which have been attributed to the network topological effects. Especially Te-As-Se compositions are perspective materials for manufacturing optical fibers because of their low phonon energy, low optical losses and good thermal and chemical stability.

The variaty of light-induced structural transformation in amorphous chalcogenide films is wide and attracts scientific as well as technical interest [6,7]. Among them, photo-induced diffusion has potential application in optoelectronics (photoresists, optical memories, optoelectronic circuits, etc.). The presence of localized states in the gap region is the dominant factor for the photo-induced effects in such type of materials. The lone-pair character of the valence tails leads to very rich behavior under the influence of light. The illumination by band gap light of many amorphous chalcogenides changes their internal and / or surface structure, and the optical absorption edge will have a red or blue shift [8]. To knowledge of the photo-interaction in such films is a crucial point in understanding the basic mechanism and its technological applications such as device making.

Various device applications like rectifiers, photocells, xerography, switching and memory, etc., have made selenium (Se) attractive. Unfortunately, pure Se element has disadvantages like short lifetime and low sensitivity [9]. This problem can be overcome by alloying Se with some impurity atoms (As, Te, Bi, Ge, Ga, Sb, etc.), which gives higher sensitivity, higher crystallization temperature and smaller aging effects [6,7]. Chalcogenide glasses in general and vitreous Te-based alloys in particular have been the subject of extensive work, with an emphasis on structure change due to their new technological applications in optical data storage, memory devices, CO_2 detection [4,10]. The addition of an impurity has a pronounced effect on the optical properties of amorphous materials, and this effect can be widely different for different impurities [11]. Therefore, the ternary compounds involving As-Se-Te have interesting properties as well as technological applications because they form a wide range of glassy region [1].

Photocurrent measurements have been widely used for understanding the defect states in glassy chalcogenides. In most of the chalcogenide glasses, long time exposure to light at room temperature, leads to an appreciable decrease in

photocurrent (photodegradation). This is found to be due to the formation of intimate valence alternation pairs under illumination. These defects are stable only at low temperatures and are converted by bond-switching reactions to random pairs of charged defects, known as light induced metastable defects [12,13]. These light induced metastable defects act as electron-hole trapping centers and decrease the photocurrent.

Recombination is a key factor when describing photocarrier transport in chalcogenide glasses because it strongly affects the electrical and optical response of the chalgonide glass at all levels of external excitation. In order to determine the quality of a semiconductor, an important parameter is the photocarrier lifetime, because it provides information on the distribution of defects exist in the material. The defect and impurity levels affect the carrier lifetime directly by supplying an alternative recombination path or by acting as trapping centers. The carrier lifetime distribution of a material, therefore, provides a sensitive measure of sample quality.

In the present work, we use frequency-resolved photocurrent (FRPC) spectroscopy on a-As and its compounds, at different light intensities and applied voltages. The exponent ν in the power-low relationship, $I_{ph} \propto G^{\nu}$, between photocurrent and the carrier generation rate is also determined at different frequencies, wavelengths, and materials. The results are discussed in terms of the proposed models that try to explain the photocurrent response in relation to the localizes states.

2. Experimental details

We produced the thin film of samples of a-As and its compounds by using a thermal evaporation unit. The materials used for these samples were from BDH chemicals with a high purity of 99.9992 %. Mostly we put co-planar Al or Au electrodes on the samples by using a suitable Al foil mask and the thermal evaporation unit. However, instead of using a crucible, the Al or Au ingots were evaporated directly from tungsten spiral. For electrode spacing, the different size Cu wires ranging between 0.1 mm and 0.2 mm were used as masks. Copper external leads were contacted with Ag paint. The current-voltage (I-V) measurements taken in dark proved that the contacts were perfectly ohmic. As noted previously [14], gold contacts perform better in injecting hole carriers and thus give larger photocurrents than aluminium contacts for these a-As and its chalcogenide compounds.

The samples were excited by a HeNe or an Ar laser. An acousto optic modulator (IntraAction Corp., Model AOM-125) was used to modulate the light sinusoidally in the frequency range of 10 Hz to 100 kHz. The modulation amplitude amounted to 46 % of the bias light intensity. The modulated photocurrent signal excited in this way was measured and analysed by a lock-in amplifier (SR 530 Stanford Research System). The intensity of the excitation light was reduced by neutral density filters.

3. Theory

There are many transient photocurrent techniques [15-17] aimed primarily at probing the thermalization of photoexcited carriers in amorphous materials. On a longer time-scale, the decay of the photocurrent in the presence of recombination gives information about both deep recombination centers and traps in thermal equilibrium with the band. The response time is generally measured by measuring the time for the photocurrent to decay to some fraction of its initial value. Measurement of the modulation frequency dependence of the photocurrent is a complementary method of measuring the response time. Oscillatory modulation allows the investigation of details in the steady-state system response, whereas transient decay measurements average over a range of system conditions.

The frequency-resolved photocurrent (FRPC) spectroscopy technique has already been described [18-20]. In its simplest form, the optical excitation of a sample is modulated with a small amplitude sinusoid and the sample response to this modulation is measured either in-phase or in-quadrature to the phase of the excitation modulation, using a lock-in dedection. Logarithmically sweeping the modulation frequency then generates a lifetime distribution directly.

In the mathematical analysis of frequency-resolved spectroscoy (FRS) method, the in- phase FRS gives the integral of lifetime distribution, between the limits $\tau\sim(2\pi\omega)^{-1}$ and ∞, while the in-quadrature FRS gives the lifetime distribution directly. For a system with a single characteristic lifetime τ, the in-quadrature FRS spectrum is a symmetric band, of half width 0.7 decades peaked at the frequency

$$f_{peak} = \frac{1}{2\pi\tau} \tag{1}$$

The lock-in output from all lifetime components as the frequency is swept is given by

$$S(\omega) = \int_0^\infty P(\tau)s(\omega,\tau)d\tau \tag{2}$$

where $P(\tau)$ is the lifetime distribution, and $s(\omega,\tau)$ is the response function. For quadrature the lock-in response function is given by

$$s(\omega,\tau) = \frac{g_r}{(\omega\tau + \frac{1}{\omega\tau})} \tag{3}$$

while in-phase FRS, it takes the following form

$$s(\omega,\tau) = \frac{g_r}{(1+\omega^2\tau^2)} \tag{4}$$

where g_r is the excitation rate. For comparison, the in-quadrature and phase response functions of a-As are represented together in Fig.1. Althoug the in-quadrature FRS is the most useful form, the in-phase version can also give important additional information on the existence of fast processes beyond the time domain of the in-quadrature measurements. It is worth remembering that if one knows the quadrature response from $\omega = 0 \rightarrow \infty$ (which one does not), a Kramers-Kronig transform will give the in-phase response. That is all the information is in either response, if complete in ω.

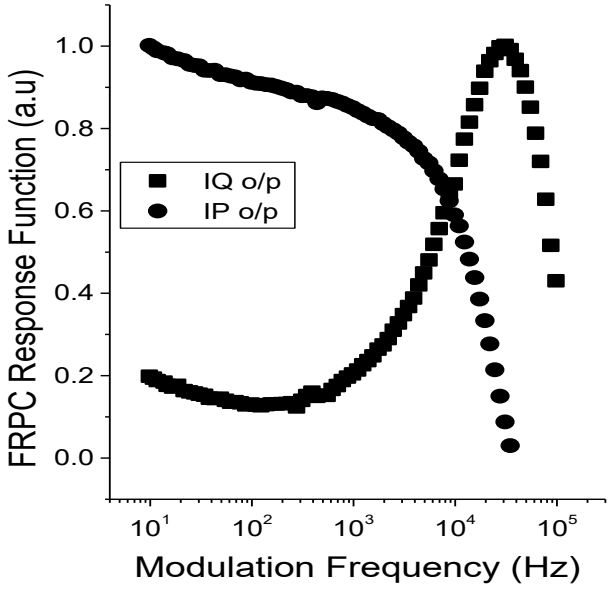

Fig.1. Freqency-resolved photocurrent (FRPC) response function of a-As for the in-quadrature (Eq. (3)) and in-phase (Eq. (4)) with a single well defined lifetime. Excitation: HeNe laser (632.8 nm, 2314 μW). Applied voltage: 500 V. (a.u, arbitrary units).

4. Results and discussion

The in-phase and in-quadrature frequency-resolved photocurrent (IP-FRPC and IQ-FRPC)) responses of the samples in the frequency interval between 10 Hz and 100 kHz were measured as a function of the intensity of the excitation light and applied voltages. Since the energy of the excitation light is much higher than the optical band gap of these materials, we assume that the carriers are

photoexcited between extended states and then a trap limited recombination occurs at room temperature.

Fig. 2 shows IQ-FRPC and IP-FRPC spectra of a-As for different excitation intensities of HeNe laser (632.8 nm). Applied voltage was 500 V. As seen from the IQ-FRPC spectra, there is only one single broad spectra. This means that there is only one characteristic lifetime.

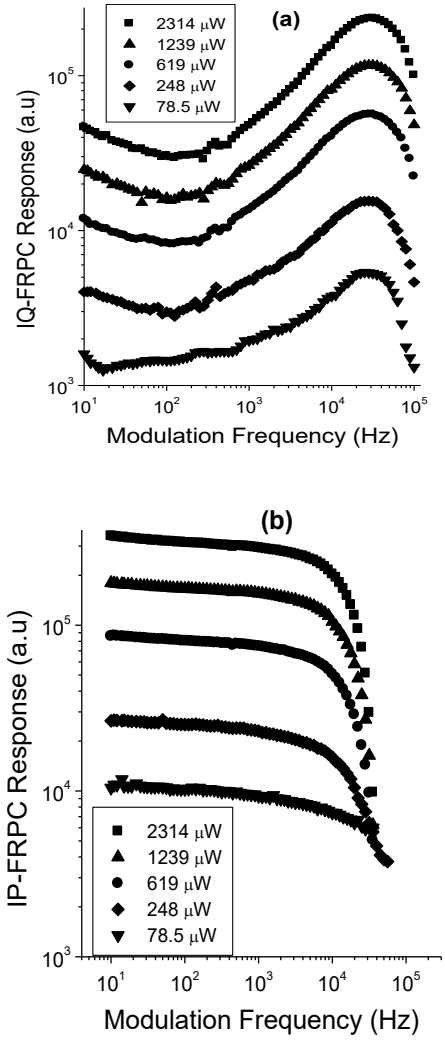

Fig. 2. (a) IQ-FRPC and (b) IP-FRPC spectra of a-As for different excitation intensities of HeNe laser (632.8 nm).

Using Eq. (1), a lifetime of about 5 μs was calculated from the peak frequency of 31622 Hz. Fig. 3 shows the effect of applied voltage on the IQ-

FRPC and IP-FRPC spectra. In Figs. 2 and 3, however, the lifetime is found to be independent of excitation intensity and applied voltage. The magnitude of IQ- and IP-FRPC decreases with decreasing light intensities and voltages as expected. At room temperature, the photocarriers may be thermally ionized from recombination or trapping states, in which only one recombination path is present.

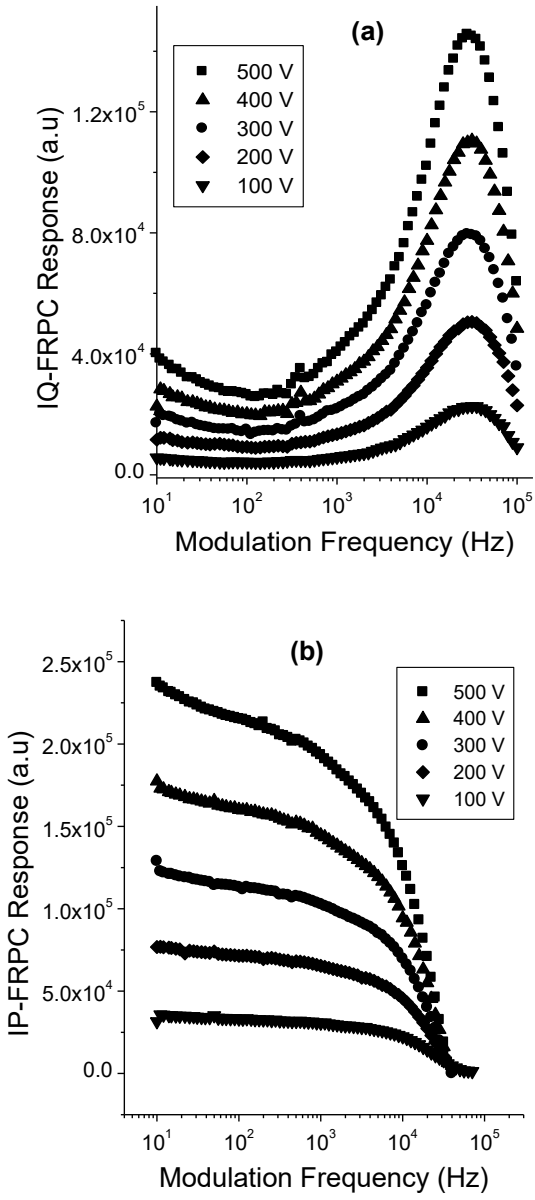

Fig. 3. (a) IQ-FRPC and (b) IP-FRPC spectra in a-As at different applied voltages. Excitation: HeNe (632.8 nm, 2314 μW).

The next series of our experiments concerns the light intensity dependence of photocurrent, I_{ph}. For these measurements, the light intensity was increased in steps from 23.1 μW up to 2314 μW. Fig. 4 shows the light intensity dependence of photocurrent at two different outputs (IP and IQ) and modulation frequencies (10 Hz and 1 kHz). According to the power-law relatioship, $I_{ph} \propto G^{\nu}$, between light generation flux and photocurrent, the plot between $ln(I_{ph})$ and $ln(G)$ should be straight line. The exponent ν is calculated from the slope of the curve plotted in Fig. 4. However the result of 10 Hz of IQ o/p for ν is not reliable much in this type of experiment, so we can not plot it due to very small signal dedected at this frequency.

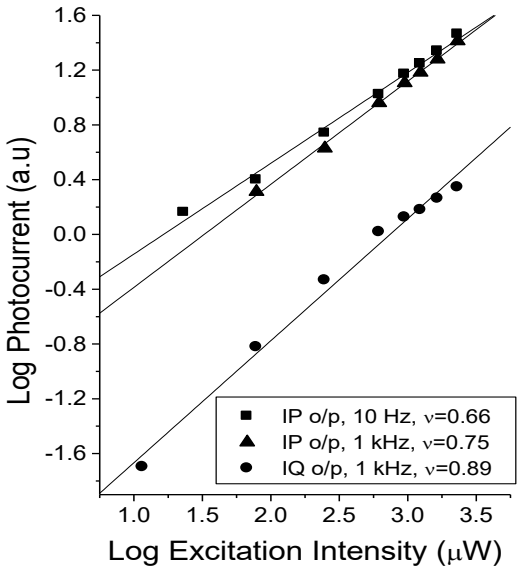

Fig. 4. Excitation (HeNe) intensity dependence of photocurrent of a-As at two different IP and IQ outputs, and frequencies. The calculated values of exponent ν in $I_{ph} \propto G^{\nu}$ are also shown on the figure.

As seen from Fig. 4, the exponent, ν, inreases with increasing modulation frequency due to the release rate of fotocarriers from the deep level traps. There is also a difference between IP and IQ outputs for ν at the same frequency of 1 kHz. We have no idea for this result now. It may be the lock-in amplifier effect.

We have also examined the effect of different excitation wavelengths on ν. Table 1 shows this result for a-As. The blue light (476.5 nm) has a larger ν value than that of other wavelengths of 632.8 nm and 528.0 nm due to the high absorption of excitation light at low wavelengths.

Table 1. Comparison of the exponent ν in $I_{ph} \propto G^{\nu}$ at three different excitation wavelengths. V_{app} = 500 V, T = 290 K.

Wavelength (nm)	632.8	528.0	476.5
Exponent, ν	0.72±0.03	0.72±0.07	0.85±0.09

The intensity and the photon energy dependence of FRPC response at room temperature may be interpreted through the kinetics of photoinduced transitions and thermal relaxations between the extended and localized states, or in terms of the charged defect concept.

Rose [21] suggests that $\nu = 1$ corresponds to monomolecular recombination and $\nu = 0.5$ to bimolecular recombination. However, in the case of continuous distribution of traps the value of ν may be anywhere between 0.5 and 1.0 depending on the light intensity and temperature range.

It is now well known that the value of the exponent ν differs in various materials. In most cases, a sublinear dependence is found and the exponent ν in the power-law relation $(I_{ph} \propto G^{\nu})$ has quite complicated variations with photon energy, light intensity, temperature, modulation frequency and applied field [11]. Table 2 shows a comparative ν values for a-As and its compounds at the same experimental conditions. All results lie between about 0.59 and 0.72, indicating the presence of a continuous distribution of localized states in the energy gaps of materials used.

Table 2. A comparison of the exponent ν in $I_{ph} \propto G^{\nu}$ for different compounds of a-As under identical conditions. Exc.: HeNe (2314 μW), V_{app} = 500 V, T = 290 K.

Materials	Exponent, ν
a-As	0.72 ± 0.03
a-AsS	0.66 ± 0.01
a-As_2S_3	0.69 ± 0.07
a-AsTe	0.70 ± 0.04
a-AsSe	0.60 ± 0.07
a-As_2Se_{4-8}	0.59 ± 0.03
a-As_2S_3Se	0.69 ± 0.02

The exponet ν in power-law could qualitatively be associated with the amount of recombination centers located in energy gap; a higher value of ν, in general, implies a higher rate of carrier recombination. In this respect, the pure a-As has a larger photocarrier recombination rate than other materials given in Table 2. The addition of S, Te and Se to As increases the charged defects.

However a full interpretation of the results given in Table 1 and 2, clearly needs a sufficiently detailed knowledge of the recombination mechanism which is not presently available.

Fig. 5 shows the FRPC response vs the applied voltage for IP and IQ outputs. As seen, both outputs are linear with different slopes under the blue illumination of 476.5 nm.

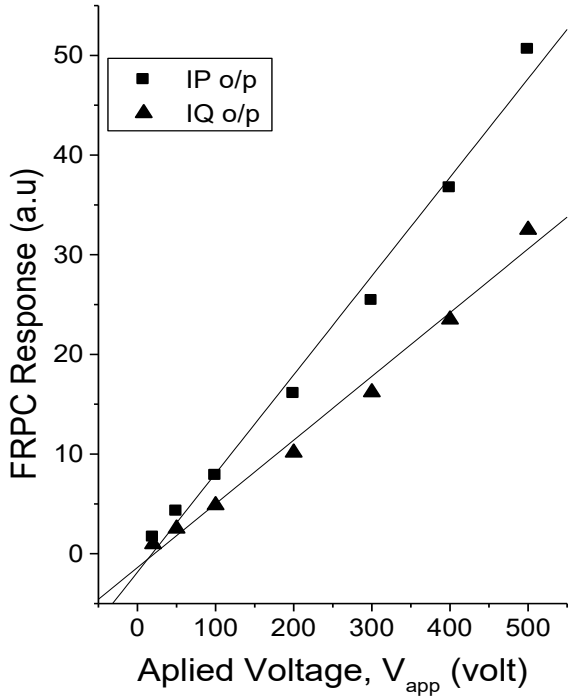

Fig. 5. Applied voltage dependence of IP- and IQ-FRPC response of a-As. f=10 Hz. Intensity:1052 μW from Ar laser (476.5 nm). T=290 K.

5. Conclusions

Amorphous semiconductors and in particular chalcogenide glasses are drawing a lot of attention due to manifold applications in different fields. To optimise these materials for possible applications it is essential to understand the carrier lifetime, recombination and transport mechanisms that operate in them. Measurement of photocurrent serves as an important tool to understand the recombination kinetics, which in turn gives information about the localized states present in amorphous semiconductors.

Recombination is influenced both by material properties and by external parameters, such as excitation light intensity, wavelength, temperature, applied field and modulation frequency. Especially the recombination lifetime is one of the critical parameters in the search for cost-competitive photovoltaic technologies. Each technology has specific materials issues with respect to the role of recombination lifetime in potential success of that technology. In a-As, a small single lifetime of 5 μs was determined for the excitation intensity between

78.5 μW and 2314 μW at room temperature. However, this lifetime is found to be independent of the excitation light intensity and the applied electric field.

We also measured the exponent ν in the power-law, $I_{ph} \propto G^{\nu}$. At room temperature the photocurrent is found to be sublinear in photon flux, with the exponent of 0.66-0.89 in the measured frequency and intensity ranges for a-As. The exponent, ν was also compared for different compounds of a-As, under the same experimental conditions. All ν values are found to be between 0.59 and 0.72, which indicate the presence of the continuous distribution of localized states in their band gaps.

The ν value of a-As was found to be a little excitation wavelength dependent. The dependence of ν can be related to the light absorption profiles of a-As.

However, IP and IQ outputs of the lock-in amplifier give a little different, but complicated results for ν. We think that this is due to instrumental effect.

Our presented results of the recombination lifetime and intensity dependence of photocurrent show that the recombination occurs through the trap states at room temperature. Therefore the relase rate from traps controls both the lifetime and photocurrent processes.

References

[1] Wu, Z., Xu, Y., Zhang, P., Qi, D., Ma, C., Li, W., J. Non-Cryst. Solids **527**, (2020) 119755.

[2] Sing, P. R. , Zulfequar, M., Kumar, A., Dwivedi, P. K., J. Non-Cryst. Solids **476**, (2017) 46.

[3] Shiryaev, V. S. , Churbanov, M. F., J. Non-Cryst. Solids **475**, (2017) 1.

[4] Brandova, D., Suoboda, R., Liska, M., Malek, J., J. Non-Cryst. Solids **475**, (2017) 121.

[5] Mehta, N., Journal of Scientific and Industrial Research **65**, (2006) 777.

[6] Al-Ghamdi, A. A., Vacuum **80**, (2006) 400.

[7] Saitar, M., Ledru, Hamou, A., Saffarani, G., Phys. B **245**, (1998) 256.

[8] de Neufville, J. P., Moss, S. C., Ovshinsky, S. R., J. Non-Cryst. Solids **13**, (1974) 191.

[9] Kaplan, R., Solar Energy **84**, (2010) 401.

[10] Maurugeon, S., Bureau, S. B., Faber, A., Zhang, X., Geliesen, W., Lucas, J., J. NoCryst. Solids **355**, (2009) 2074.

[11] Kaplan, R., Sol. Energy Mater. Sol. Cells **85**, (2005) 545.

[12] Shimakawa, K., Kolobov, A., Elliott, S. R., Adv. Phys, **44(6)**, (1995) 475.

[13] Iovu, M. S., Shutov, S. D., Popescu, M., J. Non-Cryst. Solids **299-302,** (2002) 924.

[14] Marshall, J. M., Owen, A. E., Philos. Mag. **24**, (1971) 1281.

[15] Depinna, S. P., Dunstan, D. J., Phil. Mag. B **50**, (1984) 579.

[16] Searle, T. M., Phil. Mag. Lett., **61**, (1990) 251.

[17] Main, C., Webb, D. P., Bruggemann, R., Reynolds, S., J. Non-Cryst. Solids **137-138**, (1991) 951.

[18] Wagner, D., Irsigler, P., Dunstan, D. J., J. Physics C: Solid State Physics **17**, (1984) 6793.

[19] Lourenco, M. A., Homewood, K. P., McLellan, R. D., J. Appl. Phys. **73(6)**, (1993) 2958.

[20] Lourenco, M. A., Homewood, K. P., Semicond. Sci. Technol. **8**, (1993) 1277.

[21] Rose, A., Concept in photoconductivity and Allied Problems, Krieger, 1978.

Effects of the Perpendicular Applied Magnetic Field and the Second Order Anisotropy on the Domain Structure in Ultrathin Films

Bengü KAPLAN

Prof. Dr., University of Mersin, Physics Division,
Department of Mathematics and Science Education, Çiftlikköy Campus,
33343 Mersin, Turkey. bkaplan@mersin.edu.tr
Orcid ID: 0000-0002-1334-6137

1. Introduction

Over the past several yearsRE-TM (Rare Earth-Transition Metals) thin films have been widely investigated due to their macroscopic physical properties such as remarkable structural, mechanical and thermal characteristics which originate from the intrinsic of the material. RE-TM alloys usually present perpendicular magnetic anisotropy and, when they are prepared in the form of thin films, they represent periodic magnetic domain above a certain critical thickness, with lateral dimensions in the range of a few hundred nanometers [1-4].Various methods were used to specify the first- and second-order anisotropy constants which successfully applied on intermetallic crystals[5] and magnetic thin films [6].

More recently, Alvarez-Prado et al.[7] have determined the anisotropy contributions in the second-order approximation in amorphous Nd-Co thin films by micromagnetic simulations so that these films exhibit stripe shaped periodic magnetic domains with local out-of-plane magnetization components due to their perpendicular magnetic anisotropy. They have observed that the first- and second-order anisotropy constants, K_1 and K_2 respectively, must be used to properly describe the variation of the stripe domains with the in-plane applied field. Their method presents that an accurate description of magnetic anisotropy in Nd-Co amorphous films needs including the second-order anisotropy constant,K_2, despite being one order of magnitude smaller than K_1. The second-order anisotropy K_2 plays a crucial role in the magnetic behaviour, resulting in magnetization of ultrathin magnetic films [8]. Theoretical models should regard especially by considering the role of finite-size walls [9].

It is of interest to study the magnetostatic solution for the total energy of the stripe pattern for well-separated walls with the perpendicular applied magnetic field,H, by considering anisotropies in the second-order approximation. In this work, we would like, however, to consider the magnetization processand also compare the results with experimental observations at low and room temperatures.

2. Calculations and discussion

In this work the film is taken as an infinite slab parallel to the $x-y$ plane with thickness L along the z coordinate. We presume a stripe configuration of walls which is the equilibrium configuration for the continuum model [10,11]. We take into account only the situation in which the domain walls are sufficiently widely separated for the interactions between walls to be neglected. The dipolar energy depends on the value of the perpendicular magnetization in

the film. The average perpendicular magnetization will vanish over the region of the wall and this effect causes strong changes in the dipolar energy. Since our theory is valid only for well- separated walls in which ω represents the domain wall width, we use the continuum model to calculate the dipolar energy throughout. The quantity ω is not constant and depends on film parameters, in particular, on the film thickness L, as well. Given a regular array of stripe pattern and assuming that the finite wall width,ω, is important when compared with the stripe period in which the exchange energy would be important. Within these assumptions, the total energy of the system is given by[12,13]:

$$U_t = \{U_d + U_e + U_{a1}\}sin^2\theta + U_{a2}sin^4\theta - (U_{a1} + U_{a2}) + U_o - U_z \quad (1)$$

where θ is the angle between magnetization and normal to the film plane. The first term of the curly brackets, which denotes the magnetostatic energy, is found by expanding the magnetic potential in a Fourier series and matching to the boundary conditions as explained in a previous work [13]. For wider domain walls the magnetostatic energy per unit area is given by:

$$U_d = (2\pi M_o^2 a_o)n_l\left[\left(1 - \frac{4\xi}{\pi^2}\right) - \frac{2}{\pi}\mathcal{N}(\xi)(ka_o)n_l\right] \quad (2)$$

where M_o is the saturation magnetization, a_o is the lattice spacing, n_l is the number of atomic layers, ξ is defined as ω/D , $k = 1/D$, $\mathcal{N}(\xi) = 2P + \ln(\frac{1}{\xi})$, and the value of P is obtained from the finite series [11] and is $P \cong 0.635$. The second term of the curly brackets in Eq. 1 is the exchange energy per unit area in the wall and is given by [10]

$$U_e = \frac{\pi^2}{2\xi}\frac{A}{a_o}(ka_o)^2 n_l \quad (3)$$

where $A = 2JS^2/a_o$, and $2JS^2$ is the interaction energy between the nearest neighbours. The third term of the curly brackets in Eq. 1 is the anisotropy energy per unit area in the wall which is written as [10,13]

$$U_{a1} = -\frac{K_s^1}{2}\left(1 - \frac{4\xi}{\pi^2}\right)n_l \quad (4)$$

where$K_s^1 = K_1 a_o$ represents the first-order anisotropy energy per unit of area.In Eq. 1, U_{a2} represents the second-order anisotropy energy per unit of area which is written as similar to Eq. 4 above in which K_s^2 indicates the second-order anisotropy energy per unit of area. In Eq. 1, U_o is anisotropy energy which is independent of the angle and is usually ignored. The last term in Eq. (1) correspons to the Zeeman energy. We first define a normalized energy, $E = \frac{U_t}{E_o}$where $E_o = 2\pi M_o^2 a_o$, and$n_l = \frac{L}{a_o}$,$R = \frac{A}{a_o E_o}$,$f_1 = \frac{K_s^1}{2E_o}$,$f_2 = \frac{K_s^2}{2E_o}$, $f_3 = f_1 + f_2$ and therefore the expression for E is given by

$$E = n_l \left[\left\{ (1 - f_1)\left(1 - \frac{4\xi}{\pi^2}\right) - \frac{2}{\pi}\mathcal{N}(\xi)(ka_o)n_l + \frac{\pi^2 R}{2\xi}(ka_o)^2 \right\} sin^2\theta - f_2\left(1 - \frac{4\xi}{\pi^2}\right) sin^4\theta + f_3\left(1 - \frac{4\xi}{\pi^2}\right) - h\, cos\theta \right] \quad (5)$$

Byminimizing of Eq. 5 with respect to(ka_o) and θ we obtain Eqs. 6 and 7 respectively in the following:

$$(ka_o) = \frac{2\xi\mathcal{N}(\xi)n_l}{\pi^3 R} \quad (6)$$

and

$$-\frac{h}{2} = \left[(1 - f_{eff})\left(1 - \frac{4\xi}{\pi^2}\right) - \frac{2\xi N^2(\xi) n_l^2}{\pi^4 R} \right] cos\theta + 2f_2\left(1 - \frac{4\xi}{\pi^2}\right) cos^3\theta \quad (7)$$

where $h = \frac{H}{2\pi M_o}$ and also $f_{eff} = f_1 + 2f_2$ [7] which is the effective uniaxial anisotropy constant. From Eq. 6 we can see that the actual values of D and ω depend on R, and therefore on the way of dealing with the exchange energy.

The surface anisotropy constants display different behaviours with film thickness, with the first-order presenting the usual inverse of ferromagnetic layer thickness. Besides this inverse of thickness behaviour, the second order also comes up with a constant value[14].

Alvarez-Prado et al.[7] experimentally showed that the amorphous Nd-Co thin films exhibit stripe shaped periodic magnetic domain with local out-of-

plane magnetization components due to their perpendicular magnetic anisotropy. They observed that the first and second anisotropy constans must be used to properly describe the variation of the stripe domains with the out- and in-plane applied magnetic field. Experimentally the stripe period is of the order of 180 nm at 300 K with a decreasing as a function of field obtain from the magnetic force microscope measurements. At low fields they reported that there is a small deviation between the calculated and experimental behaviour. One of the simulated magnetization components is parallel to the external field in which this component only takes significant values at the domain walls so that increases at high temperatures. The values they used are the following: $L = 100\,nm$, $M_S = 1.06 \times 10^6\,A/m$, $K_1 = 8.7 \times 10^5\,{}^{J}/_{m^3}$and $K_2 = 3.4 \times 10^5\,{}^{J}/_{m^3}$ at 10 K. They also used for the exchange stiffness constant $A = 0.7 \times 10^{-11}\,{}^{J}/_{m}$ which is typical of amorphous RE-TM alloys for all temperatures.

Further, inserting Eq. 6 into Eq. 5, we get the normalized minimum free energy which is given by

$$E_{min} = n_l\left[\left\{(1-f_1)\left(1-\frac{4\xi}{\pi^2}\right)-\frac{2\xi\mathcal{N}^2(\xi)n_l^2}{\pi^4 R}\right\}sin^2\theta - f_2\left(1-\frac{4\xi}{\pi^2}\right)sin^4\theta + f_3\left(1-\frac{4\xi}{\pi^2}\right) - h\,cos\theta\right] \quad (8)$$

It is easy to show that as ξ varies in the interval $10^{-1}-1$, f_2 attains its minimum value for $\xi = 1$, and then increases monotonically for decreasing ξ.

Figures 1(a) and (b) present the normalized minimum free energy of the stripe domain structure vs. R in units of E_o in films of the $100\,nm$, in which $f_1 = 0.96$, $f_2 = 0.38$at 300 K and also $f_1 = 0.62$, $f_2 = 0.24$ at 10 K respectively which are experimental data of Ref.[7].

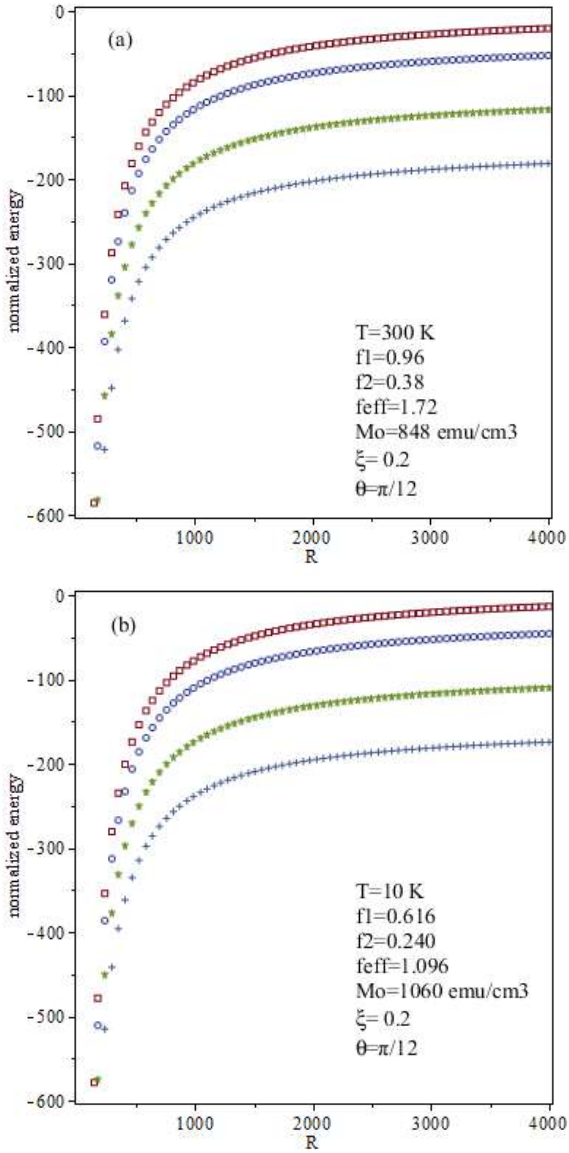

Fig. 1 The normalized minimum energy as a function of R for $L = 100\,nm$ at 300 K (a) and 10 K (b).

As can be seen from these figures, $R \cong 3400$ which is saturation point at $\xi = 0.2$ and $\theta = \pi/12$. Although it is not shown here, we have found the similar figures for different values of θ and ξ. We assume $0 \leq h \leq 0.5$ for the amorphous Nd-Co thin film[7].

Parts (a) and (b) in Figure 2 represent the $^{M}/_{M_o}$ vs. $^{H}/_{4\pi M_o}$ with the field applied perpendicular to the film. It can be seen that calculated magnetization curves are given for some values of ξ.

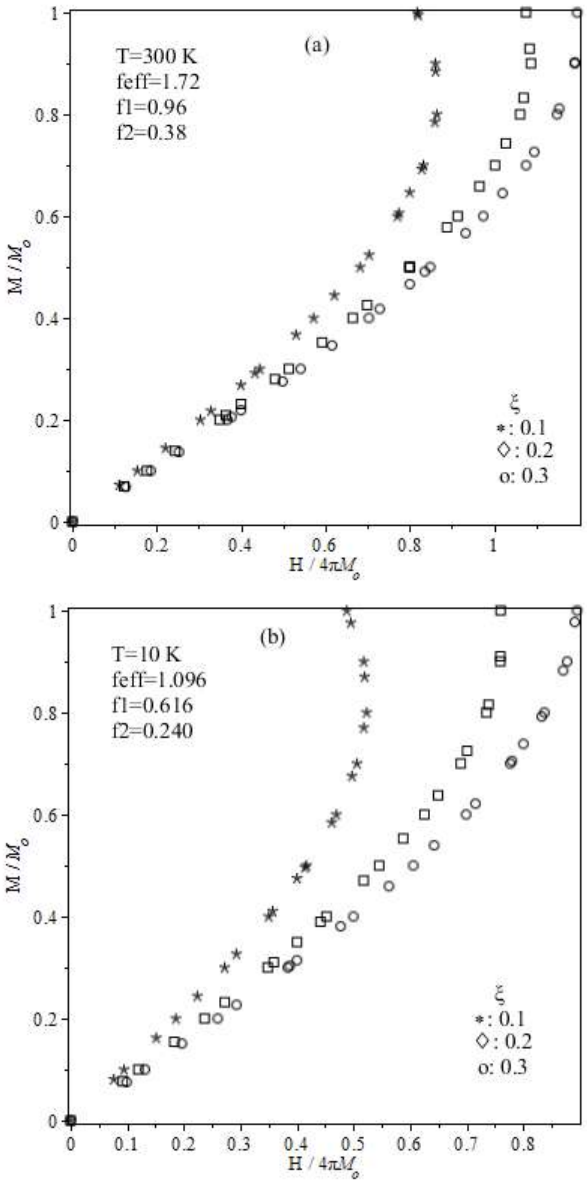

Fig. 2 Magnetization process for the stripe domain structure with several parameter of ξ at 300 K (a) and 10 K (b).

The magnetization curves are not straight line in general, as would be expected from classical continuum theory but show characteristic deviations. Saturation occurs in a field smaller than $4\pi M_o$, which is agreement with the Ref.[7]. For small ξ, the film can be magnetized easily, because the normalized saturation field is small. With increasing ξ, the normalized saturation field increases, corresponding to the fact that the energy difference between the saturation state and the demagnetized state becomes larger for the larger value of ξ. In the linear model, when ξ tends to 1, it corresponds to a vanishing domain but as the domain width varies very rapidly in this region, and thus the contribution of the walls to the total energy soon becomes very small.

In Figures 3(a,b) we quote the experimental data of Ref.[7], fitted Eqs. (6) and (7) to the experimental data.

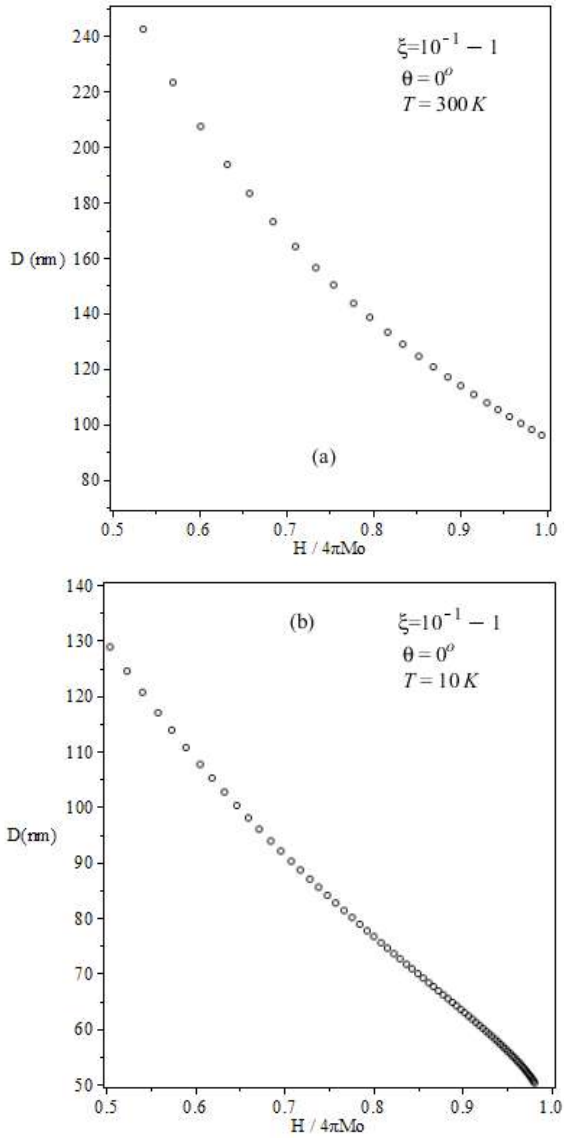

Fig. 3 Field dependent stripe domain period at 300 K (a) and 10 K (b).

This fitting was made by using the $\theta = 0^{\circ}$at low and room temperatures. Its variation with the applied magnetic field is displayed in Fig. 3(a) for 300 K. The value of D near remanence is of the order of 240 nm which is close to their simulation value[7]. As can be seen in Fig. 3(b), at low temperature, the value of D is near remanence is of the order of 130 nm which is smaller than the room temperature result. At low temperatures, the effective film anisotropy is larger than the magnetostatic energy indicating a strong perpendicular magnetic

anisotropic material but, as temperature increases, the material could have a transition to a weak perpendicular magnetic anisotropy regime. In particular, at 300 K, $f_{eff} = 1.72$ and, at 10 K, $f_{eff} = 1.09$. This anisotropy behaviour is characteristic of two magnetically coupled 3d-4f sublattices with competing anisotropies.

3. Conclusions

Asa conclusion, we determined the total energy of the magnetized film including the magnetostatic energy, anisotropy energies in the second-order approximation, and the exchange energy in perpendicular applied magnetic field by using a continuum model. It is found that the total energy depends on anisotropy constants, crystallographic orientation and film thickness. Also we have derived a good expression for the equilibrium width of the domain pattern.

The magnetization process due to the external perpendicular field was calculated numerically for the stripe domain structure under the assumption of the well-separeted walls. The numerical calculations indicated that the magnetization process hascharacteristic deviations. The domain size and also calculated magnetization curve were compared with the experimental data for amorphous Nd-Co thin films and good coincidence was obtained between both curves.

REFERENCES

1. Ge, Y., Heczko, O., Södenberg, O., Lindroos, V. K.,*J. Appl. Phys*. 96(2004) 2159.
2. Ge, Y., et al.*Mater. Sci. Eng*. A 436-440(2006) 961.
3. Ullakko, K., Huang, J. K., Kantner, C., Kokorin, V. V., O'Handly, R. C.,*Appl. Phys. Lett.*69(1996) 1966.
4. Chernenko, V. A., L'vov, V. A., Golub, V., Aseguinolaza, I. R., Barandiaran, J. M.,*Phys. Rev*. B84(2011) 054450.
5. Gerstein, G., et al.*Funct. Mater. Lett*. 10 (4)(2017) 1750044.
6. Rames, M., Heczko, O., Sozinov, A., Ullakko, K., Straka, L.,*Scripta Materialla*142(2018) 61.
7. Alvarez-Prado, L. M., et al. *J. Magn. Magn. Mat*er. 456(2018) 251.
8. Yang, G., et al. *Applied Surface Science*353(2015) 489.
9. Donzelli, O., Bassani, B., Spizzo, F., Palmeri, D.,*J. Magn. Magn. Mat*er. 320(2008)e261.
10. Yafet, Y. and Gyorgy, E. M.,*Phys. Rev*. B 38(1988) 9145.
11. Kaplan, B. and Gehring, G. A.,*J. Magn. Magn. Mater*. 128(1993) 111.
12. Nakagawa, S., et al.*Journal de Physique,* Colloque C8, Supplement au n^{o} 12, (1988) Tome 49.
13. Kaplan, B.,*J. Magn. Magn. Mater*. 288 (2005) 178.
14. Oliveira, A. B., et al. *J. Magn. Magn. Mater*. 469(2019) 64-68.

Prediction of Icing Risk Degree on Aircraft with Machine Learning Algorithms

Fatmanur ATEŞ [1] and Ramazan ŞENOL [2]

[1] Affiliation 1; fatmanurates@isparta.edu.tr
[2] Affiliation 2; ramazansenol@isparta.edu.tr
** Correspondence: fatmanurates@isparta.edu.tr;*

1. Introduction

Since prehistorical times, humans have invented for reasons such as facilitating their daily lives and ensuring their safety. However, inventions in history brought along some problems. The biggest problem that arose from the invention of aircraft were the fatal accidents caused by aircraft. Focusing on taking precautions by learning from bad experiences, human beings also try to eliminate or minimize fatal accidents caused by aircraft. One of the most important types of accidents that require precautions, which is the subject of fatal accidents in aviation almost every year, is icing. According to the Air Safety Institute, 388 accidents, which represent 12 percent of all aircraft accidents during 1990-2000, occurred due to ice. [1]. This figure shows the significance of ice-related accidents and indicates that it is something that should be paid attention to. Precautions have also been taken against ice-related accidents and are still being taken. Anti-Icing systems have been recommended to prevent ice formation, and de-icing systems have been recommended to eliminate current icing. These mechanistic, chemical, electrical, and energy rules are being used and developed today [2]. These systems are generally available in aircraft, but are usually left to pilot use. Pilots operate the anti-icing and de-icing systems when he or she detects the presence of icing. This can cause accidents due to the pilot's carelessness or inexperience. [3]. The fact that the anti-icing and de-icing systems are not completely under the control of the pilot, and that they are activated automatically is an important issue for the safe flight of the aircraft. Anti-icing and de-icing systems can be activated automatically, depending on the degree of icing risk in aircraft. When the icing risk level is 3, ice prevention and removal systems should be activated [14]. The degree of icing risk depends on different parameters, but among these parameters, parameters such as temperature and humidity are the most decisive.

With regard to icing on aircraft, there has been work by scientists from many fields. Palacios et. al. have introduced a non-thermal ultrasonic-based anti-icing system for rotor blades. They have studied the effects of ultrasonic waves on icing strength at different frequencies and amplitudes [4]. Aykanet. al. have tried to detect and control the icing on wings of the F16 fighter jet during a flight. They identified the aircraft’s icing model with the parameters known as stability variants and determined the icing after monitoring the changes in the Extended Kalman filter (EKF) innovation process of the aircraft’s dynamic characteristics [5]. Boduroğlu studied on a thermal anti-icing system applicable to the wings of a Boeing 737-800 aircraft. Thermal anti-icing systems operate by blowing hot air on wings which are exposed to icing. In the study, the heat required against icing was calculated using boundary layer equations, thereby

obtaining the hot air blowing capacity [6]. Fenar tried to predict the icing risk in his study using artificial neural networks. Initially, artificial neural networks were trained with ambient temperature, amount of water in the air, and freezing point, then the icing risk was estimated accordingly [3]. Johansen and Sorensen recommended an electro thermal-based autonomous icing protection system for drones. They have an electrothermal welding on the surface of the aircraft, a central control unit as well as an icing protection solution. The control unit is equipped with a built-in bundle of atmospheric sensors measuring ambient atmospheric conditions. When an icing risk arises, control algorithms check the energy supplied to electro-thermal sources for heat control [7]. Gliwaet. al. provided automatic control of anti-icing system for Diamod DA42 aircraft. They created their work by using Matlab's Fuzzy Logic Toolbox package. They took four parameters into consideration; weather temperature, cloud water content, temperature of the plane and rain. In the first stage, they determined the potential ice density in the aircraft and then automatically adjusted the anti-icing system [8]. In its study, Akbal used numerical calculations on the aircraft wing to calculate the ice thickness and determine the type of ice in the area where the maximum air velocity was seen. He calculated the time after which the accumulation of ice on the wings switched to the glassy ice and the thickness of the water layer on the surface during the transition to the glassy ice [9]. Akbal also developed a computer program using Fortran, Techplot, and GetGraphDigitizer software for glaciation simulation on wings, tail, and cylinder geometries to solve the icing problem [10]. Vertuccioet. get. designed a thermal anti-icing system to prevent icing on aircraft surfaces using flexible graphene film/paper. They used less power than other solutions to break the ice with the flexible heating paper they designed [11] while offering high mechanical properties. Li et. al, estimates maximum ice thickness, icing area, and icing risk rating using XGBoost supervised learning algorithm. In XGBoost model, the liquid water content, droplet diameter and exposure time were set as input parameters. They used precision, recall, F-score and confusion matrix in their icing risk rating estimation. Out of 521 data, 512 data was classified correctly, whereas 9 data was classified incorrectly. The accuracy, precision and F-score values were above 0.95 [12]. Shen et. al. combined the mass and temperature transfer model of anti-icing surface with the shell temperature equations to simulate aircraft thermal anti-icing systems and to decode the combined heat transfer of air droplet flow and solid surface. The method, which has been developed based on the heat flow, can directly decode the thermodynamic model of the back-flow water, while temperature-based

methods have been shown to have reached the solution at a higher calculation rate [13].

In the study, icing risk degree estimation was made using data consisting of temperature, humidity, rain and aircraft temperature input parameters. For icing risk estimation, k nearest neighbor algorithm (KNN), support vector machines (SVM), random forest algorithm (RF), bagging algorithm, augmentation algorithm and decision trees (DT) were applied. In addition, an artificial neural network model was created and training was provided in this model. In order to increase the model performances, hyper parameter tuning was done manually for the models. Results are given with accuracy, precision, sensitivity, and f-score. Among the applied artificial intelligence models, the model that gives the most optimum result has been proposed. The proposed model is modeled using Simulink/Waijungblockchain and embedded in STM32F4 Discovery board. Outputs are observed with the help of a led.

2. Materials and Methods

2.1. Icing on Aircrafts

Icing in aircraft is a major risk related to flight safety caused by atmospheric conditions that depend on meteorological conditions. Ice in aircraft can occur while the aircraft is on the land or in the air [14]. Icing density in aircraft is divided into different categories. The objective is to define and report on the icing. To determine the severity of the icing, the US Federal Aviation Company has identified four main categories, namely trace, light, moderate and severe. These categories and their descriptions are given in Table 1 [14, 15].

Table 1 Identification of icing risk levels [15]

Category	Description
Trace	This is the degree of icing that is noticeable, although difficult to see. Appears as a white line. De-icing and anti-icing equipment is not required unless the icing condition lasts more than one hour.
Light	If aircraft icing continues for more than 1 (one) hour, the white-line ice forming at the front edge of the wings starts to expand and the aircraft's performance is affected. Therefore, the icing protection system needs to be operated.
Moderate	Even a short-term icing period is very dangerous. With the anti-icing system or icing-protection system, the icing must be prevented or removed from the aircraft. It may be necessary to stop ice, change altitude and change direction in the moderate-level icing.
Severe	At this stage, the aircraft should return to safe airspace conditions as soon as possible. The aircraft needs to change altitude or direction. Because even if the ice-protection or anti-icing equipment is activated, the icing is unstoppable, and the effect of the icing is not diminished.

If the pilot is late to operate the de-icing and anti-icing system, as illustrated by table 1, the aircraft may be losing control and causing an accident. If the icing occurs when the aircraft is on the ground and the aircraft takes off, a possible accident may be inevitable. On December 27, 1991, icing on the wings of Flight 751 for Scandinavian Airlines have not been detected, and shortly after taking off the plane crashed [9], which can be regarded as a concrete example. To avoid the pilot-induced errors, Systems are being developed to determine whether or not there is icing in the aircraft and detect its degree.

2.2. Artificial Intelligence (AI)

Artificial intelligence has arisen through an effort to put uniquely human qualities into machines that support computers or computers. In artificial intelligence, the goal is to artificially transfer the behavior of assets to machines. Machine learning is a subset of artificial intelligence. Machine learning is the application for parsing, learning, and forecasting data using algorithms [16]. In the literature, machine learning strategies are studied under three key topics: supervised learning, unsupervised learning and reinforcement learning. In the supervised learning model, the model is trained by providing input data and output data. On the other hand, in unsupervised learning, the output data is not given to the network, thus learning is possible according to the relationship between entries. Reinforcement learning uses a benchmark that evaluates and compares the obtained output with the input. [17] The study uses RF, KNN, DT, SVM, bagging, boosting and ANN. The machine learning methods used in the study are explained below.

2.2.1. K-Nearest Neighbor Algorithm: The KNN algorithm was first applied in the 1950s. It is a supervised algorithm that can be used for both classification and regression. In other words, a newly added data to the network whose class is unknown, is first compared with other data in the training set and a distance measurement is made, then the most optimal class is found for the data that has not yet been assigned to a class according to the calculated distance, and the data is included in that class. The most important point in KNN is to find the appropriate k value, which gives the number of neighbors [18]. Different methods are used in distance calculations to find the nearest neighbor. The most commonly used distance measure is Euclidean. Apart from the Euclidean distance, different distance calculation criteria such as Manhattan, Minkowski, Chebyshev are also available in the literature [18].

2.2.2. Artificial Neural Networks: Artificial neural networks are machine learning methods inspired by the behavior of neurons in the brain and central nervous system. In neural networks, the input data is fed to the network with

one or more hidden layers with weights. The output of the layers is decided by operations with weight and bias values. The learning rate used in the model allows the weight and bias values to be adjusted [19]. Artificial neural networks have different types of uses such as DNN (Deep Neural Network), RNN (Recurrent Neural Network), MLP (Multiple Layer Perceptron) [20].

2.2.3. Support Vector Machines: Support vector machine (SVM) is one of the artificial intelligence algorithms frequently used in classification processes. It was developed by Vladimir Vapnik and Alexey Chervonenkis at the end of the 1960s [21]. It is used to classify linear and nonlinear data sets. It includes different methods according to whether the data is linearly separated or not. If the data can be fully parsed linearly, the hyperplane is used to determine the data classes, if the data cannot be linearly decomposed, kernel functions are used [22].

2.2.4. Decision Trees: Another method frequently used in classification and regression processes is decision trees. Decision trees are formed in the form of a tree structure. It can work with categorical and numerical data and its rules can be expressed simply [23]. Decision trees consist of roots, nodes, and leaves. The stem cell forms the first cell of the decision trees. Observations are classified according to the root "yes" or "no" condition. Then there are nodes under the stem cells. Observations are classified with the help of nodes. At the bottom of the decision tree algorithm are leaves. Leaves give the classification result. There are different types such as ID3, C4.5, CART.

2.2.5. Random Forest Algorithm: It is one of the classification and regression algorithms that contains many decision trees in a random forest. It is a model introduced by Breiman in 2001 [24, 25]. In the random forest algorithm, subsets are randomly selected from the data set and trained. Decision trees are created for training subsets. Decision trees make predictions based on data sets, and the average of the predictions is effective in classifying the problem. For this reason, random forest usually gives more accurate results than a single decision tree [25].

2.2.6. Bagging Algorithm:It was proposed by Breinman in 1996. The working logic is to work with smaller datasets produced by dividing the training data into subsets. Here, different combinations of training data are generated and multiple instances are created. Working with different training sets in this algorithm provides successful results [26].

2.2.7. Boosting Algorithm: The boosting algorithm is an ensemble classifier algorithm that works with the logic of obtaining strong classifiers from weak classifiers. The community of weak classifiers is combined using the majority vote method [27].

2.3. Performance Evaluation Metrics

Performance evaluation metrics are used in evaluating trained models. Performance evaluation metrics allow models to be compared to their evaluation result. Generally, it is achieved by using the error matrix that is created for binary classification. Error matrix given on Table 2 [28]. In Table 2, True Positive (TP) represents data that is correctly tagged for the positive class. True Negative (TN) represents the correctly tagged data for the negative class. False Positive (FP) represents mistagged data from the negative class, and False Negative (FN) represents data that is mistagged from the positive class.

Table 2. Error matrix consisting of binary class [28]

		Prediction Class	
		Positive	**Negative**
Actual Class	Positive	True Positive (TP)	False Negative (FN)
	Negative	False Positive (FP)	True Negative (TN)

Evaluation metrics used to evaluate classification performance are given in Table 3. [28].

Table 3. Performance evaluate metrics

Performance Evaluation Metric	**Formula**	**Definition**
Accuracy	$\frac{\boldsymbol{TP} + \mathrm{T}\boldsymbol{N}}{\boldsymbol{TP} + \mathrm{F}\boldsymbol{P} + \mathrm{T}\boldsymbol{N} + \mathrm{F}\boldsymbol{N}}$	It is the ratio of correctly classified data belonging to positive and negative classes to all data.
Recall	$\frac{\boldsymbol{TP}}{\boldsymbol{TP} + \mathrm{F}\boldsymbol{N}}$	It is the ratio of correctly classified data belonging to the positive class to all the data belonging to the positive class.
Precision	$\frac{\boldsymbol{TP}}{\boldsymbol{TP} + \mathrm{F}\boldsymbol{P}}$	It is the ratio of correctly classified data belonging to the positive class to all positively labeled data.
F-Score	$\frac{\mathbf{2} * \mathrm{Recall} * \mathrm{Precision}}{\mathrm{Recall} + \mathrm{Precision}}$	The sensitivity and precision of performance evaluation criteria is the harmonic mean.

2.4. Dataset

The degree of icing data set was based on the works in literature and the experimental data used by Gliwaetet al. for aerospace students from the Polish Air Force. The data set consists of four inputs and one outputs. Temperature and humidity are the most important parameters that affect icing. The degree of icing has been estimated by taking into account temperature, humidity, aircraft temperature and precipitation. The data set contains 3,025 pieces of data. For the four input values, the output is created as "no icing (0)", "trace(1)", "moderate(2)" and "severe (3)". Therefore, icing risk rating is estimated based on four degree [8]. The data set was given to the created architectures using 10-fold cross validation. Thus, it was ensured that the entire data set was used as training and test data. An example part of the dataset is given in Table 4.

Table 4. Sample part of the data set

Input Parameters				**Output Parameters**
Precipitation(mm)	**Aircraft Temperature (C°)**	**Humidity (gr/m³)**	**Temperature (C°)**	**Icing Risk Degree**
-0,2	-29	-0,8	-55	0
-0,5	-28	-0,1	0	0
-0,8	-25	0,4	-50	2
-0,8	-15	0	20	1
-0,8	-30	0,5	-15	2
-0,1	-17	-0,5	-40	0
-0,5	-11	-0,2	-15	2
-0,2	-18	4,5	-2	3
-0,1	-25	5	15	1
-0,2	0	1,3	-2	3
1	48	1,1	-18	2
1,2	10	4	4	3
.	.	.	.	.
.	.	.	.	.
.	.	.	.	.
2,5	-23	0,9	-5	3
2,5	5	0	-55	2
2,5	2	4,8	-55	2
3,3	-14	1,3	10	1

2.5. Waijung Blokset

The Waijung block set is a toolbox working under Simulink developed by Taiwanese company Aimagin. It is possible to develop Simulink based applications using Waijung block sets. The block set can be downloaded

directly from the web page "WaijungBockset" [29]. It is preferred for programming because of the simplicity of the block set and its application development capacity[30].

2.6. Method

In the study, Gliwa et al. Firstly, data preprocessing was performed on the dataset obtained based on the literature. Seven different machine learning models were established and trained by performing 10-fold cross validation on the dataset. Certain hyperparameters in each machine learning model are optimized by manual tuning. The hyperparameters that give the most optimum results for the models were found. All results are evaluated and the model that gives the optimum result is proposed for icing risk degree estimation. The results were evaluated using the performance evaluation metrics accuracy, precision, sensitivity and f-score. The model that gave the optimum result for the study was modeled in Simulink and the simulation results were observed. Then it was embedded in the STM32F4 discovery control card using waijungblocksets. RGB LED is used to observe different outputs from the control card by giving different input values. The flow chart for the method followed in the study is given in figure 1.

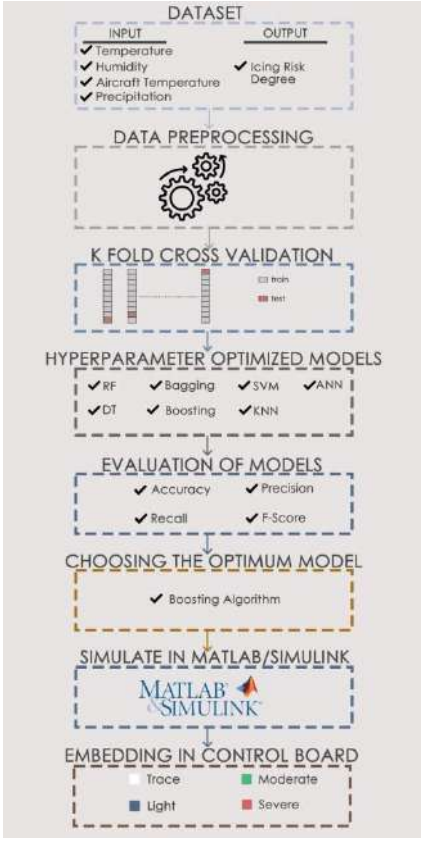

Fig 1. Workflow

3. Results

3.1. Application Results of AI Methods

Ten-fold cross validation was used in the artificial intelligence models applied in the study. In this section, the results of artificial intelligence algorithms applied to the data set are given.

3.1.1. ANN Application Results

In the study, feedback artificial neural network, which is one of the artificial neural network types, was used. The performance of the model has been optimized by changing the number of layers and the number of neurons. The optimum classification accuracy of the model was obtained when the number of layers was 1 and the number of neurons was 25. The values for the model's confusion matrix are given in Table 5. When Table 5 was examined, a total of 1923 data were classified correctly, while 1102 data were classified incorrectly.

Table 5. Artificial neural networks confusion matrix

Confisuon Matrix				
Actual / Predict	**No Icing**	**Light**	**Moderate**	**Severe**
No Icing	662	157	102	3
Light	183	402	141	10
Moderate	77	86	360	149
Severe	5	17	172	499

3.1.2. KNN Application Results

For KNN algorithm, an artificial intelligence method used to classify data set, a model was trained for different k neighboring values, and the optimum classification accuracy was obtained by selecting a k value of 14. Euclid distance was used for the distance calculations of K neighbors. Fig.2 shows the accuracy given by the model with different k values.

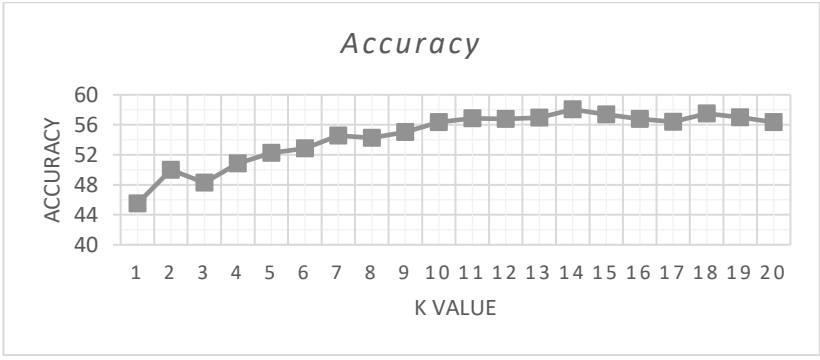

Fig. 2. Accuracy results for different k values

Selecting K value 14 trained the model and the confusion matrix is given in table 6. When Table 6 is examined, a total of 1,754 data are classified correctly and 1,271 data is classified incorrectly.

Table 6. KNN confusion matrix

Confusion Matrix				
Actual / Predict	**No Icing**	**Light**	**Moderate**	**Severe**
No Icing	532	207	167	18
Light	170	344	164	58
Moderate	71	90	416	95
Severe	21	35	173	464

3.1.3. SVM Application Results

Support vector machines have been trained on data sets using different core functions, and optimum classification accuracy is achieved when using radial basis kernel function. Figure 3 shows the change in accuracy of the model based on the kernel functions.

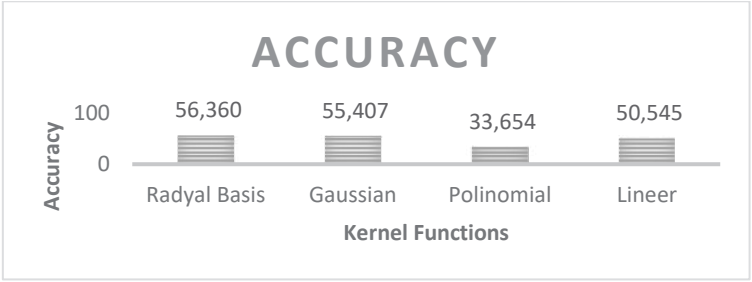

Fig. 3. The accuracy of the model using different kernel functions

The accuracy model obtained when using radial basis kernel function is given in Table 7. When Table 7 was examined, the model classified 1,705 data correctly and 1,320 data incorrectly.

Table 7. SVM confusion matrix

Confusion Matrix				
Actual / Predict	**No Icing**	**Light**	**Moderate**	**Severe**
No Icing	570	176	162	16
Light	209	303	183	41
Moderate	66	97	397	112
Severe	27	23	208	435

3.1.4. Decision Tree Application Results

CART algorithm, one of the decision tree methods, was used in the study. The accuracy matrix of the decision tree algorithm applied to the data set is given in Table 8. The algorithm 2315 classified data correctly, but 710 data incorrectly.

Table 8. Decision trees confusion matrix

Confusion Matrix				
Actual / Predict	**No Icing**	**Light**	**Moderate**	**Severe**
No Icing	774	141	6	3
Light	131	494	106	5
Moderate	33	59	507	73
Severe	8	5	140	540

3.1.5. Random Forest Algorithm Application Results

The random forest algorithm was applied by changing the number of decision trees it contains. The model was trained continuously by using the number of decision trees 10,50,100,150,200 and some values in between. Optimum classification accuracy was obtained when the number of decision trees was 19. Figure 4 shows a visual of the model's accuracy change in the number of different decision trees.

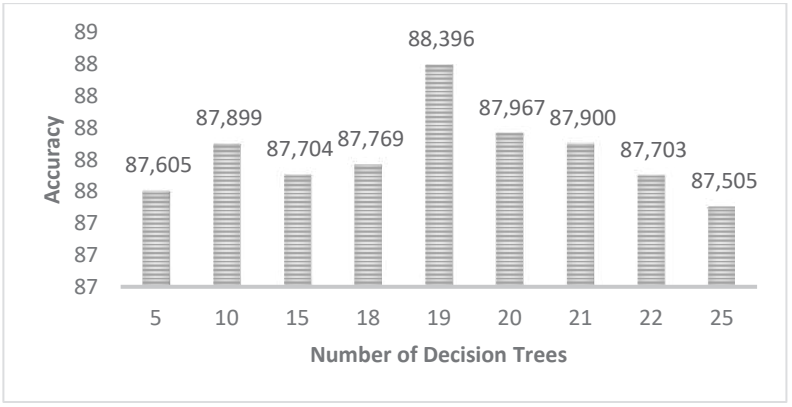

Fig. 4. Accuracy change of the model at different number of decision trees

The confusion matrix of the trained model is given when 19 decision trees are selected in Table 9. Accordingly, a total of 2,674 data were classified as correct and 351 data were classified as incorrect.

Table 9. Random forest confusion matrix

Confusion Matrix				
Actual / Predict	**No Icing**	**Light**	**Moderate**	**Severe**
No Icing	853	60	10	1
Light	87	619	26	4
Moderate	23	49	568	32
Severe	2	7	50	634

3.1.6. Bagging and Boosting Algorithm Application Results

The confusion matrix for the bagging algorithm applied to the data set is given in Table 10, and the confusion matrix for the boosting algorithm is given in Table 11. Adaboost, one of the increment algorithm types, was used.

Table 10. Bagging algorithm application results

Confusion Matrix				
Actual / Predict	**No Icing**	**Light**	**Moderate**	**Severe**
No Icing	835	84	4	1
Light	178	483	70	5
Moderate	37	47	519	69
Severe	7	6	92	588

Table 11. Boosting algorithm application results

Confusion Matrix				
Actual / Predict	**No Icing**	**Light**	**Moderate**	**Severe**
No Icing	847	66	9	2
Light	72	629	30	5
Moderate	27	50	567	28
Severe	3	8	45	637

3.2. Determination of the Optimum Classification Method

Seven different artificial intelligence algorithms have been applied to the data set. Algorithms are evaluated with performance evaluation metrics, and results are given in Table 12.

Table 12. Evaluation of classification methods with performance evaluation metrics

Artificial Intelligence Algorithm / Performance Evaluation Metric	ANN	KNN	SVM	Decision Tree	Random Forest	Bagging	Boosting
Recall	0.6352	0.5904	0.5744	0.7656	0.8849	0.8034	**0.8867**
Precision	0.6296	0.5829	0.5618	0.7606	0.8811	0.7952	**0.8836**
Accuracy	0.6357	0.5805	0.5636	0.7653	0.8840	0.8017	**0.8859**
F score	0.6324	0.5867	0.5680	0.7631	0.8830	0.7993	**0.8851**

The best way to classify the data set is to be called the boosting algorithm from ensemble methods by Table 11. The sensitivity for the boosting algorithm from ensemble models was found at 88.67%, while precision is 88.36%, accuracy is 88.59%, and F score is 88.51%.

3.3. Analyzing Optimum Classification Method in Simulink

For the optimum AI algorithm embedded in the simulation, the input values are randomly determined by using Repeating Sequence Stair. In Simulink diagram shown in figure 5, sample time was selected at 0.1.

The random temperature values for input repeatedly during the simulation period have been set to [3 -2 1 0 -20 -15 4 2 1 -1 -3 -15 20 30 -57 -45 25 27 20]. Besides, random humidity values are [-1 4 0.1 0.5 -0.1 3 0.8 1 -0.7 0 0.1 0.4 0.7 -0.1 -0.2 4 2 -0.3 2 3]. Random precipitation values are [3 -1 1 0 -0.2 -0.3 -0.4 2 1 1 3 -0.5 -0.2 -0.3 1 0 0.1 2 3 1 0 3 2] and random aircraft temperature values are [54 -20 10 2 -5 -15 4 2 -11 1 -3 40 -15 20 30 -25 -20 -27 55]. Simulation time is 10 seconds.

The codes written in the MATLAB workspace were summoned from Simulink using a function block and embedded in the STM32F4 board with the help of the waijungblokset. The codes written in the MATLAB workspace were summoned from Simulink using a function block and embedded in the STM32F4 board with the help of the waijungblokset.

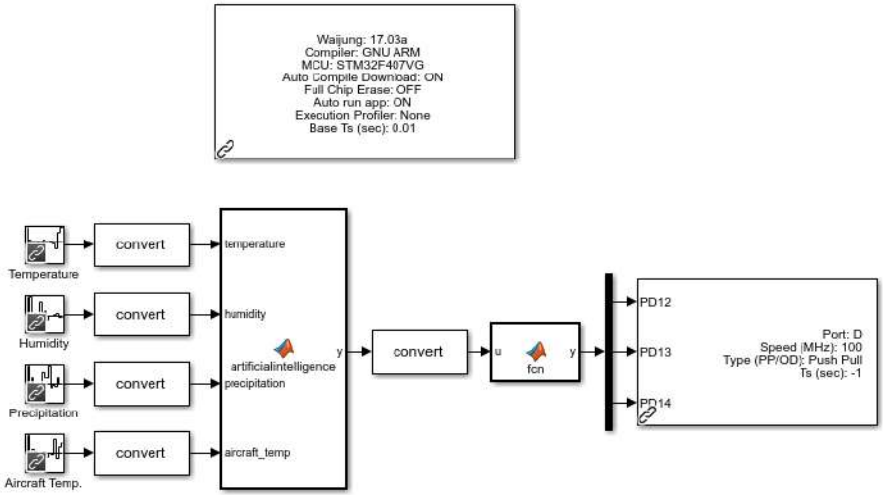

Fig. 5. Embedding the optimum classification method into the STM32F board

With an RGB led, it is possible to see the icing risk ratings generated by signals applied to random input as 0 (no icing) with no light, icing risk rating 1 (light) with blue light, icing risk 2 (moderate) with green light and icing risk 3 (severe) with red light. It can be seen in Figure 6, Figure 7 shows icing risk ratings graphs in the output, depending on the input parameters.

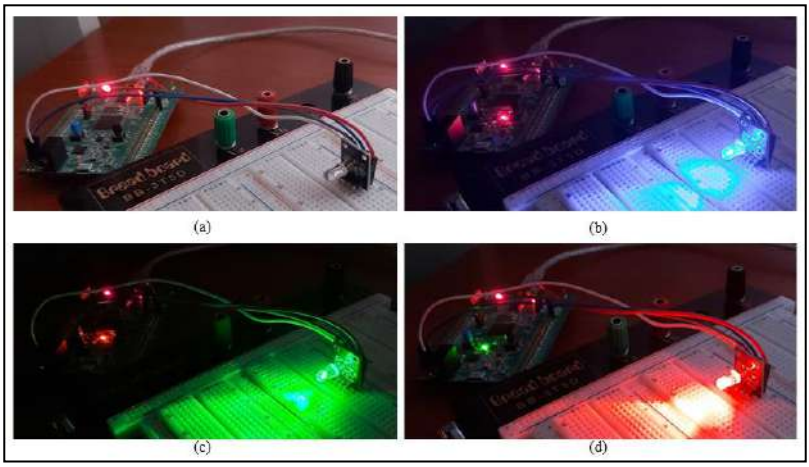

Fig. 6. Icing risk levels observed with the help of RGB LED (a) Trace (b) Light (c) Moderate (d) Severe

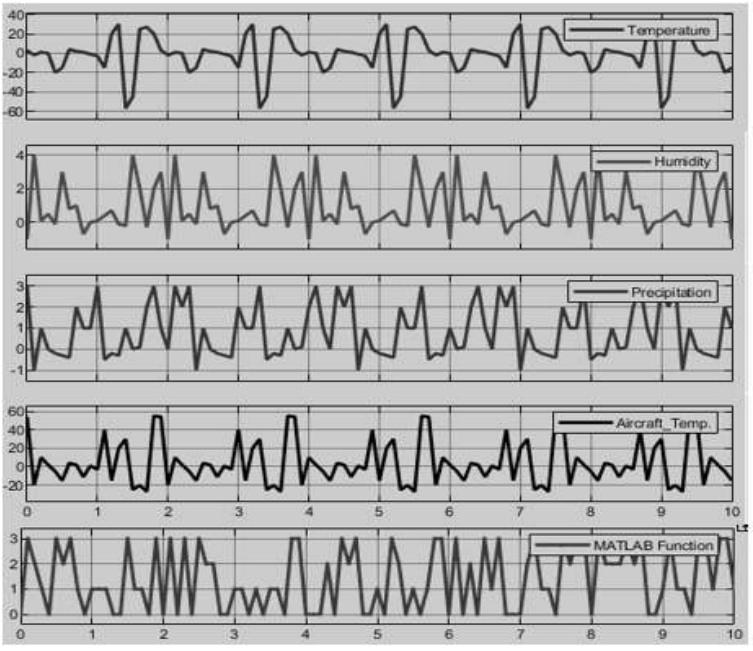

Fig. 7. Input and output graphs by random inputs

4. Conclusions

Icing on aircraft is one of the most important causes of accidents in aviation today. In this study, it was tried to determine the degree of icing risk based on data such as temperature, humidity, precipitation and aircraft temperature taken from a sample aircraft. An alternative method has been proposed for the studies on determining the degree of icing risk. There are different studies with a different number of parameters for determining the degree of icing risk, but in this study, the most important parameters affecting the icing risk degree and the number of parameters have been estimated by keeping the number of parameters high, and the performance of seven different artificial intelligence methods on determining the risk degree has been tested, and the most optimal method has been proposed for the problem. Thus, it is aimed to work with a minimum parameter number error in determining the degree of risk. Because many parameters are effective in the formation of the icing risk level, but some of them do not affect the change of the risk level too much. Estimating with parameters that are very influential on the degree of icing risk brings closer the real result. In the study, an interim study was carried out to automatically decide on the activation of the anti-icing and de-icing systems. Depending on the value of the icing risk level, de-icing and anti-icing systems can be activated automatically, and errors caused by the pilot can be prevented. In the study, not only did it give alternative results to the methods applied in the literature, but it was embedded in the STM32F4 discovery card in order to be applied on a real system. Accordingly, the icing risk degree can be estimated according to the input data, and anti-icing systems can be activated and deactivated. In the study, the highest performance classification was performed with the augmentation algorithm, one of the ensemble learning algorithms. The sensitivity of the augmentation algorithm was 88.67%, the precision was 88.36%, the accuracy was 88.59%, and the F score was 88.51%. The trained parameters of the augmentation algorithm are saved and called in order to be used for estimation in new input data that can be entered from the simulink via the function block in the simulink. By giving random inputs from the simulink, the icing risk degree estimation was made with the augmentation algorithm, which has the best performance in classification, and the results are shown with graphics. The model simulated in Simulink is embedded in the STM32F4 discovery card with the help of the blocks in the waijungblokset library. Since icing prediction is not yet implemented on a real or prototype aircraft, the accuracy of the output has been observed with the help of RGB LEDs connected to the control card output. At the end of the study, the system that predicts the degree of icing risk, which can actually be applied as a solution to the problem, is designed, simulated and

embedded in the control card in an operational manner. By estimating the degree of icing risk, anti-icing and anti-icing systems can be activated and icing accidents caused by the pilot can be prevented. In the next phase of the study, it is aimed to obtain data from a prototype aircraft and to estimate the degree of icing risk and to observe and examine the commissioning and de-icing of anti-icing systems. In addition, it is aimed to develop and test new methods that can increase the accuracy for icing risk degree and icing density estimation.

References

1. AOPA Air Safety Foundation, Aircraft Icing, AOPA Epilot, 2008.
2. Ünlü, D. &Hilmioğlu, N. (2017). UçaklardaBuzlanmaveBuzlanmayıÖnleyecekYöntemler. SürdürülebilirHavacılıkAraştırmalarıDergisi, 2(2), 75-80. Doi: https://doi.org/10.23890/SUHAD.2017.0204
3. Fenar, S. (2016). UçaklardaUçuşEsnasındaMeydanaGelebilecekBuzlanma Risk Derecesinin YSA KullanılarakTahminEdilmesi. (YüksekLisansTezi, ErciyesÜniversitesi Fen BilimleriEnstitüsü)
4. Palacios, J.L., Smith, E. C., Gao, H., & Rose, J.L., (2006). Ultrasonic shear wave anti-icing system for helicopter rotor blades. In Annual Forum Proceedings-American Helicopter Society (p. 1492). Amerıcan Helıcopter Socıety, Inc
5. Aykan, R., Hacıyev, Ç.,&Çalışkan, F. (2011). EKF veyapaysinirağlarıileuçakkanatbuzlanmalarınıntespitiveyenidenşekillendirilebilirkontrol. İTÜDERGİSİ/d, 5(2), 122-132.
6. Boduroğlu, K. (2014, Haziran). UçaklardaAerodinamikYapısalveSistemselProblemlereYolAçanDonmaProblemininİrdelenmesi (YüksekLisansTezi, YıldızTeknikÜniversitesi, Fen BilimleriEnstitüsü)
7. Johansen, T. A., Sorensen, K.L. (2017). Flight test results for autonomous icing protection solution for small unmanned aircraft. In 2017 International Conference on Unmanned Aircraft Systems (ICUAS). June 13-16, Miami, 971-980. Doi: https://doi.org/10.1109/ICUAS.2017.7991301
8. Gliwa, W., Grzesik, N., &Kuźma, K. (2018). Fuzzy logic controller design for the anti-icing system in the DA42 diamond aircraft. In AIP Conference Proceedings (p. 020017). AIP Publishing LLC. Doi: https://doi.org/10.1063/1.5066479
9. Akbal, Ö. (2019). UçaklardaBuzlanmanınNümerikOlarakİncelenmesiveUçuşProfiliBoyuncaHavaTahminModeliUygulaması. (YüksekLisansTezi, İstanbul TeknikÜniversitesi Fen BilimleriEnstitüsü)
10. Dökme, R. (2019). KanatProfiliÜzerindeOluşanBuzunİkiBoyuttaMatematikselModellenmesiveSayısalÇözümü (YüksekLisansTezi, İstanbul TeknikÜniversitesi, Fen BilimleriEnstitüsü)

11. Vertuccio, L., De Santis, F., Pantani, R., Lafdi, K. & Guadagno, L. (2019). Effective de-icing skin using graphene-based flexible heater. Composites Part B: Engineering, 162, 600-610. Doi: https://doi.org/10.1016/j.compositesb.2019.01.045
12. Li, S., Qin, J., He, M., & Paoli, R. (2020). Fast Evaluation of Aircraft Icing Severity Using Machine Learning Based on XGBoost. Aerospace, 7(4), 36. Doi: https://doi.org/10.3390/aerospace7040036
13. Shen, X., Guo, Q., Lin, G., Zeng, Y. & Hu, Z. (2020). Study on Loose-coupling Methods for Aircraft Thermal Anti-Icing System. Energies, 13(6), 1463. Doi: https://doi.org/10.3390/en13061463.
14. Çoban, R. (2018). HavacılıkSektöründeBuzlanmaRiskiÜzerineBirUçakKazasıAraştırması. HavacılıkEmniyetiYönetimiSistemiSempozyumu Ankara-Türkiye, 261-287.
15. Cao, Y., Tan, W. & Wu, Z. (2018). Aircraft icing: An ongoing threat to aviation safety. Aerospace science and technology, 75, 353-385. Doi: https://doi.org/10.1016/j.ast.2017.12.028
16. AYLAK, B. L., Okan, O. R. A. L., & YAZICI, K. (2021). YapayZekaveMakineÖğrenmesiTekniklerininLojistikSektöründeKullanımı. El-Cezeri Journal of Science and Engineering, 8(1), 74-93.
17. Atalay, M., &Çelik, E. (2017). Büyükverianalizindeyapayzekâvemakineöğrenmesiuygulamalari-artificial intelligence and machine learning applications in big data analysis. Mehmet AkifErsoyÜniversitesiSosyalBilimlerEnstitüsüDergisi, 9(22), 155-172.
18. Dilki, G. &Başar, Ö.D. (2020). İşletmelerinİflas Tahmininde K-En Yakın KomşuAlgoritmasıÜzerindenUzaklıkÖlçütlerininKarşılaştırılması. İstanbul TicaretÜniversitesi Fen BilimleriDergisi, 19(38), 224-233.
19. Shenfield, A., Day, D., &Ayesh, A. (2018). Intelligent intrusion detection systems using artificial neural networks. Ict Express, 4(2), 95-99.
20. Tang, J., Yuan, F., Shen, X., Wang, Z., Rao, M., He, Y., ...& Wu, H. (2019). Bridging biological and artificial neural networks with emerging neuromorphic devices: fundamentals, progress, and challenges. Advanced Materials, 31(49), 1902761.
21. Coşkun, H. (2016). Ekstrasistolkalpseslerinindestekvektörmakineleriylesınıflandırılmasınayönelik android uygulamasıgeliştirilmesi. (YüksekLisansTezi, SüleymanDemirelÜniversitesi Fen BilimleriEnstitüsü)

22. Metlek, S. &Kayaalp, K. (2020). Makineöğrenmesinde, teoridenörnekmatlabuygulamalarınakadardestekvektörmakineleri. İksad Publishing House, Ankara.
23. Akalın, F. (2020). İnceBağırsakGörüntüleriÜzerindeSezgiselAlgoritmaTeknikleriilePolipTeşhisi. (YüksekLisansTezi, SakaryaÜniversitesi Fen BilimleriEnstitüsü)
24. Breiman, L. (2001). Random Forests. Machine Learning, 45(1), 5-32. Doi: https://doi.org/10.1023/A:1010933404324
25. Speiser, J.L., Miller, M.E., Tooze, J. & Ip, E. (2019). A comparison of random forest variable selection methods for classification prediction modeling. Expert systems with applications, 134, 93-101. Doi: https://doi.org/10.1016/j.eswa.2019.05.028
26. Güzel, S. (2018). Veri Madenciliğinde Sınıflandırma Algoritmaları Kullanılarak Hepatit Hastalığının Tespiti. (Yüksek Lisans Tezi, Kahramanmaraş Sütçü İmam Üniversitesi Fen Bilimleri Enstitüsü)
27. Kıvrak, M. (2021). Sınıflandırma Problemlerinde Topluluk Öğrenme Yöntemlerinin İncelenmesi ve Küçük Hücreli Dışı Akciğer Kanseri Verileri Üzerine Bir Uygulaması. (Doktora Tezi, İnönü Üniversitesi Sağlık Bilimleri Enstitüsü)
28. Yavanoğlu, Ö. (2017). Stilistik Özellikler Kullanılarak Yazar Tanıma İşinde Yapay Sinir Ağlarının Başarımının Değerlendirilmesi: Türkçe Köşe Yazıları. (Yüksek Lisans Tezi, Hacettepe Üniversitesi Fen Bilimleri Enstitüsü)
29. WaijungBlokset, "https://waijung1.aimagin.com/" (Son Erişim: 08.07.2021)
30. Kizir, S., Yaren, T., Kelekçi, E. (2019). Matlab Simulink Destekli Gerçek ZamanlıKontrol. Ankara, Seçkinyayınları.

An Instance Use of Intuitionistic Fuzzy TOPSIS in Multi-Criteria Decision Making Process: Supplier Selection

Feride TUĞRUL

Department of Mathematics, Faculty of Science,
Kahramanmaraş Sutcu Imam University,
Kahramanmaraş, Türkiye
Orcid ID: 0000-0001-7690-8080

1. INTRODUCTION

With the increase in production, natural resources have decreased significantly. Gases, waste materials, toxic chemicals, waste water and many other harmful substances from the production areas have disturbed the balance of natüre (Günay, 2017).With the increase in consumption, the wastes generated after use have seriously threatened human health and the ecological balance of the world.Today, the protection of natural resources and ecosystems and the reduction of the negative effects of all activities carried out by human beings to maintain their lives are topics that researchers focus on.Supply chain (SC) addresses the environmentally conscious approach of products throughout their entire life cycle. Future supply chain management (SCM) systems will be an important competitive factor due to environmental degradation such as decreasing raw material resources, filling up of landfills and increasing pollution. Because of these reasons suppliers, The most significant step of SCM is the act of choosing suppliers. (Shang et al., 2010).

The purpose of SCM is to clarify the significance of the environment while creating value in the company's SC. SCMprovides to purified from the negative effects of all kinds of wastes such as energy, emissions, chemicals and solid wastes on the environment (Hsu ve Hu, 2008).While businesses aim to increase their efficiency and profitability with applications, they want to create awareness by minimizing their negative effects on the environment. The most important purpose of SCM is to diminish the negative effects of businesses on the natural environment. The supply chain includes purchasing, production, distribution, packaging and all logistics activities (Erol, 2018). Choosing the supplier that provides the best quality product or service in the right place, at the proper time and in the proper amount is very important in terms of managing the supply chain correctly.Choosing the right supplier and the quality of the supplier are the most important steps to be successful in the long run.

In recent years, it has become difficult to choose among the many options encountered due to the progress of technology. MCDM methods attract the attention of many researchers in terms of facilitating the selection and providing a more objective field for decision makers. This field, where many methods such as PROMETHEE, TOPSIS, AHP, etc. were used, has developed with both classical sets, fuzzy sets and IF sets. Moreover it is available for applications in education, transportation, agriculture, engineering, algebraic structures, medicine and various fields (Çuvalcıoğlu et al., 2015; Kutlu et al., 2020; Tuğrul et al., 2020; Tuğrul and Çitil, 2021, 2022; Tuğrul, 2022a, 2022b, 2022c).

The intuitionistic fuzzy TOPSIS method was utilized for the SCM in this study.With the appearance of fuzzy sets, researchers looked at their research in

a new and completely different way (Zadeh, 1965).Thanks to the intuitionistic fuzzy sets (IFS) built by Atanassov on the basis of fuzzy logic in 1983 explained the undecided situations, making the work of researchers much easier (Atanassov, 1983).Recently the IFSs continue to attract the attention of many researchers both in practice and theory (Çuvalcıoğlu, 2014, 2017; Çuvalcıoğlu et al., 2018, 2019) . The method used in this study can be changed and different perspectives on supplier selection methods can be presented by conducting statistical-based studies with different perspectives (Şahin et al., 2018; Kaya et al., 2019; Karaokur et al., 2019; Sözeyatarlar et al., 2021; Çanga et al., 2021; Yavuz and Şahin, 2022).Thanks to the TOPSIS method, positive ideal and negative ideal distances are figured out. In addition, it is a great advantage for DMs to indicate their views objectively thanks to linguistic terms. Thanks to this method, in which the contributions of the decision makers are also activated, a ranking among the alternatives is obtained by assigning a degree of importance to all criteria separately. There are many application studies in the literature with TOPSIS, fuzzy TOPSIS and intuitionistic fuzzy TOPSIS (Boran et al., 2009, 2012; Boran, 2011; Büyüközkan and Güleryüz, 2015; Damgacı et al., 2017; Rouyendegh, 2011, 2015; Rouyendeghand Saputro, 2014; Rouyendeghet al., 2018, 2020; Tekez and Bark, 2016).

After researchers working on SCM with classical decision making methods, studies with fuzzy and IFS, MCDM have attracted the notice of scientists and continue to increase rapidly today.Bulgurcu examined evaluate the efficiency of green SCM using the TOPSIS (Bulgurcu, 2018).Zaralı researched the green supplier selection in the machine manufacturing sector (Zaralı, 2021).Rouyendegh et al. handled the supplier selection issue with different methods together with intuitionistic fuzzy TOPSIS (Rouyendeghand Saputro, 2014; Rouyendegh et al., 2020).Boran et al. applied using the TOPSIS methodin the same field (Boran et al., 2009). Kılıç researchedSCM with the fuzzy TOPSIS method (Kılıç, 2012).Tian et al. established a new technique by considering the TOPSIS method from a different perspective in the green supplier selection (Tian et al., 2018).

2. PRELIMINARIES

Definition 1:(Atanassov, 1983, 1986)Let $X \neq \emptyset$. An intuitionistic fuzzy set A in X;

$$A = \{\langle x, \mu_A(x), \nu_A(x)\rangle |\ x \epsilon X\}, (1.1)$$

$$\mu_A(x), \nu_A(x), \pi_A(x): X \rightarrow [0,1] (1.2)$$

$$\mu_A(x) + \nu_A(x) + \pi_A(x) = 1 \ (1.3)$$

The algorithm, in which the calculations of the IF TOPSIS method take place step by step, consists of a total of 7 steps. In calculations, m represents alternatives and n represents criteria (Rouyendegh, 2015):

Step 1: For the first step, the importance of the decision makers (DMs) is determined. λ represents significance of each DM.

Table 1. Values for Importance of DMs

Linguistic Terms	IFNs
Very Important	(0.8,0.1)
Important	(0.5,0.2)
Medium	(0.5,0.5)
Bad	(0.3,0.5)
Very Bad	(0.2,0.7)

$L = l_1, l_2, \dots, l_n$is set of DMs. $Dl = [\mu l, \nu l, \pi l]$ is determined:

$$\lambda l = \frac{\left[\mu l + \pi l\left(\frac{\mu l}{\mu l + \nu l}\right)\right]}{\sum_{l=1}^{k}\left[\mu l + \pi l\left(\frac{\mu l}{\mu l + \nu l}\right)\right]} \qquad (1.4)$$

where $\lambda l \in [0,1]$ and $\sum_{l=1}^{k} \lambda l = 1$.

Step 2: Table 2 is utilized to evaluate the significance of the criteria (W).

Table 2. Values for Evaluating Criteria

Linguistic Terms	IFNs
Very Important	(0.9,0.1)
Important	(0.75,0.2)
Medium	(0.5,0.45)
Unimportant	(0.35,0.6)
Very Unimportant	(0.1,0.9)

Thanks to the IFWA operator, importance of the criteria are decided (Xu, 2007):

$$w_j = IFWAr_\lambda\left(w_j^{(1)}, w_j^{(2)}, \dots, w_j^{(l)}\right)$$
$$= \lambda_1 w_j^{(1)} \oplus \lambda_2 w_j^{(2)} \oplus, \dots, \oplus \lambda_k w_j^{(k)}$$
$$= [1 - \prod_{l=1}^{k}\left(1 - \mu_{ij}^{(l)}\right)^{\lambda l}, \left(\prod_{l=1}^{k}\left(\nu_{ij}^{(l)}\right)^{\lambda l}\right),$$
$$\prod_{l=1}^{k}\left(1 - \mu_{ij}^{(l)}\right)^{\lambda l} - \prod_{l=1}^{k}\left(\nu_{ij}^{(l)}\right)^{\lambda l}] \quad (1.5)$$

Step 3: Each of the alternatives is evaluated individually by all decision makers for each criterion. Calculations are made using of the values in Table 3 and R matrix is created.

Table 3. Values for Evaluating Criteria

Linguistic Terms	IFNs
Very Good (VG)	(1.00,0.00)
Good (G)	(0.85,0.05)
MediumGood (MG)	(0.70,0.20)
Fair (F)	(0.50,0.50)
Medium Poor (MP)	(0.40,0.50)
Poor (P)	(0.25,0.60)
Very Poor (VP)	(0.00,0.90)

$$R^l = (r_{ij}^{(l)})_{m*n}$$
$$\lambda = \lambda_1, \lambda_2, \dots, \lambda_k$$
$$R = (r_{ij})_{m' \times n'}$$
$$r_{ij} = IFWAr_\lambda\left(r_{ij}^{(1)}, r_{ij}^{(2)}, \dots, r_{ij}^{(l)}\right) \quad (1.6)$$

Step 4: The Aggregated Intuitionistic Fuzzy Decision Matrix (AIFDM) namely S matrix is acquired.

$$S = R \times W$$
$$R \otimes W = \left(\mu_{ij}^{'}, \nu_{ij}^{'}\right)$$
$$= \{\langle \mu_{ij} \times \mu_j, \nu_{ij} + \nu_j - \nu_{ij} \times \nu_j \rangle\} \quad (1.7)$$

Step 5: Considering that there are J_1 benefit and J_2 cost criteria, the A^+positive and A^-negative ideal solution are acquired:

$$A^+ = \left(r_1^{'*}, r_2^{'*}, \dots, r_n^{'*}\right), r_j^{'*} = \left(\mu_j^{'*}, \nu_j^{'*}, \pi_j^{'*}\right) \quad (1.8)$$
$$A^- = \left(r_1^{'-}, r_2^{'-}, \dots, r_n^{'-}\right), r_j^{'-} = \left(\mu_j^{'-}, \nu_j^{'-}, \pi_j^{'-}\right) \quad (1.9)$$

where $j = 1,2,\dots,n$ and

$$\mu_j^{'*} = \left\{\left(\max_i\{\mu_{ij}^{'}\} j \in J_1\right), \left(\min_i\{\mu_{ij}^{'}\} j \in J_2\right)\right\}$$
$$\nu_j^{'*} = \left\{\left(\min_i\{\nu_{ij}^{'}\} j \in J_1\right), \left(\max_i\{\nu_{ij}^{'}\} j \in J_2\right)\right\}$$
$$\mu_j^{'-} = \left\{\left(\min_i\{\mu_{ij}^{'}\} j \in J_1\right), \left(\max_i\{\mu_{ij}^{'}\} j \in J_2\right)\right\}$$
$$\nu_j^{'-} = \left\{\left(\max_i\{\nu_{ij}^{'}\} j \in J_1\right), \left(\min_i\{\nu_{ij}^{'}\} j \in J_2\right)\right\}$$

Step 6: In this step, separation measuresS_i^+ and $S_i^-$are calculated using the normalized Hamming distance. It is shown in studies that the normalized Hamming distance gives more accurate results than other distance measures(Szmidt and Kacprzyk, 2000; Çitil, 2019).

$$S_i^+ = \frac{1}{2n}\sum_{i=1}^{n}\left[\left|\mu_{ij}^{'} - \mu_{ij}^{'*}\right| + \left|\nu_{ij}^{'} - \nu_{ij}^{'*}\right| + \left|\pi_{ij}^{'} - \pi_{ij}^{'*}\right|\right]$$
$$S_i^- = \frac{1}{2n}\sum_{i=1}^{n}\left[\left|\mu_{ij}^{'} - \mu_{ij}^{'-}\right| + \left|\nu_{ij}^{'} - \nu_{ij}^{'-}\right| + \left|\pi_{ij}^{'} - \pi_{ij}^{'-}\right|\right]$$

Step 7: Closeness coefficient values are obtained for each alternative.

$$C_i^* = \frac{S_i^-}{S_i^+ + S_i^-},$$

where $0 \le C_i^* \le 1$.While interpreting the C_i^* values obtained, it should be noted that the higher the value, the higher the chance of choosing the alternative.

3. NUMERICAL EXAMPLE

In this study, the selection mechanism was established to decide the most suitable supplier. Considering the production and marketing processes of the factory, decision making application was made to determine the most suitable one among the 3 suppliers. In this application, where the opinions of 2 expert DMs in the field were taken, 3 suppliers were evaluated according to a total of 6 criteria.The S set represented the suppliers, that is, the alternatives, and the C set represented the criteria. The criteria are as follows:

C_1: Delivery Time
C_2: Cost
C_3: Qualitative
C_4: Communication system
C_5: Technology
C_6: Institutionalization

Step 1:A total of 2 DMs' opinions were indicated for the IF TOPSIS method. Both the evaluation of the criteria, the determination of their importance and the assessment of the alternatives according to each criterion were indicated. The significance of the first and second DMs was determined as VI and I respectively, and the values obtained with the help of equation (1.4) were 0.554455 and 0.445545 respectively.

Step 2: The values in Table 4 of the opinions obtained by equation (1.5) were shown in Table 5.

Table 4. Opinions of decision makers as to criteria

	DM_1	DM_2
C_1	I	VI
C_2	VI	I
C_3	I	M
C_4	M	U
C_5	VI	I
C_6	I	VI

Table 5. Weights of criteria

C_1	(0.834, 0.147)
C_2	(0.849, 0.136)
C_3	(0.659, 0.287)
C_4	(0.438, 0.512)
C_5	(0.849, 0.136)
C_6	(0.834, 0.147)

The opinions of the DMs were specified in Table 6.

Table 6. Opinions of DMs as to alternatives

	C_1	C_2	C_3	C_4	C_5	C_6
DM_1						
S_1	VG	F	G	G	MG	MG
S_2	G	MG	MG	MG	F	G
S_3	MG	G	MP	F	G	VG
DM_2						
S_1	G	MP	MG	VG	G	F
S_2	MG	F	G	G	MP	MG
S_3	G	MG	F	MP	MG	G

Step 3-4: *R* matrix and *S* matrix were obtained in Table 7 and 8.

Table 7. R Matrix

	C_1	C_2	C_3	C_4	C_5	C_6
S_1	(1.000, 0.000)	(0.458, 0.500)	(1.000, 0.000)	(1.000, 0.000)	(0.779,0.108)	(0.623, 0.301)
S_2	(0.796, 0.093)	(0.623, 0.301)	(0.850, 0.050)	(0.778, 0.108)	(0.458, .500)	(0.796, 0.093)
S_3	(0.779,0.108)	(0.796,0.093)	(0.447,0.500)	(0.458,0.500)	(0.796,0.093)	(1.000,0.000)

Table 8. S Matrix

	C_1	C_2	C_3	C_4	C_5	C_6
S_1	(0.834,0.147)	(0.389,0.568)	(0.659,0.287)	(0.438,0.512)	(0.662,0.229)	(0.519, 0.404)
S_2	(0.663,0.226)	(0.529,0.396)	(0.561,0.323)	(0.342,0.564)	(0.389,0.568)	(0.663,0.226)
S_3	(0.650,0.239)	(0.676,0.216)	(0.295,0.644)	(0.200,0.756)	(0.676,0.216)	(0.834,0.147)

Step 5: Values of A^+ and A^-were calculated in Table 9.

Table 9. Values of A^+ and A^-

	A^+	A^-
C_1	(0.834, 0.147)	(0.650, 0.239)
C_2	(0.676, 0.216)	(0.389, 0.568)
C_3	(0.659, 0.287)	(0.295, 0.644)
C_4	(0.438, 0.512)	(0.200, 0.756)
C_5	(0.676, 0.216)	(0.389, 0.568)
C_6	(0.834, 0.147)	(0.519, 0.404)

Step 6-7: For each alternative, the separation measures obtained using the normalized Hamming distance were calculated and shown in Figure 1. In addition, the closeness coefficient values required for the net ranking were also included in Table 10 and was shown in Figure 2.

Table 10. Values of S^+, S^- and C_j^*

	S^+	S^-	C_j^*
S_1	0.11325	0.18859	0.62480
S_2	0.17794	0.14589	0.45051
S_3	0.13213	0.16961	0.56212

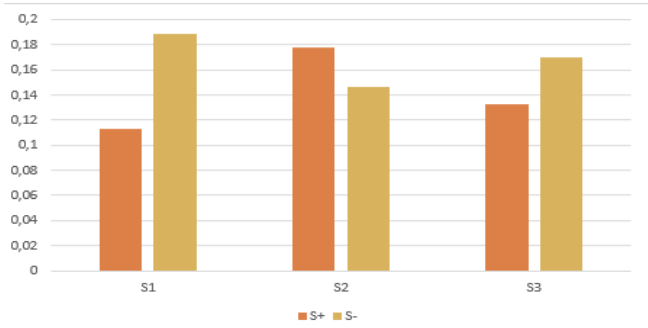

Figure 1. Graphics of Separation Measures

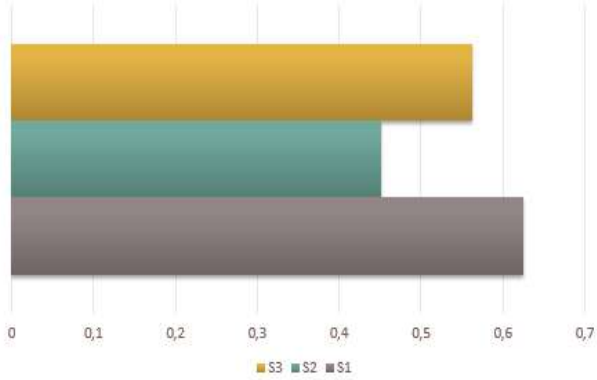

Figure 2. Graphics of Closeness Coefficient Values

When the values in Figure 2 and Table 10 are interpreted, the order among suppliers is S_1-S_3-S_2. In accordance with the criteria determined by the DMs, the most suitable supplier is S_1.

4. CONCLUSION

This study focused on supplier selection, which is investigated by the IF TOPSIS method. The opinions of 2 expert DMs were indicated. While deciding the weights of the criteria, the opinions of the DMs were taken into account. Alternatives were evaluated individually according to each criterion. The feature that distinguishes this method from other methods is that it evaluates alternatives depending on their distance from ideal solutions. In addition, the part that distinguishes this application from other existing studies is that it is calculated using the normalized Hamming distance. The criteria in the selection of the current supplier may be changed depending on the decision makers, different methods may be used. The quality and quantity of alternatives may vary. This study, which is thought to guide future studies, will contribute to the supply chain management system.

REFERENCES

1. Atanassov, K.T. (1983). Intuitionistic Fuzzy Sets, VII ITKR's Session, Sofia, June 1983 (Deposed in Central Sci. - Techn. Library of Bulg. Acad. of Sci., 1697/84) (in Bulg.). Reprinted: Int. J. Bioautomation, 20(S1), 1-6, 2016.
2. Atanassov, K.T. (1986). Intuitionistic Fuzzy Sets. Fuzzy Sets and Systems, 20(1), 87-96.
3. Boran, F.E., Genç, S., Kurt, M., Akay, D. (2009). A Multi-Criteria Intuitionistic Fuzzy Group Decision Making For Supplier Selection With TOPSIS Method. Expert Systems with Applications, 36(8), 11363-11368.
4. Boran, F.E. (2011). An Integrated Intuitionistic Fuzzy Multi Criteria Decision Making Method For Facility Location Selection. Mathematical and Computational Applications, 16(2), 487-496.
5. Boran, F.E., Boran, K., Menlik, T. (2012). The Evaluation of Renewable Energy Technologies For Electricity Generation in Turkey Using Intuitionistic Fuzzy TOPSIS. Energy Sources, Part B: Economics, Planning and Policy, 7(1), 81-90.
6. Bulgurcu, B. (2018). An Intuitionistic Fuzzy Group Decision-Making to Measure the Performance of Green Supply Chain Management with TOPSIS Method. In (Ed.), Multi-Criteria Methods and Techniques Applied to Supply Chain Management. IntechOpen. https://doi.org/10.5772/intechopen.73701.
7. Büyüközkan, G., Güleryüz, S. (2015). An Application of Intuitionistic Fuzzy Topsis on Mobile Phone Selection. In 2015 IEEE International Conference on Fuzzy Systems (FUZZ-IEEE),1-8.
8. Çanga, D., Yavuz, E., Efe, E.(2021) Prediction of Egg Weight Using MARS data mining Algorithm through R. Kahramanmaraş Sütçü İmam University Journal of Agriculture and Nature, 24(1), 242-251.
9. Çitil, M. (2019). Application of the Intuitionistic Fuzzy Logic in Education. Communications in Mathematics and Applications, 10(1), 131-143.
10. Çuvalcıoğlu, G. (2014). Some Properties of Controlled Set Theory. Notes on Intuitionistic Fuzzy Sets, 20(2), 37-42.
11. Çuvalcıoğlu, G., Yilmaz, S., Bal, A. (2015). Some Algebraic Properties of the Matrix Representation of intuitionistic Fuzzy Modal Operators. Notes on Intuitionistic Fuzzy Sets, 21(2), 6-18.
12. Çuvalcıoğlu, G. (2017). Some Properties of t-intuitionistic Fuzzy-Rings. Sakarya University Journal of Science, 21(6), 1182-1187.

13. Çuvalcıoğlu, G., Tarsuslu, S., Bal, A., Artun, G. (2018). Intuitionistic Fuzzy Modal Operators in Intelligent System for Pesticide and Fertilization. Annals of Fuzzy Mathematics and Informatics, 16(1), 117-132.
14. Çuvalcıoğlu, G., Bureva, V., Michalíková, A. (2019). Intercriteria Analysis Applied To University Ranking System Of Turkey. Notes on Intuitionistic Fuzzy Sets, 25(4), 90-97.
15. Damgacı, E., Boran, K., Boran, F.E. (2017). Evaluation of Turkey's Renewable Energy Using Intuitionistic Fuzzy TOPSIS Method. Journal of Polytechnic, 20(3), 629-637.
16. Erol, Ö. (2018). Green Supplier Selection Based On Multi-Criteria Decision Making Approach: A Case Study in a Company Manufacturing Wind Turbine Tower. Selçuk Unıversity, Graduate School Of Natural And Applied Science, Konya.
17. Günay, S.N. (2017). Green Supplier Selection Based on Ahp and Vikor Methods and an Application. M.Sc. Thesis, Gazi University, Graduate School Of Natural And Applied Sciences, Ankara.
18. Hsu, C. W., Hu, A. H. (2008). Green Supply Chain Management in the Electronic Industry. International Journal of Environmental Science and Technology, 2(5), 208.
19. Karaokur, Ö., Kaya, F., Yavuz, E., Yenipınar, A. (2019). Comparison of Commonly Used Statistics Package Programs. Black Sea Journal of Engineering and Science, 2 (1), 26-32.
20. Kaya, F ,Yavuz, E , Koç, Ş , Karaokur, Ö . (2019). A Study on Determination of Outlier Observations by Using Chi-Square Threshold Value. Black Sea Journal of Engineering and Science, 2 (1), 7-10.
21. Kılıç, H.S. (2012). Supplier Selection Application Based On A Fuzzy Multiple Criteria Decision Making Methodology. AJIT-e: Online Academic Journal of Information Technology, 3(8), 7-18.
22. Kutlu, F., Tuğrul, F., Çitil, M. (2020). Introduction to Temporal Intuitionistic Fuzzy Approximate Reasoning, Commun. Fac. Sci. Univ. Ank. Ser. A1 Math. Stat., 69(1), 232-251.
23. Rouyendegh, B.D. (2011). The DEA And Intuitionistic Fuzzy TOPSIS Approach To Departments' Performances: A Pilot Study. Journal of Applied Mathematics, 2011, doi:10.1155/2011/712194.
24. Rouyendegh, B.D., Saputro, T.E. (2014). Supplier Selection Using Integrated Fuzzy TOPSIS And MCGP: A Case Study. Procedia-Social and Behavioral Sciences, 116, 3957-3970.

25. Rouyendegh, B.D. (2015). Developing an Integrated ANP and Intuitionistic Fuzzy TOPSIS Model For Supplier Selection. Journal of Testing and Evaluation, 43(3), 664–672.
26. Rouyendegh, B.D., Yıldızbaşı, A., Arıkan, Ü.Z. (2018). Using Intuitionistic Fuzzy TOPSIS in Site Selection Of Wind Power Plants in Turkey. Advances in Fuzzy Systems, 2018,https://doi.org/10.1155/2018/6703798.
27. Rouyendegh, B.D., Yıldızbaşı, A., Üstünyer, P. (2020). Intuitionistic Fuzzy TOPSIS Method For Green Supplier Selection Problem. Soft Computing, 24(3), 2215-2228.
28. Shang, K., Lu, C., Li, S. (2010). A Taxonomy of Green Supply Chain Management Capability Among Electronics-Related Manufacturing Firms in Taiwan. Journal of Environmental Management, 91, 1218-1226.
29. Sözeyatarlar, M., Şahin, M., Yavuz, E. (2021). Statistical Relations Measures. Journal of Universal Mathematics, 4(2), 283-295.
30. Szmidt, E., Kacprzyk, J. (2000). Distances Between Intuitionistic Fuzzy Sets. Fuzzy Sets Syst., 114, 505-518.
31. Şahin, M., Yavuz, E., Üçkardeş, F. (2018). Multicollinearity Problem and Bias Estimates in Japanese Quail. Pakistan J. Zool., 50(2), 757-761.
32. Tekez, E.K., Bark, N. (2016). Supplier Selection For Furniture Industry with Fuzzy TOPSIS Method. Sakarya Unıversity Journal of Science, 20(1), 55-63.
33. Tian, Z. P., Zhang, H. Y., Wang, J. Q., Wang, T. L. (2018). Green Supplier Selection Using Improved TOPSIS And Best-Worst Method Under Intuitionistic Fuzzy Environment. Informatica, 29(4), 773-800.
34. Tuğrul, F., Çitil, M., Karasolak, B., Dağlı, M. (2020). Interpretation of Physical Conditions of Schools with Fuzzy Multi Criteria Decision Making, Journal of Universal Mathematics, 3(1), 46-52.
35. Tuğrul, F., Çitil, M. (2021). A New Perspective on Evaluation System in Education with Intuitionistic Fuzzy Logic and PROMETHEE Algorithm, Journal of Universal Mathematics, 4(1), 13-24.
36. Tuğrul, F., Çitil, M. (2022). Application of Mathematical Modeling in Multi Criteria Decision Making Process: Intuitionistic Fuzzy PROMETHEE, Journal of Mathematical Sciences and Modelling, 5(2), 48-56.
37. Tuğrul, F. (2022a). Personnel Selection Utilizing The Decision Making Mechanism Created with The Intuitionistic Fuzzy TOPSIS Method, Mugla Journal of Science and Technology, 8(2), 16-21.

38. Tuğrul, F. (2022b). An Evaluation of Supermarkets From the Lens of Multiple Criteria: The Intuitionistic Fuzzy TOPSIS Method,Black Sea Journal of Engineering and Science, 5(4), 146-150.
39. Tuğrul, F. (2022c). An Innovative Application on Supermarket Selection Through Using Intuitionistic Fuzzy TOPSIS Method, Sakarya University Journal of Science, 26(5), 2029-2039.
40. Xu, Z.S. (2007). Intuitionistic Fuzzy Aggregation Operators. IEEE Transactions on Fuzzy Systems, 15, 1179-1187.
41. Yavuz, E, Şahin, M. (2022). Semiparametric Regression Models and Applicability in Agriculture, Black Sea Journal of Agriculture, 5(2), 160-166.
42. Zadeh, L.A. (1965). Information and Control, Fuzzy sets, 8(3), 338-353.
43. Zaralı, F. (2021). Intuitionistic Fuzzy Green Supplier Selection and an Application in the Machine Manufacturing Sector. Journal of Turkish Operations Management, 5(1), 676-687.

Metal Organic Frameworks and Gas Adsorption

Fuat ASLAN

[1]Instructor, Necmettin Erbakan University,
Science and Technology Research and Application Center (BİTAM),
Konya, Turkey, e-mail: faslan@erbakan.edu.tr
(ORCID: https://orcid.org/0000-0002-6830-6490)

INTRODUCTION

The applications of adsorption science are of importance in industry and environmental protection. The most important issue here is the choice of adsorbent. Among the adsorbents used, there are materials such as silica gels, zeolites, activated carbon, cellulose, chelating resins, polyurethane foam and functionalized graphene(Sitko et al., 2015). Although adsorption studies mostly find application in aqueous solutions, research has also focusedon gas adsorption studies.

An efficient, effective, energy-saving and environmentally friendly methodsare needed for gas adsorption and separation. Metal organic frameworks (MOFs) are a class of microporous materials that are of great importance in gas storage and separation processes due to their large surface areas, surface functionalization, adjustable pore sizes and controllable properties, as well as their chemical stability (Li, Kuppler, & Zhou, 2009; Xu et al., 2021). Some examples of MOFs with porous structures are given in Figure 1.

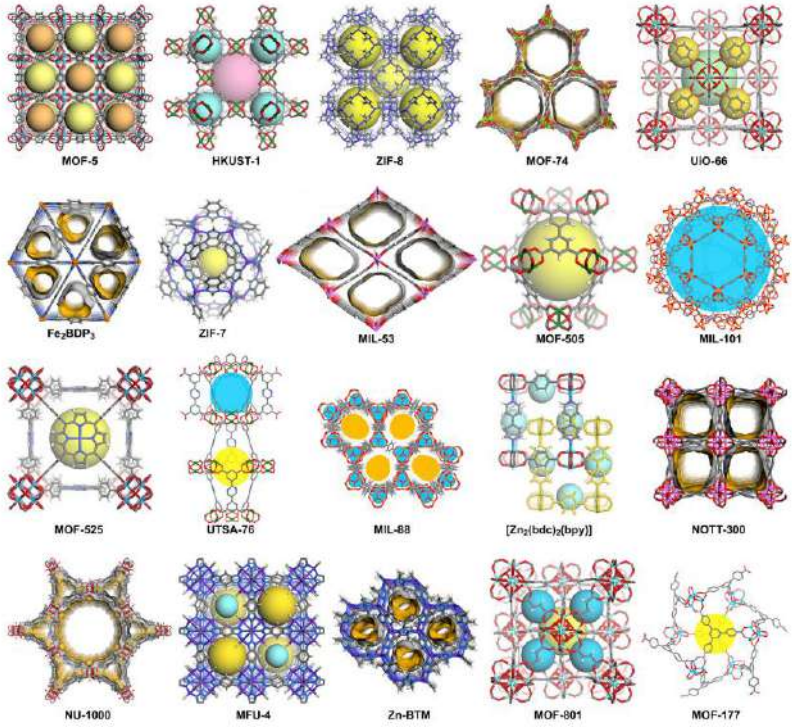

Figure 1 Representative Porous Structures of Metal Organic Frameworks(Lin, Xiang, Zhou, & Chen, 2020).

MOFs are organic-inorganic structures called metal-ligand coordination polymers. It consists of two basic components, metal salts and linkers. Because

of their versatile coordination numbers, most metal ions are transition metals with various geometries. They form coordination networks with organic ligands(Alhamami, Doan, & Cheng, 2014).

An exampleMOF formation and functionalization is shown in Figure 2. Zirconium-based UiO-66-NH2 MOF was synthesized by solvothermal method using zirconium tetrachloride as metal salt and 2-aminoterephthalic acid as linker, and functional group of 6-amino-4-hydroxy-2-mercaptopyrimidine (AHMP) were attached through glutaraldehydecrosslinkerin subsequent steps.

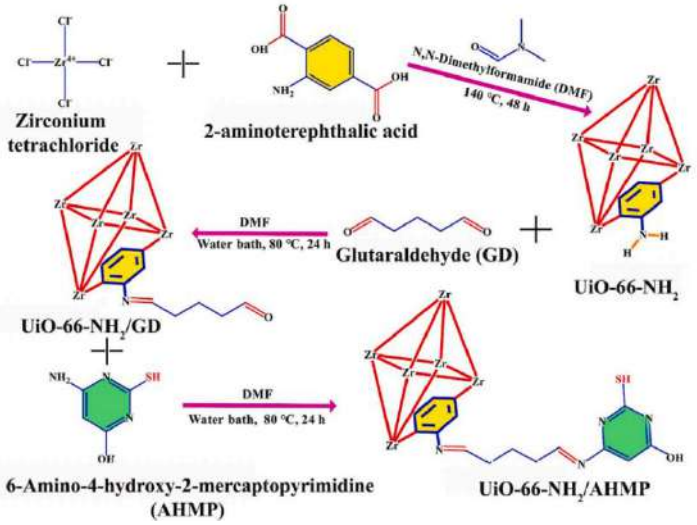

Figure 2 Synthesis steps of a functionalized MOF of UiO-66-NH_2/AHMP(Ruan et al., 2022).

MOFSynthesis Methods

MOF syntheses are generally liquid-phase syntheses in which metal salt and ligand solutions are mixed in certain reaction conditions. In liquid phasereactions, the choice of solvent, reactivity, solubility, redox potential, stability constant etc. factors are of importancefortheformation of MOFs.Moreover, thesolidphasereactionsareoftenpreferredduetotheirreaction rate andease. However, difficulties may be encountered in obtaining crystals in solid state synthesis. While only mechanochemical method has been used in solid state synthesis of MOFs, methods such as hydrothermal, solvothermal, microwave, electrochemical and sonochemicalhas beenused in liquid phase synthesis (Dey, Kundu, Biswal, Mallick, & Banerjee, 2014). The most preferred hydrothermal, solvothermal and microwave synthesis methods in MOFproduction is discussed in thefollowingsections.

Hydrothermal and Solvothermal Synthesis

It is one of the most widely used synthesis methods in the production of MOFs. In this method, metal salt dissolved in a certain amount of solvent and organic linker are generally reacted in an autoclave under pressure at a certain time and temperature. Here, the reaction time can take from a few hours to several days. When water is used as a solvent during the dissolution of ligands, it is called hydrothermal while other organic solvents are beingused, it is called solvothermal(Lee, Kim, & Ahn, 2013). Both hydrothermal and solvothermal reactions are carried out under autogenous pressure(Dey et al., 2014). The organic solvents generally used during the solvothermal synthesis of MOFs are dimethyl formamide (DMF), diethyl formamide (DEF), acetonitrile, acetone, ethanol, methanol etc.Recently, MIL-101(Fe) MOF was synthesized by solvothermal method and As(V) adsorption studies was successfully completed by using MOF structure (Figure 3).

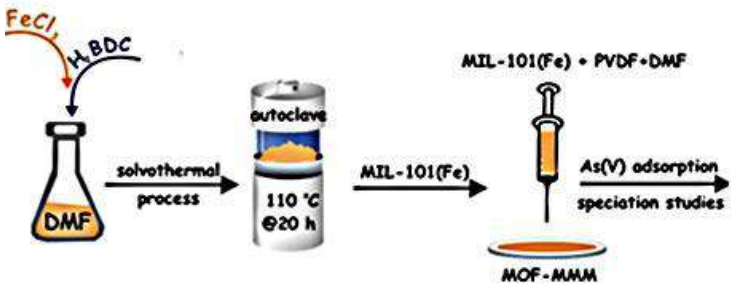

Figure 3 Solvothermalsynthesis of MIL-101(Fe) MOF and its attachment tomembrane surface (Aslan & Tor, 2022).

Microwave Synthesis

Microwave provides rapid MOF synthesis under thermal conditions in a short time such as one hour. In the microwave device, the reaction takes place by adjusting theparameters such as time, temperature, pressure, and ramp heating. The heating time of the solution in the teflon cells in the device is shortened by applying oscillating electric field in the microwave technique.In addition, phase selectivity, narrow particle size distribution, and easy morphology control can be obtained during the reaction that could result in high quality crystals (Klinowski, Almeida Paz, Silva, & Rocha, 2011; Lee et al., 2013). In a study by Xiaofei et al., it is emphasized that in the synthesis of MOF-74, reaction takes 20 hours to 3 days by the solvothermal method, but the microwave-assisted method significantly reduces the processing time, increases product yield with an improved product quality.

Recently, MiL-101 MOF was synthesized by different researchers in a reaction time less than 1 hour, with a smaller size between 40-100 nm, more uniform crystal structure, large surface area and high pore volume (Wu et al., 2013). In another study, the synthesis of MOFwas achieved by forming coordination networks of metal salts with organic ligands in a teflon cell by using microwave (Figure 4).

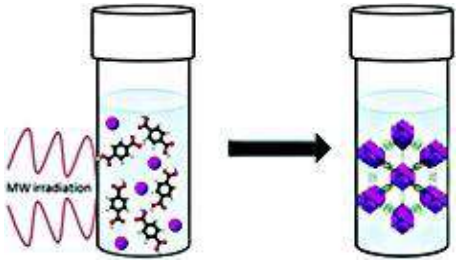

Figure 4 Microwave synthesis of MOF(Taddei et al., 2015).

Gas Adsorption

Toxic gases are an environmental problem for all humanity. Adsorption is one of the most promising methodsfor removing and storing gases. In recent years, MOFs have been preferred as membranes for the removal, separation, and storage of gases due to their high surface area, tunability and different interactions. Pore size and ambient conditions are prerequisites for high gas adsorption in MOFs (Fan, Zhang, Kang, Liu, & Sun, 2021). Moreover, different composite structures of MOFs were prepared and used in gas adsorption studiesin many studies. As an example, it has been determined in some studies that graphene oxide (GO) has a positive effect on the retention of small molecules such as ammonia when its composite (GO-MOF) is formed with MOFs. This increase is due to the formation of new porous portions at the interface between GO and MOF units (Ahmed & Jhung, 2014).

For a good separation in the membrane, the gas transport mechanism should be known. The main mechanisms controlling the gas flow process are the molecular sieving, Knudsen diffusion, surface diffusion, and solution diffusion. There are two important methods for gas systemsin membrane separation processes; transportation through dense and through porous membranes(Zou, Zhu, & Print, 2020). The separation process depends on the pore size distribution, temperature, pressure, and interface interaction. Knudsen diffusion has lower selectivity than surface diffusion whilemolecular sieving membranes having high selectivity. The first separation study with MOFs was carried out by the Knudsen mechanism on membranes prepared by attaching MOF-5 to

porous alumina substrates(Yoo, Lai, & Jeong, 2009). In molecular sieving, membranes prepared with MOFs are ideal because a porous membrane structure is needed that allows the passage of one gas molecule while preventing the passage of the others (Caro, 2011).

As MOFs can show different adsorption capacity for various gases, analytical methods have been applied to investigate mixed gas separation. Natural gas mixtures could be separated by gas chromatography through a MOF structure (Figure 5). MOFs are mostly preferred for gas separation applications as they provide effective separation than zeolite materials. For example, various MOFs have been used in carbon dioxide capture, natural gas purification, toxic gas removal and separation studies of olefin/paraffin, alkyne/olefin, acetylene/carbon dioxide, hexane isomers, xylene isomers, xenon/krypton, hydrogen isotopes (Lin et al., 2020).

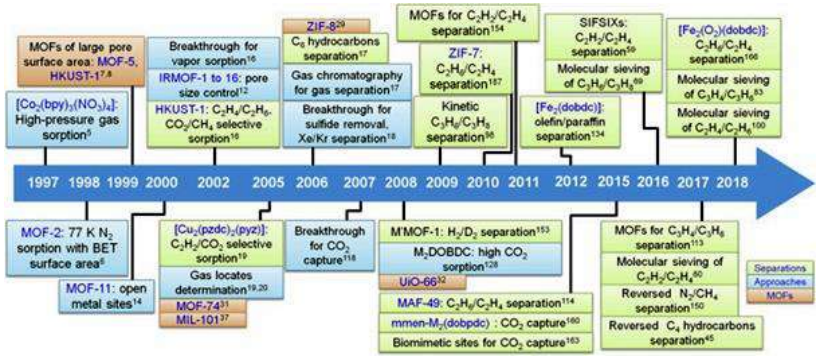

Figure 5 Developments in gas studies using MOFs (Lin et al., 2020).

Many revolutionary studies have been carried out in this field to capture CO_2 in the first decade of the applications using MOFs and to separate the light hydrocarbons emerged in the second decade. MOFs still provides their popularity today, attracting academic and industrial attention(Fakhraei Ghazvini, Vahedi, Najafi Nobar, & Sabouri, 2021; Lin et al., 2020).

As a result, metal organic frameworks (MOFs) are extremely advanced materials compared to other adsorbents used in gas storage and separation processes, as well as in aqueous solutions, with the advantages of their chemical stability, high surface area, surface functionalization and adjustable pore sizes. Due to these important features, the studies in environmental applications, catalysis applications, sensors, renewable energy and biomedical field are rapidly proceedingusing MOF structures.

References

1. Ahmed, I., & Jhung, S. H. (2014). Composites of metal-organic frameworks: Preparation and application in adsorption. Materials Today, 17(3), 136–146. https://doi.org/10.1016/j.mattod.2014.03.002
2. Alhamami, M., Doan, H., & Cheng, C. H. (2014). A review on breathing behaviors of metal-organic-frameworks (MOFs) for gas adsorption. Materials, 7(4), 3198–3250. https://doi.org/10.3390/ma7043198
3. Aslan, F., & Tor, A. (2022). Chemosphere Determination and speciation of trace inorganic arsenic species in water samples by using metal organic framework mixed-matrix membrane and EDXRF spectrometry. Chemosphere, 307(P1), 135661. https://doi.org/10.1016/j.chemosphere.2022.135661
4. Caro, J. (2011). Are MOF membranes better in gas separation than those made of zeolites? Current Opinion in Chemical Engineering, 1(1), 77–83. https://doi.org/10.1016/j.coche.2011.08.007
5. Dey, C., Kundu, T., Biswal, B. P., Mallick, A., & Banerjee, R. (2014). Crystalline metal-Organic frameworks (MOFs): Synthesis, structure and function. Acta Crystallographica Section B: Structural Science, Crystal Engineering and Materials, 70(1), 3–10. https://doi.org/10.1107/S2052520613029557
6. Fakhraei Ghazvini, M., Vahedi, M., Najafi Nobar, S., & Sabouri, F. (2021). Investigation of the MOF adsorbents and the gas adsorptive separation mechanisms. Journal of Environmental Chemical Engineering, 9(1), 104790. https://doi.org/10.1016/j.jece.2020.104790
7. Fan, W., Zhang, X., Kang, Z., Liu, X., & Sun, D. (2021). Isoreticular chemistry within metal–organic frameworks for gas storage and separation. Coordination Chemistry Reviews, 443, 213968. https://doi.org/10.1016/j.ccr.2021.213968
8. Klinowski, J., Almeida Paz, F. A., Silva, P., & Rocha, J. (2011). Microwave-assisted synthesis of metal-organic frameworks. Dalton Transactions, 40(2), 321–330. https://doi.org/10.1039/c0dt00708k
9. Lee, Y. R., Kim, J., & Ahn, W. S. (2013). Synthesis of metal-organic frameworks: A mini review. Korean Journal of Chemical Engineering, 30(9), 1667–1680. https://doi.org/10.1007/s11814-013-0140-6
10. Li, J. R., Kuppler, R. J., & Zhou, H. C. (2009). Selective gas adsorption and separation in metal-organic frameworks. Chemical Society Reviews, 38(5), 1477–1504. https://doi.org/10.1039/b802426j

11. Lin, R. B., Xiang, S., Zhou, W., & Chen, B. (2020). Microporous Metal-Organic Framework Materials for Gas Separation. Chem, 6(2), 337–363. https://doi.org/10.1016/j.chempr.2019.10.012
12. Ruan, W., Liu, H., Qi, Y., Zhou, M., Wu, H., & Yang, H. (2022). Post-modification of Uio-66-NH2 based on Schiff-base reaction for removal of Hg2+ from aqueous solution: Synthesis, adsorption performance and mechanism. Fuel, 319(January), 123816. https://doi.org/10.1016/j.fuel.2022.123816
13. Sitko, R., Janik, P., Zawisza, B., Talik, E., Margui, E., & Queralt, I. (2015). Green Approach for Ultratrace Determination of Divalent Metal Ions and Arsenic Species Using Total-Reflection X-ray Fluorescence Spectrometry and Mercapto-Modified Graphene Oxide Nanosheets as a Novel Adsorbent. Analytical Chemistry, 87(6), 3535–3542. https://doi.org/10.1021/acs.analchem.5b00283
14. Taddei, M., Dau, P. V., Cohen, S. M., Ranocchiari, M., Van Bokhoven, J. A., Costantino, F., Vivani, R. (2015). Efficient microwave assisted synthesis of metal-organic framework UiO-66: Optimization and scale up. Dalton Transactions, 44(31), 14019–14026. https://doi.org/10.1039/c5dt01838b
15. Wu, X., Bao, Z., Yuan, B., Wang, J., Sun, Y., Luo, H., & Deng, S. (2013). Microwave synthesis and characterization of MOF-74 (M = Ni, Mg) for gas separation. Microporous and Mesoporous Materials, 180, 114–122. https://doi.org/10.1016/j.micromeso.2013.06.023
16. Xu, G. R., An, Z. H., Xu, K., Liu, Q., Das, R., & Zhao, H. L. (2021). Metal organic framework (MOF)-based micro/nanoscaled materials for heavy metal ions removal: The cutting-edge study on designs, synthesis, and applications. Coordination Chemistry Reviews, 427, 213554. https://doi.org/10.1016/j.ccr.2020.213554
17. Yoo, Y., Lai, Z., & Jeong, H. K. (2009). Fabrication of MOF-5 membranes using microwave-induced rapid seeding and solvothermal secondary growth. Microporous and Mesoporous Materials, 123(1–3), 100–106. https://doi.org/10.1016/j.micromeso.2009.03.036
18. Zou, X., Zhu, G., & Print, M. (2020). Microporous Materials for Separation Membranes. Chromatographia, 83(12), 1561–1562. https://doi.org/10.1007/s10337-020-03968-y

Structural Behaviors of Nicotinamide Complexes of Cd(II) Arylcarboxylates

Hacali Necefoğlu[1], Füreya Elif Öztürkkan[2]*, Tuncer Hökelek[3]

[1]Kafkas University, Department of Chemistry, Kars, Türkiye
[2]Kafkas University, Department of Chemical Engineering, Kars, Türkiye
[3]Hacettepe University, Department of Physics, Ankara, Türkiye
** E-mail: fozturkkan36@gmail.com*

INTRODUCTION

Many coordination compounds containing carboxylate groups have been the subject of many staudies due to their structural properties and application areas. Many parameters such as the central metal atom, the main and auxiliary ligands used, and their functional groups being nucleophilic or electrophilic, pH, solvent, synthesis method, and temperature affect the structural diversity. Cadmium complexes also attract the attention of inorganic chemists due to their structural properties. The attractiveness of cadmium lies in the fact that in the case of the chemistry of carboxylates, it can be considered as a fairly close analog of Mn(II), Fe(II), Co(II), Ni(II), Cu(II), and Zn(II). The properties of cadmium compounds significantly expand the possibilities for the synthesis of carboxylate complexes in comparison with the use of compounds with 3d-metals (Sen et al., 1999). Thus, the noticeably greater stability of cadmium complexes makes it possible to carry out many syntheses of its carboxylate complexes in aqueous media. The main differences in the composition and structure of cadmium and 3d-metal complexes are because a noticeably longer cadmium-element bond length leads to a significant decrease in steric effect, and the ability of cadmium to exhibit large coordination number can manifest itself in the fact that, unlike 3d elements, it can form complexes of different structures with ligands of a similar nature. And the ability to exhibit a coordination number greater than six can lead to the formation of the same types of metal backbones with monodentate and chelating ligands. In the case of cadmium compounds, the influence of the nature of the carboxylate anion is much stronger. The greater stability of cadmium complexes is also reflected in the formation of stable intermediates with coordinated solvent molecules, which is much less common in the case of 3d metals (Bhattacharya, Dey, & Ghoshal, 2013; Khattak et al., 2022). It should be noted that the structure of Cd(II) complexes differs significantly from the complexes of 3d metals, including Zn(II), and the variation of the molecules of the N-donor ligand and carboxylate anions, which are part of the complexes, makes it possible to trace dependence of the structure and properties of compounds on the steric features of the ligands. A typical difference between the chemistry of Cd(II) and Zn(II) can be shown using acetate complexes as an example. Zinc(II) acetate is a mononuclear coordination compound $[Zn(H_2O)_2(OAc)_2]$. Whereas in the case of cadmium(II) acetate, due to the chelate-bridging coordination of carboxylate anions, the already polymeric complex $[Cd(H_2O)_2(OAc)_2]_n$(Shemelev, 2020).

Cadmium(II) has four, five, six, seven, and eight coordination numbers. In a study comparing the structures of the 200 cadmium (II) complexes whose crystal structure was determined, it was found that in 19.8 % of these

complexes, coordination numbers of cadmium had four and five. In addition, in 56 % of these complexes, the coordination number of cadmium was reported to be six. In the same study, seven-coordinate cadmium (II) complexes were reported to be less common in the literature (Sen et al., 1999).

In this study, the structures of nicotinamide complexes of cadmium arylcarboxylates with monomeric, dimeric, ionic, polymeric, and supramolecular structures were discussed.

Mononuclear Complexes

Among the nicotinamide complexes of Cd(II) arylcarboxylates, two mononuclear compounds whose crystal structures have been studied are known. The Cd atom in the nicotinamide complex of cadmium 2-nitrobenzoate lies on a center of inversion in an all-trans octahedral environment. In the structure where all ligands are monodentate coordinated, there are also two uncoordinated water molecules (Figure 1).In the crystal, the complex interacts with the uncoordinated water molecules through O-H···O and N-H···O hydrogen bonds, forming a layered network. Cd-O_{COO}, Cd-$O_{w,}$ and Cd-N bond lengths are 2.325 Å, 2.326 Å, and 2.329 Å, respectively [4]. A similar configuration is observed around the Cd atom in the *N, N′*-diethylnicotinamide complex of cadmium 4-cyanobenzoate (Cd-O_{COO}, Cd-$O_{W,}$and Cd-N bond lengths are 2.259 Å, 2.319 Å, and 2.334 Å, respectively). This type of structure is frequently encountered in monomeric nicotinamide complexes of 3d-metal arylcarboxylates (Çaylak, Hökelek, & Necefoğlu, 2007; Hökelek, Çaylak, & Necefoğlu, 2007; Hökelek & Necefoğlu, 2007a, 2007b; Necefoğlu, Özbek, Öztürk, Tercan, & Hökelek, 2011; O. Şahin, Büyükgüngör, Köse, & Necefoglu, 2007; Onur Şahin, Büyükgüngör, Köse, Ozturkkan, & Necefoglu, 2007).

An example of a second mononuclear structure is the nicotinamide complex of Cd(II) 2,4,6-trimethylbenzoate (Figure 1). In this structure, 2,4,6-trimethylbenzoate anions are coordinated as bidentate (Cd-O_{COO} 2.297 Å and 2.527 Å), while nicotinamide (Cd-N 2.371 Å) and water molecules (Cd-O_w 2.306 Å) are monodentate. There is a pentagonal bipyramidal coordination circle around the cadmium atom, and the coordination number of cadmium is seven (Figure 1) (Hökelek, Özkaya, & Necefoğlu, 2018). The cadmium atom shows similar structural behavior in the isonicotinamide complex of cadmium 4-formylbenzoate, where Cd-O_{COO} 2.307-2.606 Å, Cd-O_w 2.327 Å, Cd-N 2.320 and 2.336 Å (Hökelek, Yılmaz, Tercan, Gürgen, & Necefoğlu, 2009).

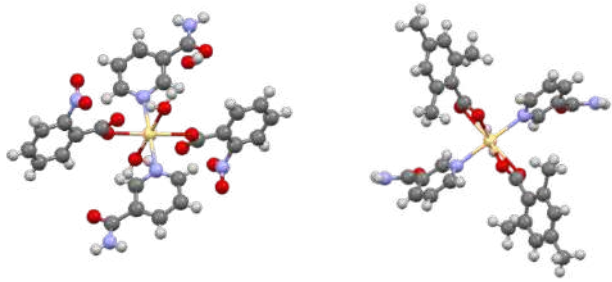

Figure 1. Molecular structures of the nicotinamide complex of cadmium 2-nitrobenzoate (in left) (Zhang, Yang, Lin, & Ng, 2009)and the nicotinamide complex of Cd(II) 2,4,6-trimethylbenzoate (in right) (Hökelek et al., 2018).

Binuclear Complexes

Binuclear complexes of cadmium arylcarboxylates with the formula $[Cd_2(ArCOO)_4(NA)_2(H_2O)_2]$ (ArCOO – arylcarboxylate anion, NA - nicotinamide molecule) appear in two different structures. The first of these structures is schematically given in Figure2.

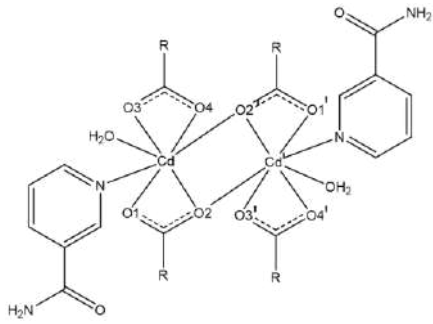

Figure 2. The general molecular structure of the nicotinamide complexes of Cd(II) 4-methyl- (Dincel, Tercan, Çimen, Necefoğlu, & Hökelek, 2012), 4-methylamino-(Hökelek, Sağlam, Tercan, Aybirdi, & Necefoğlu, 2010), 4-dimethylamino- (Hökelek, Süzen, Tercan, Aybirdi, & Necefoğlu, 2010) and 3-fluorobenzoates (Öztürkkan Özbek, Sertçelik, Yüksek, Elmalı, & Şahin, 2020).

As seen in the figure, in the nicotinamide complexes of Cd(II) 4-methyl-(Dincel et al., 2012), 4-methylamino-(Hökelek, Sağlam, et al., 2010), 4-dimethylamino- (Hökelek, Süzen, et al., 2010)(Hökelek, Süzen, et al., 2010)and 3-fluorobenzoates (Öztürkkan Özbek et al., 2020)one of arylcarboxylate anions around the cadmium atom acts as tridentate ligands (Figure 2). Namely, molecules of the complexes are built from centrosymmetric binuclear metal fragments interconnected by two chelate-bridging acid anions, and cadmium atoms complete the environment by coordinating one chelating acid anion, one

monodentate nicotinamide, and one water molecule. The coordination number of each cadmium atom in such dimeric complexes is seven. The bond lengths formed by the cadmium atom and the distances between the two cadmium atoms and the selected bond angles are given in Table 1.

Table 1. The bond lengths and angles of the binuclear complexes.

R	4-CH_3-C_6H_4COO (Dincel et al., 2012)	4-CH_3NH-C_6H_4COO (Hökelek, Sağlam, et al., 2010)	4-$(CH_3)N$-C_6H_4COO(Hökelek, Süzen, et al., 2010)	3-F-C_6H_4COO(Öztürkkan Özbek et al., 2020)
Cd-O1	2.635 Å	2.510 Å	2.571 Å	2.285 Å
Cd-O2	2.272 Å	2.319 Å	2.285 Å	2.585 Å
Cd'-O2	2.527 Å	2.563 Å	2.576 Å	2.591 Å
Cd-O3	2.374 Å	2.384 Å	2.351 Å	2.198 Å
Cd-O4	2.340 Å	2.317 Å	2.336 Å	2.697 Å
Cd-O_w	2.299 Å	2.315 Å	2.317 Å	2.383 Å
Cd-N	2.324 Å	2.327 Å	2.334 Å	2.249 Å
Cd…Cd'	3.780 Å	3.820 Å	3.812 Å	4.078 Å
O1-Cd-O2	52.85°	54.22°	53.78°	53.09°
O3-Cd-O4	55.62°	55.71°	55.96°	52.90°
Cd-O2-Cd'	103.78°	102.88°	103.13°	144.10°

In the isonicotinamide complex of Cd(II) 3-hydroxybenzoate, which has a similar cluster structure, unlike the binuclear complexes mentioned above, the coordination number of the cadmium atom is 6 due to the absence of a water molecule around the coordination. In addition, four uncoordinated water molecules in this compound intermolecular O-H···O and N-H···O hydrogen bonds link the molecules into a three-dimensional network. The distance between two cadmium molecules is 3.818 Å (Zaman, Çaylak Delibaş, Necefoğlu, & Hökelek, 2012).

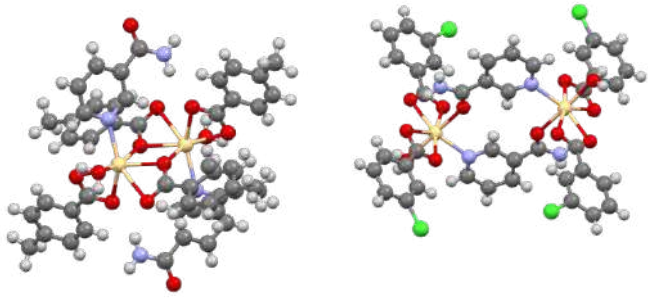

Figure 3. Molecular structures of the nicotinamide complex of cadmium 4-methylbenzoate (in left) (Zaman et al., 2012)and the nicotinamide complex of Cd(II) 3-chlorobenzoate (in right) (Bozkurt, Dilek, Çaylak Delibaş, Necefoğlu, & Hökelek, 2013).

In the centrosymmetric binuclear nicotinamide complex of cadmium(II) 3-chlorobenzoate, the Cd(II) atom is coordinated by one hetero-N atom from one bridging nicotinamide ligand (Cd-N 2.338 Å) and one O_{CO} atom from another symmetry-related bridging nicotinamide ligand(Cd-O_{CO} 2.318 Å), four O_{COO} atoms from two 3-chlorobenzoate ligands (Cd-O_{COO} 2.323 Å, 2.480 Å, 2.545 Å, 2.311 Å) and one water molecule (Cd-O_w 2.302 Å) in a pentagonal bipyramidal geometry (Figure 3). The Cd···Cd' distance is 7.165 Å (Bozkurt et al., 2013).

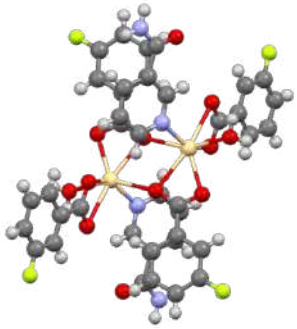

Figure 4. Molecular structure of the nicotinamide complex of cadmium 3-fluorobenzoate (Öztürkkan Özbek et al., 2020).

Unlike the nicotinamide complex of Cd(II) 3-fluorobenzoate, which is synthesized by crystallization at room temperature, the complex with the same formula obtained by hydrothermal synthesis is isomorphic to the nicotinamide complex of Cd(II) 3-chlorobenzoate mentioned above. In this complex, which has a binuclear structure, two nicotinamide molecules act as a bidentate-bridge (Cd-N 2.341 Å, Cd-O_{CO} 2.330 Å) between two cadmium atoms Cd …Cd' 7.204 Å). By the coordination of four chelated oxygen atoms from 3-fluorobenzoate anions (Cd-O_{COO} 2.302 Å, 2.533 Å, 2.342 Å, 2.442Å) and one water molecule (Cd-Ow 2.315 Å), the coordination environment of the cadmium atom is completed to the pentagonal-bipyramid (Figure 4) (Öztürkkan Özbek et al., 2020).

Complexes with ionic, supramolecular, and coordination polymer structures

Among the nicotinamide complexes of cadmium arylcarboxylates, there is an ionic complex. In this complex, where 4-formylbenzoate is the primary ligand, there are two nicotinamide molecules coordinated over the pyridine ring

nitrogen atom and four coordinated water molecules in the cationic unit (Figure 5). There are two 4-formylbenzoate anions in the anionic unit. In the three-dimensional network, cationic and anionic units are connected through hydrogen bonds. The Cd-N bond distance is 2.305 Å (Deng, Gao, & Ng, 2007).

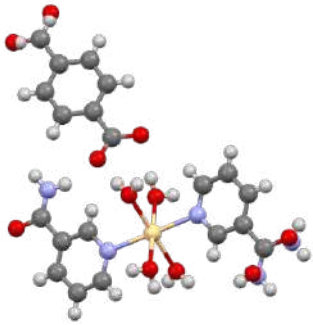

Figure 5. Molecular structure of the nicotinamide complex of cadmium 3-formylbenzoate (Deng et al., 2007).

The cadmium 2-hydroxybenzoate nicotinamide complex is an example of a supramolecular structure. There are two independent molecules in the asymmetric unit of the crystal structure. There is octahedral coordination around the cadmium atom in one unit and pentagonal bipyramidal coordination in the other unit (Figure 6). The unit with octahedral coordination has a trans structure. All ligands were monodentate coordinated. In the other unit, two 2-hydroxybenzoate anions are bidentate chelate coordinated, and water and nicotinamide molecules are monodentate coordinated. The structure also contains four uncoordinated water molecules. Cd-N1 (six coordinated unit) and Cd-N2 (seven coordinated unit) bond distances are 2.3118 Å and 2.2824 Å, respectively (Çaylak Delibaş, Necefoğlu, & Hökelek, 2013).

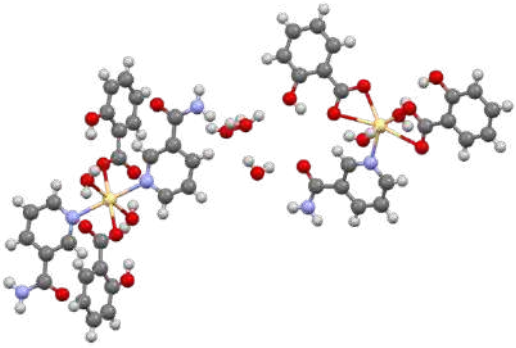

Figure 6. Molecular structures of the nicotinamide complex of cadmium 2-hydroxybenzoate (Çaylak Delibaş et al., 2013).

The cadmium benzenedicarboxylate nicotinamide complex has a coordination polymer structure. In the crystal structure, there is a bidentate chelate 1,4-benzenedicarboxylate anion, two nicotinamide molecules, two bidentate bridge 1,4-benzenedicarboxylate anion around the cadmium atom. In three-dimensional networks, $NH\cdots O_{(COO)}$ is connected by hydrogen bonds. Cd-N distances are determined as 2.358 Å and 2.348 Å. The bond distances between the bidentate chelate coordinate 1,4-benzenedicarboxylate anion and cadmium are 2.297 (Cd-O5) and 2.465 (Cd-O6) Å. Cd-O3 and Cd-O4 distances in carboxylate anion bridges are 2.167 Å and 2.224 Å, respectively (Figure 7)(Chisca et al., 2018).

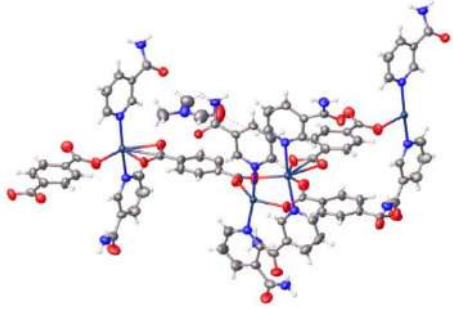

Figure 7. Molecular structures of the nicotinamide complex of cadmium 1,4-benzenedicarboxylate (Chisca et al., 2018).

CONCLUSION

In this study, the crystal structures of nicotinamide complexes of cadmium arylcarboxylates were discussed. These complexes exhibit different structural properties such as monomeric, dimeric, ionic, polymeric and supramolecular. Six of these complexes, which have eleven different examples in the literature, have a dimeric structure. The coordination number of cadmium in all dimeric complexes is seven, and these dimeric complexes contain the water molecule. The number of coordination in the monomeric complex containing 2-nitrobenzoate anion is six, while the number of coordination in the monomeric complex containing 2,4,6-trimethylbenzoate anion is seven. The 4-formylbenzoate anion in the ionic complex is located outside the coordination sphere. The main ligand of the polymeric complex is terephthalic acid, and it is the only complex that does not contain a water molecule among the nicotinamide complexes of cadmium aryl carboxylate. The asymmetric unit in the supramolecular complex, which has interesting structural architecture, contains two different molecules. In the supramolecular structure, 2-

hydroxybenzoate ligand is a monodentate coordinate in one molecule and a bidentate coordinate in another. In a study in which nicotinamide complexes of cadmium 3-fluorobenzoate were synthesized by classical and hydrothermal methods, 3-fluorobenzoate anions form a bridge in the complex synthesized by the classical method, while nicotinamide molecules form a bridge in the complex synthesized by the hydrothermal method.

As a result, nicotinamide complexes of cadmium arylcarboxylates have different structural properties. Arylcarboxylates with different functional groups may have different coordination abilities. Cd-O and Cd-N bond distances can vary in monomeric, dimeric, and coordination polymer structures. While arylcarboxylates can be coordinated in the form of monodentate, bidentate chelate, and bidentate bridge in crystal structures, there are examples of structures where they are not coordinated. Nicotinamide molecules can be coordinated as monodentate or bidentate bridges.

REFERENCES

1. Bhattacharya, B., Dey, R., & Ghoshal, D. (2013). Synthesis, crystal structure and photo luminescent property of a 3D metal-organic hybrid of Cd(II) constructed by two different bridging carboxylate. *Journal of Chemical Sciences*, *125*, 661–666.
2. Bozkurt, N., Dilek, N., Çaylak Delibaş, N., Necefoğlu, H., & Hökelek, T. (2013). Di-μ-nicotinamide-κ $^{2}N^{1}$: O;κ ^{2}O: N^{1} -bis[aquabis(3-chlorobenzoato-κ ^{2}O , O')cadmium]. *Acta Crystallographica Section E Structure Reports Online*, *69*, m389–m390.
3. Çaylak Delibaş, N., Necefoğlu, H., & Hökelek, T. (2013). Diaquabis(2-hydroxybenzoato-κ O^{1})bis(nicotinamide-κ N^{1})cadmium–diaquabis(2-hydroxybenzoato-κ $^{2}O^{1}$, $O^{1'}$)(nicotinamide-κ N)cadmium–water (1/2/4). *Acta Crystallographica Section E Structure Reports Online*, *69*, m191–m192.
4. Çaylak, N., Hökelek, T., & Necefoğlu, H. (2007). Diaquabis(4-fluorobenzoato-κ O)bis(nicotinamide-κ N^{1})cobalt(II). *Acta Crystallographica Section E Structure Reports Online*, *63*, m1341–m1343.
5. Chisca, D., Croitor, L., Petuhov, O., Kulikova, O. V., Volodina, G. F., Coropceanu, E. B., … Fonari, M. S. (2018). Tuning structures and emissive properties in a series of Zn(II) and Cd(II) coordination polymers containing dicarboxylic acids and nicotinamide pillars. *CrystEngComm*, *20*, 432–447.
6. Deng, Z.-P., Gao, S., & Ng, S. W. (2007). Tetraaquabis(nicotinamide-κ N)cadmium(II) bis(4-formylbenzoate). *Acta Crystallographica Section E Structure Reports Online*, *63*, m2323–m2323.
7. Dincel, Ö., Tercan, B., Çimen, E., Necefoğlu, H., & Hökelek, T. (2012). Bis(μ-4-methylbenzoato)-κ ^{3}O , O': O;κ ^{3}O: O, O'-bis[aqua(4-methylbenzoato-κ ^{2}O , O')(nicotinamide-κ N^{1})cadmium]. *Acta Crystallographica Section E Structure Reports Online*, *68*, m1510–m1511.
8. Hökelek, T., Çaylak, N., & Necefoğlu, H. (2007). Diaquabis(4-bromobenzoato-κ O)bis(nicotinamide-κ N^{1})cobalt(II). *Acta Crystallographica Section E Structure Reports Online*, *63*, m1873–m1874.
9. Hökelek, T., & Necefoğlu, H. (2007a). Diaquabis[4-(dimethylamino)benzoato-κ O](nicotinamide-κ N^{1})cobalt(II) dihydrate. *Acta Crystallographica Section E Structure Reports Online*, *63*, m1078–m1080.

10. Hökelek, T., & Necefoğlu, H. (2007b). Diaquabis[4-(dimethylamino)benzoato-κ *O*](nicotinamide-κ N^1)manganese(II) dihydrate. *Acta Crystallographica Section E Structure Reports Online*, *63*, m1279–m1281.
11. Hökelek, T., Özkaya, S., & Necefoğlu, H. (2018). Crystal structure and Hirshfeld surface analysis of aquabis(nicotinamide-κ N^1)bis(2,4,6-trimethylbenzoato-κ ^2O , O')cadmium(II). *Acta Crystallographica Section E Crystallographic Communications*, *74*, 246–251.
12. Hökelek, T., Sağlam, E. G., Tercan, B., Aybirdi, Ö., & Necefoğlu, H. (2010). Bis[μ-4-(methylamino)benzoato]-κ ^3O , O': O ;κ ^3O : O , O'-bis{aqua[4-(methylamino)benzoato-κ ^2O , O'](nicotinamide-κ N)cadmium(II)}. *Acta Crystallographica Section E Structure Reports Online*, *66*, m1559–m1560.
13. Hökelek, T., Süzen, Y., Tercan, B., Aybirdi, Ö., & Necefoğlu, H. (2010). Bis[μ-4-(dimethylamino)benzoato]-κ ^3O , O': O ;κ ^3O : O , O'-bis{aqua[4-(dimethylamino)benzoato-κ ^2O , O'](nicotinamide-κ N^1)cadmium(II)}. *Acta Crystallographica Section E Structure Reports Online*, *66*, m782–m783.
14. Hökelek, T., Yılmaz, F., Tercan, B., Gürgen, F., & Necefoğlu, H. (2009). Aquabis(4-formylbenzoato-κ $^2O^1$, $O^{1'}$)bis(isonicotinamide-κ N^1)cadmium(II) monohydrate. *Acta Crystallographica Section E Structure Reports Online*, *65*, m1416–m1417.
15. Khattak, Z. A. K., Ahmad, N., Younus, H. A., Ullah, H., Yu, B., Munawar, K. S., … Verpoort, F. (2022). Synthesis of 3D Cadmium(II)-Carboxylate Framework Having Potential for Co-Catalyst Free CO2 Fixation to Cyclic Carbonates. *Inorganics*, *10*, 162.
16. Necefoğlu, H., Özbek, F. E., Öztürk, V., Tercan, B., & Hökelek, T. (2011). Diaquabis(4-bromobenzoato-κ *O*)bis(nicotinamide-κ N^1)copper(II). *Acta Crystallographica Section E Structure Reports Online*, *67*, m900–m901.
17. Öztürkkan Özbek, F. E., Sertçelik, M., Yüksek, M., Elmalı, A., & Şahin, E. (2020). The superiority of the classical synthesis compared to the hydrothermal synthesis upon the structural, optical absorption and fluorescent properties of new Cd(II) 3-fluorobenzoate complexes with Pyridine-3-carboxamide/Pyridine-3-carboxylate. *Inorganica Chimica Acta*, *509*, 119694.
18. Şahin, O., Büyükgüngör, O., Köse, D. A., & Necefoglu, H. (2007). Trans-Diaqua-bis(3-hydroxy-benzoato-κO1)bis-(nicotinamide-

κN1)copper(II). *Acta Crystallographica Section C: Crystal Structure Communications*, *63*, m510–m512.

19. Şahin, Onur, Büyükgüngör, O., Köse, D. A., Ozturkkan, E. F., & Necefoglu, H. (2007). Diaquabis(4-fluorobenzoato-κ *O*)bis(nicotinamide-κ *N*)cobalt(II). *Acta Crystallographica Section C Crystal Structure Communications*, *63*, m243–m245.
20. Sen, S., Kumar Saha, M., Kundu, P., Mitra, S., Kruger, C., & Bruckmann, J. (1999). Synthesis and structure of a heptacoordinated cadmium(II) complex. *Inorganica Chimica Acta*, *288*, 118–121.
21. Shmelev M. A. (2020). Polynuclear Homo- and Heterometallic Complexes of Cd(II) with Aromatic Monocarboxylic Acid Anions. N. S. Kurnakov Institute of General and Inorganic Chemistry, Russian Academy of Sciences. PhD Thesis, Moscow, p. 12.
22. Zaman, I. G., Çaylak Delibaş, N., Necefoğlu, H., & Hökelek, T. (2012). Bis(μ-3-hydroxybenzoato)-κ $^{3}O^{1}$, $O^{1'}$: O^{1} ;κ $^{3}O^{1}$: O^{1} , $O^{1'}$ -bis[(3-hydroxybenzoato-κ ^{2}O , O')(isonicotinamide-κ N^{1})cadmium] tetrahydrate. *Acta Crystallographica Section E Structure Reports Online*, *68*, m198–m199.
23. Zhang, K.-L., Yang, B., Lin, J.-G., & Ng, S. W. (2009). Trans,trans,trans-Diaquabis(nicotinamide-κN)bis-(2-nitro-benzoato-κO)cadmium(II) dihydrate. *Acta Crystallographica Section E: Structure Reports Online*, *65*, m292–m292.

Evaluation of anticarcinogenic effects of extracts of *Rosa canina* L. fruits

Füreya Elif ÖZTÜRKKAN and Giray Buğra AKBABA

General Characteristics of *Rosa canina* L.

Rosa canina L., an angiosperm and perennial herb, is a member of the L. Rosaceae family.(Demir and Özcan 2001; Tomljenovic and Pejić 2018).The approximate height of this perennial plant is 2-3 m(Demir and Özcan 2001).Rosehip is a fruit with a length of 16-20 mm and a width of 10-14 mm (Figure 1). The color of the petals is pale pink.The taxonomic classification of *Rosa canina* L. is as follows:

Kingdom	Plantae
Class	Magnoliopsida
Order	Rosales
Family	Rosaceae
Genus	Rosa L.
Species	*Rosa canina* L.- dog rose(URL-1)

Figure 1. Fruits of *Rosa Canina* L. (rosehip).

Rosa canina L. is widely grown in Africa, Asia, and Europe due to the lack of a special climate and soil requirement(URL-2) (Figure 2). It is a plant that grows in almost every region of Türkiye.The fruit of the plant is known as rose hips, and it may be consumed fresh as well as made into syrup, jam, marmalade, flour, and tea (Ayati et al. 2019; Dénes et al. 2012).Rosehip is widely used in folk medicine for the treatment of gastrointestinal diseases, respiratory system ailments, hypertension, and kidney Stones (Ayati et al. 2019; Patel 2017).

In addition, many researchers have reported that rosehip has antioxidant(Czyzowska et al. 2015), anticancer(Mármol et al. 2020), anti-inflammatory(Chrubasik-Hausmann et al. 2014), antiobesity(Goto et al. 2012), antidiabetic(Andersson et al. 2011), antibacterial(Wang, Liang, and Cock 2020), antidepressant(Parandin 2019), hepatoprotective (Sadeghi et al. 2016)and antiulcerogenic(Gurbuz et al. 2003) properties.

For this reason, the plant is thought to have an important place in both folk medicine and modern medicine. Rosehip is used in cosmetics as well as food (Taneva et al. 2016).

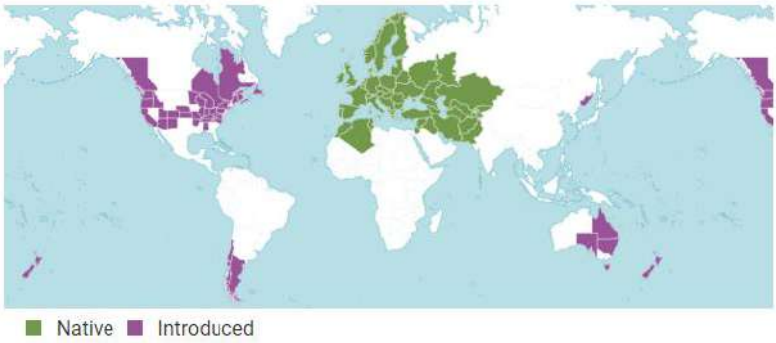

Figure 2. Distribution map of *Rosa Canina* L. (URL-2).

The fruits of *Rosa canina* L. (rosehip) contain phytochemicals such as phenolic compounds, flavonoids, anthocyanins, tannins, and carotenoids (Tahirović and Bašić 2017). It has been determined that these edible fruits contain many phenolic components such as quercetin, gallic acid, epicatechin, salicylic acid, rutin, elagic acid, myricetin, chlorogenic acid, vanilic acid, catechin hydrate, syringic acid and sinapic acid (Cosmulescu, Trandafir, and Nour 2017). When evaluated in terms of mineral content, it has been reported that rosehip fruit, which is rich in calcium, magnesium, and iron, contains traces of sodium, copper, chromium, zinc, and boron. (Cosmulescu et al. 2017; Ercisli 2005). Rosehip contains Thiamin (B_1), Riboflavin (B_2), Niacin (B_3), Pantothenic acid (B_5), Vitamin B_6, and Vitamin A, with a predominance of Vitamin C(Fan, Pacier, and Martirosyan 2014).The biological activity of rosehip is attributed to its rich phytochemical content(Sahingil and Hayaloglu 2022).It has been reported that the chemical composition of the plant varies depending on the region where it was collected, climate, soil quality, degree of maturity, cultivation method, and storage conditions (Fan et al. 2014).

Anticarcinogenic Effects

Effects of Rosa canina L. *on Breast Cancer*

Berköz et al. obtained 70% ethanol extracts of *Rosa canina* L. fruits, which they collected from Mersin, Turkey.The effects of the samples prepared in the concentration range of 12.5-100 µg/mL of these extracts on MCF-7 and MDA-MB-468 breast cancer cells were investigated by apoptosis assay and colorimetric methods MTT and Caspase-3 activity assay.According to the

results obtained using the MTT method, *Rosa canina* L. fruit extracts at a concentration of 25 µg/mL caused significant cytotoxicity on both cell lines at 48 hours of exposure.In addition, when exposures of 24, 48, and 72 hours are taken into account, it has been reported that more cell death occurs as the application time and concentration increase. The findings of the apoptosis assay show that apoptosis occurs on these extracts on both cell lines.However, the findings of Caspase-3 enzyme test, which is another colorimetric method, show that apoptosis occurs in MDA-MB-468 breast cancer cells at a concentration of 25 µg/mL, and no increase in apoptosis occurs on MCF-7 cells in 6, 12 and 24 hours application. According to the results of this study, hydroalcoholic extracts of *Rosa canina* L. fruits have been suggested as anticarcinogenic agents for breast cancer (Berkoz et al. 2019). In another study by Nadpal et al., the effects of water and methanol extracts of fresh and air-dried fruits, and jam and puree of a *Rosa canina* L. sample collected in Serbia, on MCF-7 cells were investigated by the sulphorhodamine B method, but they could not obtain any IC_{50} values (Nađpal et al. 2016). The cytotoxic effects of 80% methanol extracts and methanol extracts containing 0.5% TFA of mature *Rosa canina* L. fruits collected from Northern Portugal were investigated on MCF-7 cells. It has been reported that these extracts exhibited 50% grown inhibition value at a concentration higher than 400 µg/mL(Guimarães et al. 2014).

Effects of Rosa canina L. *on ColonCancer*

The effects of water and methanol extracts of fresh and air-dried fruits of *Rosa canina* L. and its jam and puree were investigated on HT-29 colon cancer cells by the sulphorhodamine B method. But it was determined that all investigated extracts, jam, and puree had any effect on this cell line(Nađpal et al. 2016).Guimaraes et al. investigated the effects of methanol extracts containing 0.5% TFA and methanol-water extracts of ripe *Rosa canina* L. fruits on HCT-15 colon cancer cells using the sulforhodamine B method. They determined the grown inhibition values for these extracts as 243.51 and 243.67 µg/mL, respectively.In addition, according to this result, it was determined that the rosehip extracts used in this study caused more cytotoxic effects on HCT-15 colon cancer cells than MCF-7 cells (Guimarães et al. 2014).Turan et al. investigated the cytotoxic effects of rosehip fruits collected from eastern Turkey and cisplatin on WiDr cells by MTT method.According to the findings of the researchers, when WiDr cells were exposed to fruit extract and cisplatin for 72 hours, the IC_{50} values were determined as 270.00 and 1.30 µg/mL, respectively. However, when the findings of the study were evaluated in general, it was emphasized that *Rosa canina* fruits, which are rich in polyphenols, could be a natural anticarcinogenic agent for WiDr cells(Turan et al. 2018).

Effects of Rosa canina L. *on BrainCancer*

Cagle et al. determined that methanolic rosehip extracts in the concentration range of 25 µg/mL-1 mg/mL exhibited a significant cytotoxic effect on A-172 cells. These extracts caused a decrease in the proliferation of U-251 MG and U-1242 MG cells at concentrations of 1 mg/mL, 250 µg/mL, and 25 µg/mL. According to these findings, methanolic rosehip extracts (North Carolina, USA) caused a decrease in cell proliferation rate in human brain tumor cell lines(Cagle et al. 2012).

Effects of Rosa canina L. *on Lung Cancer*

Guimaraes et al. studied the effects of *Rosa canina* L. fruits on breast and colon cancer cells as well as on NCI-H460 lung cancer cells.While the grown inhibition value for rosehip extracts obtained with 80% methanol solvent was found as 254.69 µg/mL, this value was determined as 305.97 µg/mL for methanol extracts containing 0.5% TFA.This clearly shows that while methanol-water extract causes more cytotoxicity on lung cancer than on breast cancer cells, this cytotoxic effect is similar to the effect on colon cancer cells(Guimarães et al. 2014). In a study on the effects of rosehip on A549 lung cancer cells, the MTT method was used and the exposure time was determined as 72 hours.The cytotoxic effects of DMSO extracts of ripe fruits collected from eastern Turkey were compared with the effects of cisplatin. IC_{50} values were determined as 142.5 and 0.69 µg/mL for the extract and cisplatin, respectively. The apoptotic and cytotoxic effect exhibited by these extracts has been attributed to their phenolic content (Kilinc et al. 2020).

Effects of Rosa canina L. *on LiverCancer*

Fetni et al. investigated the anticarcinogenic effects of rosehip fruit extracts in the concentration range of 0.1-250 µg/mL, collected from Algeria, on HepG2 liver cancer. The IC_{50} value was determined as 30.44 µg/mL. It has been reported that rosehip extracts reduce cell proliferation as the concentration increases, and even at 250 ppm concentration, approximately 75% cell inhibition occurs. The average GI50 value reported by Guimaraes et al. on the same cell line is 270 µg/mL (Guimarães et al. 2014).

Effects of Rosa canina L. *on CervixCancer*

Nadpal et al. reported that water and methanol extracts of fresh and air-dried fruitsand jam of rosehip sample collected from Serbia did not cause cytotoxicity on HeLa cells, while the IC_{50} value for puree was 498 µg/mL. In the study findings of this research group, no IC_{50} value could be determined for breast and colon cancer. The only cell line with reported cytotoxicity is the HeLa cell line (Nađpal et al. 2016). The cytotoxic effects of rosehip on HeLa cells were also investigated by Guimaraes et al. The GI_{50} values determined for

hydromethanolic and methanol extracts containing 0.5% TFA using the SRB method are 253.03 and 311.16 μg/mL, respectively. When these findings were evaluated, Guimaraes and his research group, who investigated the effects of rosehip on breast, lung, colon, cervix, and liver cancer cells, reported that rosehip extracts caused the most cytotoxicity on colon cancer cells (Guimarães et al. 2014).

Effects of Rosa canina L. *on Neuroblastoma Cancer*

Fetni et al. investigated the cytotoxic effects on SH-SY5Y neuroblastoma cells of rosehipextracts collected from Algeria (in the concentration range of 0.1-250 μg/mL). They reported the IC_{50} value as 18.15 μg/mL. The same research group reported that similar to the effects of rosehip extracts on liver HepG2 liver cancer cells, cell proliferation decreased as the concentration increased and approximately 70% cell inhibition occurred at the highest concentration of the study, 250 μg/mL. However, the anticarcinogenic effect of these extracts, whose effects were examined, on SH-SY5Y neuroblastoma cells is greater than the effect on HepG2 liver cancer cells (Fetni, Bertella, and Ouahab 2020).

Effects of Rosa canina L. *on Thyroid Cancer*

Naseri and his study group investigated the anticarcinogenic effects on B-CPAP and Thr.C1-PI 33, which are thyroid cancer cells,of 80% ethanol extracts of rosehip fruits collected in winter in Iran using Trypan blue and MTT methods. It has been reported that extracts in the concentration range of 6.25-800 μg/mL cause more cytotoxicity due to increasing doses and exposure times (24, 48, and 72 hours). In the comparison made in the same study, it was emphasized that rosehip extracts were more cytotoxic on Thr.C1-PI 33 cells (Naseri et al. 2022).

Results and Recommendations

In this study, studies on the anticarcinogenic properties of *Rosa canina* L., which can be consumed in the form of dried and fresh fruit, jam, puree, and tea, were reviewed. It was determined that the effects of extracts of fruits obtained by using different solvents on breast, colon, brain, thyroid, cervix, and neuroblastomacancers were investigated.Since the cytotoxicity determination method, the concept expressing cytotoxicity such as IC_{50} and GI_{50}, the place where the plant is collected and the extraction solvent is different, it is not possible to compare the anticarcinogenic effects on the same cell line in detail.However, when evaluated in general, it is possible to say that the plant has an anti-carcinogenic effect on these cancer cells.In this context, it is necessary to investigate the properties of different in vitro/in vivo antitumoral

methods, different cell lines, different extraction methods, different extraction solvents, and fruits from different localities. Alternative medicine needs more detailed research to use plants in the treatment of diseases.Since *Rosa canina* L., which grows in many parts of the world, is also used in folk medicine, there is an important literature gap on its anticarcinogenic properties. We think that this study will guide further research.

References

Andersson, Ulrika, Emma Henriksson, Kristoffer Ström, Jan Alenfall, Olga Göransson, and Cecilia Holm. 2011. "Rose Hip Exerts Antidiabetic Effects via a Mechanism Involving Downregulation of the Hepatic Lipogenic Program." *American Journal of Physiology-Endocrinology and Metabolism* 300(1):E111–21. doi: 10.1152/ajpendo.00268.2010.

Ayati, Zahra, Mohammad S. Amiri, Mahin Ramezani, Elahe Delshad, Amirhossein Sahebkar, and Seyed A. Emami. 2019. "Phytochemistry, Traditional Uses and Pharmacological Profile of Rose Hip: A Review." *Current Pharmaceutical Design* 24(35):4101–24. doi: 10.2174/1381612824666181010151849.

Berkoz, M., F. Ozkan-Yilmaz, A. Ozluer-Hunt, M. Yildirim, O. Allahverdiyev, and A. Aslan. 2019. "Rosa Canina L. Ethanolic Extract Induces the Antiproliferative and Apoptosis Potential in MCF-7 and MDA-MB-468 Cell Lines." *Fresenius Environmental Bulletin* 28(5):3718–23.

Cagle, Patrice, Ombeni Idassi, Janelle Carpenter, Radiah Minor, Ipek Goktepe, and Patrick Martin. 2012. "Effect of Rosehip (Rosa Canina) Extracts on Human Brain Tumor Cell Proliferation and Apoptosis." *Journal of Cancer Therapy* 03(05):534–45. doi: 10.4236/jct.2012.35069.

Chrubasik-Hausmann, S., C. Chrubasik, E. Neumann, and U. Müller-Ladner. 2014. "A Pilot Study on the Effectiveness of a Rose Hip Shell Powder in Patients Suffering from Chronic Musculoskeletal Pain: ROSE HIP SHELL POWDER FOR MUSCULOSKELETAL PAIN." *Phytotherapy Research* 28(11):1720–26. doi: 10.1002/ptr.5192.

Cosmulescu, Sina, Ion Trandafir, and Violeta Nour. 2017. "Phenolic Acids and Flavonoids Profiles of Extracts from Edible Wild Fruits and Their Antioxidant Properties." *International Journal of Food Properties* 20(12):3124–34. doi: 10.1080/10942912.2016.1274906.

Czyzowska, A., E. Klewicka, E. Pogorzelski, and A. Nowak. 2015. "Polyphenols, Vitamin C and Antioxidant Activity in Wines from Rosa Canina L. and Rosa Rugosa Thunb." *Journal of Food Composition and Analysis* 39:62–68. doi: 10.1016/j.jfca.2014.11.009.

Demir, Fikret, and Musa Özcan. 2001. "Chemical and Technological Properties of Rose (Rosa Canina L.) Fruits Grown Wild in Turkey." *Journal of Food Engineering* 47(4):333–36. doi: 10.1016/S0260-8774(00)00129-1.

Dénes, Andrea, Nóra Papp, Dániel Babai, Bálint Czúcz, and Zsolt Molnár. 2012. "Wild Plants Used for Food by Hungarian Ethnic Groups Living in

the Carpathian Basin." *Acta Societatis Botanicorum Poloniae* 81(4):381–96. doi: 10.5586/asbp.2012.040.

Ercisli, Sezai. 2005. "Rose (Rosa Spp.) Germplasm Resources of Turkey." *Genetic Resources and Crop Evolution* 52(6):787–95. doi: 10.1007/s10722-003-3467-8.

Fan, Cui, Callen Pacier, and Danik M. Martirosyan. 2014. "Rose Hip (Rosa Canina L): A Functional Food Perspective." *Functional Foods in Health and Disease* 4(12):493–509. doi: 10.31989/ffhd.v4i12.159.

Fetni, Samira, Nabil Bertella, and Ammar Ouahab. 2020. "LC–DAD/ESI–MS/MS Characterization of Phenolic Constituents in Rosa Canina L. and Its Protective Effect in Cells." *Biomedical Chromatography* 34(12):e4961. doi: 10.1002/bmc.4961.

Goto, Tsuyoshi, Aki Teraminami, Joo-Young Lee, Kana Ohyama, Kozue Funakoshi, Young-Il Kim, Shizuka Hirai, Taku Uemura, Rina Yu, Nobuyuki Takahashi, and Teruo Kawada. 2012. "Tiliroside, a Glycosidic Flavonoid, Ameliorates Obesity-Induced Metabolic Disorders via Activation of Adiponectin Signaling Followed by Enhancement of Fatty Acid Oxidation in Liver and Skeletal Muscle in Obese–Diabetic Mice." *The Journal of Nutritional Biochemistry* 23(7):768–76. doi: 10.1016/j.jnutbio.2011.04.001.

Guimarães, Rafaela, Lillian Barros, Ricardo C. Calhelha, Ana Maria Carvalho, Maria João R. P. Queiroz, and Isabel C. F. R. Ferreira. 2014. "Bioactivity of Different Enriched Phenolic Extracts of Wild Fruits from Northeastern Portugal: A Comparative Study." *Plant Foods for Human Nutrition* 69(1):37–42. doi: 10.1007/s11130-013-0394-5.

Gurbuz, I., O. Ustun, E. Yesilada, E. Sezik, and O. Kutsal. 2003. "Anti-Ulcerogenic Activity of Some Plants Used as Folk Remedy in Turkey." *Journal of Ethnopharmacology* 88(1):93–97. doi: 10.1016/S0378-8741(03)00174-0.

Kilinc, Kagan, Selim Demir, Ibrahim Turan, Ahmet Mentese, Asim Orem, Mehmet Sonmez, and Yuksel Aliyazicioglu. 2020. "Rosa Canina Extract Has Antiproliferative and Proapoptotic Effects on Human Lung and Prostate Cancer Cells." *Nutrition and Cancer* 72(2):273–82. doi: 10.1080/01635581.2019.1625936.

Mármol, Inés, Nerea Jiménez-Moreno, Carmen Ancín-Azpilicueta, Jesús Osada, Elena Cerrada, and María Jesús Rodríguez-Yoldi. 2020. "A Combination of Rosa Canina Extracts and Gold Complex Favors Apoptosis of Caco-2 Cells by Increasing Oxidative Stress and

Mitochondrial Dysfunction." *Antioxidants* 9(1):17. doi: 10.3390/antiox9010017.

Nađpal, Jelena D., Marija M. Lesjak, Filip S. Šibul, Goran T. Anačkov, Dragana D. Četojević-Simin, Neda M. Mimica-Dukić, and Ivana N. Beara. 2016. "Comparative Study of Biological Activities and Phytochemical Composition of Two Rose Hips and Their Preserves: Rosa Canina L. and Rosa Arvensis Huds." *Food Chemistry* 192:907–14. doi: 10.1016/j.foodchem.2015.07.089.

Naseri, R., E. A. Jegarloee, M. Kamani, F. K. Hematabadi, I. Rashidi, M. Zhaleh, and C. Jalili. 2022. "Anti-Proliferative and Apoptotic Effects of Rosa Canina Fruit Extract on Thyroid Cancer Cells (B-CPAP and Thr.C1-PI 33)." *World Cancer Research Journal* 9(March 2022). doi: 10.32113/wcrj_20223_2246.

Parandin, Rahmatollah. 2019. "Antidepressant Effects of a Hydroalcoholic Extract of Rosa Canina L. on the Depression InDuced by Reserpine in Balb/c Mice." *ISMJ* 22(5):333–46. doi: 10.29252/ismj.22.5.333.

Patel, Seema. 2017. "Rose Hip as an Underutilized Functional Food: Evidence-Based Review." *Trends in Food Science & Technology* 63:29–38. doi: 10.1016/j.tifs.2017.03.001.

Sadeghi, Heibatollah, Saleh Hosseinzadeh, Mehdi Akbartabar Touri, Mehdi Ghavamzadeh, Mehrzad Jafari Barmak, Moslem Sayahi, and Hossein Sadeghi. 2016. "Hepatoprotective Effect of Rosa Canina Fruit Extract against Carbon Tetrachloride Induced Hepatotoxicity in Rat." *Avicenna Journal of Phytomedicine* 6(2):181–88.

Sahingil, D., and A. A. Hayaloglu. 2022. "Enrichment of Antioxidant Activity, Phenolic Compounds, Volatile Composition and Sensory Properties of Yogurt with Rosehip (Rosa Canina L.) Fortification." *International Journal of Gastronomy and Food Science* 28:100514. doi: 10.1016/j.ijgfs.2022.100514.

Tahirović, Azra, and Nađad Bašić. 2017. "Determination Of Phenolic Content And Antioxidant Activity Of Rosa Canina L. Fruits In Different Extraction Systems." *Radovi Šumarskog Fakulteta Univerziteta u Sarajevu* 47(1):47–59. doi: 10.54652/rsf.2017.v47.i1.66.

Taneva, Ira, Nadezhda Petkova, Ivan Dimov, Ivan Ivanov, and Panteley Denev. 2016. "Characterization of Rose Hip (Rosa Canina L.) Fruits Extracts and Evaluation of Their in Vitro Antioxidant Activity." *Journal of Pharmacognosy and Phytochemistry* 5(2):35–38.

Tomljenovic, Nikola, and Ivan Pejić. 2018. "Taxonomic Review of the Genus Rosa." *Agriculturae Conspectus Scientificus* 83(2):139–47.

Turan, Ibrahim, Selim Demir, Kagan Kilinc, Serap Ozer Yaman, Sema Misir, Hanife Kara, Berna Genc, Ahmet Mentese, Yuksel Aliyazicioglu, and Orhan Deger. 2018. "Cytotoxic Effect of Rosa Canina Extract on Human Colon Cancer Cells through Repression of Telomerase Expression." *Journal of Pharmaceutical Analysis* 8(6):394–99. doi: 10.1016/j.jpha.2017.12.005.

(URL-1) https://www.itis.gov/servlet/SingleRpt/SingleRpt?search_topic=TSN&search_value=24819#null) Access date: 06.10.2022

URL-2 https://powo.science.kew.org/taxon/urn:lsid:ipni.org:names:731955-1 access date: 06.10.2022

Wang, Yujun, Yushu Liang, and Ian Cock. 2020. "Rosa Canina L. Fruit Extracts Inhibit the Growth of Bacterial Triggers of Some Autoimmune Inflammatory Diseases and Potentiate the Activity of Conventional Antibiotics." *Pharmacognosy Communications* 10:7–17. doi: 10.5530/pc.2020.1.3.

Recent Advances in Microwave-Assisted Multicomponent Reactions

Rahmi KASIMOĞULLARI[1], Gönül YILDIZ[2]

[1]Professor Dr., Faculty of Arts and Sciences/Department of Chemistry,
Kütahya Dumlupınar University, Kütahya, Turkey,
e-mail: rahmi.kasimogullari@dpu.edu.tr
[2]Responsible Author, Research Assistant,
Faculty of Arts and Sciences/Department of Chemistry,
Kütahya Dumlupınar University, Kütahya, Turkey,
Orcid number: 0000-0002-1886-5964 , e-mail: gonul.yildiz@dpu.edu.tr

1. Introduction

Microwave, typically electromagnetic radiation, is located between infrared IR and radio waves. Microwave technology has a wide range of applications in organic chemical synthesis today [1].Today, microwave technology is widely used in organic chemical synthesis. The absorption and transmission of microwave radiation are fundamentally different from conventional heating. Traditional heating uses convection and conduction to transfer energy from the surface to the ground, requiring the vessel to be superheated to reach the target temperature. This is an inefficient heating method because the surface temperature is higher than the bulk temperature. On the other hand, microwave radiation occurs through efficient internal heating due to the direct correlation of microwave energy to the batch reaction mixture[2].

Only one or two compounds are involved in a chemical reaction. Reactions that form products from three or more different starting compounds in a single vessel are called multicomponent reactions (MCRs) [3]. In recent years, multicomponent reactions have received great attention due to the minimization of operating steps, energy consumption, cost, time, and the number of reagents [4]. Microwave-assisted reactions, on the other hand, have advantages such as shorter reaction times, higher yields, and less by-product formation. It significantly accelerated the reaction rates of many chemical reactions. In addition, some reactions that cannot be performed or are difficult with classical methods have been made possible with the microwave method [5].

2. Three-component microwave assisted reactions

Khan *et al* (2022) synthesized the compound 3-nitro-*N*,2-diphenyl-2*H*-chromen-4-amine in the microwave with 91%yield efficiency in a short time, based on the (*E*)-2-(2-nitrovinyl)phenol compound, aniline and benzaldehyde compounds (three-components). DMSO was used as solvent and L-proline as catalyst in this reaction. This reaction in the microwave has provided another advantage in addition to creating products in a short time and using a cheap and easily available catalyst [6].

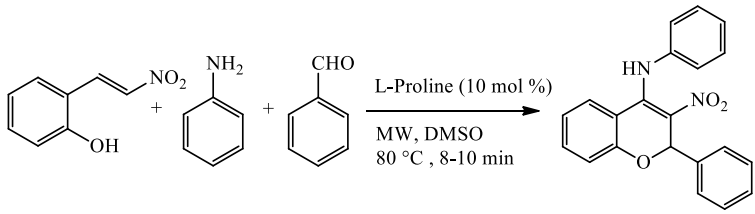

Jamali *et al* (2022) synthesized 2-hydroxy-4-(4-hydroxyphenyl)-5*H*-indeno[1,2-*b*]pyridine-5-one compound with 95% yield efficiency in a single container in the microwave based on the compounds 1*H*-indene-1,3(2*H*)-dione,

acetamide, and 4-hydroxybenzaldehyde. Different methods were tried in the study. For example; Although the reaction time is continued for up to 8 hours using the same components and catalyst, the reaction is not completed. But this reaction took place in the microwave with the same components and catalyst in 5 minutes [7].

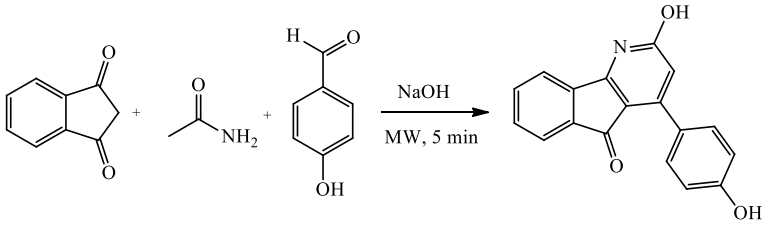

Kumar *et al* (2020) reacted 4-amino-2*H*-chromen-2-one (2 eq.) and 4-nitrobenzaldehyde (1 eq.) compounds in the microwave in acetonitrile and ethylene glycol. As a result of the multicomponent reaction, they obtained the compound 7-(4-nitrophenyl)dichromeno[4,3-*b*:3',4'-*e*]pyridine-6,8(7*H*,14*H*)-dione with 92% yield efficiency [8].

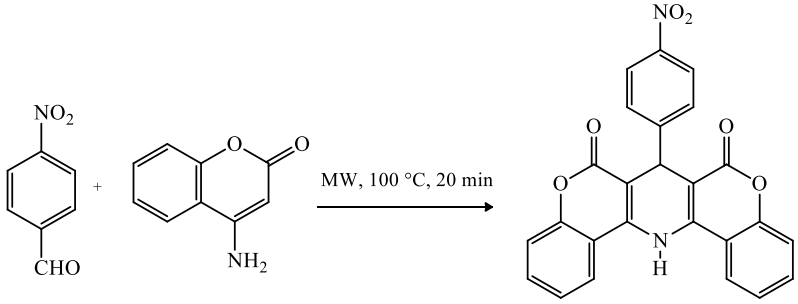

Teleb *et al* (2021) synthesized the 7-(4-methoxyphenyl)-3-phenyl-9-(thiophen-2-yl)pyrido[3',2':4,5]thieno[3,2-*d*]pyrimidin-4(3*H*)-one compound with high efficiency in the microwave using the multicomponent technique. Starting compounds; consist of three components: 1,1-dimethoxy-*N*,*N*-dimethylmethanamine, aniline, and ethyl 3-amino-6-(4-methoxyphenyl)-4-(thiophen-2-yl)thieno[2,3-*b*]pyridine-2-carboxylate. Using the same temperature (110 °C) and the same solvent (Dioxane), 2 different methods were tried and the effect on yield was investigated. In the study, the target product was synthesized with 69% yield efficiency in 10 hours with the traditional method, while it was synthesized in the microwave with 77% yield efficiency in 45 minutes [9].

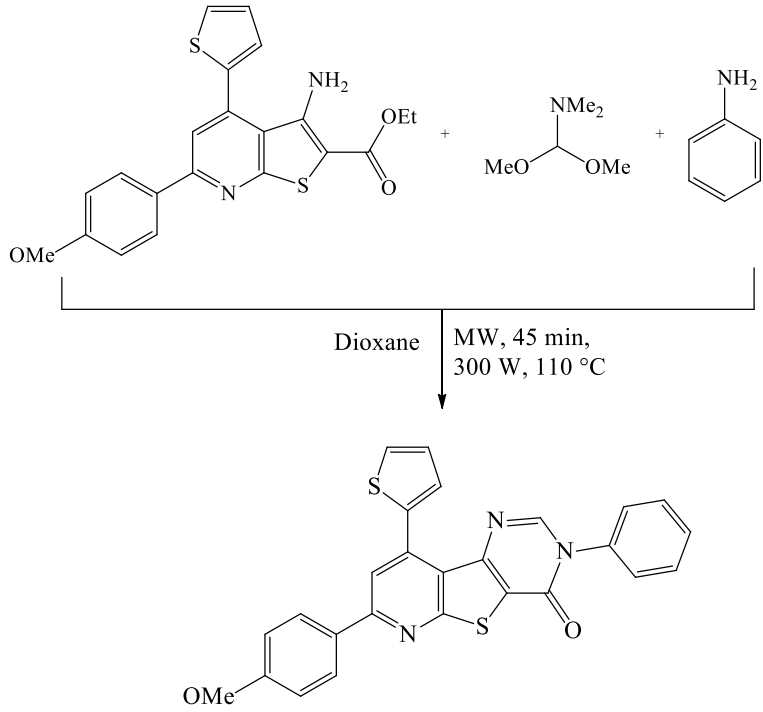

The compound 5-nitro-1,3,6-triphenyl-1,2,3,4-tetrahydropyrimidine was synthesized by Gülbenek *et al* (2022) using a multicomponent reaction technique. (*E*)-*N*-(2-nitro-1-phenylvinyl)aniline,formaldehyde, and aniline were used as components. As a result of this reaction in the microwave, the target product was realized with 78% yield efficiency in 40 minutes. The same components were realized with 40% yield efficiency in 18 hours under the Et_3N catalyst [10].

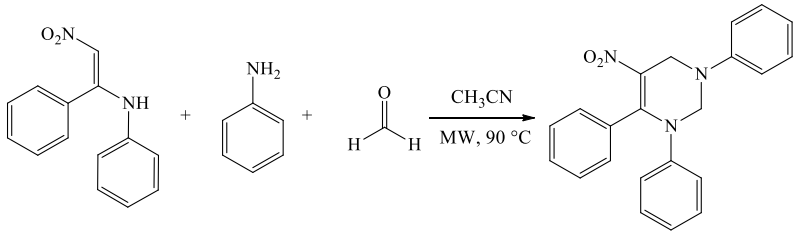

Lim *et al.* (2018) synthesized 7-amino-substituted 4-aminopyrazolo[1,5-*a*][1,3,5]triazine-8-carboxylates derivatives in a tep container based on three-components. For this, 5-aminopyrazole-4-carboxylates, trimethyl orthoformate, and cyanamide compounds were used. As for solvents, different solvents were tried, but the highest yield was observed to be realized in methanol. In this study, the reactions were carried out with high efficiency in 25 minutes in the microwave [11].

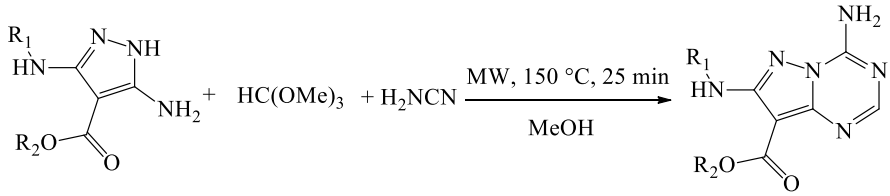

R_1	R_2
Ph	Et
3-Me-Ph	Me
3-I-Ph	Et
4-F-Ph	Et
4-Cl-Ph	Me

3. Four-component microwave assisted reactions

In 2006, Adib *et al.* and colleagues first mixed aldehyde and ketone at room temperature for 2.5 hours in the presence of sodium hydroxide. Then hydroxylamine and acetic acid were mixed at room temperature for 2.5 hours. These two mixtures were taken and placed in the microwave and 2,4,6-triarylpyrimidines derivatives were synthesized. The efficiency of these reactions, which take place in 3 minutes at 150 °C, is in the range of 86–95% yields [12].

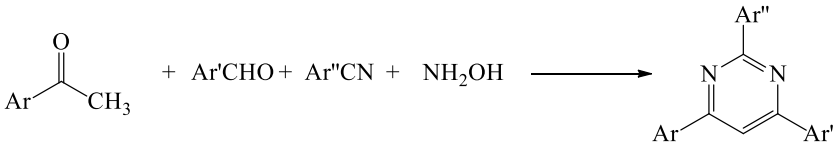

Ar	Ar'	Ar"
Ph	Ph	Ph
4-CH_3-Ph	4-MeO-Ph	4-Br-Ph
	4-Cl-Ph	4-Cl-Ph
	4-NO_2-Ph	4-CH_3-Ph
		4-MeO-Ph

Mohammadrezaei *et al.* (2019) synthesized the compound 3-methyl-16-(4-nitrophenyl)benzo[*a*]pyrano[3',4':5,6]pyrano[2,3-*c*]phenazin-1(16*H*)-one with four-components by multicomponent reaction method. This reaction, which was catalyzed by phosphotungstic acid, took place in the microwave with an efficiency of 88% yield in 20 minutes [13].

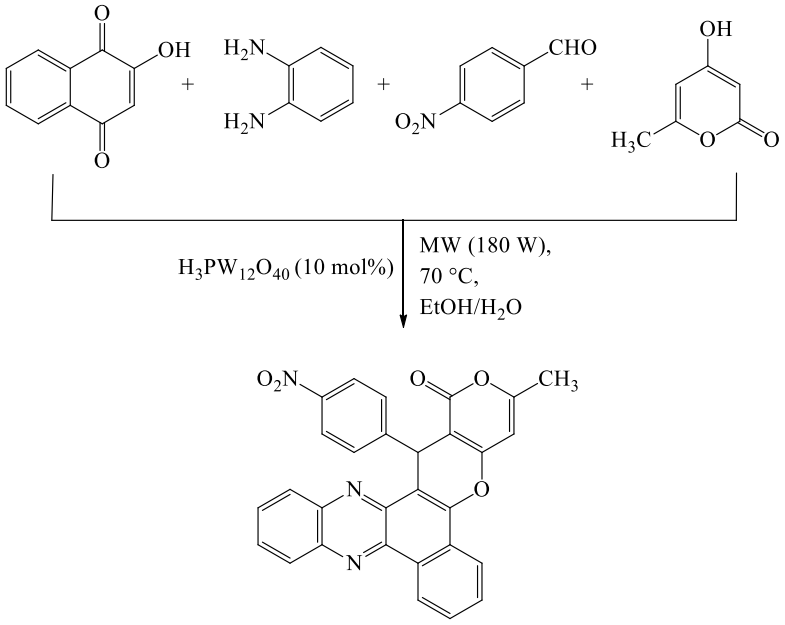

Lian *et al* (2014) synthesized new arylboronic acid derivatives using a four-component Ugi reaction method. These reactions occurred under appropriate conditions (45 minutes, 45 °C, 150 W) with efficiencies in the range of 52-81% in the microwave [14].

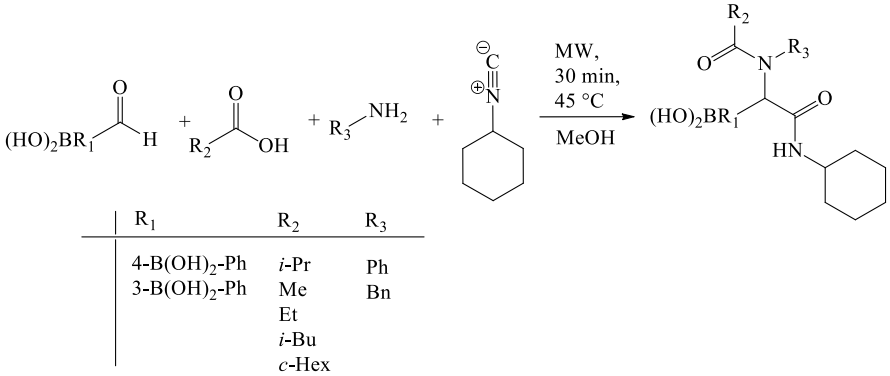

R_1	R_2	R_3
4-$B(OH)_2$-Ph	*i*-Pr	Ph
3-$B(OH)_2$-Ph	Me	Bn
	Et	
	i-Bu	
	c-Hex	

Miranda *et al.* (2020) synthesized ethyl 3-(tert-butylamino)-2-(*N*-(cyclohexylmethyl)benzamido)-3-oxopropanoate compound in a microwave using a four-component multicomponent reaction technique. In this study, four-components in the reaction; benzoic acid, ethyl 2-oxoacetate, phenylmethanamine and 2-isocyano-2-methylpropane were used. As a result of this reaction in indium(III) chloride and 2,2,2-trifluoroethanol, the target product has a yield of 49% [15].

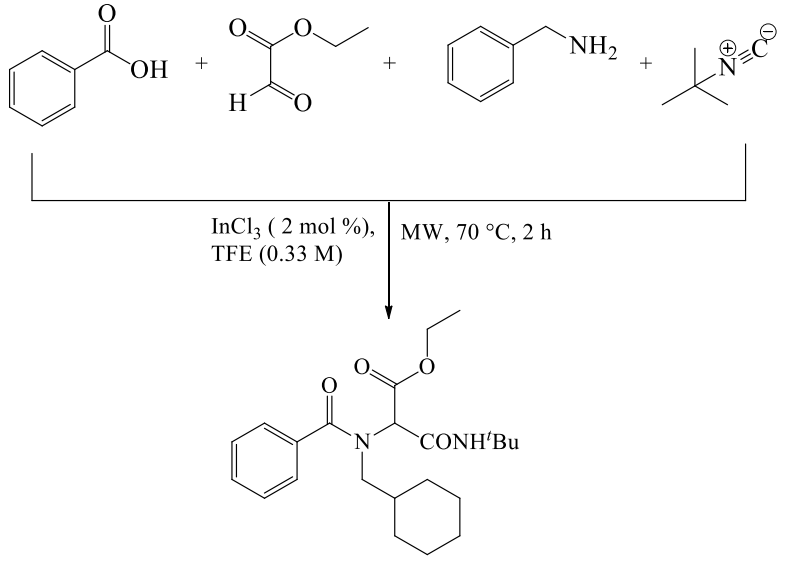

In their study, Thi *et al*. synthesized the new podophyllotoxin-naphthoquinone and its derivatives by a microwave-assisted four-component reaction of 2-hydroxy-1,4-naphthoquinone, aromatic benzaldehyde, thromone acid, and ammonium acetate. The reaction time is 15 minutes and the yield of the products obtained as a result of this reaction is in the range of 78-82% yield [16].

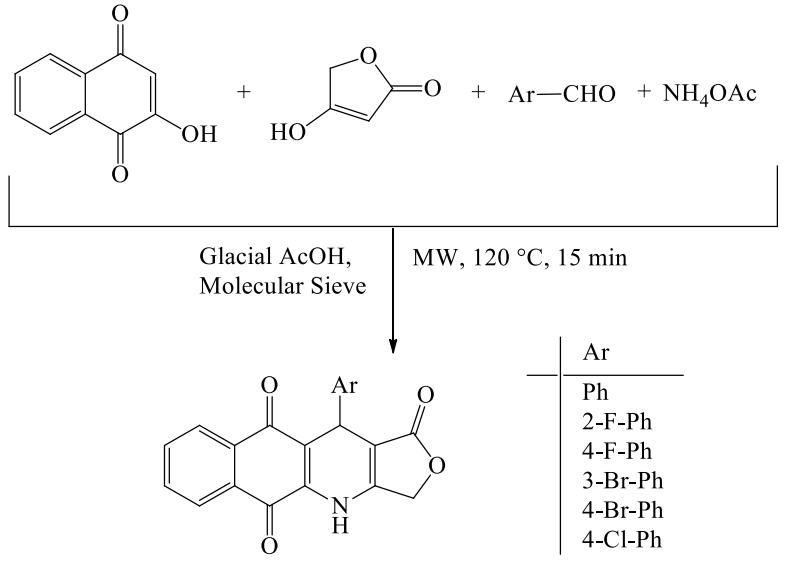

Tangeti *et al.* (2016) obtained coumarin-containing dihydrofuran-derived compounds by multicomponent reaction in a single container. By developing an effective method, 4-hydroxy-6-methyl-2*H*-pyran-2-one, 2-hydroxy aromatic aldehydes, aromatic aldehyde, and pyridinium ylide compounds were reacted in

the microwave under appropriate conditions. The 12 compounds synthesized in this study have yields in the range of 71-89% yield [17].

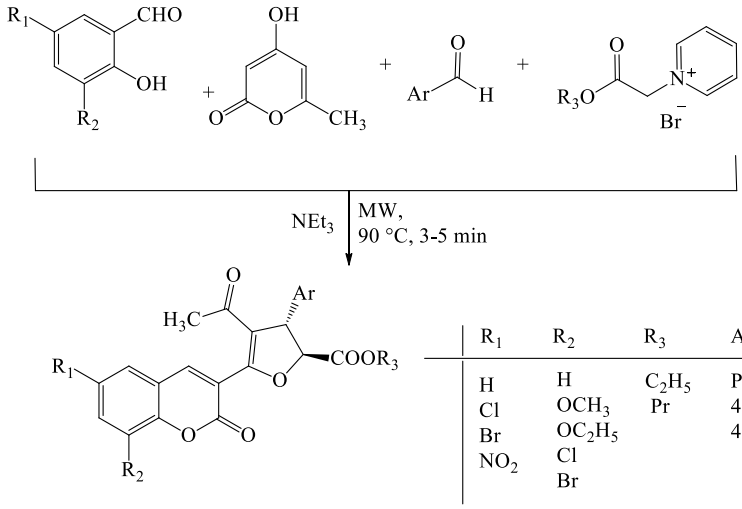

R_1	R_2	R_3	Ar
H	H	C_2H_5	Ph
Cl	OCH_3	Pr	4-NO_2-Ph
Br	OC_2H_5		4-N(CH_3)$_2$-Ph
NO_2	Cl		
	Br		

Conclusion

To date, researchers have performed numerous microwave-assisted multicomponent reactions and evaluated the results. Especially in cases where a long-term reaction is required, the microwave method is very effective to shorten the reaction times and increase the yield of the products. In this review, the advantages of microwave, microwave-assisted three-component and four-component multicomponent reactions were examined. Based on multiple components, it will offer advantages for researchers who want to carry out the reaction in a shorter time with high efficiency and want it to be economical.

References

1. Alsafi, M. A., Al-Dhuwayin, B. H., El-Sofany, W. I., Rateb, H. S., & Flefel, E. M. (2022). Functionalization of novel anti-microbial drug based on molecular docking study for nicotinonitrile analogs prepared by microwave irradiation. *Journal of Molecular Structure*, *1264*, 133261. DOI: 10.1016/j.molstruc.2022.133261
2. Adhikari, A., Bhakta, S., & Ghosh, T. (2022). Microwave-assisted synthesis of bioactive heterocycles: An overview. *Tetrahedron*, 133085. DOI: 10.1016/j.tet.2022.133085
3. Ugi, I., Dömling, A., & Hörl, W. (1994). Multicomponent reactions in organic chemistry. *Endeavour, 18*(3), 115-122.
4. Jadhav, C. K., Nipate, A. S., Chate, A. V., Pathan S. J., Malwankar K. A., Warawdekar U. K., & Gill, C. H. (2020). Rapid Multicomponent Tandem Annulation in Ionic Liquids: A Convergent Access to *N*-alkylated pyridines as Potential Anticancer Scaffolds. *Journal of Heterocyclic Chemistry.* DOI:10.1002/jhet.4187
5. Das, A., & Banik, B. K. (2021). Foundational principles of microwave chemistry. *Microwaves in Chemistry Applications*, *3*–26. DOI: 10.1016/b978-0-12-822895-1.00005-9
6. Khan, D., Sharma, S., & Shukla, P. (2022). Microwave assisted L-proline catalyzed one-pot three–component reaction for the synthesis of 4-aminoaryl-2-phenyl-2*H*-3-nitrochromene hybrid via Domino Michael-Henry-Michael addition reaction. *Journal of Heterocyclic Chemistry*. *59*:1064–1072. DOI: 10.1002/jhet.4447
7. Jamali, M., Sardarian, A. R., Rezaei, F., Ghanbari, M. M., & Mohajeri, A. (2022). Highly efficient microwave-assisted solvent free sequential one-pot multicomponent synthesis of novel 2-hydroxy indenopyridin-5-ones and mechanismic computational study. *Journal of Heterocyclic Chemistry*, *59*(1), 161-171. DOI: 10.1002/jhet.4375
8. Kumar, A., Mahiya, K., Prasad, A. K., & Singh, S. K. (2022). Multicomponent Synthesis of 4-Aryl-1,4-Dihydro-Oxochromeno[3,2-*b*] Oxoindeno[6,5-*e*]Pyridine. *Polycyclic Aromatic Compounds*, *42*(5), 2555-2567. DOI: 10.1080/10406638.2020.1852269.
9. Mohamed Teleb, M. A., Mekky, A. E., & Sanad, S. M. (2021). 3-Aminothieno[2,3-*b*]pyridine-2-carboxylate: Effective precursor for microwave-assisted three components synthesis of new pyrido[3′,2′:4,5]thieno[3,2-*d*]pyrimidin-4(3*H*)-one hybrids. *Journal of Heterocyclic Chemistry*, *58*(9), 1825-1835. DOI: 10.1002/jhet.4313

10. Gülbenek, C., Yıldırım, M., & Yıldırım, A. (2022). Microwave-mediated approach to highly substituted nitropyrimidines via double Mannich reactions and their biological properties. *Tetrahedron*, *120*, 132904. DOI: 10.1016/j.tet.2022.132904
11. Lim, F. P. L., Halcovitch, N. R., Tiekink, E. R., & Dolzhenko, A. V. (2018). A new microwave-assisted, three-component reaction of 5-aminopyrazole-4-carboxylates: Selective synthesis of substituted 5-aza-9-deaza-adenines. *Tetrahedron*, *74*(15), 1868-1879. DOI: 10.1016/j.tet.2018.02.054
12. Adib, M., Mahmoodi, N., Mahdavi, M., & Bijanzadeh, H. R. (2006). Microwave-assisted simple, one-pot, four-component synthesis of 2,4,6-triarylpyrimidines under solvent-free conditions. *Tetrahedron Letters*, *47*(52), 9365-9368. DOI: 10.1016/j.tetlet.2006.10.090
13. Mohammadrezaei, M., Mohebat, R., & Tabatabaee, M. (2019). Microwave-assisted Multi-component Domino Reaction for the Green Synthesis of Novel Benzo[*a*]pyrano[3',4':5,6]pyrano[2,3-*c*]phenazines Using $H_3PW_{12}O_{40}$ as Efficient, Cost-effective and Recyclable Catalyst. *Organic Preparations and Procedures International*, *51*(5), 477-485. DOI: 10.1080/00304948.2019.1653128
14. Lian, R. C., Lin, M. H., Liao, P. H., Fu, J. J., Wu, M. J., Wu, Y. C., ... & Pan, P. S. (2014). Direct synthesis of the arylboronic acid analogues of phenylglycine via microwave-assisted four-component Ugi reaction. *Tetrahedron*, *70*(9), 1800-1804. DOI: 10.1016/j.tet.2014.01.016
15. Borja-Miranda, A., Valencia-Villegas, F., Lujan-Montelongo, J. A., & Polindara-García, L. A. (2020). Synthesis of polysubstituted isoindolinones via radical cyclization of 1,3-dicarbonyl Ugi-4CR adducts using tetrabutylammonium persulfate and TEMPO. *The Journal of Organic Chemistry*, *86*(1), 929-946. DOI: 10.1021/acs.joc.0c02441
16. Thi, Q. G. N., Le-Nhat-Thuy, G., Thi, T. A. D., Thi, P. H., Tuan, A. N., Thi, T. H. N., ... & Van Nguyen, T. (2021). Synthesis of novel potent cytotoxicy podophyllotoxin-naphthoquinone compounds via microwave-assited multicomponent domino reactions. *Bioorganic & Medicinal Chemistry Letters*, *37*, 127841. DOI: 10.1016/j.bmcl.2021.127841
17. Tangeti, V. S., Varma K, R., Siva Prasad, G. V., & Satyanarayana, K. V. V. V. (2016). Synthesis of C3-dihydrofuran substituted coumarins via multicomponent approach. *Synthetic Communications*, *46*(7), 613-619. DOI: 10.1080/00397911.2016.1159696

Chemical Characteristics, Synthetic Methods, and Recent Developments in the Research Field of Pyrazole Derivatives

Gönül YILDIZ[1], Rahmi KASIMOĞULLARI[2]

Responsible Author, Research Assistant,
Faculty of Arts and Sciences/Department of Chemistry,
Kütahya Dumlupınar University, Kütahya, Turkey,
Orcid number: 0000-0002-1886-5964 , e-mail: gonul.yildiz@dpu.edu.tr
[2]Professor Dr., Faculty of Arts and Sciences/Department of Chemistry,
Kütahya Dumlupınar University, Kütahya, Turkey,
e-mail: rahmi.kasimogullari@dpu.edu.tr

1. Introduction

Pyrazoles (Fig. 1), are aromatic diazoles with five-membered ring that exhibit a wide range of chemical and biological characteristics and they also have reached substantial popularity owing to their multipleuses [1].

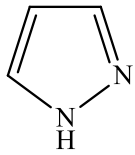

Figure 1: Structure of pyrazole

The pyrazole ring containing nitrogen is pyridine and pyrrole-like molecule. The nitrogen atom 1 makes the ring "pyrrole-similar" since its unrequited electrons are conjugated by an aromatic system. The nitrogen atom 2 makes the ring "pyridine-similar" because the unrequited electrons are not affected by resonance, as in the pyridine system. These structural differences make pyrazole to react with acids and bases [2] (Fig. 2).

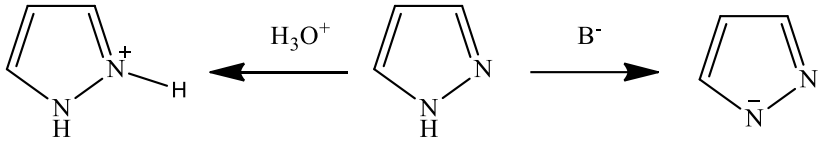

Figure 2: Cations and anions obtained from pyrazole.

Pyrazole and its derivatives are very active groups of compounds, exhibiting an extensive range of pharmacological activities such as anti-tuberculosis, anti-tumor, cardiovascular, analgesic, anti-bacterial, anti-convulsant, and anti-inflammatory activities [3]. Therefore, these compounds are synthesized and evaluated as target structures by many researchers for their biological activity[4]. The structures of some pyrazole compounds marketed in different countries as pharmacological agents are shown in Table 1.

Table 1. List of some pyrazole compounds marketed as pharmacological agents.

Pyrazole Derivative	Structure	Pharmacological Property
Crizotinib [5]	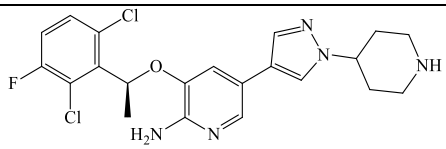	Anti-cancer
Antipyrine [6]	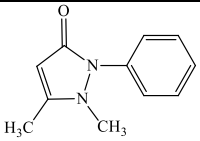	Non-steroidal anti-inflammatory drug (NSAID)
Fomepizole [7]	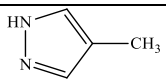	Antidote for methanol poisoning
Mepiprazole [8]	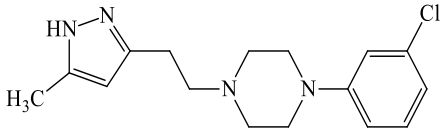	Minor tranquilizer

2. Synthesis of pyrazole derivatives

Various processes with their references were reported for the synthesis of pyrazoles listed below with explanations:

From ethyl 2,4-dioxopentanoate: Karrouchi *et al*. synthesized ethyl 5-hydroxy-1-isonicotinoyl-3-methyl-4,5-dihydro-1*H*-pyrazole-5-carboxylate with nearly 85% yield as a result of condensation reaction between ethyl 2,4-dioxopentanoate and isonicotinohydrazide [9] (Scheme 1).

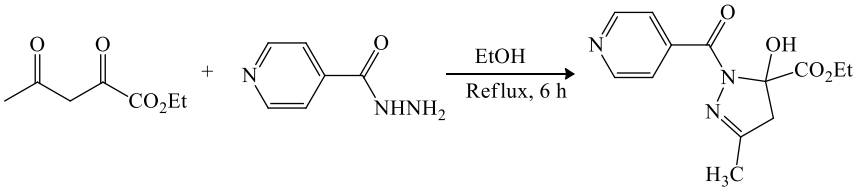

Scheme 1

From furandione: Sener *et al.* synthesized a new compound containing pyrazole carboxylic acid with the reaction between furandione derivative compounds and nitrophenyl-hydrazine derivative compounds. Then, this compound was converted to acid chloride, nitrile, ester, and amides [10] (Scheme 2).

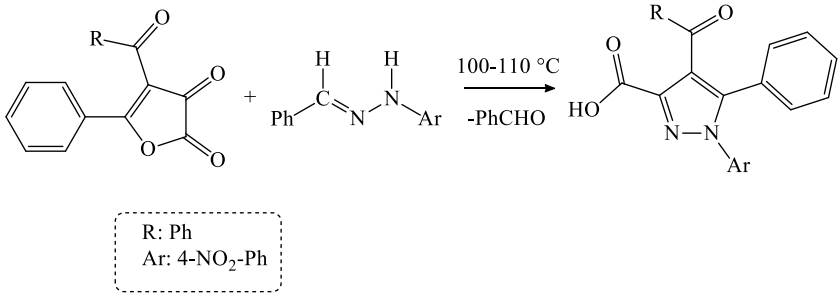

Scheme 2

In 2015, Kasımoğulları *et al.* synthesized new pyrazole carboxylic acid derivatives with high yield using different functional groups (R: OEt and Ar: 3-NO_2-Ph) with the same method. The synthesized pyrazole carboxylic acid compound was converted to the amide derivative at the beginning and then the full reduction reaction was carried out. The resulting product was treated with *β*-naphthol as a result of the diazotization reaction [11] (Scheme 3).

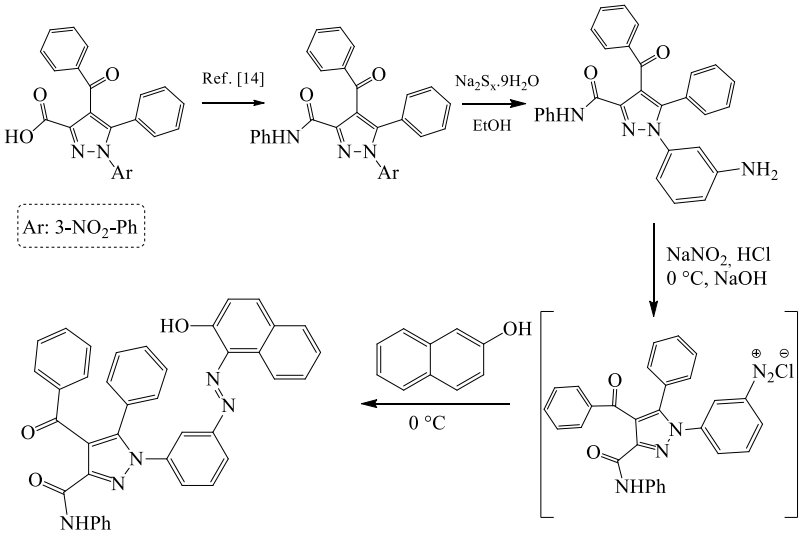

Scheme 3

From asetofenon: Yan *et al*. firstly synthesized the compound (*E*)-1-phenyl-2-(1-phenylethylidene) hydrazine with the reaction between acetophenone and phenylhydrazine compounds. This synthesized compound was converted to 1,3-diphenyl-1*H*-pyrazole-4-carbaldehyde with 81% yield under Vilsmeier-Haack (DMF-$POCl_3$) conditions [12] (Scheme 4).

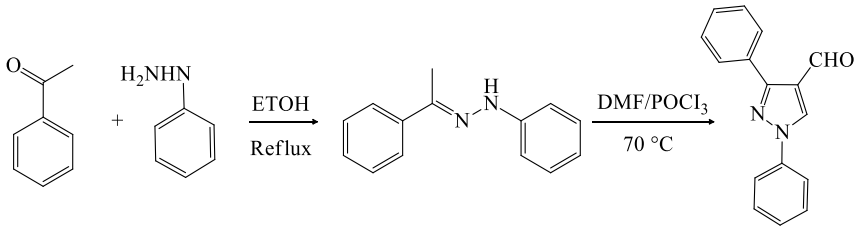

Scheme 4

From 4-methylbenzaldehyde: Muhammed TK *et al.*synthesized the (*E*)-1-phenyl-3-(*p*-tolyl)prop-2-en-1-one compound by Claisen Schmidt condensation of the acetophenone compound with 4-methylbenzaldehyde. This synthesized compound was further modified by cyclization with acetic acid and hydrazine hydrate to yield 1-(3-phenyl-5-(*p*-tolyl)-4,5-dihydro-1*H*-pyrazol-1-yl)ethanone compound [13](Scheme 5).

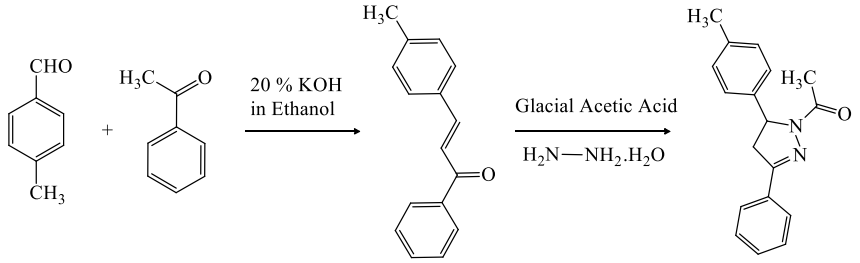

Scheme 5

From N'-(2-oxo-2-phenylethyl)benzohydrazide: Ardakani *et al.* synthesized functionalized 2,3-dihydro1*H*-pyrazoles with a high yield as a result of the three-component closure reaction between alkyl isocyanides and *N*'-(2-oxo-2-phenylethyl)benzohydrazide [14](Scheme 6).

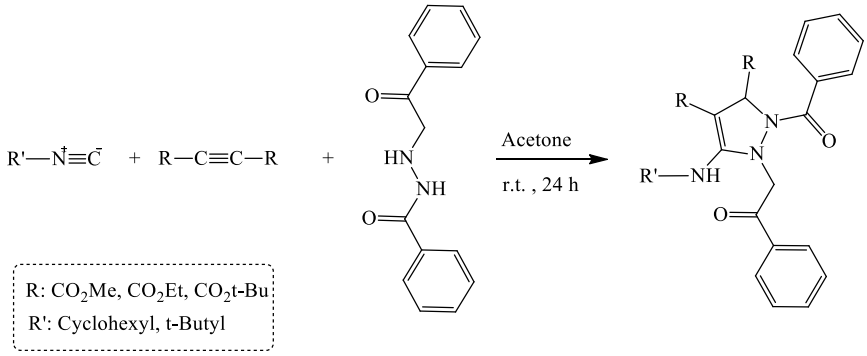

Scheme 6

From aniline and aniline derivative: Demirçalı synthesized aniline and aniline derivative compounds with phenylcarbonohydrazonoyl dicyanide and its derivatives by the reaction with malononitrile solution in pyridine at 0–5 °C. Then, the derivatives of 4-(phenyldiazenyl)-1*H*-pyrazole-3,5-diamine were synthesized by combining arylazo malononitrile compounds with hydrazine [15] (Scheme 7).

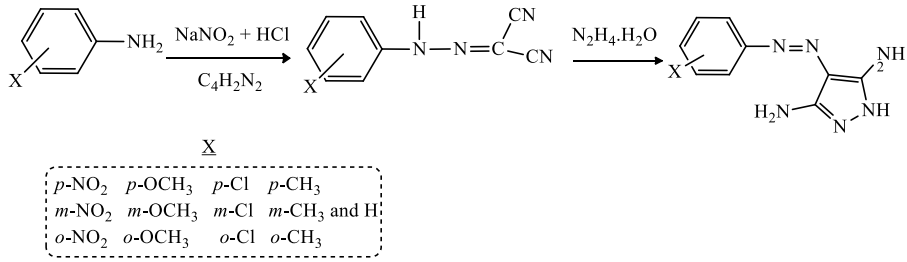

Scheme 7

3. Isolation of natural pyrazoles, their medicinal importance, and synthetic ways.

3.1. *Fluviols*

Fluviols are antibiotics rich in bicyclic nitrogen categorized as Fluviol A, Fluviol B, Fluviol C, Fluviol D, and Fluviol E. Fluviols are produced by *Pseudomonas fluorescenes*. According to the biological activity studies of Smirnov *et al*., among these Fluviols, Fluviol E showed broad antibacterial activity by inhibiting the growth of gram-positive and gram-negative bacteria. Furthermore, it halted the growth of Ehrlich carcinoma by up to 40%. Fluviol C shows a lower antibacterial potency and a less toxicity than Fluviol E and a modest anti-tumor activity by inhibiting the growth of Ehrlich carcinoma by 64%. Fluviol A, the demethylated derivative of Fluviol E, has a low toxicity and

shows potent anti-tumor effects by inhibiting the growth of Ehrlich carcinoma by 83% [16] (Fig. 3).

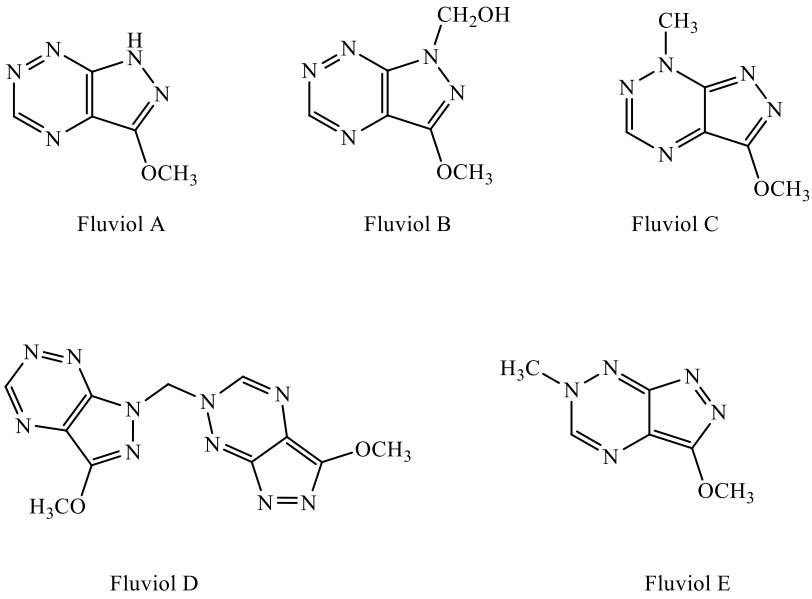

Figure 3

3.2. *L-α-Amino-β-(pyrazolyl-N)-propanoic acid*

L-α-amino-*β*-(pyrazolyl-*N*)-propionic acid or named as [(*S*)-*β*-pyrazolylalanine or *β*-pyrazol-1-yl-L-alanine] is a histidine isomer. It is isolated as a first time in 1957 from *Citrullus vulgaris* juice. It is also the first natural product example of pyrazole with anti-diabetic activity [17] (Fig. 4).

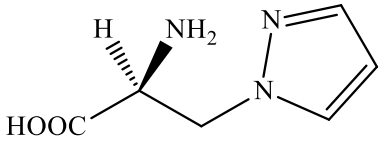

Figure 4

3.3. *Withasomnine*

Withasomnine is a pyrazole alkaloid and was first isolated from the stems of the *Withania Somnifera* Dun (*Solanaceae*) plant in 1966. This herb, especially used medicinally, is native to South Africa and India [18]. Traditionally, this plant is widely used worldwide as an immuno-modulator, anti-inflammatory, anti-stress, anti-cancer, anti-dementia, cardio-protective, health booster for mental and physical health, low blood pressure, diabetes treatment, aphrodisiac, enhances memory, and etc. The plant is also effective against different types of

cancers and problems of colon, blood, breast, lung, prostate, skin, liver, blood, and kidney [19] (Fig. 5).

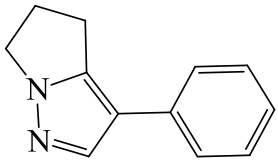

Figure 5

4. Biological Activity of Pyrazole

Theattendance of pyrazole compounds such as*celecoxib*(Anti-inflammatory and analgesic agent),*CDPPB*(antipsychotic), *Rimonabant*(CB1 receptor modulator),*Difenamizole*(Pain relief), *Betazole* (H2 receptor agonist), *Fezolamine* (Antidepressant)aspharmacological agents of several therapeutic classes provides a wide rangeof biological activities [20]. These examples of pyrazoles have been shown in Fig. 6.

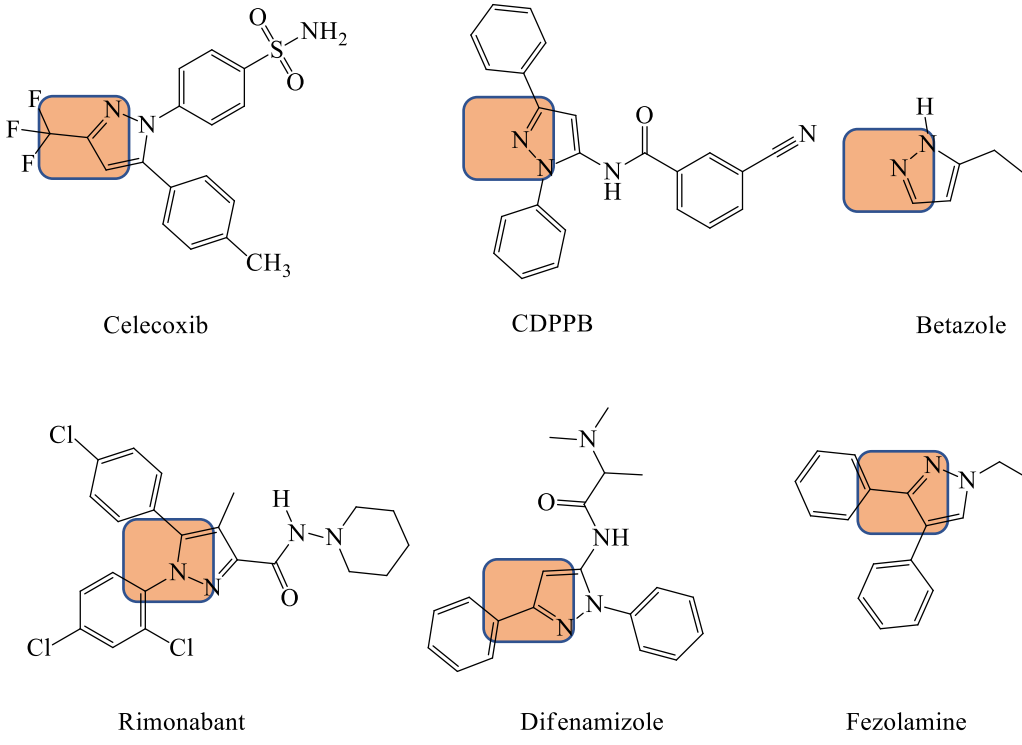

Figure 6: Some pharmacologically significant active pyrazoles.

Pyrazole as anti-tubercular activity: Compounds synthesized by Pathak *et al.* were analyzed with in vitro anti-tubercular activity upon *Mycobacterium tuberculosis* H37Rv strain by radiometric measurements with BACTEC 460. Among these compounds with higher activity upon *M. tuberculosis* H37Rv were discovered with the *N*-((2*R*,3*R*)-3-chloro-2-(2-hydroxyphenyl)-4-oxoazetidin-1-yl)-3-(4-chlorophenyl)-1*H*-pyrazole-5-carboxamide (MIC^b: 0.35 μg/mL) compound [21] (Fig. 7).

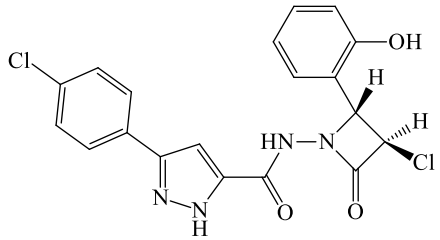

Figure 7

Shingare *et al.* synthesized new sulfonamide compounds with pyrazole oxadiazole derivatives starting from the 1-(3-fluoro-4-methoxyphenyl)ethanone compound and investigated their anti-tubercular activities. Anti-tubercular activity screening was evaluated upon M. tuberculosis H37Rv strain with the utilization of a standard drug called Isoniazid. Most of the synthesized compounds displayed the least activity than the norm drug Isoniazid. 2-(5-(3-fluoro-4-methoxyphenyl)isoxazol-3-yl)-5-(4-fluorophenyl)-1,3,4-oxadiazole compound showed the highest activity against tuberculosis H37Rv strain [22] (Fig. 8).

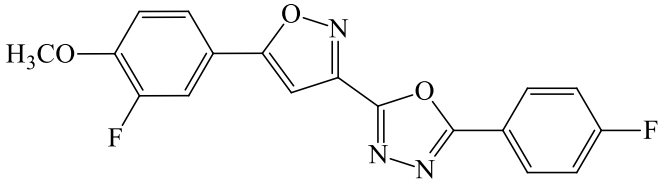

Figure 8

***Pyrazole as anti-tumor activity*:**Novel 1,5-diaryl substituted pyrazole secnidazole ester derivatives were synthesized by Teng *et al* and their anti-tumor activities upon four tumor cell lines were investigated. 1-(2-methyl-5-nitro-1*H*-imidazol-1-yl)propan-2-yl-1-phenyl-5-(*m*-tolyl)-1*H*-pyrazole-3-carboxylate compound proved to have the best considerable inhibiting activities upon human tumor cell lines of NCI-H460, MCG-803 and Skov-3. On the BEL-7404 cell, 1-(2-methyl-5-nitro-1*H*-imidazol-1-yl)propan-2-yl and 5-(4-iodophenyl)-1-phenyl-1*H*-pyrazole-3-carboxylate compounds showed the best activity [23] (Fig. 9).

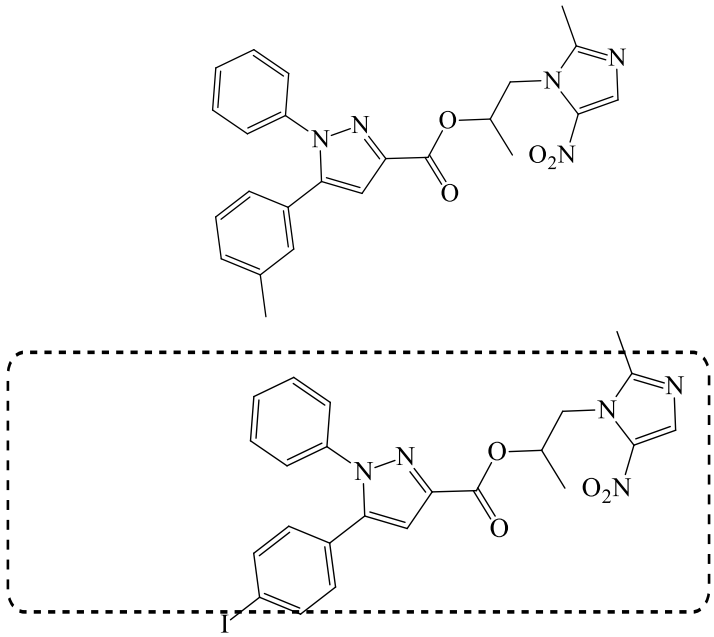

IC_{50}: 2.03 μM for BEL-7404 cell (liver tumor cell)
1.34 μM for NCI-H460 cell (lung tumor cell)
0.14 μM for MCG-803 cell (gastric tumor cell)
0.87 μM for Skov-3 cell (ovarian tumor cell)

Figure 9

Because the ALK5 inhibitor plays an important function in the pathogenesis of many illnesses such as malicious tumors and texture fibrosis, Wang *et al*. synthesized varieties of 4-(pyridin-4-oxy)-3-(tetrahydro-2*H*-pyran-4-yl)-pyrazole derivatives and studied the behavior of these compounds against the ALK5 inhibitor. According to the results obtained, 2-(4-(4-((4-((1-cyclopropyl-3-(tetrahydro-2*H*-pyran-4-yl)-1*H*-pyrazol-4-yl)oxy)pyridin-2-yl)amino)-2-(trifluoromethyl)phenyl)piperazin-1-yl)ethanol compound showed moderate ALK5 inhibitory activity (IC_{50} = 25 nM) [24] (Fig. 10).

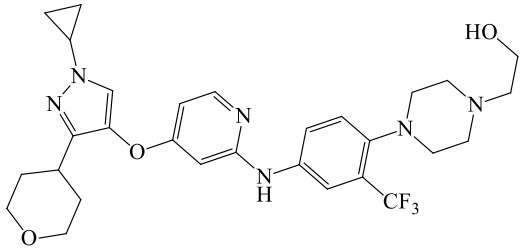

Figure 10

***Pyrazole as anti-malarial activity*:** Seven compounds (thiazolyl-pyrazole derivatives) synthesized by Bansal *et al.* were studied for their anti-malarial effects upon the human malaria parasite *Plasmodium falciparum*. All tested compounds represented reasonable activity with IC_{50} ranging from 0.23 to 0.9 µ/ml. Among these compounds, 2,6-dichloro and 4-fluoro substitutions showed great activity upon *P. falciparum* with IC_{50} values equal to 0.23 and 0.31 µg/mL, respectively [25] (Fig. 11).

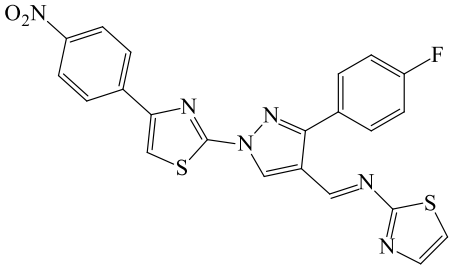

(*E*)-*N*-((3-(4-fluorophenyl)-1-(4-(4-nitrophenyl)thiazol-2-yl)-1*H*-pyrazol-4-yl)methylene)thiazol-2-amine

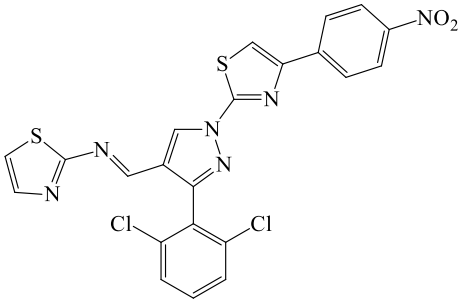

(*E*)-*N*-((3-(2,6-dichlorophenyl)-1-(4-(4-nitrophenyl)thiazol-2-yl)-1*H*-pyrazol-4-yl)methylene)thiazol-2-amine

Figure 11

For neuroprotective activity: Neelarapu *et al.* investigated their neuro-protective potential by developing various pyrazole-based diazide analogs. According to the results for the synthesized compounds, N^1-(1-(3-azido-5-(azidomethyl)benzyl)-1*H*-pyrazol-4-yl)-N^6-hydroxyadipamide compound showed neuro-protective enzyme activity with histone deacetylase 3 by obtaining IC_{50} value of 17 nM. It has emerged as the most remarkable neuroprotective agent that inhibits HDAC3 [26] (Fig. 12).

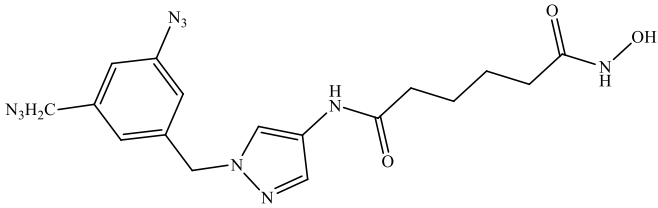

Figure 12

Pyrazole as anti-leishmanial activity: A variety of hybrid molecules containing pyrazole and various five-member heterocyclic molecules were synthesized by Bekhit *et al.* As a result of its evaluation in terms of serial anti-leishmanial activity developed, the*N*-(4-acetyl-5-(1-(4-bromophenyl)-3-(4-nitrophenyl)-1*H*-pyrazol-4-yl)-4,5-dihydro-1,3,4-thiadiazol-2-yl)-*N*-phenylacetamide compound showed the best activity. The *in vitro* anti-leishmanial activity of this compound on *Leishmaniaaethiopica* resulted in an IC50 value of 0.0142 ±0 .004 µg/ml [27] (Fig. 13).

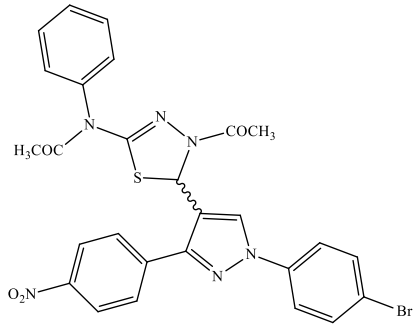

Figure 13

Pyrazole as anti-psychotic activity: 3-aryl-5-acylpiperazinyl-pyrazoles derivatives were prepared by Hoveyda *et al.* and their activities against the G protein-coupled human tachykinin NK3 receptor (*h*NK3-R) was investigated. Among them, the (5-(4-chlorophenyl)-1-methyl-1*H*-pyrazol-3-yl)(4-(2-methoxyphenyl)piperazin-1-yl) methanone compound had exhibited the best anti-psychotic activity with an IC_{50} value of 180 nM [28] (Fig. 14).

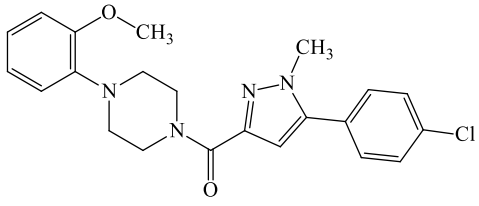

Figure 14

Pyrazole as anti-fungal activity: Zhang *et al.* synthesized innovative 4,5-dihydro-1*H*-pyrazole derivative compounds to examine their anti-fungal activities. They examined their anti-fungal activities on five plants (*Rhizoctonia cerealis, Sclerotinia sclerotiorum, Coniella diplodiella, Physalospora piricola, and Penicillium digitatum*) by the pathogenic fungi and most compounds were found to exhibit important anti-fungal activity measured as 20 μg/mL. The most important result of their study is that the two compounds presented magnificent antifungal activity upon *Sclerotinia sclerotiorum* and preferable activity to the trading fungicide penthiopyrad [29]. The chemical formula and EC_{50} values of these two compounds are given below (Fig. 15).

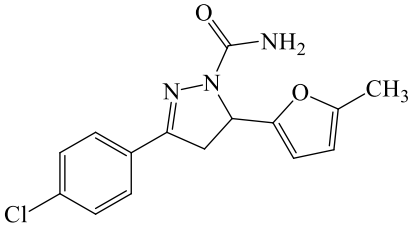

(EC_{50} value of = 0.138 μg/mL)

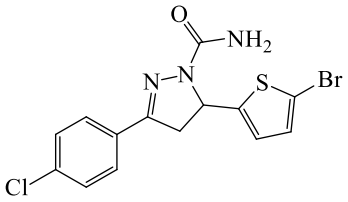

(EC_{50} value of = 0.081 μg/mL)

Figure 15

Conclusion

To date, many collaborating team have synthesized numerous pyrazole derivatives and tested their biological activities and evaluated the results. Since pyrazole derivatives have wide range of biological activity, they can be further synthetically diversified and studied for potential use against many illnesses. In this review, the chemical properties, synthesis methods, natural formations, and various biological activities of pyrazole derivatives were discussed. It will present advantages for researchers who plan to study pyrazoles for their biological activity and give a comprehensive understanding of the function of pyrazoles.

Acknowledgement

We would like to thank Dr. Ayhan YILMAZ from Kütahya Dumlupınar University for his contributions.

References

1. Brown, A. W. (2018). Recent developments in the chemistry of pyrazoles. *Advances in Heterocyclic Chemistry*, *126*, 55-107. DOI:10.1016/bs.aihch.2018.02.001
2. Faria, J. V., Vegi, P. F., Miguita, A. G. C., Dos Santos, M. S., Boechat, N., & Bernardino, A. M. R. (2017). Recently reported biological activities of pyrazole compounds. *Bioorganic &Medicinal Chemistry*, *25*(21), 5891-5903. DOI:10.1016/j.bmc.2017.09.035
3. Quejada, L. F., de Almeida, R., Vegi, P. F., dos Santos, M. S., Bernardino, A. M. R., Vericimo, M. A., & Faria, R. X. (2022). Rotenone enhances antifungal activity of novel pyrazoles against Candida spp. *European Journal of Medicinal Chemistry Reports, 5*, 100045. DOI: 10.1016/j.ejmcr.2022.100045
4. Küçükgüzel, Ş. G., & Şenkardeş, S. (2015). Recent advances in bioactive pyrazoles. *European Journal of Medicinal Chemistry*, *97*, 786-815. DOI:10.1016/j.ejmech.2014.11.059
5. Sun, H. Y., & Ji, F. Q. (2012). A molecular dynamics investigation on the crizotinib resistance mechanism of C1156Y mutation in ALK. *Biochemical and Biophysical Research Communications*, *423*(2), 319-324. DOI:10.1016/j.bbrc.2012.05.120
6. Bromm, B., Forth, W., Richter, E., & Scharein, E. (1992). Effects of acetaminophen and antipyrine on non-inflammatory pain and EEG activity. *Pain*, *50*(2), 213-221. DOI:10.1016/0304-3959(92)90165-8
7. Lepik, K. J., Levy, A. R., Sobolev, B. G., Purssell, R. A., DeWitt, C. R., Erhardt, G. D., ... & Brignall, J. L. (2009). Adverse drug events associated with the antidotes for methanol and ethylene glycol poisoning: a comparison of ethanol and fomepizole. *Annals of Emergency Medicine*, *53*(4), 439-450. DOI:doi:10.1016/j.annemergmed.2008.05.008
8. Fong, M. H., Garattini, S., & Caccia, S. (1982). 1-m-Chlorophenylpiperazine is an active metabolite common to the psychotropic drugs trazodone, etoperidone and mepiprazole. *Journal of Pharmacy and Pharmacology*, *34*(10), 674-675. DOI:10.1111/j.2042-7158.1982.tb04701.x
9. Karrouchi, K., Mortada, S., Issaoui, N., El-guourrami, O., Arshad, S., Bouatia, M., ... & Brandán, S. A. (2022). Synthesis, crystal structure, spectroscopic, anti-diabetic, anti-oxidant and computational investigations of Ethyl 5-hydroxy-1-isonicotinoyl-3-methyl-4,5-dihydro-1*H*-pyrazole-5-carboxylate. *Journal of Molecular Structure*, *1251*, 131977. DOI:10.1016/j.molstruc.2021.131977

10. Sener, A., Kasimogullari, R., Sener, M. K., & Genc, H. (2004). Studies on reactions of cyclic oxalyl compounds with hydrazines or hydrazones. 2. Synthesis and reactions of 4-benzoyl-1-(4-nitrophenyl)-5-phenyl-1*H*-pyrazole-3-carboxylic acid. *Chemistry of Heterocyclic Compounds*, *40*(8), 1039-1046. DOI:10.1023/b:cohc.0000046695.00178.79
11. Kasımoğulları, R., Duran, H., Yağlıoğlu, A. Ş., Mert, S., & Demirtaş, İ. (2015). Design, synthesis, characterization, and anti-proliferative activity of novel pyrazole-3-carboxylic acid derivatives. *Monatshefte für Chemie-Chemical Monthly*, *146*(10), 1743-1749. DOI:10.1007/s00706-015-1450-7
12. Yan, R., Huang, X., Deng, X., & Song, M. (2021). Synthesis and Activity Evaluation of Some Pyrazole–Pyrazoline Derivatives as Dual Anti-Inflammatory and Anti-microbial Agents. *Polycyclic Aromatic Compounds*, 1-14. DOI:10.1080/10406638.2021.1919156
13. TK, S. M., Das, A., Revanasiddappa, B. C., Sreeraj, K., & Shijith, K. V. (2022). Synthesis, Molecular Docking, and In-Vivo Anti-Inflammatory Screening of Novel Substituted Pyrazole Analogues. *Journal of Molecular Structure*, 132415. DOI:10.1016/j.molstruc.2022.132415
14. Shaker Ardakani, L., Mosslemin, M. H., Hassanabadi, A., & Hashemian, S. (2021). Reaction between Benzoic Acid *N*′-(2-Oxo-2-Phenyl-Ethyl) Hydrazide and Acetylenic Esters in the Presence of Alkyl Isocyanides: One-Pot Synthesis of Highly Functionalized 2,3-Dihydro-1*H*-Pyrazoles. *Polycyclic Aromatic Compounds*, 1-7. DOI:10.1080/10406638.2021.1991396
15. Demirçalı, A. (2021). Novel heterocyclic disazo dyes containing pyrazole and phenylpyrazole. part 1: Synthesis, characterization, solvent polarity and acid-base sensitive characteristics. *Journal of Molecular Structure*, *1231*, 129960. DOI:10.1016/j.molstruc.2021.129960
16. Smirnov, V. V., Kiprianova, E. A., Garagulya, A. D., Esipov, S. E., & Dovjenko, S. A. (1997). Fluviols, bicyclic nitrogen-rich antibiotics produced by *Pseudomonas Fluorescens*. *FEMS Microbiology Letters*, *153*(2), 357-361. DOI:10.1111/j.1574-6968.1997.tb12596.x
17. Kumar, V., Kaur, K., Gupta, G. K., & Sharma, A. K. (2013). Pyrazole containing natural products: Synthetic preview and biological significance. *European Journal of Medicinal Chemistry*, *69*, 735-753. DOI:10.1016/j.ejmech.2013.08.053
18. Schröter, H. B., Neumann, D., Katritzky, A. R., & Swinbourne, F. J. (1966). Withasomnine: A pyrazole alkaloid from Withania somnifera

Dun. *Tetrahedron*, *22*(8), 2895-2897. DOI:10.1016/S0040-4020(01)99082-9

19. Singh, N., Yadav, S. S., Rao, A. S., Nandal, A., Kumar, S., Ganaie, S. A., & Narasihman, B. (2021). Review on anti-cancerous therapeutic potential of Withania somnifera (L.) Dunal. *Journal of Ethnopharmacology*, *270*, 113704. DOI:10.1080/00304948.2021.1904750
20. Bennani, F. E., Doudach, L., Cherrah, Y., Ramli, Y., Karrouchi, K., & Faouzi, M. E. A. (2020). Overview of recent developments of pyrazole derivatives as an anti-cancer agent in different cell line. *Bioorganic Chemistry*, *97*, 103470. DOI:10.1016/j.bioorg.2019.103470
21. Pathak, R. B., Chovatia, P. T., & Parekh, H. H. (2012). Synthesis, anti-tubercular and anti-microbial evaluation of 3-(4-chlorophenyl)-4-substituted pyrazole derivatives. *Bioorganic & Medicinal Chemistry Letters*, *22*(15), 5129-5133.DOI:10.1016/j.bmcl.2012.05.063
22. Shingare, R. M., Patil, Y. S., Sangshetti, J. N., Patil, R. B., Rajani, D. P., & Madje, B. R. (2018). Synthesis, biological evaluation and docking study of some novel isoxazole clubbed 1,3,4-oxadiazoles derivatives. *Medicinal Chemistry Research*, *27*(4), 1283-1291.DOI: 10.1007/s00044-018-2148-2
23. Teng, Q. H., Sun, G. X., Luo, S. Y., Wang, K., & Liang, F. P. (2021). Design, syntheses and anti-tumor activities evaluation of 1,5-diaryl substituted pyrazole secnidazole ester derivatives. *Journal of Heterocyclic Chemistry*, *58*(8), 1656-1664. DOI:10.1002/jhet.4302
24. Wang, Z., Zhang, Y., Wang, H., Wang, X., Yu, Z., & Zhao, L. (2022). Synthesis and Biological Evaluation of 4-(pyridine-4-oxy)-3-(tetrahydro-2*H*-pyran-4-yl)-pyrazole Derivatives as Novel, Potent of ALK5 Receptor Inhibitors. *Bioorganic & Medicinal Chemistry Letters*, 128552. DOI:10.1016/j.bmcl.2022.128552
25. Bansal, K. K., Bhardwaj, J. K., Saraf, P., Thakur, V. K., & Sharma, P. C. (2020). Synthesis of thiazole clubbed pyrazole derivatives as apoptosis inducers and anti-infective agents. *Materials Today Chemistry*, *17*, 100335. DOI:10.1016/j.mtchem.2020.100335
26. Neelarapu, R., Holzle, D. L., Velaparthi, S., Bai, H., Brunsteiner, M., Blond, S. Y., & Petukhov, P. A. (2011). Design, synthesis, docking, and biological evaluation of novel diazide-containing isoxazole-and pyrazole-based histone deacetylase probes. *Journal of Medicinal Chemistry*, *54*(13), 4350-4364. DOI:10.1021/jm2001025
27. Bekhit, A. A., Hassan, A. M., Abd El Razik, H. A., El-Miligy, M. M., El-Agroudy, E. J., & Bekhit, A. E. D. A. (2015). New heterocyclic hybrids

of pyrazole and its bioisosteres: design, synthesis and biological evaluation as dual acting anti-malarial and anti-leishmanial agents. *European Journal of Medicinal Chemistry*, *94*, 30-44. DOI:10.1016/j.ejmech.2015.02.038

28. Hoveyda, H. R., Roy, M. O., Blanc, S., Noël, S., Salvino, J. M., Ator, M. A., & Fraser, G. (2011). Discovery of 3-aryl-5-acylpiperazinyl-pyrazoles as antagonists to the NK3 receptor. *Bioorganic & Medicinal Chemistry Letters*, *21*(7), 1991-1996. DOI:10.1016/j.bmcl.2011.02.033
29. Zhang, T., Liu, H., Lu, T., Zhang, G., Xiao, T., Cheng, W., ... & Tang, X. (2022). Novel 4,5-dihydro-1*H*-pyrazole derivatives as potential succinate dehydrogenase inhibitors: design, synthesis, crystal structure, biological activity and molecular modeling. *Journal of Molecular Structure*, *1249*, 131537. DOI:10.1016/j.molstruc.2021.131537

String Cloud with Strange Quark Matter in Lyra Geometry for Non-Static Universe

[1]Asst. Prof. Halife ÇAĞLAR and [2]Assoc. Prof. Doğukan TAŞER

[1]Department of Electricity and Energy, Biga Vocational School,
Çanakkale Onsekiz Mart University, 17400, Çanakkale, Turkey
https://orcid.org/0000-0003-2877-1221
[2]Department of Electricity and Energy, Çan Vocational School,
Çanakkale Onsekiz Mart University, 17400, Çanakkale,
Turkey https://orcid.org/0000-0002-8622-6830

Introduction

The basis of gravitational theories begins with Newton's theory. Although Newton's theory was successful in studying the motions of the earth and determining the orbits of planets and other celestial bodies, it failed to cosmologically explain some issues. On the other hand, General Relativity (GR) theory was the first theory that succeeded in explaining geometrically the gravitational field (Einstein, 1916). In General Relativity, the Lagrangian density of the geometric part is theoretically defined by the Ricci curvature scalar. However, the progression of the planet's perihelion is the most valid theory of gravity, which provides tests such as gravitational deflection and redshift of light. Later, the first geometric unified theory was proposed by Weyl (1918) to unify both gravity and electrodynamics. This theory has not received much attention due to the failure of length conversions. Lyra (1951) suggested an alteration of Riemannian geometry by adding a tuning function to the structureless manifold. In this theory differently from Weyl theory, the integrability of the length transformation of a vector under parallel transformations is also eliminated. A new scalar-tensor theory and an analogy of Einstein's field equations in Lyra manifold were proposed in literature (Sen, 1957; Sen and Dun, 1970).

In the Lyra geometry, Halford (1970) indicated constant displacement vector behaves like a cosmological constant, Λ, in general relativity. Because of dynamical structure of displacement vector, it is not constant in general. Many cosmological hot topics are deeply studied in Lyra geometry. There are many cosmological models in literature.Bhardwaj and Rana (2020) studied Bianchi-III metricin the presence of two different cosmic matter forms in a nonsingular hybrid universe. Bishi and Lepse (2021) investigated particle creation by way of quadratic deceleration parameter for FRW universe in Lyra geometry. Ram and Verma (2022) analyzed anisotropic dark energy model with massive scalar field for Bianchi space-time in Lyra manifold. In literature, there are many different cosmological considerationswithin the context of Lyra geometry.

All considerations have referred that there were several phase transitions during evolvement of the early ages of the universe. Throughout these phase transitions occurring in early ages, the symmetry of universe is spontaneously broken. It is thought that as a result of the symmetry distortion, material forms called topological defects occurred. These forms of matter are called as monopole, string, domain walls and texture (Vilenkin, 1953). Cosmic strings are forms of cosmic matter that are formed as one-dimensional objects during axis symmetry breaking (Kibble, 1976). Cosmic strings have a substantial place from the point of astrophysics. It is thought that strings hadasignificant place in the constitution of galaxies due to density fluctuations of it(Zel'dovich,

1980). It is known that strings could be coupled with gravitational field (Yadav et. al., 2011). In consequence, examination of the gravitational effect caused by the strings is a quite significant issue. At the same time, the Quark-Gluon Plasma phase transition, called the quark-hadron transition, occurred at the cosmic temperature of T~ 200 MeV in the early stages of the universe (Yavuz, 2005). Some astrophysical objects such as neutron stars and quark-gluon plasma in these early times of the universe may have originated from quark matter (QM). In this study, we considered quark pressure is given by

$$p_q = \frac{\rho_q}{3}. \quad (1)$$

Here ρ_q represents the quark energy density. Total energy density is described as

$$\rho = \rho_q + B_c \quad (2)$$

where$B_c$is the QM bag constant.Total pressure is given by

$$p = p_q - B_c. \quad (3)$$

To examine early universe, cosmic string and QM forms are examined in the literature within the scope of many different theories, both separately and in the form of QM attached to a string. Mahanta and Biaswal (2012) investigated both string and domain walls in the presence ofQM in Lyra geometry. Katore and Hatkar (2015) examined to strange quark matter (SQM)with stringin that theory. Çağlar and Aygün (2016) studied bulk viscous with string cloud attached to SQM for n-dimensional FRW universe within the scope of Lyra manifold.

In this study, Einstein-Rosen universe with SQMcoupled to string cloud in Lyra geometry. In the next section, cosmological quantities for the model have been represented and field equations for Lyra geometry have been reminded. We have attained to field equations for the model in Lyra manifold. Exact solutions of the model have gained without using any geometrical and physical approximation. All results have concluded in last section.

Model and Field Equations

Line element for non-static Einstein-Rosen metric is described as

$$ds^2 = e^{(2\alpha-2b)}(-dt^2 + dr^2) + r^2e^{-2b}d\varphi^2 + e^{2b}dz^2 \quad (4)$$

whereα and$b$ are metric potentials depending on time, *t*. In this study, we have examined SQMcoupled to string cloud. Matter distribution for string cloud is described as

$$T_{ik} = \rho u_i u_k - \rho_s X_i X_k \quad (5)$$

whereρ and ρ_s are energy density and string tension density, respectively. $u_i$andX_i are four velocity and space like vectors. Four velocity and space like vector satisfy following relation (Yavuz, 2005).

$u_i u^i = -x_i x^i = 1 \text{and} u^i X_i = 0.$ (6)

Also, Connectionamongtwo densitiesis given by

$\rho = \rho_p + \rho_s.$ (7)

Here ρ_p represents particleenergy density. If we consider quark matter as particle, it is possible to use Eq. (2) in Eq. (7). Thus, total particle energy density has been obtained as follows:

$\rho = \rho_q + \rho_s + B_c$ (8)

From Eqs. (5) and (8), the energy momentum tensor of SQMcoupled to string cloud can be written as (Pradhan et.al, 2007; Katore, 2012)

$T_{ik} = (\rho_q + \rho_s + B_c)u_i u_k - \rho_s X_i X_k.$ (9)

The field equation for Lyra geometry (Sen, 1957; Sen and Dunn 1971) is given by

$R_{ij} - \frac{1}{2} g_{ij} R + \frac{3}{2}\phi_i \phi_j - \frac{3}{4} g_{ij}\phi_k \phi^k = -\chi T_{ij}$ (10)

whereϕ_i is called as displacement vector and given as $\phi_i = [0,0,0,\beta(t)]$.The components of the displacement vector could be constant or scalar functions that depend on the coordinates. The field equations for examined SQM coupled string cloudin non-static Einstein-Rosen universe in Lyra manifold are obtained in the following forms:

$e^{2(b-\alpha)}\left(b'^2 + \frac{3}{4}\beta^2\right) = \rho_s,$ (11)

$e^{2(b-\alpha)}\left(\alpha'' + b'^2 + \frac{3}{4}\beta^2\right) = 0,$ (12)

$e^{2(b-\alpha)}\left(\alpha'' - 2b'' + b'^2 + \frac{3}{4}\beta^2\right) = 0,$ (13)

$e^{2(b-\alpha)}\left(-b'^2 - \frac{3}{4}\beta^2\right) = \rho_q + \rho_s + B_c,$ (14)

$e^{2(b-\alpha)}\frac{\alpha'}{r} = 0.$ (15)

Obtained differential equation system contains three unknown functions. One can get exact solutions of the model without using any geometrical or physical approximation. From Eqs. (11)-(15), we get metric potential, α and b as follows:

$b(t) = k_1 t + k_2$ (16)

$\alpha(t) = k_3.$ (17)

Also, displacement vector, SQM energy density and string cloud energy density are attained by using Eqs. (11)-(15) with (16) and (17), in the following form:

$$\beta^2 = -\frac{4}{3}k_1^2. \quad (18)$$

$$\rho_q = -B_c \quad (19)$$

$$\rho_s = 0. \quad (20)$$

Quark pressure has been attainedfromEqs. (19) and (1) as follows

$$p_q = \frac{-B_c}{3} \quad (21)$$

All solutions of the model have been obtained as mentioned above, also widely discussed in following section.

Conclusion

In this study, Einstein-Rosen universe have been investigated in Lyra alternative gravitation theory with SQM coupling to string cloud matter distribution. By using Eqs. (16) and (17) in Eq. (4), it is possible to rewrite line element ofEinstein-Rosen universe for constructed model as:

$$ds^2 = e^{-2(k_1t+k_2-k_3)}(-dt^2 + dr^2) + r^2e^{-2(k_1t+k_2)}d\varphi^2 + e^{2(k_1t+k_2)}dz^2. \quad (22)$$

It is seenfrom Eq. (22) that Einstein-Rosen line element gives time dependent and non-scalar universe model. Because of displacement vectorβ^2has been obtained depending onconstantk_1, one can say that it plays the role of cosmological constant. This result agrees with Halford (1970) study which has suggested that displacement vector field behaves like cosmological constant.Since cosmic string have been obtained $\rho_s = 0$ as seen in Eq. (20), one can say that string cloud does not survive depending on solutions of the examined model in this study. Many scientists (Krori et.al, 1994; Reddy, 2003; Sahoo and Mishra, 2013) have studied cosmic string model in framework variousalternative gravitation theories,and they have found that their models do not allow to survive cosmic string.Otherwise, accordingly Eqs. (19) and (22),we have assumed negative value of Bag constant$B_c$to gain meaningful results for themodel by supporting with Begun et.al (2011) study. Also, kinematical quantities such as volume, average scale factor, Hubble parameter, shear scalar and deceleration parameter are attained for constructed model following forms

$$V = \sqrt{-g} = re^{-2(k_1t+k_2-k_3)}, \quad (23)$$

$$\mathcal{R} = r^{\frac{1}{3}}e^{-\frac{2}{3}(k_1t+k_2-k_3)} \quad (24)$$

$$H = \frac{1}{3}(lnV)' = -\frac{2}{3}k_1, \quad (25)$$

$$\Theta = 3\mathrm{H} = -2\mathrm{k}_1, \quad (26)$$

$$\sigma^2 = \frac{1}{2}\sigma_{ij}\sigma^{ij} = \frac{4}{3}{k_1}^2e^{2(k_1t+k_2-k_3)} \quad (27)$$

$$q = -3\Theta^{-2} - \left(\Theta_{,i}u^{,i} + \frac{1}{3}\Theta^{2}\right) = -1. \quad (28)$$

Here deceleration parameter q is an important quantity to describe fate of universe.Expanding of the model is with accelerating or decelerating when$q < 0$or $q > 0$ respectively (Bolotin et. al., 2015).According to Eq. (28), we can say that Einstein-Rosen universe is expanding with acceleration in framework Lyra theory with SQM attached to cosmic string.

All solutions of the universe model reduce from Lyra theory to General Relativity when displacement vector is zero. In our solutions $k_1$is an important constant. If we chose $k_1 = 0$, displacement vector becomes zero and all solutions turns to GR solutions. The line element of Einstein-Rosen universe for our model can be written in GR theory as

$$ds^2 = e^{-2(k_2-k_3)}(-dt^2 + dr^2) + r^2e^{-2k_2}d\varphi^2 + e^{2k_2}dz^2. \quad (29)$$

It is clearly seen that the line element does not depend on cosmic time *t*, and it gives static universe in GR theory.

References

1. Bhardwaj V. K. and Rana M. K. (2020). Bianchi–III Transitioning Space-Time in a Nonsingular Hybrid Universewithin Lyra's Cosmology. *Gravitation and Cosmology*26 (1), 41–49.
2. Begun V. V., Gorenstein M. I. and Mogilevsky O. A. (2011), Modified Bag Models for the quark-Gluon Plasma Equation of State. *Int. J. Mod. Physics E* 20 (8), 1805.
3. Bishi B. K. and Lepse P. V. (2021). Particle Creation and Quadratic Deceleration Parameter in Lyra Geometry. *New Astronomy* 85, 101563.
4. Bolatin Y.L., CherkaskiyV.A., LemetsO.A., YerokhinD.A. and ZazunovL.G. (2015). Cosmology in Terms of The Deceleration Parameter. Part I. e-print:arXiv:1502.00811v.
5. Çağlar H. and Aygün S. (2016). Exact Solutions of Bulk Viscous with String Cloud Attached To Strange Quark Matter for Higher Dimensional FRW Universe in Lyra Geometry. *AIP Conference Proceedings* 1722, 050001.
6. Einstein A (1916). Die Grundlage der Allgemeinen Relativitätstheorie. *Ann. Phys.* (Lpz.) 49, 769.
7. Katore S. D. (2012).Strange Quark Matter Attached to String Cosmologyin FRW Space-Time. *Int. J. Theor. Phys.* 51, 83
8. Katore S. D. and Hatkar S. P. (2015). Strange Quark Matter Coupled To String Cloud in Lyra Geometry. *Astrophys. Space Sci.* 357:55.
9. Kibble, T. W. B. (1976).Topology of Cosmic Domains and Strings. J. *Phys. A: Math Gen*. 9, 1387.
10. Krori,K. D., Chaudhury T. and MahantaC. R. (1994). Strings in Some Bianchi Type Cosmologies.*Gen. Rel. and Grav.* 26 (3),265.
11. Lyra G.(1951). Über-Eine Modifikation der Riemannschen Geometrie. *Math. Z*. 54, 52.
12. Mahanta K. L. and Biswal A. K. (2012). String Cloud and Domain Walls with QuarkMatter in Lyra Geometry. *Journal of Modern Physics*3, 1479-1486.
13. Pradhan A, Khadekar G. S., Mishra M. K. and Kumbhare S. (2007). Higher Dimensional Strange Quark Matter Coupled to the String Cloud with Electromagnetic Field Admitting One Parameter Group of Conformal Motion. *Chin. Phys. Lett.* 24 (10), 3013.
14. Ram S. and Verma M. K. (2022). Dynamics of Bianchi Type-VI_0Anisotropic Dark Energy CosmologicalModel with Massive Scalar Field in Lyra Manifold. *Indian J Phys* 96(4), 1269–1275.

15. Reddy D. R. K. (2003). Non-Existence of Cosmic Strings in Bimetric Theory Of Gravitation. *Astrophys. And Space Sci.* 286 (3), 397
16. Sahoo P. K. and Mishra B. (2013). Axially Symmetric Space-Time with Strange Quark Matter Attached to String Cloud inBimetric Theory. *Int. J. Pure and Applied Math.* 82, 87.
17. Sen D. K.(1957). A Static Cosmological Model. *Z. Phys.* 149, 311.
18. Sen D. K. and Dunn K. A.(1971). A Scalar-Tensor Theory of Gravitation in A Modified Riemannian Manifold. *J. Math. Phys.* 12, 578.
19. Vilenkin, A. and Shellard, E. P. S. (1994). Cosmic Strings and Other Topological Defects.*(Cambridge University Press, Cambridge).*
20. Weyl H.(1918). Gravitation und Elektrizität. Sitzungsber. *Preuss.Akad.Wiss.* 465.
21. Yadav, A. K., Yadav, V. K. and Yadav, L. (2011).Bianchi Type-V String Cosmological Models in General Relativity.*Pramana* 76, 681-690.
22. Yavuz, I., Yılmaz, İ. ve Baysal, H. (2005).Strange quark matter attached to the string cloud in the spherical symmetric space–time admitting conformal motion.*Int. J. Mod. Phys. D* 14, 1365.
23. Zel'dovich, Ya. B. (1980).Cosmological fluctuations produced near a singularity.*Mon. Not. R. Astron. Soc.* 192, 663.

Fluorescent Interaction of Benzotiazole Based Fluorescent Compounds with Various Metal Ions

Asst. Prof.Dr. Hülya ELMALI GÜLBAŞ

Usak University, Banaz Vocational School,
Department of Chemistry and Chemical Processing Technologies,
Chemical Tecnology Programme,64500 Usak, Turkey,
Orcid ID: 0000-0002-6041-6054

1.Introduction

The harm of toxic metals to human health and our environment is well known. Therefore, environmental pollution danger to humankind and other living things. The most important damages for environment caused by toxic metals or cations are manifested in soil and/or water. However, these pollutions increase with industrialization due to the need for technology and the increasing human population, so studies on the creation and development of new methods and technologies for wastewater treatment procedures are gaining in importance. As an industrial sector, wastewater from metal, paper, leather, paint and textile industries contains large amounts of heavy metals. Uncontrolled release of such wastewater to the environment causes toxic and mutagenic effects on the environment and the living things in that environment [1-3].

It is known that heavy metals such as mercury, cadmium and lead are toxic metals and they cause especially digestive system, immune system, heart, kidney and neurological diseases. In today's conditions, metal analyzes are generally performed using voltammetric, chromatographic or spectroscopic methods. Although these analysis methods allow the analysis of elements at low concentrations, they are not suitable for analysis under certain conditions. However, fluorimetric methods have many advantages such as being more selective, lower cost and more sensitive than other methods. For this reason, the detection of these ions in many studies conducted in recent years has attracted great interest in analytical chemistry, biology and environmental chemistry. The different types of enzymes, biosensors and chemosensors molecules that can detect cations and anions have been designed [4]. In these studies, selective fluorescence sensors were developed and designed for the detection of cations, especially toxic metals [5].

Chemosensors are designed with the basic principle of monitoring the changes in physical properties resulting from host-guest interactions that occur in the molecule in the presence of a guest. Fundamental principle of chemosensor design have been that the chemosensor exhibits a a qualitative answer to a given analyte, but another type of answer to diffferent analytes. It also allows to a quantitative specification for a broad range of analyte concentrations. [6].

Between the chemosensors, fluorescent sensors have been effectively reaserched because of their high selectivity and sensitivity. Espesially, fluorescent sensors, which exhibited the shift of emission bands after linking to analytes, constitute a very interesting research topic because they allow the ratiometric detection of analytes. The last decades, A number of fluorescent

sensors have been reported that notable selectivity and sensitivity for a special metal ion [7].

The design and synthesis of receptors for the identification of heavy metalsconstitute very important issues. In addition, selective recognition of cations like Cd(II), Pb(II) and Hg(II) in the presence of other cations is also very important. Because the polluting effects and toxicities of cations like Pb(II), Cd(II) and Hg(II) are known. Therefore, early determination of such cations is very important for the prevention of environmental pollution. Therefore, great attempted have been made over the past years to produce and develop selective cation receptors [8].

In general, chemosensor studies require a receptor group or ligand that can selectively identify cations, and a method that physically detects signal changes and shows the interaction between the two groups [9].

As a result of various modifications, such receptors can be selectively complexed against desired metal ions [10,11]. While designing such cation receptors; In the preferred ligand, there should be sufficient number of donor atoms to ensure coordination, the size of the surface on which the receptor groups in the designed sensor structure will provide coordination should be such as to include the metal cation, and the ends containing the donor groups should be flexible enough to ensure the formation of coordination spheres [12].

It is important to provide metal sensor applications of benzothiazole-based fluorescent-active amide and amine molecules, which have a structure that can pave the way for new applications with the development of a new, selective sensor that is easy to synthesize. It is expected that thiazole-based amide and amine derivatives, which are very rare in the literature, will add a new dimension to their applications [13].

Benzothiazoles are group of heterocyclic compounds exhibiting various pharmacological activities such as antibacterial [14], anticancer [15], anti-inflammatory, analgesic antidiabetic, etc.

Benzothiazole is a heterocyclic ring system formed by the fusion of the thiazole ring to the benzene ring at the 4 and 5 positions. The sulfur atom is numbered as 1 and is called 1,3-benzothiazole. Its closed formula is C_7H_5NS. Its molecular weight is 135.18 g/mol. It is liquid at room temperature and its boiling point is 227°C. The molecular structure of benzothiazole is given in Figure 1.

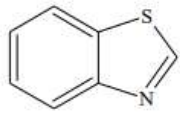

Figure 1Molecular Structure of Benzotiazole

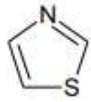

Figure 2 Molecular structure of tiazole

Fluorescent sensors in the benzothiazole structure show excellent coordination ability because of the presence of a thiazole ring. [16]. To date, several fluorophoric benzothiazole scaffold compounds have been reported in the literature. Theavailabilityof electron-withdrawing or electron-donating groups on the molecule results in a "Turn on-Turn off" "on-off" fluorescence response.

Benzothiazoles have high quantum yields, large Stokes shifts due to their stable conjugated structure. The perfect photophysical features of benzothiazoles, like good photostability, have attracted the noticed to researchers who want to synthesize fluorescent compounds and chemosensors [17]. The chemosensors mostly consist of two parts. They consist of a benzothiazole moiety that acts as a fluorophore and a minor organic identification group that added to the benzothiazole ring. Figure 3 shows the overall structure.

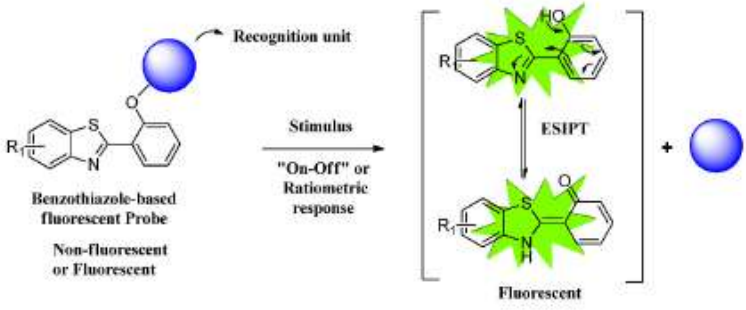

Figure 3 General mechanism of fluorescence response of benzothiazole-based fluorescent sensors [17].

Although there are studies on fluorescent sensors containing benzothiazole and their interaction with various metal ions, there is no systematic study on

these studies in the literature. In this study, some benzothiazole compounds in the literature are summarized. Thus, it is aimed to create a basic resource for researchers who may want to work on benzothiazole fluorescent compounds [18].

2. Some Benzothiazole Compounds in the Literature

In the study of Leslee et al., a thiazole-based 2-(benzothiazol-2-yl)-1-((9-ethyl-9H-carbazole-6yl)methylene)hydrazine (CBT-1) sensor was synthesized. As a consequence of the analysis they have been defined by as a consequence of the analysis, that the CBT-1 sensor has been selective for Hg2+ ions in the precence of different metal ions. The CBT-1 sensor shows colorimetric and fluorimetric color changes in the presence of Hg +2 ions.It was determined that the sensor mechanism resulted from the intramolecular charge transfer between Hg2+ ions and the carbazole and benzothiazole moiety in the molecular structureIn the study, the linking mechanism of CBT-1 and Hg2+ cation was determined by various spectroscopic techniques like UV-vis, fluorescence, Mass, FT-IR and calculation studies. The molecular structure and synthesis reaction of the CBT-1 compound are given in Figure 4. The proposed detection mechanism of CBT-1 for Hg^{2+} ions is shown in Figure 5. [19].

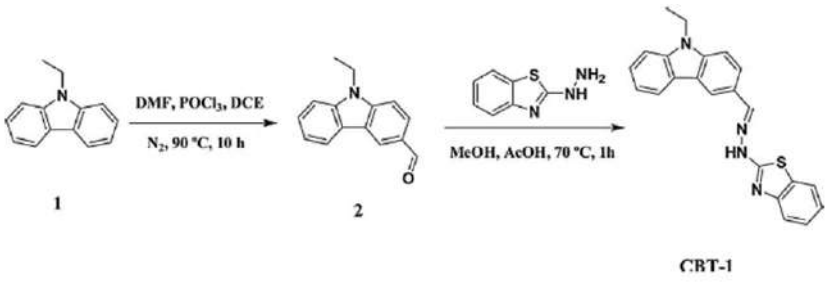

Figure 4 Synthesis reaction of 2-(benzothiazol-2-yl)-1-((9-ethyl-9H-carbazole-6yl)methylene)hydrazine (CBT-1) [19].

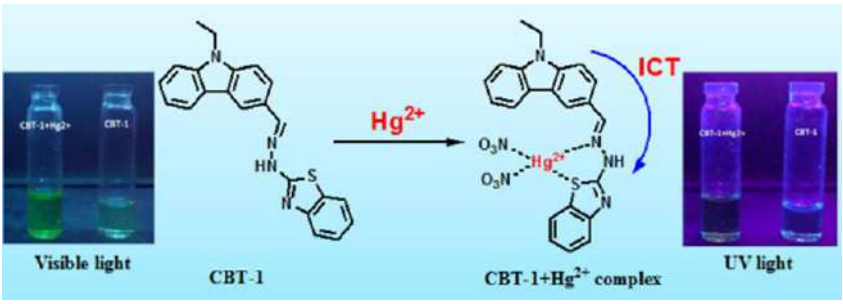

Figure 5 Recommended detection mechanism of CBT-1 with Hg2+ ion[19].

In the study of Halay et al., two triazine-based thiazole derivatives containing chiral aminoalcohol groups, (2R,2'R)-2,4,6-triamine-N^2-[2-(4-benzothiazolyl)phenyl]-N^4,N^6- [di(butan-1-ol)]-1,3.5 triazine (Tr1) and (1S,1'S,2R,2'R)-2,4,6-triamine-N^2-[2-(4 benzothiazolyl) Chiral enantiomeric recognition properties of compounds synthesized and synthesized with phenyl]-N^4,N^6-[di(1,2-) diphenylethanol)]-1,3,5 triazine (Tr2). Fluorescence against carboxylic acid enantiomers like2-chloromandelic acid and mandelic acid. It was investigated in DMSO/H2O (30:70) mixture using spectroscopic tecniques. It was determined that chiral molecules did not show fluorescence emission in DMSO solutions, It was observed that the emission increased 38 and 43 times for butan-1-ol and diphenylethanol derivatives, such as compounds with aggregation-related emission (AIE) character, when the percentage of water in the solution was increased. As a result of the study, it was identifited that R-isomers of carboxylic acids form more suitable complexes against chiral selectors than S-isomers.Scheme 1. Synthesis of fluorescent sensor candidate molecules Tr1 and Tr2 is shown. Figure 6. The fluorescent photograph of Tr1 in pure DMSO (left cell) and DMSO/H_2O mixture (right cell) is shown. Figure 7. The fluorescent photograph of Tr2 in DMSO/H_2O mixtures with 0% and 95% H_2O fractions is shown [20].

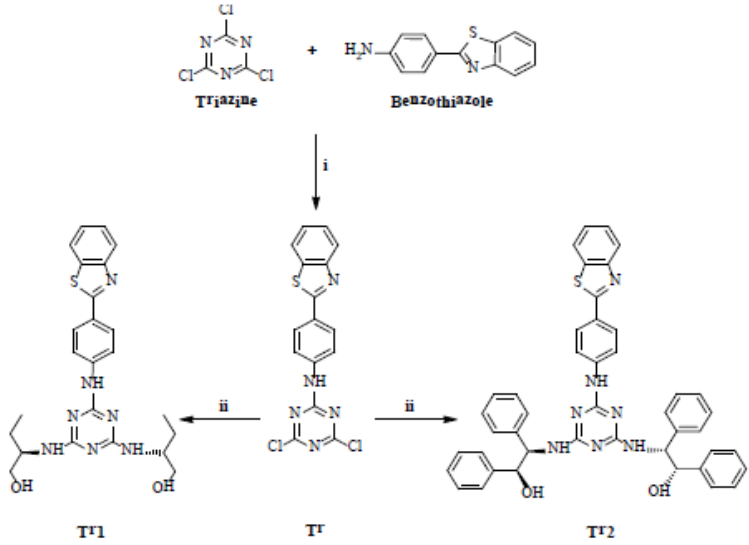

Figure 6 Synthesis reaction of Tr1 and Tr2 [20]

Figure 7 Fluorescence photograph of **Tr1** in pure DMSO (cell on the left) and in DMSO/H_2O mixture (cell on the right).[20]

Figure 8 Fluorescence photograph of **Tr2** in DMSO/H2O mixtures with 0% and 95% H_2O fraction[20].

In another study by Bozkurt et al., 25,27-bis(N-(benzothiazole-4-yl)-acetamide)-26,28-dihydroxy-calix, a fluorescent probe based on the Calyx[4]arene-benzothiazole platform. [4]arene (V) compound was synthesized. Photophysical properties of the synthesized fluorescent compound were investigated in THF/H_2O (70:30) mixture using fluorescence spectroscopy. It was determined that Compound V was a compound with aggregation-induced emission (AIE) character. As a result of fluorescence spectroscopy examination of Compound V against various ions, it was determined that Compound V was sensitive and selective towards chloride ions. Compound V is reported to be the first for the determination of chloride ions by fluorescence spectroscopy. The synthesis of Compound V is shown in Figure 9. The fluorescent appearance of sensor V in THF-H_2O solutions with increasing water fractions is shown. Figure 10 and Figure 11 show a photograph (70:30, v/v) of Sensor V's fluorometric responses to various anions in THF-H_2O [21].

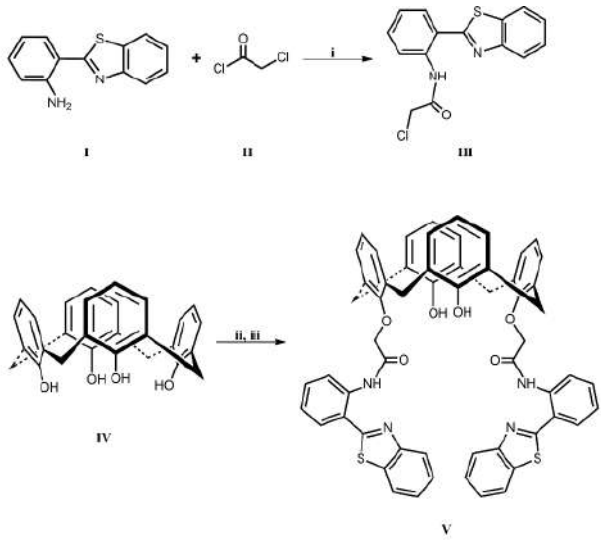

Figure 9 Synthesis reaction of Compound **V** [21].

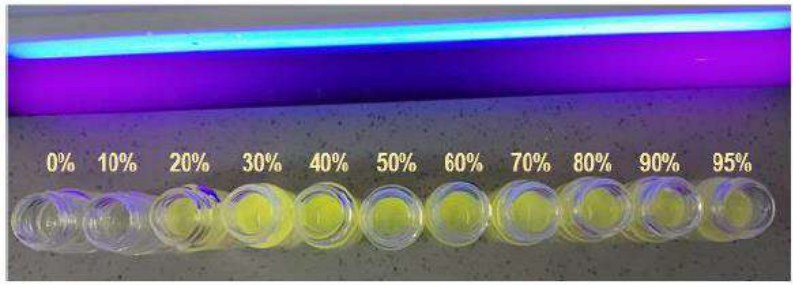

Figure 10 Fluorescence photograph of sensor **V** in THF-H_2O solutions with different water fractions[21].

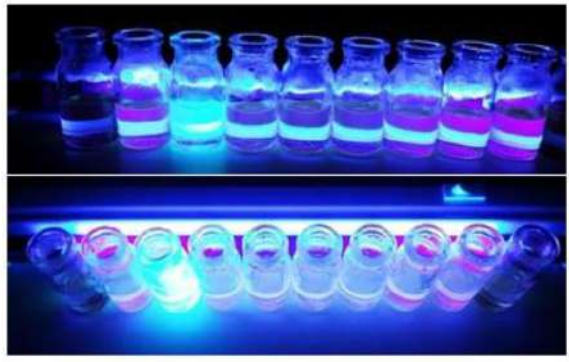

Figure 11 Photograph of Sensor V's fluorometric responses to several ions in THF-H_2O (70:30, v/v)[21].

In the study of Karpagam et al., thiophene conjugated benzothiazole compounds L1 and L2, which have the potential to be used as a portable chemosensor in the future, were synthesized. The fluorescence properties of the synthesized compounds were compared. Research with UV-vis and photoluminescence (PL) studies that was determined that L1 and L2 ligands were selective among various metal ions towards Cd+2 and Cu+2 ions, respectively. It was determined that the L2 compound was selective towards the Cd^{+2} metal cation. The synthesis of compound L2 is shown in Figure 12. The proposed mechanism is shown in Figure 13 [22].

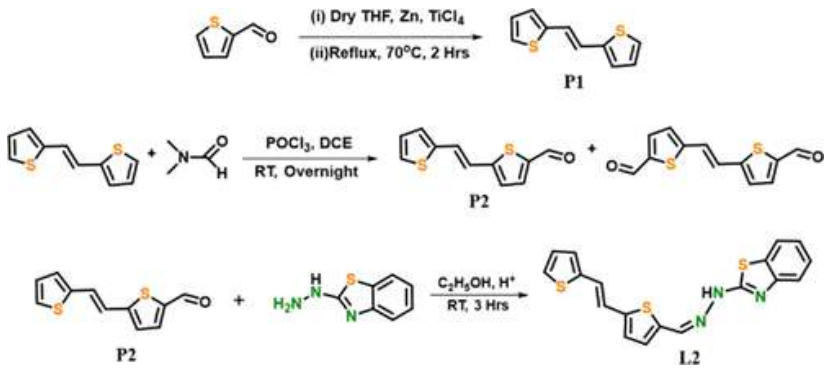

Figure 12 Synthesis reaction of L2 [22].

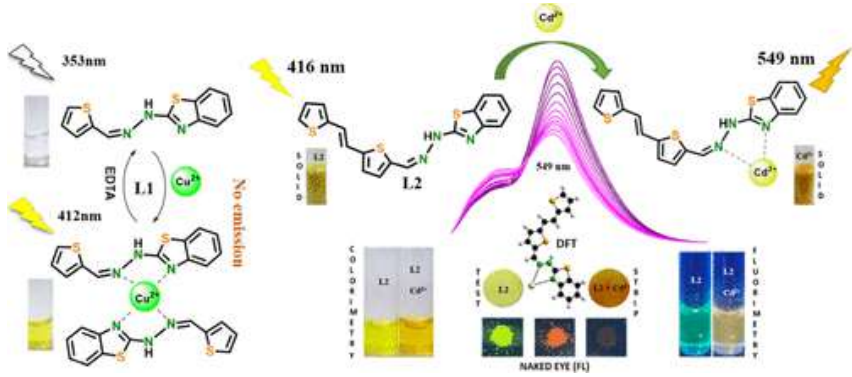

Figure 13 Recommended detection mechanism of L1 and L2 with Cu^{+2} and Cd^{+2}ions[22].

In the study of Wang et al., diethylamine coumarin compound 1 containing benzothiazole terminal group was synthesized. The molecular structure of Compound 1 is shown in Figure 14The selectivity of Compound 1 towards CN^- and Cu^{+2} ions was studied. In the study, limits of detection for compound 1 for

CN− and Cu2+ in acetonitrile were determined as in the order of 0.0071 μM(CN−) and 0.014 μM(Cu2+)' in fluorescence spectroscopy.The sensitivity and selectivity of Compound 1 for the recognition of CN- and Cu+2 cations can be observed colorimetrically with the naked eye in solution and on test paper. It was observed that the color changed from reddish brown to white after the addition of cyanide or copper ions to the test paper. Figure 15 shows the proposed sensitivity mechanism of Compound 1 to CN^- and Cu^{+2} ions [23].

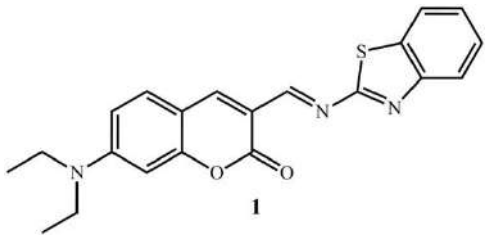

Figure 14 Molecular structure of 1

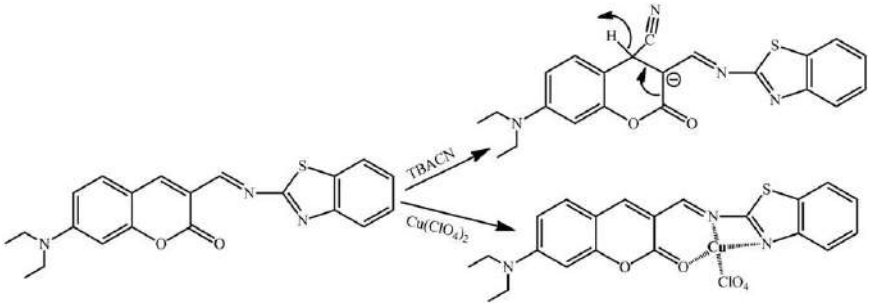

Figure 15 Recommended sensing mechanism of Compound 1 for CN^- and Cu^{+2} [23].

In the study of Chen et al., a new AIE active fluorescent benzothiazole derivative chemosensor 1 was synthesized. The Chemosensor 1 synthesis reaction is shown in Figure 16. Chemosensor 1 was determined to show 'turn off' selectivity and sensitivity against CN- in pure aqueous medium. In addition, the detection limit of 0.22 m (9.44 ppm), which is lower than the maximum cyanide level (1.9 m) in drinking water allowed by the World Health Organization (WHO), was reached by using Chemosensor 1 in the study. The biological applications of Compound 1 were examined and Compound 1 was determined exhibit low cytotoxicity and membrane permeability.In addition, Chemosensor 1-based test strips were also determined by applications to be able to detect CN^-appropriately. Figure 17 shows the predicted mechanism of sensitivity to CN^- cations of chemosensory 1 [24].

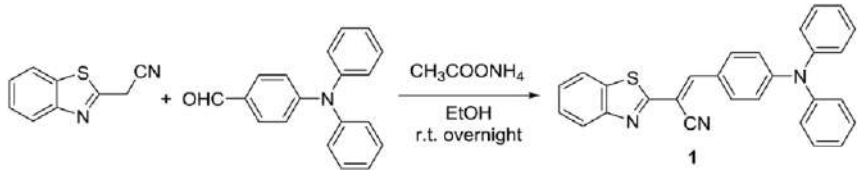

Figure 16 Synthesis reaction of 1 [24].

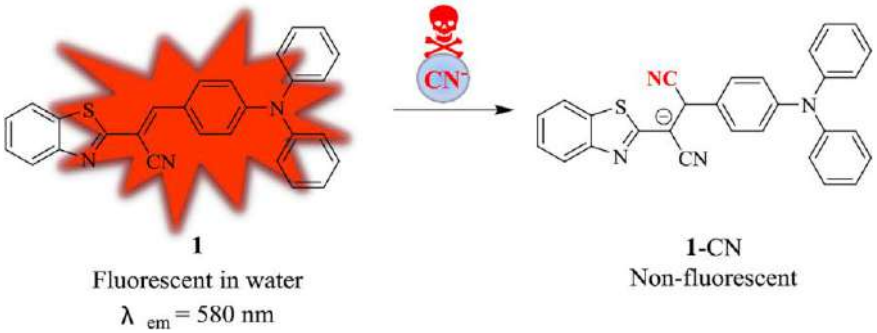

Figure 17 Recommended detection mechanism of Compound 1 for CN^- [24].

In the study of H. J. Jung et al. in 2008, benzothiazole, called Receptor 3, was prepared by the condensation reaction of isophthalaldehyde with 2-(2-aminophenyl)-benzothiazole. The molecular structure of the receptor 3 is shown. In the study, it was predicted that it could be an alternative to benzoimidazole compounds in metal sensor synthesis due to the sulfur atoms, which are potential donor groups in the benzothiazole ring in the structure of Receptor 3. In the study, it was determined that Receptor 3 has high linking affinity for a wide variety of metal ions and exhibits metal ion complexation using alternative linking sites with various metal ions, therefore it is not selective for any metal ion. Figure 18 shows the molecule structure of the Receptor 3 [25].

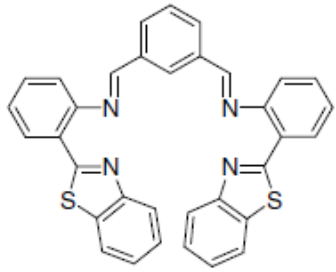

3

Figure18 Molecular Structure of receptor 3 [25].

3. General Aspect of Study

In our study, some benzothiazole derivative compounds used as fluorescent active chemosensors in the literature and their behavior against various metal ions were investigated. Although benzothiazole derivative compounds are a highly studied group in the literature, especially due to their biological activities, there is a wide area for studies on the synthesis of benzothiazole derivative fluorescent active compounds. With derivatization of the benzothiazole structure, the synthesis of new fluorescently active compounds is highly possible. This will continue to make the subject of benzothiazole derivative fluorescent active compound synthesis attractive for the scientific world in the coming years.

References

1. Malik, A., 2004, "Metal Bioremediation through growing cells", *Environmental International,* 30, 261-278.
2. Nies, D. H., 2003, "Efflux-mediated heavy metal resistance in prokaryotes", *FEMS Microbiology Reviews*, 27, 313-339.
3. Bruins, M. R., Kapil, S., Oehme, F.W., 2000, "Microbial resistance to metals in the environment", *Ecotoxicology and Environmental Safety*, 45, 198-207.
4. Alpat, K., Yüksel, U., Akçay, H., 2005, "Development of a novel carbon paste electrode containing a natural zeolite fort he voltammetric determination of copper*", Electrochemistry Communications*, 7(2), 130-134.
5. Leray, I., Valeur, B., 2009, Extended Calix[4]arene-Based Receptors for Molecular Recognition and Sensing *Eur. J. Inorg. Chem.,* 3525–3535.
6. G.J. He, X.L. Zhang, C. He, X.W. Zhao, C.Y. Duan, Ratiometric fluorescencechemosensors for copper(II) and mercury(II) based on FRET systems, Tetrahedron 66 (2010) 9762–9768;
7. Martinez-Manez, R., Sancenon, F., 2003, "Fluorogenic and chromogenic chemosensors and reagents for anions", *Chem. Rev*., 103(11), 4419-4476.
8. Lu, H. J., Fan, Y. T., Wu, Y. J., Yin, M. C., 2001, "Tripodal lipophilic ionophores: synthesis, cation binding and transport through liquid membranes", *Polyhedron* 20, 3281-3286.
9. Goodall, M., Kelly, P. M., Peter, D., 1997, "Selective cation binding with cis, cis-1,3,5-trioxycyclohexyl based ligands", *J. Chem. Soc. Perkin Trans*. *2*, 59-70.
10. Coskun, A., Akkaya, E. U., 2005, "Ion sensing coupled to resonance energy transfer: a highly selective and sensitive ratiometric fluorescent chemosensor for Ag(I) by a modular approach", *Journal of the American Chemical Society*, 127, 10464-10465.
11. Kim, S. H., Kim, H. J., Yoon, J., Kim, J. S., 2007, "Calixarenes in the Nanoworld Fluorescent Chemosensors", *Springer*, 311–333.
12. Bozdemir, O. A., Guliyev, R., Buyukcakir, O., Selcuk, S., Kolamen, S., Gulseren, G., Nalbantoglu, D., Boyaci, H., Akkaya, E. U., 2010, " Selective Manipulation of ICT and PET Processes in Styryl-Bodipy Derivatives: Applications in Molecular Logic and Fluorescence Sensing of Metal Ions", *Journal of the American Chemical Society,* 132, 8029-8036.

13. F.D. Natale, A. Lancia, A. Molino, M.D. Natale, D. Karatza, D. Musmarra, Captureof mercury ions by natural and industrial materials, J. Hazard. Mater. 132 (2006)220–225
14. A. Renzoni, F. Zino, E. Franchi, Mercury levels along the food chain and riskfor exposed populations, Environ. Res. A 77 (1998) 68–72;
15. J.M. Benoit, W.F. Fitzgerald, A.W.H. Damman, The biogeochemistry of anombrotrophic bog: evaluation of use as an archive of atmospheric mercurydeposition, Environ. Res. A 78 (1998) 118–133.
16. Jian Hua Wanga, Yao Ming Liub, Zhen Ming Donga, Jian Bin Chaob, Hui Wangc,∗, Yu Wanga, New colorimetric and fluorometric chemosensor for selective Hg^{2+} sensing in a near-perfect aqueous solution and bio-imaging, Journal of Hazardous Materials 382 (2020) 121056
17. S. Das, H. K. Indurthi, P. Asati, P. Saha, D. K. Sharma, Benzothiazole based fluorescent probes for the detection of biomolecules, physiological conditions, and ions responsible for diseases , Dyes and Pigments 199 (2022) 110074
18. Dhaka, G.; Singh, J.; Kaur, N.; 2017, "Benzothiazole based chemosensors having appended amino group(s): Selective binding of Hg^{2+} ions by three related receptors" Inorganica Chimica Acta 462, 152–157.
19. D. Britto C. Leslee, K. Sekara,, M. M. Kothotti, Carbazole-hydrazinobenzothiazole a selective turn-on fluorescent sensor for Hg2+ions – Its protein binding and electrochemical application studies, Journal of Photochemistry & Photobiology, A: Chemistry 415 (2021) 113303
20. S. Bozkurt, E. Halay, Synthesis of Benzothiazole Bearing Calixarene as a Chemical Sensor with Triggered Fluorescence Property for Chlorite Ion, *European Journal of Science and Technology No. 21, pp. 486-492, January 2021*
21. E. HALAY, S. BOZKURT, Synthesis and enantiomeric recognition studies of triazine-based chiral fluorescent compounds, *J. BAUN Inst. Sci. Technol., 20(2), 124-134, (2018).*
22. P. Purushothaman, S. Karpagam, Thiophene-Appended Benzothiazole Compounds for Ratiometric Detection of Copper and Cadmium Ions with Comparative Density Functional Theory Studies and Their Application in Real-TimeSamples, ACS Omega 2022, 7, 41361−41369
23. K. Wang, W. Feng, Y. Wang, D. Cao , R. Guan, X. Yu, Q. Wu,A coumarin derivative with benzothiazole Schiff's base structure as

chemosensor for cyanide and copper ions, Inorganic Chemistry Communications 71 (2016) 102–104
24. X. Chena, L. Wanga, X. Yanga, L. Tanga, Y. Zhoub, R. Liub, J. Qua,A new aggregation-induced emission active fluorescent probe forsensitive detection of cyanide, Sensors and Actuators B 241 (2017) 1043–1049
25. Highly Fe3+ selective ratiometric fluorescent probe based on imine-linked benzimidazole, Hee Jung Jung, Narinder Singh, Doo Ok Jang , Tetrahedron Letters 49 (2008) 2960–2964.

Nanofertilizer and Antibacterial Properties of Green Synthesized ZnO Nanoparticle using Echinops viscosus subsp. bithynicus

Kağan VERYER[1] , Yusuf ZALAOĞLU[2] , Fuat BOZOK[3] , Nazmi SEDEFOĞLU[4]

[1] *Res. Asst., Department of Biology, Faculty of Arts and Sciences, Osmaniye Korkut Ata Univer-sity, 80000, Osmaniye, Türkiye, kaganveryer@osmaniye.edu.tr*

[2]*Assoc. Prof. Dr., Department of Electricity and Energy, Osmaniye Korkut Ata University, 80000, Osmaniye, Türkiye, yzalaoglu@osmaniye.edu.tr*

[3]*Assoc. Prof. Dr., Department of Biology, Faculty of Arts and Sciences, Osmaniye Korkut Ata University, 80000, Osmaniye, Türkiye, fbozok@osmaniye.edu.tr*

[4]*Asst. Prof. Dr., Department of Physics, Faculty of Arts and Sciences, Osmaniye Korkut Ata University, 80000, Osmaniye, Türkiye, nazmisedefoglu@osmaniye.edu.tr*

INTRODUCTION

Nanoparticles (NPs) are materials smaller than 100 nm that are frequently used in medicine, food, agriculture, and other industries (Jadoun et al. 2013; Rennick et al. 2021; Shilpi et al. 2021). These particles can produce with various methods in nanotechnology. The various methods to produce nanoparticles have been extensively researched and published, but some methods are both expensive and environmentally harmful (Tao et al. 2021; Farhadi et al. 2022).

Green synthesis has long been used as a cheap and clean alternative method (Elumalai et al. 2010; Duan et al. 2015; Irshad et al. 2018). In this environmentally friendly method, biological agents such as mushrooms and plant extracts are used to produce nanoparticles. Recently studies indicated that ZnO, Ag, Au, and other nanoparticles were successfully synthesized by using plant extracts (Parveen et al. 2016). ZnO is a precious metal oxide used in many devices and industries such as nano sensors, energy storage, and cosmetics thanks to its chemical properties (Jones et al. 2008; Thema et al. 2015). If the dimension of materials shrinks to the nanometer size, obtained the new materials earn unique electrical, optical, and mechanical features. However, the new materials may earn a detrimental effect on human healthcare and the environment. But, the toxic effect of ZnONPs is quite low, and this situation makes it a valuable nanoparticle for biomedical and other applications. Moreover, in earlier studies, the chemical and physical properties of ZnONPs produced with green synthesis by using various extracts were investigated by different researchers (Kalpana et al. 2018; Sharmila et al. 2019; Mohamed et al. 2020; Thi et al. 2020; Rambabu et al. 2021; Karthik et al. 2022; Sebuso et al. 2022).

In this study, green synthesized ZnO-NP was obtained with extract of *Echinopsviscosus* subsp. *bithynicus* belonging to the family Asteraceae. This is the first report on nano fertilizer and antimicrobial properties of ZnO-NP with *E. viscosus* subsp. *bithynicus* collected from Osmaniye province of Türkiye.

MATERIAL AND METHODS

Preparation of Plant-extract

The flowers of *Echinopsviscosus* subsp. *bithynicus* were collected from Osmaniye province of Türkiye and powdered by a blender. 10 g powdered flowers were boiled in 100 ml dH_2O for one hour at 100 ºC. And then, the extract obtained was cooled down at room temperature and filtered by using Whatman No. 1 filter paper.

ZnO-NP Production

5 g $(CH_3COO)_2Zn.2H_2O$ were mixed with 25 ml plant extract and 25 ml ethanol at 100 ºC until the solution has completely evaporated. Then, it was calcinated at 800°C for 60 min. Finally, a white powder was obtained.

XRD analysis

The structural properties of ZnO-NPs were investigated using CuKa (1.541 Å) RigakuMiniflex with Powder XRD and 2θ ranging between 20-70º. All the characteristic peaks of ZnO indicating planes were taken from the literature.

Effect of ZnO nanoparticles on Plant Growth

Two different seeds (*Lepidiumsativum* and *Zea mays*) purchased from the local market of Osmaniye were used for nanofertilizer of ZnO-NPs produced by *Echinopsviscosus* subsp. *bithynicus* extract. The seeds of *L. sativum* (n=50) and *Z. mays* (n=15) were placed into petri dishes (9 cm diameter, with two layers of Whatman No.1 paper) and ZnO-NPs was added to petri dishes at different concentrations (62.5, 125, 250, and 500 ppm) (Singh et al. 2019). The experiment was carried out in 3 replications.

Effect of ZnO nanoparticles on chlorophyll and carotenoid contents

0.1 g leaves from germinated seeds were taken and crushed in acetone solution (80%) with mortar and pestle then centrifuged at 4000 rpm for 10 minutes. Absorbance values of supernatants were measured at 480, 510, and 663 wavelengths with a spectrophotometer. Total chlorophyll and carotenoid contents were estimated by the methods of Arnon (1949) and Duxbury and Yentsch (1956), respectively.

Antibacterial Effect of ZnO nanoparticles

The antibacterial impact of ZnO-NPs has been studied using the Kirby-Baurer disc diffusion technique and McFarland turbidity. In the current investigation, two bacterial strains (*Escherichia coli* and *Bacillus subtilis*) were cultivated in liquid Luria Bertani-broth until McFarland turbidity occurred, then this bacterial solution was spread out to cover the entire surface of the Mueller-Hinton agar (MHA). The Kirby-Bauer disc diffusion method was used to examine the effects of sterile discs impregnated with ZnO-NP and kanamycin (control) at 50mg were placed on MHA and cultivated for 24 h in an incubator. The inhibition zones have been measured with a ruler (Gülmez and Algur, 2019).

Statistical Analysis

Statistical data were calculated using the Graphpad prism program version 9.3.1 and given in tables in the findings section. Statistical analysis of all data was evaluated with One-Way Anova according to SEM (standard error of the mean).

RESULTS AND DISCUSSION

The structural properties of ZnO-NPs were shown in Fig 1. As seen in Fig 1, all the characteristic peaks of ZnO such as (100), (002), (101), (102), (110), (103), (200), (112), and (201) planes were acquired the samples prepared, indicating that hexagonal wurtziteZnO without secondary phases was crystallized (JCPDS Card No 36-1451) (Vidya et al. 2013). No characteristic peaks of organic residues were observed. The highest intensity plane of obtained ZnO-NPs was determined as (111). Therefore, the (111) orientation was taken into account in the calculations done in order to determine the particle size of the sample. (111) Peak was located at 36.454^{o} with a FWHM of 0.181^{o}. Using the diffraction intensity of the (111) peak from the Debye-Sherrer equation, the average grain size of ZnO-NPs was around 48 nm.

$D = 0.89\lambda / \beta \cos \theta$

where the constant of shape factor is 0.89, the X-ray wavelength is 1.5148 Å, the full width at half maximum intensity (FWHM) is measured in radians, and the diffraction Bragg angle is measured in degrees.

Fig. 1. XRD results of ZnONPs

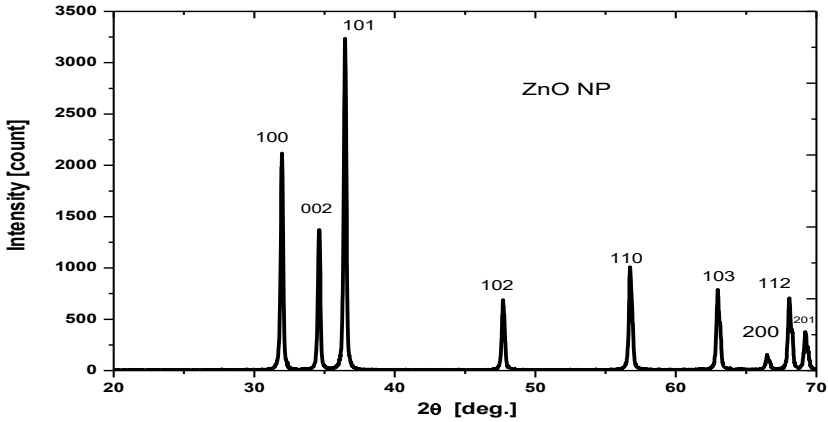

ZnO-NPs produced increased statistically the plumule elongation of *Lepidium sativum* at 62,5 and 125 ppm concentrations and *Zea mays* at 125, 250, and 500 ppm concentrations, although decreased the radicle elongation of both plants when compared to the control (Fig 2-3). Chlorophyll (a and b) and carotenoid contents of both *L. sativum* and *Z. mays* were increased significantly by applying ZnO-NPs at the lowest concentration (62,5 ppm) (Fig 4-5).

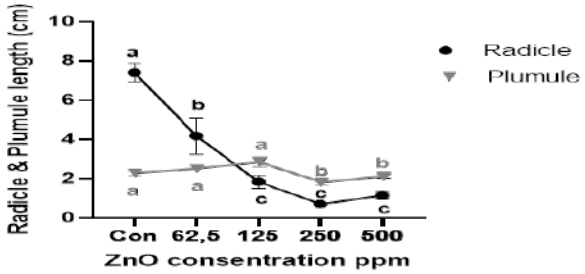

Fig. 2. ZnO-NPs effect on radicle and plumule of *L. sativum*

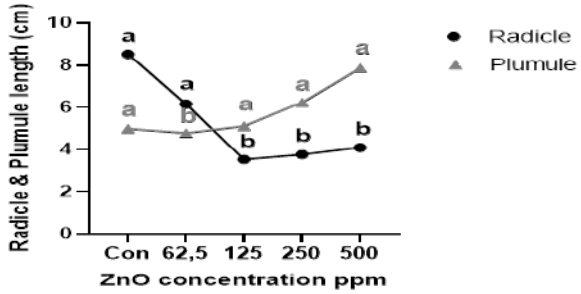

Fig. 3. ZnO-NPs effect on plumule and radicle of *Z. Mays*

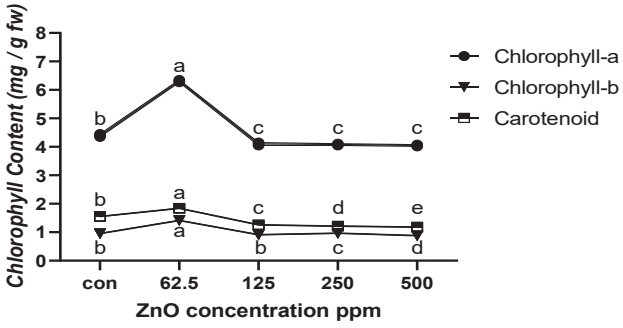

Fig. 4. ZnO-NPs effect on total chlorophyll and carotenoid contents of *L. sativum*

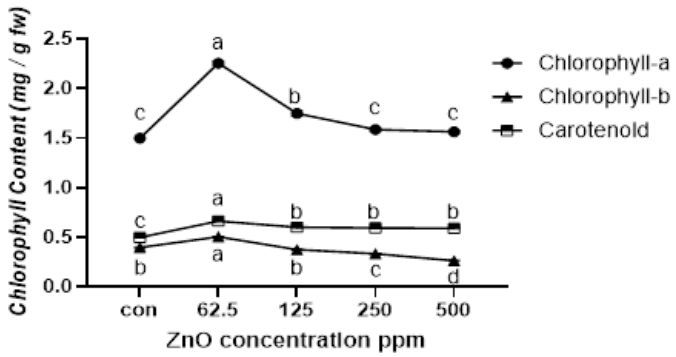

Fig. 5. ZnO-NPs effect on total chlorophyll and carotenoid contents of Z. mays

In this study, it was found that green synthesized ZnO-NPs showed a significant antibacterial effect against two bacterial species. In Fig 6, the antibacterial activity of ZnO-NPs has been demonstrated. ZnO-NP was more effective against *E. coli* than *B. subtilis*. The activities of green synthesized ZnO-NPs against both *E. coli* and *B. subtilis* were found to be higher than the negative control (dH_2O) and lower than the kanamycin antibiotic used as a positive control.

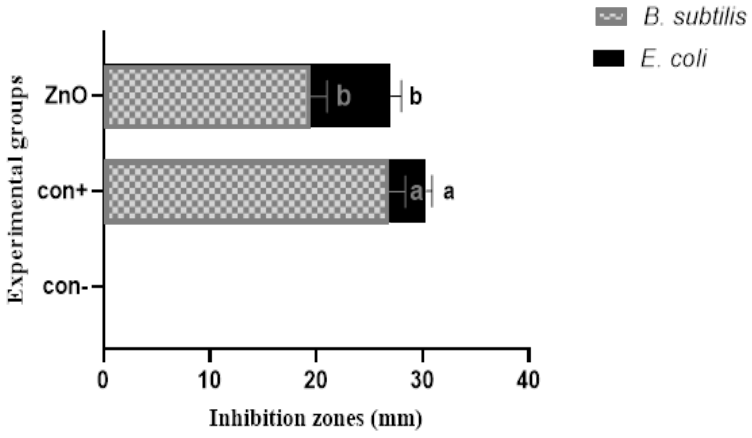

Fig. 6. ZnO-NPs effect on two strains of bacteria

ZnO nanoparticles are a valuable industrial material but producing ZnO is costly and environmentally harmful. Green synthesis is a good alternative method to this dilemma. In the present study, ZnO-NP is produced from *E. viscosus* subsp. *bithynicus* water extract with an inexpensive and eco-friendly method, and this shows similarities with previous studies (Agarwal et al. 2017; Nava et al. 2017; Khatami et al. 2018; Bandeira et al. 2020). In the literature, plenty of methods have for the identification of nanoparticles. Some of them are fourier transform infrared spectroscopy, energy dispersion analysis of X-ray, transmission electron microscopy, UV-visible diffuse reflectance spectroscopy, atomic force microscope, field emission scanning electron microscopy, scanning electron microscopy, photoluminescence analysis, thermogravimetric analysis, differential scanning calorimetry, X-ray diffraction, and so on. The fact that the NP used in the present study is ZnO-NPs has been proven by comparing with the ZnO-NPs specific XRD card number (JCPDS Card No 36-1451) of the peaks obtained using the XRD method [12, 16]. In the previous studies, high concentrations of ZnO-NPs have an inhibitory effect on plant germination. In most studies, the positive effects of ZnO used in low concentrations on the germination of different seeds (tomato, green and red beans) have been proven (Sabir et al. 2014; Hussain et al. 2015; Nguyen et al. 2021; Khan et al. 2021).

Increasing antibiotic resistance of bacteria against antibiotics that are used constantly has become a serious issue nowadays, and innovative approaches are required to this predicament, one of these innovative approaches is nanoparticles (Aslam et al. 2018). The antibacterial properties of ZnO-NPs to use make it more effective (Gunalan et al. 2012; Raghavendra et al. 2017; Suresh et al. 2018; Anand et al. 2019; Umavathi et al. 2021; Gharpure et al. 2022). This study is similar to previous studies in terms of antibacterial activity. Elumalai et al. (2015) investigated antimicrobial activities of green synthesized ZnO-NPs using leaf extract of *Azadirachta indica* collected from Annamalai Nagar, Tamil Nadu, India on the different bacterial strains (S. *aureus, B. subtilis, P. aeruginosa, P. mirabilis,* and *E. coli*) and found that ZnO-NPs affected significantly against all tested strains. In the other studies, ZnO-NPs were obtained by using *Atalantia monophyla* leaves collected from India and *Amygdalus scoparia* stem bark collected from Iran and it was determined that two bacterial strains such as *E. coli* and *B. subtilis* tested in the present studywere significantly inhibited by these ZnO-NPs, respectively (Vijayakumar et al. 2018; Jobie et al. 2021).

CONCLUSIONS

To the best of our knowledge, this is the first report on nano fertilizer and antibacterial properties of green synthesized ZnO-NPs using the extract of *E. viscosus* subsp. *bithynicus,* collected from the East Mediterranean of Türkiye. According to the XRD data, ZnO-NPs with wurtzite structure and free of the secondary phase and impurity were synthesized. ZnO-NPs produced increased the plumule elongation of both *Lepidium sativum* and *Zea mays*, although decreased the radicle elongation of both plants when compared to the control. And also, it has been proven that ZnO-NP has significant antimicrobial activity against *Escherichia coli* and *Bacillus subtilis*. Further studies could be done in real field conditions to confirm the nano fertilizer properties of green synthesized ZnO-NPs by using different plant extracts.

REFERENCES

1. Jadoun S., Arif R.N., Jangid, K., Meena, R.K. (2020).Green synthesis of nanoparticles using plant extracts: A review.*Environmental Chemistry Letters*, 19(1), 355-374.
2. Rennick, J. J.A., Johnston, P.R., Parton, R.G. (2021). Key principles and methods for studying the endocytosis of biological and nanoparticle therapeutics.*Nature Nanotechnology*, 16(3), 266-276.
3. Shilpi, S., Zeba, U., Atanas, A.G.S., Vinod, K., Pratap, S.N., Azeem, A., Ahmed, M., Ram, P., Govid, G., Minaxi, S., Atul, B. (2021). Biological nanofactories: Using living forms for metal nanoparticle synthesis.*Mini-Reviews in Medicinal Chemistry*, 21(2), 245-265.
4. Tao, H., Wu, T., Aldeghi, M., Wu, T.C., Guzik, A.A., Kumacheva, E. (2021). Nanoparticle synthesis assisted by machine learning.*Nature Reviews Materials*, 6 (8), 701-716.
5. Farhadi, L., Mohtashami, M., Saeidi, J., Nezhad, M.A., Taheri, G., Taheri, R.K., Shirvan, A.R., Shamloo, E., Ghasemi, A. (2022). Green synthesis of chitosan-coated silver nanoparticle, characterization, antimicrobial activities, and cytotoxicity analysis in cancerous and normal cell lines.*Journal of Inorganic and Organometallic Polymers and Materials*, 2022, 1-13.
6. Elumalai, E.K., Prasad, T.N.V.K.V., Kambala, V., Nagajyothi, P.C., David, E. (2010). Green synthesis of silver nanoparticle using *Euphorbia hirtaL*and their antifungal activities.*Archives of Applied Science Research*, 2(6), 76-81.
7. Duan, H., Wang, D., Li, Y. (2015). Green chemistry for nanoparticle synthesis.*Chemical Society Reviews Journal,* 44 (16), 5778-5792.
8. Irshad, S., Salamat, A., Anjum, A.A., Sana, S., Saleem, R.S., Naheed, A. (2018). Green tea leaves mediated ZnO nanoparticles and ıts antimicrobial activity.*Cogent Chemistry*, 4(1), 146920.
9. Parveen, K., Banse, V., Ledwani, L. (2016). Green synthesis of nanoparticles: their advantages and disadvantages, *AIP Conference Proceedings*, 020048 (1), 1724.
10. Jones, N., Ray, B., Ranjit, K.T. (2008). Manna, A.C., Antibacterial activity of ZnO nanoparticle suspensions on a broad spectrum of microorganisms. *FEMS Microbiology Letters*, 279 (1), 71-76.
11. Thema, F.T., Manikandan, E., Dhlamini, M.S., Maaza, M. (2015). Green synthesis of ZnO nanoparticles via *Agathosma betulina* natural extract. *Materials Letters*, 161, 124-127.

12. Kalpana V.N., Rajeswari V.D. (2018). A review on green synthesis, biomedical applications, and toxicity studies of ZnO NPs.*Bioinorganic Chemistry and Applications*, 2018, 3569758.
13. Sharmila, G., Thirumarimurugan, M., Muthukumaran, C. (2019). Green synthesis of ZnOnanoparticles using*Tecoma castanifolia*leaf extract: Characterization and evaluation of its antioxidant, bactericidal and anticancer activities.*Microchemical Journal*, 145, 578-587.
14. Mohamed, A.A., Elghait, M.A. (2020). Ahmed, N.E., Salem, S.S., Ecofriendly mycogenic synthesis of ZnO and CuO nanoparticles for *in vitro* Antibacterial, antibiofilm, and antifungal applications.*Biological Trace Element Research*, 199 (7), 2788-2799.
15. Thi, T.U.D., Nguyen, T.T., Thi, Y.D., Thi, K.H.T., Phan, B.T., Pham, K.N. (2020). Green synthesis of ZnOnanoparticles using orange fruit peel extract for antibacterial activities, *RSC Advances,* 10 (40), 23899-23907.
16. Rambabu, K., Bharath, G., Banat, F., Show, P.L. (2021). Green synthesis of zinc oxide nanoparticles using *Phoenix dactylifera* waste as bioreductant for effective dye degradation and antibacterial performance in wastewater treatment.*Journal of Hazardous Materials*, 402, 123560.
17. Karthik, K.V., Raghu, A.V., Reddy, K.R., Ravishankar, R., Sangeeta, M., Shetti, N.P., Reddy, C.V. (2022). Green synthesis of Cu-doped ZnO nanoparticles and its application for the photocatalytic degradation of hazardous organic pollutant.*Chemosphere*, 287(2), 132081.
18. Sebuso, D.P., Kuvarega, A.T., Lefatshe, K., King'ondu, C.K., Numan, N., Maaza, M., Muiva, C.M. (2022). Green synthesis of multilayer graphene/ZnO nanocomposite for photocatalytic applications.*Journal of Alloys and Compounds*, 900(2022), 163526.
19. Şenkardeş, İ., Bulut, G., Doğan, A., Tuzlacı, E. (2019). An ethnobotanical analysis on wild edible plants of the Turkish Asteraceae, Taxa.*Agriculturae Conspectus Scientificus*, 84 (1), 17-28.
20. Singh, J., Kumar, S., Alok, A., Upadhyay, S.K., Rawat, M., Tsang, D.C.W., Bolan, N., Kim, K.H. (2019). The potential of green synthesized zinc oxide nanoparticles as nutrient source for plant growth.*Journal of Cleaner Production*, 214, 1061-1070.
21. Arnon, D.I. (1949). Copper enzymes in ısolated chloroplasts. polyphenoloxidase in *Beta vulgaris*.*Plant Physiology*, 24 (1), 1-15.
22. Duxbury, A.C., Yentsch, C.S. (1956). Plankton pigment nomographs. University of Washington, *Tech. rep.*, 56.

23. Gülmez, Ö., Algur, Ö.F. (2019). Bazı bitkilerin alkol ekstrelerinin antimikrobiyal özelliklerinin belirlenmesi. *Journal of Science of East,* 2 (2), 54-60.
24. Vidya, C., Hiremath, S., Chandraprabha, M.N., Antonyaj, M.A.L., Gopal, I.V., Jain, A., Bansal, K. (2013). Green synthesis of ZnOnanoparticles by *Calotropis gigantea*.*International Journal of Current Engineering and Technology*, 1(1),118-120.
25. Agarwal, H., Kumar, S.V., Rajesjkumar, S. (2017). A review on green synthesis of zinc oxide nanoparticles–An eco-friendly approach.*Resource-Efficient Technologies*, 3 (4), 406-413.
26. Nava, O.J., Luque, P.A., Gutiérrez, C.M.G., Nestor, A.R.V., Beltrán, A.C., González, M.L.M., Olivas, A. (2017). Influence of *Camellia sinensis*extract on zinc oxide nanoparticle green synthesis.*Journal of Molecular Structure*, 1134, 121-125.
27. Khatami, M., Varma, R.S., Zafarnia, N., Yaghoobi, H., Sarani, M., Kumar, V.G. (2018). Applications of green synthesized Ag, ZnO and Ag/ZnO nanoparticles for making clinical antimicrobial wound-healing bandages.*Sustainable Chemistry and Pharmacy*, 10, 9-15.
28. Bandeira, M., Giovanela, M., Ely, M.R., Devine, D.M., Crespo, J.D.S. (2020). Green synthesis of zinc oxide nanoparticles: a review of the synthesis methodology and mechanism of formation. *Sustainable Chemistry and Pharmacy*, 15(2020), 100223.
29. Sabir, S., Arshad, M., Chaudhari, S.K. (2014). Zinc oxide nanoparticles for revolutionizing agriculture: Synthesis and applications.*The Scientific World Journal,* 2014, 952494.
30. Hussain, I., Singh, N.B., Singh, A., Singh, H., Singh, S.C. (2015). Green synthesis of nano zinc oxide and evaluation of its ımpact on germination and metabolic activity of *Solanum lycopersicum*.*Journal of Biotechnology,* 233, 84-94.
31. Nguyen, D.T.C., Le, H.T.N., Nguyen, T.T., Nguyen, T.T.T., Bach, L.G., Nguyen, T.D., Tran, T.V. (2021). Multifunctional ZnO nanoparticles biofabricated from *Canna indica*L. flowers for seed germination, adsorption, and photocatalytic degradation of organic dyes.*Journal of Hazardous Materials*, 420(2021), 126586.
32. Khan, M.I., Fatima, N., Shakil, M., Tahir, M.B., Riaz, K.N., Rafique, M., Iqbal, T., Mahmood, K. (2021). Investigation of *in-vitro*antibacterial and seed germination properties of green synthesized pure and nickel doped ZnO nanoparticles, *Physica B: Condensed Matter*, 601(2021), 412563.

33. Aslam, B., Wang, W., Arshad, M.I., Khurshid, M., Muzammil, S., Rasool, M.H., Nisar, M.A., Alvi, R.F., Aslam, M.A., Qamar, M.U., Salamat, M.F.K., Baloch, S. (2018). Antibiotic resistance: A rundown of aglobal crisis.*Infection and Drug Resistance,* 11, 1645-1658.
34. Gunalan, S., Sivaraj, R., Rajendran, V. (2012). Green synthesized ZnO nanoparticles against bacterial and fungal pathogens.*Progress in Natural Science: Materials International*, 22(6), 693-700.
35. Raghavendra, M., Yatish, K.V., Lalithamba, H.S. (2017). Plant-mediated green synthesis of ZnO nanoparticles using*Garcinia gummi-gutta*seed extract: Photoluminescence, screening of their catalytic activity in antioxidant, formylation and biodiesel production.*The European Physical Journal Plus,* 132(8), 1-12.
36. Suresh, J., Pradheesh, G., Alexramani, V., Sundrarajan, M., Hong, S.I. (2018). Green synthesis and characterization of Zinc oxide nanoparticle using ınsulin plant (*Costus pictus D. Don*) and investigation of its antimicrobial as well as anticancer activities.*Advances in Natural Sciences: Nanoscience and Nanotechnology*, 9 (1), 015008.
37. Anand, G.T., Renuka, D., Ramesh, R., Anandaraj, L., Sundaram, S.J., Ramalingam, G., Magdalane, C.M., Bashir, A.K.H., Maaza, M., Kaviyarasu, K. (2019). Green Synthesis Of ZnO Nanoparticle using *Prunus dulcis* (Almond Gum) for antimicrobial and supercapacitor applications. *Surfaces and Interfaces*, 17(2019), 100376.
38. Umavathi, S., Mahboob, S., Govindarajan, M., Ghanim, K.A.A., Ahmed, Z., Virik, P., Mulhm, N.A., Subash, M., Gopinath, K., Kavitha, C. (2021). Green synthesis of ZnO nanoparticles for antimicrobial and vegetative growth applications: A novel approach for advancing efficient high quality health care to human wellbeing.*Saudi Journal of Biological Sciences*, 28(3), 1808-1815.
39. Gharpure, S., Yadwade, R., Ankamwar, B. (2022). Non-antimicrobial and non-anticancer properties of ZnO nanoparticles biosynthesized using different plant parts of *Bixa orellana*.*American Chemical Society*, 2022, 1914-1933.
40. Elumalai, K., Melmurugan, S. (2015). Green synthesis, characterization and antimicrobial activities of zinc oxide nanoparticles from the leaf extract of *Azadirachta indica* (*L.*).*Applied Surface Science*, 345, 329-336.
41. Vijayakumar, S., Mahadevan, S., Arulmozhi, P., Sriram, S., Praseetha, P.K. (2018). Green synthesis of Zinc oxide nanoparticles using *Atalantia monophylla*leaf extracts: characterization and antimicrobial analysis.*Materials Science in Semiconductor Processing,* 82, 39-45.

42. Jobie, F.N., Ranjbar, M., Moghaddam, A.H., Kiani, M., Green synthesis of Zinc oxide nanoparticles using *Amygdalus scoparia* Spach stem bark extract and their applications as an alternative antimicrobial, anticancer, and anti-diabetic agent.*Advanced Powder Technology*, 32(6), 2043-2052.

Some New Generalizations Of Fractional Hardy-Type Integral On Time Scale Calculus

Dr. Lütfi Akın

Mardin Artuklu University
ORCID: 0000-0002-5653-9393

1. Introduction

The discrete Hardy inequality, which has a very important place in the literature, was developed by G. H. Hardy [1]. Let(b_n) be a sequence of non-negative real numbers and for $c > 1$, $c \in R$, then we have

$$\sum_{m=1}^{\infty}\left(\frac{b_1 + b_2 + b_3 + \cdots + b_m}{m}\right)^c < \left(\frac{c}{c-1}\right)^c \sum_{m=1}^{\infty} b_m^c.$$

The classical Hardy inequality was proved by G.H. Hardy [2]. If w^c is integrable for $w(\tau) \geq 0$and $c > 1$, then

$$\int_0^{\infty}\left(\frac{1}{s}\int_0^{s} w(\tau)d\tau\right)^c ds \leq \left(\frac{c}{c-1}\right)^c \int_0^{\infty} w^c(s)ds. \qquad (1)$$

Later, the inequality (1) was generalized by G. H. Hardy[3]. Let $c > 1$, $w(\tau) > 0$ and w integrable on $(0,\infty)$, then we have

$$\int_0^{\infty}\left(\frac{1}{t^n}\int_t^{\infty} w(\tau)d\tau\right)^c dt \leq \left(\frac{c}{1-n}\right)^c \int_0^{\infty}\frac{1}{t^{n-c}} w^c(t)dt, \quad n < 1, \qquad (2)$$

$$\int_0^{\infty}\left(\frac{1}{t^n}\int_0^{t} w(\tau)dr\right)^c dt \leq \left(\frac{c}{n-1}\right)^c \int_0^{\infty}\frac{1}{t^{n-c}} w^c(t)dt, \quad n > 1. \qquad (3)$$

In [4], Hardy and Littlewood developed the discrete versions of the inequalities (2) and (3) previously proved. If (b_n) is a sequence of non-negative terms for $c > 1$, then we have

$$\sum_{n=1}^{\infty}\frac{1}{n^k}\left(\sum_{m=n}^{\infty} b_m\right)^c \leq M\sum_{n=1}^{\infty}\frac{1}{n^{k-c}} b_n^c, \quad k < 1,$$

$$\sum_{n=1}^{\infty}\frac{1}{n^k}\left(\sum_{m=1}^{n} b_m\right)^c \leq M\sum_{n=1}^{\infty}\frac{1}{n^{k-c}} b_n^c, \quad k > 1,$$

where$M$ is a non-negative constant. For more detailed information on Hardy inequalities, see [5-8].

Let $H_\propto$ and $\widetilde{H}_\propto$ be a fractional Hardy-type integral operator and its adjointon $(0,\infty)$,

$$H_\propto v(t) = \frac{1}{t^{1-\propto}}\int_0^{t} v(s)ds, \qquad \widetilde{H}_\propto v(t) = \int_t^{\infty}\frac{1}{t^{1-\propto}} v(s)ds,$$

where$0 \leq \propto < 1$ (see [9]). When $\propto = 0$, we denote H_0 as H and $\widetilde{H}_0$ as $\widetilde{H}$. In [1,4], G.H. Hardy established the Hardy-type integral inequalities

$$\int_0^\infty |Hv(x)|^p dx \leq \left(p'\right)^p \int_0^\infty |v(x)|^p dx, \quad p > 1,$$

$$\int_0^\infty \left|\widetilde{H}v(x)\right|^p dx \leq p^p \int_0^\infty |v(x)|^p dx, \quad p > 1,$$

where $1/p + 1/p' = 1$. The above Hardy-type integral inequalities have many applications in analysis (for details see [10-12]).

2. Mathematical background on time scales

Studies on time scales for half a century, especially integral inequalities and dynamic equations, have gained a very important place in the world of mathematics and science.In this chapter, we will give some concepts that will be necessary for us to prove our results (for details [13-17, 20, 21]). A time scale is known as a completely arbitrary, non-empty closed subset of real numbers and it is denoted by $\mathbb{T}$ notation. The $(0,\infty)_{\mathbb{T}}$ is denoted by $(0,\infty) \cap \mathbb{T}$.

Themappings$\sigma, \rho: \mathbb{T} \to \mathbb{T}$definedby$\sigma(t) = \inf\{s \in \mathbb{T}: s > t\}$ ($\sigma(t)$ is forwardjumpoperator), $\rho(t) = \sup\{s \in \mathbb{T}: s > t\}$ ($\rho(t)$ is backwardjumpoperator), for$t \in \mathbb{T}$.

- If$\sigma(t) > t$, then$t$ is right-scattered and if $\sigma(t) = t$, then t is called right-dense.
- If$\rho(t) < t$, then$t$ is left-scattered and if $\rho(t) = t$, then t is called left-dense.
- Lettwomappings$\mu, \vartheta: \mathbb{T} \to \mathbb{R}^+$ such that $\mu(t) = \sigma(t) - t$, $\vartheta(t) = t - \rho(t)$ are called graininess mappings.
- If$\mathbb{T}$ has a left-scattered maximum m, then $\mathbb{T}^k = \mathbb{T} - \{m\}$. Otherwise $\mathbb{T}^k = \mathbb{T}$. Briefly

$$\mathbb{T}^k = \begin{cases} \mathbb{T} \setminus (\rho \sup \mathbb{T}, \sup \mathbb{T}], & \text{if} \quad \sup \mathbb{T} < \infty, \\ \mathbb{T}, & \text{if} \quad \sup \mathbb{T} = \infty. \end{cases}$$

Bythesameway

$$\mathbb{T}_k = \begin{cases} \mathbb{T} \setminus [\inf \mathbb{T}, \sigma(\mathbb{T})], & |\inf \mathbb{T}| < \infty, \\ \mathbb{T}, & \inf \mathbb{T} = -\infty. \end{cases}$$

Assumethat$\varphi: \mathbb{T} \to \mathbb{R}$ is a function and $t \in \mathbb{T}^k (t \neq min\mathbb{T})$,

- Ifφ is $\Delta -$ differentiable at point$t$, then φ is continuous at point t.
- Ifφ is left continuous at point t and t is right-scattered, then φ is $\Delta -$ differentiable at point t,

$$\varphi^{\Delta}(t) = \frac{\varphi^{\sigma}(t) - \varphi(t)}{\mu(t)}.$$

Let$t$ be a right-dense,

- Ifφ is $\Delta -$ differentiable at point t and $\lim_{s\to t}\frac{\varphi(t)-\varphi(s)}{t-s}$, then
$$\varphi^{\Delta}(t) = \lim_{s\to t}\frac{\varphi(t) - \varphi(s)}{t - s}.$$
- Ifφ is $\Delta -$ differentiable at point t, then $\varphi^{\sigma}(t) = \varphi(t) + \mu(t)\varphi^{\Delta}(t)$.
- If$\mathbb{T} = \mathbb{R}$, then $\varphi^{\Delta}(t) = \varphi'(t)$.
- If$\mathbb{T} = \mathbb{Z}$, then $\varphi^{\Delta}(t)$ reduces to $\Delta\varphi(t)$.

Let $\varphi: \mathbb{T} \to \mathbb{R}$ and $\varphi^{\sigma}: \mathbb{T} \to \mathbb{R}$ by $\varphi^{\sigma}(t) = \varphi(\sigma(t))$ for all $t \in \mathbb{T}$, i.e., $\varphi^{\sigma} = \varphi \circ \sigma$ and let $\varphi: \mathbb{T} \to \mathbb{R}$ and $\varphi^{\rho}: \mathbb{T} \to \mathbb{R}$ by $\varphi^{\rho}(t) = \varphi(\rho(t))$ for all $t \in \mathbb{T}$, i.e., $\varphi^{\rho} = \varphi \circ \rho$.

The Hilger derivative (delta derivative) $\varphi^{\Delta}(t)$ is defined as follows.

Foreverye$\varepsilon > 0$ and $s, t \in V$ there exists a neighborhood V of t such that
$$\left|\varphi\big(\sigma(t)\big) - \varphi(s) - \varphi^{\Delta}(t)(\sigma(t) - s)\right| \leq |\sigma(t) - s|.$$

SupposethatΦ: $\mathbb{T} \to \mathbb{R}$ is defined$\Delta -$antiderivative of $\varphi: \mathbb{T} \to \mathbb{R}$, then $\Phi^{\Delta} = \varphi(t)$holdsforall$t \in \mathbb{T}$ and we define the Cauchy $\Delta -$integral of φ by
$$\int_{s}^{t} \varphi(\tau)\Delta\tau = \Phi(t) - \Phi(s),$$

for$s, t \in \mathbb{T}$. Supposethattworeal-valued$rd -$continuous functions$v, w : \mathbb{R} \to \mathbb{R}$ is Hilger (delta) differentiable, then$v \circ w: \mathbb{R} \to \mathbb{R}$ is Hilger (delta) differentiableand

$$(v \circ w)^{\Delta}(x) = \left\{\int_{0}^{1} v'(w(x) + \varphi\mu(x)w^{\Delta}(x))\, d\varphi\right\} w^{\Delta}(x). \tag{4}$$

If v, w satisfy the conditions of [14, Theorem 1.90], then $v \circ w: \mathbb{T} \to \mathbb{R}$ is Hilger (delta) differentiable such that

$$(v \circ w)^{\Delta}(x) = v'\big(w(d)\big)w^{\Delta}(x) \tag{5}$$

where$d \in [x, \sigma(x)]$.

Toproveourfindings, wewillconsiderthefollowingnotations,

$$\begin{cases} (wv)^{\Delta} = w^{\Delta}v + w^{\sigma}v^{\Delta} = wv^{\Delta} + w^{\Delta}v^{\sigma}, \\ \left(\frac{w}{v}\right)^{\Delta} = \frac{w^{\Delta}v - wv^{\Delta}}{vv^{\sigma}} \end{cases} \tag{6}$$

where$vv^{\sigma} \neq 0$ and $v^{\sigma} = v \circ \sigma$.

A function$\pi: \mathbb{T} \to \mathbb{R}$is regressiveprovided$1 + \mu(s)\pi(s) \neq 0,\ s \in \mathbb{T}$. In[14, Theorem 1.90], theKeller'schainrule isdefinedby

$$\left(\Theta^{\delta}(s)\right)^{\Delta} = \delta \int_0^1 \left[w\Theta^{\delta} + (1-w)\Theta\right]^{\delta-1} dw\Theta^{\Delta}(s), \tag{7}$$

where$\delta \in \mathbb{R}$.

If$a, b \in \mathbb{T}$and$u, v \in C_{rd}(\mathbb{T})$($C_{rd}(\mathbb{T})$ is set of all rd −continuous functions), then

$$\int_a^b u(x)v^{\Delta}(x)\Delta x = [u(x)v(x)]_a^b - \int_a^b v^{\sigma}(x)u^{\Delta}(x)\Delta x. \tag{8}$$

In [14], Hölder's inequality [states that two real-valued rd −continuous functions $w, \varphi: \mathbb{T} \to \mathbb{R}$, $a, b \in \mathbb{T}$, then

$$\int_a^b |w(x)\varphi(x)|dx \leq \left(\int_a^b \left(w(x)\right)^{\propto} dx\right)^{\frac{1}{\propto}} \left(\int_a^b \left(\varphi(x)\right)^{\beta} dx\right)^{\frac{1}{\beta}}. \tag{9}$$

where$\propto > 1$ and $1/\propto + 1/\beta = 1$.

Fortheremainder of ourwork, wewillassumethatthefunctionsv_k, φ_k, and g_k in theexpressions of ourtheoremsarepositivefunctionsandrd −continuous.Wewillalsoneedthefollowingarithmetic-geometricinequalitytohelp us withtheproofs. (see [18, page 17])

$$\prod_{k=1}^{m} {\delta_k}^{\beta_k} < \sum_{k=1}^{m} \delta_k\beta_k, \tag{10}$$

where$\sum_{k=1}^{m} \beta_k = 1$. Now, let us define the operators

$$D_k(\theta) = \frac{1}{v_k(\theta)} \int_a^{\theta} v_k(s)\varphi_k(s)\mu_k(s)\Delta s, \tag{11}$$

$$H_{k,\propto}\varphi(\theta) = \frac{1}{\theta^{1-\propto}} \int_a^{\theta} \varphi_j(s)\Delta s, \tag{12}$$

where$\theta \in [a, \infty)_{\mathbb{T}}$ and $k = 1,2, \ldots, m$.

3. Main Result

Theorem 3.1. Let $\beta_k < \delta_k$ and $1 < \beta_k < \gamma_k$ for $k = 1,2,\dots,m$ such that $\sum_{k=1}^{m} \beta_k = 1$. Let $v_k(\theta)$ be a non-increasing and non-negative functions for $k = 1,2,\dots,m$, and let $g_k(\theta)$ be a non-decreasing and non-negative functions for $k = 1,2,\dots,m$. If there exist constants $\rho_k > 0$ for $k = 1,2,\dots,m$ satisfying

$$\left[\frac{H^{\sigma}_{k,\propto}\varphi(\theta)}{H_{k,\propto}\varphi(\theta)}\right]^{\frac{\delta_k}{\beta_k}} \frac{\gamma_k H_{k,\propto}\varphi(\theta) {v_k}^{\Delta}(\theta)}{(\delta_k - \beta_k)\varphi_k(\theta)v_k(\theta)} + 1$$

$$\geq \left[\frac{H^{\sigma}_{k,\propto}\varphi(\theta)}{H_{k,\propto}\varphi(\theta)}\right]^{\frac{\delta_k}{\beta_k}} \frac{\gamma_k H_{k,\propto}\varphi(\theta) {g_k}^{\Delta}(\theta)}{(\delta_k - \beta_k)\varphi_k(\theta)g^{\sigma}_k(\theta)} + \frac{1}{\rho_k}, \tag{13}$$

then for any constants $C_k > 0$, we have

$$\int_b^{\infty} \prod_{k=1}^{m} \left([D^{\sigma}_k(\theta)]^{\gamma_k} \frac{[g^{\sigma}_k(\theta)\varphi_k(\theta)]^{\beta_k}}{\left[H^{\sigma}_{k,\propto}\varphi(\theta)\right]^{\delta_k}} \right) \Delta\theta$$

$$\leq \left[\prod_{k=1}^{m} \frac{1}{C_k^{\gamma_k}}\right] \sum_{k=1}^{m} L_k \int_b^{\infty} g^{\sigma}_k(\theta)\varphi_k(\theta)\mu_k^{\frac{\gamma_k}{\beta_k}}(\theta) \frac{\left(H^{\sigma}_{k,\propto}\varphi(\theta)\right)^{\frac{\delta_k}{\beta_k}\left(\frac{\gamma_k}{\beta_k}-1\right)}}{\left(H_{k,\propto}\varphi(\theta)\right)^{\frac{\gamma_k}{\beta_k}\left(\frac{\delta_k}{\beta_k}-1\right)}} \Delta\theta, \tag{14}$$

where $L_k = \beta_k \left(C_k \frac{\rho_k \gamma_k}{\delta_k - \beta_k}\right)^{\frac{\gamma_k}{\beta_k}}$.

Proof. If we integrate the left-hand side of (14) for $\vartheta(\theta) = -\int_{\theta}^{\infty} \varphi_k(s) \left(H^{\sigma}_{k,\propto}\varphi(s)\right)^{-\frac{\delta_k}{\beta_k}} \Delta s$, then we have

$$\int_b^{\infty} \frac{g^{\sigma}_k(\theta)\varphi_k(\theta)[D^{\sigma}_k(\theta)]^{\frac{\gamma_k}{\beta_k}}}{\left(H^{\sigma}_{k,\propto}\varphi(\theta)\right)^{\frac{\delta_k}{\beta_k}}} \Delta\theta = -\int_b^{\infty} \vartheta(\theta) \left(g_k(\theta) D_k^{\frac{\gamma_k}{\beta_k}}(\theta) \right)^{\Delta} \Delta\theta, \tag{15}$$

where we use (8) with

$$\begin{cases} \lambda^{\sigma}(\theta) = g^{\sigma}_k(\theta)[D^{\sigma}_k(\theta)]^{\frac{\gamma_k}{\beta_k}} \\ \vartheta^{\Delta}(\theta) = \dfrac{\varphi_k(\theta)}{\left(H^{\sigma}_{k,\propto}\varphi(\theta)\right)^{\frac{\delta_k}{\beta_k}}} \end{cases},$$

to obtain

$$\int_b^{\infty} \frac{g_k^{\sigma}(\theta)\varphi_k(\theta)[D_k^{\sigma}(\theta)]^{\frac{\gamma_k}{\beta_k}}}{\left(H_{k,\propto}^{\sigma}\varphi(\theta)\right)^{\frac{\delta_k}{\beta_k}}}\Delta\theta$$

$$= \vartheta(\theta)g_k(\theta)D_k^{\frac{\gamma_k}{\beta_k}}(\theta)I_b^{\infty} - \int_b^{\infty} \vartheta(\theta)\left(g_k(\theta)D_k^{\frac{\gamma_k}{\beta_k}}(\theta)\right)^{\Delta}\Delta\theta.$$

From (7), we obtain that

$$\left(\left(H_{k,\propto}\varphi(s)\right)^{1-\frac{\delta_k}{\beta_k}}\right)^{\Delta}$$

$$= \left(1-\frac{\delta_k}{\beta_k}\right)\int_0^1 \left(\tau H_{k,\propto}^{\sigma}\varphi(s) + (1-\tau)H_{k,\propto}(s)\right)^{-\frac{\delta_k}{\beta_k}} d\tau H_{k,\propto}^{\Delta}\varphi(s)$$

$$\leq \left(1-\frac{\delta_k}{\beta_k}\right)\int_0^1 \left(\tau H_{k,\propto}^{\sigma}\varphi(s) + (1-\tau)H_{k,\propto}^{\sigma}\varphi(s)\right)^{-\frac{\delta_k}{\beta_k}} d\tau H_{k,\propto}^{\Delta}\varphi(s)$$

$$= \left(1-\frac{\delta_k}{\beta_k}\right)\left(H_{k,\propto}^{\sigma}\varphi(s)\right)^{-\frac{\delta_k}{\beta_k}}\varphi_k(s),$$

so

$$\left(H_{k,\propto}^{\sigma}\varphi(s)\right)^{-\frac{\delta_k}{\beta_k}}\varphi_k(s) \leq \frac{\beta_k}{\beta_k-\delta_k}\left(\left(H_{k,\propto}\varphi(s)\right)^{1-\frac{\delta_k}{\beta_k}}\right)^{\Delta}.$$

Therefore

$$\vartheta(\theta) = -\int_{\theta}^{\infty}\left(H_{k,\propto}^{\sigma}\varphi(s)\right)^{-\frac{\delta_k}{\beta_k}}\varphi_k(s)\Delta s \leq \frac{\beta_k}{\beta_k-\delta_k}\int_{\theta}^{\infty}\left(\left(H_{k,\propto}\varphi(s)\right)^{1-\frac{\delta_k}{\beta_k}}\right)^{\Delta}\Delta s$$

$$= \frac{\beta_k}{\delta_k-\beta_k}\left(\left(H_{k,\propto}\varphi(s)\right)^{1-\frac{\delta_k}{\beta_k}} - I_k\right) \leq \frac{\beta_k}{\delta_k-\beta_k}\left(H_{k,\propto}\varphi(s)\right)^{1-\frac{\delta_k}{\beta_k}}. \qquad (16)$$

Combining (15) and (16) weobtainthat

$$\int_b^{\infty} \frac{g_k^{\sigma}(\theta)\varphi_k(\theta)[D_k^{\sigma}(\theta)]^{\frac{\gamma_k}{\beta_k}}}{\left(H_{k,\propto}^{\sigma}\varphi(\theta)\right)^{\frac{\delta_k}{\beta_k}}}\Delta\theta$$

$$\leq \frac{\beta_k}{\delta_k-\beta_k}\int_b^{\infty}\left(H_{k,\propto}\varphi(\theta)\right)^{1-\frac{\delta_k}{\beta_k}}\left(g_k(\theta)D_k^{\frac{\gamma_k}{\beta_k}}(\theta)\right)^{\Delta}\Delta\theta. \qquad (17)$$

If we use the definition of $D_k(\theta)$, the multiplication rule (6) gives:

$$D_k^{\Delta}(\theta)=\frac{[v_k(\theta)\varphi_k(\theta)\mu_k(\theta)]}{v_k(\theta)}+\left(-\frac{v_k^{\Delta}(\theta)}{v_k(\theta)v_k^{\sigma}(\theta)}\right)\int_b^{\sigma(\theta)}v_k(s)\varphi_k(s)\mu_k(s)\Delta s$$

$$=\varphi_k(\theta)\mu_k(\theta)-\frac{v_k^{\Delta}(\theta)D_k^{\sigma}(\theta)}{v_k(\theta)}\geq 0.$$

Applyingthechainruleforc $\in[\theta,\sigma(\theta)]$,

$$\pi^{\Delta}\big(\eta(\theta)\big)=\pi'\big(\eta(c)\big)\pi^{\Delta}(\theta), \qquad (18)$$

weobtainthat

$$\left(D_k^{\frac{\gamma_k}{\beta_k}}(\theta)\right)^{\Delta}=\frac{\gamma_k D_k^{\frac{\gamma_k}{\beta_k}-1}(c)}{\beta_k}D_k^{\Delta}(\theta).$$

Since $D_k^{\Delta}(\theta)\geq 0$and $\sigma(\theta)\geq c$, we have that

$$\left(D_k^{\frac{\gamma_k}{\beta_k}}(\theta)\right)^{\Delta}\leq\frac{\gamma_k D_k^{\sigma\left(\frac{\gamma_k}{\beta_k}-1\right)}(\theta)}{\beta_k}\left[\varphi_k(\theta)\mu_k(\theta)-\frac{v_k^{\Delta}(\theta)D_k^{\sigma}(\theta)}{v_k(\theta)}\right]$$

$$=\frac{\gamma_k\varphi_k(\theta)\mu_k(\theta)D_k^{\sigma\left(\frac{\gamma_k}{\beta_k}-1\right)}(\theta)}{\beta_k}-\frac{\gamma_k v_k^{\Delta}(\theta)D_k^{\frac{\sigma\gamma_k}{\beta_k}}(\theta)}{\beta_k v_k(\theta)},$$

and we obtain that

$$\left(g_k(\theta)D_k^{\frac{\gamma_k}{\beta_k}}(\theta)\right)^{\Delta}=D_k^{\frac{\gamma_k}{\beta_k}}(\theta)g_k^{\Delta}(\theta)+\left(D_k^{\frac{\gamma_k}{\beta_k}}(\theta)\right)^{\Delta}g_k^{\sigma}(\theta)$$

$$\leq D_k^{\frac{\sigma\gamma_k}{\beta_k}}(\theta)g_k^{\Delta}(\theta)+\frac{\gamma_k g_k^{\sigma}(\theta)\varphi_k(\theta)\mu_k(\theta)D_k^{\sigma\left(\frac{\gamma_k}{\beta_k}-1\right)}(\theta)}{\beta_k}$$

$$-\frac{\gamma_k g_k^{\sigma}(\theta)v_k^{\Delta}(\theta)D_k^{\frac{\sigma\gamma_k}{\beta_k}}(\theta)}{\beta_k v_k(\theta)}.$$

Substituting (19) into (17), we have that

$$\int_b^{\infty} \frac{g_k^{\sigma}(\theta)\varphi_k(\theta)D_k^{\frac{\sigma\gamma_k}{\beta_k}}(\theta)}{\left(H_{k,\propto}^{\sigma}\varphi(\theta)\right)^{\frac{\delta_k}{\beta_k}}}\Delta\theta \le \frac{\beta_k}{\delta_k-\beta_k}\int_b^{\infty}\left(H_{k,\propto}\varphi(\theta)\right)^{1-\frac{\delta_k}{\beta_k}} g_k^{\Delta}(\theta)D_k^{\frac{\sigma\gamma_k}{\beta_k}}(\theta)\Delta\theta$$

$$+\frac{\gamma_k}{\delta_k-\beta_k}\int_b^{\infty}\left(H_{k,\propto}\varphi(\theta)\right)^{1-\frac{\delta_k}{\beta_k}} g_k^{\sigma}(\theta)\varphi_k(\theta)\mu_k(\theta)D_k^{\sigma\left(\frac{\gamma_k}{\beta_k}-1\right)}(\theta)\Delta\theta$$

$$-\frac{\gamma_k}{\delta_k-\beta_k}\int_b^{\infty}\frac{g_k^{\sigma}(\theta)v_k^{\Delta}(\theta)}{v_k(\theta)}\left(H_{k,\propto}\varphi(\theta)\right)^{1-\frac{\delta_k}{\beta_k}} D_k^{\frac{\sigma\gamma_k}{\beta_k}}(\theta)\Delta\theta.$$

Thisand (13) implythat

$$\int_{\square}^{\infty} \frac{\square_{\square}^{\square}(\square)\square_{\square}(\square)}{\left(\square_{\square,\propto}^{\square}\square(\square)\right)^{\frac{\square\square}{\beta\square}}}\square_{\square}^{\frac{\square\square\square}{\square\square}}(\square)\Delta\square$$

$$\le \frac{\rho_k\gamma_k}{\delta_k-\beta_k}\int_b^{\infty}\left(H_{k,\propto}\varphi(\theta)\right)^{1-\frac{\delta_k}{\beta_k}} g_k^{\sigma}(\theta)\varphi_k(\theta)\mu_k(\theta)D_k^{\sigma\left(\frac{\gamma_k}{\beta_k}-1\right)}(\theta)\Delta\theta$$

$$=\frac{\rho_k\gamma_k}{\delta_k-\beta_k}\int_b^{\infty}\left(\frac{\left(H_{k,\propto}\varphi(\theta)\right)^{1-\frac{\delta_k}{\beta_k}} g_k^{\sigma}(\theta)\varphi_k(\theta)\mu_k^{\frac{\gamma_k}{\beta_k}}(\theta)}{\left(H_{k,\propto}^{\sigma}\varphi(\theta)\right)^{-\frac{\delta_k}{\beta_k}\left(\frac{\gamma_k}{\beta_k}-1\right)}}\right)^{\frac{\beta_k}{\gamma_k}}$$

$$\times\left(\frac{g_k^{\sigma}(\theta)\varphi_k(\theta)D_k^{\frac{\sigma\gamma_k}{\beta_k}}(\theta)}{\left(H_{k,\propto}^{\sigma}\varphi(\theta)\right)^{\frac{\delta_k}{\beta_k}}}\right)^{\frac{\gamma_k-\beta_k}{\gamma_k}}\Delta\theta.$$

ByapplyingHölder'sinequality, weobtain

$$\int_{b}^{\infty} \frac{g_k^{\sigma}(\theta)\varphi_k(\theta)D_k^{\frac{\sigma\gamma_k}{\beta_k}}(\theta)}{\left(H_{k,\propto}^{\sigma}\varphi(\theta)\right)^{\frac{\delta_k}{\beta_k}}}\Delta\theta$$

$$\leq \frac{\rho_k\gamma_k}{\delta_k-\beta_k}\left(\int_{b}^{\infty} \frac{\left(H_{k,\propto}\varphi(\theta)\right)^{1-\frac{\delta_k}{\beta_k}} g_k^{\sigma}(\theta)\varphi_k(\theta)\mu_k^{\frac{\gamma_k}{\beta_k}}(\theta)}{\left(H_{k,\propto}^{\sigma}\varphi(\theta)\right)^{-\frac{\delta_k}{\beta_k}\left(\frac{\gamma_k}{\beta_k}-1\right)}}\Delta\theta\right)^{\frac{\beta_k}{\gamma_k}}$$

$$\times\left(\int_{b}^{\infty} \frac{g_k^{\sigma}(\theta)\varphi_k(\theta)D_k^{\frac{\sigma\gamma_k}{\beta_k}}(\theta)}{\left(H_{k,\propto}^{\sigma}\varphi(\theta)\right)^{\frac{\delta_k}{\beta_k}}}\Delta\theta\right)^{\frac{\gamma_k-\beta_k}{\gamma_k}}.$$

Thisgives us that

$$\int_{\square}^{\infty} \frac{\square_{\square}^{\square}(\square)\square_{\square}(\square)\square_{\square}^{\frac{\square\square}{\square\square}}(\square)}{\left(\square_{\square,\propto}^{\square}\square(\square)\right)^{\frac{\square}{\square\square}}}\Delta\square$$

$$\leq\left(\frac{\rho_k\gamma_k}{\delta_k-\beta_k}\right)^{\frac{\gamma_k}{\beta_k}}\int_{b}^{\infty} \frac{g_k^{\sigma}(\theta)\varphi_k(\theta)\mu_k^{\frac{\gamma_k}{\beta_k}}(\theta)\left(H_{k,\propto}^{\sigma}\varphi(\theta)\right)^{\frac{\delta_k}{\beta_k}\left(\frac{\gamma_k}{\beta_k}-1\right)}}{\left(H_{k,\propto}^{\sigma}\varphi(\theta)\right)^{\frac{\gamma_k}{\beta_k}\left(\frac{\delta_k}{\beta_k}-1\right)}}\Delta\theta.$$

Forany$C_k > 0$, and by using the inequality (10), we obtain

$$\prod_{k=1}^{m}\left(\frac{g_k^{\sigma}(\theta)\varphi_k(\theta)\left(D_k^{\sigma}(\theta)\right)^{\gamma_k}}{\left(H_{k,\propto}^{\sigma}\varphi(\theta)\right)^{\delta_k}}\right)$$

$$=\prod_{k=1}^{m}\frac{1}{C_k^{\gamma_k}}\left\{\left(C_k\frac{D_k^{\sigma}(\theta)[g_k^{\sigma}(\theta)\varphi_k(\theta)]^{\frac{\beta_k}{\gamma_k}}}{\left(H_{k,\propto}^{\sigma}\varphi(\theta)\right)^{\frac{\delta_k}{\gamma_k}}}\right)^{\frac{\gamma_k}{\beta_k}}\right\}^{\beta_k}$$

$$= \left[\prod_{k=1}^{m} \frac{1}{C_k^{\gamma_k}}\right] \prod_{k=1}^{m} \left\{ \left(C_k \frac{D_k^{\sigma}(\theta)[g_k^{\sigma}(\theta)\varphi_k(\theta)]^{\frac{\beta_k}{\gamma_k}}}{\left(H_{k,\propto}^{\sigma}\varphi(\theta)\right)^{\frac{\delta_k}{\gamma_k}}} \right)^{\frac{\gamma_k}{\beta_k}} \right\}^{\beta_k}$$

$$\leq \left[\prod_{k=1}^{m} \frac{1}{C_k^{\gamma_k}}\right] \sum_{k=1}^{m} \frac{\beta_k C_k^{\frac{\gamma_k}{\beta_k}} g_k^{\sigma}(\theta)\varphi_k(\theta)\left(D_k^{\sigma}(\theta)\right)^{\frac{\gamma_k}{\beta_k}}}{\left(H_{k,\propto}^{\sigma}\varphi(\theta)\right)^{\frac{\delta_k}{\gamma_k}}}.$$

Herewith

$$\int_b^{\infty} \prod_{k=1}^{m} \left(\frac{g_k^{\sigma}(\theta)\varphi_k(\theta)\left(D_k^{\sigma}(\theta)\right)^{\gamma_k}}{\left(H_{k,\propto}^{\sigma}\varphi(\theta)\right)^{\delta_k}} \right) \Delta\theta$$

$$\leq \left[\prod_{k=1}^{m} \frac{1}{C_k^{\gamma_k}}\right] \sum_{k=1}^{m} \beta_k C_k^{\frac{\gamma_k}{\beta_k}} \int_b^{\infty} \frac{g_k^{\sigma}(\theta)\varphi_k(\theta)\left(D_k^{\sigma}(\theta)\right)^{\frac{\gamma_k}{\beta_k}}}{\left(H_{k,\propto}^{\sigma}\varphi(\theta)\right)^{\frac{\delta_k}{\gamma_k}}} \Delta\theta$$

$$\leq \left[\prod_{k=1}^{m} \frac{1}{C_k^{\gamma_k}}\right] \sum_{k=1}^{m} L_k \int_b^{\infty} g_k^{\sigma}(\theta)\varphi_k(\theta)\mu_k^{\frac{\gamma_k}{\beta_k}}(\theta) \frac{\left(H_{k,\propto}^{\sigma}\varphi(\theta)\right)^{\frac{\delta_k}{\beta_k}\left(\frac{\gamma_k}{\beta_k}-1\right)}}{\left(H_{k,\propto}^{\sigma}\varphi(\theta)\right)^{\frac{\gamma_k}{\beta_k}\left(\frac{\delta_k}{\beta_k}-1\right)}} \Delta\theta,$$

where$L_k = \beta_k \left(\frac{\rho_k \gamma_k C_k}{\delta_k - \beta_k}\right)^{\frac{\gamma_k}{\beta_k}}$.

Corollary 3.2. Let$\varphi_k(\theta) = g_k(\theta) = 1, v_k(\theta)$be non increasingandnon-negativefunctionsfor$k = 1,2, \dots, m$,and define

$$D_k(\theta) = \frac{1}{v_k(\theta)} \int_b^{\theta} v_k(s)\mu_k(s)\Delta s, \tag{21}$$

where$\theta \in [b, \infty)_{\mathbb{T}}$. If there exist constants $\rho_k > 0$for$k = 1,2, \dots, m$ satisfying $\left(\frac{\gamma_k}{\delta_k - \beta_k}\right)\frac{(\theta - b)v_k^{\Delta}(\theta)}{v_k(\theta)} \geq \frac{1}{\rho_k} - 1$, then, for any constants $C_k > 0$, we have

$$\int_b^{\infty} \prod_{k=1}^{m} \left(\frac{\left(D_k^{\sigma}(\theta)\right)^{\gamma_k}}{(\sigma(\theta) - b)^{\delta_k}} \right) \Delta\theta$$

$$\leq \left[\prod_{k=1}^{m} \frac{1}{C_k^{\gamma_k}}\right] \sum_{k=1}^{m} L_k \int_b^{\infty} \mu_k^{\frac{\gamma_k}{\beta_k}}(\theta) \frac{(\sigma(\theta)-b)^{\frac{\delta_k}{\beta_k}\left(\frac{\gamma_k}{\beta_k}-1\right)}}{(\theta-b)^{\frac{\gamma_k}{\beta_k}\left(\frac{\delta_k}{\beta_k}-1\right)}} \Delta\theta,$$

where $L_k = \beta_k C_k^{\frac{\gamma_k}{\beta_k}} \left(\frac{\rho_k \gamma_k}{\delta_k - \beta_k}\right)^{\frac{\gamma_k}{\beta_k}}$.

Remark 3.3. In Corollary 3.2, if we take $\mathbb{T} = \mathbb{R}, b = \propto = 0$ and replace $\mu_k(\theta)$ by $\frac{\mu_k(\theta)}{\theta}$, we obtain Theorem 1 in [19] proved by Cheung et al.

4. Conclusion

In this study, we focused on fractional Hardy-type integral inequalities, generalizing and improving the results presented in previous studies. To be more specific, we have created some new generalizations of fractional Hardy type integral inequalities in time scale calculation. These generalizations shed light on the solution of problems that arise in business, economics, physics, optics and other branches of science as well as mathematics.

References

5. Hardy, G.H. (1920).Note on a theorem of Hilbert, *Math. Z.* 6(3–4), 314–317.
6. Hardy, G.H. (1925).Notes on somepoints in the integral calculus, LX. An inequalitybetweenintegrals, *Mess. Math*. 54,150–156.
7. Hardy, G.H.,Littlewood, J.E. (1927).Elementarytheoremsconcerningpowerserieswithpositivecoefficientsand moment constants of positivefunctions, *J. ReineAngew. Math*. 157, 141–158.
8. Hardy, G.H. (1928).Notes on somepoints in the integral calculus, LXIV. *Mess. Math*. 57, 12–16.
9. Ahmad, W.,Khan, K.A., Nosheen, A., Sultan, M.A. (2019).Copson, Leindlertypeinequalitiesforfunction of severalvariables on time scales, *PunjabUniv. J. of Math*. 51(8),157–168.
10. Ashraf, M.S.,Khan, K.A., Nosheen, A. (2019).Hardy-Copsontypeinequalities on time scalesforthefunctions of n independentvariables, *Int. J. Anal. Appl.* 17(2), 244–259.
11. Baric, J., Bibi, R., Bohner, M., Nosheen, A., Pecaric, J. (2015).Jenseninequalitiesandtheirapplications on time scales, Element, Zagreb, Croatia.
12. Nosheen, A.,Nawaz, A., Khan, K.A., Awan, K.M. (in press)MultivariateHardyandLittlewoodinequalities on time scales, *Arap Journal of Mathematical Science*.
13. Li, W.,Liu, D., Liu, J. (2019).WeightedinequalitiesforfractionalHardyoperatorsandcommutators, *Journal of Inequalitiesand Applications* 2019:158, 1-14.
14. Bradley, J. (1978).Hardyinequalitieswithmixednorms. *Can. Math. Bull.* 21(4), 405-408.
15. Kufner, A.,Persson, L.E. (2003).WeightedInequalities of HardyType. World Scientific, Singapore.
16. Opic, B.,Kufner, A. (1990).Hardy-TypeInequalities. PitmanResearchNotes in Mathematics Series, LongmanScientificand Technical, Harlow, Essex.
17. Bohner, M.,Georgiev, S.G. (2016).Sequencesand Series of Functions. In: MultivariableDynamicCalculus on Time Scales, SpringerInt. Publ. Switzerland.
18. Bohner, M.,Peterson, A. (2001).DynamicEquations on Time Scales. An Introductionwith Applications, Birkhauser, Boston.

19. Agarwal, R.P.,Bohner, M., O'Regan, D., Saker, S.H. (2011).SomeWirtinger-typeinequalities on time scalesandtheirapplications, *Pacific J. Math.* 252, 1–26.
20. Akın, L. (2020). On theFractionalMaximal Delta IntegralTypeInequalities on Time Scales. *FractalFract*. 4, 26, 1-10.
21. Akın, L. (2020). On someresults of weightedHöldertypeinequality on time scales. *Middle East Journal of Science* 6(1), 15-22.
22. Hardy, G.H.,Littlewood, J.E., Polya, G. (1952).Inequalities, 2nd edn. Cambridge UniversityPress, Cambridge.
23. Cheung, W.-S.,Hanjs, Z, Pecari´c, J. (2000).SomeHardy-typeinequalities. *J. Math. Anal. Appl*. 250, 621–634.
24. Akın L. (2021). A New ApproachfortheFractionalIntegralOperator in Time ScaleswithVariableExponentLebesgueSpaces. *FractalFract*. 5(7), 1-13.
25. Akın L. (2021). On innovations of n-dimensional integral-typeinequality on time scales. *Adv. Differ. Equ*. 2021:148.

On New Dynamic Fractional Integral Inequalities On Time Scales

Dr. Lütfi Akın[1], Prof. Dr. Yusuf Zeren[2]

Mardin Artuklu University
ORCID: 0000-0002-5653-9393

Yıldız Technical University
ORCID: 0000-0001-8346-2208

1. Introduction

Inequalities, fractional integral operators, and dynamic equations have many important roles in time scales. The theory of time scales has applications not only in mathematics, but also in business, economics, physics, optics, etc. In this work, we will prove new dynamic fractional maximal type integral inequalities that provide more application in the mathematical literature as a result of generalizing inequalities using Keller's chain rule on time scales. The theory of time scales is based on Stefan Hilger [10]. For decades several dynamic inequalities and integral type equations have been established on time scales $\mathbb{T}$ [1-4, 14, 16-20]. The most important application areas that time scales offer us are integral inequalities, differential calculus and difference calculus, i.e, when $\mathbb{T} = \mathbb{R}$, $\mathbb{T} = \mathbb{N}$ and $\mathbb{T} = q^{\mathbb{N}_0} = \{q^t : t \in \mathbb{N}_0\}$ for $q > 1$. For details, the reader can refer to books [5, 6]. Anastassiou [4] introduced some features of fractional calculus on time scales, which are very important for our convenience in practice. Saker and O'Regan [14] proved some new dynamic inequalities on time scales. Akin [2] demonstrated some properties of the integral type inequalities on time scales. Rahman et al. [12] demonstrated tempered fractional integral inequalities for convex functions. Uçar et al. [18] showed a generalization of fractional integral type inequalities over time scales. Dynamic equations and integral type inequalities on time scales have many applications that help us solve problems in various scientific disciplines. For example, quantum mechanics, fluid dynamics, economics, and population dynamics [8, 9, 13, 17, 21, 22, 23].

2. Mathematical Background

In this chapter, necessary information will be given to guide us in proving our main conclusions. A time scale $\mathbb{T}$ is a closed non-empty subset of the real numbers $\mathbb{R}$. Throughout this work, wesuppose that $\sup \mathbb{T} = \infty$ and define $[t_0, \infty)_{\mathbb{T}}$ by $[t_0, \infty)_{\mathbb{T}} = [t_0, \infty) \cap \mathbb{T}$. The notation $f^{\sigma}(t) = f(\sigma(t))$.

Definition 2.1 [14] The mappings$\sigma, \rho : \mathbb{T} \to \mathbb{T}$are defined by$\sigma(t) = inf\ \{s \in \mathbb{T} : s > t\}$, $\rho(t) = \sup\{s \in \mathbb{T} : s > t\}fort \in \mathbb{T}$. Respectively, $\sigma(t), \rho(t)$ are forward jump operator and backward jump operator.

Definition 2.2 [14] Let two mappings $\mu, \vartheta : \mathbb{T} \to \mathbb{R}^+$ such that $\mu(t) = \sigma(t) - t$, $\vartheta(t) = t - \rho(t)$ are called graininess mappings.

Remark 2.3 [14]

- If $\sigma(t) > t$, then t is right-scattered.
- If $\rho(t) < t$, then t is left-scattered.
- If $\sigma(t) = t$, then t is called right-dense.
- If $\rho(t) = t$, then t is called left-dense.
- Let $f: \mathbb{T} \to \mathbb{R}$ and $\Theta: \mathbb{T} \to \mathbb{R}$ be any functions for $t \in \mathbb{T}$. Define $\Theta^{\Delta}(t)$ to be the number with the property that given any $\varepsilon > 0$ there is a neighborhood V of t with

$$\left|\left[\Theta\left(\sigma(t)\right) - \Theta(s)\right] - \Theta^{\Delta}(t)[\sigma(t) - s]\right| \leq \varepsilon|\sigma(t) - s|,$$

for all $s \in V$.

- If a time scale $\mathbb{T}$ has a left-scattered, then $\mathbb{T}^k = \mathbb{T} - \{k\}$. Otherwise $\mathbb{T}^k = \mathbb{T}$. Briefly

$$\mathbb{T}^k = \begin{cases} \mathbb{T} \setminus (\rho \sup \mathbb{T}, \sup \mathbb{T}], & \text{if} \quad \sup \mathbb{T} < \infty, \\ \mathbb{T}, & \text{if} \quad \sup \mathbb{T} = \infty. \end{cases}$$

By the same way

$$\mathbb{T}_k = \begin{cases} \mathbb{T} \setminus [\inf \mathbb{T}, \sigma(\inf \mathbb{T})], & |\inf \mathbb{T}| < \infty, \\ \mathbb{T}, & \inf \mathbb{T} = -\infty. \end{cases}$$

In [14], assume that $f: \mathbb{T} \to \mathbb{R}$ is a function and let $t \in \mathbb{T}^k (t \neq min\mathbb{T})$.

- If f is $\Delta -$ differentiable at point t, then f is continuous at point t.
- If f is left continuous at point t and t is right-scattered, then f is $\Delta -$ differentiable at point t,

$$f^{\Delta}(t) = \frac{f^{\sigma}(t) - f(t)}{\mu(t)}.$$

- Let t is right-dense. If f is $\Delta -$ differentiable at point t and $\lim_{s \to t} \frac{f(t)-f(s)}{t-s}$, then

$$f^{\Delta}(t) = \lim_{s \to t} \frac{f(t) - f(s)}{t - s}.$$

- If f is $\Delta -$ differentiable at point t, then $f^{\sigma}(t) = f(t) + \mu(t) f^{\Delta}(t)$.

Remark 2.4 [14]

i. If $\mathbb{T}=\mathbb{R}$, then $\sigma(s)=s,\ \mu(s)=0,\ g^{\Delta}(s)=g'(s),\ \int_a^b g(s)\Delta s=\int_a^b g(s)ds.$

ii. If $\mathbb{T}=\mathbb{Z}$, then $\sigma(s)=s+1,\ \mu(s)=1,\ g^{\Delta}(s)=\Delta g(s),\ \int_a^b g(s)\Delta s=\sum_{s=a}^{b-1} g(s).$

iii. If $\mathbb{T}=\lambda\mathbb{Z},\ \lambda>0,$ then $\sigma(s)=s+\lambda,\ \mu(s)=\lambda, \theta^{\Delta}(s)=\Delta_{\lambda}\theta(s)=\frac{\theta(s+\lambda)-\theta(s)}{(p-1)s}$,

and $\int_a^b g(s)\Delta s=\sum_{k=0}^{\frac{b-a}{\lambda}-1} g(a+k\lambda)\lambda.$

iv. If $\mathbb{T}=\{s: s=p^k, k\in\mathbb{N}_0, p>1\}$, then $\sigma(s)=ps,\ \mu(s)=(p-1)s,$ $\Theta^{\Delta}(s)=\Delta\Theta(s)=\frac{\Theta(ps)-\Theta(s)}{(p-1)s}$,

and $\int_{s_0}^b g(s)\Delta s=\sum_{k=n_0}^{\infty} g\left(p^k\right)\mu(p^k)$, where $s_0=p^{n_0}$.

v. If $\mathbb{T}=\mathbb{N}_0^2=\{n^2: n\in\mathbb{N}_0\}$, then $\sigma(s)=\left(\sqrt{s}+1\right)^2,\ \ \mu(s)=1+2\sqrt{s},$ $\Delta_{\mathbb{N}}\theta(s)=\frac{\theta(\sigma(s))-\theta(s)}{1+2\sqrt{s}}$.

Definition 2.5 [14]If $L^{\Delta}(s)=l(s)$, then delta integral of l is defined by

$$\int_a^s l(t)\Delta t=L(s)-L(a).$$

In [5], if $l\in C_{rd}(\mathbb{T})$ ($C_{rd}(\mathbb{T})$ is set of all $rd-$continuous functions), then delta (Hilger) integral $L(s)=\int_{s_0}^s l(t)\Delta t$ exists, $s_0\in\mathbb{T}$ and satisfies $L^{\Delta}(s)=l(s),\ s\in\mathbb{T}$. We will use the following notations product lf and quotient l/f rules for delta derivative ($ff^{\sigma}\neq 0, f^{\sigma}=f\circ\sigma$),

$$\begin{cases}(lf)^{\Delta}=l^{\Delta}f+l^{\sigma}f^{\Delta}=lf^{\Delta}+l^{\Delta}f^{\sigma},\\ \left(\frac{l}{f}\right)^{\Delta}=\frac{l^{\Delta}f-lf^{\Delta}}{ff^{\sigma}}\end{cases}\tag{2.1}$$

Definition 2.6 [5] A function $\pi:\mathbb{T}\to\mathbb{R}$is regressive provided $1+\mu(s)\pi(s)\neq 0,\ s\in\mathbb{T}$. The Keller's chain rule [5, Theorem 1.90] defined by

$$\left(\Theta^{\delta}(s)\right)^{\Delta}=\delta\int_0^1\left[g\Theta^{\delta}+(1-g)\Theta\right]^{\delta-1}dg\,\Theta^{\Delta}(s).\tag{2.2}$$

Using $f^{\sigma}(s)=f(s)+\mu(s)f^{\Delta}(s)$, we obtain

$$\left(\Theta^{\delta}(s)\right)^{\Delta} = \delta \int_0^1 \left[\Theta + g\mu(s)\Theta^{\Delta}(s)\right]^{\delta-1} dg\Theta^{\Delta}(s). \tag{2.3}$$

The integration is given by

$$\int_a^b f(s)\, g^{\Delta}(s)\Delta s = [f(s)g(s)]_a^b - \int_a^b f^{\Delta}(s)g^{\sigma}(s)\Delta s, \tag{2.4}$$

In [11], the inverse Hölder inequality to help us with our results is defined as follows. Let $a, b \in \mathbb{T}$ and $f, g \in C_{rd}(\mathbb{T}, \mathbb{R})$, we have

$$\left[\int_a^b |f(s)|^q \, \Delta s\right]^{\frac{1}{q}} \left[\int_a^b |g(s)|^p \, \Delta s\right]^{\frac{1}{p}} \leq C_p \int_a^b f(s)g(s)\Delta s, \tag{2.5}$$

where $p > 1$ and$\frac{1}{p}+\frac{1}{q}=1$.

Definition 2.7 [3] Let be $\Omega \subset \mathbb{R}^n$ (Ω is open set) and $0 < a < n$. $M_a f$ is defined by

$$M_a f(s) = \sup_{B \ni s} \frac{1}{|B|^{1-\frac{a}{n}}} \int_{B\cap\Omega} f(y)dy.$$

Definition 2.8 [4, Lemma 2; 7] If $f \in C_{rd}(\mathbb{T}, \mathbb{R})$, then

$$\int_s^{\sigma(s)} f(y)\Delta y = \mu(s)f(s),$$

and fractional maximal type $\Delta -$ integral is defined by

$$M_a f(s) = \sup_{B \ni s} \frac{1}{|B|^{1-\frac{a}{n}}} \int_a^s f(y)\Delta y,$$

where $f, M_a f \in L_1([a, s] \cap \mathbb{T})$ and L is Lebesgue $\Delta -$ integrable functions set on $[a, s] \cap \mathbb{T}$ for $s \in [a, s] \cap \mathbb{T}$.

3. Main Results

In this study, we will accept the functions in the theorems as non-negative and assume that they have integrals.

Theorem 3.1 Let $\mathbb{T}$ be a time scale with$q < p < 0$ and $a \in (0, n) \cap \mathbb{T}$ such that $\frac{p}{q} \geq 2$ and $\delta > 1$. Suppose that f is a non-negative function and delta integral $\int_a^n \big(\sigma(s)\big)^{\frac{p-q\delta}{q}} f^{\frac{p}{q}}(s)\Delta s$ exists. If

$$M_a f(s) = \sup_{B \ni s} \frac{1}{|B|^{1-\frac{a}{n}}} \int_a^s f(y)\Delta y, \tag{3.1}$$

where $s \in [a, n] \cap \mathbb{T}$, then

$$\int_a^n \frac{f^{\frac{p}{q}}(s)}{\big(\sigma(s)\big)^{\delta-\frac{p}{q}}} \Delta s \leq C_p \left(\frac{q(1-\delta)}{p}\right)^{\frac{p}{q}} \int_a^n \frac{\big(M_a f(s)\big)^{\frac{p}{q}}(s)}{\big(\sigma(s)\big)^{\delta}} \Delta s. \tag{3.2}$$

Proof If we integrate the left-hand side of (3.2) by (2.4) with $y^{\Delta}(s)\sigma^{\delta}(s) = 1$ and $x(s) = \big(M_a f(s)\big)^{\frac{p}{q}}$, we obtain

$$\int_a^n \frac{\big(M_a f(s)\big)^{\frac{p}{q}}}{\big(\sigma(s)\big)^{\delta}} \Delta s = y(s)(M_a f)^{\frac{p}{q}}(s) I_a^n + \int_a^n y^{\sigma}(s) \left(-(M_a f)^{\frac{p}{q}}(s)\right)^{\Delta} \Delta s, \tag{3.3}$$

where $y(s) = \int_a^s \big(\sigma(t)\big)^{-\delta} \Delta t$. Using (2.2) and $\sigma(t) \leq t$, we obtain

$$\big(t^{1-\delta}\big)^{\Delta} = (1-\delta) \int_0^1 [g\sigma(t) + (1-g)t]^{-\delta} dg$$

$$\leq (1-\delta) \int_0^1 [g\sigma(t) + (1-g)\sigma(t)]^{-\delta} dg = \frac{1-\delta}{\sigma^{\delta}(t)}.$$

Hence

$$y^{\sigma}(s) = \int_a^{\sigma(s)} [\sigma(t)]^{-\delta}\Delta t \geq \frac{1}{1-\delta}\int_a^{\sigma(s)} \left(t^{1-\delta}\right)^{\Delta}\Delta t$$

$$= \frac{1}{(1-\delta)\left(\sigma(s)\right)^{\delta-1}} - \frac{1}{(1-\delta)a^{\delta-1}} \geq \frac{\left(\sigma(s)\right)^{1-\delta}}{1-\delta}. \tag{3.4}$$

Combining (3.3), (3.4) and using $y(a) = 0$, we have

$$\frac{q(1-\delta)}{p}\int_a^n \frac{\left(M_a f(s)\right)^{\frac{p}{q}}}{\left(\sigma(s)\right)^{\delta}}\Delta s \geq \int_a^n \frac{f(s)\left(-\left(M_a f(s)\right)^{\frac{p}{q}}\right)^{\Delta}}{\left(\sigma(s)\right)^{\delta-1}}\Delta s. \tag{3.5}$$

Applying delta derivative (chain rule) $f^{\Delta}\left(f(s)\right) = f'(f(c))f^{\Delta}(s)$, we obtain

$$\frac{q}{p}\left(\left(M_a f(s)\right)^{\frac{p}{q}}\right)^{\Delta} = M_a f^{\frac{p}{q}-1}(c)\left(M_a f(s)\right)^{\Delta}, \tag{3.6}$$

where $c \in [s, \sigma(s)]$. Since $(M_a f)^{\Delta}(s) + f(s) \leq 0$ and $c \leq s$, we obtain

$$-\frac{q}{p}\left(\left(M_a f(s)\right)^{\frac{p}{q}}\right)^{\Delta} \geq \left(M_a f(s)\right)^{\frac{p-q}{q}} f(s). \tag{3.7}$$

Substituting (3.7) into (3.5), we obtain

$$\frac{q(1-\delta)}{p}\int_a^n \frac{\left(M_a f(s)\right)^{\frac{p}{q}}}{\left(\sigma(s)\right)^{\delta}}\Delta s \geq \int_a^n \frac{\left(M_a f(s)\right)^{\frac{p-q}{q}}}{\left(\sigma(s)\right)^{\delta-1}} f(s)\Delta s,$$

and

$$\frac{q(1-\delta)}{p}\int_a^n \frac{\left(M_a f(s)\right)^{\frac{p}{q}}}{\left(\sigma(s)\right)^{\delta}}\Delta s \geq \int_a^n \frac{\left(\left(\sigma(s)\right)^{\delta}\right)^{\frac{p-q}{p}}\left(M_a f(s)\right)^{\frac{p-q}{q}}}{\left(\sigma(s)\right)^{\delta-1}\left(\left(\sigma(s)\right)^{\delta}\right)^{\frac{p-q}{p}}} f(s)\Delta s. \tag{3.8}$$

If we use the inverse Hölder inequality (2.5) to the right side of inequality (3.8), then we obtain

$$C_p \int_a^n \left[\frac{\left(\left(\sigma(s) \right)^{\delta} \right)^{\frac{p-q}{p}} f(s)}{\left(\sigma(s) \right)^{\delta-1}} \right] \left(\left(\sigma(s) \right)^{\delta} \right)^{\frac{q-p}{p}} \left(M_a f(s) \right)^{\frac{p-q}{q}} \Delta s$$

$$\geq \left[\int_a^n \left[\frac{\left(\left(\sigma(s) \right)^{\delta} \right)^{\frac{p-q}{p}} f(s)}{\left(\sigma(s) \right)^{\delta-1}} \right]^{\frac{p}{q}} \Delta s \right]^{\frac{q}{p}} \left[\int_a^n \frac{\left(M_a f(s) \right)^{\frac{p}{q}}}{\left(\sigma(s) \right)^{\delta}} \Delta s \right]^{1-\frac{q}{p}}.$$

Substituting (3.9) into (3.8), we obtain

$$\int_a^n \frac{f^{\frac{p}{q}}(s)}{\left(\sigma(s) \right)^{\delta-\frac{p}{q}}} \Delta s \leq C_p \left(\frac{q(1-\delta)}{p} \right)^{\frac{p}{q}} \int_a^n \frac{\left(M_a f(s) \right)^{\frac{p}{q}}}{\left(\sigma(s) \right)^{\delta}} \Delta s. \tag{3.10}$$

Thus, proof of inequality (3.2) is completed. If we take $\delta < 1, a = 0$ and $\frac{p}{q} > 1$, then Theorem 3.1 reduces to Hardy-Littlewood inequality.

Remark 3.2 If we use $(M_a f)^{\Delta}(s) \geq 0$, we have

$$\int_a^n \frac{\left(M_a f(s) \right)^{\frac{\sigma p}{q}}}{\left(\sigma(s) \right)^{\delta}} \Delta s \geq \int_a^n \frac{\left(M_a f(s) \right)^{\frac{p}{q}}}{\left(\sigma(s) \right)^{\delta}} \Delta s,$$

and

$$\left(\frac{q(1-\delta)}{p} \right)^{\frac{p}{q}} \int_a^n \frac{f^{\frac{p}{q}}(s)}{\left(\sigma(s) \right)^{\delta-\frac{p}{q}}} \Delta s \leq \int_a^n \frac{\left(M_a f(s) \right)^{\frac{\sigma p}{q}}}{\left(\sigma(s) \right)^{\delta}} \Delta s.$$

In the further stages of the study, we will suppose that there exists constants $L > 0, t \geq a$ with

$$\frac{t}{\sigma(t)} \geq \frac{1}{L}. \tag{3.11}$$

Theorem 3.3 Let $\mathbb{T}$ be a time scales with$q < p < 0$ and $a \in (0, n) \cap \mathbb{T}$ such that $\frac{p}{q} \geq 2$ and $\delta < 1$. Suppose that f is a non-negative function and Hilger (delta) integral $\int_a^n \big(\sigma(s)\big)^{\frac{p-q\delta}{q}} f^{\frac{p}{q}}(s)\Delta s$ exists. If

$$M_a f(s) = \sup_{B \ni s} \frac{1}{|B|^{1-\frac{a}{n}}} \int_a^s f(y)\Delta y, \tag{3.12}$$

where $s \in [a, n] \cap \mathbb{T}$, then

$$\int_a^n \frac{f^{\frac{p}{q}}(s)}{s^{\delta-\frac{p}{q}}}\Delta s \leq C_p \left(\frac{q(\delta-1)}{pL^{\delta}}\right)^{\frac{p}{q}} \int_a^n \frac{(M_a f)^{\frac{\delta p}{q}}(s)}{s^{\delta}}\Delta s. \tag{3.13}$$

Proof If we integrate the left-hand side of (3.13) by (2.4) with $x^{\Delta}(s)s^{\delta} = 1$ and $y^{\sigma}(s) = \big(M_a f(s)\big)^{\frac{\sigma p}{q}}$, then we obtain

$$\int_a^n \frac{(M_a f)^{\frac{\delta p}{q}}(s)}{s^{\delta}}\Delta s = x(s)(M_a f)^{\frac{p}{q}}(s)I_a^n$$

$$+ \int_a^n (-x(s))\left((M_a f)^{\frac{p}{q}}(s)\right)^{\Delta}\Delta s, \tag{3.14}$$

where

$$x(s) = -\int_a^s t^{-\delta}\Delta t. \tag{3.15}$$

If we apply the chain rule (2.3), then we obtain

$$\left(-t^{1-\delta}\right)^{\Delta} = (\delta-1)\int_0^1 [g\sigma(t) + (1-g)t]^{-\delta} dg$$

$$\leq (\delta-1)\int_0^1 [g\sigma(t)+(1-g)\sigma(t)]^{-\delta}dg = \int_0^1 \frac{\delta-1}{\sigma^{\delta}(t)}dg = \frac{\delta-1}{\sigma^{\delta}(t)}. \qquad (3.16)$$

From (3.11) and (3.16), we see that $(Lt)^{\delta}\left(-t^{1-\delta}\right)^{\Delta} \leq \delta-1$. Then

$$(\delta-1)\int_s^0 t^{-\delta}\Delta t \leq L^{\delta}\int_s^0 \left(-t^{1-\delta}\right)^{\Delta}\Delta t = -L^{\delta}\left(t^{1-\delta}\right)I_s^0 = L^{\delta}s^{1-\delta}. \qquad (3.17)$$

Hence

$$(\delta-1)x(s) = (\delta-1)\int_s^n -t^{\delta}\Delta t \geq L^{\delta}s^{1-\delta}. \qquad (3.18)$$

From (3.12), (3.14), (3.15) and (3.18), we obtain

$$\int_a^n f(s)s^{1-\delta}\left((M_af)^{\frac{p}{q}}(s)\right)^{\Delta}\Delta s \leq \frac{q(\delta-1)}{pL^{\delta}}\int_a^n s^{-\delta}(M_af)^{\frac{p\sigma}{q}}(s)\Delta s. \qquad (3.19)$$

Using the chain rule (See [5])

$$f^{\Delta}f(s) = f'\big(f(c)\big)f^{\Delta}(s),$$

where $c \in [s,\sigma(s)]$ such that

$$p(M_af)^{\frac{p-q}{q}}(c)(M_af)^{\Delta}(s) = q\left((M_af)^{\frac{p}{q}}(s)\right)^{\Delta}. \qquad (3.20)$$

Since $(M_af)^{\Delta}(s) \geq 0$ and $\sigma(s) \geq c$, we obtain

$$q\left((M_af)^{\frac{p}{q}}(s)\right)^{\Delta} \geq p\big(M_af(s)\big)^{\frac{\sigma(p-q)}{q}}f(s). \qquad (3.21)$$

Substituting (3.21) into (3.19), we have

$$\int_a^n f(s)s^{1-\delta}\left(\left(M_a f(s)\right)^{\frac{\sigma(p-q)}{q}}\right)^{\Delta}\Delta s \le \frac{q(\delta-1)}{pL^{\delta}}\int_a^n s^{-\delta}(M_a f)^{\frac{p\sigma}{q}}(s)\Delta s.$$

Hence, we obtain

$$\int_a^n s^{-\delta}(M_a f)^{\frac{p\sigma}{q}}(s)\Delta s$$

$$\ge \frac{q(\delta-1)}{pL^{\delta}}\int_a^n \left[\frac{f(s)s^{\frac{\delta(p-q)}{p}}}{s^{\delta-1}}\right]\left[\frac{\left(M_a f(s)\right)^{\frac{\sigma(p-q)}{q}}}{s^{\frac{\delta(p-q)}{p}}}\right]\Delta s. \tag{3.22}$$

If we use the inverse Hölder inequality (2.5), then we have

$$C^p\int_a^n \left[\frac{f(s)s^{\frac{\delta(p-q)}{p}}}{s^{\delta-1}}\right]\left[\frac{\left(M_a f(s)\right)^{\frac{\sigma(p-q)}{q}}}{s^{\frac{\delta(p-q)}{p}}}\right]\Delta s$$

$$\ge \left[\int_a^n \left[\frac{f(s)s^{\frac{\delta(p-q)}{p}}}{s^{\delta-1}}\right]^{\frac{p}{q}}\Delta s\right]^{\frac{q}{p}}\left[\int_a^n s^{-\delta}(M_a f)^{\frac{p\sigma}{q}}(s)\Delta s\right]^{\frac{p-q}{p}}. \tag{3.23}$$

Substituting (3.23) into (3.22), we obtain

$$\left[\int_a^n \left[\frac{f(s)s^{\frac{\delta(p-q)}{p}}}{s^{\delta-1}}\right]^{\frac{p}{q}}\Delta s\right]^{\frac{q}{p}}\left[\int_a^n s^{-\delta}(M_a f)^{\frac{p\sigma}{q}}(s)\Delta s\right]^{\frac{p-q}{p}}$$

$$\le \frac{q(\delta-1)}{pL^{\delta}}\int_a^n s^{-\delta}(M_a f)^{\frac{p\sigma}{q}}(s)\Delta s.$$

Herewith, we obtain the following inequalities

$$\int_a^n \frac{f^{\frac{p}{q}}(s)}{s^{\delta-\frac{p}{q}}}\Delta s \leq C_p\left(\frac{q(\delta-1)}{pL^{\delta}}\right)^{\frac{p}{q}}\int_a^n \frac{(M_a f)^{\frac{\delta p}{q}}(s)}{s^{\delta}}\Delta s.$$

Thus, proof of inequality (3.13) is completed.

If we take $\delta > 1$, $a = 0$ and $\frac{p}{q} > 1$, then Theorem 3.3 reduces to Hardy-Littlewood inequality.

Remark 3.4 Let $\sigma(s) \geq s$, inequality of (3.13). If we get $M_a f(s) = \sup_{B \ni s} \frac{1}{|B|^{1-\frac{a}{n}}} \int_a^s f(y)\Delta y$, for $s \in (a,n) \cap \mathbb{T}$, then we have

$$\int_a^n s^{\frac{p}{q}-\delta}((M_a f(s))^{\Delta})^{\frac{p}{q}}\Delta s \leq \left(\frac{q(\delta-1)}{pL^{\delta}}\right)^{\frac{p}{q}}\int_a^n \frac{(M_a f)^{\frac{\sigma p}{q}}(s)}{\sigma^{\delta}(s)}\Delta s. \tag{3.24}$$

If we write $\sigma^{\delta}(s)$ instead of s^{δ} on the right side of inequality (3.13), it would be very easy for us to reach the following conclusion.

Corollary 3.5 Let $a \in (0,n) \cap \mathbb{T}$, $q < p < 0$, $\delta < 1$ and let $\frac{p}{q} = 2m+1, m \in \mathbb{Z}$. Suppose that f is a non-negative function and Hilger (delta) integral

$$\int_a^n \sigma^{\frac{p}{q}-\delta}(s)\left(\frac{\sigma(s)}{s}\right)^{(\delta-1)\frac{p}{q}} f^{\frac{p}{q}}(s)\Delta s,$$

exists, then it would be very easy for us to reach the following conclusion

$$\int_a^n \frac{f^{\frac{p}{q}}(s)}{\sigma^{\delta-\frac{p}{q}}(s)}\left(\frac{\sigma(s)}{s}\right)^{(\delta-1)\frac{p}{q}}\Delta s \leq \left(\frac{q(\delta-1)}{p}\right)^{\frac{p}{q}}\int_a^n \frac{(M_a f)^{\frac{\sigma p}{q}}(s)}{\sigma^{\delta}(s)}\Delta s.$$

We can now give the following two theorems, which are no more general than the theorems we proved above.

Theorem 3.6 Let $\mathbb{T}$ be a time scales with$\frac{p}{q} \geq 2$ and$a \in (0, n) \cap \mathbb{T}$ such that $\delta < 1$. Suppose that f is a non-negative and Hilger (delta) integral $\int_a^n s^{\frac{p-q\delta}{q}} f^{\frac{p}{q}}(s)\Delta s$ exists. If

$$M_a f(s) = \sup_{B \ni s} \frac{1}{|B|^{1-\frac{a}{n}}} \int_a^s f(y)\Delta y, \tag{3.25}$$

where $s \in [a, n] \cap \mathbb{T}$, then

$$\int_a^n s^{-\delta+\frac{p}{q}} f^{\frac{p}{q}}(s)\Delta s \leq C_p \left(\frac{\delta - 1}{2^{\frac{p}{q}-1} L^{\delta}} \right)^{\frac{p}{q}} \int_a^n \frac{(M_a f)^{\frac{\sigma p}{q}}(s)}{s^{\delta}} \Delta s. \tag{3.26}$$

Proof If we follow a path like the proof of inequality (3.13), then we get

$$\int_a^n \frac{(M_a f)^{\Delta}(s)}{s^{\delta-1}} \Delta s \leq \frac{\delta - 1}{L^{\delta}} \int_a^n \frac{(M_a f)^{\frac{\sigma p}{q}}(s)}{s^{\delta}} \Delta s. \tag{3.27}$$

Applying the following inequality with chain rule (2.3)

$$a^{\gamma} + b^{\gamma} \leq (a + b)^{\gamma} \leq 2^{\gamma-1}(a^{\gamma} + b^{\gamma}),$$

If we take $a, b \geq 0$ and $\gamma \geq 1$, then we have

$$\left((M_a f)^{\frac{p}{q}}(s) \right)^{\Delta} \leq 2^{\frac{p-2q}{p}} \frac{p}{q} \int_0^1 \Big[(g M_a^{\sigma} f(s))^{\frac{p-q}{q}} + \big((1-g) M_a f(s) \big)^{\frac{p-q}{q}} \Big] dg \big(M_a f(s) \big)^{\Delta}$$

$$= 2^{\frac{p-2q}{p}} \Big[(M_a f(s))^{\frac{\sigma(p-q)}{q}} + (M_a f(s))^{\frac{(p-q)}{q}} \Big] \big(M_a f(s) \big)^{\Delta}$$

$$\leq 2^{\frac{p-q}{p}} \Big[\big(M_a f(s) \big)^{\frac{\sigma(p-q)}{q}} \Big] f(s). \tag{3.28}$$

Hence

$$\int_a^n \frac{(M_a f)^{\frac{\sigma p}{q}}(s)}{s^{\delta}}\Delta s \geq \frac{2^{\frac{p-q}{p}}L^{\delta}}{\delta-1}\int_a^n \frac{(M_a f)^{\frac{\sigma(p-q)}{q}}(s)}{s^{\delta-1}}f(s)\Delta s, \tag{3.29}$$

and thus

$$\int_a^n \frac{(M_a f)^{\frac{\sigma p}{q}}(s)}{s^{\delta}}\Delta s$$

$$\geq \frac{2^{\frac{p-q}{p}}L^{\delta}}{\delta-1}\int_a^n \left[s^{\frac{\sigma(p-q)}{p}}s^{1-\delta}f(s)\right]\left[\left(s^{\frac{-\delta(p-q)}{p}}\right)\left(M_a f(s)\right)^{\frac{\sigma(p-q)}{q}}\right]\Delta s. \tag{3.30}$$

If we use the right-hand inverse Hölder inequality (2.5), then we obtain

$$\int_a^n \frac{(M_a f)^{\frac{\sigma p}{q}}(s)}{s^{\delta}}\Delta s$$

$$\geq \frac{2^{\frac{p-q}{p}}L^{\delta}}{\delta-1}\left[\int_a^n \left[s^{\frac{\sigma(p-q)}{p}}s^{1-\delta}f(s)\right]^{\frac{p}{q}}\Delta s\right]^{\frac{q}{p}}\left[\int_a^n s^{-\delta}\left(M_a f(s)\right)^{\sigma}\Delta s\right]^{\frac{(p-q)}{p}}.$$

Thus, we obtain

$$\int_a^n s^{-\delta+\frac{p}{q}}f^{\frac{p}{q}}(s)\Delta s \leq C_p\left(\frac{\delta-1}{2^{\frac{p}{q}-1}L^{\delta}}\right)^{\frac{p}{q}}\int_a^n \frac{(M_a f)^{\frac{\sigma p}{q}}(s)}{s^{\delta}}\Delta s.$$

The proof of inequality (3.26) is completed.

If we take $\delta > 1, a = 0$, then Theorem 3.6 reduces to Hardy-Littlewood inequality.

Theorem 3.7 Let $\mathbb{T}$ be a time scales with $\frac{p}{q} \geq 2$ and $a \in (0, n) \cap \mathbb{T}$ such that $\delta < 1$. Suppose that f is a non-negative and Hilger (delta) integral $\int_a^n s^{\frac{p-q\delta}{q}} f^{\frac{p}{q}}(s)\Delta s$ exists. If

$$M_a f(s) = \sup_{B \ni s} \frac{1}{|B|^{1-\frac{a}{n}}} \int_a^s f(y)\Delta y, \tag{3.31}$$

where $s \in [a, n] \cap \mathbb{T}$, then

$$\int_a^n s^{-\delta+\frac{p}{q}} f^{\frac{p}{q}}(s)\Delta s \leq C_p \left(\frac{\delta - 1}{2L^{\delta}}\right)^{\frac{p}{q}} \int_a^n \frac{(M_a f)^{\frac{\sigma p}{q}}(s)}{s^{\delta}} \Delta s. \tag{3.32}$$

Proof The reader can easily prove Theorem 3.7 by considering the proof of Theorem 3.6.

4. Conclusion and Recommendations

In this study, a generalization of the new dynamic fractional Maximal type integral inequalities has been established by using Keller's chain rule and the inverse Hölder inequality with $\Delta -$ derivative on time scale. As a result of the generalization of these inequalities, we can reach the solutions to the problems we encounter in the literature more easily. Our works can be extended to $\nabla -$ derivative and $\diamond_{\alpha} -$ derivative. More different inequalities can be obtained. These inequalities that we have obtained also have application areas outside of mathematics. We have mentioned some of them in our references.

References

1. Agarwal, R.P., Bohner, M., O'Regan, D., Saker, S.H. (2011). Some Wirtinger-type inequalities on time scales and their applications. *Pacic J. Math.* 2011; 252: 1-26.
2. Akın, L.(2020). On the Fractional Maximal Delta Integral Type Inequalities on Time Scales. *Fractal Fractional*. 4(2), 26: 1-10.
3. Akın, L. (2019). Compactness of Fractional Maximal Operator in Weighted and Variable Exponent Spaces. *Erzincan Univ.J. Sci. Technol*. 12: 185-190.
4. Anastassiou, G.A. (2010). Principles of delta fractional calculus on time scales and inequalities. *Math. Comput. Model*. 52: 556-566.
5. Bohner, M., Peterson, A.(2001). Dynamic Equations on Time Scales: An Introduction with Applications. Birkhauser, Boston.
6. Bohner, M., Peterson, A. (2003). Advances in Dynamic Equations on Time Scales. Birkhauser, Boston.
7. Bohner, M., Agarwal, R.P. (1999). Basic calculus on time scales and some of its applications. *Result. Math*.35: 3-22.
8. Dananea, J., Allalia, K., Hammouch, Z. (2019). Mathematical analysis of a fractional differential model of HBV infection with antibody immune response. *Chaos Solut. Fractals.*136: 109787.
9. Ghanbari, B., Gu• nerhan, H., Srivastava, H.M. (2020). An application of the Atangana-Baleanu fractional derivative in mathematical biology: A three-species predator-prey model. *Chaos Solut. Fractals*. 138: 109910.
10. Hilger, S. (1990). Analysis on measure chains a unified approach to continuous and discrete calculus. *Results Math*. 18: 18-56.
11. Nehari, Z. (1968). Inverse Hölder inequalities. *Journal of Mathematical Analysis and Applications.* 21(2), 405-420.
12. Rahman, G., Nisar, K.S., Abdeljawad, T. (2020). Tempered Fractional Integral Inequalities for Convex Functions. *Mathematics*. 8: 500.
13. Singh, J., Kumar, D., Hammouch, Z., Atangana, A. (2018). A fractional epidemiological model for computer viruses pertaining to a new fractional derivative. *Appl. Math. Comput*. 316: 504-515.
14. Saker, S.H., O'Regan, D. (2016). Hardy and Littlewood Inequalities on Time Scales. *Bull. Malays. Math. Sci. Soc*. 39:527-543.
15. Saker, S.H. (2010). Oscillation Theory of Dynamic Equations on Time Scales: Second and Third Orders. Lambert Academic Publishing, Germany.
16. Tuna, A., Kutukcu, S. (2008). Some integrals inequalities on time scales. *Appl.Math.Mech. Eng. Ed.*29: 23-29.

17. Tassaddiq, A., Rahman, G., Nisar, K.S., Samraiz, M. (2020). Certain fractional conformable inequalities for the weighted and the extended Chebyshev functionals. *Adv. Dier. Equ*. 2020: 1-9.
18. Uçar, D., Hatipoğlu, V.F., Akincali, A. (2018). Fractional Integral Inequalities On Time Scales. *Open J. Math. Sci*. 2:361-370.
19. Akın, L. (2021). A New Approach for the Fractional Integral Operator in Time Scales with Variable Exponent Lebesgue Spaces. *Fractal Fract*. 5(7), 1-13.
20. Akın, L. (2021). On innovations of n-dimensional integral-type inequality on time scales. *Adv. Differ. Equ*. 148 (2021).
21. Tisdell, C.C., Zaidi, A. (2008). Basic qualitative and quantitative results for solutions to nonlinear dynamic equations on time scales with an application to economic modelling. *Nonlinear Anal.,* 68, 3504–3524.
22. Brigo, D., Mercurio, F. (2000). Discrete time vs continuous time stock-price dynamics and implications for option pricing. *Finance Stochast*., 4, 147–159.
23. Seadawy, A.R., Iqbal, M., Lu, D. (2019). Nonlinear wave solutions of the Kudryashov–Sinelshchikov dynamical equation in mixtures liquid-gas bubbles under the consideration of heat transfer and viscosity. *Journal of Taibah University for Science,* 13(1), 1060-1072.

Determining The Correct Sample Size in Survey and Experimental Studies

Assoc. Prof. Meral YAY

Mimar Sinan Fine Arts University
Science and Letters Faculty Department of Statistics
ORCID: 0000-0003-1857-8719

In recent years, one of the remarkable issues in scientific research is the need for researchers to work with a correctly determined sample size. More detailed information on how the sample size is calculated during the publication process is requested, and its stages are expected to be explained in detail. Sample size determination plays an important role in social sciences, business, health sciences, agricultural science research and survey research.Inappropriate sample size can lead to false inferences on the population. Examining the entire population on which the research will be conducted brings about a loss of time, effort and cost. Instead of the whole population, it is a more accurate way to work with samples selected from the population with appropriate sampling methods and representing the population well. At this point, researchers try to find an answer to the question "how many units of sample should I choose". Optimal sample size depends upon many considerations such as statistical test used, precision of the measures and design of the study. Therefore, researchers use various methods to select samples representing the entire population, to analyze the data from the selected samples, and to estimate the parameters of the population, making it very important to determine the appropriate sample size to answer the research question [In J et all, 2020 & Kang, 2015]. It may not be possible to detect a possible difference in tests with very small samples. On the contrary, even a small difference may appear statistically significant in tests with large samples. Therefore, the sample size used in the study should be neither too small nor too large for a desired comparison.

In scientific research, it is a basic statistical principle to define sample size before starting a study to avoid bias when interpreting results. With the help of a sufficiently large sample, it becomes possible to reach results that will be valid for the population parameters and to make reliable estimations. At this point, the need for statistical methods and statisticians is obvious. While statisticians determine whether any observed relationship in the sample actually exists; If the relationship is based on coincidence, they also play an important role in the reason why. Sampling methods are used to make more precise estimates in a shorter time at low cost. It is extremely important to use the correct sampling method and to determine the sample size correctly. No matter how well the study is conducted, it may be insufficient to detect sample effects or relationships when it is studied with a small sample. Or, if the sample is chosen larger than necessary, the cost will increase first, and then the complexity of the study and erroneous results will be encountered. Therefore, sample size is an important factor in any scientific research.

Sample size determination is the technique of selecting the number of observations from a population to be included in a sample.It is an important part

of research aimed at making inferences about the population.The sample size used in a study is determined by the cost of data collection and sufficient statistical power (Singh &Masuku, 2014).At this stage, it should be considered whether the study is a survey study or an experimental study.In determining the sample size, the type of research has an important place in the roadmap.While the concept of precision is used in survey studies, power is used in experimental studies.In a survey study, the method followed in the calculation of the sample size is common in the estimates made regarding the population mean or proportion.In survey studies, "d" is the tolerable amount of variation in estimating the population mean and is called “the level of accepted error”, whereas "d" represents the level of tolerable error in estimating the population proportion, and is called “the margin of error”. (Verma, 2020).In other words, while estimating the mean in a survey study, the level of acceptance "d" should be taken into account in calculating the sample size, while the error of margin "E" should be determined in the proportion estimation. The flow diagram to be followed in determining the sample size in estimating the population mean or proportion in survey studies is as in Diagram1.

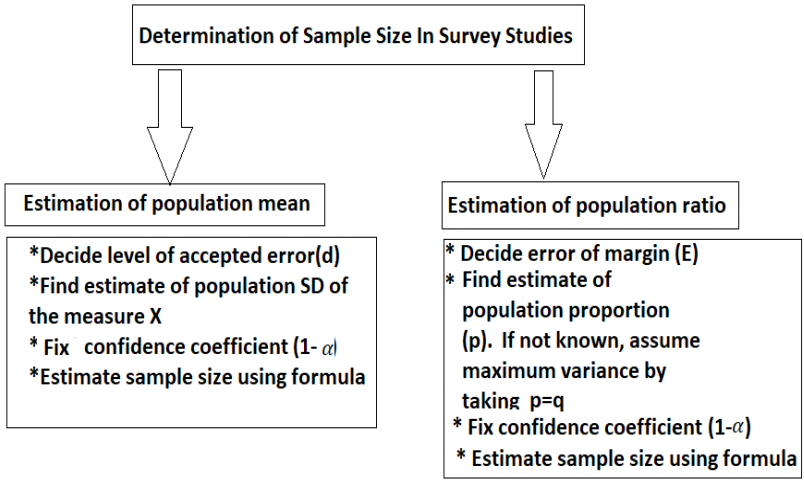

Diagram 1. Determination sample size in estimating population mean or proportion in survey studies

When a sample of size "n" is drawn from a normally distributed population with N(μ, σ^2) parameters, the distribution of sample means is also normal and is expressed by N(μ, σ^2/n).In this case, (1-α)x100% confidence limits of the population mean are obtained with $\bar{x} \pm z\alpha_{/2} \frac{\sigma}{\sqrt{n}}$. For example, if the estimate is

desired to be within "±d" of the true population mean, the sample size that needs to be studied to have such precision is determined as

$$n = z^2_{\alpha/2} \frac{\sigma^2}{d^2} \quad (1)$$

In this equation, "α" is the level of significance which depends upon how much confidence one wishes to have in estimation. *"d"*is the amount of error which one can tolerate inestimating mean and it is called as the level of accepted error. In other words *"d"*is a decisiononthe tolerable limits of errors is made, i.e. the researcher makes a statement that it does not matter if his sample estimate does not differ from true population value by a certain amount. In clinical studies, it can be defined as the minimum difference to be considered clinically significant between the mean or ratio of the two groups. The difference between groups (d) represents the absolute difference between groups to be compared in clinical studies. If the primary variable of interest (primary outcome) in a clinical trial is a ratio, then the difference in the observation rate of the event of interest between the treatment group and the control group represents *"d"*. When the number of groups is more than two, then it is expressed as the difference between the highest rate and the lowest rate. When the event of interest is a quantitative value, the difference between the treatment group mean and the control group mean represents *"d"*. Dividing the obtained difference by the standard deviation of the control group gives the effect size. The denominator standardizes the difference by transforming the absolute difference into standard deviation units. Cohen's term *"d"* is an example of this type of effect size index. Cohen classified effect sizes as small (*"d"* = 0.2), medium (*"d"* = 0.5), and large (*"d"* ≥ 0.8) (Sullivan &Feinn, 2012). The standard deviation is used to estimate the population variance of the predicted outcome variable in calculating the sample size. Because population variance is often unknown, researchers use estimates derived from previous studies. If the population has a homogeneous structure, the small sample size will be sufficient for the study, as the standard deviation will be low, while the required sample size will increase as it moves away from homogeneity. The value of σ is obtained from similar studies conducted earlier. In practice, there are very few or no cases where the population variance is known.If estimated with "s" from previous similar studies, "$t^2_{\alpha/2;n-1}$"is used instead of "$z^2_{\alpha/2}$" to estimate the sample size.

In a survey study in which the sample size is determined in the estimation of the population proportion, let "x" be the number of observations with the desired characteristics, and let "x/n" be the estimator of the population proportion. In this case, the "$\hat{p} = x/n$" distribution fits the binomial distribution

and is also equal to the mean of the distribution.When "n" is large enough, the distribution of "$\hat{p}$" fits the normal distribution with mean "p"and variance "pq/n".Usually, "p" is unknown; therefore, the maximum variance is often used for sample size estimation.When “E” is defined as the margin of error on both sides of the population proportion "p", then the 95% confidence limits for the proportion are obtained with $\hat{p} \pm z_{\alpha/2}\sqrt{\frac{pq}{n}}$. Considering the margin of error of "E" on both sides, the sample size can be calculated as follows:

$$n = z^2_{\alpha/2}\frac{pq}{E^2} \quad (2)$$

When the population proportion is not known, the sample size is obtained as follows by writing the ratio estimate obtained from the sample instead:

$$n = z^2_{\alpha/2}\frac{\hat{p}\hat{q}}{E^2} \quad (3)$$

These formulas introduced by Cochran (1963) were developed to find sample sizes for large population proportions.In the case of small population proportions, the sample size obtained from the above formula is assumed to be "$n = n_0$” and the following correction is made:

$$n = \frac{n_0}{1+\frac{n_0-1}{N}} \quad (4)$$

With this adjustment, it can significantly reduce the required sample size for small populations and is also called population correction.

Two main purposes are taken into consideration while calculating the sample size.The first objective is to estimate a minimum sample size that may be sufficient to achieve the target accuracy in an estimate for a given population parameter.As a result, the researcher aims to produce an estimate that is expected to be equally accurate as an actual parameter in the target population. The second aim is to determine the level of statistical significance (ie"p" value < 0.05) obtained with the desired effect sizes. A certain statistical test will be applied that will determine the statistical significance level and the "p" value will be calculated using this test. The optimal sample size is determined on the basis of precision or power in the run.As stated before, while determining the sample size, the basis of precision is taken into account in survey studies, while it is determined on the basis of power in experimental studies. The flow diagram to be followed in determining the sample size in estimating the population parameter in experimental studies is as in Diagram 2.

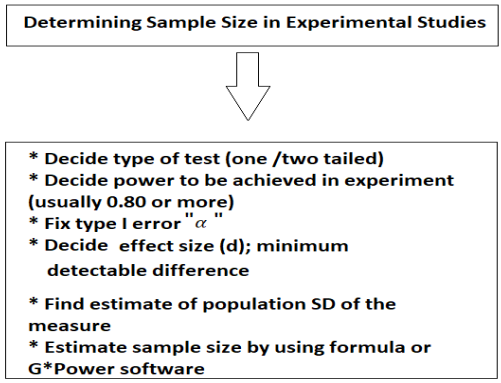

Diagram 2. Determining sample size in experimental studies

In experimental studies, the sample size for any study depends on the acceptable level of significance, power of the study, effect size and standart deviation in the population. The main purpose of experimental research is to investigate the cause-effect relationship between an intervention and some variables of interest. The researcher investigating the relationship uses the "p" value, that is, the "level of significance", to see the effect of the intervention. When the "p" value is found to be less than 0.05, it is stated that the researcher is 95% sure that the effect exists. However, if the null hypothesis is rejected even though it is true, Type 1 error (α) occurs and this error corresponds to a cut-off value for statistical significance. Therefore, the cut-off value chosen represents the probability of a Type I error with a risk of "false positives" that is considered tolerable in the study. The accepted significance level for the "α" error conventionally used is 0.05, i.e. there is a 5% probability that the observed difference or effect is due to chance.When the null hypothesis is accepted, another type of error is committed due to accepting a wrong hypothesis, which is the beta error, which is defined as the Type II error. This error corresponds to the occurance of a false negative result. The sum of positive results is the sum of true positives and false negatives (β error). Power, on the other hand, is the probability of detecting a true positive result, and is expressed as "1-β" by subtracting false negatives from the sum of positive results.The larger the sample size, the greater the power of a test. A study is considered adequately powered if it has a power of 0.80 or higher in scientific studies, that is, there is at least an 80% chance of correctly detecting a true difference or effect and rejecting a false null hypothesis (Columb&Stevens, 2008).

And also a significant "p" value does not mean anything unless the size of the effect is actually known. At this point, the researcher needs to decide on the significant effect size before starting the experiment. The reason for this is that the sample size depends on the determined effect size. The effect size can be defined as the minimum detectable difference in rejecting the investigated hypothesis. While the sample size is large, even a small effect may cause the null hypothesis to be rejected, while in a smaller sample, the null hypothesis may not be rejected even for a large effect. Particularly in clinical studies, calculating the sample size is critical so that it has enough power to show clinically significant differences. The effect size shows the difference or strength of relationships. It also represents a minimal clinically meaningful difference. As the size, distribution, and units of the effect size vary between studies, standardization of the effect size is usually performed for sample size calculation and power analysis. With the help of power analysis, the probability of correctly rejecting the null hypothesis can be calculated. Power analysis also reveals how likely it is to detect a statistically significant effect in the data, given that it actually exists in the population. As a result, considering the power of a test, it is mentioned together with the determination of the appropriate sample size at the planning stage.Another factor that plays a role in determining the sample size is variability. The standard deviation, which gives a measure of the distribution and variability of the population, is a measure that should be taken into account when calculating the sample size. Because the researcher has to estimate the variation in the measurements. It is very clear that when the population is homogeneous, the standard deviation, which is the measure of variability, will be small and therefore a smaller sample will be needed. This leads to an increase in test power.

In an experimental study in which the population mean is estimated;Depending on the given "$\alpha, \beta$and d", the sample size to be studied is calculated as follows (Borkowf, Johnson & Albert, 2018&Rosner, 2011):

$$n = \frac{\left(z_{1-\alpha/2}+z_{1-\beta}\right)^2\sigma^2}{d^2} \qquad (5)$$

In this equation;$z_{1-\alpha/2}$ is z-value for α = 0.05 (for example, if α=0.05, then $1-\alpha/2$= 0.975 and z=1.960; $z_{1-\beta}$is z-value for the desired power and “d” is the level of accepted error (the difference between sample mean and population mean).$1-\beta$ is the selected power, and $z_{1-\beta}$is the value from the standard normal distribution holding $1-\beta$ below it. Sample size estimates for hypothesis testing are often based on achieving 80% or 90% power. The $z_{1-\beta}$

values for these popular scenarios are $z_{0.80}$ = 0.84 for 80% power; and $z_{0.90}$ =1.282 for 90% power.

When estimating the population proportion;the sample size to be studied is calculated as follows:

$$n = \frac{\left(z_{1-\alpha/2}+z_{1-\beta}\right)^2 pq}{E^2} \quad (6)$$

$z_{1-\alpha/2}$and$z_{1-\beta}$ are defined as above and "E" is the error of margin (the difference between sample proportion and population proportion). In this book chapter, sample size determination formulas and applications for only a single population mean and ratio are given.Sample size studies for two or more samples will be included in future studies.

References

1. Borkowf, C. B., Johnson, L. L., Albert, P.S. (2018). Power and sample size calculations. *Principles and practice of clinical research.*359-372.
2. Columb, M. O., Stevens,A. (2008). Power Analysis and Sample Size Calculations.*Current Anaesthesia and Critical*.*19.* 12–14.
3. In, J., Kang H., Kim J. H., Kim T. K., Ahn E. J., Lee D. K., Lee S., Park J. H. (2020). Tips for troublesome sample-size calculation. *Korean Journal Anesthesiol*, *73*, 114-120.
4. Kang H. (2015). Sample size determination for repeated measures design using G Power software. *Anesth Pain Med*,*10*, 6-15.
5. Rosner, B. (2011) *Fundamentals of biostatistics.* Boston. Brooks/Cole.
6. Singh, A. S., Masuku, M. B. (2014). Sampling techniques and determination of sample size in applied statistics research: an overview.*International Journal of Economics, Commerce and Management United Kingdom,2-11,* 1-22.
7. Sullivan, G. M., Feinn, R. (2012). Using effect size- or why the p value is not enough.*The Journal of Graduate Medical Education.4(3).* 279–282.
8. Verma, J. P., Verma, P. (2020).*Determining sample size and power in research studies: A manuel for researchers.* Singapore.Springer.

Examination of Influence of Eu impurity in Superconductors on Young's modulus of elasticity with Vickers hardness findings

M. Oz , A.T. Ulgen

1. Introduction

The discovery of the superconductivity phenomenon with no resistance (Onnes, 1911; Oh, Kim, Jeong, Hyun, & Kim, 2007; Chen, 2002) has directly guided academic researchers in the usage of superconducting materials in the basic technological,sensitive process control, industrial, medical, high-energy, electro-optic, power transmission cable, spintronics, medical diagnosis, renewable energy, levitated trains, motors, future hydrogen society, particle accelerators, refrigeration, and large-scale application fields (Buckel and Kleiner, 2004; Xu, et al., 2012;Choi, et al., 2011; Akkurt & Yildirim, 2016; Zalaoglu, et al., 2021; Erdem, et al., 2021; Coombs, 2011; Werfel, et al., 2011). Especially, recent studies on type-II superconducting ceramic compounds (after the discovery of $La_{2-x}Ba_xCuO_4$ ceramic superconducting material (Bednorz & Müller, 1986; Ford & Saunders, 2004) haveattracted considerable interest in the material research community.Among the type-II superconducting ceramic compounds, the Bi-based ceramic family with the main three participantspossesses largercritical current density carrying density ability, greater critical transition temperature (onset and offset), and higher magnetic fieldcarrying capability (Turkoz, et al., 2019; Chen et al., 2002; Takayama-Muromachi, 1998; Yamauchi & Karppinen, 2000; Zalaoglu, Akkurt, Oz, & Yildirim, 2017). Similarly, no power consumption is another desirable property that consents the Bi-containing superconducting solid materials to use in much more application fields(Ateş, 2013; Ateş, 2016). It is obvious that with the improvement in the essential characteristic features; namely,crystallinity quality, electrical, superconducting, flux pinning,microstructural, physical, modulation, pairing mechanism, crystallization reaction kinetics, nucleation stability, crystallization temperature, formation of discrete pancakelike, morphological, slip system, key mechanical performance, and mechanical representative properties; these kinds of superconducting materials bargain much more fieldsin the potential application areas. In addition, material science is much more in the relationship different branch of technological and industrial applications (Ateş, Keskin, Totic, & Yeşil, 2014; Ateş, Onur Ugur, Akbiyikli, Polat, & Keskin, 2016).

In the present work, the effect of europium impurity addition amount ($0 \leq x \leq 0.1$) on some importantmechanical performance quantities (fracture toughness, elastic stiffness coefficient, ductility, and brittleness index)using the conventional Vickers microhardness tests executed at various applied microindentation test loads between 0.245N and 2.940 N.At the same time, we determine the relationship between mechanical performance behavior and the europium impurity addition amount and applied test loads. The experimental

results show that the increases in both the applied test loads negatively affect the mechanical performance features pertain to the bulk Bi-2212 superconducting ceramics as a conclusion of the increase in crystal structure difficulties based on the microvoids, strains, omnipresent flaws, borderline coupling and connectivity between the head-to-head layers in the solid crystal system.

2. Experimental details and related computational findings

This research is a continuum of systematic characterization analysisdepend on inspection of the change of basic characteristic properties; namely superconducting, physical, electrical, pairing mechanism, clustering, crystallinity quality, nucleation stability, microstructural, flux pinning, crystallization temperature, crystallization reaction kinetics, formation of discrete pancakelike, morphological, slip system, key mechanical performance, and mechanical characteristic properties of bulk Bi-2212 superconducting solid constituents. In the following study, the main part of europium impurity addition on the fracture toughness (K_{IC}), ductility (D), elastic stiffness coefficient (C_{11}), and brittleness index (B)properties deduced from the Vickers microindentation hardness tests using a SHIMADZU HVM-2 model digital tester in openmedium atmosphere is thoroughly examined with the aid of related equations (1–4):

$K_{IC} = \sqrt{2E\alpha}$ (here, α is related to the surface energy value) (1)

$$B = \frac{H_v}{K_{IC}} \quad (2)$$

$$D = \frac{1}{B} \quad (3)$$

$$C_{11} = H_v^{7/4} \quad (4)$$

here, the change of K_{IC}, D, C_{11} and Bquantities as a function of both the utilized test loads and Eu addition level is extensively inspected by Vickers microindentation hardness test loads intervals of 0.245 N-2.940 N applying to the distinctnominated sites of sample surfaces for the timeperiod of 10 seconds. Besides, the measurements are taken 5 times by the calibrated microscope to determine the average indentation diagonal lengths evaluated from the average of two impression lengths. Moreover,material preparation processes including purity of chemical powders, heat-treatment methods,impurity addition amount, ambient conditions, heating- cooling rates calcination/sintering temperatures,

press loads-time, milling process,and experimental measurement test tools such as instruments, digital tester are clearly depicted in Ref. (Ulgen, Terzioglu, & Yildirim, 2022). Also, one can seeall the electrical conductivity and related superconducting findings can be observed in detail in Ref. (Ulgen, Terzioglu, & Yildirim, 2022).the pure and Eu-added Bi-2212 superconducting materials arranged by the weight-to-weight ratios intervals x = 0.0, 0.01, 0.03, 0.05, 0.07, and 0.10are thereafterabbreviated pure (unadded), Eu-1, Eu-2, Eu-3, Eu-4, and Eu-5, respectively.

3. Results and discussion

3.1. Variation of fracture toughness, ductility, elastic stiffness coefficients, and brittleness index of bulk $Bi_{2.1}Sr_{2.0}Ca_{1.1}Cu_{2.0}O_y$ ceramic solids

We investigate the differentiation of some critical mechanical performance quantities including fracture toughness (K_{IC}), ductility (D), elastic stiffness coefficient (C_{11}), and brittleness index (B)propertiesby means of the Vickers microindentation hardness test results deduced from 0.245 N-2.940 N carrying out test loads with the aid of related equations. One can see every computation in Table 1.

It is understandable from the table given in the following part that all properties are detected to depend seriously on both the practical test loads and the europium impurity addition amount. These findings show us that the europium impurity is successfully added in $Bi_{2.1}Sr_{2.0}Ca_{1.1}Cu_{2.0}O_y$ crystal structure. As for numerical values, the fracture toughness features are noted to increase regularly as the impurity increases in the crystal nature. This means that being of europium impurity provoke enhancement in the permanent crystal nature problems, microcrystal coalescence orientations, microvoids, granularity degree, and formation of flaws, voids, and cracks. In other words, the fracture toughness parameter is responsible for the critical stress strength factor of a challenging crystal medium. Accordingly, resistance towards the samples to the initiation of flaws, voids and crack propagation gets less and less depending on the addition amount. Furthermore, the experimental findings show that with the raise in the utilized test load the K_{IC} values are obtained to increase systematically due to the compression of the granular structure of the Bi-2212 crystal solid.

Numerically, the pure sample is observed to have the K_{IC} value of 0.19244 $MPam^{1/2}$ at the preferred test load of 0.245 N and the value is found to lessening monotonously with rising test load. In the case of the highest applied test load of 2.940 N K_{IC} value is noted to be about 0.18727 (smallest) $MPam^{1/2}$ for the unadded material. Even, this behavior (nonlinear lessening in the K_{IC}properties

with the applied test load) is attributed to the standard indentation size effect (ISE) characteristic properties. As for the Eu-5 sample, the K_{IC} values are calculated between 0.27503 MPam$^{1/2}$ and 0.25050 MPam$^{1/2}$ under 0.245 N and 2.940 N applied test loads, respectively.

Table 1. Variation of K_{IC}, D, C_{11} and Bpropertiesdetermined from microindentation test loads. *The elastic modulus values are deduced from Ref. (Turkoz, Erdem, & Yildirim, 2022)

Samples	*F (N)*	*Kıc (MPam$^{1/2}$)*	*C_{11} (GPa)$^{7/4}$*	*B (m$^{-1/2}$)*	*D (m$^{1/2}$)*	*E* (GPa)*
	0.245	0,192434597	0,23403222	2,26622451	0,441	35.7443
	0.490	0,189992148	0,223799666	2,237460882	0,447	34.8427
Pure	0.980	0,188263582	0,216753829	2,21710432	0,451	34.2116
	1.960	0,187744187	0,214667987	2,210987229	0,452	34.0230
	2.940	0,187268693	0,212771076	2,205387312	0,453	33.8509
	0.245	0,212777002	0,22122637	1,984706976	0,504	34.6132
	0.490	0,208373097	0,205610974	1,943629023	0,515	33.1952
Eu-1	0.980	0,205888679	0,197157891	1,920455281	0,521	32.4084
	1.960	0,205288976	0,195155289	1,914861709	0,522	32.2199
	2.940	0,204870771	0,193767346	1,910960742	0,523	32.0887
	0.245	0,255313119	0,209267405	1,602346175	0,624	33.5313
	0.490	0,246937814	0,186209704	1,549782895	0,645	31.3674
Eu-2	0.980	0,242115872	0,173790939	1,519520375	0,658	30.1544
	1.960	0,241159752	0,171400669	1,513519554	0,661	29.9167
	2.940	0,240564353	0,169924194	1,509783119	0,662	29.7691
	0.245	0,259425702	0,187062032	1,479036186	0,676	31.4494
	0.490	0,249007177	0,162062107	1,419637798	0,704	28.9741
Eu-3	0.980	0,243486822	0,149831879	1,388165476	0,720	27.7037
	1.960	0,242078048	0,146819531	1,380133401	0,725	27.3840
	2.940	0,242005548	0,146665759	1,379720434	0,725	27.3676
	0.245	0,275357621	0,170743782	1,322643618	0,756	29.8511
	0.490	0,262863791	0,145131837	1,262631109	0,792	27.2037
Eu-4	0.980	0,255269726	0,130979278	1,226154015	0,816	25.6546
	1.960	0,253099253	0,127122703	1,215728599	0,823	25.2857
	2.940	0,253428056	0,127701661	1,217308	0,821	25.2202
	0.245	0,275025	0,14890221	1,224616	0,817	27.6053
	0.490	0,261505	0,124818158	1,164414	0,859	24.9579
Eu-5	0.980	0,253348	0,111714332	1,128093	0,886	23.4252
	1.960	0,250719	0,107709764	1,116389	0,896	22.9416
	2.940	0,250495	0,107373276	1,115392	0,897	22.9006

Other materials exhibit moderate fracture toughness values (but increase trend with impurity level). In this respect, it can be concluded that the pure sample with better crystallinity quality exhibits the least response and gentle to the applied test load. Conversely, the Eu-5 identified compoundwith the worst crystal quality performs the highest response and sensitive to the microindentation test load applied.Furthermore, the Vickers microindentation test results permitone to determine the role of europium impurity mixing on another mechanical performance parameter of elastic stiffness coefficient. According to Table 1, we can simplycomprehend that the elastic stiffness coefficient is noted to decrease constantly with enhancing both the europium impurity level in the Bi-2212 ceramic structure and applied test loads. In this regard, pure material has the largest values at any applied loads. Namely, maximum C_{11} parameter of 0.23403(GPa)$^{7/4}$ at the applied test load of 0.245 N for the unadded sample and the C_{11} value gets smaller and smaller with the increase in the applied test load and reaches the local minimum value of 0.21277 (GPa)$^{7/4}$. Besides, the global smallest C_{11} values are observed for the Eu-5 ceramic sample. When a load of 0.245 N is exerted to the material surface, the C_{11} value is attributed to be about 0.14890 (GPa)$^{7/4}$. In the matter of a maximum test load of 2.940 N, the Eu-5 sample exhibits the global smallest C_{11} parameter of 0.10737 (GPa)$^{7/4}$. It is apparent from the decline in the C_{11} parameters with both the utilized test loads and Eu impurity level that the crystal structure problems based on the microvoids, strains, omnipresent flaws, coupling and connectivity between the adjacent layers begin predominantly in the Bi-2212 superconducting solid system. We also determine the effect of europium impurity addition and applied test loads on the sustainability degree of plastic decomposition under the microindentation test loads applied throughout the fiasco (called ductility parameter) behavior of the Bi-2212 ceramic system with the aid of Vickers microhardness test loads. Unlike the elastic stiffness coefficients, the ductility parameter is found to augment continuouslyas both the applied test loads and Eu impurity amount increase. On this basis, the minimum ductility value of 0.441 $m^{1/2}$ is attributed to the sample that does not include impurity under 0.245 N applied test load. The *D* parameter of unadded material is found to increase systematically up to the local maximum value of 0.453 $m^{1/2}$when the applied test load is 2.940 N. In view of the highest addition ratio of x=0.10, the bulk Eu-5 superconducting sample possesses the highest results at the applied test loads. In this context, the Eu-5 sample shows the ductility value of 0.817 $m^{1/2}$ at 0.245 N applied test load when the global maximum D value of 0.897 $m^{1/2}$ is obtained at 2.940 N applied test load. The rapid decrement stems from the increase in the granular medium in

the Bi-2212 superconducting solids. Lastly, we focus sensitively on the change of brittleness index fitting to the bulk Bi-2212 superconducting solids with the europium addition ratio and applied test loads with the help of Vickers microindentation hardness test results. The experimental foundations are mathematically given in Table 1. It is realized from the table that the findings for the brittleness index depend totally on both the applied test loads and the europium impurity addition amount. With the increase in both the applied test load and europium impurity addition amount in the bulk Bi-2212 crystal solidthe brittleness index parameters are obtained to reduce systematically. On this basis, the unadded sample has the largest B parameter of 2.26622 $m^{-1/2}$at the applied test load of 0.245 N when the parameter is attributed to decrease towards to the value of 2.20539 $m^{-1/2}$(for 2.940 N) with the increment in the settled load. On the other hand, the smallest values are recorded for the Eu-5 sample. Namely, the B values are found to be in a range of 1,22462 $m^{-1/2}$(at 0.245 N applied test load) -1,11539 $m^{-1/2}$(at 2.940 N applied test load).It is apparent that the granular structure of the Bi-2212 superconducting system varies not the applied test loads but europium impurity addition amount.

3.2. Link between Vickers hardness values and applied test loads

According to Part 3.1.of this study, there appears a strong relationship between applied test loads and Vickers microindentation hardness parameters due to the change of main mechanical performance quantities with the europium addition amount. The strong link can be shown by the fitting equations from the fourth-order formulations to catch the maximum correlation value of R^2=1. The fitting relations are provided in Table 2.

Table 2. Link between Vickers microhardness and applied test loads for all solid ceramic compounds

Samples	*Fitting equations for Eu added Bi-2212 ceramic samples
Pure	$y = 0.00526x^4 - 0.03719x^3 + 0.09243x^2 - 0.09837x + 0.45518$
Eu-1	$y = 0.01076x^4 - 0.07317x^3 + 0.17231x^2 - 0.16888x + 0.45437$
Eu-2	$y = 0.01610x^4 - 0.10988x^3 + 0.26013x^2 - 0.25633x + 0.45785$
Eu-3	$y = 0.01924x^4 - 0.13123x^3 + 0.31153x^2 - 0.30991x + 0.42329$
Eu-4	$y = 0.01996x^4 - 0.13491x^3 + 0.31689x^2 - 0.31246x + 0.39624$
Eu-5	$y = 0.02035x^4 - 0.13650x^3 + 0.31602x^2 - 0.30267x + 0.44082$

It is apparent from the table thatall the termsincludingx^4, x^3,x^2, and x are found to depend on considerably the europium impurity addition amount. The variation of independent variables shows that the europium impurity is successfully added in the $Bi_{2.1}Sr_{2.0}Ca_{1.1}Cu_{2.0}O_y$ crystal structure. Moreover, the dependency of the x^4parameter is realized to increase systematically from 0.00526to 0.02035. The increase in the independent variable of x^4results from the augmentation of crystal structure problems based on the microvoids, strains, omnipresent flaws, coupling and connectivity between the adjacent layers in the bulk Bi-2212 crystal system. Thus, it is clear that the pure sample with stronger mechanical performance quantities presents the least response and sensitive to the applied test load while the Bi-2212 prepared by the maximum Eu impurity addition rate exhibits the highest response and precise to microindentation test load applied due to the worst crystal quality.

3.3. Roleof Eu impurity onmodulus of elasticity for Bi-2212 ceramic system

We inspectthe role of Eu impurity addition and applied test loads in the bulk Bi-2212 ceramic structure on the elasticity modulus using the granularity degree (porosity) deduced from the Vickers microindentation hardness tests (Abdeen, et al., 2016).The relation between Young's moduli of elasticity and porosities given below is used to find relative degrees ofgranularitypertaining to the pure and Eu-added Bi-2212 ceramic compounds(Callister, & Rethwisch, 2018):

$$E = E_0(1-1.9P+0.9P^2) \quad (4)$$

in Eq. 4, the E_0 parameter is determined to be about 35.7443 GPa (cited from a full-text titled "Investigation of the effect of Eu impurity on slip systems in Bi-2212 crystal system with Vickers microindentation hardness method")that belongs to the pure sample at microindentation test load of 0.245 N as a result of the highest (densest material) elastic modulus parameter among the measurements. One can see other elasticity moduli (called from Turkoz, Erdem, & Yildirim, 2022) in Table 1, also. The relative granularity degree parameters calculated according toYoung's modulus parameter are arithmetically provided in Table 3.

Table 3. Variation ofgranularity degree parameters as a function of Eu impurity addition amount and applied indentation test loads.

Samples	*Applied Indentation Test Loads (N)*				
	0.245	***0.490***	***0.980***	***1.960***	***2.940***
	Relative volume fraction porosity (%)				
Pure	-----	1.3360	2.2815	2.5656	2.8257
Eu-1	1.6788	3.8226	5.0319	5.3238	5.5274
Eu-2	3.3105	6.6544	8.5795	8.9612	9.1989
Eu-3	6.5257	10.4900	12.5903	13.1262	13.1538
Eu-4	9.0668	13.4299	16.0816	16.8394	16.7246
Eu-5	12.7548	17.3001	20.0419	20.9255	21.0007

According to the table, it is based on the fact that the relative granularity degree parameters harshly depend on both the europium impurity addition level and applied microindentation test loads. In more detail, granularity degree is found to reduce considerably with increasing the europium impurity addition level. In this respect, the minimum relative penetrability value is noted to be about 1.3360 % at 0.490 N microindentation test load applied. The parameter climbs systematically with the addition level. At the same applied test load, the porosity value is measured to be about 17.3001 % for the bulk Eu-5 superconducting sample. Besides, at 0.245 N microindentation test load applied the Eu-5 material possesses the degree of the granularity value of 12.7548 %. At the same time, the raise in the applied test load leads to an increment in the degree of the granularity value. On this context, the maximum porosity parameter is measured to be about 21.0007 % for the Eu-5 sample with the most granular structure at the applied microindentation test load of 2.940 N. The findings show that both the europium impurity additionalrate and applied microindentation test loads trigger the induction of new permanentcrystal structure problems founded on the microvoids, strains, omnipresent flaws, coupling and connectivity between the adjacent layersin the bulk Bi-2212 crystal solids. Correspondingly, the mechanical performances and durable tetragonal phase as well as the stabilization of the bulk Bi-2212 superconducting nature cannot stand the maintenance of europium impurity in the Bi-2212 crystal structure.

4. Conclusion

In the presentstudy, there seems to be a strong link between theEu impurity addition mechanism and mechanical performances, durable tetragonal phase, and stabilization of granular $Bi_{2.1}Sr_{2.0}Ca_{1.1}Cu_{2.0}O_y$ crystal structure. The experimental values are determined from Vickers microindentation hardness experiments is accomplished at changed applied test loadsvarying from 0.245 N to a load of 2.940 N. The Eu-added Bi-2212 superconducting ceramic compounds are produced in different Eu molar concentrationsby the standard solid-phase reaction way. The observed Vickers microhardness curves allow us to calculate numerically the fracture toughness (K_{IC}), ductility (D), elastic stiffness coefficient (C_{11}), and brittleness index (B) properties of the Bi-2212 ceramic structure. It is determined that all the mechanical performance parameters are observed to relymuscularly on both applied test loads and the europium impurity addition amount. Thus, it is obvious that the europium impurity is successfully introduced in the $Bi_{2.1}Sr_{2.0}Ca_{1.1}Cu_{2.0}O_y$ crystal solid nature. Moreover, he existence of europium impurity in the Bi-2212 ceramic system rises the crystal construction problems based on the microvoids, strains, omnipresent flaws, coupling and connectivity between the adjacent layers in bulk Bi-2212 crystal solid system. Hence, the experimental results illustrate that the pure sample exhibits much stronger mechanical performance quantities than the other ones. Similarly, the same material presents the least reply and sensitive to the applied test load while the Bi-2212 organized by the maximum Eu impurity additional level exhibits the highest response and critical to the microindentation test load applied because of the worst crystal quality.

References

1. Abdeen, W., Marahba, S., Awad, R., Abou Aly, A. I., Ibrahim, I. H., & Matar, M. (2016). Electrical and mechanical properties of (Bi, Pb)-2223 substituted by holmium. Journal of Advanced Ceramics, 5(1), 54-69.
2. Akkurt, B., Erdem, U., Zalaoglu, Y., Ulgen, A. T., Turgay, T., & Yildirim, G. (2021). Evaluation of crystallographic and electrical-superconducting features of Bi-2223 advanced ceramics with vanadium addition. Journal of Materials Science: Materials in Electronics, 32(4), 5035-5049.
3. Akkurt, B., Yildirim, G. (2016). Change of mechanical performance and characterization with replacement of Ca by Gd nanoparticles in Bi-2212 system and suppression of durable tetragonal phase by Gd. Journal of Materials Science: Materials in Electronics, 27(12), 13034-13
4. Ateş A., Onur Ugur L., Akbiyikli R., Polat H., Keskin I., (2016),Soil liquefaction induced settlements with interaction of earthquake hazard analysis in vicinity Duzce city (Turkey), [in:] Journal of Current Construction Issues. Civil Engineering Present Problems, Innovative Solutions- Sustainable Development in Construction, ed. Jarosław Górecki, BGJ Consulting,
5. Ateş, A. (2013). The effect of polymer-cement stabilization on the unconfined compressive strength of liquefiable soils. International Journal of Polymer Science, 2013.
6. Ateş, A. (2016). Mechanical properties of sandy soils reinforced with cement and randomly distributed glass fibers (GRC). Composites Part B: Engineering, 96, 295-304.
7. Ateş, A., Keskin, I., Totic, E., & Yeşil, B. (2014). Investigation of soil liquefaction potential around efteni lake in Duzce Turkey: Using empirical relationships between shear wave velocity and SPT blow count (N). Advances in Materials Science and Engineering, 2014.
8. Bednorz, J. G.,& Müller, K. A. (1986). Possible highT c superconductivity in the Ba− La− Cu− O system. Zeitschrift für Physik B Condensed Matter, 64(2), 189-193.
9. Callister, W. D.,& Rethwisch, D. G. (2018). Materials science and engineering: an introduction (Vol. 9, pp. 96-98). New York: Wiley.
10. Chen, M., Paul, W., Lakner, M., Donzel, L., Hoidis, M., Unternaehrer, P., Weder, R., Mendik, M. (2002). 6.4 MVA resitive fault current limiter based on Bi-2212 superconductor. Physica C: Superconductivity, 372, 1657-1663.

11. Choi, K. Y., Jo, I. S., Han, S. C., Han, Y. H., Sung, T. H., Jung, M. H., Park, G.S. Lee, S. I. (2011). High and uniform critical current density for large-size YBa2Cu3O7− δ single crystals. Current Applied Physics, 11(4), 1020-1023.
12. Coombs, T. A. (2011). A finite element model of magnetization of superconducting bulks using a solid-state flux pump. IEEE transactions on applied superconductivity, 21(6), 3581-3586.
13. Erdem, U., Akkurt, B., Ulgen, A. T., Zalaoglu, Y., Turgay, T., & Yildirim, G. (2021). Effect of annealing ambient conditions on crack formation mechanisms of bulk Bi-2212 ceramic systems. Journal of Asian Ceramic Societies, 9(3), 1214-1227.
14. Ford, P. J.,& Saunders, G. A. (2004). The rise of the superconductors. CRC press.
15. Kleiner, R.,& Huebener, R. P. (2004). Superconductivity: fundamentals and applications. Wiley-VCH.
16. Oh, S. Y., Kim, H. R., Jeong, Y. H., Hyun, O. B., & Kim, C. J. (2007). Joining of Bi-2212 high-Tc superconductors and metals using indium solders. Physica C: Superconductivity and its applications, 463, 464-467.
17. Onnes, H.K. (1911), Further experiments with Liquid Helium. D. On the change of Electrical Resistance of Pure Metals at very low Temperatures, etc. V. The Disappearance of the resistance of mercury, Koninklijke Nederlandsche Akademie van Wetenschappen Proceedings, 14 113–115.
18. Takayama-Muromachi, E. (1998). High-pressure synthesis of homologous series of high critical temperature (Tc) superconductors. Chemistry of materials, 10(10), 2686-2698.
19. Turkoz, M.B., Erdem, U., Yildirim, G., Investigation of effect of Eu impurity on slip systems in Bi-2212 crystal system with Vickers microindentation hardness method, 5. Uluslararası Fen Bilimleri ve İnovasyon Kongresi, 11-12 Kasım 2022, Ankara, Turkiye.
20. Turkoz, M. B., Zalaoglu, Y., Turgay, T., Ozturk, O., Akkurt, B., & Yildirim, G. (2019). Evaluation of key mechanical design properties and mechanical characteristic features of advanced Bi-2212 ceramic materials with homovalent Bi/Ga partial replacement: Combination of experimental and theoretical approaches. Ceramics International, 45(17), 21183-21192.
21. Ulgen, A.T., Terzioglu, C., Yildirim, G., (2022), Change of Basic Electrical Conductivity and Superconducting Features of Bi-2212 Superconducting Ceramics with Europium Addition, International Research in Engineering Sciences II, Eğitim Yayınevi, 23-42.

22. Werfel, F. N., Floegel-Delor, U., Rothfeld, R., Riedel, T., Goebel, B., Wippich, D., & Schirrmeister, P. (2011). Superconductor bearings, flywheels and transportation. Superconductor Science and Technology, 25(1), 014007.
23. Xu, H. H., Cheng, L., Yan, S. B., Yu, D. J., Guo, L. S., & Yao, X. (2012). Recycling failed bulk YBCO superconductors using the NdBCO/YBCO/MgO film-seeded top-seeded melt growth method. Journal of applied physics, 111(10), 103910.
24. Yamauchi, H.,& Karppinen, M. (2000). Application of high-pressure techniques: stabilization and oxidation-state control of novel superconductive and related multi-layered copper oxides. Superconductor Science and Technology, 13(4), R33.
25. Zalaoglu, Y., Akkurt, B., Oz, M., & Yildirim, G. (2017). Transgranular region preference of crack propagation along Bi-2212 crystal structure due to Au nanoparticle diffusion and modeling of new systems. Journal of Materials Science: Materials in Electronics, 28(17), 12839-12850.
26. Zalaoglu, Y., Erdem, U., Bolat, F. C., Akkurt, B., Turgay, T., & Yildirim, G. (2021). Improvement in fundamental electronic properties of Bi-2212 electroceramics with trivalent Bi/Tm substitution: a combined experimental and empirical model approach. Journal of Materials Science: Materials in Electronics, 32(14), 19846-19858. 043.

Measurement uncertainty in spectrophotometric total antioxidant capacity (TAC)-DPPH analysis

Gülsüm ÇİÇEK[1], Mehmet KILINÇER[2] and Mustafa ÖZYÜREK[1*]

1Istanbul University-Cerrahpaşa, Faculty of Engineering, Department of Chemistry,Analytical Chemistry Division, 34320 Avcilar - Istanbul, Turkey
2 Department of Dioxin and Food Packaking, Istanbul Food Control Laboratory, Istanbul, Turkey

INTRODUCTION

Reactive oxygen/nitrogen species (ROS/RNS) produced during aerobic metabolism play an important role in biological and biochemical processes, homeostasis and cell signal transduction.A significant increase in ROS levels resulting in oxidative stress which was related to development of many disorders such as DNA-based cancer tumor growth, cardiovascular diseases and neurological disorders **[1,2]**.Oxidative stress is also a state of imbalance between ROS/RNS generation and antioxidant defence system that cause an interruption of the redox signal in an living organism. Due to unhealthy nutrition schemes, it is associated with many metabolic disorders, and it is stated that antioxidant intake can be increased properly.Therefore, the regulation of oxidative stress plays a key role into protect cell and tissue homeostasis. Because of significant role of various food antioxidants in the prevention of these oxidative stress-based diseases, various total antioxidant activity (TAA)/capacity (TAC) assays have been developed. TAC analysis methods are generally classified as electron transfer (ET), hydrogen atom transfer (HAT), and mixed HAT/ET- based assays**[3,4]**:

i. HAT based TAC assays: peroxyl radical scavenging (ORAC, TRAP),
ii. ET based TAC assays: reduction of metal ion (CUPRAC, FRAP)
iii. ET/HAT based mixed TAC assays: organic radical scavenging (DPPH, ABTS)

DPPH method is one of the widely used standard spectrophotometric ET/HAT based methods for measuring the TAC of complex food and biological samples, evaluating the potential of free radical scavenge of an antioxidant and determining the antioxidant properties of pure compounds**[5,6]**.When stabil DPPH radical interacts with hydrogen/electron donors, it is reduced to hydrazine. The dark purple colored DPPH radical gives maximum absorption at a wavelength of 515-520 nm. By adding antioxidant to ethanol or methanolic DPPH solution, a decrease in absorbance occurs and the color of the radical changes from dark purple to yellow with the presence of antioxidant compounds/real matrixes **[7]**. It is natural that the ability to scavenge the DPPH radical cannot be directly correlated with the ability to scavenge ROS and RNS radicals that are active in physiological conditions.

The measurement uncertainty is a parameter that reported together with the result of a measurement or a test and represents the probability distributions of the componentsin measurement results. It is also a statistical parameter that defines a range that includes the value of a measurable quantity**[8,9]**. Thus, it defines the range of values that can be encountered in relation to the measured quantity. That is: the uncertainty of measurement is calculated and when given

together; within which limits the measurement can take place and confidence/quality indicates the level.

The aim of this study is to determine the measurement uncertainty of TAC in apple juice using DPPH method. To the best of our knowledge, there is no detailed measurement uncertainty study based on the DPPH test with bottom-up approach for the TAC determination of commercial apple juice. For this purpose, EURACHEM-CITAC **[10]** and ISO-5725 **[11]** guides were mainly taken to express the uncertainty of measurement and in experimental studies, the uncertainty components were performed according to the ISO/IEC 17025: 2017 **[12]** standards with a bottom-up approach.

EXPERIMENTALS

Chemicals

Trolox (TR) (98%), DPPH (2,2-diphenyl-1-picrylhydrazyl) and ethanol (EtOH) were obtained from Sigma Aldrich (Steinheim, Germany). Stock solution of TR (1 $mmolL^{-1}$) was prepared in EtOH and then trolox for calibration was diluted with ethanol to give standart solutions of 0.2 mmol L^{-1}. Concentrations ranging from 4.0 to 24.0$\mu molL^{-1}$ for the DPPH method are obtained. Stock solution of DPPH (1 $\mu molL^{-1}$) radical was prepared in EtOH.

TAC-DPPH Assay

Since the DPPH method is easy and has high sensitivity, it is one of the methods that has been widely used in natural antioxidant determinations recently. Figure 1 shows the mechanism by which the DPPH radical – less stable free nitrogenous radical – interacts with antioxidant compounds and takes up hydrogen. The antioxidant effect of a compound is proportional to the inhibition of the DPPH radical. The DPPH radical is purple at 515-520 nm and shows strong absorption. As the DPPH radical is inhibited by the antioxidant compounds, the color changes from purple to yellow, then measured by the decrease in absorption at 517 nm using Agilent Cary 100 Bio model UV–Vis spectrophotometer (Australia), in accordance with the following (Eq 1.)**[13,14]**.

$DPPH^{\bullet} + ArOH \rightarrow DPPH + ArO^{\bullet} + H^{+}$ (Eq. 1)

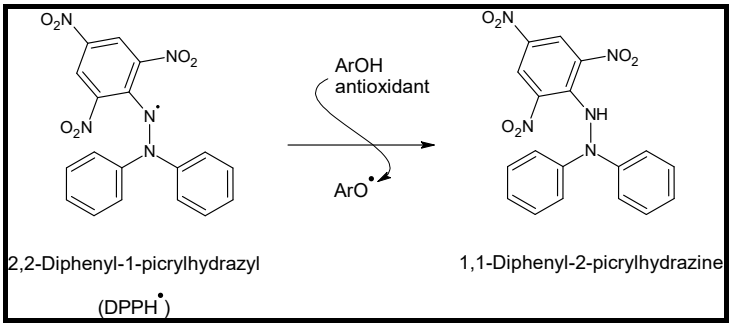

Figure 1. Mechanism of interaction of DPPH radical with antioxidant compounds.

To a test tube were added 0.4 mL of 10^{-3} M DPPH solution, (x) mL apple juice and (4.6-x) mL of EtOH (final volume: 5 mL). The mixture was incubated for 30 minutes in the dark at room temperature and the decrease in absorbance of the DPPH radical was measured at 517 nm wavelength against the EtOH solution.

0.4 mL DPPH + x mL AOX + (4.6-x) mL EtOH (V_{total}= 5.0 mL)

The TAC-DPPH value of AOX samples (mM TR) was calculated using the following Eq.2:

$$\text{TAC} - \text{DPPH (mM TR)} = \frac{\Delta A}{\varepsilon} \times df1(rxn\ dilution) \times 1000 \text{(Eq.2)}$$

ΔA: A_0-A_1; A_0 and A_1, Absorbancesof the DPPH radical in the absence and presence of samples (A_{517}), respectively

Ɛ: The molar absorptivity of TR ($Lmol^{-1}cm^{-1}$) usingTAC-DPPH assay

df1: The reaction dilution (x mL sample diluted to 5.0 mL reaction volume)

Plotting the ΔA of DPPH radical (initial conc. of DPPH radical; 0.4 mL, 1 mM) in the presence of TR versus TR concentration (4-24 μmol L^{-1})gave the standard calibration curve.

RESULTS AND DISCUSSION

Evulation of Uncertainty

The uncertainty of measurement shows the distribution of possibilities that can be detected in relation to the measured amount.Therefore, the uncertainty of the measurement or calculated value should be given together when giving the measurement result. According to the international metrology dictionary (International vocabulary of metrology, VIM) **[8,15,16]**, it is a parameter that represents the probability distributions of the components in measurement resultsand it should be given as a result of each measurement and reflects the level of trust of the analysis. Thus, it gives information about the quality of measurement by using the result indicating the extent to which the result

represents the real value. The laboratories should systematically examine all sources of uncertainty under their own conditions and report the uncertainty values together with the measurement result**[17,18]**. The individual sources of uncertainty that significantly affecting of the TAC-DPPH measurement were shown in a fishbone diagram (Figure 2).

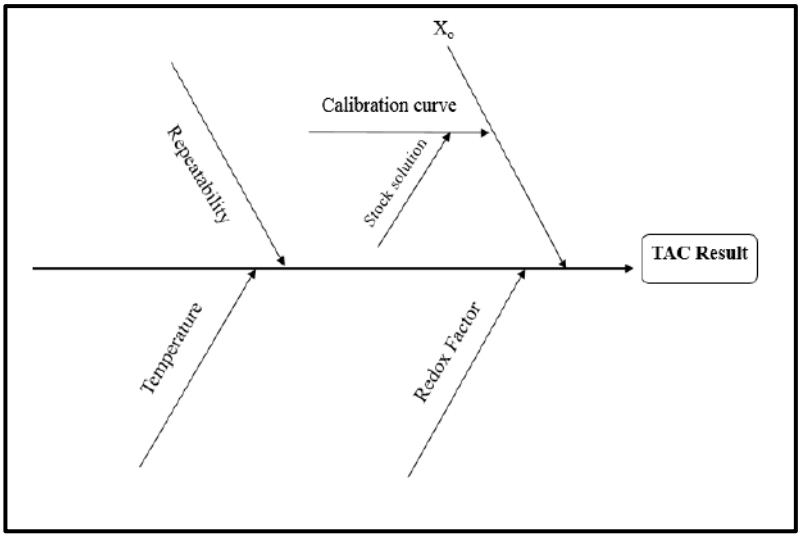

Figure 2. Fishbone diagram for measurement uncertainty in TAC-DPPH determination of apple juice.

The uncertainty value of TAC was calculated using Eq 3. **[17]**.

$TAC_{Uncertainty} = 2.X_0 \,.\, f_{rep} \,.\, f_T .\; f_{c_{TR}} . f_{RF}$(Eq.3)

- X_0 : the calibration curve uncertainty,
- f_{rep} : the repeatability uncertainty,
- f_T : the temperature uncertainty,
- $f_{c_{TR}}$: TR standard solution uncertainty,
- f_{RF} : the uncertainty of redox factor (RF) in TAC-DPPH test

TR Standard Solution Uncertainty, $U_r(C_{TR})$

The mass (m), volume (V) and purity (P) uncertainties affecting the final concentration of the reference standard solution (C_{TR}) were combined and the uncertainty of measurement was calculated.

Quantity/Unit	Estimate	Uncertainty	Distribution Factor	u(x)	u(x)/x
Mass/g	0.0125	-	-	4.2×10^{-5} [a]	0.0034
Purity	0.98	0.02	$rectangular\ \sqrt{3}$	0.0118	0.0118
Volume/mL	50		$triangular\ \sqrt{6}$	-	0.0015

a : mass balances standard uncertainty

Reference standard TR solution (C_{TR}=1 mM) was prepared inEtOH (96%)using Eq. 4:

$$C_{TR} = \frac{m_{TR} .p}{MW_{TR}.V} \text{ (Eq. 4)}$$

(MW_{TR}: molecular weight of TR)

The measurement uncertainty of the C_{TR} solution was calculated according to the equation 5.

$$u_r\,(C_{TR}) = \frac{u(C_{TR})}{C_{TR}} = \sqrt{(u_r(m)^2 + u_r(P)^2 + u_r(V)^2)} \text{(Eq. 5)}$$

$$u_r(C_{TR}) = \sqrt{(0.0034)^2 + (0.0118)^2 + (0.0015)^2} = 0.0124$$

The Calibration Curve Uncertainty, $u_r(X_o)$

In the DPPH method, six concentrations between 4.10^{-3} and 24.10^{-3} mmol L^{-1} were examined. Each of all concentrations for intra-day repeatability was performed three times and for six days for recurrence between days. According to EURACHEM/CITAC **[10]** guide, the calibration curveuncertainty was calculated as follows:

$$var\,(X_o) = \frac{var(y_{obs})}{b^2} + \frac{S^2}{b^2}\left[\frac{1}{\sum w_i} + \frac{(X_o - \bar{X})^2}{\sum(w_i X_i^2) - \frac{\sum(w_i X_i)^2}{\sum w_i}}\right] \text{(Eq. 6)}$$

where:

- var(y_{obs}): the variance of the observed variable
- S : RMSD
- b : the slope
- Xo andX_i: the concentration obtained from calibration curve and reference solutions, respectively
- $\overline{X}$: the mean of the concentrations used in the formation of calibration curve

$$u(X_O) = \sqrt{var(X_O)} = 0.00006 \text{ mmol/L} \quad \text{(Eq. 7)}$$

$$u_r\,(X_O) = \frac{u(X_O)}{X_O} = \frac{0.00006}{0.02483} = 0.00243$$

Repeatability Uncertainty, u_{pr}

Repeatability of the TAC of apple juice by using the DPPH method was calculated. The TAC of apple juice was experimentally determined by analyzing ten independent measurements for six days.According to the ISO 5725-3:1994 standard, the repeatability uncertaintyof the DPPH method was calculated **[11]** (Table 2).

Table 2. TAC-DPPHresults of apple juice samples(μmol L^{-1}).

Measurement	**1**	**2**	**3**	**4**	**5**	**6**	
1	597.7	597.2	596.5	597.9	599.8	598.0	
2	599.8	596.5	597.2	598.6	598.3	598.4	
3	597.9	598.0	600.5	598.7	597.4	599.5	
4	597.5	599.8	599.1	559.4	597.0	598.1	
5	598.2	597.8	597.5	599.6	597.3	598.0	
6	597.4	599.4	598.4	598.6	598.0	599.8	
7	600.4	598.5	598.2	600.5	597.9	599.3	
8	599.4	597.3	597.9	597.9	597.7	599.5	
9	596.9	599.9	597.7	599.7	597.7	598.6	
10	597.4	597.2	597.3	599.2	599.6	599.9	
							$\overline{\overline{X}}$ [a]
$\overline{X}$ [b]	598.3	598.2	598.0	598.9	598.1	598.9	598.41
S^2_{rj} [c]	1.418	1.418	1.267	0.746	0.899	0.553	

[a] general mean; [b] the mean and [c]the variance of the group; n=5

The variance homogeneity of the TAC-DPPH data series was tested by the Cochran's test(Eq. 8) for the DPPH method, and the results confirmed the homogeneity of variances (d= 6;(v) = n-1 = 9).

$$C_{exp} = \frac{S^2_{rjmax}}{\sum_{j=1}^{d} S^2_{rj}} = 0.2250 \leq C_{tab.(v,d)}(p = 0.95\,\%) = 0.3584$$

(Eq. 8)

where:

$C_{crit\ and}\ C_{exp}$: critical and experimentally found value, respectively,

S^2_{rj} S^2_{rjmax}: the estimated and the highest variance, respectively.

Application of DPPH method In-day certainty, (S^2_r) and intermediate-precision ($S^2_{I(T)}$)were calculated using Eq. 9 and Eq. 10 respectively.

$$S_r^2 = 1/d \sum_{j=1}^{d} S_{rj}^2 = 1.050(\mu mol/L)^2 \text{(Eq. 9)}$$

$$S_r = 1.025\ (\mu mol/L)$$

$$S_{I(T)}^2/(S_r^2/n) = 1.03 \leq F\ (p = 95\%;\ v_{IM} = 5, v_r = 54) = 2.386 \text{(Eq.10)}$$

The variance coefficient (CV) of TAC-DPPH method in repeatability analysis was calculated using Eq. 11.

$$CV = \frac{S_r}{\overline{X}} = \frac{1.025}{598.414} = 0.0017 \text{(Eq. 11)}$$

To determine the uncertainty of measurement from the certainty in DPPH test was calculated using Eq. 12

$$u_{(rep)} = \frac{CV}{\sqrt{n}} = \frac{0.0017}{\sqrt{3}} = 0.0098\ (n = 3) \text{(Eq. 12)}$$

The individual random effects in the TAC-DPPH measurement (Table 3) were analyzed by one-way ANOVA.

Table 3. Evaluation of TAC-DPPH results of apple juices with respect to the one-way ANOVA.

Summary

Groups	Count	Sum	Average	Variance
1	10	5982.851	598.2851	1.41867
2	10	5981.715	598.1715	1.41832
3	10	5980.475	598.0475	1.26748
4	10	5989.627	598.9627	0.74608
5	10	5980.992	598.0992	0.89930
6	10	5989.212	598.9212	0.55286

ANOVA

Variance Sources	SS	df	MS	F	P_{value}	$F_{criteria}$
Between Groups	8.670786	5	1.734157	1.650861	0.162417	2.38607
Within Groups	56.72464	54	1.050456			
Total	65.39542	59				

($F_{exp.}$=1.65 < $F_{crit.}$=2.38)

Temperature Uncertainty

DPPH analyzes were performed in room temperature conditions. Water bath was used to determine the uncertainty associated with temperature. For this purpose, the water bath is set to 25 ± 0.3. The temperature uncertainty ($u_{r(T)}$) was calculated as follows (Eq. 13):

$$u_{(T)} = \frac{\triangle T}{\sqrt{6}} = 0.122$$

$$u_{r\,(T)} = \frac{u_{(T)}}{T} = 0.00489 \text{(Eq. 13)}$$

CONCLUSIONS

In this study, the bottom-up approaches for the measurement uncertainty of TAC-DPPH analysis of commercial apple juice sample were assessed, and the related expanded uncertainty was calculated at 95% confidence interval (coverage factor of 2).The individual uncertainty components in TAC-DPPH measurements of apple juice were listed in Table 4. Seemingly, the relative contributions of each components to the combined uncertainty of TAC-DPPHwas given in a bar diagram (Figure 3)and the roles played in the expanded uncertainty were also clarified. As a result, $u_r(C_{TR})$, presented the highest contrubution to the extended uncertainty.

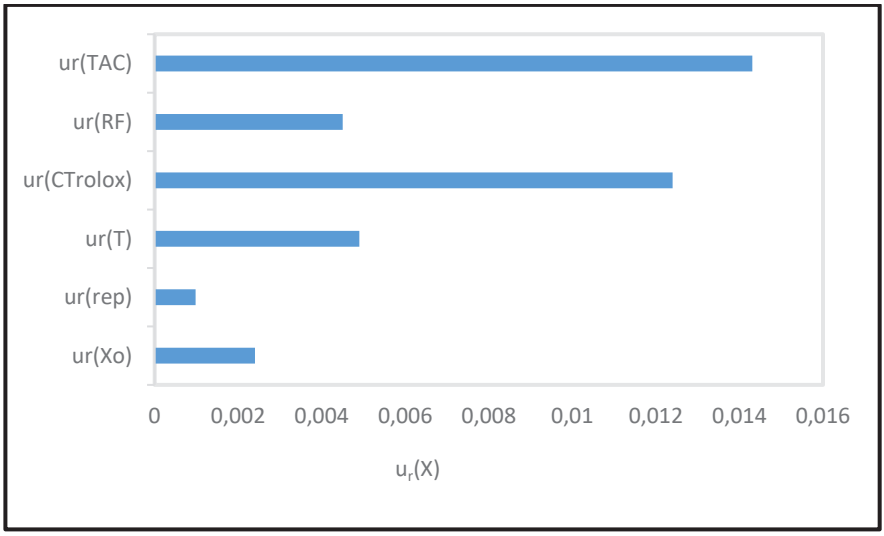

Figure 3. Uncertainty contrubutions of all sources in spectrophotometric TAC-DPPH measurements of apple juice.

Table 4. The individual uncertainties of the sources in spectrophotometric TAC-DPPH measurements of apple juice in accordance with the EUROCHEM Guide.

Quantity	Relative uncertainty	Uncertainty
X_0	$u_r(X_0)$	0.0024
f_{rep}	$u_r(rep)$	0.0009
f_T	$u_r(T)$	0.0049
$f_{C_{Trolox}}$	$u_r(C_{Trolox})$	0.0124
f_{RF}	$u_r(RF)$	0.0045
	$u_r(TAC)$	0.0143
	$U(TAC)^a\ (k=2)$	17.11

[a]U(TAC) as μmol L^{-1} and TAC-DPPH of the apple juice = 598.41 μmol L^{-1}.

$$\frac{u(TAC)}{TAC} = \sqrt{\left(\frac{u(X_O)}{X_O}\right)^2 + u(rep)^2 + \left(\frac{u(T)}{T}\right)^2 + \left(\frac{u(pH)}{pH}\right)^2 + \left(\frac{u(C_{TR})}{C_{TR}}\right)^2 + \left(\frac{u(RF)}{RF}\right)^2}$$ (Eq. 14)

$$U(TAC) = u_{r(TAC)} \times 2$$ (Eq. 15)

REFERENCES

1. C. A. Juan, J. M. P. de la Lastra, F. J. Plou & E. Pérez-Lebeña. The chemistry of reactive oxygen species (ros) revisited: Outlining their role in biological macromolecules (dna, lipids and proteins) and induced pathologies. Int. J. Mol. Sci., 22(9):4642, 2021.
2. G. Vitiello, L. Serpe & A. Blázquez-Castro. The role of reactive oxygen species in chemical and biochemical processes editorial on the research topic the role of reactive oxygen species in chemical and biochemical processes. Front. Chem., 9:33, 2021.
3. S. Jiang, H. Liu & Chunbao Li. Dietary regulation of oxidative stress in chronic metabolic diseases. Foods, 10(8):1854, 2021.
4. A. Karadag, B. Ozcelik & S. Saner. Review of methods to determine antioxidant capacities. Food Anal.Methods, 2(1):41–60, 2009.
5. K. Mishra, H. Ojha & N. K. Chaudhury. Estimation of antiradical properties of antioxidants using DPPH assay: A critical review and results. Food Chem., 130(4):1036–1043, 2012.
6. J. D. Yeo & F. Shahidi. Critical re-evaluation of dpph assay: Presence of pigments affects the results. J. Agric. Food Chem., 67(26):7526–7529, 2019.
7. Y. Carmona-Jiménez, M. V. García-Moreno, J. M. Igartuburu & C. G. Barroso. Simplification of the DPPH assay for estimating the antioxidant activity of wine and wine by-products. Food Chem., 165:198–204, 2014.
8. S. L.R. Ellison & A. Williams. Quantifying uncertainty in analytical measurement. 2012.
9. Evaluation of measurement data - Guide to the expression of uncertainty in measurement. JCGM 100: 2008.
10. EURACHEM/CITAC guide quantifying uncertainty in analytical measurement. Third Edition, 2012.
11. ISO 5725-3:1994/cor.1:2001 Accuracy of measurement methods and results – part 3: Intermediate measures of the precision of a standard measurement method.
12. ISO/IEC 17025:2017 General requirements for the competence of testing and calibration laboratories. Geneva, 2017.
13. M. Moniruzzaman,M. I. Khalil, S. A. Sulaiman&S. H. Gan. Advances in the analytical methods for determining the antioxidant properties of honey: a review. African Journal of Traditional, Complement. Altern. Med., 9(1):36-42, 2012.
14. B. Kuswandi,M. Fantoni, M. A.Hidayat,&I. Y. Ningsih. Paper microzone plate based on DPPH as a simple colorimetric assay of the total

antioxidant content of herbal extracts. J.Food Sci. Technol., 57(5):1971-1976, 2020.
15. I. Iso and BIPM OIML. Guide to the expression of uncertainty in measurement. Geneva, Switzerland, 122:16–17, 1995.
16. J. Kristiansen. The guide to expression of uncertainty in measurement approach for estimating uncertainty: an appraisal. Clin. Chem., 49(11):1822–1829, 2003.
17. I. Leito, L. Jalukse & I. Helm. Estimation of measurement uncertainty in chemicalanalysis (analytical chemistry) course. University of Tartu: Tartu, Estonia, 2018.
18. E. Prenesti,S. Berto, F. Gosmaro, P. Fisicaro, M. Bagnati&G. Bellomo. Measurement uncertainty evaluation of the total antioxidant capacity of human plasma tested by the CUPRAC-BCS method. Measurement, 152:107289. 2020.

A Mini-Overview of Microbial L-Asparaginase and Its Current Industrial Applications

Nihan ARABACI

Research Assistant Dr., Department of Biology,
Faculty of Arts and Sciences, Cukurova University,
Adana, Türkiye, narabaci@cu.edu.tr
ORCID: 0000-0003-3829-6495

1. Introduction

L-asparaginase (L-ASNase, EC 3.5.1.1.) is a member of amidohydrolase group enzymes and catalyzes the breakdown of the amino acid L-asparagine into L-aspartic acid and ammonia (NH_3) (Nunes et al. 2020). L-ASNase, which is frequently preferred in industrial areas such as food, therapeutic, and biosensor applications due to this mechanism of action, is an extremely important biocatalyst of the global enzyme market (Barros et al. 2022).

Because of the hydrolytic catalysis feature, L-ASNase can be used as a significant chemotherapeutic agent for the treatment of a variety of lymphoproliferative disorders and lymphomas, especially Acute Lymphoblastic Leukemia (ALL) and Hodgkin's Lymphoma (Cachumba et al. 2016). In addition, it is a very valuable enzyme because it plays a role in the inhibition of acrylamide, which occurs as a side reaction during the industrial processing of food (Narta et al. 2007).

According to molecular studies, L-ASNase is usually found in tetramer form. However, there are also hexameric, dimeric, and monomeric forms of asparaginases isolated from various sources (Jia et al. 2021). Most of the L-ASNase enzymes isolated from bacteria consist of quaternary and tertiary structures. (Batool et al. 2016). This enzyme can be obtained in nature from a wide variety of organism sources, from prokaryotes to vertebrates (Eisele et al. 2011).

This chapter summarizes the importance of L-ASNase, the different sources from which this enzyme is obtained, and its applications in various fields.

2. Mechanism of Action

The mechanism by which the L-ASNase enzyme catalyzes the hydrolysis of L-ASNase to L-aspartic acid and NH_3 occurs in two steps (Fig 1):

Firstly, a strong base (NH_2) activates the nucleophilic residue of L-ASNase. The activated enzyme attacks the amide carbon atom of L-asparagine (substrate). Thus, the beta-acyl-enzyme intermediate product is generated. In the second stage, the nucleophile activated by a water molecule attacks the ester carbon, forms L-aspartic acid and liberates the ammonia molecule (Cachumba et al. 2016).

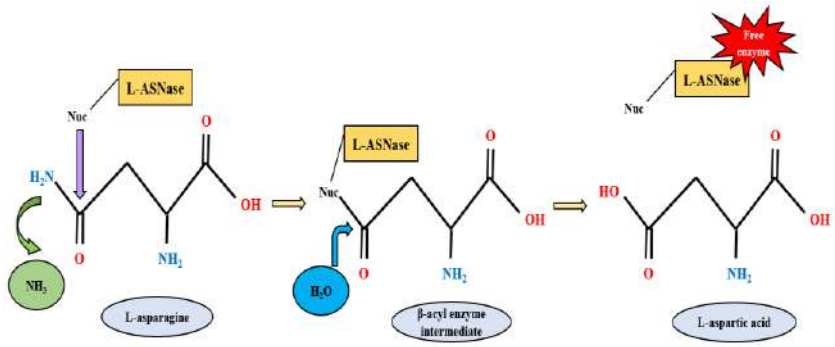

Fig 1. Hydrolysis reaction mechanism of L-asparaginase. Nuc: nucleophile (by author)

3. Various Sources of L-asparaginase

L-ASNase enzyme can be isolated in nature from a wide variety of organism sources, from prokaryotes to vertebrates (Eisele et al. 2011). Apart from human beings, the L-ASNase enzyme is naturally expressed and produced by many organisms, including plants, animals, and microorganisms (bacteria, Actinomycetes, algae, fungi, and yeast) (Wakil and Adelegan, 2019). However, the extraction of this enzyme from plants and animals is quite difficult. Therefore, researchers have turned to a wide range of microbial sources to isolate L-ASNase (Batool et al. 2016). The L-ASNase-producing microorganism can be isolated from the environment such as soil, water, marine/river sediment, sea sponges, algae, and plants (Jia et al. 2021). In this chapter, only L-ASNase enzymes of microbial origin are mentioned.

3.1. Bacterial Sources

Microorganisms, especially bacterial strains, are preferred over other sources of L-ASNase production because they have some advantages: rapid growth in short fermentation times, ease of upstream and downstream processing in industrial scale production, ease of production with high yield and purity, having low production costs, being more stable, growing easily in the presence of simple substrates, being easily genetically modifiable, etc (Lopes et al. 2015; Vimal and Kumar, 2017; Chand et al. 2020).

L-ASNase has been isolated from both Gram-positive and Gram-negative bacterial strains which can grow in different environments. Gram-positive bacteria have a wider production range than Gram-negative bacteria (Asthana and Azmi, 2003).

Bacterial L-ASNases are divided into two types based on their cellular locations and on the activity towards L-asparagine and L-glutamine: Type I and

type II L-ASNase (Izadpanah et al., 2018). Type I L-ASNases are found in the cytosol (cytosolic asparaginases) and show a lower affinity for L-asparagine and a higher affinity for L-glutamine. Type II L-ASNases are found in the periplasmic spaces and show a high affinity for L-asparagine and less affinity for L-glutamine. Specifically, they are produced extracellularly (Olivieria et al. 2021).

L-ASNase type II shows better antitumor activity than type I and is used as a chemotherapeutic agent (Zhang et al. 2015). It is also used in the food industry to remove asparagine before food processing to reduce acrylamide formation (Hendriksen et al. 2009).

Although L-ASNase enzymes are obtained from many bacterial strains (Table 1), *Escherichia coli* and *Erwinia chrysanthemi* have been used frequently in industrial and clinical applications for many years due to their high affinity and low glutaminase activities (Kotzia and Labrou, 2005). Table 1 displays various bacterial L-ASNase sources.

3.2. Fungal Sources

Fungal sources, like bacteria, are microorganisms that produce L-ASNase with high efficiency (Chand et al. 2020). The L-ASNase enzymes they produce are used as food processing agents, especially in the food industry (Aiswarya and Baskar, 2018). From a health point of view, fungal L-ASNases are thought to cause less immunogenicity because they are cellularly closer to humans as compared to bacteria (Chand et al. 2020).

It has been reported that bacterial L-ASNases can cause some immunological side effects that limit their use, such as allergic reactions, thrombosis, hyperglycemia, and coagulation abnormality (Doriya and Kumar, 2016). However, compared to bacteria, fungi are more closely related to humans. Therefore, fungal L-ASNases may have fewer immunological adverse effects (Shrivastava et al. 2012). Asparaginase from some fungal genera, such as Fusarium, Penicillium, and Aspergillus, exhibited anti-lymphoma activity and had no effect on L-glutamine (Nagarethiam et al. 2012). Furthermore, it is very easy to purify fungal L-ASNase is produced extracellularly. Therefore, it has recently gained importance as a source of L-ASNase, and several L-ASNase-producing fungal sources are shown in Table 1.

3.3. Actinomyces Sources

Like bacteria and fungi, Actinomycetes are good producers of the L-ASNase enzyme (Sahu et al. 2007). They are abundant in soil, water, sediments, and nature worldwide, but it has been reported that the enzyme obtained from species living in fish especially shows high activity (Batool et al. 2016). Many studies

have been reported on the L-ASNase enzyme isolated from strains of the genus Streptomyces, a member of the Actinomycetes group (Usha et al. 2011; Sudhir et al. 2012; Meena et al. 2015; Saleena et al. 2022). Some Actinomycetes strains producing L-ASNase are given in Table 1.

3.4. Yeast Sources

Yeasts have been becoming an attractive alternative source for L-ASNase production. Some investigations have reported the use of the yeasts *Saccharomyces* sp., *Pichia* sp., *Candida* sp., *Spobolomyces* sp., *Hansenula* sp., and *Rhodotorula* sp. for L-ASNase production (Cachumba et al. 2016). It has also been mentioned that the enzyme obtained from yeast shows antitumor activity (Nagarethiam et al. 2012). In a study, it was stated that a protein expression system based on the L-ASNase enzyme was developed in *Pichia pastoris* yeast (Sajitha et al. 2015). They reported that this new system could be effective in the production of humanized enzymes by glycosylation patterns similar to those of mammals. Some of the L-ASNase-producing yeasts are also listed in Table 1.

3.5. Algal Sources

In recent years, the reasons why blue-green microalgae used in the production of L-ASNase have been preferred as an interesting alternative source are: high nutritional content, low production costs, high-efficiency enzyme production, ease of cultivation, harvestability, no seasonal variation, etc (Abd El Baky and El Baroty, 2016). Some of the L-ASNase-producing algae included in various research are represented in Table 1.

Table 1. L-asparaginase-producing microbial sources

L-ASNase Source	Reference
Bacteria	
Acinetobacter baumannii	Muslim (2014)
Bacillus amyloliquefaciens MKSE	Yim and Kim (2019)
Bacillus licheniformis	Gulati et al. (1997)
Bacillus pumilus	Sindhwad and Desai (2015)
Bacillus sonerensis	Aly et al. (2020)
Escherichia coli MTCC 739	Vidya et al. (2011)
Pectobacterium carotovorum MTCC 1428	Kumar et. al. (2011)
Streptococcus sp. D2	Wakil and Adelegan (2015)
Thermococcus gammatolerans EJ3	Zuo et al. (2014)
Actinomycetes	
Nocardiopsis alba NIOT-VKMA08	Meena et al. (2015)
Streptomyces brollosae NEAE-115	El-Naggar et al. (2018)
Streptomyces ginsengisoli	Deshpande et al. (2014)
Streptomyces koyangensis SK4	Saleena et al. (2022)
Streptomyces noursei MTCC 10469	Dharmaraj et al. (2011)
Streptomycetes parvulus KUAP106	Usha et al. (2011)
Algae	
Chlamydomonas sp.	Paul (1982)
Chlorella vulgaris	Ebrahiminezhad et al. (2014)
Spirulina maxima	Abd El Baky and El Baroty (2016)
Fungi	
Aspergillus alliaceus	Gulati et al. (1997)
Aspergillus niger	Mishra (2006)
Aspergillus terreus	Aiswarya and Baskar (2018)
Cladosporium sp.	Kumar and Manonmani (2013)
Fusarium solani	Nakahama et al. (1973)
Flammulina velutipes	Eisele et al. (2011)
Penicillium crustosum NMKA 511	Khalil et al. (2011)
Rhizomucor miehei	Huang et al. (2014)
Trichoderma viride Pers: SF Grey	Lincoln et al. (2015)
Yeast	
Candida utilis	Kil et al. (1995)
Candida utilis ATCC9950	Momeni et al. (2015)
Pichia polymorpha	Foda et al. (1980)
Saccharomyces cerevisiae	Bon et al. (1997)
Yarrowia lipolytica DSM3286	Darvishi et al. (2019)

4. L-asparaginase Applications

4.1. The Role of L-ASNase as an Anticancer Drug

L-ASNase is one of the therapeutic agents combined with drugs used in the treatment of many cancers, such as ALL (Acute Lymphoblastic Leukemia), Hodgkin's disease, chronic lymphatic leukemia, myelomonocytic leukemia, melanosarcoma, reticulosarcoma, and lymphosarcoma (Kidd, 1953; Broome. 1961).

The L-ASNase enzyme catalyzes the breakdown of the non-essential L-asparagine amino acid in the blood, which is not needed by normal cells but is needed by cancer cells, into aspartate and ammonia (Chand et al. 2020). Healthy cells can synthesize L-asparagine from L-aspartic acid through the asparagine synthetase enzyme (Mostafa et al. 2019). However, tumor cells lack this enzyme (Fig 2).

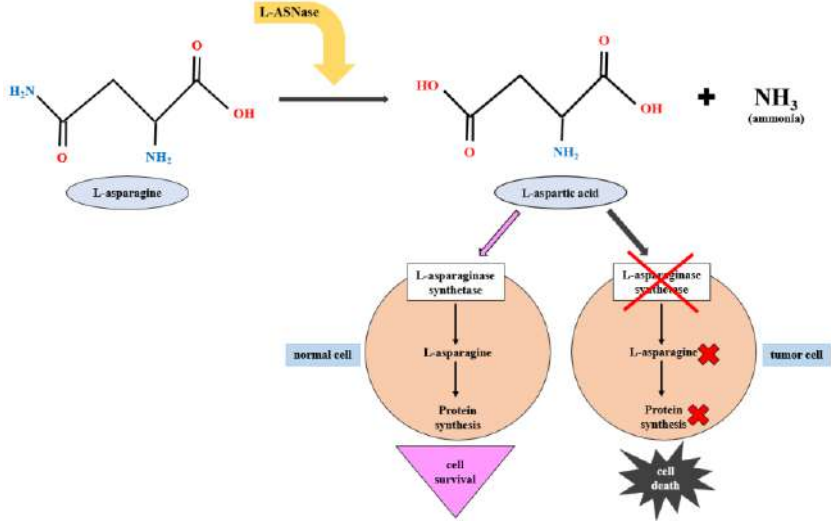

Fig 2. Effect of L-ASNase on normal and tumor cells (by author)

In the absence of L-asparagine, malignant cells cannot perform their vital activities such as protein and DNA synthesis and die off (Salzer et al. 2014; Batool et al. 2016). This enzyme provides significant healing against cancer by depriving cancerous cells of the amino acid L-asparagine.

There are three types of L-ASNase used as drugs in the treatment of ALL: asparaginase (from *E. coli*), Pegaspargase (L-ASNase from *E. coli* and attached to polyethylene glycol), and Erwinia asparaginase (from *E. caratovora*) (Chand et al. 2020). Cristanaspase (USA), L-Asnase (USA), Elspar (USA), Leumase (Japan), Crasntin (Germany), Kidrolase, Oncaspar, Crisantas, Erwinase, Pasum, PEGasparaginase, Pegasparagasum are also commercially available therapeutic

L-ASNase products. Today, they are used in drug formulations together with various chemotherapeutic agents such as prednisone, methotrexate, and vincristine (Vimal and Kumar, 2017).

4.2. The Role of L-ASNase in Food Industry

In the food industry, heat treatment is applied to foods (biscuits, cookies, snacks, coffee, bread, French fries, cereals, etc.) to improve or preserve their nutritional properties. L-asparagine, which is found in most starchy foods, reacts with the reduced sugar during heat treatment (above 120°C) to form acrylamide (C_3H_5NO) (Fig 3), a carcinogenic and neurotoxic by-product of the Maillard reaction (browning process) (Mottram et al. 2002). When L-ASNase is used before frying and cooking, the amino acid L-asparagine, one of the precursors of acrylamide, is hydrolyzed and the amount of acrylamide formed in foodstuffs is reduced (Yim and Kim, 2019).

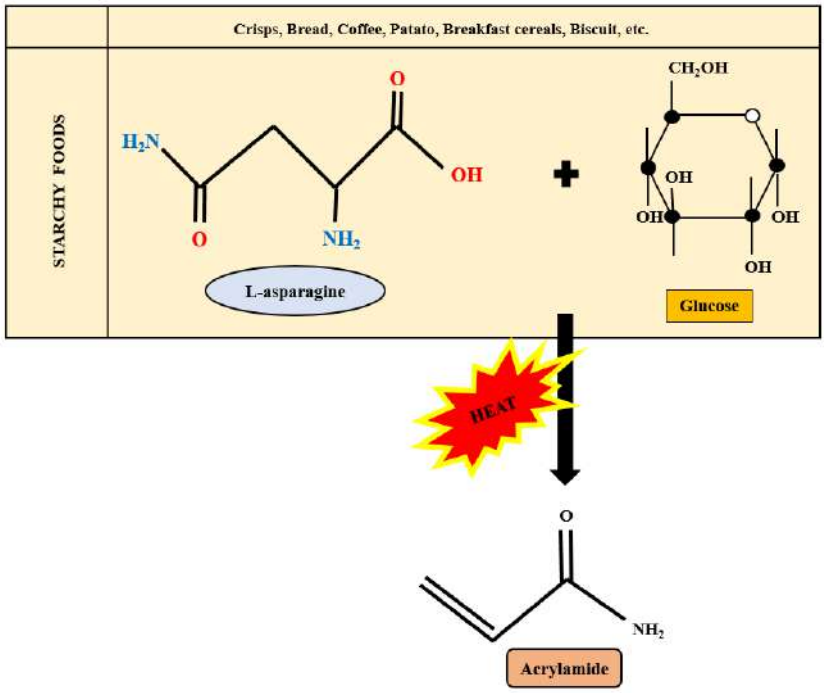

Fig 3. Acrylamid formation in starchy foods (by author)

Two commercially available brands of asparaginases for reducing acrylamide in starchy foods are Acrylaway® (Novozymes, Denmark) from *Aspergillus oryzae* and PreventAse™ (DSM Food Specialties Den-mark) from *Aspergillus niger* (Adebo et al. 2017).

4.3. The Role of L-ASNase in Biosensors

Many spectroscopic techniques such as XPS, XRD, TEM, and SEM are costly and difficult applications used in the determination of L-asparagine (Zubavichus et al. 2004). For this reason, the demand for the development of inexpensive, reliable, and practical biosensors has increased. Therefore, researchers have developed biosensors to analyze L-asparagine levels in the food industry and in the treatment of leukemia (Verma et al. 2007). The mechanism of action of this biosensor is based on the activity of the L-ASNase enzyme. Ammonium ions released as a result of hydrolysis of asparagine with L-ASNase enzyme cause changes in pH, color, and absorption. In this way, the amount of asparagine is determined (Batool et al. 2016).

4.4. The Role of L-ASNase in Amino Acid Metabolism

L-ASNase is involved in the biosynthesis of amino acids threonine, lysine isoleucine, and methionine, which are members of the aspartic family (Qeshmi et al. 2018). Aspartic acid, which is the direct precursor of these amino acids, occurs as a result of the hydrolysis of asparagine by L-ASNase or from the Krebs cycle. At the end of the hydrolysis reaction, commercially important amino acids lysine, threonine, and methionine are formed from aspartic acid (Batool et al. 2016).

5. Conclusion

In this chapter, various sources and industrial applications of the L-ASNase enzyme have been presented. The microbial L-ASNase isolated from various microorganisms has a very important place in the industry, both as a therapeutic agent and playing a key role in the reduction of acrylamide. Considering the wide application possibilities of the enzyme in modern fields such as health, food, and biosensor applications, it seems that there is a lot of research to be done on this fabulous enzyme.

6. References

1. Abd El Baky, H. H., El Baroty, G. S. (2016). Optimization of growth conditions for purification and production of L-asparaginase by *Spirulina maxima*. *Evidence-Based Complementary and Alternative Medicine*, 2016.
2. Adebo, O. A., Kayitesi, E., Adebiyi, J. A., Gbashi, S., Temba, M. C., Lasekan, A., Phoku, J. Z., Njobeh, P. B. (2017). Mitigation of acrylamide in foods: An African perspective, B. S. R. Reddy, *Acrylic Polymers in Healthcare*, (s. 152-172), London: Intech.
3. Aiswarya, R., Baskar, G. (2018). Enzymatic mitigation of acrylamide in fried potato chips using asparaginase from *Aspergillus terreus*. *International Journal of Food Science & Technology*, *53*(2), 491-498.
4. Aly, N., El-Ahwany, A., Ataya, F. S., Saeed, H. (2020). *Bacillus sonorensi*s L. Asparaginase: Cloning, expression in *E. coli* and characterization. *The Protein Journal*, 39(6), 717-729.
5. Asthana, N., Azmi, W. (2003). Microbial L-asparaginase: A potent antitumour enzyme. *Indian Journal of Biotechnology*, 2, 184-194.
6. Barros, R. A., Cristóvão, R. O., Carabineiro, S. A., Neves, M. C., Freire, M. G., Faria, J. L., Santos-Ebinuma, V. C., Tavares, A. P. M., Silva, C. G. (2022), Immobilization and Characterization of L-Asparaginase over Carbon Xerogels. *BioTech*, *11*(2), 10.
7. Baskar, G., Renganathan, S. (2011). Optimization of media components and operating conditions for exogenous production of fungal L-asparaginase. *Chiang Mai J Sci*, 38(2), 270-279.
8. Batool, T., Makky, E. A., Jalal, M., Yusoff, M. M. (2016). A comprehensive review on L-asparaginase and its applications. *Applied biochemistry and biotechnology*, 178(5), 900-923.
9. Bon, E. P., Carvajal, E., Stanbrough, M., Rowen, D., Magasanik, B. (1997). Asparaginase II of *Saccharomyces cerevisiae*. *Applied biochemistry and biotechnology*, 63(1), 203-212.
10. Broome, J. D. (1961). Evidence that the L-asparaginase activity of guinea pig serum is responsible for its anti lymphoma effects. *Nature*, 191(4793), 1114-1115.
11. Cachumba, J. J. M., Antunes, F. A. F., Peres, G. F. D., Brumano, L. P., Santos, J. C. D., Silva, S. S. D. (2016). Current applications and different approaches for microbial L-asparaginase production. *Brazilian journal of microbiology*, 47, 77-85.

12. Chand, S., Mahajan, R. V., Prasad, J. P., Sahoo, D. K., Mihooliya, K. N., Dhar, M. S., Sharma, G. (2020). A comprehensive review on microbial L-asparaginase: Bioprocessing, characterization, and industrial applications. *Biotechnology and applied biochemistry*, 67(4), 619-647.
13. Darvishi, F., Faraji, N., Shamsi, F. (2019). Production and structural modeling of a novel asparaginase in *Yarrowia lipolytica*. *International journal of biological macromolecules*, 125, 955-961.
14. de Oliveira, M. D., Vaz, C. J. T., de Oliveira, L. M., Guidini, C. Z. (2021). L-asparaginase: therapeutic use and applications in the food industry-a review. *Research, society and development*, 10 (10), e596101018980-e596101018980.
15. Deshpande, N., Choubey, P., Agashe, M. (2014). Studies on optimization of growth parameters for L-asparaginase production by *Streptomyces ginsengisoli*. *The Scientific World Journal*, 2014.
16. Dharmaraj, S. (2011). Study of L-asparaginase production by *Streptomyces noursei* MTCC 10469, isolated from marine sponge *Callyspongia diffusa*. *Iranian journal of biotechnology*, 9(2), 102-108.
17. Doriya, K., Kumar, D. S. (2016). Isolation and screening of L-asparaginase free of glutaminase and urease from fungal sp. *3 Biotech*, 6(2), 1-10.
18. Ebrahiminezhad, A., Rasoul-Amini, S., Ghoshoon, M. B., Ghasemi, Y. (2014). *Chlorella vulgaris*, a novel microalgal source for L-asparaginase production. *Biocatalysis and Agricultural Biotechnology*, 3(2), 214-217.
19. Eisele, N., Linke, D., Bitzer, K., Na'amnieh, S., Nimtz, M., Berger, R. G. (2011). The first characterized asparaginase from a basidiomycete, *Flammulina velutipes*. *Bioresource technology*, 102(3), 3316-3321.
20. El-Naggar, N. E. A., Deraz, S. F., El-Ewasy, S. M., Suddek, G. M. (2018). Purification, characterization and immunogenicity assessment of glutaminase free L-asparaginase from *Streptomyces brollosae* NEAE-115. *BMC Pharmacology and Toxicology*, 19(1), 1-15.
21. Foda, M. S., Zedan, H. H., Hashem, S. A. (1980). Formation and properties of L-glutaminase and L-asparaginase activities in *Pichia polymorph*a. *Acta Microbiologica Polonica*, 29(4), 343-352.
22. Gulati, R., Saxena, R. K., Gupta, R. (1997). A rapid plate assay for screening L-asparaginase producing microorganisms. *Letters in applied microbiology*, 24(1), 23-26.
23. Hendriksen, H. V., Kornbrust, B. A., Østergaard, P. R., Stringer, M. A. (2009). Evaluating the potential for enzymatic acrylamide mitigation in a range of food products using an asparaginase from *Aspergillus oryzae*. *Journal of agricultural and food chemistry*, 57(10), 4168-4176.

24. Huang, L., Liu, Y., Sun, Y., Yan, Q., Jiang, Z. (2014). Biochemical characterization of a novel L-Asparaginase with low glutaminase activity from *Rhizomucor miehei* and its application in food safety and leukemia treatment. *Applied and environmental microbiology*, 80(5), 1561-1569.
25. Jia, R., Wan, X., Geng, X., Xue, D., Xie, Z., Chen, C. (2021). Microbial L-asparaginase for application in acrylamide mitigation from food: Current research status and future perspectives. *Microorganisms*, 9(8), 1659.
26. Khalil, N. M., Rodríguez-Couto, S., El-Ghany, M. N. A. (2021). Characterization of *Penicillium crustosum* L-asparaginase and its acrylamide alleviation efficiency in roasted coffee beans at non-cytotoxic levels. *Archives of Microbiology*, 203(5), 2625-2637.
27. Kidd, J. G. (1953). Regression of transplanted lymphomas induced in vivo by means of normal guinea pig serum: I. course of transplanted cancers of various kinds in mice and rats given guinea pig serum, horse serum, or rabbit serum. *The Journal of experimental medicine*, 98(6), 565-582.
28. Kil, J. O., Kim, G. N., Park, I. (1995). Extraction of extracellular L-asparaginase from *Candida utilis*. *Bioscience, biotechnology, and biochemistry*, 59(4), 749-750.
29. Kotzia, G. A., Labrou, N. E. (2005). Cloning, expression and characterisation of *Erwinia carotovora* L-asparaginase. *Journal of Biotechnology*, 119(4), 309-323.
30. Kumar, S., Dasu, V. V., Pakshirajan, K. (2011). Purification and characterization of glutaminase-free L-asparaginase from *Pectobacterium carotovorum* MTCC 1428. *Bioresource technology*, 102(2), 2077-2082.
31. Kumar, N. M., Ramasamy, R., Manonmani, H. K. (2013). Production and optimization of L-asparaginase from *Cladosporium* sp. using agricultural residues in solid state fermentation. *Industrial Crops and Products*, 43, 150-158.
32. Lincoln, L., Niyonzima, F. N., More, S. S. (2021). Purification and properties of a fungal L-asparaginase from *Trichoderma viride* pers: SF GREY. *Journal of Microbiology, Biotechnology and Food Sciences*, 2021, 310-316.
33. Lopes, A. M., Oliveira-Nascimento, L. D., Ribeiro, A., Tairum Jr, C. A., Breyer, C. A., Oliveira, M. A. D., Monteiro, G., de Souza-Motta, C. M., de Oliveira Magalhães, P., Avendaño, J. G. F., Cavaco-Paulo, A. M., Mazzola, P. G., de Oliveira Rangel-Yagui, C., Sette, L. D., Converti, A., Pessoa, A. (2017). Therapeutic L-asparaginase: upstream, downstream and beyond. *Critical reviews in biotechnology*, 37(1), 82-99.

34. Meena, B., Anburajan, L., Sathish, T., Vijaya Raghavan, R., Dharani, G., Valsalan Vinithkumar, N., Kirubagaran, R. (2015). L-Asparaginase from *Streptomyces griseus* NIOT-VKMA29: optimization of process variables using factorial designs and molecular characterization of L-asparaginase gene. *Scientific reports*, 5(1), 1-12.
35. Mishra, A. (2006). Production of L-asparaginase, an anticancer agent, from *Aspergillus niger* using agricultural waste in solid state fermentation. *Applied Biochemistry and Biotechnology*, 135(1), 33-42.
36. Momeni, V. Alemzadeh, I., Vosoughi, M. (2015). Enhancement of L-asparaginase production by *Candida utilis* in a 13 L fermenter and its purification. *International Journal of Engineering*, 28(8), 1134-1139.
37. Mottram, D. S., Wedzicha, B. L., Dodson, A. T. (2002). Acrylamide is formed in the Maillard reaction. *Nature*, 419(6906), 448-449.
38. Mostafa, Y., Alrumman, S., Alamri, S., Hashem, M., Al-izran, K., Alfaifi, M., Elbehairi, S. E., Taha, T. (2019). Enhanced production of glutaminase-free L-asparaginase by marine *Bacillus velezensis* and cytotoxic activity against breast cancer cell lines. *Electronic Journal of Biotechnology*, 42, 6-15.
39. Muslim, S. N. (2014). Production, purification and characterization of a novel L-asparaginase from *Acinetobacter baumannii* with anticancerous activity. *Int. J. Curr. Eng. Technol.*, 4(1), 6-11.
40. Nagarethinam, S., Naik, A. N., Udupa, N., Rao, V. J., Vanathi, M. B. (2012). Microbial L-Asparaginase and its future prospects. *Asian Journal of Medical Research*, 1(4), 159-168.
41. Nakahama, K., Imada, A., Igarasi, S., Tubaki, K. (1973). Formation of L-asparaginase by Fusarium species. *Journal of General Microbiology*, 75, 269–273.
42. Narta, U. K., Kanwar, S. S., Azmi, W. (2007). Pharmacological and clinical evaluation of L-asparaginase in the treatment of leukemia. *Critical reviews in oncology/hematology*, 61(3), 208-221.
43. Nunes, J. C., Cristóvão, R. O., Freire, M. G., Santos-Ebinuma, V. C., Faria, J. L., Silva, C. G., Tavares, A. P. (2020). Recent strategies and applications for L-asparaginase confinement. *Molecules*, 25(24), 5827.
44. Paul, J. H. (1982). Isolation and characterization of a Chlamydomonas L-asparaginase. *Biochemical Journal*, 203(1), 109-115.
45. Qeshmi, F. I., Homaei, A., Fernandes, P., Javadpour, S. (2018). Marine microbial L-asparaginase: biochemistry, molecular approaches and applications in tumor therapy and in food industry. *Microbiological Research*, 208, 99-112.

46. Sahu, M. K., Sivakumar, K., Poorani, E., Thangaradjou, T., Kannan, L. (2007). Studies on L-asparaginase enzyme of actinomycetes isolated from estuarine fishes. *Journal of Environmental Biology*, 28(2), 465.
47. Sajitha, S., Vidya, J., Binod, P., Pandey, A. (2015). Cloning and expression of L-asparaginase from *E. coli* in eukaryotic expression system. *Biochemical engineering journal*, 102, 14-17.
48. Saleena, S. K., Johnson, J. I., Joseph, J. K., Padinchati, K. K., Abdulla, M. H. (2022). Production and optimization of L-asparaginase by *Streptomyces koyangensis* SK4 isolated from Arctic sediment. *Journal of Basic Microbiology*, 2022, 1-10.
49. Salzer, W. L., Asselin, B. L., Plourde, P. V., Corn, T., Hunger, S. P. (2014). Development of asparaginase *Erwinia chrysanthemi* for the treatment of acute lymphoblastic leukemia. *Annals of the New York Academy of Sciences*, 1329(1), 81-92.
50. Shrivastava, A., Khan, A. A., Shrivastav, A., Jain, S. K., Singhal, P. K. (2012). Kinetic studies of L-asparaginase from *Penicillium digitatum*. *Preparative Biochemistry and Biotechnology*, 42(6), 574-581.
51. Sindhwad, P., Desai, K., 2015. Media optimization, Isolation and purification of L-asparaginase from marine isolate. *Asian Pac. J. Health Sci*. 293, 72-82.
52. Sudhir, A. P., Dave, B. R., Trivedi, K. A., Subramanian, R. B. (2012). Production and amplification of an L-asparaginase gene from actinomycete isolate *Streptomyces* ABR2. *Annals of microbiology*, 62(4), 1609-1614.
53. Usha, R., Mala, K. K., Venil, C. K., Palaniswamy, M. (2011). Screening of actinomycetes from mangrove ecosystem for L-asparaginase activity and optimization by response surface methodology. *Polish Journal of Microbiology*, 60(3), 213-221.
54. Verma, N., Kumar, K., Kaur, G., Anand, S. (2007). L-asparaginase: a promising chemotherapeutic agent. *Critical reviews in biotechnology*, 27(1), 45-62.
55. Vidya, J., Vasudevan, U. M., Soccol, C. R., Pandey, A. (2011). Cloning, functional expression and characterization of L-asparaginase II from *E. coli* MTCC 739. *Food Technology and Biotechnology*, 49(3), 286.
56. Vimal, A., Kumar, A. (2017). Biotechnological production and practical application of L-asparaginase enzyme. *Biotechnology and genetic engineering reviews*, 33(1), 40-61.

57. Wakil, S. M., Adelegan, A. A. (2015). Screening, production and optimization of L-asparaginase from soil bacteria isolated in Ibadan, South-western Nigeria. *Journal of Basic & Applied Sciences*, 11, 39-51.
58. Yim, S., Kim, M. (2019). Purification and characterization of thermostable L-asparaginase from *Bacillus amyloliquefaciens* MKSE in Korean soybean paste. *LWT-Food Science and Technology*, 109 (2019), 415-421.
59. Zhang, S., Xie, Y., Zhang, C., Bie, X., Zhao, H., Lu, F., Lu, Z. (2015). Biochemical characterization of a novel L-asparaginase from *Bacillus megaterium* H-1 and its application in French fries. *Food Research International*, 77, 527-533.
60. Zubavichus, Y., Fuchs, O., Weinhardt, L., Heske, C., Umbach, E., Denlinger, J. D., Grunze, M. (2004). Soft X-ray-induced decomposition of amino acids: an XPS, mass spectrometry, and NEXAFS study. *Radiation Research*, 161(3), 346-358.
61. Zuo, S., Xue, D., Zhang, T., Jiang, B., Mu, W. (2014). Biochemical characterization of an extremely thermostable L-asparaginase from *Thermococcus gammatolerans* EJ3. *Journal of Molecular Catalysis B: Enzymatic*, 109, 122-129.

Acute Epileptic Seizures Induce Significant Alterations In Proteins Of Hippocampus Region: Evidence From Infrared Spectroscopic Analysis

Assist Prof. Sevgi Türker-Kaya[1]
Assoc. Prof. Doç. Gül İlbay[2]

[1]Department of Biology, Faculty of Arts and Sciences, Kocaeli University, 41380, Kocaeli, Turkey,
e-mail:sevgitrkr@gmail.com; sevgi.turker@kocaeli.edu.tr
[2]Department of Physiology, Faculty of Medicine, Kocaeli University, 41380, Kocaeli, Turkey, e-mail: gulilbay@yahoo.com

Introduction

Epilepsy is a neurological disorder characterized by transient and recurrent seizures (1-2). There is still no effective treatment strategy to eliminate the seizures due to limited knowledge about the mechanisms underlying epileptic conditions (2-3).

Generalized tonic–clonic seizures (GTCS) are observed in 90% of epileptic patients (4). Seizures either bilaterally are generated from distribute whole brain or formed from one hemisphere (5). They are identified as the activity of tonic phase with the frequency of >13 Hz and low amplitude with the frequency of ≤10 Hz, and high amplitude slow-wave oscillations (5-6). Frequent GTCS are higher risk factors for the sudden unexpected death (7). Thus, management of these seizures is of great importance. Even though their pathophysiology remains unclear (8), evidence suggests that GTCS rather affect specific brain regions most intensely, particularly the hippocampus. Indeed, the hippocampus has been shown by molecular alterations after GTCS, which represents its possible role in the generation and propagation of such seizures (8-9).

Considering the role of proteins in brain functioning, the investigation of the alterations in proteins in hippocampus brain region after GTCS would be beneficial as also suggested by previous works (9-11). Attenuated Total Reflectance Fourier Transform Infrared (ATR-FTIR) spectroscopy is suitable for this analysis. It can be applied to a variety samples, for determining protein content and secondary structure (12-14). In an ATR-FTIR spectrum of a biological sample, the Amide I band is accepted as a combination of discrete underlying modes unique to secondary structures of proteins. Using methods such as the second derivative and curve-fitting analyses it is possible to study structural components of proteins. These methods allow the quantitative estimation of protein secondary structures (15-17), which can be also confirmed by X-ray crystallography (15,18). Owing to such advantage ATR-FTIR spectroscopy has been increasingly employed to monitor the alterations in proteins induced by disease' states, which is not easily detectable by morphological methods, in native environments such as within cells and tissues (12,14,19-20).

The present work was focused on the investigation of the effects of acute GTCS on proteins in the hippocampus. For this purpose, the relative changes in the secondary structure components and amount of proteins in the hippocampus were determined by ATR-FTIR spectroscopy combined with principal component analysis (PCA).

Materials and methods

Animal experiments and sample preparation

Animal experiments were performed in compliance with the European Community Council Directive of 24 November 1986, and the procedures were hold the approval obtained by the local animal welfare authorities (KOU HAYDEK, approval number 7/3-2016). Adult Wistar male rats were divided as the control group (n = 7) and the GTCS group (n = 7). Rats had free access of food and water ad libitium under standard laboratory conditions (21°C, 12:12-h dark-light cycle: lights on at 07:00 and off at 19:00). During five days, saline solution was applied to the control group, while 60 mg/kg dose of pentylenterazol was injected i.p. to the GTCS group. After each injection, no rats in the control group had a seizure. But, all rats in the GTCS group had tonic-clonic seizures based on the Racine scale (21). Five days later, all animals were decapitated under ether anesthesia. The hippocampus regions were dissected out and kept at -80 ° C until analyses.

Hippocampus samples were chopped in homogenization buffer containing 0.25 M sucrose, 10 mM Tris−HCl, pH 7.4, 1 mM EDTA, and 1 mmol PMSF. The samples were homogenized by a Potter Elvehem type glass-Teflon homogenizer, and subsequently centrifuged at 100 000 g for 1 h at 4 °C. The pellet fractions were stored at −70 °C until spectral experimentation.

Spectral collection and data processing

Spectral acquisition was done by a Spectrum Two FT-IR spectrometer (PerkinElmer Ltd., UK), equipped with a Universal ATR accessory using the single-bounce mode. To avoid the interference of atmospheric water on spectra, the background was collected on the empty cell (no sample loaded), and was later subtracted automatically from sample spectra using Perkin-Elmer Spectrum software. 10 µl homogenate was placed on ATR-Diamond/ZnSe crystal, and spectra were obtained in 4000 to 1000 cm^{-1} region with 100 interferograms at a resolution of 4 cm^{-1}. Three independent scanning from the same hippocampus homogenate were performed. The average spectra of the replicates from one hippocampus were examined during the spectral analysis (22-24). Since water absorption modes in samples overlap protein bands (1700-1500 cm^{-1}), the buffer was scanned and subtracted from each sample spectrum using Perkin Elmer software. These subtracted spectra were used for spectral analysis. The band positions were obtained using the frequency corresponding to the center of 80% x-height of the peak. The Amide I and Amide II peak areas were calculated. In addition, Amide I/Amide II and Amide I/Amide I+Amide II

ratios were obtained by dividing the integrated area of Amide I to Amide II, and Amide I to the sum of the areas of Amide I and Amide II, respectively.

Estimation of protein secondary structures

The Amide I band (1720-1590 cm^{-1}) was analyzed by Peak Spectroscopy Software (Operant LLC, US). Sub-bands under Amide I mode were acquired by taking second derivative of spectra with the 7–9 point Savitsky–Golay smoothing function and polynomial order of 2. The identified hidden peaks were assigned, and negative value peak intensity were measured.

With the same program curve fitting was performed on baseline corrected Amide I. Secondary structure calculations were performed using selected bands. During the fitting procedure using Gaussian peak-fit components, peak height was free. Fifty iterated optimization algorithm was done in each fit. The iteration was performed when the coefficient of determination (R^2) became 1 (%100) and was stopped until the best fit was obtained (chi-square $\leq 1.10^{-6}$). The analysis results were expressed as peak position and as the percentage area.

Measurement of protein amount (Bradford assay)

Bradford assay, a well-adopted test, was performed to determine the protein content of groups. The samples were homogenized in cold 100 mM buffer containing protease inhibitors (pH 7.4). Standard protein solutions were prepared by using bovine serum albumin at different concentrations (0, 0.125, 0.25, 0.50, 0.75, 1 mg/mL). Upon adding Bradford reagent on the tubes of hippocampus samples and standards, all samples were incubated for 5 min and absorbance values were measured at 595 nm.

Principal Component Analysis (PCA)

PCA was utilized by Unscrambler 10.4 (Camo Software, Oslo, Norway) on normalized second derivative spectra that smoothed with the Savitzky–Golay algorithm based on the selected spectral region between Amide I band (1720-1590 cm^{-1}).

Statistical Analysis

The results were expressed as 'mean ± standard deviation'. All data were analyzed by ANOVA test. A 'p' value less than or equal to 0.05 was considered as statistically significant. The degree of significance was signed as less than or equal to $p \leq 0.05$*.

Results and Discussion

The current study performed infrared spectroscopic analysis of the proteins in native environment (14,16,22-23). It is worth mentioning that this technology is restricted to give information about proteins in a biological sample without focusing on specific ones, thus the obtained spectral data from the hippocampus

homogenates only gives data about the whole protein profile of the hippocampus including every kinds of proteins within the cell. On the account of this, the present work study was conducted to determine the relative changes in the secondary structure components and amount of proteins in the hippocampus region after acute GTCS, as similarly in previous reports (16,22-23).

Figure 1A illustrates the average absorbance spectra of the hippocampus homogenates for the control and the GTCS group in the region of 1840-1480 cm^{-1}. The bands centred at around 1655 cm^{-1} and 1545 cm^{-1} are assigned to the Amide I and the Amide II vibrations of proteins. The mode at 1655 cm^{-1} (Amide I) corresponds to the C=O stretching of proteins. Each type of secondary structure correlates to this C=O frequency due to its unique molecular geometry and hydrogen bond pattern (11,22). The band located at 1545 cm^{-1} (Amide II) is attributed to the N-H bending and the C-N stretching modes of proteins (15,18,22-24). Principally, spectral analysis of these modes gives structural and quantification information about proteins within the biological samples without the need for isolation (23-25). According to Beer-Lambert law, the area of the Amide absorptions offers relative information for the content of proteins, which has been previously confirmed by biochemical assays (25-26). The alterations in protein amount of the samples were detected by calculating the integrated areas of Amide I and II modes. In addition, to minimize differentiation of experimental conditions such as alterations in thickness, the area ratios of Amide I/Amide II and Amide I+Amide II were calculated as in previous reports (14,24-25,27). Results of those measurements were given in Figure 1B and 1C.

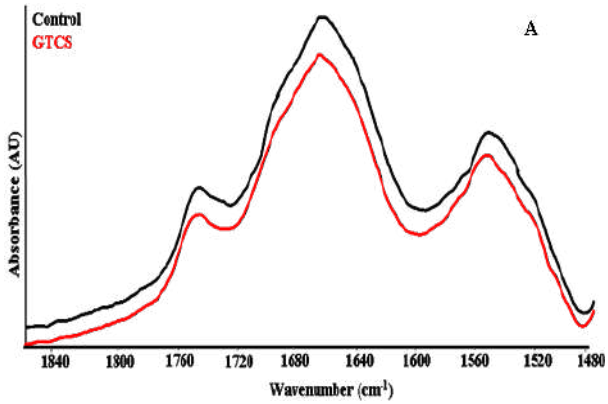

Figure 1. (A) Average absorption infrared spectra of the hippocampus for control and GTCS groups in the region between 1840-1480 cm^{-1}.

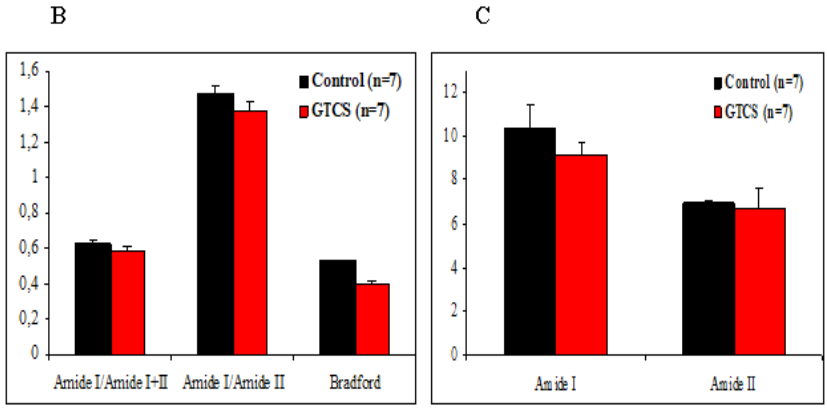

Figure 1. (B) Measurements of integrated areas of Amide I and Amide II modes. **(C)** Amide I/Amide II and Amide I/Amide I+Amide II area ratios, Bradford assay results for control and GTCS groups.

As shown in Figure 1A, 1B, 1C, the Amide I, Amide II areas, and Amide I/Amide II and Amide I/Amide I+Amide II ratios significantly ($p \leq 0.05$*) decreased for the GTCS group in comparison with the control one, which was also affirmed by the Bradford assay (also given in Figure 1C). This result may suggest that GTCS cause a decrement in whole protein content in the hippocampus. Previous proteomic analyses on the hippocampus after GTCS have shown that some proteins like neurogranin (28) and NMDA receptor (29) increase. Moreover, the immediate-early and growth factor genes are activated following these types of epileptic activities (29-30). Taking this into account, it seems that there is a tendency to an elevated level of protein content in the hippocampus after GTCS. But, it should be emphasized that proteins are under attack of free radicals, produced in a very high amount during epileptic seziures. These molecules cause protein degradation (14,22,25). Thus, it is highly probable that newly synthesized proteins upon GTCS might also be disrupted and degraded by free radicals. In addition, despite the studies reported an increased level of specific proteins in the hippocampus after GTCS, there are also works showing that a variety of proteins in the hippocampus such as stress-induced phosphoprotein 1, coronin-1 SIR2-like Dynamin-1 Synapsin-1 are down-regulated (28). In sum, as stated before, the findings in the current study are related to the whole protein profile in the hippocampus region, therefore; cumulative protein content in the hippocampus might be lowered due to GTCS. Such decline in protein content in the hippocampus after acute GTCS may result in susceptibility to proteolysis, tissue damage, and neurotoxicity (31).

Such circumstances may further cause spontaneous and repetitive epileptic activities, also in turn epileptogenesis.

The Amide I/Amide II area ratio (in Figure 1C) is also related with a change in the protein secondary structure in the diseased tissues in comparison to the normal ones (14,25,27). Even though epilepsy is not a condition for specific protein misfolding, it contains pathological events such as alteration in ion homeostasis, and protein oxidation. These situations may result in the disruption of the hydrogen bonding of polypeptide chains, further stimulate protein aggregation. To better estimate this, the variations in protein secondary structure the Amide I mode (1720-1590 cm^{-1}) was further analyzed as previously done by us (22-23,32) and others (15-16,33). The Amide I band consists of many overlapping modes that represent different secondary structure elements of proteins such as alpha-helix, β-sheet, and β-turn (16-17,32). However, such secondary structure components may not be readily observed in an absorbance spectrum. Therefore, a second derivative spectrum is used to sharpen hidden peaks (15,32). The second derivative spectra of the control and the GTCS groups were illustrated in Figure 2A. The obtained the sub-bands under Amide I mode in second derivative spectra were assigned according to the literature. The mode at around 1710 cm^{-1} is from β turns, the band at around 1695 cm^{-1} and 1675 cm^{-1} are generally attributed to anti-parallel β and parallel β, respectively. The peak at around 1655 cm^{-1} is due to α-helix. Next two modes located at around 1635 cm^{-1} and 1625 cm^{-1} are associated with β sheet and β turn. Intermolecular aggregated β structure appears at around 1615 cm^{-1} (14-15,22-23,33).

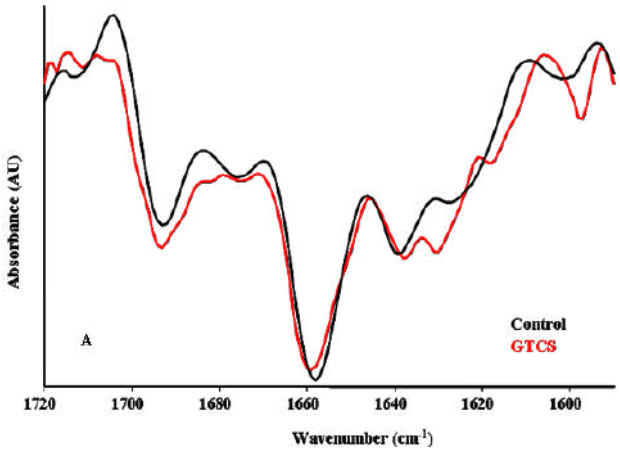

Figure 2. (A) Average second derivative spectra of the hippocampus for control and GTCS groups in the region between 1720-1590 cm^{-1}.

Table 1. Numerical data of analysis of second derivative and curve fitting for control and GTCS groups. The values are the mean ± standart deviation for each sample. The degree of significance was denoted as ($p \leq 0.05$*).

	Control (n=7)		GTCS (n=7)	
Second Derivative				
	Wavenumber (cm^{-1})	Intensity (10^{-3})	Wavenumber (cm^{-1})	Intensity (10^{-3})
β turns	1711.22±0.53	-0.003±0.0001	1709.84±0.39	-0.002±±0.0001↓
Anti-parallel β	1695.10±0.49	-0.018±0.0002	1692.90±1.05	-0.023±0.0003*↑
Parallel β	1678.32±1.65	-0.009±0.0013	1676.05±1.09	-0.009±0.0005
α-helix	1656.28±0.57	-0.062±0.0027	1655.01±0.46	-0.060±±0.0098↓
β sheet	1635.73±0.84	-0.028±0.0064	1633.92±1.04	-0.031±0.0076*↑
β turns	1630.09±1.55	-0.011±0.0009	1630.55±1.61	-0.020±0.0055**↑
Int. agg. β	-	-	1615.61±0.48	-0.005±0.0008*↑
Curve Fit				
	Wavenumber (cm^{-1})	Peak Area (%)	Wavenumber (cm^{-1})	Peak Area (%)
β turns	1707.09±0.45	0.41±0.009	1706.57±1.29	0.74±0.012*↑
Anti-parallel β	1695.67±0.26	4.41±0.92	1692.45±1.13	11.00±1.69*↑
Parallel β	1678.09±1.83	11.65±2.06	1678.04±0.54	7.59±1.85*↓
α-helix	1659.09±1.16	57.35±2.48	1659.67±1.09	50.33±1.44*↓
β sheet	1633.34±1.51	23.49±0.45	1634.45±1.18	26.69±0.62*↑
Int. Agg. β	1615.04±0.77	2.69±0.83	1616.21±0.69	3.65±0.08*↑

Table 1 demonstrates the second derivative intensity values of each mode under Amide I mode of the groups. As illustrated in Figure 2A and Table 1, there some considerable differences between the control and the GTCS second derivative spectra. Indeed, there was a slight decrement in β turns (1710 cm^{-1}) and in α-helix (1655 cm^{-1}). A significant ($p \leq 0.05$*) increment in anti-parallel β (1695 cm^{-1}) and β sheet (1635 cm^{-1}) was obtained. More importantly, intensity values of β turn mode at around 1625 cm^{-1} were dramatically increased for the GTCS group. It has been shown for chronic pilocarpine evoked seizures (34) that the obvious appearance of a distinct mode between 1630–1625 cm^{-1} may be associated with protein aggregation. As being supportive of this, a pronounced change in GTCS spectrum was found for a band specific for intermolecular aggregated β structure (1615 cm^{-1}), which could not be observed in the control group.

To validate the results from the second-derivative analysis, curve fitting of the Amide I region (1720–1590 cm^{-1}) was also utilized. The fitted images of the samples illustrate the different components in the Amide I band (Figure 2B and 2C). In curve fitting analysis, seven different curves obtained from second derivative spectra were applied. But, six modes were fitted for both groups. As mentioned in the Material and Methods part, since the peak height was free, the best fit was obtained for six modes for the control (R^2 3.30-3.40x$10^{-7;}$ chi-square 100 %) and the GTCS (R^2 5.50-5.60x10^{-7}; chi-square 100 %). Each component to the Amide I band is indicated in Figure 2B for control and Figure 2C for the GTCS group.

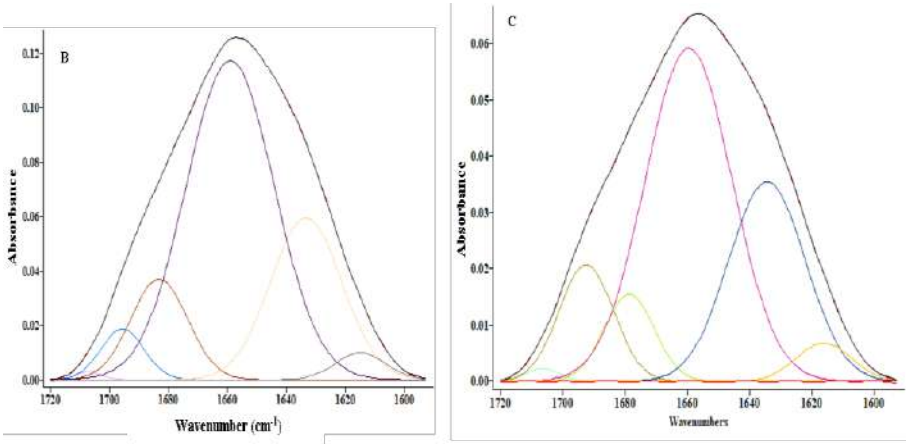

Figure 2. (B) Curve fitted Amide I mode for control. (C) Curve fitted Amide I mode for GTCS group.

As given in the table, the results of curve fitting revealed consistent results to the second derivative analysis. To the results, there was a significant ($p \leq 0.05$*) decrease in parallel β (11.65 to 7.59 %) (1675 cm^{-1}) and α-helix (57.35 to 50.33 %) (1655 cm^{-1}), but a remarkable ($p \leq 0.05$*) increment in β turns (0.41 to 0.74 %) (1710 cm^{-1}), anti-parallel β (4.41 to 11.00 %) (1695 cm^{-1}), β sheet (23.49 to 26.69 %) (1635 cm^{-1}) and intermolecular aggregated β (2.69 to 3.65 %) (1615 cm^{-1}) for GTCS group. As given in Table 1, curve fit analysis revealed mostly consistent results to the second derivative analysis. But, it should be mentioned that the only discrepancy in the results of both analyzes was observed in β turn mode at1710 cm^{-1}. While the intensity value of this band decreased in the second derivative spectra, it increased in the curve fit analysis. The reason for this may be that, as mentioned above, 7 bands defined in the second derivative

spectra were fit as 6 bands during the curve fit analysis, since the peak height was free.

Hence, all obtained data from second derivative analysis and curve fitting elicited that acute GTCS lead to structural changes in proteins of the hippocampus. This finding is that α-helix structure decreased, while β structures elevated. The reduction in α-helix might be come out from the increment in β structures, which was in consistent with β-sheet formation as suggested in the literature (35-36). This result is also supported by the studies on the hippocampus after chronic pilocarpine-induced seizures (34,37). The elevated level of β structures in the GTCS group may mean that an increment in the intermolecular hydrogen-bonding forms protein aggregation with high molecular weight, assigned to irreversible insoluble structures (36,38). This was also observed by an increase in the mode of intermolecular aggregated β structure (around 1615 cm^{-1}). In addition, such structural variations may be caused by disruptions of hydrogen or disulfide bonds. This break may cause a partial unfolding of the polypeptide chain. It lead to a disorganization of the internal structure of proteins (39).

The found in the present study acute GTCS-induced structural alterations might be resulted from the different phenomenon. One is the high level of free radical production during epileptic activities reported for the whole-brain (22,23) and hippocampus (40,41). As also mentioned, the attack of free radical action to proteins may exhibit secondary structural differentiation together with spontaneous fragmentations and proteolysis (42). Particularly, it has been reported that these species generated during epileptic activities can induce the formation of β sheet rich proteins (43). Other explanation might be the altered redox potential that can modify the structure of proteins (44). In addition, the dysfunction of some heat shock proteins might bring out misfolded proteins as reported for the epileptic hippocampus (45). Furthermore, as shown (45), epileptic seizures cause synaptic reorganization of hippocampal circuitry. Such alteration requires new protein synthesis, which may further contribute to the general protein profile of the hippocampus. Overall, structural variations in proteins of the hippocampus may be an indication of structural variations in already existed proteins and/or newly expressed protein types, as well.

It is also worth noting that our preparation contains all membrane compartments, these parameters may be also attributed to the differences in all membrane proteins in the hippocampus from control and GTCS groups from a general perspective. As an example, a decline in α-helix structure might be from variations in membrane lipids, which tightly interact with membrane proteins. It

has been reported that any conformational variation in membrane lipids due to peroxidation may directly trigger the structural arrangement of membrane proteins. This further means that membrane-embedded domains of such proteins are then conformationally changed to stabilize membrane curvature (23).

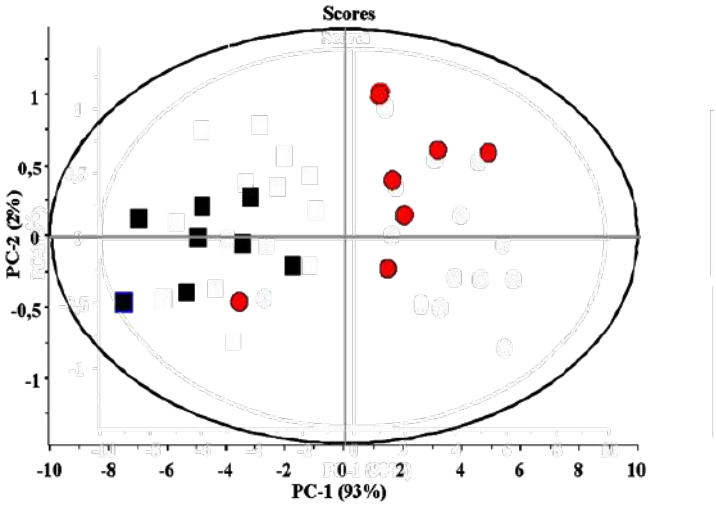

Figure 3. (A) Principal component analysis of hippocampus homogenates of control (black) and GTCS (red) in 1720-1590 cm^{-1} spectral range.

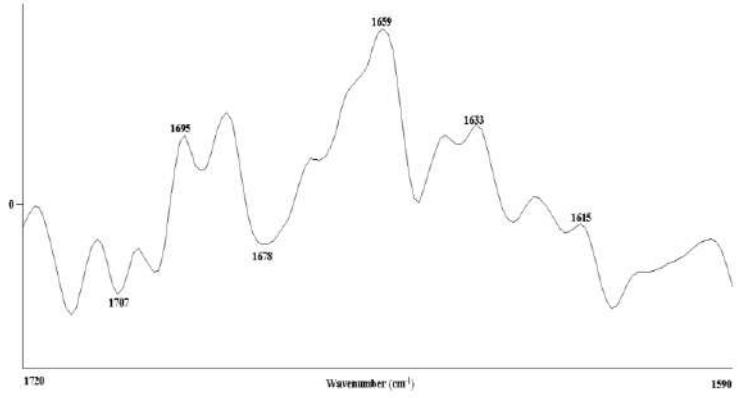

Figure 3. (B) PC-1 loading plot in the region of 1720-1590 cm^{-1}.

To further examine structural differences in proteins of the control and GTCS samples, PCA was utilized. Fig. 3A and Fig 3B demonstrates the score plot obtained along PC1 versus PC2, and loading plot, respectively. As illustrated in score plot, there is a relatively distinct distribution trend between the two sample groups along PC1, while PC1 (93%), and PC2 (2.0%) with 95% of the total variability. This shows that there are significant variations in secondary structure in proteins of the control and GTCS group, and PC1 is mainly responsible for this discrimination. Indeed, the loading plot PC1 reveals spectral characteristics that further play role in discrimination of hippocampus samples of GTCS group from control. PC1 explains 93 % of total variance. Along PC1, the discriminating is positively correlated loadings at 1695, 1655, and 1633 cm^{-1} (anti-parallel β, α-helix and β sheet, respectively), whereas negatively correlated loadings at 1707, 1678, and 1615 cm^{-1} (β turns, paralel β, and intermolecular aggregated β, respectively). All these results are in agreement in the second derivative and curve fit analysis.

Conclusion

Our result suggests that ATR-FTIR spectroscopy together with PCA analysis was successfully utilized to detect the effects of acute GTCS on the structure and amount of proteins in hippocampus brain region of Wistar rats. In particular, a decrease in protein content was observed. Additionally, an altered structural profile of proteins was predicted as an increase in total β structures whereas a decrease α-helix. These results indicate possible consequences of acute GTCS on hippocampus proteins, which may further cause to development of epileptogenesis as well as affect the proper function of the hippocampus such as memory and function. In sum, the current study can contribute to epilepsy research aimed at treatment strategies. To clarify the effects of acute GTCS on hippocampus proteins additional studies performing on different animal models should be done.

References

1. Lamberink, H., Motte, W., Blümcke, I., & Braun, K.P. (2020). Seizure outcome and use of antiepileptic drugs after epilepsy surgery according to histopathological diagnosis: a retrospective multicentre cohort study. Lancet Neurology, 19, 748-757.
2. Falco-Walter, J. J., Scheffer, I. E., & Fisher, R. S. (2018). The new definition and classification of seizures and epilepsy. Epilepsy Research, 139, 73–79.
3. Grigoletto, J., Oliveira, C. V. de, Grauncke, A. C. B., Souza, T. L. de, Souto, N. S., Freitas, M. L. de, … Oliveira, M. S. (2016). Rosmarinic acid is anticonvulsant against seizures induced by pentylenetetrazol and pilocarpine in mice. Epilepsy & Behavior, 62, 27–34.
4. Fan, D., Duan, L., Wang, Q., & Luan, G. (2017). Combined Effects of Feedforward Inhibition and Excitation in Thalamocortical Circuit on the Transitions of Epileptic Seizures. Frontiers in Computational Neuroscience, 11, 59-68.
5. Berg, A. T., Berkovic, S. F., Brodie, M. J., Buchhalter, J., Cross, J. H., van Emde Boas, W., Scheffer, I. E. (2010). Revised terminology and concepts for organization of seizures and epilepsies: Report of the ILAE Commission on Classification and Terminology, 2005-2009. Epilepsia, 51(4), 676–685.
6. Hammond N (2016): Tonic-clonic seizures, Reference Module in Biomedical Sciences.
7. Duncan, S., & Brodie, M. J. (2011). Sudden unexpected death in epilepsy. Epilepsy & Behavior, 21(4), 344–351.
8. Wang, Z., Wang, X., Rong, R., Xu, Y., Zhang, B., & Wang, Z. (2019). Impaired hippocampal functional connectivity in patients with drug resistant, generalized tonic-clonic seizures. NeuroReport, 30(10), 700–706.
9. Temp, F. R., Marafiga, J. R., Milanesi, L. H., Duarte, T., Rambo, L. M., Pillat, M. M., & Mello, C. F. (2017). Cyclooxygenase-2 inhibitors differentially attenuate pentylenetetrazol-induced seizures and increase of pro- and anti-inflammatory cytokine levels in the cerebral cortex and hippocampus of mice. European Journal of Pharmacology, 810, 15–25.
10. Chen, K. D., Hall, A. M., Garcia-Curran, M. M., Sanchez, G. A., Daglian, J., Luo, R., & Baram, T. Z. (2021). Augmented seizure susceptibility and hippocampal epileptogenesis in a translational mouse model of febrile status epilepticus. Epilepsia, 62(3), 647–658.

11. Chwiej, J., Skoczen, A., Janeczko, K., Kutorasinska, J., Matusiak, K., Figiel, H., Setkowicz, Z. (2015). The biochemical changes in hippocampal formation occurring in normal and seizure experiencing rats as a result of a ketogenic diet. The Analyst, 140(7), 2190–2204.
12. Tiernan, H., Byrne, B., & Kazarian, S. G. (2020). Insight into Heterogeneous Distribution of Protein Aggregates at the Surface Layer Using Attenuated Total Reflection-Fourier Transform Infrared Spectroscopic Imaging. Analytical Chemistry, 92(7), 4760–4764.
13. Lilo, T., Morais, C. L. M., Ashton, K. M., Pardilho, A., Davis, C., Dawson, T. P., … Martin, F. L. (2019). Spectrochemical differentiation of meningioma tumours based on attenuated total reflection Fourier-transform infrared (ATR-FTIR) spectroscopy. Analytical and Bioanalytical Chemistry, 412(5), 1077–1086.
14. Gurbanov, R., Bilgin, M., & Severcan, F. (2016). Restoring effect of selenium on the molecular content, structure and fluidity of diabetic rat kidney brush border cell membrane. Biochimica et Biophysica Acta (BBA) - Biomembranes, 1858(4), 845–854.
15. Sadat, A., & Joye, I. J. (2020). Peak Fitting Applied to Fourier Transform Infrared and Raman Spectroscopic Analysis of Proteins. Applied Sciences, 10(17), 5918.
16. Tidy, R. J., Lam, V., Fimognari, N., Mamo, J. C., & Hackett, M. J. (2017). FTIR studies of the similarities between pathology induced protein aggregation in vivo and chemically induced protein aggregation ex vivo. Vibrational Spectroscopy, 91, 68–76.
17. Kong, J., & Yu, S. (2007). Fourier Transform Infrared Spectroscopic Analysis of Protein Secondary Structures. Acta Biochimica et Biophysica Sinica, 39(8), 549–559.
18. Schleich, T., Stevens, A., & Michael, D. P. (1992). FT-IR spectroscopic elucidation of lens crystallin protein secondary structure in solution. Experimental Eye Research, 55, 195.
19. Elsohaby, I., McClure, J. T., Riley, C. B., Shaw, R. A., & Keefe, G. P. (2015). Quantification of bovine immunoglobulin G using transmission and attenuated total reflectance infrared spectroscopy. Journal of Veterinary Diagnostic Investigation, 28(1), 30–37.
20. Balázs, B., Farkas, G., Berkesi, O., Gyulai, R., Berkó, S., Budai-Szűcs, M., Csányi, E. (2014). Protein structure is changed in psoriatic skin on the unaffected region — Imaging possibility with ATR-FTIR spectroscopy. Microchemical Journal, 117, 183–186.

21. Racine, R. J. (1972). Modification of seizure activity by electrical stimulation: II. Motor seizure. Electroencephalography and Clinical Neurophysiology, 32(3), 281–294.
22. Turker, S., Ilbay, G., Severcan, M., & Severcan, F. (2014). Investigation of compositional, structural, and dynamical changes of pentylenetetrazol-induced seizures on a rat brain by ft-ir spectroscopy. Analytical Chemistry, 86(3), 1395–1403.
23. Turker, S., Severcan, M., Ilbay, G., & Severcan, F. (2014). Epileptic seizures induce structural and functional alterations on brain tissue membranes. Biochimica et Biophysica Acta (BBA) - Biomembranes, 1838(12), 3088–3096.
24. Elibol-Can, B., Jakubowska-Dogru, E., Severcan, M., & Severcan, F. (2011). The effects of short-term chronic ethanol intoxication and ethanol withdrawal on the molecular composition of the rat hippocampus by ft-ir spectroscopy. Alcoholism: Clinical and Experimental Research, 35(11), 2050–2062.
25. Bozkurt, O., Haman Bayari, S., Severcan, M., Krafft, C., Popp, J., & Severcan, F. (2012). Structural alterations in rat liver proteins due to streptozotocin-induced diabetes and the recovery effect of selenium: Fourier transform infrared microspectroscopy and neural network study. Journal of Biomedical Optics, 17(7), 0760231.
26. Wu, C.-F., Chen, Y.-L., Chen, C.-C., Yang, T.-T., & Chang, P.-E. (2007). Applying open-path Fourier transform infrared spectroscopy for measuring aerosols. Journal of Environmental Science and Health, Part A, 42(8), 1131–1140.
27. High-resolution diffusion tensor imaging in the substantia nigra of de novo Parkinson disease. (2009). Neurology, 72(23), 2059–2059.
28. Wu, L., Peng, J., Wei, C., Liu, G., Wang, G., Li, K., & Yin, F. (2011). Characterization, using comparative proteomics, of differentially expressed proteins in the hippocampus of the mesial temporal lobe of epileptic rats following treatment with valproate. Amino Acids, 40(1), 221–238.
29. Ben-Ari, Y. (2001). Cell Death and Synaptic Reorganizations Produced by Seizures. Epilepsia, 42, 5–7.
30. Funke, M. G., Amado, D., Cavalheiro, E. A., & Naffah-Mazzacoratti, M. G. (1998). Tyrosine phosphorylation is increased in the rat hippocampus during the status epilepticus induced by pilocarpine. Brain Research Bulletin, 47(1), 87–93.

31. Berdichevsky, Y., Dzhala, V., Mail, M., & Staley, K. J. (2012). Interictal spikes, seizures and ictal cell death are not necessary for post-traumatic epileptogenesis in vitro. Neurobiology of Disease, 45(2), 774–785.
32. Türker-Kaya, S., Mutlu, O., Çelikyurt, İ. K., Akar, F., & Ulak, G. (2016). Tianeptine, olanzapine and fluoxetine show similar restoring effects on stress induced molecular changes in mice brain: An FT-IR study. Spectrochimica Acta Part A: Molecular and Biomolecular Spectroscopy, 161, 178–185.
33. Raouf, G., Qusti, S., Ali, A.M., & Dakhakhni, T.H. (2012). The Mechanism of 2,4-dichlorophenoxyacetic acid neurotoxicity on rat brain tissue by using FTIR spectroscopy. Life Science Journal, 9, 4-11.
34. Chwiej, J., Dulinska, J., Janeczko, K., Dumas, P., Eichert, D., Dudala, J., & Setkowicz, Z. (2010). Synchrotron FTIR micro-spectroscopy study of the rat hippocampal formation after pilocarpine-evoked seizures. Journal of Chemical Neuroanatomy, 40(2), 140–147.
35. Palaniappan, PL. RM., & Vijayasundaram, V. (2009). The FT-IR study of the brain tissue of Labeo rohita due to arsenic intoxication. Microchemical Journal, 91(1), 118–124.
36. Creighton, T., (1984). Pathways and mechanisms of protein folding. Advances in Biophysics, 18, 191.
37. Dong, A., Malecki, J. M., Lee, L., Carpenter, J. F., & Lee, J. C. (2002). Ligand-Induced Conformational and Structural Dynamics Changes inEscherichia coliCyclic AMP Receptor Protein. Biochemistry, 41(21), 6660–6667.
38. Ami, D., Natalello, A., Taylor, G., Tonon, G., & Maria Doglia, S. (2006). Structural analysis of protein inclusion bodies by Fourier transform infrared microspectroscopy. Biochimica et Biophysica Acta (BBA) - Proteins and Proteomics, 1764(4), 793–799.
39. Toyran, N., Zorlu, F., & Severcan, F. (2005). Effect of stereotactic radio surgery on lipids and proteins of normal and hypo fused rat brain homogenates: A Fourier transform infrared spectroscopy study. International Radiation Journal, 81, 911–918.
40. Furukawa, A., Kawamoto, Y., Chiba, Y., Takei, S., Hasegawa-Ishii, S., Kawamura, N., Shimada, A. (2011). Proteomic identification of hippocampal proteins vulnerable to oxidative stress in excitotoxin-induced acute neuronal injury. Neurobiology of Disease, 43(3), 706–714.

41. Liu, J., Wang, A., Li, L., Huang, Y., Xue, P., & Hao, A. (2010). Oxidative stress mediates hippocampal neuron death in rats after lithium–pilocarpine-induced status epilepticus. Seizure, 19(3), 165–172.
42. Waldbaum, S., & Patel, M. (2010). Mitochondria, oxidative stress, and temporal lobe epilepsy. Epilepsy Research, 88(1), 23–45.
43. Wang, L., Li, B., & Tian, L. F. (2013). A novel multi-modal medical image fusion method based on shift-invariant shearlet transform. The Imaging Science Journal, 61(7), 529–540.
44. Siesjö, B. K. (1988). Acidosis and ischemic brain damage. Neurochemical Pathology, 9(1-3), 31–88.
45. Bausch, S. B., & McNamara, J. O. (1999). Experimental partial epileptogenesis. Current Opinion in Neurology, 12(2), 203–209.

An Antioxidant: Selenium

Dr. Öğr. Üyesi SUZAN ONUR

Karabuk University
Faculty Of Health Sciences
Physiotherapy And Rehabilitation Department
Orcid: 0000-0001-8145-609

INTRODUCTION

As an essential mineral, selenium (Se) has an important role in the homeostasis of the human body and especially for the regular functioning of the immune system (Tajaddini et.al., 2015; Hoffmann and Berry, 2008; Rayman, 2000).

In addition to being involved in the structure of many enzymes, selenium plays a role in many events such as thyroid hormone mechanism, antioxidant enzyme defense, and regulation of the immune system (Iglesias et.al., 2013). Recent studies have shown that selenium deficiency may be associated with aging, cancer, insulin resistance, diabetes, cardiovascular and neurodegenerative diseases, increased mortality risk, immune system diseases (Roman et.al., 2014; Rayman, 2012).

Formerly known only for its high toxicity, especially as a carcinogenic compound, Se has been used in many researches as an essential trace element, an anticarcinogenic nutrient and a chemopreventive agent.

History and General Properties

Selenyum is named after the ancient Greek goddess of the moon, 'Selene' (Köhrle, 1999). Se, which Schwartz and Foltz proposed to be essential for mammals in 1957 (Schwartz and Foltz, 1957), was first discovered by Brezilius and Gahn in 1817 and described as an essential trace element commonly found in nature (Wilber, 1980; Köhrle, 1999).

Selenium, which is found in biological systems, is an element of amino acids that participate in the protein structure and is a nonmetal found in many oxidation states in oxygen series. For the first time in the 1930s, cows were tried to get alkaline disease by eating plants grown in Se rich soils. Studies of Se's nutritional deficiency in sheep, pigs, and cattle continued until 1973, when the biochemical function of the element was found. Researchers have discovered that Se is an essential part of the glutathione peroxidase (GSH-Px) enzyme system (Burk and Levender, 1999). Glutathione is a methionine derivative that combines with Se to form GSH-Px. In addition to its role in protecting the cell membrane by inhibiting lipid peroxidation, it has been shown to have a synergistic effect with chemoteuriapine agents thanks to its interaction with antioxidants (Dai et.al., 1999) and to increase the therapeutic effect, reducing the toxic side effects of cisplatin (Yang et.al., 2000).

Its importance in the human diet was discovered in 1979. Scientists in China have observed that children growing up in Se poor soils suffer from a disease of cardiomyopathy known as Keshan disease, and when Se is added to the diet, the symptoms of the disease regress. These discoveries have led to extensive work

to discover Se's unknown role in the human body. All these studies have also prompted the World Health Organization (WHO) to conduct research on the dietary intake of Se. The daily dietary intake of the element (RDA: Recommemded Daily Allowance) was determined in 1989 (Burk and Levender, 1999; Groff et.al., 1995).

In group VI A of the periodic table (Hall, 2007), there are 6 naturally occurring isotopes and are among the rarest trace elements (Neve et al., 1985; Foster and Surnar, 1997). Se is an essential element for almost all animals (Kumpulainen, 1989). Se, which appears as an intermediate product during the purification of metal ores, especially copper, is similar to sulfur, which is in the same group in terms of its physical and chemical properties (Wilber, 1980). The inorganic shapes of Se are H_2Se, H_2SeO_3 and H_2SeO_4; hydrogen sulfide is analogous with sulfides and sulfates and is present in nature in the form of compounds with a valence of -2, 0, +4 and +6. But selenoamino acids such as Se-methionin, Se-cystine, Se-cysteine, and other organic Se compounds such as selenoglutation, dimethylcelide, trimethylselenium are generally more reactive than their sulfurous counterparts (Stadtman, 1980).

1A																	8A
H	2A											3A	4A	5A	6A	7A	He
Li	Be											B	C	N	O	F	Ne
Na	Mg	3B	4B	5B	6B	7B	8	8B 9	10	1B	2B	Al	Si	P	S	Cl	Ar
K	Ca	Sc	Ti	V	Cr	Mn	Fe	Co	Ni	Cu	Zn	Ga	Ge	As	Se	Br	Kr
Rb	Sr	Y	Zr	Nb	Mo	Tc	Ru	Rh	Pd	Ag	Cd	In	Sn	Sb	Te	I	Xe
Cs	Ba	La	Hf	Ta	W	Re	Os	Ir	Pt	Au	Hg	Tl	Pb	Bi	Po	At	Rn

Figure 1. Periodic Table

Se, which is an indispensable component of the important metabolic pathways of the human body shows its biological effects through selenoproteins, which have the amino acid selenocysteine in their structure (Rayman, 2000; Asayan and Baylan, 2011). Proteins that have been added to the region in the form of selenocysteine are defined as selenoproteins and these proteins require Se to perform their functions. Although it is estimated that there are around 100 selenoproteins in the human body, only 30 have been identified (Bal et.al., 2015; Iglesias et.al., 2013).

The most important of these are;

- glutathione peroxidase,
- thioredoxine reductase and

- iodothyronine is a family of deiodinase enzymes (Beckett and Arthur, 2005).

Selenoproteins, cancer and many chemical toxicities are also the most necessary antioxidant enzymes; thyroid and thyroid regulate hormone functions, are structural proteins in sperm for reproductive function, and perform many vital functions in the human body, such as being able to reduce virulence in many viral infections, including HIV-1 (Weeks et. al., 2012).

The effects and properties of selenium can be classified as follows:

1.Structural Properties: Selenoproteins

- Selenoprotein P (SePP)
- Glutathione peroxidase (GSH-Px)
- Ioidine deodinase (ID)
-Thioredoxin reductase (TrxR)
- Other selenoproteins

2. Thyroid hormone synthesis and metabolism

3. Antioxidant defense and immune effects

- Protect endotelial cells from peroxnitrite damage.
- Reduces the effect of reactive oxygen species such as hydrogen peroxide and lipid hydroperoxide.
- It is responsible for regulating many antioxidants.
- Reduces cytokine release.
- Protects immune cells from oxidative stress.

Selenoprotein P (SePP)

Selenium is known to exhibit many of its biological functions through SePPs (Rayman, 2000). SePP which produces about 60% of the Se in the plasma, is the main carrier protein of Se (Brown and Arthur, 2001; Pappa et al., 2006; Rayman, 2012), as well as vascular endothelial cells (Brown and Arthur, 2001). Since they have Se storage sites, they are also the body's Se storage protein. For this reason, it is one of the main indicators of the body's Se level (Pappa et al., 2006; Rayman, 2012). Due to all these properties, the effects of Se on human health can be easily explained by knowing the function of selenoproteins in metabolism (Rayman, 2000). In addition to these duties, SePP also acts as a chelator of some heavy metals (Pappa et al., 2006; Rayman, 2012).

Although the function of SePP is not fully known, it is stated that it is an antioxidant of endothelial cells damaged by free radicals defined as peroxynitrate (Brown and Arthur, 2001). Se levels and activities of Se carrier proteins such as SePP and Se-containing enzymes such as GSH-Px in the body

can be measured to obtain information about Se levels in the body. It is recommended that the amount of SePPs, which have an important role in providing systemic homeostasis, should be as high as possible. Studies on this subject show that; when 125µg Se is taken daily, the GSH-Px-3 concentration is 125µU/L and the Se concentration in serum is 79µg/L. (Burk et.al., 2006; Hollenbach et.al., 2008; Hoeflich et.al., 2010; Combs et.al., 2011).

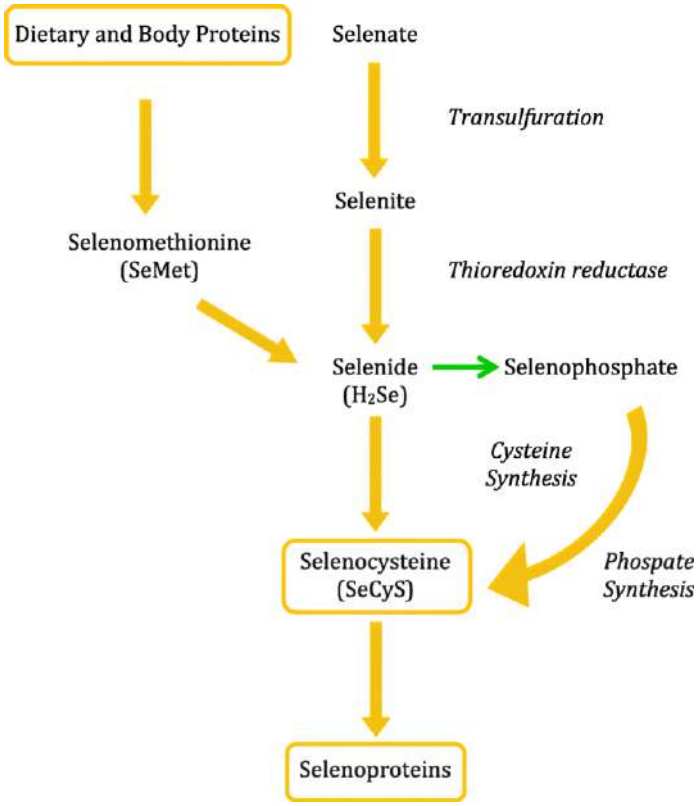

Figure 2. The main metabolic steps of metabolism of inorganic and organic Se. Both inorganic (selenite) and organic (selenomethionine, SeMet) are converted to selenide (H_2Se) before the formation of selenocysteine (SeCys) and its insertion in bioactive selenoproteins (Duntas, 2020).

Glutathione Peroxidase (GSH-Px)

Glutathione peroxidase, is also present in sitozole and is involved in the glutathione-dependent detoxification of hydrogen peroxide (H_2O_2) (Brigelius-Flohe, 2006; Conrad et al., 2007; Brigelius-Flohe and Kipp, 2009; Bouayed and Bohn, 2010; Lubos et al., 2011).

Eight isoforms of GSH-Px, one of the first selenoproteins identified as Se in

its structure, classified according to their structure and localization, have been identified (Muller et al., 2007). Se is needed for GSH-Px to exert its effect better (Akyıldız et al., 2014). The basic selenoprotein found in most tissues in animals (Sonet et.al., 2018) and a Se-dependent antioxidant enzyme capable of protecting mammalian cells against oxidative stress (Sunde et al., 2018). Because it is one of the selenoproteins most sensitive to variation of Se concentration, it is often used to assess Se state at the cellular or organism level (Sonet et al., 2018).

GSH-Px, which is part of a multicomponent antioxidant-protective system in the cell (Combs, 1984; Robinson and Thomson 1983), whose main function is to protect the cell and lipid membranes from oxidative stress (Ruseva et al., 2013). The system also contains other cellular preservatives such as calatalase, superoxide dismutase and vitamin E. In this way, it protects phospholipids and critical proteins containing unsaturated fatty acids in the cell from the harmful effects of reactive oxygen compounds and free radicals. The hydroxyl radical ($OH^{\cdot}$) is the task of GSH-Px to prevent the formation of reactive oxygen compounds and H_2O_2 concentrations by decreasing it. (Combs, 1984; Robinson and Thomson 1983). They also catalyze the reaction that leads to the reduction of H_2O_2 and organic peroxides (ROOH) by forming elenous acid or alcohols as intermediates (Ruseva et.al., 2013). GSH-Px, which catalyzes the conversion of P-eroxides to alcohols, causes membrane lipids, erythrocytes, cell membrane, cellular and subcellular membranes to be protected from oxidative effects (Oldfield, 1987).

Thioredoxin Reductase (TrxR)

Thioredoxin reductase is found in cytosol and mitochondria. In addition to reducing the oxidized form of cytosolic TR, it catalyzes all reactions of tioredoxin and glutaredoxin (Su et al., 2005; Turanov et al., 2006; Holmgren and Lu, 2010; Turanov et al., 2010).

Thioredoxin reductase is an enzyme containing selenocysteine (Brown and Arthur, 2001; Hashemy, 2006). TrxR is responsible for the reduction of oxidized thioredoxin (Tamura and Stadtman, 1996). Catalyzes the NADPH-dependent reduction of thioredoxin (Brown and Arthur, 2001; Hashemy, 2006). TrxR enzymes detoxify peroxides as well as maintain the reduction status of transcription factors. Thanks to these effects, it regulates cell growth and aging. TrxR is present in many antioxidant systems containing vitamin C along with thioredoxin, which has led to its effects being analyzed as a target agent in antitumor therapy (Brown and Arthur, 2001; Hashemy, 2006). Furthermore, the

tasks of TrxRs include oxidized glutathione, dihydroascorbic acid, lipid peroxidases, vitamin K, and the reduction of H_2O_2 (Tamura and Stadtman, 1996).

Iodothyronine Deiodinase (ID)

Selenocysteine is a family of enzymes containing and is responsible for catalyzing thyroid hormone activation (Kohrle et.al., 2005). The DIO family, which catalyzes the conversion of thyroxine to the biologically active hormone T3, has 3 different isoforms. These are DIO1, DIO2 and DIO3; they are all membrane-bound enzymes, with identical sequence homology and catalytic properties (Lu and Holmgren, 2009). DIO1, DIO2, DIO3; while located in the plasma membrane, it causes plasma T3 production by separating iodine from T4. It also provides T3 deiodination and inactivation (Schomburg and Köhrle, 2008; Maia et al., 2011; Dentice and Salvatore, 2011; Williams and Duncan Bassett, 2011).

Other Selenoproteins

15 kDa selenoprotein (Sep15) from the selenoproteins found in the endoplasmic reticulum (ER); regulated by ER stress, UDP-glucose: while glucoprotein interacts with glucosyltransferase and is involved in glucoprotein folding (Labunskyy et.al., 2005; Ferguson et.al., 2006; Labunskyy et.al., 2007; Labunskyy et al., 2009), Selenoprotein M (SelM); responsible for protecting neurons from oxidative stress (Reeves et al., 2010). Selenoprotein H (SelH); is located in the nucleus and protects the cells from H_2O_2. Mitochondrial biogens and increases CytC production (Dtwoet et.al., 2007; Panee et.al., 2007; Mendelev et.al., 2011). Selenoprotein K (SelK) from selenoproteins located in the membrane of the endoplasmic reticulum; while Ca^{+2} affects cell functions by taking part in the release of Ca^{+2} (Verma et.al., 2011), Selenoprotein N (SEPN1) controls the redox balance in the release of inthalelilar calcium from the channels (Jurynec et al., 2008; Shchedrina et al., 2010). Selenoprotein S (SelS); is upregulated in glucose deficiency and increase in proinflammatory cytokines (Shchedrina et.al., 2010; Ye et.al., 2004). Selenoprotein P (SePP) is found in plazma and is responsible for transporting Se to peripheral tissues, so its antioxidant efficacy has been mentioned (Burk and Hill, 2009; Richardson, 2005; Schweizer et.al., 2004). Selenoprotein R (SelR) in cytosol, it is used to convert methionine-R-sulfoxide groups in proteins to methionine (Lee et.al., 2009). Selenoprotein T (SelT) while located in the endoplasmic reticulum and golgi apparatus, its functions include redox regulation and cell adhesion (Sengupta et.al., 2009). Selenoprotein I (SelI) is in the membrane (Kryukov and Gladyshev, 2002), Selenoprotein V (SelV) is included in cytosol (Dikiy et al., 2007),

Selenoprotein O (SelO) in mitochondria (Kryukov et al., 2003) and Selenoprotein W (SelW) are included in cytosol (Noh et.al., 2010).

Distribution on Earth

The main source of the element Se is reported as the molten volcanic rocky masses covering the earth's core (Neve et.al., 1985). In addition to being found all over the world, there are great differences in its distribution between regions (Neve et.al., 1985; Akkus et.al., 1995; Yaylalı and Sözer, 1995). As a result of measurements made in different regions of the world, serum Se concentration has been found to vary according to country, geographical region, ethnicity and other habits (Stuss et.al., 2017). Se is an element of great metabolic importance, and since it passes from the soil to plants in the food chain, its intake varies by geographical region. (Brown and Arthur, 2001).

Selenium Sources

The most important source for human beings is plant and animal foods (Yaylalı and Sözer, 1995). Plants take Se from the soil in which they are grown (Groff et.al., 1995) and store it according to its concentration in the soil, even if they do not need it. The Se content of plants varies according to the type of plant and the Se content of the soil, so that plants growing in Se rich soils absorb and accumulate high amounts of Se (Yaylalı and Sözer, 1995). It is known that some foods contain high levels of Se, usually more Se than foods of animal origin, especially meat, than in plants (Burk et.al., 1999; Groff et.al., 1995). It is also believed that seafood is the best source of Se, with the exception of some fish (Groff et.al., 1995). Fruits and vegetables (except mushrooms and garlic), milk and dairy products (except eggs, some cheeses and butter), fats, beverages and many baby foods are very poor foods in terms of Se. It is also reported that there is a small amount of Se in drinking water (Neve et.al., 1985; Akkus et.al., 1991; Yanardag and Sickle, 1999).

Daily Intake Levels

The main source of selenium is dietary nutrients, which are found in insignificant amounts in water and air (Roman et.al., 2014). Se is found as selenochisteine in foods of animal origin and selenomethionine in plant-based foods. Thought to account for at least 50% of the amount of Se in the diet, it is mainly selenomethionine, which is found mainly in the diet (Mueller et.al., 2009).

The amount of Se that should be taken in the diet is calculated based on the maximum plasma GSH-Px activity (Hurst et.al., 2010). The minimum amount of Se that should be taken in humans is 10µg/day; maximum 400µg/day (Mueller

et.al., 2009). The mean plasma Se level should be 125ng/mL (Rocourt and Cheng, 2013). Epidemiological studies have revealed that Se deficiency can cause significant health problems in many countries of the world (Holben and Smith, 1999). An Se, which is vital for humans, is an element that can be toxic depending on the dose and specification (Solovyev et.al., 2018). According to the World Health Organization, taking Se at 400–700µg may cause toxic effects (Kieliszek and Błażejak, 2013). For this reason, it is recommended that the daily intake of Se should not exceed 70µg/day (Kieliszek and Błażejak, 2013).

According to the data of the Food and Nutrition Board of the National Academy of Science; 40-70µg in men and 45–55µg in women 60–70µg during pregnancy and lactation is recommended daily Se intake (Slencu et.al., 2014).

Societies' eating habits and life styles can cause significant changes in the daily intake and amount of Se in the body. Inspired by the studies carried out, the term "Reference Selenium Dose (RSD)" has been used. Patterson and Levander (1997) set the average RSD value of 350µg/day for a 70kg person (Patterson and Levander, 1997). According to these researchers, the amount of Se that should be taken daily with food is 150µg, while the amount that should be taken with supplements is 200µg. Due to the limited therapeutic index of Se, overdose can be observed as a result of consuming high amounts of Se-rich foods as well as using them as supplements (Fordyce, 2007).

The recommended daily intake levels for Se are shown in Table 1.

Table 1: Recommended daily intake levels for selenium
(Institute of Medicine US Panel on Dietary Antioxidants and Related Compounds, 2000)

Age	Woman	Male	Gestation period	Breastfeeding period
1–3	20 µg/day Se	20 µg/day Se	-------	--------
4–8	30 µg/day Se	30 µg/day Se	--------	--------
9–13	40 µg/day Se	40 µg/day Se	--------	--------
14–18	55 µg/day Se	55 µg/day Se	60 µg/day Se	70 µg/day Se
19–30	55 µg/day Se	55 µg/day Se	60 µg/day Se	70 µg/day Se
31–50	55 µg/day Se	55 µg/day Se	60 µg/day Se	70 µg/day Se
51–70	55 µg/day Se	55 µg/day Se	--------	--------
>70	55 µg/day Se	55 µg/day Se	--------	--------

Absorption of Selenium in the Body

Selenium, which is usually found in organic form, is taken from natural sources (Davis et al., 2017). Many forms of Se enter the body as part of the amino acids in proteins. The first significant form of Se to enter the body is

selenomethionine and selenosistein, which are found in animals and plants (Burk et.al., 1999).

Organic Se is noted to be higher in terms of bioavailability (Pérez-Corona et al., 2011). It is reported that absorption first occurs around the small intestine and is almost never in the stomach. In contrast, selenomethionine has been shown to absorb close to 100% of the small intestine (Groff et. al., 1995). In a study conducted by Pérez-Corona et al., it was found that 85-95% of organic Se and 10% of inorganic Se were absorbed from the intestine (Pérez-Corona et.al., 2011). The absorption of Se in the form of selenomethionine is quite high as it is by active transport (Stadtman, 1980; Robinson and Thomson, 1983). Selenomethionine has been shown to be absorbed close to 100% in the small intestine. The absorption of inorganic forms of Se varies depending on luminal factors, which can reach up to 50% to 100%. Also the level of Se in the body does not interfere with this absorption (Groff et. al., 1995). Se, which is absorbed in the body, is first transported by binding to plasma proteins. For binding, it must initially be retained by erythrocytes and metabolized by reduced glutathione (GSH) and reduced to H_2Se. (Stadtman, 1980). After absorption, erythrocytes, globulin and albumin bind and circulated and distributed to various organs and tissues (Combs et al., 2011).

Inhibition or encouragement of Se absorption is also closely related to many nutritional factors (Groff et.al., 1995). The content of vitamins A, E, C and protein in the diet is also noted to increase Se absorption (Stadtman, 1980; Robinson and Thomson, 1983). In contrast, heavy metals (such as mercury) reduce the absorbent of the element through precipitation (Groff et. al., 1995).

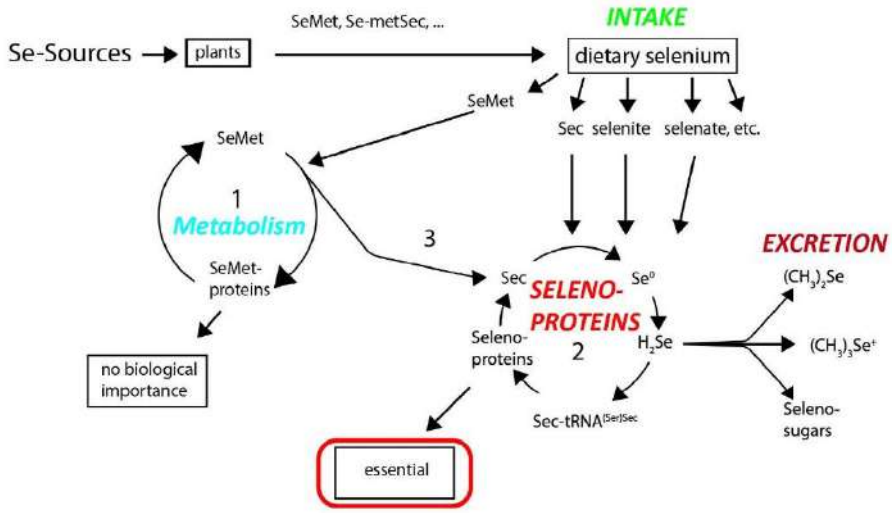

Figure 2. Metabolism of Se-containing compounds in human body. SeMet derived from plants is directly used for protein synthesis (1, SeMet cycle). Se released from SeMet and other compounds takes part in the Sec synthesis followed by the production of Sec-containing selenoproteins (2, selenoprotein cycle). H_2Se is one of the intermediates in the generation of Sec-tRNA(Ser)Sec. Excessive Se is excreted from the body in the urine as trimethylselenonium ion and via respiratory tract in a form of dimethyl selenide. Se is also found in the urine in the content of selenosugars. Whether selenosugars take part in Se recirculation from the primary urine remains unknown (Waldemar, 2022).

Transport of Selenium in the Body

According to a hypothesis, the mechanism of transport of selenium is that it enters red blood cells through diffusion and is transported in the body in this way. Free Se binds to lipoproteins such as VLDL (Very Low Density Lipoproteins) and LDL (Low Density Lipoproteins) in the body. A plasma protein called selenoprotein P is considered as a second transporter (Groff et.al., 1995). According to another view, the presence of selenocystein inhibits the protein's transport ability (Burk and Levender, 1999).

Once Se taken through diet is absorbed by the digestive system, it is mostly carried to the liver, where it is metabolized, used for the production of selenoprotein, and redistributed to other tissues through the blood. For this reason, the liver is a central organ in Se metabolism. Se is used to synthesize the amino acid selenocystein (Sec), which is found in the active site of selenoenzymes (Seale et.al., 2018). Approximately 80% of the initial absorption of Se is regulated by the presence or absence of protein and other trace elements

(Ardüser et.al., 1986). Transport of Se in the body; it is realized by binding to proteins in the blood (serum albumin, SEPP1, Glutathione peroxidase-3) (Fairweather-Tait et.al., 2011). The bioavailability was found to be approximately 14% of the original Se content in the food ingested. It has been reported that approximately 2-20mg of Se is present in an adult human body and can be detected through many tissues, urine, nails and hair (Ashton et.al., 2009).

Storage of Selenium in the Body

The heart, liver, kidney, lungs, pancreas, and muscles contain high levels of Se as part of glutathione. It is stated that it is most commonly found in the liver (Burk and Levender, 1999, Groff et.al., 1995). It has been reported that it is noteworthy that red blood cells contain 4 times more glutathione than plasma (Powers and Ji, 1999).

Removal of Selenium from the Body

Selenate, selenomethionine, or Se, which is taken organically by natural means in different ways, after absorption, turns into selenite as a result of catabolism. While the metabolisation of Se occurs by reduction, GSH is needed and stimulated in anaerobic conditions in the presence of NADPH. In this way H_2Se-shaped Se, which is formed as a result of GSH-dependent metabolism in the erythrocyte and released into the plasma, either binds to proteins or undergoes methylation. As a result of methylation, $(CH_3)_2Se$ and $(CH_3)_3Se^+$ are formed as the main products. Since H_2Se has high toxicity, the most important detoxifycation mechanism is noted as the methylation pathway (Ganther, 1966).

Selenium is removed from the body in two basic ways: urinary (50-60%) and fecal (40-50%) system (Groff et.al., 1995). Physiologically, the homeostasis of Se in the body is regulated by urine under reception conditions. 20-50% of the Se excreted in the urine is in the form of $(CH_3)_3$ Se because it has a high solubility. High dose Se intake leads to the removal of the element by ventilation with the lungs in the form of $(CH_3)_2Se$ (Combs and Combs, 1984; Burk and Levender, 1999; Groff meat. al., 1995). Loss through the lungs is characterized by the smell of garlic caused by volatile Se compounds. Fecal excretion is not very common, but instead urinary excretion is the main pathway followed in the normal physiological process (Burk and Levender, 1999; Groff et al., 1995).

Physiological Role of Selenium

It has been reported that many of the 11 Se-containing proteins (selenoproteins) in animals are characterized by their enzymatic functions, whereas their biochemical functions have only recently been determined.

According to some hypotheses, cytochrome P450 has functions in the maintenance of the system, DNA repair, enzyme activation and the functioning of the immune system. A well-known function of Se is its role in the GSH-Px enzyme system. Untill today, 4 different GSH-Px have been defined. The total GSH-Px in the cell is distributed in a 2:1 ratio between cytosol and mitochondrial matrix. These enzymes have been determined to be the main antioxidant defense systems in the body. Reduced glutathione is the first line of defense in the body against free radicals. The glutathione enzyme system plays a key role in the coordination of water and fat-soluble antioxidant defense systems (Balakrishnan and Anuradha, 1998). Peroxidases inhibit cell peroxidation by breaking down hydrogen peroxide and lipid peroxides using reduced GSH-Px (Burk and Levender, 1999; Groff et.al., 1995). Adequate levels of the substrate and reduced glutathione in the cell are needed in the form of GSH-Px to exhibit antioxidant properties (Ji, 1995). When reduced glutathione is used to remove hydrogen peroxide from the body, oxidized glutathione is formed. Glutathione oxidized by the glutathione reductase enzyme is converted into reduced glutathione to become an antioxidant again. More specifically, this enzyme also catalyzes the conversion of thyroxine (T4) to triiodothyronine (T3), and this phenomenon is observed to be Se-dependent (Del Maestro, 1991). Powers and Ji (1999) reported in a published summary that reduced glutathione has the ability to recharge antioxidants in the body. According to this publication; glutathione acts as an electron donor for vitamins C and E to regain their original electron configurations (Powers and Ji, 1999).

Selenium Excess

When selenium is taken in excess, it exhibits prooxidant properties and can induce free radical production, causing DNA damage. It can also bind to thiol groups of proteins whose function is to repair DNA damage, causing them to become inactive (Letavayová et.al., 2008).

An excess of Se in the body can best be determined by the loss of hair and nails. In addition, dental disorders, skin and nervous system lesions may alsobe observed. Although it can cause miscarriages, there is no evidence of teratogenic effect. The first symptoms of acute intoxication include nausea, vomiting and diarrhea; in the following few weeks, pathological changes in the nails and hair loss are noticeable. Other findings include temporary ECG change, liver dysfunction and garlic-scented breathing (Akkus et.al., 1991).

Selenium Toxicity

Selenium is known to be highly toxic in both animals and humans. Although the LD50 value is given as 0.4-6.4 mg/kg Se for different species, it has been reported that this varies according to the type of Se compound (Harr and Muth, 1972). Selenium toxicity (selenosis) has been reported to be acute or chronic, but it is rarely seen in humans. Among its symptoms are; nausea, vomiting, abdominal pain, diarrhea, hair loss, fracture of nails, and peripheral neuropathy (Duntas and Benvenga, 2015).

Selenium, when consumed in high quantities over a long period of time, can ultimately increase blood Se levels by 100µg/dL (Koller et al., 1986). Some of the common symptoms identified for Se toxicity are gastrointestinal pain, hair loss, white patches, the smell of garlic in the breath, fatigue, irritability, and mild nerve damage (Spiller and Pfiefer, 2007).

Some plants that grow in alkaline soil cause chronic Se poisoning, which is called 'alkaline disease' or 'short tail' disease. Among the characteristic features of this disease are; mane, bristle and hair loss, nails, stoppage of development, stiffness in the joints, severe damage to the liver and heart, hepatic cirrhosis and anemia. In acute Se poisoning caused by taking a lethal amount of Se with plants that store Se or feeds containing high amounts of Se; deterioration in vision, staggering, respiratory distress appear. This condition, known as 'blind staggering', results in death within 24 hours (Wilber, 1980; Burk, 1978).

Selenium Deficiency

Selenium deficiency occurs when an imbalance occurs between the nutritional Se required by the organism and the bioavailable Se in the diet (Neve et.al., 1985; Akkuş et al., 1991).

Selenium deficiency leads to functional or picile disorders in many organs and systems in humans, resulting in certain diseases and causing a wide range of symptoms, some of which can be fatal. Two of these are dilated cardiomyopathy (Keshan disease) and endemic osteoarthropathy (Kashin-Beck disease). The first evidence for this was obtained in 1979 when scientists in China found Keshan and Kashin-Beck's disease, which is characterized by Se deficiency (Burk and Levender, 1999; Groff et.al., 1995). Keshan disease usually affects children and young women, while Kashin-Beck's disease has an impact in the pre-adolescent period. This disease results in various types of osteoarthritis (calcification) (Burk and Levender, 1999).

Selenium deficiency symptoms are weight loss, muscle aches, loss of pigment in the hair and skin, and whitening of the nail beds (Groff et.al., 1995). In addition, other diseases in which Se deficiency plays an important role have been

reported as sudden infant death syndrome, arrhythmia, infertility in men, stroke, prostate cancer, nephropathy, heart diseases, autoimmune-other immune diseases and thyroid diseases (Mistry et.al., 2012; Hendrickx et.al., 2013; Ruseva et.al., 2013; Roman et.al., 2014).

Selenium deficiency can also occur from interaction with other elements. When lead (Pb) interacts with Se, it provides a significant decrease in the tissue concentration of the element. Although the mechanism of this phenomenon is not fully explained, it is suggested that it is due to the fact that both elements bind to sulfidril groups. In addition, iron (Fe) and copper (Cu) also interact with Se, inhibiting the uptake of the element into tissue. When the level of methionine in the body decreases, it closes this gap by binding selenomethionine to body proteins, which reduces the level of freely Se accessible in the body (Burk and Levender, 1999).

Selenium and Oxidative Stress

In oxygenated breathing organisms, free oxygen radicals are inevitably formed. These active oxygen radicals, superoxide, hydrogen peroxide, free hydroxyl radical, and the resulting lipid peroxides and other similar derivatives, cause significant changes by affecting molecules such as proteins, carbohydrates, lipids and DNA in different parts of the cell. In particular, unsaturated fatty acids in cells are very good targets for these (Karataş et al., 2006).

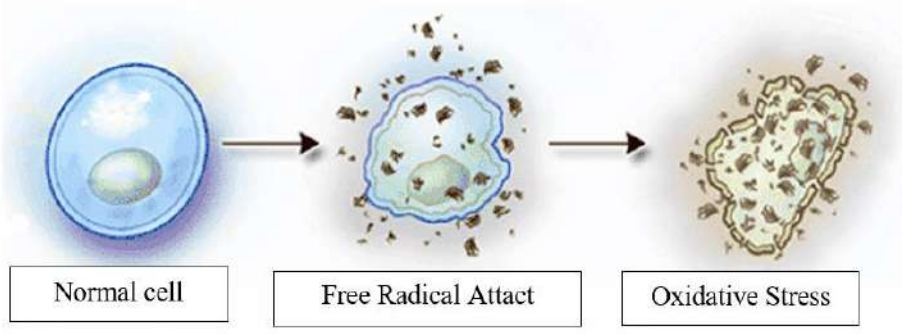

Free radicals; are reactive and short-lived molecules containing uncommon electrons. These molecules can be formed both as a by-product of normal metabolism and under the influence of drugs and other harmful chemicals. Many diseases are caused by tissue destruction, free radicals and lipid peroxidation. Free radical reactions in the organism are controlled by many antioxidant systems. Antioxidants function as structures that prevent or break chains of free radical formation. As long as the rate of formation of free radicals is in balance with the speed of defense systems consisting of some endogenous antioxidant enzymes, such as catalase (Cat), glutathione peroxidase (GSH-Px), and

superoxide dismutase (SOD), which neutralize or reduce them, the organism is not affected. However, if this balance is disturbed, free radicals begin to be harmful and show their effects in the form of oxidative stress (Kurt et.al., 2005).

Selenium, which is involved in the regulation of many functions, is an important trace element for metabolism found in the structure of enzymes. In particular, the presence of antioxidant enzymes such as GPx and TrxR in its structure suggests that there may be a relationship between Se levels and oxidative stress. Adequate levels of Se intake help these enzymes work optimally and prevent oxidative stress (Galan-Chilet et.al., 2014). Se has a direct role in antioxidant protection. This is because selenoproteins, which protect cells against oxidative damage by catalyzing the reduction of hydrogen peroxide by glutathione, are located in the active center of GSH-Px. Seleno-glutathione peroxidase provides an important line of defense against free radicals that are effective against hydrogen peroxide and lipid peroxidation (Rayman, 2000). There is a very important relationship between Se levels in the body and GSH-Px and TrxR activities. In order for these enzymes to reduce H_2O_2 levels, optimum concentrations of Se in biological fluids and intracellular are required to be achieved, which is shown to regulate inflammatory and immune responses (Beckett and Arthur, 2005; Duntas, 2006). Furthermore, when Se intake is at adequate levels, intracellular GSH-Px and TrxR enzymes are reported to protect the thyroid from oxidative stress (Sun et.al., 1999; Becker et.al., 2000). It is known that oxidative stress increases with age and aging is characterized by deficiency of Se due to inadequate nutrient intake, decreased physical function, or serious pathologies (Giovannini et.al., 2018).

RESULT

There is a direct relationship between serum selenium levels and dietary selenium. For this reason, it can be said that when the serum selenium level is at the desired level, health can be protected, many chronic diseases can be prevented and the aging process can be slowed down.

As a result, it turns out that meeting the Se needs of the organism at the optimum level is very important for human health.

REFERENCES

1. Akkuş İ, Şekeroğlu MR, Üner A, Aköz M, Kurt E: Selenyum: Dağılışı, Metabolizması ve Fizyopatolojisi. S.Ü. Tıp Fak Dergisi. 1991;4:547-51.
2. Ardüser F, Wolffram S, Scharrer E, Schneider B. Transport of selenate and selenite across the brush border membrane of rat and sheep small intestine. Biological Trace Element Research. 1986;9(4):281-290.
3. Ashton K, Hooper L, Harvey LJ, Hurst R, Casgrain A, Fairweather-Tait SJ. Methods of assessment of selenium status in humans: a systematic review. The American journal of clinical nutrition. 2009;89(6):2025-2039.
4. Aşayan T, Baylan M. Çiftlik Hayvanlarının Beslenmesinde Organik Selenyumun Önemi. Süleyman Demirel Üniversitesi Ziraat Fakültesi Dergisi. 2011;6(1):34-43.
5. Bal C, Büyükşekerci M, Ercan M, Hocaoğlu A, Çelik HT, Abuşoğlu S, et al. Farklı selenyum seviyelerinin tiroid hormon sentezi üzerine etkisi. Turk Hij Den Biyol Derg. 2015;72(4):311-6.
6. Balakrishnan SD, Anuradha CV. Exercise, Depletion of Antioxidants and Antioxidant Manipulation, Cell Biochem Funct. 1998;16:269-275.
7. Becker K, Gromer S, Schirmer RH, Müller S. Thioredoxin reductase as a pathophysiological factor and drug target. European Journal of Biochemistry. 2000;267(20):6118-6125.
8. Beckett GJ, Arthur JR. Selenium and endocrine systems. J Endocrinol, 2005;184(3): 455-65.
9. Brigelius-Flohe R. Glutathione peroxidases and redox-regulated transcription factors. Biological Chemistry. 2006;387(10/11):1329-1335.
10. Brigelius-Flohe R, Kipp A. Glutathione peroxidases in different stages of carcinogenesis. Biochimica et Biophysica Acta (BBA)-General Subjects. 2009;1790(11):1555-1568.
11. Bouayed J, Bohn T. Exogenous antioxidants—double-edged swords in cellular redox state: health beneficial effects at physiologic doses versus deleterious effects at high doses. Oxidative Medicine and Cellular Longevity. 2010;3(4):228-237.
12. Brown KM, Arthur JR. Selenium, selenoproteins and human health: a review. Public Health Nutr. 2001;4:593-9.

13. Burk RF, Levender OA. In: Modern Nutrition in Health and Disease, Ninth Edition, Edited by M. Shils, J olson, M. Shike and A. C. Ross. Baltimore: Williams&Wilkinis. 1999; 265-276.
14. Burk RF, Hill KE. Selenoprotein P-expression, functions, and roles in mammals. Biochimica et Biophysica Acta (BBA)-General Subjects. 2009;1790(11):1441-1447.
15. Burk, R.F. Selenium in Nutrition. Wld. Rev. Nutr. Diet. 1978; 30:88-106. 1447.
16. Combs GF, Combs SB. The Nutritional Biochemistry of Selenium. Ann. Rev. Nutr. 1984; 4:257-280.
17. Combs GF, Watts JC, Jackson MI, Johnson LK, Zeng H, Scheett AJ, Uthus EO, Schomburg L, Hoeg A, Hoefig CS, Davis CD, Milner JA. Determinants of selenium status in healthy adults. Nutrition Journal. 2011;10(1):75.
18. Dai J, Weinberg RS, Waxman S, Jing Y. Malignant Cells Can Be Sensitized to Undergo Growth Inhibition and Apoptosis by Arsenic Trioxide Through Modulation of the Glutathione Redox System, The American Society of Hematolgy. 1999;0006-4971/99/9301-0016.
19. Davis T, Tiwary AK, Stegelmeier BL, Pfister JA, Panter KE, Hall JO. Comparative oral dose toxicokinetics of sodium selenite and selenomethionine. Journal of Applied Toxicology. 2017;37(2):231-238.
20. Dentice M, Salvatore D. Deiodinases: the balance of thyroid hormone: local impact of thyroid hormone inactivation. The Journal of Endocrinology. 2011;209(3):273-282.
21. Dikiy A, Novoselov SV, Fomenko DE, Sengupta A, Carlson BA, Cerny RL, Ginalski K, rishin NV, Hatfield DL, Gladyshev VN. SelT, SelW, SelH, and Rdx12: genomics and molecular insights into the functions of selenoproteins of a novel thioredoxin-like family. Biochemistry. 2007;46(23):6871-6882.
22. Duntas LH. The role of selenium in thyroid autoimmunity and cancer. Thyroid. 2006;16(5):455-460.
23. Duntas LH, Benvenga S. Selenium: an element for life. Endocrine. 2015;48:756-75.
24. Duntas LH. Selenium and at-risk pregnancy: challenges and controversies. Thyroid Research. 2020;13:16.

25. Ferguson AD, Labunsky, VM, Fomenko DE, Araç D, Chelliah Y, Amezcua CA, Rizo J, Gladyshev VN, Deisenhofer J. NMR structures of the selenoproteins Sep15 and SelM reveal redox activity of a new thioredoxin-like family. Journal of Biological Chemistry. 2006;281(6):3536-3543.
26. Fairweather-Tait SJ, Bao Y, Broadley MR, Collings R, Ford D, Hesketh JE, Hurst R. Selenium
27. in human health and disease. Antioxidants & redox signaling. 2011;14(7):1337-1383.
28. Fordyce F. Selenium geochemistry and health. AMBIO: a Journal of the Human Environment. 2007;36(1):94-98.
29. Foster LH, Surnar S: Selenium in Health and Disease: A review. Crit Rev Food Sci Nutr. 1997;37(3):21,1-28.
30. Galan-Chilet I, Tellez-Plaza M, Guallar E, De Marco G, Lopez-Izquierdo R, Gonzalez-Manzano I, Carmen Tormos M, Martin-Nuñez GM, Rojo-Martinez G, Saez GT, Martín-Escudero JC, Redon J, Javier Chaves F. Plasma selenium levels and oxidative stress biomarkers. A gene–environment interaction population-based study. Free Radical Biology and Medicine. 2014;74:229-236.
31. Ganther HE. Enzymatic Synthesis of Dirnethyl Selenide from Sodium Selenite in Mouse Liver Extracts. Biochemistry. 1966;5:1089-1098.
32. Giovannini S, Onder G, Lattanzio F, Bustacchini S, Di Stefano G, Moresi R, Landi F. Selenium concentrations and mortality among community-dwelling older adults: results from IlSIRENTE study. The journal of nutrition, health & aging. 2018;22(5):608-612.
33. Groff JL, Gropper SS, and Hunt SM. Microminerals in Advenced Nutrition and Human Metabolism, Minneapolis: West Publishing Company, Minneapolis. 1995;381-384.
34. Hall JO. Veterinary Toxicology, Edited by Ramesh C. Gupta, ISBN: 978-0-12-370467-2, Selenium. Bölüm 34; 2007.
35. Harr JR, Muth OH. Selenium Poisoning in Domestic Animals and its Relationship to Man. Clin. Toxicol. 1972;5:175-186.
36. Hashemy S, Ungerstedt J, Zahedi Avval F, Holmgren A. Motexafin gadolinium, a tumor-selective drug targeting thioredoxin reductase and ribonucleotide reductase. J Biol Chem. 2006;281:10691-7.
37. Hendrickx W, Decock J, Mulholland F, Fairweather-Tait S, Bao YP.

Selenium biomarkers in prostate cancer cell lines and influence of selenium on invasive potential of PC3 cells. Frontiers in Oncology. 2013;3:239.

38. Hoeflich J, Hollenbach B, Behrends T, Hoeg A, Stosnach H, Schomburg L. The choice of biomarkers determines the selenium status in young German vegans and vegetarians. British Journal of Nutrition. 2010;104(11):1601-1604.
39. Hoffmann PR, Berry, M. J. The influence of selenium on immune responses. Molecular Nutrition ve Food Research. 2008;52(11):1273-1280.
40. Holbe D, Smith AM. The diverse role of selenium within selenoproteins: a review. Journal of the American Dietetic Association. 1999;99(7):836-843.
41. Hollenbach B, Morgenthaler NG, Struck J, Alonso C, Bergmann A, Köhrle J, Schomburg L. New assay for the measurement of selenoprotein P as a sepsis biomarker from serum. Journal of Trace Elements in Medicine and Biology. 2008;22(1):24-32.
42. Holmgren A, Lu J. Thioredoxin and thioredoxin reductase: current research with special reference to human disease. Biochemical and Biophysical Research Communications. 2010;396(1):120-124.
43. Hurst R, Armah CN, Dainty JR, Hart DJ, Teucher B, Goldson AJ, et al. Establishing optimal selenium status: results of a randomized, double-blind, placebo-controlled trial. The American Journal of Clinical Nutrition. 2010;91(4):923-31.
44. Iglesias P, Selgas R, Romero S, Díez JJ. Selenium and kidney disease. J Nephrol. 2013;26(2):266-72.
45. Institute of Medicine (US) Panel on Dietary Antioxidants and Related Compounds. Dietary Reference Intakes for Vitamin C, E, Selenium and Carotenoids. Washington (DC): National Academies Press (US). 2000. 7, Selenium. Available from: https://www.ncbi.nlm.nih.gov/books/NBK225470. Erişim Tarihi: 15.11.2022.
46. Ji LL. Exercise and Oxidative Stress: Role of the Cellular Antioxidant Systems. In: Exercise and Sport Science Reviews, edited by J Holloszy. Baltimore: Wilkins and Wilkins. 1995;135-166.
47. Jurynec MJ, Xia R, Mackrill JJ, Gunther D, Crawford T, Flanigan KM, Abramson JJ, Howard MT, Grunwald DJ. Selenoprotein N is required

for ryanodine receptor calcium release channel activity in human and zebrafish muscle. Proceedings of the National Academy of Sciences. 2008;105(34):12485-12490.

48. Karataş F, Aşkın U, Halifeoğlu İ, Dönder E. Guatrlı Hastalarda Antioksidan Vitaminler (A, E ve C), Selenyum Gulutatyon Peroksidaz (GSH-Px) Düzeylerinin Araştırılması, F.Ü. Sağ. Bil. Der. 2006;20(4):277-280.

49. Kieliszek M, Błażejak S. Selenium: significance, and outlook for supplementation. Nutrition. 2013;29(5):713-718.

50. Kohrle J, Jakob F, Contempre B, Dumont JE. Selenium, the thyroid, and the endocrine system. Endocrine Reviews. 2005;26(7):944-984.

51. Kohrle J. The trace element selenium and the thyroid gland. Biochimie. 1999; 81:527-33.

52. Koller LD, Exon JH. The two aces of selenium-deficiency and toxicity are similar in animals and man. Canadian Journal of Veterinary Research. 1986;50(3):297.

53. Kryukov GV, Gladyshev VN. Mammalian selenoprotein gene signature: identification and functional analysis of selenoprotein genes using bioinformatics methods. Methods in Enzymology. 2002;347: 84-100.

54. Kryukov GV, Castellano S, Novoselov SV, Lobanov A V, Zehtab O, Guigó R, Gladyshev VN. Characterization of mammalian selenoproteomes. Science. 2003;300(5624):1439-1443.

55. Kumpulainen J: Selenium: Requirement and Supplementation. Acta Pediatr Scand Suppl. 1989;351:114-7.

56. Kurt H, Başaran A, Aral E, Sıçanlarda Karbon Tetrakloritin (CCl4) Oluşturduğu Oksidatif Stresin Kateşin ve Likopen İle Önlenmesi, Doktora Tezi, Osmangazi Üniversitesi, Sağlık Bilimleri Enstitüsü. 2005.

57. Labunskyy VM, Ferguson AD, Fomenko DE, Chelliah Y, Hatfield DL, Gladyshev VN. A novel cysteine-rich domain of Sep15 mediates the interaction with UDP-glucose: glycoprotein glucosyltransferase. Journal of Biological Chemistry. 2005;280(45):37839-37845.

58. Labunskyy VM, Hatfield DL, Gladyshev VN. The Sep15 protein family:roles in disulfide bond formation and quality control in the endoplasmic reticulum. IUBMB Life. 2007;59(1):1-5.

59. Labunskyy VM, Yoo M-H, Hatfield DL, Gladyshev VN. Sep15, a thioredoxin-like selenoprotein, is involved in the unfolded protein response and differentially regulated by adaptive and acute ER stresses. Biochemistry. 2009;48(35):8458-8465.
60. Lee BC, Dikiy A, Kim H-Y, Gladyshev VN. Functions and evolution of selenoprotein methionine sulfoxide reductases. Biochimica et Biophysica Acta (BBA)-General Subjects. 2009;1790(11):1471-1477.
61. Letavayová L, Vlasáková D, Spallholz JE, Brozmanová J, Chovanec M. Toxicity and mutagenicity of selenium compounds in Saccharomyces cerevisiae. Mutation Research/Fundamental and Molecular Mechanisms of Mutagenesis. 2008;638(1-2):1-10.
62. Lubos E, Loscalzo J, Handy DE. Glutathione peroxidase-1 in health and disease: from molecular mechanisms to therapeutic opportunities. Antioxidants ve Redox Signaling. 2011;15(7):1957-1997.
63. Lu J, Holmgren A. Selenoproteins. Journal of Biological Chemistry. 2009;284(2):723-727.
64. Maia AL, Goemann IM, Souza Meyer EL, Wajner SM. Type 1 iodothyronine deiodinase in human physiology and disease. Journal of Endocrinology. 2011;209(3):283-297.
65. Mendelev N, Mehta SL, Witherspoon S, He Q, Sexton JZ, Li, PA. Upregulation of human selenoprotein H in murine hippocampal neuronal cells promotes mitochondrial biogenesis and functional performance. Mitochondrion. 2011;11(1):76-82.
66. Mistry HD, Pipkin FB, Redman CW, Poston L. Selenium in reproductive health. American Journal of Obstetrics and Gynecology. 2012;206(1):21-30.
67. Mueller AS, Mueller K, Wolf NM, Pallauf J. Selenium and diabetes: an enigma? Free radical research. 2009;43(11):1029-59.
68. Neve J, Vertongen F, Molle L: Seleniuro Deficiency. Clin Endocrinol Metabol. 1985; 14:629-56.
69. Noh OJ, Park YH, Chung YW, Kim IY. Transcriptional regulation of selenoprotein W by MyoD during early skeletal muscle differentiation. Journal of Biological Chemistry. 2010;285(52):40496-40507.
70. Oldfield JE. The two faces of selenium. J Nutrition. 1987;117:2002-2008.
71. Panee J, Stoytcheva ZR, Liu W, Berry MJ. Selenoprotein H is a redox-sensing high mobility group family DNA-binding protein that up-

regulates genes involved in glutathione synthesis and phase II detoxification. Journal of Biological Chemistry. 2007;282(33):23759-23765.

72. Patterson BH, Levander A. Naturally occurring selenium compounds in cancer chemoprevention trials: a workshop summary. Cancer Epidemiology and Prevention Biomarkers. 1997;6(1):63-69.

73. Pérez-Corona M, Sánchez-Martínez M, Valderrama M, Rodríguez M, Cámara C, Madrid Y. Selenium biotransformation by Saccharomyces cerevisiae and Saccharomyces bayanus during white wine manufacture: laboratory-scale experiments. Food Chemistry. 2011;124(3):1050-1055.

74. Powers SK, Ji LL, Leeuwenburgh C. Exercise Training-Induced Alterations in Skeletal Muscle Antioxidant Capacity: a Brief Review, Medicine & Science in Sports & Exercise. 1999;31(7):987-997.

75. Rayman MP. The importance of selenium to human health. Lancet. 2000;356:233-41.

76. Rayman MP. Selenium and human health. Lancet. 2012;379:1256–68.

77. Reeves MA, Bellinger FP, Berry MJ. The neuroprotective functions of selenoprotein M and its role in cytosolic calcium regulation. Antioxidants and Redox Signaling. 2010;12(7):809-818.

78. Richardso, DR. More roles for selenoprotein P: local selenium storage and recycling protein in the brain. Biochemical Journal. 2005;386(2):E5.

79. Robinson MF, Thomson CD. The Role of Selenium in the Diet. Nutr. Abs. Rev. Clin. Nutr. Series A. 1983;53:3-26.

80. Rocourt CR, Cheng WH. Selenium supranutrition: are the potential benefits of chemoprevention outweighed by the promotion of diabetes and insulin resistance? Nutrients. 2013;5(4):1349-65.

81. Roman M, Jitaru P, Barbante C. Selenium biochemistry and its role for human health. Metallomics. 2014;6(1):25-54.

82. Ruseva B, Himcheva I, ve Nankova D. Importance of selenoproteins for the function of the thyroid gland. Medicine. 2013;3(1):60-64.

83. Schomburg L, Köhrle J. On the importance of selenium and iodine metabolism for thyroid hormone biosynthesis and human health. Molecular Nutrition ve Food Research. 2008;52(11):1235-1246.

84. Schweizer U, Bräuer AU, Köhrle J, Nitsch R, Savaskan NE. Selenium and brain function: a poorly recognized liaison. Brain Research

Reviews. 2004;45(3):164-178.

85. Seale LA, Ha HY, Hashimoto AC, Berry MJ. Relationship between selenoprotein P and selenocysteine lyase: Insights into selenium metabolism. Free Radical Biology and Medicine. 2018;127:182-189.

86. Sengupta A, Carlson BA, Labunskyy VM, Gladyshev VN, Hatfield DL. Selenoprotein T deficiency alters cell adhesion and elevates selenoprotein W expression in murine fibroblast cells. Biochemistry and Cell Biology. 2009;87(6):953-961.

87. Shchedrina VA, Zhang Y, Labunskyy VM, Hatfield DL, Gladyshev VN. Structure–function relations, physiological roles, and evolution of mammalian ER-resident selenoproteins. Antioxidants and Redox Signaling. 2010;12(7):839-849.

88. Solovyev N, Drobyshev E, Bjørklund G, Dubrovskii Y, Lysiuk R, Rayman MP. Selenium, selenoprotein P, and Alzheimer's disease: is there a link? Free Radical Biology and Medicine. 2018;127:124-133.

89. Spiller HA, Pfiefer E. Two fatal cases of selenium toxicity. Forensic science international. 2007;171(1):67-72.

90. Stuss M, Michalska-Kasiczak M, Sewerynek E. The role of selenium in thyroid gland pathophysiology. Endokrynologia Polska. 2017;68(4):440-465.

91. Su D, Novoselov SV, Sun Q-A, Moustafa ME, Zhou Y, Oko R, Gladyshev VN. Mammalian selenoprotein thioredoxin-glutathione reductase roles in disulfide bond formation and sperm maturation. Journal of Biological Chemistry. 2005;280(28):26491-26498.

92. Sun H, Feng B. Speciation of organic and inorganic selenium in selenium-enriched eggs by hydride generation atomic fluorescence spectrometry. Food Analytical Methods. 2011;4(2):240-244.

93. Sun Q-A, Wu Y, Zappacosta F, Jeang K-T, Lee BJ, Hatfield DL, Gladyshev VN. Redox regulation of cell signaling by selenocysteine in mammalian thioredoxin reductases. Journal of Biological Chemistry. 1999;274(35):24522-24530.

94. Şlencu BG, Ciobanu C, Cuciureanu R. Selenium content in foodstuffs and its nutritional requirement for humans. Clujul Medical. 2014;85(2):139-145.

95. Tajaddini MH, Keikha M, Razzazzadeh A, Kelishadi R. A systematic review on the association of serum selenium and metabolic syndrome. J Res Med Sci. 2015;20:782-9.

96. Tamura T, Stadtman TC. A new selenoprotein from human lung adenocarcinoma cells: purification, properties, and thioredoxin reductase activity. Proceedings of the National Academy of Sciences. 1996;93(3):1006-1011.
97. Turanov A A, Su D, Gladyshev VN. Characterization of alternative cytosolic forms and cellular targets of mouse mitochondrial thioredoxin reductase. Journal of Biological Chemistry. 2006;281(32):22953-22963.
98. Turanov AA, Kehr S, Marino SM, Yoo M-H, Carlson BA, Hatfield DL, Gladyshev VN. Mammalian thioredoxin reductase 1: roles in redox homoeostasis and characterization of cellular targets. Biochemical Journal. 2010;430(2):285-293.
99. Verma S, Hoffmann FW, Kumar M, Huang Z, Roe K, Nguyen-Wu E, Hashimoto AS, Hoffmann PR. Selenoprotein K knockout mice exhibit deficient calcium flux in immune cells and impaired immune responses. The Journal of Immunology. 2011;186(4):2127-2137.
100. Yanardağ R, Orak H. Seleniuro content of milk and milk products of Turkey - Part ll. Biol Trace Elem Res. 1999;68:79-9 5.
101. Yang Z, Faustino PJ, Andrews PA, Monastra R, Rasmussen AA, Ellison CD, Cullen KJ. Decreased Cisplatin/DNA Adduct Formation is Associated with Cisplatin Resistance in Human and Neck Cancer Cells Lines, Cancer Chemother Pharmacol. 2000;46:255-262.
102. Yaylalı B, Sözer V. İnsan hastalıklarında eser elementler. Endokrinolojide yönelişler. 1995;4:25-33.
103. Ye Y, Shibata Y, Yun C, Ron D, Rapoport TA. A membrane protein complex mediates retro-translocation from the ER lumen into the cytosol. Nature. 2004;429(6994): 841.
104. Waldemar B. Minich Selenium Metabolism and Biosynthesis of Selenoproteins in the Human Body. Bıochemıstry. 2022;62:369-390.
105. Weeks BS, Hanna MS, Cooperstein D. Dietary selenium and selenoprotein function. Med Sci Monitor. 2012;18(8): RA127.
106. Wilber CG. Toxicology of Selenium: A Review. Clin. Toxicol. 1980;17:171-230.
107. Williams GR, Duncan Bassett J. Local control of thyroid hormone action: role of type 2 deiodinase. Journal of Endocrinology. 2011;209(3):261-272.

Antioxidants

Dr. Öğr. Üyesi SUZAN ONUR[1]
Prof. Dr. ADNAN AYHANCI[2]

[1]Karabuk University, Faculty Of Health Sciences
Physiotherapy And Rehabilitation Department
Orcid: 0000-0001-8145-6090
[2]Eskisehir Osmangazi University, Faculty Of Science
Biology Department
Orcid: 0000-0003-4866-981

INTRODUCTION

Oxidative stress can be explained as the deterioration of the balance between the peroxidation in the lipid layer of the cells as a result of the production of free radicals and the antioxidant defense system of the body (Cochranc, 1991), that is, oxidative stress occurs when the balance between oxidant and antioxidant systems cannot be achieved(Patlevič et al., 2016). Impaired cellular metabolism, molecular breakdown and tissue damage, which are disrupted as a result of oxidative stress to which the organism is exposed when oxidants are increased or antioxidants are insufficient (Bullock et al., 1954).

One of the two main sources of oxidant substances are reactive oxygen products, the most important of which are hydroxyl radical (•OH), superoxide anion ($O_2•^-$), hydroperoxyl radical ($HO_2•$), single oxygen ($1O_2$) and hydrogen peroxide (H_2O_2) (Patlevič et al., 2016) (Figure 1).Free radicals and reactive oxygen species (ROT) cause oxidative damage to lipid, carbohydrate, protein and nucleic acids (Yoshikawa and Naito, 2002).

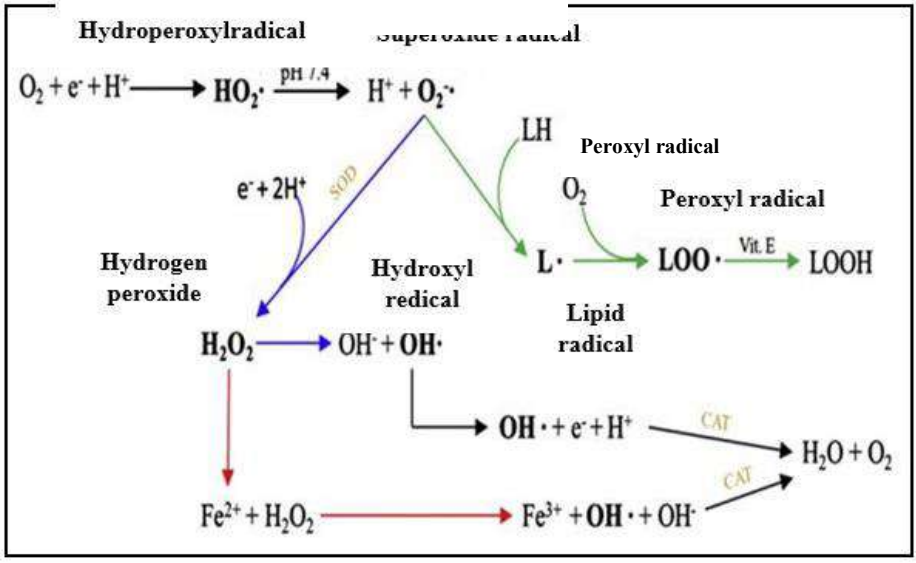

Figure 1. The sequence of reactions that cause the formation of reactive oxygen species. The green arrows represent lipid peroxidation, the blue arrows represent the Haber-Weiss reaction, and the red arrows represent the Fenton reaction (Carocho and Ferreira, 2013).

The task of oxidative balance is to protect the cell, which is disrupted by the action of free radicals, from the harmful effects of free radicals. Cells produce

antioxidants to neutralize free radicals and protect them from their harmful effects (Yoshikawa and Naito, 2002).

ANTIOXIDANTS

Cells and tissues have a system that inhibits radical products and reactions (Şener and Berrak, 2009). In the structure of living things, there are mechanisms developed to neutralize the negative effects of emerging free radicals, which can operate both inside and outside the cell (Bayır, 2008; Coral, 2004). Defense systems that prevent the formation of reactive oxygen species, prevent the damage caused by these substances and work in the body to provide detoxification are defined as "antioxidant defense systems" or "antioxidants" (Şener and Berrak, 2009). They are antioxidants that protect cells directly or indirectly from drugs, carcinogens and the harmful effects of toxic radical reactions (Bayır, 2008; Coral, 2004). To this end, antioxidants work continuously to keep the reactive substances and their reactions in balance (Byung 1994). As a result of this study, the organism keeps the biochemical products that show free radical properties that occur during physiological activity at a level known as "oxidant-antioxidant balance". More than the presence of radicals, it is indicated that the disruption of this balance between oxidants and antioxidants in favor of any of them can be dangerous for the organism. (Karlsson, 1997). Antioxidants are defined as substances that prevent the progression of autooxidation/peroxidation by reacting rapidly with radicals (Aydemir and Karadağ, 2009). Antioxidant vitamins also show their effects with the following mechanisms while maintaining the oxidant-antioxidant balance of the organism. These;

- bind or stabilize the resulting free radicals with their collecting and relieving effects (Zintzen, 1997; Young and Woodside, 2001),
- inhibit free radical-producing chemical reactions with a chain-breaking effect (Gutteridge, 1995; Van-Der-Meulen et al., 1997),
- reduce the reaction rate by suppressive effect (Packer, 1991),
- repair biological molecular damageto lipids, proteins and DNA (Evelson, 1997),
- stop oxidation reactions by inhibiting cellular kinase losses (Van-Der-Meulen et al., 1997; Evelson, 1997),
- to increase the synthesis of antioxidant enzymes and non-enzymatic antioxidants present in the organism (Gutteridge, 1995).

Antioxidant defense is also classified as "enzymatic antioxidant defense" and "nonenzymatic defense" (Kirkman et al., 1987), more specifically as cellular,

membranal and extracellular according to whether the components are enzymatic or not (Aydın et al., 2001). Its antioxidant activity depends on the type of oxidative substrate and oxidative stress. According to Packer et al., when evaluating the antioxidant potential of a substance; should be considered as its specificity in removing free radicals, interaction withother antioxidants, metal chalazion activity, effects on gene expression, bioavailability, localization and repair of thatoxidative damage. If an antioxidant can meet all of these criteria, it should be considered the ideal antioxidant (Packer et al., 1995).

CLASSIFICATION OF ANTIOXIDANTS

When classifying antioxidants, they are grouped into two main groups as endogenous and exogenous. Both groups areused to maintain oxidant/antioxidant balance while protecting the body from free radicals and neutralizing free radicals (Sen and Chakraborty, 2011).

ENDOGENOUS ANTIOXIDANTS

Endogenous antioxidants, which provide suppression of oxidant effects occurring in living things in daily life and are primarily used in this regard (Karlsson et al., 1997; Byung, 1994). Enzymatic and non-enzymatic aredivided into two subgroups (Akagün and Alabaş, 2009; Pham-Huy et al., 2008; Aydemir and Karadağ, 2009; Sen et al., 2010) (Figure 2).

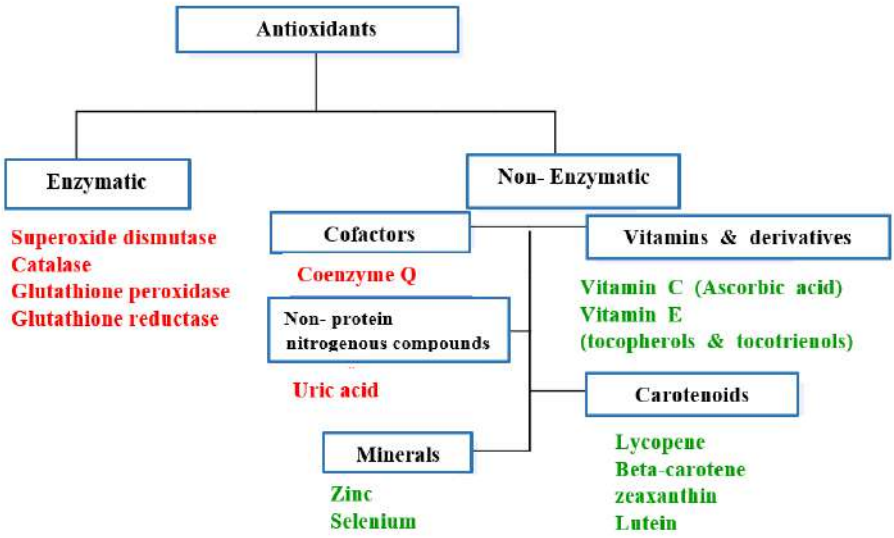

Figure 2. Classification of natural antioxidants. Endogenous antioxidants are sown in red and exogenous antioxidants in green (Carocho and Ferreira, 2013).

ENZIMATIC ANTIOXIDANTS

The enzymatic antioxidants that form the enzymatic defense line are superoxide dismutase (SOD), catalase (CAT), glutathione peroxidase (GPx), and glutathione reductase (GR) (Sen et al., 2010, Pham-Huy et al., 2008; You and Chakraborty, 2011; Valko et al., 2007). Of these, CAT, SOD and GPx are antioxidant enzymes with a very high effect in living things (Cheeseman and Sloter, 1993), and GR is shown as an example of first-order enzymatics and GR is shown as an example of second-order enzymatics (Pellegrini et al., 2009; Ratnam, 2006) (Figure 3).

Superoxide Dismutase Enzyme (SOD)

Forming the first line of defense against reactive oxygen species (Sen et al., 2010; Sen and Chakraborty, 2011) this enzyme reduces the effect of superoxide radicals by catalyzing the conversion of the radical ($O_2^{\bullet -}$), hydrogen peroxide (H_2O_2) and molecular oxygen (O_2) (Larson, 1988; Young and Woodside, 2001). The resulting H_2O_2 is removed from the environment by means of CAT or GPx (Young and Woodside, 2001). Zinc (Zn), an important mineral involved in this event, forms the active site of the SOD enzyme (Larson, 1998).

$$2H^+$$

$$O_2^{\bullet -} + O_2^{\bullet -} \rightarrow H_2O_2 + O_2$$

$$SOD$$

There are three forms of SOD in humans. Of these, superoxide dismutase (Cu/Zn SOD) containing copper (Cu) and zinc (Zn) is found in cytosol, superoxide dismutase (MnSOD) containing manganese (Mn) is found in mitochondria, and extracellular superoxide dismutase (EC SOD) is found in extracellular fluids (Sen and Chakraborty, 2011; Young and Woodside, 2001).

One of the most abundant SOD isoenzymes in cells, cytosolic dimeric Cu /Zn SOD, is called cytoplasmic SOD (SOD1), while it consists of two equal subunits containing one Cu and one Zn atom in each subunit (Mruk, 2002; Nordberg and Arner, 2001). Another SOD isoenzyme, Mn SOD, is known as mitochondrial SOD (SOD2) because it is a mitochondrial enzyme, consists of four equal subunits and contains Mn^{+3} in its active site. Like Cu/Zn SOD, they both catalyze the same reaction (Fridovich 1995; Orbea et al., 2000). EC SOD is called SOD3 and has a Cu and a Zn atom in each of its subunits, which are necessary for enzymatic activity. SOD3 is primarily and intensively found in

the extracellular matrix, cell surfaces (Gao et al., 2008), plasma, lymph and synovial fluid, especially in the vessel walls(Fattman, 2003). SOD3 is secreted and synthesized by fibroblast cells, glia cells, and endothelial cells (Gao et al., 2008). In addition, vascular smooth muscle cells have been reported to synthesize SOD3 to a large extent (Fattman, 2003).

Catalase (CAT)

The catalase enzyme is a metalloenzyme recognized as one of the most effective protein catalysts that promote the redox reaction (Larson, 1988) and is found mainly in peroxisomes (Ighodaro and Akinloye, 2018), but less so in the mitochondria and endoplasmic reticulum (Limon-Pacheco and Gonsebatt, 2009). Each subunit of the catalase, whose subunit consists of four proteins, contains a Hem group and a NADPH molecule (Young and Woodside, 2001; Kirkman and Galiano, 1987). That is, catalase is a hemoprotein that contains a single ferriprotoporphyrin in each polypeptide subunit structure (Ighodaro and Akinloye, 2018). In most cases, the NADPH molecule is close to the surface and tightly bound (Zamocky and Koller, 1999). The toxic H_2O_2 produced as a result of SOD enzyme activity is converted to H_2O and O_2 by the action of the catalase enzyme (Duthie et al., 1989; Limon-Pacheco and Gonsebatt, 2009).

Catalase

$$2\ H_2O_2 \rightarrow 2\ H_2O + O_2$$

In order to neutralize hydrogen peroxide in plants as well, catalase forms the compound H_2O_2 as an intermediate product in the first stage of the reaction, while in the second stage it forms H_2O and O_2, during which it provides enzyme release (Gechev et al., 2003).

The superoxide radical is converted to H_2O_2 by means of SOD. The resulting H_2O_2 acts as a precursor when OH• is formed, the most reactive type of oxygen, catalyzed by Cu and Fe ions through the Fenton reaction (Cheung et al., 2001; Larson, 1988).

Glutathione Peroxidase (GSHPx)

Glutathione peroxidase is a highly important antioxidant that breaks down H_2O_2into H_2O in mitochondria and sometimes cytosols (Fattman, 2003). Protects cells against oxidative damage from H_2O_2 and prevents OH• from H_2O_2(Cnubben et al., 2001; Reiter et al., 1995).

Glutathione peroxidase acts as an enzyme that metabolizes H_2O_2 and organic hydroperoxides (lipid hydroperoxides, DNA hydroperoxides) using glutathione (GSH) as the electron source. Itconsists of four protein subunits, each of which contains a Se atom (Sen and Chakraborty, 2011), and often its activity depends on selenium. For this reason, it is defined in two ways as selenium-dependent (Se-GPx) and non-selenium-dependent (GST). (Cnubben et al., 2001). While Se-GPx, which has selenium in its active region, is effective against $H_2O_2$and organic hyperoxides; GST is mainly involved in the metabolization of organic hydroperoxides (Cnubben et al., 2001; Reiter et al., 1995). During these metabolization reactions, GSH oxidizes H_2O_2 as hydrogen donor and GSH oxidizes as hydroperoxides are reduced (Reiter et al., 1995). Oxidized glutathione is defined as glutathione disulfide (GSSG), and together with the GR enzyme, oxidized glutathione is reduced back to reducted glutathione. During this reduction reaction, the GR enzyme uses NADPH as an electron donor (Sen and Chakraborty, 2011; Reiter et al., 1995). The GSHPx enzyme converts the reduced form of glutathione (GSH) into an oxidized state (GSSG).

$$2\ GSH + H_2O_2 \xrightarrow{GSHPx} GSSG + 2\ H_2O$$

Studies have shown that low GPx levels cause the antioxidant system to malfunction. When oxidative damage occurs in membrane fatty acids and functional proteins, the occurrence of neurotoxic damage and the development of permanent damage along with neurodegeneration also indicate that the antioxidant defense system is disrupted (Chabory et al., 2009).

Glutathione Reductase (GR)

Glutathione Reductase, a flavoprotein enzyme containing flavin adenine dinucleotide (FAD), converts an electron of NADPH back into GSH by transferring it to disulfide bonds of oxidized glutathione. Therefore, NADPH is needed to prevent free radical damage and the most important source of this is the hexose monophosphate (pentose phosphate) pathway (Özkan ve Fıskın, 2004; Sen et al., 2010).

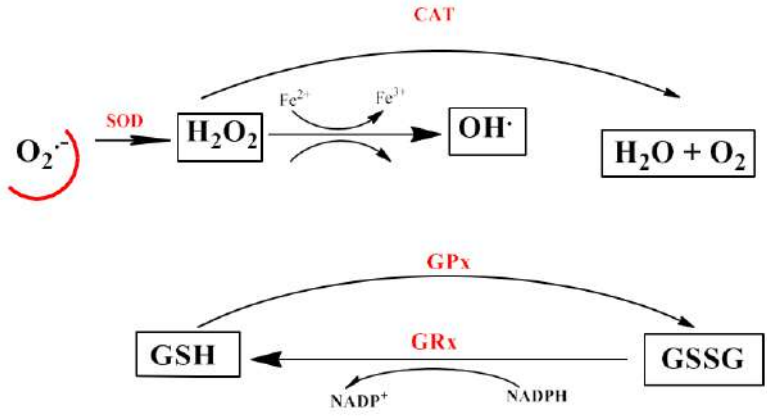

Figure 3. Enzymatic antioxidants (Rani et al., 2016).

NONENZYMATIC ANTIOXIDANTS

Non-enzymatic antioxidants are glutathione, melatonin, uric acid, bilurubin, albumin, coenzyme Q10, selenium, α-lipoic acid, ceruloplasmin and transferrin (Sen et al., 2010; Pham-Huy et al., 2008; You and Chakraborty, 2011; Valko et al., 2007; Droge, 2002; Willcox, 2004). The most important non-enzymatic antioxidants are albumin and uric acid, which are responsible for 85% of the total antioxidant capacity. Other important antioxidants are bilirubin, α-tocopherol (vitamin E), β-carotene (Liguori et al., 2018).

Glutathione (GSH)

Synthesized in almost all eukaryotic cells, GSH acts as an antioxidant in maintaining the redox state of the cell, in the operation of the detoxification system, in the synthesis of eicosanoids, in the regulation of the cell signaling mechanism, in gene expression and apoptosis, and is found in high quantities (Townsend et al., 2003). GSH is a tripeptide that carries a thiol group. Thiol groups function by using enzymatic reactions and capturing free radicals. GSH, which is a water-soluble thiol that acts as a substrate of many enzymes such as transferases, peroxidases that prevent or reduce the destructive effects of free radicals, and is present in very high concentrations in many cells, plays an important role in the enzymatic protection of biological membranes against lipid peroxidation (Di Mascio et al., 1991).

It is found in high density in all cells of plants, especially in the cytosol, endoplasmic reticulum, vacuole and mitochondria. Since it contains sulfur in its structure, it provides detoxification of xenobiotics by GSH conjugation (Lamb

and Dixon, 1997). Approximately 85-90% of GSH is in the cytoplasm, and once synthesized in the cytoplasm, it has been found that it can also be found in mitochondria, nucleus, peroxisomes, and endoplasmic reticulum (Green et al., 2006; Kalinina et al., 2014).

The synthesis of GSH occurs in two stages. In the first stage, glutamine-cysteine binds lygas (GCL), glutamine and cysteine to form ɣ-glutamylcysteine. In the second stage, glutathione synthetase (GSS) forms the GSH molecule by binding glycine to ɣ-glutamylcysteine. GCL consists of catalytic (GCLC) and regulatory (GCLM) subunits. The catalytic subunit of the GCL is responsible for binding cysteine and glutamine for catalytic activity, while the regulatory subunit is involved in enhancing the effect of GCLC (Lagman et al., 2015; Pei et al., 2013). The cysteine residual, which is centrally located in its structure, creates its antioxidant effect. Cytotoxic H_2 directly inactivates O_2, while hydroxy radicals (OH•) neutralize superoxide anion ($O_2^{\bullet -}$) and single oxygen ($^1O_2$) without enzyme catalysis (Larson, 1988; Avsian-Kretchmer et al., 1999).

GSH provides amino acid transport through the plasma membrane while recreating some important antioxidants. In addition to all this, it carries out the regulation of vitamins E and C (Sen and Chakraborty, 2011). Ascorbatine, a water-soluble and powerful antioxidant, regenerates ascorbatglutathione by cycle (Lamb and Dixon, 1997).

Melatonin

Melatonin (N-acetyl-5-methoxy-tryptamine) is basically synthesized endogenously from the pineal gland, tryptophan in the dark, and many other places (Hevia et al., 2014).

Melatonin, which reduces the harmful effects of free radicals, protects macromolecules from oxidative damage in all intracellular compartments, while protecting both nuclear DNA and mitochondrial DNA, as well as proteins and lipids. Since it is active everywhere as a direct free radical scavenger and an indirect antioxidant, it has a fairly wide range of protection, and thanks to this, it cleans up different types of reagents and free radicals, including hydroxyl radical, hydrogen peroxide, singlet oxygen, nitric oxide, peroxynitriteanion and peroxynitric acid. In addition to all these activities, it stimulates some of the antioxidant enzymes containing SOD, CAT, GPx and GR, while experimentally increasing the level of intracellular GSH by stimulation of melatonin, ɣ-glutamyl cysteine synthetase, prooxidative such as lipoxygenase and nitric oxide synthase enzymes. It can help the cell membrane resist oxidative damage

by hardening cellular membranes. In addition, when increasing the efficiency of the electron transport system, free radical generation and electron leakage are reduced (Reiter et al., 2006).

Uric Acid

Uric acid, the final oxidation product of purine catabolism in humans (Iliesiu et al., 2010; Kumar et al., 2015), shows activity endogenously as a free radical scavenger and as a powerful antioxidant (Sinha et al., 2009; Kumar et al., 2015). It has the task of chelating transition metals, while inactivating hydroxyl, singlet oxygen, superoxide, peroxynitrite anion, peroxynitric acid (Kumar et al., 2015; Waring, 2002). It is a powerful singlet oxygen, peroxyl radical (ROO•) and OH• scavenger (Sinha et al., 2009). In addition, it is stated that it acts as a protective function by preventing lipid peroxidation, is a powerful free radical scavenger, as well as acting as chelators of metal ions such as Fe and Cu, and is responsible for about half of the total antioxidant capacity of the blood. (Kumar et al., 2015; Waring, 2002).

Bilirubin

It is basically caused by the breakdown of erythrocytes that have expired, the breakdown of Heme proteins in erythrocytes, and acts as a highly effective antioxidant. It exerts its chain-breaking effect by especially affecting peroxil radicals. Bilirubin, which is taken up by the liver during its circulation, is excreted in bile or urine after being bio transformed (Gutteridge, 1995; Burtis and Ashwood, 2005).

Although bilirubin is known to have an antioxidant effect on lipid peroxidation in the intracellular environment, it has been stated that it has antioxidant, cytoprotective and anti-inflammatory effects in recent years (Rye et al., 1997; Liu et al., 2008).

Albumin

Albumin is a key protein found in highly soluble human plasma, as well as one of the most important and effective antioxidants in plasma. In healthy adults, about 70-80% of the cysteine 34 found in albumin contains free sulfidril groups. The rest forms a disulfide with various compounds such as cysteine, homocysteine or GSH. Thanks to the reduced cysteine 34, albumin can sweep OH•. Hypochlorous acid (HOCl) forms a powerful oxidant compound. Activephagocytes such as neutrophils and monocytes provide release of myeloperoxidase enzyme. While this enzyme catalyzes the formation of HOCl, albumin cansweep the formed HOCl oxidants, thereby preventing the

replacement of the α-antiprotease in the primary biological target of HOCl (Roche et al., 2008).

Albumin, which is the main member of the primary extracellular antioxidant 80 defense system, resists free radicals on its own because it carries one sulfhydryl group in each molecule, while tightly binding copper and iron weakly and remains on the surface of the metal to which it is attached. This metal can participate in Haber-Weiss reactions, but is immediately neutralized by the resulting OH• albumin. This damage to albumin is not very significant because albumin is very abundant in plasma and free radicals are neutralized by other antioxidants (Soriani et al., 1994). In addition to many of its functions in the body, albumin binds copper ion and inhibits lipid peroxidation due to copper ion. In addition, serum albumin has been reported to have an important role as an antioxidant in extracellular fluids (Rye et al., 1997; Roche et al., 2008).

For all these reasons, serum bilirubin, uric acid, and albumin levels may be thought to reduce oxidative stress and be indicative of antioxidant status in the body (Li et al., 2018). In addition, the other plasma proteins ceruloplasmin and transferrin have been shown to exhibit antioxidant activity (Soriani et al., 1994).

Coenzyme Q10 (CoQ10)

CoQ10, which is found in all living cells, increases immune resistance while protecting the body against free radicals, but is also necessary for the production of energy by mitochondria (Sumien et al., 2009). CoQ10, which is found in almost all cell membranes and lipoproteins, is a cofactor for at least three mitochondrial enzymes (Complex I, II, III) found in the inner membrane of mitochondria and its role in oxidative phosphorylation is very important (Gürkan and Bozdağ-Dündar, 2005).

As an antioxidant, CoQ10 has functions such as sweeping free radicals and suppressing lipid and protein peroxidation. The reduced form of CoQ10 is ubiquinol (CoQH2) and acts as a lipophilic antioxidant, participating in electron and proton transport in the electron transport system, as well as giving electrons to neutralize oxidants and showing a highly potent antioxidant activity. In this way, CoQ10 provides highly effective protection against toxic ROS such as H2O2 and O 2•−. In addition, while inhibiting lipid peroxidation similarly to vitamin E, it works synergistically with α-tocopherol and recreates its active forms through a similar mechanism to vitamin C (Gürkan and Bozdağ-Dündar, 2005).

α-Lipoic acid (ALA)

ALA, which is anantioxidant that can be dissolved in both oil and water, stands out among the antioxidants that are gaining importance today with its effects such as removing free radicals, regenerating other antioxidants, binding heavy metals and facilitating their excretion, and it is stated that it can be called universal antioxidant because it shows all these effects. As with some foods, it is a natural substance that is synthesized in the body. It is abundant in animal and plant tissue, which are abundant in mitochondrial complexes (Kramer, 2001).

Lipoic acid is a naturally occurring compound that acts as a cofactor in mitochondrial enzymes involved in energy production and metabolism (Cadenas, 2001). One of the main components of the antioxidant cycle is vitamin E. This vitamin works to stop high free radical reactivation in membranes and adipose tissue Researchers have shown in recent years that lipoic acid regenerates vitamins E and vitamin C, which remove free radical damage. (Busse et al., 1992). Lipoic acid also plays an important role in mitochondrial dehydrogenase reactions. The lipoate, or its reduced form, dihydrolipoate, is reactivated by reactive oxygen compounds such as superoxide radicals, hydroxyl radicals, peroxyl radicals, and singlet oxygen. Lipoic acid also protects the membranes by influencing each other with vitamin C and glutathione, which regenerate vitamin E. It has been shown that administration of lipoic acid may be beneficialin some of the oxidative stress patterns such as diabetes, ischemia-reperfusion damage, cataract formation, HIV activation, nerve degeneration and radiation damage (Packer et al., 1995).

Selenium (Se)

Selenium (Se), which is important for the homeostasis of the human body and especially for the regular functioning of the immune system (Hoffmann and Berry, 2008; Rayman, 2000) is a highly important trace element for metabolism, found in the structure of enzymes used to regulate many functions (Galan-Chilet et al., 2014). Se, which is used for amino acid synthesis, called selenocysteine and an important basic element for selenoprotein function, has antioxidant and immunoregulatory functions. There are at least 25 selenoproteins in the human body and these are antioxidant enzymes (glutathione peroxidase), antioxidant proteins (selenoprotein) P and W) and other metabolic enzymes. It has been reported that there may be a link between Se level and oxidative stress, especially since it is found in the structure of antioxidant enzymes such as GPx and thioredoxin reductase (TrxR) (Kim et al., 2014). It suppresses ROS formation by increasing GPx activity when Se in the body is at adequate levels (Kim et al., 2014), while GPx and TrxR enzymes

work at optimal levels, which reduce H_2O_2 levels (Beckett and Arthur, 2005; Duntas, 2006; Galan-Chilet et al., 2014) and contributes to the inhibition of oxidative stress (Becker et al., 2000; Sun et al., 1999; Galan-Chilet et al., 2014). This phenomenon has also been cited as a regulator of inflammatory and immune responses (Beckett and Arthur, 2005; Duntas, 2006).

Ceruloplasmin and Transferrin

Ceruloplasmin, which is an important protein, is involved in oxidase activity and especially in iron metabolism as well as 90% of copper in serum (Cousins, 1985; Loudianos, 2000; Cox, 2002). Physiological phenomena in which ceruloplasmin takes part in metabolism; acute phase protein function, oxidation of nitric oxide, antioxidant and pro-oxidant activity, plasma ferrooxidase activity and iron homeostasisis provision, breakdown of organic substrates, ascorbate oxidase activity, copper transport and storage (Hellman, 2002; Fox, 1995).

The transfer, which is mainly found in serum and in lower concentrations in other body fluids, is known as a carrier protein responsible for transporting Fe^{+3} to cells and also as an important growth factor. Ferrous ion (Fe^{+2}) causes oxidative stress by catalyzing the conversion of H_2O_2 to the more toxic OH• by the reaction of Fenton. Transferrin, on the other hand, works as an antioxidant by reducing the concentration of free ferrous ions (Chauhan et al., 2004).

EXOGENOUS ANTIOXIDANTS

Exogenous antioxidantscan be classified into two groups as vitamin exogenous anti-oxidants and exogenous antioxidants used as medicines (Aydemir, 2009; You and Chakraborty, 2011).

Vitamin Exogenous Antioxidants

External vitamin-derived antioxidants are α-tocopherol (Vitamin E), β-carotene (Vitamin A), ascorbic acid (Vitamin C) and folic acid (Vitamin B9) (Şener, 2009; Dundar, 1999; Aydemir, 2009).

α-Tocopherol (Vitamin E)

Vitamin E is a fat-soluble vitamin with high antioxidant potential and is an asymmetrical compound with eight stereoisomers. These asymmetrical forms are classified as α, β, ɣ, δ tocopherol and α, β, ɣ, δ tocotrienol (Gutteridge, 1995; Paganga et al., 1999). Tocopherols are synthesized only by plant organisms and are found in all parts of plants (Paganga et al., 1999). The main function of α-tocopherol as an antioxidant, the most bioactive form in humans,

is toprotect against lipid peroxidation, as well as to protect cell membranes from damage by free radicals. Because Vitamin E is an active antioxidant only in membranes (Gutteridge, 1995), it protects polycentric fatty acids in membrane phospholipids from the harmful effects of oxidants by eliminating free radical species in the early stages of lipid peroxidation or preventing the formation of free radicals. Thus, it makes the first defense against oxidative stress (Jialal and Fuller, 1993).

Vitamin E breaks the chain of peroxidation by fixing free radicals, and this phenomenon occurs when $1O_2$is mostly reduced to OH• or $O_2•^{-}$. Since vitamin E uses all of the mechanisms such as the destruction of radicals, the breaking of the chain, suppression, repair of deteriorated structures and strengthening endogenous defense systems, its antioxidant capacity is quite large and high. The antioxidant effect of vitamin E on the cell membrane is usually undertaken by GPx within the cell (Dündar and Aslan, 1999). The antioxidant effect of glutathione peroxidase and α-tocopherol is complementary to each other. α-Tocopherol prevents the formation of peroxides, while GPx destroys the peroxides that have already formed (Aydın et al., 2001).

Vitamin E breaks the chain of peroxidation by fixing free radicals, and this phenomenon is usually accomplished by reducing$1O_2$to OH• or $O_2•^{-}$ (Jialal 1993). Vitamin E is used to eliminate radicals (Van Der Meulen, 1997), to break the chain (Thomas 1995), to suppress (Byung, 1994), to repair deteriorated structures (Evelson, 1997) and to strengthen endogenous defense systems (Freeman, 1982; Van Der Meulen, 1997) performs the antioxidant function by using all the mechanisms and the antioxidant capacity is very large and complete (Dündar and Aslan, 1999). As in alveolar membranes and erythrocyte membranes, the antioxidant role of vitamin E can be effective even at very high molecular oxygen concentrations (Halliwell, 1995; Jialal, 1993; Stratton, 1997).

Vitamin C

Vitamin C, also known as ascorbic acid, is a water-soluble vitamin that is essential forcollagen, carnitine, and neurotransmitter biosynthesis (Li and Schellhorn, 2007). It provides effective protection against oxidative damage by easily cleaning reactive oxygen species and reactive nitrogen species such as superoxide, hydroperoxyl, singlet oxygen, ozone, peroxynitrite, nitrogen dioxide and hypochlorous acid. It can also act as a coantioxidant by regenerating α-tocopherol from α-tocopherocil radicals that occur when radicals dissolved in lipids are cleared (Carr and Frei, 1999). In addition to all these, it

also acts as an oxidant by converting Fe^{+3} into Fe^{+2}, which increases lipid peroxidation(Dündar and Aslan, 1999).

The total antioxidant capacity in plasma consists of the activities of uric acid, especially vitamin C, and few large-molecule proteins (Bendich, 1986). With its large antioxidant capacity in water-based environments, vitamin C performs the primary antioxidant defense of blood and other body fluids by taking on a role reminiscent of the antioxidant effect of vitamin E, the powerful antioxidant of lipid environments (Niki, 1991). Vitamin C is composed of singlet oxygen (Niki, 1985), superoxide (Tanaka 1997), hydroxyl, hydroperoxyl, lipid peroxyl and lipid allocycle(Tanaka,1997; Clemens, 1987) is reported to be able to exert its antioxidant effect by removing radicals from the environment. It is suggested that the dissolution of lipid peroxides formed by the oxidation of lipid molecules in aqueous environments is also caused by the antioxidant effect of vitamin C (Niki, 1991).

In addition, vitamin Cplays a role in the reactivation of vitamin E, which has become a tocopherol radical and has lost its antioxidant properties (Levine, 1997;Levine, 1987; Tolbetr, 1985).

β-carotene

β-carotene, a fat-soluble member of carotenoids recognized as provitamins because they can convert to vitamin A, turns into retinol in the retina and is essential for vision in the dark. It is also a powerful antioxidant and the best1O2 cleanser (Pham-Huy, 2008). It performs its antioxidant activity by preventing the formation of free radicals through the suppression of singlet oxygen production from oxidation intermediates and by collecting all radicals in the environment without discrimination. This antioxidant activity is directlyproportional to the oxygen concentration in the environment where β-carotene is present (Aalt, 1991; Byung, 1994).

Folic Acid

Folic acid, a member of the water-soluble vitamin B, is involved in cell division, important for spermatogenesis in men, normal fertility in men and women, during growth periods such as pregnancy and childhood, and is essential for DNA synthesis and the production of red blood cells (Hussein, 2012). In addition to all these, it is a very powerful antioxidant that clears ROS (Ebaid,2013). Folic acid, which is known to reduce plasma homocysteine levels both alone and in combination with other B vitamins, may play an auxiliary role in preventing homocysteine-mediated oxidative vascular damage with antioxidant vitamins such as vitamins C and E (Title et al., 2000).

Cellular Antioxidant Components

Of the cellular antioxidant enzymes SOD, GSH-Px, CAT and cytochrome oxidase, it reduces reactive oxygen metabolites. The conversion ofsuperoxide to $H_2O_2$and oxygen occurs under SOD catalysis by the process of dismutation. That is, SOD acts as a catalyst in the elimination reactions of $O_2^{\bullet-}$(Aydemir and Karadağ, 2009). In addition, the activity of SOD is associated with the elements copper, zinc and manganese (Aydemir and Karadağ, 2009, Kirkman et al., 1987).

$$O_2^{\bullet-} + 2H^+ \xrightarrow{\text{SOD}} H_2O_2 + O_2$$

While reducing hydrogen peroxide, the same reactions take place, this time under the catalyst of GSH-Px and catalase. CAT catalyzes the avoidance of high concentrations of H_2O_2, GSH-Px is involved in the elimination of low concentrations of H_2O_2(Sen et al., 2010). The activity of GSH-Px is associated with the element selenium(Aydemir and Karadağ, 2009;Kirkman et al., 1987).

$$O_2 + H_2O_2 \xrightarrow[\text{Catalase}]{\text{GSH-Px}} H_2O + O_2$$

Membrane Antioxidants

On the lipid face, which is hydrophobic of membranes, unlike the intracellular medium, radicals are produced that dissolve in lipids and cannot be destroyed by cellular enzymes. The main membrane antioxidants are α-tocopherol in particular, β-carotene, ubiquinol compounds and coenzyme Q. Although α-tocopherol, a fat-soluble vitamin, is very active between membrane lipid layers, it has a very weakeffect outside the membrane and dissolves in membrane lipids, allowing the peroxidation chain to be broken (Kumar et al., 2015). β-carotene, which shows its activity according to the oxygen concentration of the environment, inhibits singlet oxygen formation as well asbeing an active radical collector. Ubiquinol, which is found at micro levels, prevents autooxidation in low-density lipoproteins (Green et al., 2006). Coenzyme Q, on the other hand, is an antioxidant that acts in mitochondrial energy metabolism (Kumar et al., 2015).

Extracellular Antioxidants

Proteins such as transferrin, lactoferrin, haptoglobins, albumin, ceruloplasmin, bilirubin, uric acid, glucose are known as essential extracellular

antioxidants (Kim et al., 2014). Antioxidant enzymes are not present in body fluids and organic products. For this reason, SOD and GSH-Px are not important as antioxidants in extracellular media and organic products (Dündar, 1999). Preventing free radical metabolites produced in the intercellular medium from encountering catalyst metal ions such as iron and copper constitutes the main pathway of extracellular antioxidant defense (Kirkman et al., 1987). Lactoferrin, hemoglobin, myoglobin, hemopexin and albumin perform more or less the same function. It has been determined that the agent that prevents radical formation in neutrophils is lactoferrin (Green et al., 2006). While ceruloplasmin binding copper, glucose, urate and bilirubin have been reported to try to remove radicals in the environment(Kirkman et al., 1987). Some extracellular antioxidants and their effects are givenin Table 1.

Table. 1. Extracellular antioxidants and their effects.

Extracellular Antioxidants	**Effects**
Ascorbic acid	Hydroxyl is a radicaleliminator. Tokoferol is a reducing antioxidant vitamin.
Transferrin	It inhibitsthe reaction of Fentonby binding free iron ions.
Lactoferrin	It binds iron ions, especially in environments with low pH.
Haptoglobins	By binding hemoglobin, it prevents the release of "heme".
Hemopexin	Inhibits oxidation by binding free heme proteins in the environment
Albumin	Collects the HOCL radical. Hem binds protein and copper metal ions.
Ceruloplasmin	Neutralizes the superoxide radical. Binds the flux ions.
Bilirubin	It acts as a peroxyl radical collector.
Mucus	It is a hydroxyl radical collector.
Uric acid	In addition toits etal binding function, it also collects different radicals.
Glucose	Hydroxyl radical is eliminated.

RESULT

In addition to the continuous oxidation events in the metabolism of living beings, oxidation events are further accelerated by reactive oxygen substances taken from outside. By attacking the components inside and outside the cell, it is necessary to control the formation and activity of these oxygen species, which damage cell functions. For this, reactive species and reaction mechanisms should be well known. Antioxidants, which act as free radical scavengers, exert a protective effect by neutralizing free radicals, which are the toxic by-product of normal cell metabolism, while also contributing to the prevention of diseases by increasing the effect of the defense system.

REFERENCES

1. Akagün, G. Alabaş 'Brassica oleracea var. Gongylodes' bitkisinin antioksidan aktivitesinin incelenmesi, Yüksek Lisans Tezi, Trakya Üniversitesi Fen Bilimleri Enstitüsü, Edirne. 2009.
2. Avsian-Kretchmer O, Eshdat Y, Gueta-Dahan Y, Ben-Hayyim G. Regulation of stressinduced phospholipid hydroperoxide glutathione peroxidase expression in citrus. Planta. 1999; 209: 469-477.
3. Aydemir B, Karadağ Sarı E. Antioksidanlar ve Büyüme Faktörleri ile İlişkisi. Kocatepe Veterinary Journal. 2009; 2(2): 56-60.
4. Aydın A, Sayal A, Işımer A. Serbest Radikaller ve Antioksidan Savunma Sistemi. Gülhane Askeri Tıp Akademisi. Ayın Kitabı No:20. GATA Basımevi, Ankara; 2001.
5. Bayır, Y. Sıçanlarda İsoprotrenol İle Oluşturulan Miyokard İnfarktüsü Modelinde DNA Hasarı ve Oksidatif Stres Üzerine Lasidipin, Ramipril ve Valsartan'nın Etkilerinin İncelenmesi. Sağlık Bilimleri Enstitüsü, Tıp Fakültesi, Biyokimya Anabilim Dalı. Doktora Tezi, Erzurum, Atatürk Üniversitesi.2008.
6. Becker, K., Gromer, S., Schirmer, R. H., Müller, S. Thioredoxin reductase as a pathophysiological factor and drug target. European Journal of Biochemistry. 2000; 267(20), 6118-6125.
7. Beckett, G. J., Arthur, J. R. Selenium and endocrine systems. Journal of Endocrinology, 2005; 184(3), 455-465.
8. Bendich, A., Machlin, L.J., Scandurra, O., Burton, G.W., Wayner, D.M. The Antioxidant Role of Vitamin C. Adv. Free Radical Biol. Med. 1986; 2:419-444.
9. Bullock M.W., Brockamann J.A., Patterson E.L.,Pierce J.V.,Macchi M.E., Proposed structures for protogen-A and protogen-B.J.Am.Chem Soc. 1954; 76:1827-1828.
10. Burtis CA, Ashwood ER. Vitaminler. Aslan D. Eds. Klinik Kimyada Temel İlkeler. Palme Yayınları, Ankara; 2005.
11. Busse E., Zimmer G., Schopohl B., Kornhuber B., Influence of α-lipoic acid on intracellular glutathione in vitro and in vivo. ArzneimForsch/Drug Res. 1992; 42: 829-832.
12. Byung, P.Y. Cellular Defenses Against Damage From Reactive Species. Physiological Reviews. 1994; 74(1):139-172.
13. Cadenas E., Handbook of antioxidants (2nd ed). Marcel Dekker Incorporated, Newyork. 2001; 23:473.
14. Carocho, M. ve Ferreira, I. C., , A review on antioxidants, prooxidants and related controversy: natural and synthetic compounds, screening and

analysis methodologies and future perspectives, Food and chemical toxicology. 2013; 51, 15- 25.
15. Carr AC, Frei B. Toward a new recommended dietary allowance for vitamin C based on antioxidant and health effects in humans. Am J Clin Nutr. 1999; 69(6): 1086-1107.
16. Chauhan A, Chauhan V, Brown WT, Cohen I. Oxidative stress in autism: Increased lipid peroxidation and reduced serum levels of ceruloplasmin and transferrin- the antioxidant proteins. Life Sci. 2004; 75: 2539–2549.
17. Chabory E, Damon C, Lenoir A, Kauselmann G, Kern H, Zevnik B, et al. Epididymis seleno-independent glutathione peroxidase 5 maintains sperm DNA integrity in mice. J Clin Invest.
18. 2009;119 (7):2074-2085.
19. Cheeseman, KH., Slater, TF. An introduction to free radical biochemistry. British Medical Bulletin. 1993; 49(3), 481-93.
20. Cheung CCC, Zheng GJ, Li AMY, Richardson BJ, Lam PKS. Relationship Between Tissue Concentrations of Polycylic Aromatic Hydrocarbons and Antioxidative Responses of Marine Mussels, Perna viridis. Aquat Toxicol. 2001; 52(3-4): 189-203.
21. Cnubben NHP, Rietjens IMCM, Wortelboer H, Van-Zanden J, Van Bladeren PJ. The Interplay of Glutathione Related Processes in Antioxidant Defense. Environ Toxicol Pharmacol. 2001; 10(4): 141- 152.
22. Cochranc, CG. Cellular injury by oxidants. The American Journal of Medicine. 1991; 92, 235-305.
23. Cousins RJ. Absorption, transport, and hepatic metabolism of copper and zinc: Special reference to metallothionein and ceruloplasmin. Physiol Rev. 1985; 65 (2):238-309.
24. Cox DW, Roberts EA. Wilson disease. Ed: Feldman M, Friedman KS, Sleisenger MH. Gastrointestinal and Liver Disease. 7th edition. by Saunders, China. 2002; 2:1269-77.
25. Çavdar C, Sifil A, Çamsarı T. Reactive oxygen particles and antioxidant defence. Office Journal of the Turkish Nephrology, Association 1997; 3 (4): 92-5.
26. Di Mascio, P. Murphy, M.E., Sies, H. Antioxidan defense system: the role of carotenoids, tocopherols, and thiols. Am. J. Clin. Nutr. 1991; 53; 194-200.
27. Droge W. Free radicals in the physiological control of cell function. Physiol Rev. 2002; 82(1): 47-95.

28. Duntas, L. H. The role of selenium in thyroid autoimmunity and cancer. Thyroid. 2006; 16(5), 455-460.
29. Duthie, G.G., Wahle, K.W.J. and James, W.P.T. Oxidants, antioxidants and cardiovascular disease. Nutr. Res. Rev. 1989; 2; 51-62.
30. Dündar Y, Aslan R. Oksidan-Antioksidan Denge ve Korunmasında Vitaminlerin Rolü. Hayvancılık Araştırma Dergisi. 1999; 9(1-2): 32-39.
31. Ebaid H, Bashandy SAE, Alhazza IM, Rady A, El-Shehry S. Folic acid and melatonin ameliorate carbon tetrachlorideinduced hepatic injury, oxidative stress and inflammation in rats. Nutr Metab. 2013; 10(20) doi:10.1186/1743-7075-10-20.
32. Evelson P, Ordonez CP, Llesuy S, Boveris A. Oxidative stress and in vivo chemiluminescence in mouse skin exposed to UVA radiation. J Photochem Photobiol B. 1997; 38(2-3): 215-9.
33. Fattman CL, Schaefer LM, Oury TD. Extracellular superoxide dismutase in biology and medicine. Free Radical Biology & Medicine. 2003; 35(3): 236–256.
34. Fox PL, Mukhopadhyay C, Ehrenwald E. Structure, oxidant activity, and cardiovascular mechanisms of human ceruloplasmin. Life Sci 1995; 56(21):1749-58.
35. Fridovich I. Superoxide Radical and Superoxide Dismutase. Annu Rev Biochem. 1995; 64: 97-112.
36. Galan-Chilet, I., Tellez-Plaza, M., Guallar, E., De Marco, G., Lopez-Izquierdo, R., Gonzalez-Manzano, I., Carmen Tormos, M., Martin-Nuñez, G.M., Rojo-Martinez, G., Saez, G. T., Martín-Escudero, J.C., Redon, J., Javier Chaves, F. Plasma selenium levels and oxidative stress biomarkers: A gene–environment interaction population-based study. Free Radical Biology and Medicine. 2014; 74, 229-236.
37. Gao F, Kinnula VL, Myllärniemi M, Oury TD. Extracellular Superoxide Dismutase in Pulmonary Fibrosis. Antioxid Redox Signal. 2008; 10(2): 343-354.
38. Gechev T, Willekens H, Van Montagu M, et al. Different responses of tobacco antioxidant enzymes to light and chilling stress. J Plant Physiol. 2003; 160: 509-515.
39. Green RM, Graham M, O'Donovan MR, Chipman JK, Hodges NJ. Subcellular compartmentalization of glutathione: correlations with parameters of oxidative stress related to genotoxicity. Mutagenesis. 2006; 21(6): 383-390.
40. Gutteridge JMC. Lipid Peroxidation and Antioxidants as Biomarkers of Tissue Damage. Clin Chem. 1995; 41(12): 1819-1828.

41. Gürkan AS, Bozdağ-Dündar O. Coenzyme Q10. Journal of Faculty of Pharmacy of Ankara. 2005; 34(2): 129-154.
42. Halliwell B, Gutteridge JMC. Free Radicals in Biology and Medicine. 3rd ed. p.10-121. Oxford University Press, New York, USA; 1999.
43. Hellman NE, Gitlin JD. Ceruloplamin metabolism and function. Annu Rev Nutr. 2002; 22:439-58;
44. Hevia D, Mayo JC, Tan DX, Rodriguez-Garcia A, Sainz RM. Melatonin Enhances Photo-Oxidation 2',7'-Dichlorodihydrofluorescein by an Antioxidant Reaction That Renders N1-Acetyl-N2-Formyl-5-Methoxykynuramine (AFMK). PLoS ONE. 2014; 9(10): e109257. doi:10.1371/journal.pone.0109257.
45. Hoffmann, P. R., Berry, M. J. The influence of selenium on immune responses. Molecular Nutrition ve Food Research. 2008; 52(11), 1273-1280.
46. Hussein HK, Elnaggar MH, Al-Zahrani NK. Antioxidant role of folic acid against reproductive toxicity of cyhalothrin in male mice. Glo Adv Res J Environ Sci Toxicol. 2012; 1(4): 66-71.
47. Ighodaro O.M., Akinloye O.A. First line defence antioxidants-superoxide dismutase (SOD), catalase (CAT) and glutathione peroxidase (GPX): Their fundamental role in the entire antioxidant defence grid. 2018; 54(4), 287-293.
48. Iliesiu A, Campeanu A, Dusceac D. Serum uric acid and cardiovascular disease. Maedica J Clin Med. 2010; 5(3): 186-192.
49. Jialal, I. And Fuller, C.J. Oxidized LDL andantioxidants. Clin. Cardiol. 1993; 16: 16-19;
50. Thomas, M.J. The Role of Free Radicals and Antioxidants. Critical Reviews in Food and Science Nutrition. 1995; 35(1-2): 21-39.
51. Kalinina EV, Chernov NN, Novichkova MD. Role of Glutathione, Glutathione Transferase, and Glutaredoxin in Regulation of Redox-Dependent Processes. Published in Uspekhi Biologicheskoi Khimii. 2014; 54: 299-348.
52. Karlsson, J., Ronneberg, R., Semb, B. () Vitamins Q and E, extracorporal circulation and hemolysis. Mol. Cell. Biochem. 1997; 173(1-2): 33-41.
53. Kim Y, Kim DC, Cho ES, Ko SO, Kwon WY, Suh GJ, Shin HK. Antioxidant and antiinflammatory effects of selenium in oral buccal mucosa and small intestinal mucosa during intestinal ischemia-reperfusion injury. J Inflamm. 2014; 11(36) doi:10.1186/s12950-014-0036-1.

54. Kirkman HN, Galiano S, Gaetani GF. The function of catalase-bound NADPH. J Biol Chem. 1987; 262(2): 660–666.
55. Kramer K., Nutra ceutials in Heath and Disease Prevention. Marcel Dekker Incorporated, New York. 2001; 8:113.
56. Kumar AN, Aruna P, Naidu JN, Kumar R, Srivastava AK. Review of Concepts and Controversies of Uric Acid as Antioxidant and Pro-Oxidant. Archives Medical Review Journal. 2015; 24(1): 19-40.
57. Lagman M, Ly J, Saing T, Kaur Singh M, Vera Tudela E, Morris D, et al. Investigating the Causes for Decreased Levels of Glutathione in Individuals with Type II Diabetes. PLoS ONE. 2015; 10(3): e0118436. doi:10.1371/journal.pone.0118436.
58. Lamb C, Dixon RA. The oxidative burst in plant disease resistance. Annu Rev Plant Physiol Plant Mol Biol 1997; 48: 251-275.
59. Larson RA. The antioxidants of higher plants. Phytochemistry. 1988; 27(4): 969-978.
60. Levine, M. New Concepts in Biology and Biochemistry of Ascorbic Acid. New Engl. J.Med. 1997; 314: 892-901.
61. Levine, M., Morita, K. Ascorbic Acid in Endocrine Systems. Vitamins and Hormons 1987; 42:2-63.
62. Li Y, Schellhorn HE. New developments and novel therapeutic perspectives for vitamin C. J Nutr. 2007; 137(10): 2171-2184.
63. Li WC, Mo LJ, Shi X, Lin ZY, Li YY, Yang Z et al. Antioxidant status of serum bilirubin, uric acid and albumin in pemphigus vulgaris. Clin Exp Dermatol 2018; 43 (2): 158-63.
64. Liguori I, Russo G, Curcio F, et al. Oxidative stress, aging, and diseases. Clin Interv Aging 2018; 13: 757-772.
65. Limon-Pacheco J, Gonsebatt ME. The role of antioxidants and antioxidantrelated enzymes in protective responses to environmentally induced oxidative stress. Mutat Res. 2009; 674(1-2): 137-147.
66. Liu Y, Li P, Lu J, Xiong W, Oger J, Tetzlaff W et al. Bilirubin possesses powerful immunomodulatory activity and suppresses experimental autoimmune encephalomyelitis. J Immunol 2008; 81 (3): 1887–97.
67. Loudianos G, Gitlin JD. Wilson's disease Sem Liv Dis 2000;20:353- 64.
68. Mercan, U. Toksikolojide serbest radikallerin önemi. Yüzüncü Yıl Üniversitesi Veterinerlik Fakültesi Dergisi. 2004; 15, 91-96.
69. Mruk DD, Silvestrini B, Meng-Yun MO, Cheng CY. Antioxidant Superoxide Dismutase - a Review: Its Function, Regulation in the Testis, and Role in Male Fertility. Contraception. 2002; 65(4): 305-311.

70. Niki, E., Kawakami, A., Yamamoto, Y., Kamiya, Y. Oxidation of Lipids. VIII. Synergistic Inhibition of oxidation of vitamin E and vitamin C. Bull. Chem. Soc. Japan. 1985; 58:1971-78.
71. Niki, E. Vitamin C as an Antioxidant. World Rev. Nutr. Diet. 1991; 64: 3-30.
72. NordbergJ, Arner SJ. Reactive Oxygen Species, Antioxidant, And The Mammalian Thioredoxin System. Free Radic Biol Med. 2001; 31(11): 1287-1312.
73. Orbea A, Fahimi HD, Cajaraville MP. Immunolocalization of Four Antioxidant Enzymes in Digestive Glands of Molluscs and Crustaceans and Fish Liver. Histochem Cell Biol. 2000; 114(5): 393-404.
74. Özkan A, Fışkın K. Serbest Oksijen Radikalleri, Karsinogenez ve Antioksidant Enzimler. TürkHematoloji Onkoloji Dergisi. 2004; 14: 52-60.
75. Packer L. Protective role of vit E in biological systems. Am J Clin Nutr. 1991; 53: 1050-5.
76. Packer L., Witt E., Tritschler H.J., α-Lipoic acid as a biological antioxidant. Science Direct-Free Radical Biology & Medicine. 1995; 19(2): 227-250.
77. Paganga G, Miller N, Rice-Evans CA. The polyphenolic content offruit and vegetables and their antioxidant activities. What does a serving constitute? FreeRadic Res. 1999; 30:153-162.
78. Patlevič P, Vašková J, Švorc P Jr, Vaško L, Švorc P. Reactive oxygen species and antioxidant defense in human gastrointestinal diseases. Integr Med Res 2016; 5: 250-258.
79. Pei S, Minhajuddin M, Callahan KP, Balys M, Ashton JM, Neering SJ, Lagadinou ED, Corbett C, Ye H, Liesveld JL, O'Dwyer KM, Li Z, Shi L, Greninger P, Settleman J, Benes C, Hagen FK,
80. Pellegrini N, Miglio C, Del Rio D, et al. Effect of domestic cooking methods on the total antioxidant capacity of vegetables. Int J Food Sci Nutr. 2009; 60 (Suppl 2): 12–22.
81. Pham-Huy LA, He H, Pham-Huy C. Free Radicals, Antioxidants in Disease and Health. Int J Biomed Sci. 2008; 4(2): 89-96.
82. Rani, V., Deep, G., Singh, R. K., Palle, K. ve Yadav, U. C. Oxidative stress and metabolic disorders: Pathogenesis and therapeutic strategies, Life Sciences. 2016; 148:183-193.
83. Ratnam DV, Ankola DD, Bhardwaj V, et al. Role ofantioxidants in prophylaxis and therapy: A pharmaceutical perspective. J Control Release 2006;113: 189–207.

84. Rayman, M.P. The importance of selenium to human health. The Lancet. 2000; 356(9225), 233-241.
85. Reiter RJ, Melchiorri D, Sewerynek E, PoeggelerB, Barlow-Walden L, Chuang J, Ortiz GG, Acuna-Castroviejo D. A review of the evidence supporting melatonin‘s role as an antioxidant. J Pineal Res. 1995; 18(1): 1-11.
86. Reiter RJ, Acuna-Castroviejo D, DunXian T, Burkhardt S. Free Radical-Mediated Molecular Damage. Mechanisms for the Protective Actions of Melatonin in the Central Nervous System. Ann N Y Acad Sci. 2006; 939(1). doi: 10.1111/j.1749-6632.2001.tb03627.x
87. Roche M, Rondeau P, Singh NR, Tarnus E, Bourdon E. The antioxidant properties of serum albümin. FEBS Lett. 2008; 582(13):1783-1787.
88. Sen S, Chakraborty R, Sridhar C, Reddy YSR, De B. Free radicals, antioxidants, diseases and phytomedicines: Current status and future prospect. International Journal of Pharmaceutical Sciences and Research. 2010; 3(1): 91-100.
89. Sen S, Chakraborty R. The Role of Antioxidants in Human Health. American Chemical Society, Oxidative Stress: Diagnostics, Prevention and Therapy. 2011; Chapter 1: 1-37.
90. Sinha S, Singh SN, Ray US. Total antioxidant status at high altitude in lowlanders and native highlanders: role of uric acid. High Alt Med Biol 2009; 10: 269-274.
91. Soriani M, Pietraforte D, Minetti M. Antioxidant potential of anaerobic human plasma: role of serum albumin and thiols as scavengers of carbon radicals. Arch Biochem Biophys 1994; 312: 180-188.
92. Sumien N, Heinrich KR, Shetty RA, Sohal RS, Forster MJ. Prolonged intake of coenzyme Q10 impairs cognitive functions in mice. J Nutr 2009; 139: 1926-1932.
93. Sun, Q.-A., Wu, Y., Zappacosta, F., Jeang, K.-T., Lee, B. J., Hatfield, D. L., Gladyshev, V. N. (). Redox regulation of cell signaling by selenocysteine in mammalian thioredoxin reductases. Journal of Biological Chemistry. 1999; 274(35), 24522-24530.
94. Şener G, Yeğen Berrak Ç. İskemi Reperfüzyon Hasarı. Klinik Gelişim Dergisi. 2009; 22: 5-13.
95. Takada Y, Hachiya M, Park SH, Osawa Y, Ozawa T, Akashi M. Role of Reactive Oxygen Species in Cells Overexpressing Manganese Superoxide Dismutase: Mechanism for Induction of Radioresistance. Molecular Cancer Research 2002;1: 137–146.

96. Title LM, Cummings PM, Giddens K, Genest JJ, Nassar BA. Effect of Folic Acid and Antioxidant Vitamins on Endothelial Dysfunction in Patients With Coronary Artery Disease. J Am Coll Cardiol. 2000; 36(3): 758-765.
97. Tolbert, B.M. Metabolism and Function of Ascorbic Acids and Metabolites. Int. J. Vitam. Nutr. Res. 1985; 27: 122-138.
98. TownsendDM, Tew KD, Tapiero H. The importance of glutathione in human disease. Biomed Pharmacother. 2003; 57(3-4): 145-155.
99. Valko M, Leibfritz D, Moncola J, Cronin MTD, Mazura M, Telser J. Free radicals and antioxidants in normal physiological functions and human disease. Int J Biochem Cell Biol. 2007; 39: 44-84.
100. Van-Der-Meulen JH, McArdle A, Jackson MJ, Faulkner JA. Contraction-induced injury to the extensor digitorum longus muscles of rats: the role of vitamin E. J Appl Physiol. 1997; 83(3): 817-23.
101. Yoshikawa, T., Naito, Y. What is Oxidative Stress? Japan Med Association Journal, 2002; 45(7), 271-276.
102. Young IS, Woodside JV. Antioxidants in Health and Disease. J Clin Pathol. 2001; 54(3): 176-186.
103. Zámocky´ M, Koller F. Understanding the structure and function of catalases: clues from molecular evolution and in vitro mutagenesis. Prog Biophys Mol Biol. 1999; 72(1): 19-66.
104. Waring WS. Uric acid: an important antioxidant in acute ischaemic stroke. QJM. 2002; 95(10): 691-693.
105. Willcox JK, Ash SL, Catignani GL. Antioxidants and prevention of chronic disease. Crit Rev Food Sci Nutr. 2004; 44(4): 275-295.

Natural Nanomaterials Prepared By Biomimetic Approaches: Ferritin Nanocages

Assist. Prof. Dr., Tuğba Nur ASLAN

Necmettin Erbakan University, Faculty of Science, Department of Molecular Biology and Genetics, Konya, Turkey
e-mail: taslan@erbakan.edu.tr
(ORCID: https://orcid.org/0000-0002-5516-3603)

INTRODUCTION

BIOMIMETIC MATERIALS

To transfer biological functions to artificial materials and nanoparticles by biomimetic approaches, it is first necessary to understand about biological processes and their structures as much as possible. Biomineralization, the process by which biological systems control the nucleation and growth of inorganic solids, occurs in most organisms. Among known examples, there exists bones, teeth, and seashells, but also proteins such as ferritins and Dps ((DNA protection during starvation) proteins, which function to store iron(Zeth, Hoiczyk, & Okuda, 2016). The cage-like structure of these proteins has an internal cavity in which the biomineralization process occurs with controlled nucleation and mineral growth of iron oxides(Yoshimura, 2006). The size of the protein interior creates an upper limit for the growth of the iron oxide particle. These protein cages are important models for understanding the biochemical basis of iron biomineralization and protein-mediated inorganic material synthesis.

Once the structure and functions of biological molecules are known, hybrid molecules including peptides, lipids and organic polymers can be synthesized and nanoporous coatings, biomimetic nanofibers, bioinorganic composites can be developed for tissue engineering. Moreover, virus-based (virosomes), mammalian cell-based (exosomes) and bacteria-fungus based (bacteria ghosts, yeast cells) nanocarrier systems are given as biomimetic examples (Aydın, Aydın, Çetiner, & Erel-Akbaba, 2022; Xie et al., 2019).

Some protein structures such as mammalian ferritin, small heatshock protein from Methanococcusjannaschii (sHsp), DNA-binding (Dps) proteins, bacteriophage MS2, lumazine synthase (LS), and viral capsids; Cowpea chlorotic mottle virus (CCMV), Cowpea mosaic virus (CPMV), Brome mosaic virus (BMV) and tobacco mosaic virus (TMV) have been used as biological reaction vessels (M. Uchida et al., 2007). These container-like cage structures can be manipulated both chemically and genetically thanks to their different surfaces to impart new functionality in such a way that the protein protects its intact structure(M. Uchida et al., 2007). All the surfaces of (inner surface, outer surface, and interfaces between subunits) can be modified for a single protein cage and it is possible to encapsulate a synthetic cargo molecule in a single cage, target it to a specific surface or cell at the same time. Thus, a single protein cage can be able to gain multiple functionality(M. Uchida et al., 2007; M. Uchida et al., 2006).Protein complexes with defined interior spaces, such as virus capsids, ferritins, DNA binding (Dps) and heat shock (sHsp) proteins, have become particularly attractive for biotechnological applications(D. He &

Marles-wright, 2015). Metallic nanoparticles and nanocomposites can be assembled both inside and on the surface of the protein cage. They can be easily produced in large quantities; they have well-characterized atomic structures; they are usually monodisperse in their solution(J. He, Fan, & Yan, 2019). When protein cages are used for material synthesis, they provide ideal nano-reaction environments for material synthesis under mild biomimetic conditions(M. Uchida, Kang, Reichhardt, Harlen, & Douglas, 2010). Since the dimensions of the nanomaterials synthesized in the interior cavity of these proteins would be as much as the protein interior space, the material size limits are certain. Proteins can be mineralized to form homogeneous and certain sized particles, some reaction parameters such as metal ion : protein ratio and reaction rate should be optimized.Among the cage-like systems used as a reaction vessel (template) from biological platforms, ferritin protein is the most widely used protein since it is naturally found in the body.

FERRITIN PROTEIN CAGE AND ITS PROPERTIES

Ferritin is found in biological species such as bacteria, plants, and mammals as the protein that stores iron in the body. In mammals, it is most abundant in the liver, spleen, and bone marrow. It storesup to 4500 Fe (III) atoms in the protein interior space and Fe (III) atom is in the form of iron (III) oxide (FeOOH) compound(Zhao et al., 2003). Ferritin has a stable and robust protein cage and has a molecular weight of 450 kDa. It consists of 24 subunits with an outer diameter of 12nm and an inner diameter of 8nm, stacked in a 4:3:2 symmetry(Chasteen & Harrison, 1999). In the protein structure, there are hydrophilic channelswhich behaves as the passageway for metal ions, and hydrophobic channelswhere proton exit, or electron entry is provided. There are eight hydrophilic and six hydrophobic channels around three-fold symmetry axis and four-fold symmetry axis of protein, respectively(Chasteen & Harrison, 1999; Kramer et al., 2004).

The protein consists of heavy (H) and light (L) polypeptide chains. These subunits are ~ %50 homologous in their amino acid sequences. The contents of H- and L- subunits vary between biological species and organ. Human H-subunit has enzymatic ferroxidase sites which is responsible for the oxidation of iron (II) to iron (III). L-subunit has no such a site but contains additional glutamate residues on the interior surface of the proteinThese negatively charged residues on the inner surfaces of L subunits facilitates mineralization to form the iron core(Zhao et al., 2003).

In ferritins, the process of storing iron includes the reaction of iron (II) ion and oxygen at a ferroxidase center in the protein interior, then biomineralization

of an insoluble ferric nanoparticle by catalyzing the oxidation of iron (II) to iron (III) at the ferroxidase center.On the other hand, ferritin protein can be synthetically obtained without an iron core by dialysis method, then the empty protein cage is called apoferritin(Chasteen & Harrison, 1999). The protein cage has 3 different surfaces; these are the inner surface, the outer surface and the inter-subunit surfaces(B. M. Uchida et al., 2007).

IRON MINERALIZATION WITHIN THE APOFERRITIN PROTEIN SHELL: MAGNETOFERRITIN FORMATION

The iron stored by ferritin in the body is not of magnetic property, but with a similar biomimetic approach, iron oxide nanoparticles could be synthesized with magnetic properties in apoferritin cages to be used as a magnetic imaging agent (Balejc, 2019; Jordan, Caplan, & Bennett, 2010).

In a typical synthesis, magnetic iron oxide nanoparticles are synthesized in the presence of Fe^{2+} and Fe^{3+} in alkaline medium by coprecipitation method. Biomineralization of magnetic iron oxide nanoparticles in the protein cage involves Fe^{2+}entry through hydrophilic channels of protein, oxidation of Fe^{2+} to Fe^{3+} at ferroxidase centers and through the reaction between Fe^{2+} and Fe^{3+} with the help of an oxidant (H_2O_2), iron oxide (Fe_3O_4) nuclei formation occurs at the nucleation sites in the cavity (Equation 1)(M. Uchida et al., 2006).Then growth of iron oxide coresoccursup to 8 nm. Magnetic iron oxide encapsulated apoferritin cages are called as magnetoferritin(Balejc, 2019).

$$3Fe^{2+} + H_2O_2 + 2H_2O \rightarrow Fe_3O_4 + 6H^+$$

Equation 1

Magnetoferritin nanocages could be synthesized by different iron loading factors, defined as Fe atom/protein cage. It was shown that magnetoferritin with the loading factor of 5000 Fe atom /protein cage could be synthesized (Aslan, Aşık, & Volkan, 2016).It is the theoretical loading factor, experimental loading factors could be determined by Bradford assay and ICP-MS analysis for protein and iron concentration determinations, respectively(Aslan et al., 2016).

Magnetic nanoparticles are of importance for their several applications such as hyperthermia, magnetic delivery, and magnetic resonance imaging (MRI). There are many examples of surface modified magnetoferritin nanocages for targeting and therapy of cancer cells in literature (Kitagawa et al., 2017; Terashima et al., 2011; M. Uchida et al., 2006). MRI efficiency of magnetoferritins were also evaluated so much up to now(M. Uchida et al., 2008). Recently, magnetoferritin nanocages were proposed as effective T2 contrast agents while magnetoferritin may not serve as T1 contrast agent in MRI(Aslan, 2022).

PROPERTIES OF APOFERRITIN

The important biological function of apoferritin is its ability to bind and store iron; iron is stored in the liver in the form of ferritin and in blood in the form of hemoglobin. Another role of apoferritin being as protecting human leukemia orendothelial cells from oxidative stresswas also demonstrated in literature(Sergeev, Dolinska, & Hejtmancik, 2019).Apoferritin produced from horse spleen was first studied and used as a template in 1978 for the synthesis of inorganic nanoparticles (Banyard, Stammers, & Harrison, 1978). Apoferritin has a robust structure that can withstand up to 70°C and a wide pH range(pH 2.0–10.0)(Heger, 2014).

Apoferritin can be reversibly separated into its subunits and reassembled into its intact structure depending on pH of the medium. Apoferritin degradation begins at pH: below ~3 and above pH: ~10 (Valero et al., 2011). Then, reassembly of apoferritin into its spherical structure occurs at pH: ~7 (Aime & Frullano, 2002). Trapping of small molecules inside the inner cavity of apoferritin is successfully achieved by disassembly route (Makino et al., 2011). The pH of apoprotein solution is arranged to below 3 or above 10, then molecules that will be encapsulated in protein cage are added to the protein solution. Then, the pH of protein solution is again arranged to pH: ~7, the dissociated subunits reassemble while reforming the 24-mer ferritin and trapping the small molecules within its interior. This procedure is referred to as disassembly/reassembly method (Figure 1).

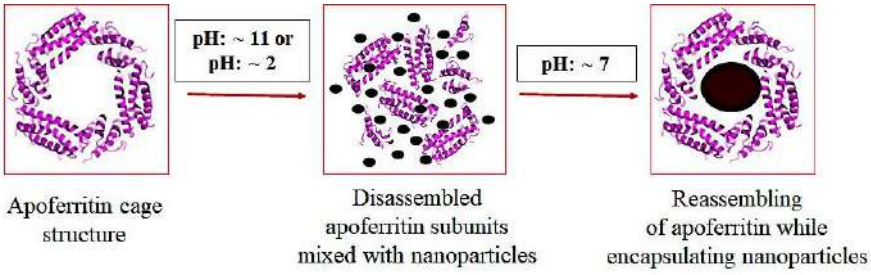

Figure 1. Disassembly/Reassembly of apoferritin for nanoparticle encapsulation.

Apoferritin and ferritin proteins that were isolated from mammalian cellsare commercially available such as horse spleen apoferritin, ferritin from human liver, however apoferritin can also be prepared by a reduction and complexation procedure by using ferritin containing iron (III) oxides (FeOOH(k)). Fe^{3+} ions that are bond to the interior protein cavity are reduced to Fe^{2+} ions by a reducing agent (thioglycolic acid, 2-2'bipyridyl)at 4 ^{0}C and under N_2 purge, Fe^{2+} ions are

then removed from protein cavity by exclusive dialysis for days. The removal of iron content is understood by observing the protein color. Dialysis is continued until the color changes from dark brown to light yellow(Funk, Lenders, Crichton, & Schneider, 1985; Ueno et al., 2004).

APPLICATIONS OF FERRITIN/APOFERRITIN IN BIOMEDICAL FIELD

In recent years, apoferritin or ferritin proteins of biological origin have been used as various nanocarrier systems for biomedical applications especially for cancer diagnosis and therapy up to now due to its biocompatibility and low cytotoxicity. Moreover, by using the amine and carboxylic functional groups from amino acid groups such as lysine, cysteine, histidine, some specific ligands could be able to be attached to the external surface of protein thus various functionalities and multifunctionality could be gained to the protein nanocarriers(Aslan et al., 2016).

In the previous studies in literature, it was observed that ferritin was easily and effectively taken up by the cells by endocytosis ways and due to the existence of receptors on cell surfaces that are specific to membranes placed on some tumor tissues. According to the results, ferritin and apoferritin systems were more toxic on cancerous cells and protein cages itself protect its biocompatibility up to higher cell viability percentages. On the other hand, cancerous cell death was generally caused by apoptosis and necrosis(Aşık, Aslan, Güray, & Volkan, 2018).

In the literature, there are some surface modifications for biological applications; fluorophore groups were bonded to amine groups of ferritin and fluorescence nanoparticles were obtained with high water solubility(Khoshnejad, Parhiz, Shuvaev, Dmochowski, & Muzykantov, 2018); cationic charged ferritin nanoparticles were prepared by surface modification of carboxylic acids with N,N-dimethyl-1,3,propanediamine for the aim of labeling cells and tissues(Jutz, Rijn, Miranda, & Bo, 2013); ferritin nanocages were modified by incorporating some small peptides on exterior surface to be used as selective targeting agent to vessel systems. As an example, RGD-4C (CDCRGDCFC) peptide selectively binds to αvβ3 αvβ5 cell receptors and can be used as targeting ligand to cancer cells since the activity of these cell receptors diminishes in angiogenic vessel system. Thus, RGD-4C peptide can be utilized for targeting to cancer cells by binding it to heat shoch proteins, ferritins, quantum dots, anticancer agents, doxorubicin, ex. It was reported that bonded RGD-4C peptides to ferritin did not disturb the intact structure of ferritin. In the study, peptide bonded ferritin displayed high binding affinity to

C-32 melanoma cells containing $\alpha_v\beta_3$ receptors on its surface (M. Uchida et al., 2006).

Gold nanoparticles were synthesized in the cavity of apoferritin as a computed tomography (CT) agent and surface of the protein was functionalized by binding a glucose analog of 2-amino-2-deoxy-glucose (2DG) molecule through EDC/NHS activation for targeting MCF-7 cells since cancer cells need more glucose due to its high metabolic activity, thus this situation increases the express of glucose transport proteins on cell surfaces(D. He & Marles-wright, 2015; B. M. Uchida et al., 2007). The uptake of the prepared nanoparticles was evaluated in breast cancer cells (MCF-7) and normal cells (MCF-10A) and the effectiveness of nanoparticles as a CT contrast agent was evaluated using micro-CT instrument. According to the results, prepared nanoparticles were displayed more uptake in MCF-7 cells and CT images of MCF-7 cells were successfully taken(Aslan, Aşık, Güray, & Volkan, 2020).

It is known that apoferritin has a self-targeting property to transferrin receptor 1 (TfR1) andit can cross the brain blood barrier due to the high expression of TfR1 in both brain endothelial and glioma cells, thusdoxorubicin anticancer drug was encapsulated unmodified apoferritin nanocage for brain targeting. The research displayed that apoferritin had significant penetrating and targeting effects in mouse glioma C6 and mouse brain endothelial bEnd.3 cell lines (Chen et al., 2017).In the other study,idarubicin anticancer drug was encapsulated within apoferritin through disassembling/reassembling procedure at pH 2 and pH 7.4 for the evaluation of the efficiency of its anticancer activity towards human breast cancer cell line (MCF-7).Free drug and drug loaded apoferritin toxicity was investigated and the results indicated that drug loaded apoferritin displayed more toxicity on MCF-7 cells. It was attributed to self-targeting ability of apoferritin on tumor cells towards highly expressed of SCARA5 receptor and transferrin 1 receptor (TfR1) (Rafipour, 2021).

There are two ways to incorporate nanoparticles in apoferritin cages; termed by reassembly and nanoreactor routes as mentioned before. It was shown in literature that luminescent PbS quantum dots for studies of biological media were successfully incorporated in apoferritin cage by two approaches(Hennequin et al., 2008).Apoferritin nanocages were designed forsynergistic combination effect of Quercetin with Curcumin on breast cancer cell (MCF7) apoptosis.Protein nanoparticles were found to increase the targeting of MCF 7 cells and displayed a synergistic cytotoxic effect for MCF10A cells (Mansourizadeh et al., 2020).

Modified protein cage structures arehighly promising candidatesin biomedical applications. As mentioned before, poor biocompatibility and

possible toxicities towards especially healthy cell and tissues created by naked nanoparticles limit their utilization in clinical applications. Thus, using biomimetic approaches would shed on light biocompatible theragnosticfor future research on these natural, versatile promising protein assemblies.

CONCLUSION

Biomimetic approaches for obtaining nanoparticles that will be used in biomedical is a current issue and attract great interest. The advantages of using biological origin templates such as ferritin and similar proteins are that they are natural carriers that do not stimulate the body's defense mechanism, since their behavior in the body is well-defined, and allows high-dose use. Nanomaterials andeven nanotheragnosticin literature are generally prepared chemically and it is known that these nanoparticles have cytotoxic or genotoxic effects in vitro to a large extent. Thanks to the biomimetic approach, disadvantages such as toxicity and biocompatibility would be prevented.

Some advantages of protein cages to be used in many applications can be summarized as.Protein cages can be used for preparation of nanometer sized nanoparticles, since nanoparticles cannot be bigger than their interior diameter, so this provides a perfect control over mineral growth. Using protein cages prevents agglomeration between particles and provides water solubility. Ferritin and similar protein cages facilitate the cell uptake of nanoparticles by endocytosis.Each modified protein cage differs in size, function, chemical and thermal stability. The preparation of metal nanoparticles in a cage-like structure allows their optical and electronic properties, catalytic activities, and antimicrobial properties to be portable.

REFERENCES

1. Aime, S., & Frullano, L. (2002). Compartmentalization of a Gadolinium Complex in the Apoferritin Cavity : A Route To Obtain High Relaxivity Contrast Agents for Magnetic Resonance Imaging. *Zuschriften*, *521*(6), 1059–1061.
2. Akbaba, H., Selamet, Y., & Kantarc, A. G. (2017). Synthesis and characterization of cationic lipid coated magnetic nanoparticles using multiple emulsions as microreactors. *Journal of Magnetism and Magnetic Materials*, *426*(July 2016), 518–524. https://doi.org/10.1016/j.jmmm.2016.11.126
3. Antonelli, A., & Magnani, M. (2022). Journal of Magnetism and Magnetic Materials SPIO nanoparticles and magnetic erythrocytes as contrast agents for biomedical and diagnostic applications. *Journal of Magnetism and Magnetic Materials*, *541*(September), 168520. https://doi.org/10.1016/j.jmmm.2021.168520
4. Aşık, E., Aslan, T. N., Güray, N. T., & Volkan, M. (2018). Cellular uptake and apoptotic potential of rhenium labeled magnetic protein cages in MDA-MB-231 cells. *Environmental Toxicology and Pharmacology*, *63*(August), 127–134. https://doi.org/10.1016/j.etap.2018.08.014
5. Aslan, T. N. (2022). Relaxivity properties of magnetoferritin : The iron loading effect. *Journal of Bioscience and Bioengineering*, *133*(5), 474–480. https://doi.org/10.1016/j.jbiosc.2022.01.005
6. Aslan, T. N., Aşık, E., Güray, N. T., & Volkan, M. (2020). The potential application of gold - apoferritin nanocages conjugated with 2 - amino - 2 - deoxy - glucose for imaging of breast cancer cells. *JBIC Journal of Biological Inorganic Chemistry*, *25*, 1139–1152. https://doi.org/10.1007/s00775-020-01830-y
7. Aslan, T. N., Aşık, E., & Volkan, M. (2016). RSC Advances Preparation and labeling of surface-modi fi ed magnetoferritin protein cages with a rhenium (I) carbonyl complex for magnetically targeted radiotherapy. *RSC Advances*, 8860–8869. https://doi.org/10.1039/c5ra19696e
8. Aydın, E., Aydın, A., Çetiner, G., & Erel-Akbaba, G. (2022). Nature-Inspired Biomimetic Nanocarrier Systems. *J. Fac. Pharm. Ankara*, *46*(2), 551–575. https://doi.org/10.33483/jfpau.1033286
9. Balejc, L. (2019). Influence of synthesis temperature on structural and magnetic properties of magnetoferritin. *Mendeleev Coomunications*, *29*, 279–281. https://doi.org/10.1016/j.mencom.2019.05.012

10. Banyard, S. H., Stammers, D. K., & Harrison, P. M. (1978). Electron Density Map of Apoferritin at 2.8-A Resolution. *1978 Nature Publishing Group*, *271*(November), 282.
11. Berry, C. C., & Curtis, A. S. G. (2003). Functionalisation of magnetic nanoparticles for applications in biomedicine. *Journal of Physics D: Applied Physics PII:*, *36*, R198–R206.
12. Chasteen, N. D., & Harrison, P. M. (1999). Mineralization in Ferritin : An Efficient Means of Iron Storage. *Journal of Structural Biology*, *194*, 182–194.
13. Chen, Z., Zhai, M., Xie, X. Y., Zhang, Y., Ma, S., Yu, F., … Mei, X. (2017). Apoferritin Nanocage for Brain Targeted Doxorubicin Delivery Apoferritin Nanocage for Brain Targeted Doxorubicin Delivery. *ACS Molecular Pharmaceutics*. https://doi.org/10.1021/acs.molpharmaceut.7b00341
14. Das, S., Bhowmick, M., Chattopadhyay, S. ., & Basak, S. (2015). Application of biomimicry in textiles. *Current Science Association*, *109*(5), 893–901. https://doi.org/10.18520/vl
15. Fisch, M. (2017). The Nature of Biomimicry : Toward a Novel Technological Culture. *Science, Technology, & Human Values*, *42*(5), 795–821. https://doi.org/10.1177/0162243916689599
16. Funk, F., Lenders, J.-P., Crichton, R. R., & Schneider, W. (1985). Reductive Mobilisation of Ferritin İron. *Eur. J. Biochem*, *152*(June), 167–172.
17. Gavas, S., Quazi, S., & Karpiński, T. M. (2021). Nanoparticles for Cancer Therapy : Current Progress and Challenges. *Nanoscale Research Letters*. https://doi.org/10.1186/s11671-021-03628-6
18. He, D., & Marles-wright, J. (2015). Ferritin family proteins and their use in bionanotechnology. *New Biotechnology*, *32*(6), 651–657. https://doi.org/10.1016/j.nbt.2014.12.006
19. He, J., Fan, K., & Yan, X. (2019). Ferritin drug carrier (FDC) for tumor targeting therapy. *Journal of Controlled Release*, *311–312*(June), 288–300. https://doi.org/10.1016/j.jconrel.2019.09.002
20. Heger, Z. (2014). Apoferritin applications in nanomedicine. *Nanomedicine*, *9*, 2233–2245.
21. Hennequin, B. B., Turyanska, L., Ben, T., Beltra, A. M., Thomas, N. R., Molina, S. I., Patane, A. (2008). Aqueous Near-Infrared Fluorescent Composites Based on Apoferritin-Encapsulated PbS Quantum Dots. *Advanced Materials*, *20*, 3592–3596. https://doi.org/10.1002/adma.200800530

22. Jeevanandam, J., Barhoum, A., Chan, Y. S., Dufresne, A., & Danquah, M. K. (2018). Review on nanoparticles and nanostructured materials : history , sources , toxicity and regulations. *Beilstein Journal of Nanotechnology*, 1050–1074. https://doi.org/10.3762/bjnano.9.98
23. Jordan, V. C., Caplan, M. R., & Bennett, K. M. (2010). Simplified Synthesis and Relaxometry of Magnetoferritin for Magnetic Resonance Imaging. *Magnetic Resonance in Medicine*, *1266*, 1260–1266. https://doi.org/10.1002/mrm.22526
24. Jutz, G., Rijn, P. Van, Miranda, B. S., & Bo, A. (2013). Ferritin : A Versatile Building Block for Bionanotechnology. *Acs Chemical Reviews*. https://doi.org/10.1021/cr400011b
25. Kahachi, H. A. H., & Jalil, W. D. A. (2019). The Implementation of Nano-Biomimicry For Sustainability In Architecture. *Journal of Engineering and Sustainable Development*, *23*(May), 2520–0917.
26. Karthick, B., & Maheshwari, R. (2008). Lotus-Inspired Nanotechnology Applications. *Resonance*, (December), 1141–1145.
27. Khoshnejad, M., Parhiz, H., Shuvaev, V. V, Dmochowski, I. J., & Muzykantov, V. R. (2018). Ferritin-based drug delivery systems : Hybrid nanocarriers for vascular immunotargeting. *Journal of Controlled Release*, *282*(March), 13–24. https://doi.org/10.1016/j.jconrel.2018.02.042
28. Kitagawa, T., Kosuge, H., Uchida, M., Iida, Y., Dalman, R. L., Douglas, T., & Mcconnell, M. V. (2017). RGD Targeting of Human Ferritin Iron Oxide Nanoparticles Enhances In Vivo MRI of Vascular Inflammation and Angiogenesis in Experimental Carotid Disease and Abdominal Aortic Aneurysm. *J. Msgn. Reson. Imaging*, *45*, 1144–1153. https://doi.org/10.1002/jmri.25459
29. Kramer, R. M., Li, C., Carter, D. C., Stone, M. O., Naik, R. R., Group, B., & Base, W. A. F. (2004). Engineered Protein Cages for Nanomaterial Synthesis. *JACS*, *126*(14), 13282–13286.
30. Li, W. A., & Mooney, D. J. (2013). Materials based tumor immunotherapy vaccines. *Current Opinion in Immunology*, *25*(2), 238–245. https://doi.org/10.1016/j.coi.2012.12.008
31. Lurie-luke, E. (2014). Product and technology innovation : What can biomimicry inspire ? *Biotechnology Advances*, *32*(8), 1494–1505. https://doi.org/10.1016/j.biotechadv.2014.10.002
32. Makino, A., Harada, H., Okada, T., Kimura, H., Amano, H., Saji, H., … Kimura, S. (2011). Effective Encapsulation of a New Cationic

Gadolinium Chelate into. *Nanomedicine: Nanotechnology, Biology, and Medicine*, *7*(5), 638–646. https://doi.org/10.1016/j.nano.2011.01.015

33. Mansourizadeh, F., Alberti, D., Bitonto, V., Tripepi, M., Sepehri, H., Khoee, S., & Geninatti, S. (2020). Biointerfaces E ffi cient synergistic combination e ff ect of Quercetin with Curcumin on breast cancer cell apoptosis through their loading into Apo ferritin cavity. *Colloids and Surfaces B: Biointerfaces*, *191*(September), 110982. https://doi.org/10.1016/j.colsurfb.2020.110982
34. Mohammed, M., Shahda, M., Abd, A., Elmokadem, E., Mohammed, M., & Elhafeez, A. (2014). Biomimicry Levels as an Approach to The Architectural Sustainability. *Port Said Engineering Research Journal*, *18*(Semtember), 117–125.
35. Nurliyana, S., Mohamed, C., Amir, Z., Jan, B. M., Khalil, M., & Azizi, A. (2022). Colloidal Stability of CA , SDS and PVA Coated Iron Oxide Nanoparticles (IONPs): Effect of Molar Ratio and Salinity. *Polymers*, 4787. https://doi.org/https://doi.org/10.3390/polym14214787
36. Rafipour, R. (2021). Apoferritin nanocages for targeted delivery of idarubicin against breast cancer cells. *Biotechnol Appl Biochem*, (April), 1061–1067. https://doi.org/10.1002/bab.2177
37. Reier, T., Oezaslan, M., & Strasser, P. (2012). Electrocatalytic Oxygen Evolution Reaction (OER) on Ru , Ir , and Pt Catalysts : A Comparative Study of Nanoparticles and Bulk Materials. *ACS Catalysis*, *2*, 1765–1722.
38. Şengel-Türk, C. T., & Hasçiçek, C. (2009). Polimerik Nanopartiküller İlaç Taşıyıcı Sistemlerde Yüzey Modifikasyonu. *Ankara Ecz. Fak. Derg.*, *38*(2), 137–154.
39. Sergeev, Y. V, Dolinska, M. B., & Hejtmancik, J. F. (2019). Apoferritin is maintaining the native conformation of citrate synthase in vitro. *HHS Public Access*, *7*(February), 680–684.
40. Shah, A., Aftab, S., Nisar, J., Naeem, M., & Jan, F. (2021). Nanocarriers for targeted drug delivery. *Journal of Drug Delivery Science and Technology*, *62*(January), 102426. https://doi.org/10.1016/j.jddst.2021.102426
41. Tang, L., He, S., Yin, Y., Liu, H., Hu, J., Cheng, J., & Wang, W. (2021). Combination of Nanomaterials in Cell-Based Drug Delivery Systems for Cancer Treatment. *Pharmaceutics*, 1–28. https://doi.org/10.3390/pharmaceutics13111888
42. Terashima, M., Uchida, M., Kosuge, H., Tsao, P. S., Young, M. J., Conolly, S. M., … Mcconnell, M. V. (2011). Human ferritin cages for

imaging vascular macrophages. *Biomaterials*, *32*(5), 1430–1437. https://doi.org/10.1016/j.biomaterials.2010.09.029
43. Torchilin, V. P. (2014). Multifunctional, stimuli-sensitive nanoparticulate systems for drug delivery. *Nature Publishing Group*, *13*(November), 813–827. https://doi.org/10.1038/nrd4333
44. Uchida, M., Klem, M. T., Allen, M., Suci, P., Flenniken, M., Gillitzer, E., … Douglas, T. (2007). Biological Containers : Protein Cages as Multifunctional Nanoplatforms **. *Advanced Materials*, *19*, 1025–1042. https://doi.org/10.1002/adma.200601168
45. Uchida, M., Flenniken, M. L., Allen, M., Willits, D. A., Crowley, B. E., Brumfield, S., … Douglas, T. (2006). Targeting of Cancer Cells with Ferrimagnetic Ferritin Cage Nanoparticles. *JACS*, *312*(16), 16626–16633.
46. Uchida, M., Kang, S., Reichhardt, C., Harlen, K., & Douglas, T. (2010). Biochimica et Biophysica Acta The ferritin superfamily : Supramolecular templates for materials synthesis. *BBA - General Subjects*, *1800*(8), 834–845. https://doi.org/10.1016/j.bbagen.2009.12.005
47. Uchida, M., Terashima, M., Cunningham, C. H., Suzuki, Y., Willits, D. A., Willis, A. F., … Douglas, T. (2008). A Human Ferritin Iron Oxide Nano-composite Magnetic Resonance Contrast Agent. *Magnetic Resonance in Medicine*, *60*, 1073–1081. https://doi.org/10.1002/mrm.21761
48. Ueno, T., Suzuki, M., Goto, T., Matsumoto, T., Nagayama, K., & Watanabe, Y. (2004). Size-Selective Olefin Hydrogenation by a Pd Nanocluster Provided in an Apo-Ferritin Cage**. *Angewandte Chemie*, *43*, 2527–2530. https://doi.org/10.1002/anie.200353436
49. Valero, E., Tambalo, S., Marzola, P., Ortega-mu, M., Javier, F. L., Santoyo-gonz, F., … Granada, U. De. (2011). Magnetic Nanoparticles-Templated Assembly of Protein Subunits : A New Platform for Carbohydrate-Based MRI Nanoprobes. *JACS*, *133*, 4889–4895.
50. Wartlick, H., Michaelis, K., Balthasar, S., Strebhardt, K., Langer, K., Wartlick, H., … Strebhardt, K. (2008). Highly Specific HER2-mediated Cellular Uptake of Antibody-modified Nanoparticles in Tumour Cells Highly Specific HER2-mediated Cellular Uptake of Antibody-modified Nanoparticles in Tumour Cells. *Journal of Drug Targeting*, *2330*, 461–471. https://doi.org/10.1080/10611860400010697
51. Williams, T. S. (2022). Advancing research efforts in biomimicry to develop nature- inspired materials , processes for space exploration and more ef fi cient aircraft. In *Biomimicry for Aerospace*. United States Government as represented by the Administrator of the National

Aeronautics and Space Administration. https://doi.org/10.1016/B978-0-12-821074-1.00014-1

52. Xie, J., Ping, H., Tan, T., Lei, L., Xie, H., & Yang, X. (2019). Progress in Materials Science Bioprocess-inspired fabrication of materials with new structures and functions. *Progress in Materials Science*, *105*(March 2018), 100571. https://doi.org/10.1016/j.pmatsci.2019.05.004
53. Yetkin, E. G. (2020). Effects of Biomimicry on Architecture. *European Journal of Natural Sciences and Medicine*, *3*(2), 106–120.
54. Yoshimura, H. (2006). Protein-assisted nanoparticle synthesis. *Colloids and Surfaces*, *283*, 464–470. https://doi.org/10.1016/j.colsurfa.2006.01.037
55. Zeth, K., Hoiczyk, E., & Okuda, M. (2016). Ferroxidase-Mediated Iron Oxide Biomineralization : Novel Pathways to Multifunctional Nanoparticles. *Trends in Biochemical Sciences*, *41*(2), 190–203. https://doi.org/10.1016/j.tibs.2015.11.011
56. Zhao, G., Bou-abdallah, F., Arosio, P., Levi, S., Janus-chandler, C., & Chasteen, N. D. (2003). Multiple Pathways for Mineral Core Formation in Mammalian Apoferritin . The Role of Hydrogen Peroxide †. *Biochemistry*, *42*, 3142–3150.

Effects Of Plant Extracts And Phytochemicals On Mirna's In Multiple Myeloma

Assist. Prof. Dr. Ela Nur ŞİMŞEK SEZER

Selçuk University, ORCID: 0000-0003-2805-7204

What is miRNA?

Since, the past, the structure of the human genome and how it plays a role in tumour biology have been emphasized. RNA acts as a messenger between the gene and the final product, hence its decoding sites are known to play an important role in gene expression and regulation (Abdellatif, 2012; O'Bryan et al., 2017). However, advances in technology have led to the discovery of transcriptional units named Ncrnas, which include lncRNAs and small non-coding RNAs, siRNAs, snoRNAs, piRNAs, and miRNAs (Irminger-Finger et al., 2014; Zhang et al., 2018; Zare et al.,2018). The flow of data generated by genome sequencing projects over the past few decades has revealed that the vast majority of eukaryotic genomes are transcribed into non-coding RNA species. Of these, microRNA (miRNA) has received great attention. miRNAs are non-coding, regulatory RNA molecules approximately 19-25 nucleotides long. They can be found in many organisms, including mammals, plants, and even viruses. They exert a negative regulatory effect on gene expression by binding to short motifs in messenger RNA (mRNA), which is largely complementary to miRNA. The reasons for this effect; interference with the translation of mRNAs; There may be cleavage of the mRNA and destabilization of the mRNA by shortening the poly(A) tail. Studies to date have shown that miRNAs play a role as important regulators in various biological events and pathological conditions. They are thought to regulate cellular gene expression at transcriptional and post-transcriptional levels (Jackson & Standart 2017). MiRNAs have very important roles in the control of gene expression as they can cause low specificity binding of the target gene to mRNAs, mRNA degradation and translation inhibition (Ambros, 2004; Bartel, 2007).

MiRNA and cancer

MiRNAs are involved in the regulation of a wide variety of cellular processes, including proliferation, differentiation and apoptosis. It is therefore not surprising that a possible dysregulation in a single miRNA-mediated pathway would have significant physiological effects on the organism. MiRNAs are pleiotropic in nature, so they can regulate multiple genes and signalling pathways (Li et al., 2010; You et al., 2017). Some studies have shown that miRNAs are abnormally expressed or mutated in cancer, suggesting that they may play a role as a new class of oncogenes or tumour suppressor genes (Gao et al., 2017). The fact that some miRNAs function as oncogenes and others as tumour suppressor genes in various cancers reveals that miRNAs are also regulators of tumour progression, metastasis and invasion (Nicoloso et al., 2009; Le Quesne & Caldas 2010). MiRNAs are involved in every stage of cancer development and progression. Altered miRNA expressions are linked to tumour onset, progression, and persistence (Sicard et

al., 2013). In addition, it also plays a role in the processes of drug resistance, invasion and metastasis. MiRNAs may play a role in many steps such as cancer development, progression and therapeutic response; they can act as a potential oncopromotor or suppressor. This supports the idea that interfering with multiple targets is a better way to target than a single gene or signalling pathway (Sumazin et al., 2011; Shah et al., 2016). In human malignancies, a higher dysregulation is observed in miRNA expression level in cancer cells compared to healthy cells. If we consider the main reasons for these changes in miRNA expression in cancer; Amplification or deletion of genes encoding miRNAs, epigenetic changes, transcriptional regulation of miRNA, and defects in miRNA biogenesis can be cited as causes.

miRNAs with Oncogenic and Tumour Suppressive properties

miRNAs can have oncogenic or tumour-suppressive properties based on the role of the mRNA they target in molecular pathways. In various cancer cases, miRNAs with increased expression levels are referred to as oncogenic miRNAs, and miRNAs that inhibit tumour formation by suppressing oncogenes are referred to as tumour suppressor miRNAs. Oncogenic miRNAs act on the cell cycle and contribute to cancer cell growth by targeting cyclin-dependent kinase (CDK) inhibitors or transcriptional repressors, of retinoblastoma family proteins. A large-scale analysis of miRNA profiles revealed that the human miR-17-92 group is upregulated in several types of cancer, including lung cancer (Volinia et al., 2006). When looking at tumour suppressor miRNAs; Let-7 is the first miRNA family discovered and most family members have been accepted as tumour suppressor miRNAs because they are found in fragile regions with multiple cancer-associated deletions, decrease in gene expression causes oncogenic differentiation (Calin & Croce, 2006). In addition, Let-7 is one of the miRNAs most associated with poor prognosis in human cancers (Malumbres, 2013). The other tumour suppressor miRNAs are miR-145, miR-143, miR-15a and miR-16-1.

Effects of plant extracts and phytochemicals on miRNA

Plant-based natural molecules have received great interest in stopping cancer progression in recent years. Natural compounds and their derivatives are widely used in clinical therapy due to their innovative structure, high biological activity and low side effects. Increasing data have revealed that some natural compounds exhibit anticancer properties through epigenetic mechanisms (Wang et al., 2013). During the antitumor effect, natural compounds have been shown to alter the expression profiles of certain miRNAs (Lin et al., 2017). Plant extracts and phytochemicals such as resveratrol, genistein, curcumin, EGCG, I3C and DIM can

abolish cancer disease and subsequent symptoms by regulating miRNAs (Li et al. 2010).

miRNA and Multiple Myeloma

Multiple myeloma (MM) is a malignant neoplasm of B lymphocyte-derived plasma cells that usually results in the production of high amounts of monoclonal antibodies (Palumbo & Anderson 2011). Multiple myeloma (MM) is characterized by the widespread proliferation of pathological plasma cells and infiltration of other tissues and organs in the bone marrow. Many studies in in-depth research on MM have supported the use of miRNAs in the prognosis and treatment of myeloma. To date, the existence of a number of miRNAs with oncogenic potential, whose overexpression is associated with the development or progression of MM, as well as miRNAs with suppressive functions and reduced expression levels that act to inhibit oncogenes and reduce tumour growth has been demonstrated. For example; lower expression levels of miR-15a, miR-25, miR-16 let-7e and miR-744 indicates poor overall survival in cases of MM, and similarly, downregulation of miR-15a, miR16 and miR-25 and upregulation of miR-92a has been reported to be associated with shorter progression-free survival (Xu et al.,2019). In addition to prognostic and predictive miRNAs in MM, there are important miRNAs in the bone marrow microenvironment, miRNAs involved in the regulation of proliferation and growth, and miRNAs that are effective in apoptosis and migration (Szudy-Szczyrek et al., 2022). Considering the significant impact of both oncomirs and tumour suppressor miRNAs on the pathogenesis and disease course of multiple myeloma, miRNA-based therapies seem to be very important in the treatment of MM.

Plant Extracts and Phytochemicals on miRNAs in Multiple Myeloma

In recent years, agents derived from plants are preferred as new cancer therapeutics. Plant extracts and phytochemicals have a very important role in cancer treatment. Studies conducted to date show that plant-based alternative and complementary treatment methods are often preferred in cancer treatment. The effects of plant-derived components, particularly on miRNA expression levels, have been studied recently. Plant extracts and phytochemicals can regulate miRNAs and extinguish cancer cell resistance to traditional therapy (Li et al. 2010). Abnormal expression of miR-21 in MM has been shown to be associated with disease progression as well as being a predictor of poor patient prognosis (Leone et al., 2013; Wang et al., 2016). miR-21 expression is related to the hypoxic environment as well as tumour development. Thus, therapeutics targeting miR-21 may hold potential for use on hypoxic cells that have survived other anti-tumor

therapy. In a study by Liu et al. (2017), they investigated the effects of gambogenic acid on miR-21 expression in hypoxic multiple myeloma cells. Gambogenic acid is one of the main components of resin, a traditional medicine derived from the *Garcinia hanburyi* tree (Song et al., 2007) and studies have reported that gambogenic acid exhibits potent and wide-ranging anti-tumour effects. When the effect of GNA on miR-21 expression in U-266 MM cell lines under normoxia and hypoxia conditions was evaluated, it was reported that GNA treatment decreased miR-21 expression more in the hypoxia group compared to the normoxia group. In another study, Hu et al. (2013) investigated the effects of berberine, a natural isoquinoline alkaloid that can be extracted from many medicinal plants such as *Hydrastis canadensis*, *Cortex phellodendri* and *Rhizoma coptidis*, on miR-21 expression levels in multiple myeloma. Berberine exhibits various pharmacological activities such as anti-inflammatory (Kuo et al., 2004), anticancer (Lin et al., 2008; Tang et al., 2009) and antioxidant (Yin et al., 2008). The effects of berberine in leukaemia and lymphoma have recently been studied using both in vivo and in vitro approaches (Wu et al., 1998; Lin et al., 2006; Yu et al., 2007). At the end of the study, it was reported that miR-21 levels were down-regulated in a dose-dependent manner with 24-hour administration of berberine (40, 80, 120 and 160 μmol/L). Berberine has also been shown to downregulate miRNA-21 expression in RPMI-8226 cells (Luo et al., 2014). Feng et al. (2015) reported that three miRNA groups (miR-106~25, miR-17~92, and miR-99a~125b) in MM cells were significantly down-regulated after treatment with berberine. Xie et al., (2016) who examined the effect of genistein (genistein is an isoflavone found in some plants that has been described as an angiogenesis inhibitor and a phytoestrogen) on the suppression of NF-kB and modulation of caspase-3 activity on U266 multiple myeloma cells, reported that genistein leads to down-regulation of NF-kB and up-regulation of micro-RNA 29b. Among ER stress-associated microRNAs, miR-211 has been reported to act as a pro-survival miRNA and inhibit the accumulation of the proapoptotic transcription factor C/EBP homologous protein (CHOP) (Chitnis et al., 2012). In the study by Cha et al. 2018, the inhibition mechanism of *Cnidium officinale* extract in lymphoma and multiple myeloma (MM) cells was investigated and the effect of *Cnidium officinale* extract on inducing apoptosis through ROS/ER stress and apoptotic mechanisms regulated by miR-211. miR-211, one of the pro-survival miRNAs, has been reported to be decreased in U937 and U266 cells as a result of the application of the extract. Another study investigated the molecular mechanism underlying the induction of apoptosis by *Salvia miltiorrhiza* and reported upregulation of miR-216b in extract-treated U266 and U937 cells compared to control group (Kim et al., 2018). A study by Lim et al., (2019) was investigated the new

anti-cancer mechanism of *Spatholobus suberectus* extract against haematological cancers (multiple myeloma and leukaemia), also the effect on ROS/ER stress and miRNA regulation. A novel anti-cancer mechanism of extract via miR-657/ER stress-mediated apoptosis was enunciated and it was reported that the expression of oncomiR-657 in SSD-treated cell lines was decreased compared to the control group.

Conclusion

In recent years, it has been shown that disorders in the regulation of miRNA cause the emergence of various diseases, especially cancer. Therefore, miRNA expression profiles are thought to be quite promising in diagnosis and treatment. The determination of miRNA expression levels in different cancer patients and the evaluation of target mRNAs will provide significant benefits in the early diagnosis of cancer and in the development of appropriate treatment methods. In addition, identifying the miRNAs expressed at different levels in healthy tissues and tumour tissue will be very useful to elucidate the role of these miRNAs in human cancers. Multiple myeloma (MM) is the second most common type of hematological cancer. Despite new and effective treatment methods, MM is still not a curable disease. Comprehensive research is increasing day by day to find new treatment options. On the other side, miRNAs have broad application prospects in the diagnosis and treatment of MM. Further work is needed to fully understand the mechanism of MM and to develop miRNA-based therapies with the use of herbal extracts and phytochemicals.

REFERENCES

1. Abdellatif, M. (2012). Differential expression of microRNAs in different disease states. *Circulation research*, *110*(4), 638-650.
2. Ambros, V. (2004). The functions of animal microRNAs. *Nature*, *431*(7006), 350-355.
3. Bartel, D. P. (2007). MicroRNAs: genomics, biogenesis, mechanism, and function. (reprinted from Cell, vol 116, pg 281-297, 2004). *Cell*, 2007;131:11-29.
4. Calin, G. A., & Croce, C. M. (2006). MicroRNA signatures in human cancers. Nature reviews cancer, 6(11), 857-866.
5. Cha, J. A., Song, H. S., Kang, B., Park, M. N., Park, K. S., Kim, S. H., ... & Kim, B. (2018). miR-211 plays a critical role in Cnidium officinale Makino extract-induced, ROS/ER stress-mediated apoptosis in U937 and U266 cells. *International journal of molecular sciences*, *19*(3), 865.
6. Chitnis, N.S.; Pytel, D.; Bobrovnikova-Marjon, E.; Pant, D.; Zheng, H.; Maas, N.L.; Frederick, B.; Kushner, J.A.; Chodosh, L.A.; Koumenis, C.; et al. miR-211 is a prosurvival microRNA that regulates chop expression in a PERK-dependent manner. *Mol. Cell,* 2012, 48, 353–364.
7. Feng, M., Luo, X., Gu, C., Li, Y., Zhu, X., & Fei, J. (2015). Systematic analysis of berberine-induced signaling pathway between miRNA clusters and mRNAs and identification of mir-99a∼ 125b cluster function by seed-targeting inhibitors in multiple myeloma cells. *RNA biology*, *12*(1), 82-91.
8. Gao, Y., Lin, L., Li, T., Yang, J., & Wei, Y. (2017). The role of miRNA-223 in cancer: Function, diagnosis and therapy. Gene, 616, 1-7.
9. Hu, H. Y., Li, K. P., Wang, X. J., Liu, Y., Lu, Z. G., Dong, R. H., ... & Zhang, M. X. (2013). Set9, NF-κB, and microRNA-21 mediate berberine-induced apoptosis of human multiple myeloma cells. *Acta pharmacologica sinica*, *34*(1), 157-166.
10. Irminger-Finger, I., Kargul, J., & Laurent, G. (2014). Non-coding RNAs: A novel level of genome complexity. *International Journal of Biochemistry and Cell Biology*, *54*, 286.
11. Jackson, R. J., & Standart, N. (2007). How do microRNAs regulate gene expression?. *Science's STKE*, *2007*(367).
12. Kim, C., Song, H. S., Park, H., & Kim, B. (2018). Activation of ER stress-dependent miR-216b has a critical role in Salvia miltiorrhiza ethanol-extract-induced apoptosis in U266 and U937 cells. International journal of molecular sciences, 19(4), 1240.
13. Kuo, C. L., Chi, C. W., & Liu, T. Y. (2004). The anti-inflammatory potential of berberine in vitro and in vivo. Cancer letters, 203(2), 127-137.

14. Le Quesne, J., & Caldas, C. (2010). Micro-RNAs and breast cancer. *Molecular oncology*, *4*(3), 230-241.
15. Leone, E., Morelli, E., Di Martino, M. T., Amodio, N., Foresta, U., Gullà, A., ... & Tassone, P. (2013). Targeting miR-21 Inhibits In Vitro and In Vivo Multiple Myeloma Cell GrowthAntitumor Activity of mir-21 Inhibitors in Multiple Myeloma. *Clinical Cancer Research*, *19*(8), 2096-2106.
16. Li Y, Kong D, Wang Z, Sarkar FH (2010) Regulation of microRNAs by natural agents: an emerging field in chemoprevention and chemotherapy research. Pharm Res 27:1027–1041.
17. Lim, H. J., Park, M. N., Kim, C., Kang, B., Song, H. S., Lee, H., ... & Kim, B. (2019). MiR-657/ATF2 signaling pathway has a critical role in Spatholobus suberectus Dunn extract-induced apoptosis in U266 and U937 cells. *Cancers*, *11*(2), 150.
18. Lin, C. C., Kao, S. T., Chen, G. W., Ho, H. C., & Chung, J. G. (2006). Apoptosis of human leukemia HL-60 cells and murine leukemia WEHI-3 cells induced by berberine through the activation of caspase-3. Anticancer research, 26(1A), 227-242.
19. Lin, J. P., Yang, J. S., Wu, C. C., Lin, S. S., Hsieh, W. T., Lin, M. L., ... & Chung, J. G. (2008). Berberine induced down-regulation of matrix metalloproteinase-1,-2 and-9 in human gastric cancer cells (SNU-5) in vitro. In vivo, 22(2), 223-230.
20. Lin, Q., Ma, L., Liu, Z., Yang, Z., Wang, J., Liu, J., & Jiang, G. (2017). Targeting microRNAs: a new action mechanism of natural compounds. Oncotarget, 8(9), 15961.
21. Liu, P., Wu, X., Dai, L., Ge, Z., Gao, C., Zhang, H., ... & Chen, B. (2017). Gambogenic acid exerts antitumor activity in hypoxic multiple myeloma cells by regulation of miR-21. *Journal of Cancer*, *8*(16), 3278.
22. Luo, X., Gu, J., Zhu, R., Feng, M., Zhu, X., Li, Y., & Fei, J. (2014). Integrative analysis of differential miRNA and functional study of miR-21 by seed-targeting inhibition in multiple myeloma cells in response to berberine. BMC systems biology, 8(1), 1-10.
23. Malumbres, M. (2013). miRNAs and cancer: an epigenetics view. Molecular aspects of medicine, 34(4), 863-874.
24. Nicoloso, M. S., Spizzo, R., Shimizu, M., Rossi, S., & Calin, G. A. (2009). MicroRNAs—the micro steering wheel of tumour metastases. *Nature Reviews Cancer*, *9*(4), 293-302.

25. O'Bryan, S., Dong, S., Mathis, J. M., & Alahari, S. K. (2017). The roles of oncogenic miRNAs and their therapeutic importance in breast cancer. *European journal of cancer*, *72*, 1-11.
26. Palumbo, A., & Anderson, K. (2011). New England journal of medicine. *NEJM*, *364*(11)), 1046-1060.
27. Shah, M. Y., Ferrajoli, A., Sood, A. K., Lopez-Berestein, G., & Calin, G. A. (2016). microRNA therapeutics in cancer—an emerging concept. *EBioMedicine*, *12*, 34-42.
28. Sicard, F., Gayral, M., Lulka, H., Buscail, L., & Cordelier, P. (2013). Targeting miR-21 for the therapy of pancreatic cancer. *Molecular Therapy*, *21*(5), 986-994.
29. Song, J. Z., Yip, Y. K., Han, Q. B., Qiao, C. F., & Xu, H. X. (2007). Rapid determination of polyprenylated xanthones in gamboge resin of Garcinia hanburyi by HPLC. Journal of separation science, 30(3), 304-309.
30. Sumazin, P., Yang, X., Chiu, H. S., Chung, W. J., Iyer, A., Llobet-Navas, D., ... & Califano, A. (2011). An extensive microRNA-mediated network of RNA-RNA interactions regulates established oncogenic pathways in glioblastoma. *Cell*, *147*(2), 370-381.
31. Szudy-Szczyrek, A., Ahern, S., Krawczyk, J., Szczyrek, M., & Hus, M. (2022). MiRNA as a Potential Target for Multiple Myeloma Therapy–Current Knowledge and Perspectives. Journal of Personalized Medicine, 12(9), 1428.
32. Tang, J., Feng, Y., Tsao, S., Wang, N., Curtain, R., & Wang, Y. (2009). Berberine and Coptidis rhizoma as novel antineoplastic agents: a review of traditional use and biomedical investigations. Journal of ethnopharmacology, 126(1), 5-17.
33. Volinia, S., Calin, G. A., Liu, C. G., Ambs, S., Cimmino, A., Petrocca, F., ... & Croce, C. M. (2006). A microRNA expression signature of human solid tumors defines cancer gene targets. *Proceedings of the National Academy of Sciences*, *103*(7), 2257-2261.
34. Wang, Y., Li, Y., Liu, X., & Cho, W. (2013). Genetic and epigenetic studies for determining molecular targets of natural product anticancer agents. Current Cancer Drug Targets, 13(5), 506-518.
35. Wang, J. H., Zhou, W. W., Liu, B. X., Man, D. L., Yang, Z. D., Liu, F. R., & Shang, H. (2016). Expression and significance of miR-21 in multiple myeloma patients. *Genet Mol Res*, *15*(1).
36. Wu, S. N., Yu, H. S., Jan, C. R., Li, H. F., & Yu, C. L. (1998). Inhibitory effects of berberine on voltage-and calcium-activated potassium currents in human myeloma cells. Life sciences, 62(25), 2283-2294.

37. Xie, J., Wang, J., & Zhu, B. (2016). Genistein inhibits the proliferation of human multiple myeloma cells through suppression of nuclear factor-κB and upregulation of microRNA-29b. Molecular Medicine Reports, 13(2), 1627-1632.
38. Xu, P., Xia, T., Ling, Y., & Chen, B. (2019). MiRNAs with prognostic significance in multiple myeloma: A systemic review and meta-analysis. Medicine, 98(33).
39. Yin, J., Zhang, H., & Ye, J. (2008). Traditional Chinese medicine in treatment of metabolic syndrome. Endocrine, Metabolic & Immune Disorders-Drug Targets (Formerly Current Drug Targets-Immune, Endocrine & Metabolic Disorders), 8(2), 99-111.
40. You, W., Xu, L., Zhang, X., Zou, H., Shi, D., Zhang, H., ... & Li, R. (2017). High-throughput screening identifies miR-451 as a pleiotropic modulator that suppresses gastric cancer metastasis. Slas Technology: Translating Life Sciences Innovation, 22(2), 136-143.
41. Yu, F. S., Yang, J. S., Lin, H. J., Yu, C. S., Tan, T. W., Lin, Y. T., ... & Chung, J. G. (2007). Berberine inhibits WEHI-3 leukemia cells in vivo. in vivo, 21(2), 407-412.
42. Zare, M., Bastami, M., Solali, S., & Alivand, M. R. (2018). Aberrant miRNA promoter methylation and EMT-involving miRNAs in breast cancer metastasis: diagnosis and therapeutic implications. *Journal of cellular physiology*, *233*(5), 3729-3744.
43. Zhang, H. D., Jiang, L. H., Sun, D. W., Hou, J. C., & Ji, Z. L. (2018). CircRNA: a novel type of biomarker for cancer. *Breast cancer*, *25*(1), 1-7.

Present And Accumulated Values For Changing And Continuous Payments

Prof. Dr. Deniz Ünal

Çukurova University, ORCID: 0000-0002-4095-3039

1. INTRODUCTION

Financial issues are an integral part of individuals' lives. Money and its time value, which are always on the agenda in the insurance sector, banking, buying and selling of stock or realty or any kind of borrowing relationship, also constitute the basic dynamics of actuarial science.

Actuarial sciences are of interest of mathematicians, statisticians, economists, and econometricians. This science is necessary especially for insurance companies because it tries to measure risks using mathematics, probability, and statistics. In short, the actuary uses mathematical and statistical techniques to determines probabilities of being in the future and the expected financial results of these events. By this knowledge, the amount of money that should now be held can be calculated by actuary, ensuring that there is enough money to pay in a possible situation. Or actuarial mathematics can be used to support solving several different problems in business and government.

Besides all these, the actuary is also concerned with the life expectancy of people. Because the completion of any payment period is also linked to the survival of individuals. For this reason, it can make premium calculations by considering the survival probabilities of individuals in all calculations. One way of calculating the survival probabilities of individuals is the use of life tables. A chart that shows the probability that individuals will die before their next birthday is called actuarial life charts. These tables are often used by life insurance companies to calculate the remaining life expectancy for people of different ages and stages, as well as the probability of survival at a certain age. The content of the table can be explained as follows. A life table is a table in which it is reported whether a certain number of people born today in any community survive tomorrow, the next day or in the following years. For example, recording numerical information such as how many of 100 people born today are alive next year or how many are alive after 5 years creates a life table for that community. Since the mortality rates of males and females are different, the actuarial life table is calculated separately for them. An actuarial life table or life table can also named as mortality table.

Actuaries working in all these fields aim to contribute to scientific developments by approaching the subject from different fields. For example, dealing with the issue of paying the debts of individuals to financial institutions, defaulting, and restructuring the debt are also fields of actuarial science. Although institutions generally work with fixed instalment payments, they may tend to meet the special payment demands of customers. Especially in periods or countries where the course of economic indicators is fluctuating, such demands may gain greater

importance. Such special demands reveal the need of institutions for flexible payment models. For this purpose, Alpman and Ünal (2019) studied payment models in which the increments are not constant, and they also calculated these models with life probabilities and presented the relationships between the models in the same study. In particular, the increase in the income of people after a certain age allows them to make their payments more easily and in higher amounts. For this reason, individuals who can make lower payments in the first period may think that they can afford higher instalments as time progresses. While planning the payments of the customers in the aforementioned structure, payment plans that increase within certain criteria may be needed. To meet this need, there are arithmetic or geometric incremental methods in the literature. In a study conducted for this purpose, in addition to arithmetic or geometric incremental methods, the accelerated method is proposed (Alpman and Ünal, 2019). For all the mentioned methods, besides providing an increase in instalments, the need for a decrease in a certain order is also taken into consideration.

In this study, in line with the purpose, the focus is on the planning stage of the payments of the products or loans purchased by the individuals or institutions. Customer-specific payment models have been discussed in order to meet the different demands of customers regarding competition conditions, economic and social conditions, and to make a difference or stand out for financial institutions.

Graduated payment mortgages (GPM) are a type of fixed rate loan with an amortization schedule that provides lower payments early on and then increases over time. Such payments are quite common in the market. In such cases, the aim is to enable individuals to take out loans. Because in some cases, people prefer periods that start with minimum payments and then reach increasing amounts. Of course, in some cases, loans with decreasing payments will be advantageous for those who can easily meet the payments in the first time but may have difficulties in the following years / processes. Different types of approaches have been made to such problems related to the variability of payments, and some studies have been conducted. For example, Tauer (1984) has addressed the problem of gradual payments using simple interest. In the study, geometric and arithmetic increment cases are also discussed as examples. Formato (1992) focused on installations other than fixed pay in his study, which dealt with the varying amounts of interest and principal included in each pay. In addition, Formato (1992) also discussed loans in which payments were skipped in the same study. He also stated that such loan payment plans are suitable for institutions and individuals where the difficulty of paying loan payouts varies throughout the year. He cited the tourism sector as an example and stated that a business in the tourism sector may find credit planning attractive, which is non-payment in certain periods. Moon (1994),

on the other hand, reconsidered and explained Formato' s calculations of skip payment loans. In addition, he expanded the study by considering the study in the context of geometric series. Eroğlu and Özdemir (2012), on the other hand, emphasized that loan repayments are generally in equal instalments, but the change in loan instalment rates will provide motivation to reach the customer. In this study, rhythmic skipping payment models were studied, emphasizing that the methods suggested by Formato (1992) and Moon (1994) could be used in case of difficulties in making loan payments in the period when the costs of the customers increased. Other examples on the variability of payments are the studies done by McNamara (1990), Cathcart et al. (2015) and Knoller et al. (2015).

In this study, which was conducted with a similar motivation, formulas were obtained by making theoretical calculations for a payment plan in which individuals or institutions will determine the increase or decrease rates indicated by "r" and which also contain continuous cash flow in certain periods. In detail, equations are given for present and accumulated values in cases of payment at the beginning of the term (annuity-immediate case) and at the end of the term (annuity-due case).

2. COMBINING ANNUITIES WITH CHANGING AND CONTINUOUS PAYMENTS

In this section, the calculation of the present and accumulated values of a payment plan in which the payments increase by a certain rate r or change with a sudden interest rate δ is studied. However, in this payment flow, where the increases are not constant, one more feature has been included in the problem. Namely, in this cash flow where each payment increases with the rate of r in the next period, the payment period is divided into two parts. This distinction is in the form of a discrete cash flow in the first part and a continuous cash flow in the second part. Calculations are made with the interest rate i in the first k periods, where there is a discrete and increasing (or decreasing for negative values of r) cash flow ($0 \leq k \leq n$). In the second part, calculations were made with instant rate δ. The continuous cash flow in the second period is determined for ρ(t)=ρ. All these problems were handled separately in annuity-due and annuity-immediate cases, and formulas for both present and accumulated values were obtained.

2.1. Annuity-immediate cases

In the calculations, with the first payment being P, each payment during the k period is handled by increasing (or decreasing with negative r values) the previous period payment by the rate r. Then the cash flows, for periods 1,2,..,k, will be as follows:

P,
P(1+r),
P $(1+r)^2$,
P $(1+r)^3$,
.
.
P $(1+r)^{k-1}$

2.1.1. Present Value:

In this case, the present value for the discrete payment period is

$\ddot{PV}_{(0,k-1)}$ = P+ $P(1+r)\,v$ +P $(1+r)^2 v^2$ + v^3 P $(1+r)^3 + \cdots +$ $v^{k-1}\,P\,(1+r)^{k-1}$

where $v = (1+i)^{-1}$ is the discount rate, r<i and $e^{\delta} = 1+i$ (Bowers, 1986). Performing some manipulations,

$$\ddot{PV}_{(0,k-1)} = P.\frac{1-\left(\frac{1+r}{1+i}\right)^k}{1-\frac{1+r}{1+i}} = P.\frac{(1+i)^k-(1+r)^k}{(1+i)^{k-1}\,(i-r)} = P.\frac{e^{\delta k}-(1+r)^k}{e^{\delta(k-1)}.\,(i-r)}$$

can be reached.

The present value can be calculated for the continuous payment period by integration with respect to t as follows,

$\ddot{PV}_{(k,n)} = \int_k^n v(k,t)\,\rho(t)\,dt$

Taking $v(k,t) = (1+i)^{k-t}$, the integration is

$= \int_k^n (1+i)^{k-t}\,\rho(t)\,dt$

Since $e^{\delta} = 1+i$ and $\rho(t)$ has a constant value ρ,

$\ddot{PV}_{(k,n)} = \int_k^n e^{-\delta(t-k)}\rho\,dt$

can be reached. Then the present value for the continuous part of the payment is

$\ddot{PV}_{(k,n)} = \rho \int_k^n e^{-\delta(t-k)}\,dt$

Taking the integration with respect to t, then

$= \frac{\rho}{\delta}\,(1-e^{-\delta(n-k)})$.

can be found.

As a result of the addition of $P\ddot{V}_{(0,k-1)}$ with $P\ddot{V}_{(k,n)}$ by taking into account the interest rate, the sum of the cash flows for the entire period is,

$P\ddot{V} = P\ddot{V}_{(0,k-1)} + v^k P\ddot{V}_{(k,n)}$.

2.1.2. Accumulated Value:

The accumulated value of the overall period for annuity-immediate case can be given as

$$A\ddot{V} = A\ddot{V}_{(0,k-1)} + A\ddot{V}_{(k,n)}$$

where $A\ddot{V}_{(k,n)}$ is the accumulated value fot the period (k,n) for annuity-immediate case and $A\ddot{V}_{(0,k-1)}$ is the accumulated value for continuous cash flow and calculated as

$A\ddot{V}_{(0,k-1)} = A(0,n).P\ddot{V}_{(0,k-1)}$.

Here $A(0,n) = (1+i)^n$ is the accumulation ratio (Bowers, 1986).

For $\rho(t) = \rho$ (constant), then

$$A\ddot{V}_{(k,n)} = \int_k^n A(t,n)\,\rho(t)\,dt$$
$$= \int_k^n \frac{1}{v(t,n)}\,\rho(t)\,dt$$
$$= \int_k^n \frac{1}{v(t,n)}\,\rho(t)\,dt$$
$$= \int_k^n (1+i)^{(n-t)}\rho\,dt$$
$$= \int_k^n e^{\delta(n-t)}\rho\,dt$$
$$= \frac{\rho}{\delta}\,(e^{\delta(n-k)} - 1)$$

can be obtained. From this finding, the formula for the accumulated value of the overall period for annuity-immediate case is

$$A\ddot{V} = A(0,n).P\ddot{V}_{(0,k-1)} + A\ddot{V}_{(k,n)}$$
$$= P.(1+i)^n \frac{e^{\delta k} - (1+r)^k}{e^{\delta(k-1)}.(i-r)} + \frac{\rho}{\delta}\,(e^{\delta(n-k)} - 1$$

2.2. Annuity-Due Case

Payments to be made at the end of each period during k periods with the first payment being P are calculated by increasing the previous period's payment by ratio r. In other words, for a cash flow:

P, P(1+r), $P(1+r)^2$, $P(1+r)^3$,….., $P\,(1+r)^{k-1}$

accumulated value calculation is given in this subsection.

2.2.1. Present Value

In case the payments are made at the end of the period, the present value for the first k periods is

$PV_{(0,k)} = P\ v + P(1+r)v^2 + P\ (1+r)^2 v^3 + P\ (1+r)^3 v^4 + \cdots + P\ (1+r)^{k-1} v^k$

$= P.\ v\ (1 + (1+r)\ v + (1+r)^2 v^2 + v^3\ (1+r)^3 + \cdots + v^{k-1}\ (1+r)^{k-1})$

$= P.\ v\ \frac{e^{\delta k} - (1+r)^k}{e^{\delta(k-1)}.(i-r)}$

$= P\ e^{-\delta}\ \frac{e^{\delta k} - (1+r)^k}{e^{\delta(k-1)}.(i-r)}$

$= P\ \frac{e^{\delta k} - (1+r)^k}{e^{\delta k}.(i-r)}$

where r <i. Present value for the continuous period is

$PV_{(k+1,n)} = \int_{k+1}^{n} v(k+1,t)\ \rho(t)\ dt$

$= \int_{k+1}^{n} (1+i)^{k+1-t}\ \rho(t)\ dt$

$= \int_{k+1}^{n} e^{-\delta(t-k-1)} \rho\ dt$

$= \frac{\rho}{\delta}\ (1 - e^{-\delta(n-k-1)})$.

Based on all these findings, taking into account the time value of money the present value for the whole period is

$$PV = PV_{(0,k)} + v^{k+1}.PV_{(k+1,n)}$$

$$= P\ \frac{e^{\delta k} - (1+r)^k}{e^{\delta k}.(i-r)} + v^{k+1}.\frac{\rho}{\delta}\ (1 - e^{-\delta(n-k-1)})\ .$$

2.2.2. Accumulated Value:

If the payments are made at the end of the period, the accumulated value of a payment schedule in which the first k payments are calculated with discrete cash flow and the next payments are calculated with continuous cash flow is shown by AV. In this case, the AV value is,

$$AV = A(0,n).PV_{(0,k)} + AV_{(k+1,n)}$$

For this sum, the accumulated value of $AV_{(k+1,n)}$ must be calculated first. For $e^{\delta} = 1 + i$ and $\rho(t) = \rho$, this value is calculated with the following formula.

$AV_{(k+1,n)} = \int_{k+1}^{n} A(t,n)\ \rho(t)\ dt = \int_{k+1}^{n} \frac{1}{v(t,n)}\ \rho(t)\ dt$

$= \int_{k+1}^{n} (1+i)^{(n-t)} \rho\ dt = \int_{k+1}^{n} e^{\delta(n-t)} \rho\ dt$

$= \frac{\rho}{\delta}\ (e^{\delta(n-k-1)} - 1)$

After calculating the accumulated value for the continuous payment period, the accumulated value for the entire cash flow is now given by the formula,

$$AV = (1+i)^n.P.\frac{e^{\delta k}-(1+r)^k}{e^{\delta k}.(i-r)}+\frac{\rho}{\delta}\left(e^{\delta(n-k-1)}-1\right)$$

3. CONCLUSION

In this study, it was started with the idea that annuity payments are shaped with customer demands. Because banks often go to debt restructuring, especially in order to prevent their loan customers from defaulting. A similar situation is frequently encountered in the structuring of tax debts to the state. In other words, in cases where a monetary relationship is established, it may be desired to ensure that individuals not to default. Therefore, different payment plans can be offered to the customer. Or banks may choose to sell loans to customers with private repayment plans that may be convenient personally. What is meant by personal convenience here is to offer the most appropriate payment advantages to individuals according to their income/expenditure status.

In this study, the theoretical formulas of payment plans, whose equations have not yet been in the literature, have been obtained. These theoretical calculations are obtained separately depending on whether the payments are made at the beginning or end of the period. The present and accumulated values of each result were calculated. While doing all of this, the case of making a part of the payment periods with continuous cash flow was also taken into consideration and the calculations related to this situation were combined with the discrete payments and general formulas were derived. Thus, the results of the alternate and continuous interest rate payment formulas have been made available to the relevant banks or financial institutions and scientists studying in the field.

REFERENCES

1. Alpman, B., & Ünal, D. (2020). Accelerating the premiums for annuities, life annuities and life insurance. *Communications in Statistics-Theory and Methods*, *49*(7), 1665-1694.
2. Bowers, N. L. (1986). *Actuarial mathematics* (No. 517/A18).
3. Cathcart, M.J., Lok, H.Y., McNeiL, A.J. and Morrison, S., 2015. Calculating Variable Annuity Liability "Greeks" Using Monte Carlo Simulation. ASTIN Bulletin., The Journal of the International Actuarial Association, 45 (2), 239-266.
4. Eroglu, A., & Ozdemir, G. (2012, May). A loan payment model with rhythmic skips. In *3rd International Symposium on Sustainable Development, Sarajevo, Bosnia and Herzegovina* (Vol. 271, p. 278).
5. Formato, R. A. (1992). Generalized formula for the periodic payment in a skip payment loan with arbitrary skips. *The Engineering Economist*, *37*(4), 355-359.
6. Knoller, C., Kraut, G., Schoenmaekers, P., 2015. On the Propensity to Surrender a Variable Annuity Contract: An Empirical Analysis of Dynamic Policyholder Behavior. The Journal of Risk and Insurance, DOI: 10.1111/jori.12076.
7. McNamara, M.J., Oppenheimer, H.R., 1990. Investment Returns of Variable Annuities: Recent Results. 6(4), 61-68.
8. Moon, I. (1994). Generalized formula for the periodic geometric-gradient series payment in a skip payment loan with arbitrary skips. *The Engineering Economist*, *39*(2), 177-185.
9. Tauer, L. W. (1984). Graduated payment loan schedules under simple interest [Farmland]. *AE Res.-New York State College of Agriculture and Life Sciences*.

Levitation Force Relaxation and Magnetic Stiffness Performances of Superconducting Maglev Systems with Different Multi-Surface HTS-PMG Arrangements

Murat Abdioglu[1,2], Ufuk Kemal Ozturk[2]

[1]Department of Mathematics and Science Education, Faculty of Education, Bayburt University, 69000, Bayburt, Türkiye.

[2]Electromagnetic Guidance and Acceleration Research Group (EMGA), Department of Physics, Faculty of Science, Karadeniz Technical University, 61080, Trabzon, Türkiye.

1. Introduction

While the need for energy in the developing world is constantly increasing, it is clear that energy sources, which are mostly dependent on fossil fuels, are also gradually depleted. For this reason, studies on reducing consumed energy are essential besides developing new energy sources. On the other hand, people's increasing need for mobility in the developing world forces researchers to seek faster and safer transportation systems. Since the discovery of the superconductivity of the ReBaCuO (Re: Rare Earth Element) compound above the boiling temperature of nitrogen (77 K) (Bednorz & Müller, 1986; M. K. Wu et al., 1987), the high-temperature superconducting (HTS) Maglev systems have become promising technologies to meet the fast, safe, and environmentally friendly transportation systems of the developing world. The discovery of HTS materials is a milestone since the superconducting materials have to be cooled below the critical temperature to be driven into the superconducting state. Because with the discovery of a superconductor with a critical temperature of 93 K, it has now become possible to cool the superconductors with liquid nitrogen. After the discovery of HTSs, various research groups have been trying to develop energy-efficient systems by utilising the magnetic levitation properties of superconductors, such as Maglev (Deng et al., 2016b; Floegel-Delor et al., 2019; Kusada et al., 2007; Ozturk, Badia-Majos, Abdioglu, Dilek, & Gedikli, 2021; Schultz et al., 2005; Richard M. Stephan & Pereira, 2020), frictionless magnetic bearings (Strasik et al., 2010; Xu, Wu, Jiao, & Zheng, 2016) and fully electric aircraft motors (Noland, 2021; Weng et al., 2021). The Maglev train technology can be dated to Alfred Zehden's patent work in 1905 named Electric Traction Apparatus (Zehden, 1905). But this technology gained the most of its popularity after announcing the Hyperloop transportation concept, based on non-contactless ultra-fast transportation in a vacuum tube (Musk, 2013).

On the other hand, the HTS Maglev systems differ from the conventional Maglev or Hyperloop systems with the feature of passive levitation. The passive levitation properties of HTS Maglev systems eliminate the negative aspects of traditional active Maglev systems, such as high cost, complexity, reliability problems, small working gaps, and errors that may occur in the power supply, control unit and electronic circuits. Therefore, studies on this technology have been increasing worldwide since the first manned HTS Maglev vehicle (Figure 1) in the Applied Superconductivity Laboratory of the Southwest Jiaotong University, China (Wang & et al., 2002). The researchers in China constructed a 45 m long HTS Maglev ring test line with a track gauge of 0.77 m, named "Super-Maglev" in 2013 (Deng et al., 2016a; Jin et al., 2021).

Figure 1. The first manned HTS Maglev test vehicle (Jin et al., 2021).

Although the wheel-rail friction is eliminated in Maglev systems via the levitated vehicle, the air friction still causes an increment in energy consumption, and it limits the maximum velocity of the system. The researchers constructed an evacuated tube with a diameter of 2 m on the "Super-Maglev" ring to explore the feasibility of combining the evacuated tube and Maglev technology, as seen in Figure 2. The system, installed in June 2014 as the first HTS Maglev Evacuated Tube Transport (HTS Maglev-ETT), can achieve a low-pressure environment of 2.9 kPa allowing the HTS Maglev vehicle to run up to 50 km/h velocity.

Figure 2. (a) The HTS Maglev ring test line in 2013 and (b) the HTS Maglev-ETT system in 2014 (Deng et al., 2016a; Deng et al., 2017).

Another research group at the Federal University of Rio de Janeiro, Brazil, fabricated a superconducting light rail vehicle named "Maglev-Cobra", operating between two buildings on the campus (R. M. Stephan, Andrade, & Ferreira, 2012). A full-scale module carrying eight people with a levitation gap of 1 cm is

shown in Figure 3a. The Maglev-Cobra prototype developed in Brazil reached level 7 in the NASA defined Technological Readiness Level (TRL) and is described as the most advanced based on this technological scale (Richard M. Stephan & Pereira, 2020). The researchers further developed their system with a 6m long vehicle composed of four modules on the test line of 200 m (Figure 3b). A short primary linear induction motor provides traction in this system.

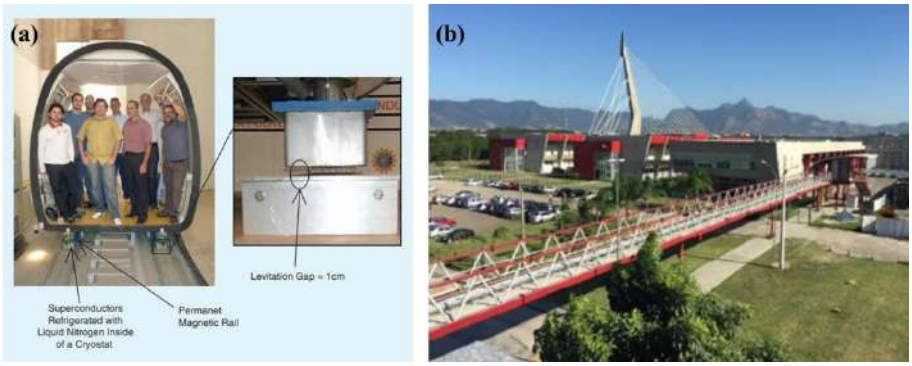

Figure 3. (a) A full-scale prototype indoor module and (b) final environment of Maglev-Cobra (Richard M. Stephan & Pereira, 2020).

Although various groups and institutes have been working on superconducting Maglev and motors worldwide, the results showed that these systems' magnetic levitation force and magnetic stiffness performance are not just at the desired level for commercial applications (M. Abdioglu et al., 2022; Deng et al., 2017; Guner, Celik, & Tomakin, 2017; Güner, 2020; Richard M. Stephan & Pereira, 2020). Therefore, the vertical magnetic levitation force for passenger and load carrying capacity, lateral guidance force and magnetic stiffness for movement stability and safety of Maglev systems should be increased. In order to improve the magnetic force properties of Maglev systems, we have proposed a novel multi-surface HTS-permanent magnetic guideway (PMG) structure which enables utilising all surfaces of the PMG unlike the arrangements in the literature, which have single-surface interactions (Murat Abdioglu et al., 2021; Ozturk, Badia-Majos, et al., 2021; Ozturk, Savaskan, et al., 2021). In our previous studies, we investigated the magnetic levitation force, guidance force, and static and dynamic stiffness performance of multi-surface arrangements. However, magnetic force relaxation is another important phenomenon in Maglev systems, except for these properties.

In the practical operations of Maglev vehicles, some intrinsic or extrinsic issues, such as flux creep and vibration of the vehicle's body, respectively, causes

a time-dependent decrement in levitation force (M. Abdioglu, Ozturk, Kabaer, & Ekici, 2018). This relaxation in levitation force results from the relaxation in magnetisation (M) and according to the standard Anderson−Kim model (Anderson & Kim, 1964) magnetisation decays with time, t as $S = (-dM/dlnt)/M_0 = -dlnM/dlnt$, where M_0 is the initial value of magnetisation. Since the relaxation of magnetisation influences the force, one can expect to have the below equation (M. Abdioglu et al., 2018):

$$(-dF\ /\ dlnt\ )/\ F_0\ =\ S \tag{1}$$

On the other hand, magnetic stiffness, which can be defined as the change in magnetic force acting on an object due to a unit change in position, directly influences the stability of Maglev vehicles. Magnetic stiffness can be better understood by considering the elastic constant in mechanical systems or the spring constant in springs. In addition to the similarity, it should be noted that unlike the elastic constant in mechanical structures, magnetic stiffness is a nonlinear function of the distance between the magnet and the superconductor. When the force (F_x) acting on the object and the displacement (x) of the object are in the same direction, the magnetic stiffness (k) is given in its simplest form (Moon, 1994):

$$F_x(x) = F(0) + \left(\frac{\partial F_x}{\partial x}\right)_{x=0}(x - x_0) \tag{2}$$

$$k_x = -\left(\frac{\partial F_x}{\partial x}\right)_{x=0} \tag{3}$$

2. Magnetic Force Relaxation and Stiffness Measurements

The reduction in levitation force with time is unavoidable, although it is undesirable. So, the stable levitation force at higher force levels is an essential parameter for the practical applicability of HTS Maglev systems. Magnetic stiffness is also significant for the safe movement of Maglev systems. We have used a triaxial magnetic force measurement system, given in Figure 4, to measure the levitation force relaxation and magnetic stiffness performances of five different multi-surface HTS-PMG arrangements shown in Figure 5.

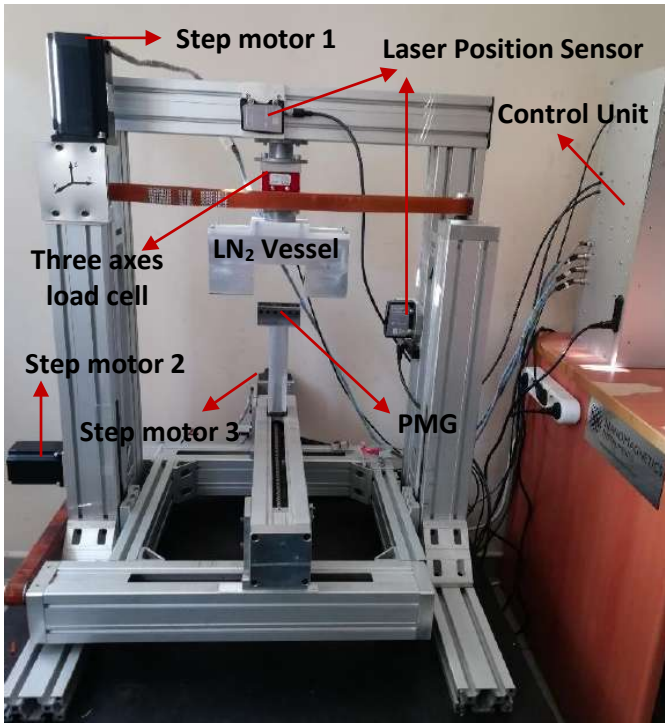

Figure 4. Triaxial magnetic levitation force measurement system.

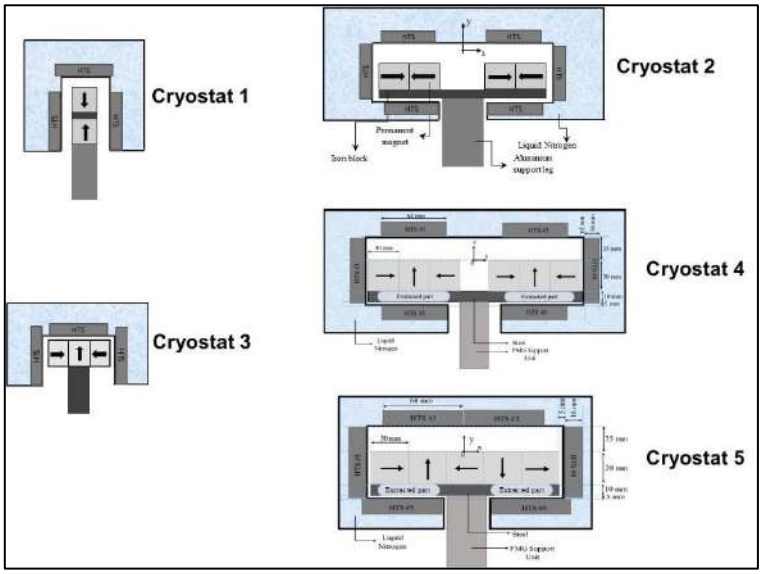

Figure 5. Schematic view of different multi-surface Cryostat-PMG arrangements.

For Cryostat 1 and Cryostat 3, magnetic force relaxation time measurements were carried out at CH=25 mm and CH=75 mm cooling heights. In these measurements, the vertical distance between the HTS-PMG is set to 75 mm after the superconductors are cooled in the respective CH. Then, the distance between the HTS-PMG is reduced to 5 mm, and the magnetic levitation force values are recorded depending on time by waiting for 200 s at this distance, where the maximum levitation force is obtained. Similarly, the magnetic relaxation time measurements with Cryostat 2, Cryostat 4 and Cryostat 5 were performed at the cooling conditions of FCH 20-30 and FCH 35-15. In these measurements, after the superconductors are cooled to the desired cooling distance, the HTS-PMG distance is adjusted to be 35-15 mm (upper gap 35 mm, lower gap 15 mm). Then, the gap between HTS-PMG is set to 5-45, and the magnetic levitation force values are recorded depending on time.

For vertical magnetic stiffness values of Cryostat 1 and Cryostat 3, minor cycles are made in the levitation force curve at z=5 mm, 9 mm, 13 mm and 17 mm vertical positions during magnetic levitation force measurement at CH=25 mm cooling height (at FCH 20-30 for Cryostat 2, Cryostat 4 and Cryostat 5). For example, for the magnetic stiffness value at the vertical position of 17 mm, after the HTSs are cooled at 25 mm cooling height, the vertical distance between the HTS-PMG is increased to 75 mm before starting the measurement. Then, to perform the measurement, the vertical gap is reduced from 75 mm to 17 mm and then increased to 19 m (Δz=2 mm). The vertical distance is then reduced to 13 mm for the next small cycle. Linear fitting is made to the cycle obtained in this way, and the magnetic stiffness value is calculated using the slope of the obtained line. The same process is repeated at z=13 mm, 9 mm and 5 mm positions to calculate the corresponding magnetic stiffness values.

3. Results and Discussion

Figure 6 shows the time-dependent graphs (relaxation time) of the magnetic levitation force measured at CH=25 mm and CH=75 mm cooling heights of different configurations of Cryostat 1 and Cryostat 3. As can be seen from the figure, as the maximum force value increases (for Cryostat 3, 3 HTS-3 PM), the reduction in levitation force becomes faster. Besides, it is seen that the Cryostat 3, 3 HTS-3 PM arrangement tends to go to zero rapidly after 150 s. This is due to the reduction in the volume of liquid nitrogen with the increasing number of superconductors in the cryostat, and therefore, getting warm of the superconductors in a shorter time and returning to the normal state.

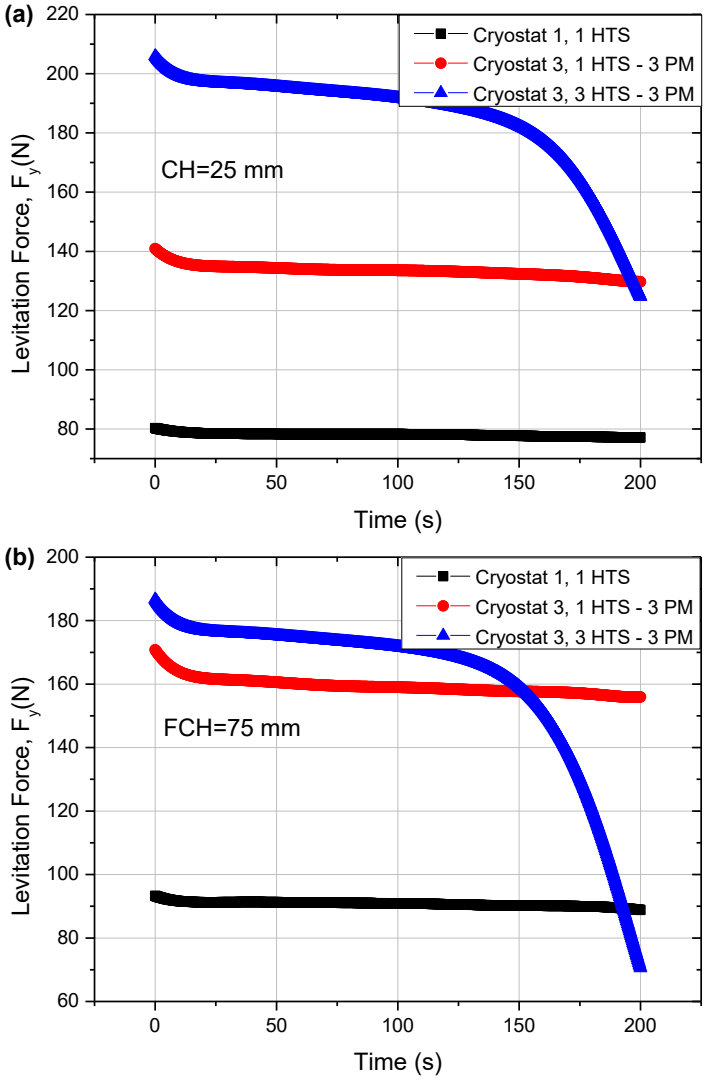

Figure 6. Time-dependent variation of magnetic levitation force measured at cooling heights CH=25 mm (a) and CH=75 mm (b) of different configurations of Cryostat 1 and Cryostat 3.

Figure 7 shows the relaxation time measurements of different arrangements of Cryostat 2, Cryostat 4, and Cryostat 5 at cooling heights of CH=25 mm and CH=35 mm. As can be seen from the figure, the reduction in force in CH=20 mm cooling height is greater for all cryostats than that in CH=35 mm cooling height. The fact that the constant force values after the relaxation in CH=20 mm are higher than that in CH=35 mm indicates that CH=20 mm can be considered as the optimum cooling height. In addition, the rapid decrease in force caused by the

early heating problem for Cryostat 3 in Figure 6 was not seen in the cryostats in Figure 7 due to the internal volume of these cryostats being large enough and getting more liquid nitrogen.

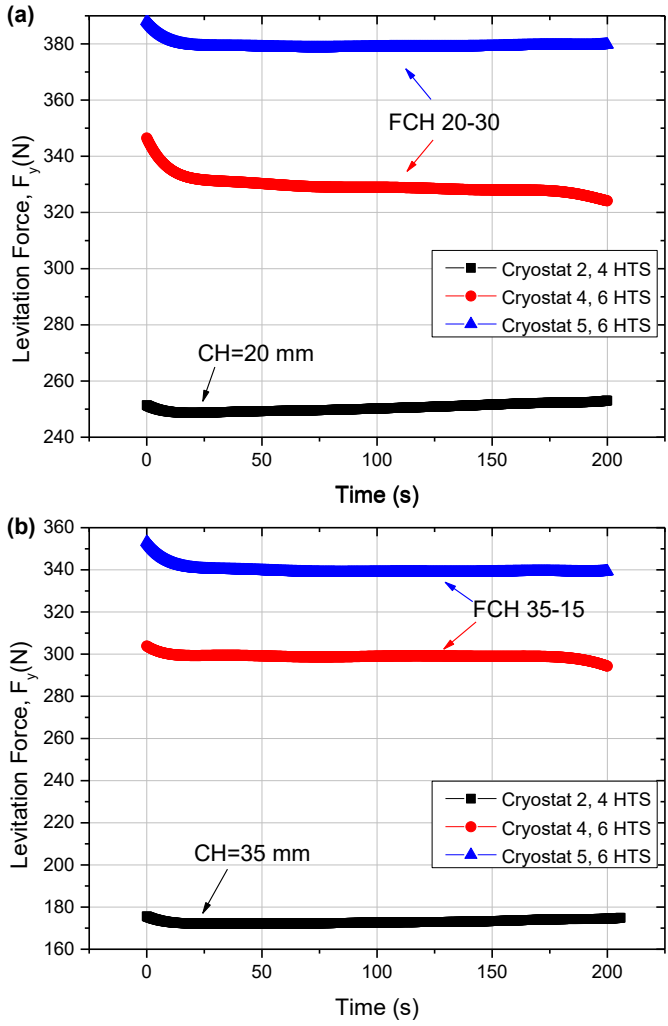

Figure 7. Time-dependent variation of magnetic levitation force measured at cooling heights CH=25 mm (a) and CH=35 mm (b) of different configurations of Cryostat 2, Cryostat 4 and Cryostat 5.

Figure 8 shows the vertical magnetic stiffness comparison of HTS-PMG arrangements with multi-surface interaction. Magnetic stiffness increases with decreasing vertical gap due to the rapidly changing force at closer distances. One can see from the figure that the multi-surface arrangements provide higher

magnetic stiffness than the single-surface arrangement (Cryostat 1, 1 HTS and Cryostat 3, 1 HTS-3 PM). In addition, the bigger magnetic stiffness values of Cryostats 2, 4, and 6 than that of Cryostats 1 and 3 can be attributed to the effective magnetic flux interaction surface and being used more number of HTSs in Cryostats 2, 4, and 6. Lastly, the nearly identical magnetic stiffness of Cryostat 4 and Cryostat 5 indicates the cost advantage of the Cryostat 5 arrangement since it includes 5 PMs while Cryostat 4 includes 6 PMs.

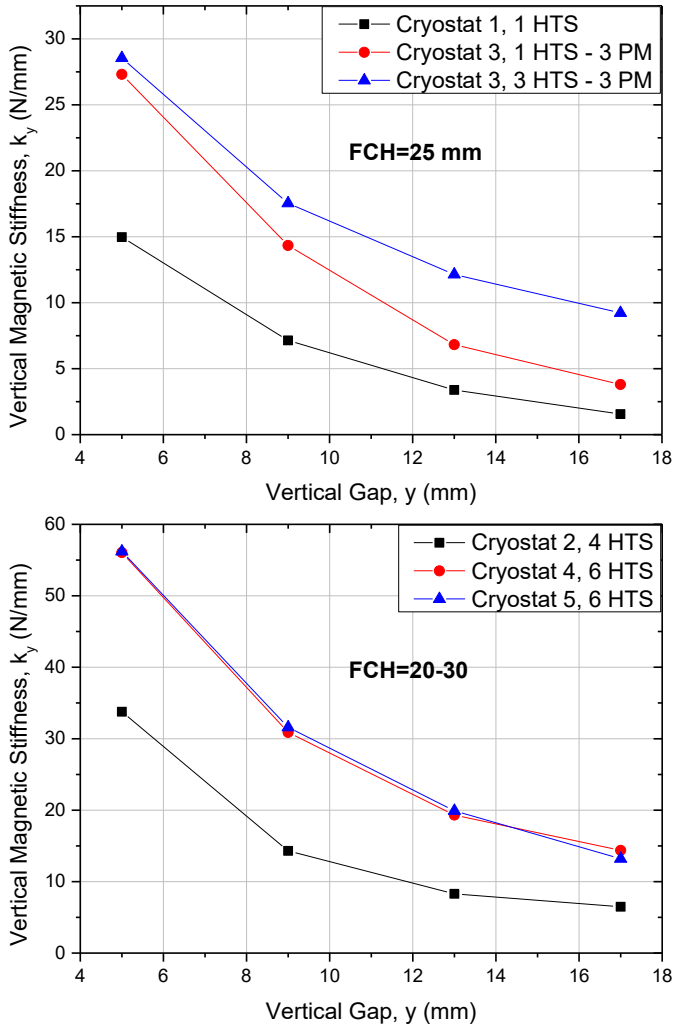

Figure 8. Vertical magnetic stiffness comparison of (a) Cryostat 1-Cryostat 3, and (b) Cryostat 2, Cryostat 4, and Cryostat 5.

4. Conclusions

Magnetic force relaxation and magnetic stiffness are essential parameters in practical applications of Maglev systems, and that's why we have investigated these parameters by using five different multi-surface HTS-PMG arrangements. It is concluded that the time-dependent relaxation in levitation force closely depends not only on the used HTS-PMG arrangement but also on the cooling height. Obtaining higher constant force values after the relaxation in CH=20 mm than that in CH=35 mm indicates that CH=20 mm can be considered as the optimum cooling height. On the other hand, magnetic stiffness also very closely depends on the used configuration. The magnetic stiffness of the multi-surface HTS-PMG arrangement is observed to be much bigger than that of the single-surface arrangement. The result of this study has the potential to enhance the applicability of the HTS Maglev vehicles in daily life.

Acknowledgment

This work was supported by the Scientific and Technological Research Council of Turkey (TUBITAK–Turkey), with project number 118F426.

References

1. Abdioglu, M., Guner, S. B. , Ozturk, K., Yang, C., Chen, I., & Celik, S. (2022). Magnetic levitation force and trapped field properties of multiseeded YBCO with triangular arrangement of seeds. *International Journal of Applied Ceramic Technology*, *19*(1), 459–466. https://doi.org/10.1111/ijac.13884
2. Abdioglu, M. Ozturk, K., Kabaer, M., & Ekici, M. (2018). Levitation and guidance force relaxations of the single−seeded and multi−seeded YBCO superconductors. *Physica C: Superconductivity and Its Applications*, *544*, 27–32. https://doi.org/10.1016/j.physc.2017.11.001
3. Abdioglu, M., Ozturk, K., Ekici, M., Savaskan, B., Celik, S., & Cansiz, A. (2021). Design and Experimental Studies on Superconducting Maglev Systems With Multisurface HTS–PMG Arrangements. *IEEE Transactions on Applied Superconductivity*, *31*(6), 1–7. https://doi.org/10.1109/TASC.2021.3085243
4. Anderson, P. W., & Kim, Y. B. (1964). Hard Superconductivity: Theory of the Motion of Abrikosov Flux Lines. *REVIEWS of MODERN PHYSICS*, *36*(1). Retrieved from https://doi.org/10.1103/RevModPhys.36.39
5. Bednorz, J. G., & Müller, K. A. (1986). Possible high Tc superconductivity in the Ba-La-Cu-O system. *Zeitschrift Für Physik B Condensed Matter*, *64*, 189–193. Retrieved from https://link.springer.com/article/10.1007/BF01303701
6. Deng, Z., Zhang, W., Zheng, J., Ren, Y., Jiang, D., Zheng, X., . . . Deng, C. (2016a). A High-Temperature Superconducting Maglev Ring Test Line Developed in Chengdu, China. *IEEE Transactions on Applied Superconductivity*, *26*(6), 1–8. https://doi.org/10.1109/TASC.2016.2555921
7. Deng, Z., Zhang, W., Zheng, J., Ren, Y., Jiang, D., Zheng, X., . . . Deng, C. (2016b). A High-Temperature Superconducting Maglev Ring Test Line Developed in Chengdu, China. *IEEE Transactions on Applied Superconductivity*, *26*(6), 1–8. https://doi.org/10.1109/TASC.2016.2555921
8. Deng, Z., Zhang, W., Zheng, J., Wang, B., Ren, Y., Zheng, X., & Zhang, J. (2017). A High-Temperature Superconducting Maglev-Evacuated Tube Transport (HTS Maglev-ETT) Test System. *IEEE Transactions on Applied Superconductivity*, *27*(6), 1–8. https://doi.org/10.1109/TASC.2017.2716842

9. Floegel-Delor, U., Schirrmeister, P., Riedel, T., Koenig, R., Kantarbar, V., Liebmann, M., & Werfel, F. N. (2019). Mobile HTS Bulk Devices as Enabling Ton-Force Technology for Maglev Trains. *IEEE Transactions on Applied Superconductivity*, *29*(5), 1–5. https://doi.org/10.1109/TASC.2019.2897216
10. Guner, S. B., Celik, S., & Tomakin, M. (2017). The investigation of magnetic levitation performances of single grain YBCO at different temperatures. *Journal of Alloys and Compounds*, *705*, 247–252. https://doi.org/10.1016/j.jallcom.2017.02.134
11. Güner, S. B. (2020). Effects of silver doping on magnetic levitation performance of MgB2 superconductors. *Cryogenics*, *108*, 103061. https://doi.org/10.1016/j.cryogenics.2020.103061
12. Jin, J., Sheng, G., Bi, Y., Song, Y., Liu, X., Chen, X., . . . Zhu, J. [Jianguo] (2021). Applied Superconductivity and Electromagnetic Devices - Principles and Current Exploration Highlights. *IEEE Transactions on Applied Superconductivity*, *31*(8), 1–29. https://doi.org/10.1109/TASC.2021.3108740
13. Kusada, S., Igarashi, M., Nemoto, K., Okutomi, T., Hirano, S., Kuwano, K., . . . Yamaji, M. (2007). The Project Overview of the HTS Magnet for Superconducting Maglev. *IEEE Transactions on Applied Superconductivity*, *17*(2), 2111–2116. https://doi.org/10.1109/TASC.2007.899691
14. M. K. Wu, J. R. Ashburn, C. J. Torng, P. H. Hor, R. L. Meng, L. Gao, . . . and C. W. Chu (1987). Superconductivity at 93 K in a new mixed-phase Y-Ba-Cu-O compound system at ambient pressure. *Physical Review Letters*, *58*(9).
15. Moon, F. C. (1994). *Superconducting Levitation*. Wiley, New York.
16. Musk, E. (2013). Hyperloop Alpha.
17. Noland, J. K. (2021). Hydrogen Electric Airplanes: A disruptive technological path to clean up the aviation sector. *IEEE Electrification Magazine*, *9*(1), 92–102. https://doi.org/10.1109/MELE.2020.3047173
18. Ozturk, K., Badia-Majos, A., Abdioglu, M., Dilek, D. B., & Gedikli, H. (2021). Experimental and Numerical Investigation of Levitation Force Parameters of Novel Multisurface Halbach HTS–PMG Arrangement for Superconducting Maglev System. *IEEE Transactions on Applied Superconductivity*, *31*(7), 1–12. https://doi.org/10.1109/TASC.2021.3106816

19. Ozturk, K., Savaskan, B., Abdioglu, M., Cansiz, A., Dilek, D. B., & Karaahmet, Z. (2021). Comparing of the Magnetic Force Parameters of Superconducting Maglev System Using Horizontal and Vertical PMG Geometry in Multi-Surface HTS-PMG Arrangement. *Journal of Superconductivity and Novel Magnetism*, *34*(12), 3151–3161. https://doi.org/10.1007/s10948-021-06072-w
20. Schultz, L., deHaas, O., Verges, P., Beyer, C., Rohlig, S., Olsen, H., . . . Funk, U. (2005). Superconductively Levitated Transport System—The SupraTrans Project. *IEEE Transactions on Appiled Superconductivity*, *15*(2), 2301–2305. https://doi.org/10.1109/TASC.2005.849636
21. Stephan, R. M., Andrade, R. de, & Ferreira, A. C. (2012). Superconducting Light Rail Vehicle: A Transportation Solution for Highly Populated Cities. *IEEE Vehicular Technology Magazine*, *7*(4), 122–127. https://doi.org/10.1109/MVT.2012.2218437
22. Stephan, R. M., & Pereira, A. O. (2020). The Vital Contribution of MagLev Vehicles for the Mobility in Smart Cities. *Electronics*, *9*(6), 978. https://doi.org/10.3390/electronics9060978
23. Strasik, M., Hull, J. R., Mittleider, J. A., Gonder, J. F., Johnson, P. E., McCrary, K. E., & McIver, C. R. (2010). An overview of Boeing flywheel energy storage systems with high-temperature superconducting bearings. *Superconductor Science and Technology*, *23*(3), 34021. https://doi.org/10.1088/0953-2048/23/3/034021
24. Wang, J. et al. (2002). The first man-loading high temperature superconducting Maglev test vehicle in the world. *Physica C: Superconductivity*, *378-381*, 809–814.
25. Weng, F., Zhang, M., Elwakeel, A., Lan, T., McNeill, N., & Yuan, W. (2021). Transient Test and AC Loss Study of a Cryogenic Propulsion Unit for All Electric Aircraft. *IEEE Access*, *9*, 59628–59636. https://doi.org/10.1109/ACCESS.2021.3073071
26. Xu, K., Wu, D., Jiao, Y. L., & Zheng, M. H. (2016). A fully superconducting bearing system for flywheel applications. *Superconductor Science and Technology*, *29*(6), 64001. https://doi.org/10.1088/0953-2048/29/6/064001
27. Zehden, A. (1905). Electric Traction Apparatus. *Patent US*, *782312 A*.

The Potential Effects Of Royal Jelly On Complex Wound Heal-Ing Process

Dr. Kaan KALTALIOGLU

Vocational School of Espiye, Giresun University, 28600, Giresun, Turkey
E-mail: kaan.kaltalioglu@gmail.com, ORCID: 0000-0002-4995-2657

INTRODUCTION

Honeybees are members of the genus *Apis* and are classified as hymenopteran insects. They are characterized by producing honey and its products that are beneficial to humans. Bee products have been used by humans for nutritional and therapeutic purposes since ancient times (Cornara, Biagi, Xiao, & Burlando, 2017). Additionally, interest in bee products and apitherapy has surged (Doko, Salaric, & Bazdaric, 2021; J.-D. Lee, Park, Chae, & Lim, 2005). Apitherapy is the use of honeybees or honeybee products as therapeutic or preventative treatments to prevent or slow the course of illness (Weis et al., 2022). Although honey is the most popular main product, various bee products (Propolis, bee venom, beeswax, and bee pollen) can be obtained from the gland secretions of honey bees and/or from different botanical materials (Cornara et al., 2017). One of these products is royal jelly, which is a white, non-fluid material generated by worker bees' mandibular and hypopharyngeal glands (Pasupuleti, Sammugam, Ramesh, & Gan, 2017). It is additionally described as a "superfood" that the queen bee consumes exclusively. Royal jelly is also offered to newly hatched honeybee larvae to aid in their development (Buttstedt, Moritz, & Erler, 2013).

ROYAL JELLY

Royal jelly, which attracts people's attention from a medical point of view, is widely used in traditional medicine as a nutritional complex to help combat many chronic health problems. In various studies, it has been determined that it has various pharmacological activities such as anti-inflammatory, antitumor, antibacterial, and antiallergic (Pasupuleti et al., 2017). The major component of royal jelly, royalactin, allows a larva to morphologically transition into a queen bee (Kamakura, 2011). It is the primary cause for the queen bee's extended lifespan compared to other bees (Pasupuleti et al., 2017).

It has been demonstrated that royal jelly contains carbohydrates, water, lipids, protein, vitamins mineral and salts (Nagai & Inoue, 2004) and approximately 185 organic compounds were detected (Pasupuleti et al., 2017). Some of the essential components that can be found include royalactin, defensin-1, adenosine monophosphate (AMP) N1-oxide,10-hydroxy-2-decenoic acid (10-HDA), major royal jelly proteins (MRJPs), prolactin, testosterone, estradiol, and progesterone (Bucekova et al., 2017; Ramadan & Al-Ghamdi, 2012; Sugiyama, Takahashi, & Mori, 2012).

Proteins constitute the majority of dry substance in royal jelly, with more than 80% containing MRJPs, which are soluble glycoproteins (The most well-known among these is royalactin, which weighs 57-kDa) (Cornara et al., 2017; Kamakura, 2011). The lipid fraction is predominantly composed of terminally and/or internally hydroxylated medium chain fatty acids with terminal mono- or dicarboxylic acid

functionalities (The most well-known among these is 10-HDA) (Li, Huang, & Xue, 2013).

The Bioactivities of Royal Jelly

The medicinal effects of royal jelly, which is an important bee product, have been the subject of various studies. According to several clinical research, royal jelly is useful in alleviating premenstrual syndrome, treating urinary issues, and enhancing the quality of life in postmenopausal women (Seyyedi, Rafiean-Kopaei, & Miraj, 2016; Taavoni, Barkhordari, Goushegir, & Haghani, 2014). Zamani et al. (2012) stated in an in vivo study that royal jelly has potential neuroprotective properties and may be beneficial against Alzheimer's disease (Zamani, Reisi, Pilehvarian, & Alaei, 2012). In addition, another study determined that royal jelly consumption improves mental health (Morita et al., 2012). Guo et al. (2009) reported that some peptides obtained from royal jelly showed strong antioxidant activity (Guo, Kouzuma, & Yonekura, 2009). It has been reported that MJRPs called jellein-I and -II show antimicrobial activity against *Escherichia coli, Bacillus subtilis, Staphylococcus aureus*, and *S. saprophyticus* microorganisms (Fontana et al., 2004). It is known that the protein called royalisin has antimicrobial effect against various bacteria (Fujiwara et al., 1990). It has also been showed that the 10-HDA component has a strong antibacterial effect against *E. coli*, *S. aureus* and *B. subtilis* bacteria (Alreshoodi & Sultanbawa, 2015). It has been stated that 10-HDA has an anti-inflammatory effect and also regulates the immune system (Gasic et al., 2007; Sugiyama et al., 2012).

WOUND HEALING

Wound healing is a biological process involving a controlled succession of many complex stages, including inflammation, proliferation, and remodeling, and regulated by growth factors secreted by numerous cells (Dindar, Kaltalioglu, & Coskun Cevher, 2017; Y.-S. S. Lee, Wysocki, Warburton, & Tuan, 2012). This process can be impeded or prevented by a number of factors (such as aging, oxidative stress, diabetes mellitus, infection) which can reduce life quality by delaying or blocking recovery (Kaltalioglu & Coskun Cevher, 2021). Approximately 1% to 2% of the population in wealthy countries is currently affected by chronic wounds (Nussbaum et al., 2018). By 2027, it is anticipated that the global market for wound care products would reach $18.7 billion (Sen, 2021; Yu, Zhang, & Guo, 2022).

ROYAL JELLY AND WOUND HEALING

Bee products or their combinations with various products have traditionally been preferred for wound treatment since ancient times (Molan, 2006). Considering the content and structure of royal jelly, it can be thought that it has a potential for use in

wound treatment. In a study, it was reported that royal jelly increases the fibroblast migration dose-dependently during the healing process and has an effect on some lipids such as cholesterol and spingonin (Kim et al., 2010). Park et al. (2011) stated that royal jelly improves collagen production and thus has a protective potential against UV rays (Park et al., 2011). El-Gayar et al. (2016) stated that royal jelly can be used to enhance wound healing as a result of an in vivo study (El-Gayar, Aboshanab, Aboulwafa, & Hassouna, 2016).

It is possible that the 10-HDA, defensin-1, and MJRPs components found in royal jelly are responsible for its favorable benefits on wound healing. 10-HDA increases collagen production, expression of growth factors that orchestrate healing process such as TGF-β, VEGF, FGF-1, and inhibits TNF-α, collagenase, lipoxygenase and cyclooxygenase (Izuta, Chikaraishi, Shimazawa, Mishima, & Hara, 2009; Kim et al., 2010; Yang et al., 2010). Moreover, Bucekova et al. (2017) reported that royal jelly is successful in wound healing treatment (Bucekova et al., 2017). They stated that royal jelly significantly increased keratinocyte migration, matrix metalloproteinase-9 production and wound closure rates, and these properties may be due to the defensin-1 protein it contains. In addition, Fratellone et al. (2015) considered that royal jelly is helpful for treating wounds and repairing tissue (Fratellone, Tsimis, & Fratellone, 2016). Collagen and growth factors are extremely important proteins for wound healing. Collagen is one of the most important proteins found in connective tissue. It has a role in the proliferation and migration of cells, in addition to provide structural support throughout the process of wound healing (Brett, 2008). Growth factors such as VEGF, TGF-β, EGF, PDGF, FGF are involved in vital processes such as new vessel formation, inflammation and re-epithelialization during the healing process (Barrientos, Stojadinovic, Golinko, Brem, & Tomic-Canic, 2008). Also, MRJP2, MRJP3, and MRJP7 promote healing process by triggering the differentiation, proliferation, and migration of epidermal keratinocyte cells (Kunugi & Mohammed Ali, 2019).

CONCLUSION

It is important to search for agents with less side effects for the correct, effective and rapid treatment of this complex process. Royal jelly is one of the candidates. Although current studies show that it has potential for wound treatment, its effectiveness in different wound types (diabetic, burn, ulcer) should be supported by pre-clinical and clinical studies.

REFERENCES

1. Alreshoodi, F., & Sultanbawa, Y. (2015). Antimicrobial Activity of Royal Jelly. *Anti-Infective Agents*, *13*(1), 50–59. https://doi.org/10.2174/2211352513666150318234430
2. Barrientos, S., Stojadinovic, O., Golinko, M. S., Brem, H., & Tomic-Canic, M. (2008). Growth factors and cytokines in wound healing. *Wound Repair and Regeneration*, *16*(5), 585–601. https://doi.org/10.1111/j.1524-475X.2008.00410.x
3. Brett, D. (2008). A Review of Collagen and Collagen-based Wound Dressings. *Wounds : A Compendium of Clinical Research and Practice*, *20*(12), 347–356. Retrieved from http://www.ncbi.nlm.nih.gov/pubmed/25941895
4. Bucekova, M., Sojka, M., Valachova, I., Martinotti, S., Ranzato, E., Szep, Z., Majtan, V., Klaudiny, J., & Majtan, J. (2017). Bee-derived antibacterial peptide, defensin-1, promotes wound re-epithelialisation in vitro and in vivo. *Scientific Reports*, *7*(1), 1–13. https://doi.org/10.1038/s41598-017-07494-0
5. Buttstedt, A., Moritz, R. F., & Erler, S. (2013). More than royal food - Major royal jelly protein genes in sexuals and workers of the honeybee Apis mellifera. *Frontiers in Zoology*, *10*(1), 72. https://doi.org/10.1186/1742-9994-10-72
6. Cornara, L., Biagi, M., Xiao, J., & Burlando, B. (2017). Therapeutic properties of bioactive compounds from different honeybee products. *Frontiers in Pharmacology*, *8*(JUN), 1–20. https://doi.org/10.3389/fphar.2017.00412
7. Dindar, B., Kaltalioglu, K., & Coskun Cevher, Ş. (2017). Effect of dual growth factor administration on oxidative markers during acute stage wound healing in rats. *Turkısh Journal of Zoology*, *41*, 841–847. https://doi.org/10.3906/zoo-1603-58
8. Doko, T., Salaric, I., & Bazdaric, K. (2021). Complementary and Alternative Medicine Use Among Croatian Health Studies Students– A Single Center Cross-Sectional Study. *Acta Medica Academica*, *49*(3), 240. https://doi.org/10.5644/ama2006-124.313
9. El-Gayar, M. H., Aboshanab, K. M., Aboulwafa, M. M., & Hassouna, N. A. (2016). Antivirulence and wound healing effects of royal jelly and garlic extract for the control of MRSA skin infections. *Wound Medicine*, *13*, 18–27. https://doi.org/10.1016/j.wndm.2016.05.004
10. Fontana, R., Mendes, M. A., Souza, B. M. de, Konno, K., César, L. M. M., Malaspina, O., & Palma, M. S. (2004). Jelleines: a family of antimicrobial

peptides from the Royal Jelly of honeybees (Apis mellifera). *Peptides*, *25*(6), 919–928. https://doi.org/10.1016/j.peptides.2004.03.016
11. Fratellone, P. M., Tsimis, F., & Fratellone, G. (2016). Apitherapy Products for Medicinal Use. *The Journal of Alternative and Complementary Medicine*, *22*(12), 1020–1022. https://doi.org/10.1089/acm.2015.0346
12. Fujiwara, S., Imai, J., Fujiwara, M., Yaeshima, T., Kawashima, T., & Kobayashi, K. (1990). A potent antibacterial protein in royal jelly. Purification and determination of the primary structure of royalisin. *The Journal of Biological Chemistry*, *265*(19), 11333–11337.
13. Gasic, S., Vucevic, D., Vasilijic, S., Antunovic, M., Chinou, I., & Colic, M. (2007). Evaluation of the Immunomodulatory Activities of Royal Jelly Components In Vitro. *Immunopharmacology and Immunotoxicology*, *29*(3–4), 521–536. https://doi.org/10.1080/08923970701690977
14. Guo, H., Kouzuma, Y., & Yonekura, M. (2009). Structures and properties of antioxidative peptides derived from royal jelly protein. *Food Chemistry*, *113*(1), 238–245. https://doi.org/10.1016/j.foodchem.2008.06.081
15. Izuta, H., Chikaraishi, Y., Shimazawa, M., Mishima, S., & Hara, H. (2009). 10-Hydroxy-2-decenoic acid, a major fatty acid from royal jelly, inhibits VEGF-induced angiogenesis in human umbilical vein endothelial cells. *Evidence-Based Complementary and Alternative Medicine : ECAM*, *6*(4), 489–494. https://doi.org/10.1093/ecam/nem152
16. Kaltalioglu, K., & Coskun Cevher, S. (2021). Isatis glauca subsp. sivasica extract contributes to diabetic wound healing process via increased collagen and nitric oxide content. *Hittite Journal of Science & Engineering*, *8*(2), 141–147. https://doi.org/10.17350/hjse19030000224
17. Kamakura, M. (2011). Royalactin induces queen differentiation in honeybees. *Nature*, *473*(7348), 478–483. https://doi.org/10.1038/nature10093
18. Kim, J., Kim, Y., Yun, H., Park, H., Kim, S. Y., Lee, K. G., Han, S. M., & Cho, Y. (2010). Royal jelly enhances migration of human dermal fibroblasts and alters the levels of cholesterol and sphinganine in an in vitro wound healing model. *Nutrition Research and Practice*, *4*(5), 362–368. https://doi.org/10.4162/nrp.2010.4.5.362
19. Kunugi, & Mohammed Ali. (2019). Royal Jelly and Its Components Promote Healthy Aging and Longevity: From Animal Models to Humans. *International Journal of Molecular Sciences*, *20*(19), 4662. https://doi.org/10.3390/ijms20194662
20. Lee, J.-D., Park, H.-J., Chae, Y., & Lim, S. (2005). An Overview of Bee Venom Acupuncture in the Treatment of Arthritis. *Evidence-Based*

Complementary and Alternative Medicine, *2*(1), 79–84. https://doi.org/10.1093/ecam/neh070

21. Lee, Y.-S. S., Wysocki, A., Warburton, D., & Tuan, T.-L. L. (2012). Wound healing in development. *Birth Defects Research Part C - Embryo Today: Reviews*, *96*(3), 213–222. https://doi.org/10.1002/bdrc.21017
22. Li, X., Huang, C., & Xue, Y. (2013). Contribution of Lipids in Honeybee (Apis mellifera) Royal Jelly to Health. *Journal of Medicinal Food*, *16*(2), 96–102. https://doi.org/10.1089/jmf.2012.2425
23. Molan, P. C. (2006). Using honey in wound care. *International Journal of Clinical Aromatherapy*, *3*(2), 21–24. Retrieved from http://hdl.handle.net/10289/2030
24. Morita, H., Ikeda, T., Kajita, K., Fujioka, K., Mori, I., Okada, H., Uno, Y., & Ishizuka, T. (2012). Effect of royal jelly ingestion for six months on healthy volunteers. *Nutrition Journal*, *11*(1), 77. https://doi.org/10.1186/1475-2891-11-77
25. Nagai, T., & Inoue, R. (2004). Preparation and the functional properties of water extract and alkaline extract of royal jelly. *Food Chemistry*, *84*(2), 181–186. https://doi.org/10.1016/S0308-8146(03)00198-5
26. Nussbaum, S. R., Carter, M. J., Fife, C. E., DaVanzo, J., Haught, R., Nusgart, M., & Cartwright, D. (2018). An Economic Evaluation of the Impact, Cost, and Medicare Policy Implications of Chronic Nonhealing Wounds. *Value in Health*, *21*(1), 27–32. https://doi.org/10.1016/j.jval.2017.07.007
27. Park, H. M., Hwang, E., Lee, K. G., Han, S.-M., Cho, Y., & Kim, S. Y. (2011). Royal jelly protects against ultraviolet B-induced photoaging in human skin fibroblasts via enhancing collagen production. *Journal of Medicinal Food*, *14*(9), 899–906. https://doi.org/10.1089/jmf.2010.1363
28. Pasupuleti, V. R., Sammugam, L., Ramesh, N., & Gan, S. H. (2017). Honey, Propolis, and Royal Jelly: A Comprehensive Review of Their Biological Actions and Health Benefits. *Oxidative Medicine and Cellular Longevity*, *2017*. https://doi.org/10.1155/2017/1259510
29. Ramadan, M. F., & Al-Ghamdi, A. (2012). Bioactive compounds and health-promoting properties of royal jelly: A review. *Journal of Functional Foods*, *4*(1), 39–52. https://doi.org/10.1016/j.jff.2011.12.007
30. Sen, C. K. (2021). Human Wound and Its Burden: Updated 2020 Compendium of Estimates. *Advances in Wound Care*, *10*(5), 281–292. https://doi.org/10.1089/wound.2021.0026
31. Seyyedi, F., Rafiean-Kopaei, M., & Miraj, S. (2016). Comparison of the Effects of Vaginal Royal Jelly and Vaginal Estrogen on Quality of Life,

Sexual and Urinary Function in Postmenopausal Women. *JOURNAL OF CLINICAL AND DIAGNOSTIC RESEARCH*, *10*(5), QC01–QC05. https://doi.org/10.7860/JCDR/2016/17844.7715

32. Sugiyama, T., Takahashi, K., & Mori, H. (2012). Royal jelly acid, 10-hydroxy-trans-2-decenoic acid, as a modulator of the innate immune responses. *Endocrine, Metabolic & Immune Disorders Drug Targets*, *12*(4), 368–376. https://doi.org/10.2174/187153012803832530
33. Taavoni, S., Barkhordari, F., Goushegir, A., & Haghani, H. (2014). Effect of Royal Jelly on premenstrual syndrome among Iranian medical sciences students: A randomized, triple-blind, placebo-controlled study. *Complementary Therapies in Medicine*, *22*(4), 601–606. https://doi.org/10.1016/j.ctim.2014.05.004
34. Weis, W. A., Ripari, N., Conte, F. L., Honorio, M. da S., Sartori, A. A., Matucci, R. H., & Sforcin, J. M. (2022). An overview about apitherapy and its clinical applications. *Phytomedicine Plus*, *2*(2). https://doi.org/10.1016/j.phyplu.2022.100239
35. Yang, X. Y., Yang, D. S., Wei-Zhang, Wang, J. M., Li, C. Y., Hui-Ye, Lei, K. F., Chen, X. F., Shen, N. H., Jin, L. Q., & Wang, J. G. (2010). 10-Hydroxy-2-decenoic acid from Royal jelly: a potential medicine for RA. *Journal of Ethnopharmacology*, *128*(2), 314–321. https://doi.org/10.1016/j.jep.2010.01.055
36. Yu, R., Zhang, H., & Guo, B. (2022). Conductive Biomaterials as Bioactive Wound Dressing for Wound Healing and Skin Tissue Engineering. *Nano-Micro Letters*, *14*(1), 1. https://doi.org/10.1007/s40820-021-00751-y
37. Zamani, Z., Reisi, P., Pilehvarian, A., & Alaei, H. (2012). Effect of Royal Jelly on spatial learning and memory in rat model of streptozotocin-induced sporadic Alzheimer′s disease. *Advanced Biomedical Research*, *1*(1), 26. https://doi.org/10.4103/2277-9175.98150

ALUMINUM OXIDE IMPURITY ADDITION EFFECT ON FUNDAMENTAL CRYSTAL STRUCTURE FOR BI2.1SR2.0CA1.1CU2.0OY SUPERCONDUCTORS

Assoc. Prof. Dr. Muhammed ÖZ[1] ,
Assoc. Prof. Dr. Mustafa Burak TÜRKÖZ[2]

[1]Bolu Abant Izzet Baysal University, https://orcid.org/0000-0003-0049-0161.
[2]Karabük University, https://orcid.org/0000-0002-4127-7650.

1. INTRODUCTION

The superconducting phenomenon was first found in 1911 by Onnes (Onnes, 1911) for heavy mercury material at 4.2 K. As is known, the behavior of superconductivity is studied by both the perfect Meissner effect and critical transition temperature values. Whereas the first coincided with the complete magnetic flux fields expulsion inside the material (Meissner and Ochsenfeld, 1933), the second parameter referred the existence of a certain transition temperature below which the compound is superconductor. Many materials such as metals, semi-metals, elements, organic compounds, alloys, metal-based compounds, fullerites, rare earth borocarbides, heavy fermions, carbon-based compounds ruteno-cuprate compounds, A-15 inorganic materials, chevrel phase, semi-metal-containing samples, magnesium diboride, chalcogens, silicon-based samples, pyrochlorine oxides, and cuprate-layered perovskite type-II materials have been included in the superconducting parents throughout the history of the phenomenon of superconductivity (Kleiner and Buckel, 2016; Guner, et. al., 2019). Also, new type compounds are being searched to show the superconducting phenomenon with higher critical transition temperatures (initial and offset), higher critical current density, greater carrying density capacity and higher magnetic field carrying capacity (Takayama, 1998; Yamauchi and Karppinen, 2000; Chen, et. al., 2002; Zalaoglu, et. al., 2020, Erdem, Zalaoglu, Ulgen, Turgay, and Yildirim, 2021). In this context, superconducting materials are basically divided in two basic parts, known as type-I known and type-II ceramic (Ginzburg, and Andryushin, 2004; Parinov, 2007; Yıldırım, 2013). Of the materials, especially the type-II materials possess rather smaller energy consumption, larger current and magnetic field carrying ability, and extremely higher operating temperature and pinning ability/capacity. Thus, the researchers have preferred the use of type-II superconducting materials in the innovative energy infrastructure, power transmission, refrigeration systems, sensitive process control, generators, future hydrogen society, spintronics, metallurgical, material science, medicine, motors, engineering, particle accelerators, levitated trains, industrial energy-related sectors, heavy-industrial technology, transformers, network, electro-optic, and large-scale application fields (Runde, 1995; Batlogg, 1998; Kuczkowski and Kusz, 1998; Buckel, 2004; Xu, et al., 2009; Coombs, 2011; Nagaya, Hirano, Naruse, Watanabe, and Tamada, 2013; Xu, et al., 2012). In this work, the variation of the basic crystallinity quality, phase analyses, average grain sizes, volume fractions, lattice cell parameters for the tetragonal crystal symmetry, grain boundary couplings, weak-interaction problems between the superconducting grains, grain alignment distributions and (mis)orientations, strength quality of connection between the grains, and crystal

structure problems of $Bi_{2.1}Sr_{2.0}Ca_{1.1}Cu_{2.0}O_y$ superconductors with the different aluminum impurity addition amount have been determined by use of the X-ray diffraction analyses. The experimental results have shown that the aluminum oxide impurity addition has been not good for fundamental crystal structure quantities.

2. EXPERIMENTAL PROCEDURES FOR $BI_{2.1}SR_{2.0}CA_{1.1}CU_{2.0}O_Y$ SUPERCONDUCTOR

In the present work, the effect of aluminum oxide impurity additions on the basic crystallinity quality, phase analyses, average grain sizes, volume fractions, lattice cell parameters for the tetragonal crystal symmetry, grain boundary couplings, weak-interaction problems between the superconducting grains, grain alignment distributions and (mis)orientations, strength quality of connection between the grains, and crystal structure problems of bulk $Bi_{2.1}Sr_{2.0}Ca_{1.1}Cu_{2.0}O_yAl_x$ superconductors has experimentally been studied by standard XRD measurements performed at 2θ angles intervals 3°-60° in the atmospheric air conditions. The aluminum oxide addition levels have been determined as $0.00 \leq x \leq 0.10$. Previously, on our studies published in "International Conference on Engineering Technologies" we inspected the influence of aluminum oxide impurity addition on some fundamental characteristics' properties including dc electrical resistivities (residual resistivity, conductivity property, residual resistivity ratios, resistivity at 90 K temperature, hole carrier concentrations per Cu ions in the Cu-O_2 layer $x^2 - y^2$ bands, resistivity at the room temperature state of 300 K, ρ_{norm}, $\Delta\rho$, offset and offset critical transition temperatures and degree of broadening parameters in the international scientific conference papers. At the same time, in the other papers, we have discussed the differentiation of formation of super-electrons, amplitude of pair wave function, homogeneities in the oxidation states, cooper-pair coupling probabilities in the strongly covalently bonded Cu-O_2 layers, hole trap energy values in the superconducting paths, metallic connections, overlapping of Cu-3d and O-2p wave functions, and crystallinity problems (related to the weak-interaction problems between the superconducting grains, stress raisers, microscopic structural faults, grain misorientations, , internal omnipresent flaws/defects/distortions/porosity, crystallinity quality problems, and grain boundary coupling problems). Also, in another paper we have tried to define a relation between the basic electrical resistivity measurements and structural flaws/defects/distortions to find the most ideal crystallinity quality of bulk $Bi_{2.1}Sr_{2.0}Ca_{1.1}Cu_{2.0}O_yAl_x$ superconductors with the maximum critical transition temperatures. Furthermore, one can encounter chemicals purities, ambient conditions, heat-treatment methods, experimental test tools, milling process, heating/cooling rates,

characterization instruments, production procedure, standard solid-state reaction route, composition contents, stochiometric ratios, and related experimental details as well as experimental test apparatus, Al molar ratios, milling process, and characterization instruments. In the present study, we have indexed the diffraction peaks observing at the XRD diffractograms with the aid of Miller indices. The Al-added samples (Bi-2212) have been prepared within the molar weights containing the ratios of 0.00, 0.01, 0.03, 0.05, 0.07 and 0.1, and they are abbreviated to be un-added, Bi/Al-1, Bi/Al-2, Bi/Al-3, Bi/Al-4, and Bi/Al-5, respectively.

3. RESULTS AND DISCUSSION

This study includes the scientific information based on the variation of the basic crystallinity quality, phase analyses, average grain sizes, volume fractions, lattice cell parameters for the tetragonal crystal symmetry, grain boundary couplings, weak-interaction problems between the superconducting grains, grain alignment distributions and (mis)orientations, strength quality of connection between the grains, and crystal structure problems inferred from the X-ray diffraction analyses taken from 2θ angles changing between of 3°-60° of solid $Bi_{2.1}Sr_{2.0}Ca_{1.1}Cu_{2.0}O_y$ superconductors with the different aluminum oxide (Al_2O_3) impurity amount ($0.0 \leq x \leq 0.10$). The XRD diffraction peaks belonging to the pure and various Al-added Bi-2212 superconductors have been depicted in Fig. 1a-c.

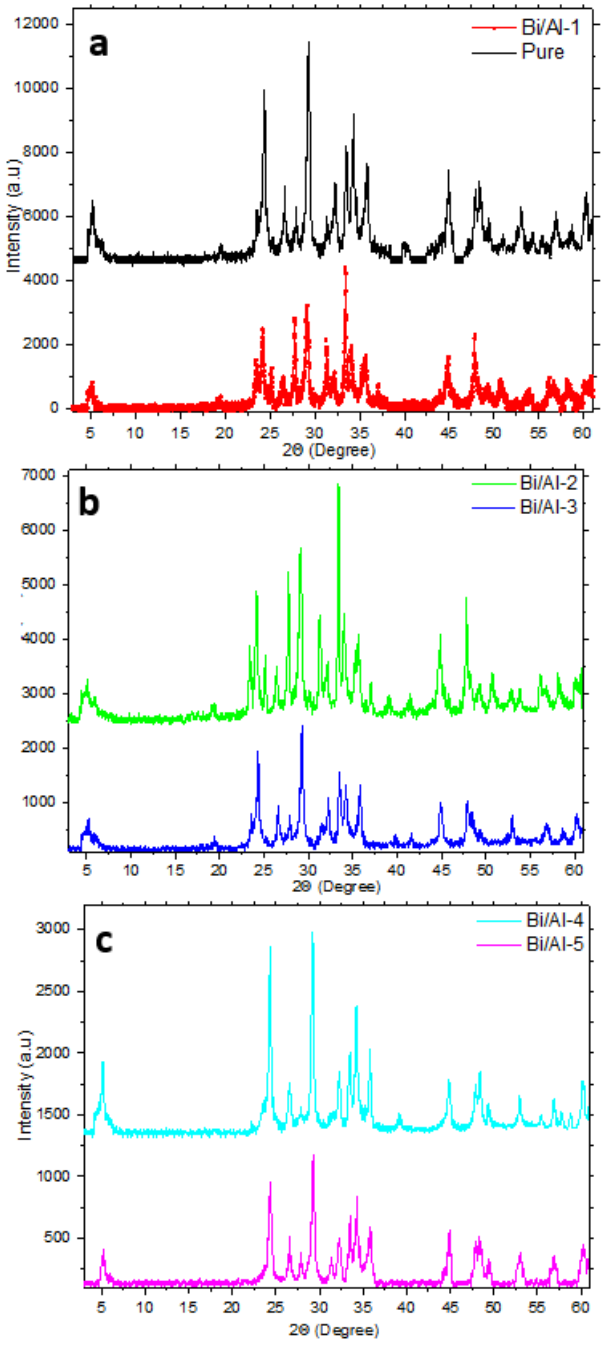

Fig. 1 Related XRD diffractograms for **a-)** pure and Bi/Al-1 superconductors; **b-)** Bi/Al-2 and Bi/Al-3 superconductors; and **c-)** Bi/Al-4 and Bi/Al-5 superconductors.

The XRD curves of Fig. 1a have displayed the bulk un-added and Bi/Al-1 superconductor when the part b of Fig. 1 has graphically indicated the XRD diffractograms for the Bi/Al-2 and Bi/Al-3 superconductors. Similarly, the part c in Fig. 1 have indicated the XRD diffraction curves for the Bi/Al-4 and Bi/Al-5 superconductors. It has been shown from the figures that the aluminum impurity addition amount has affected seriously the basic crystallinity quality, phase analyses, average grain sizes, volume fractions, lattice cell parameters for the tetragonal crystal symmetry, grain boundary couplings, weak-interaction problems between the superconducting grains, grain alignment distributions and (mis)orientations, strength quality of connection between the grains, and crystal structure problems. In fact, the increase in the Al_2O_3 impurity addition level has noted to damage considerably the fundamental crystallinity parameters mentioned above. Correspondingly, the un-added Bi-2212 superconductor has revealed the best fundamental crystallinity parameters whereas the bulk Bi/Al-5 superconductor has exhibited the worst fundamental crystallinity qualities.

3.1. Differentiations of basic crystallinity parameters of bulk $Bi_{2.1}Sr_{2.0}Ca_{1.1}Cu_{2.0}O_y$ superconductor with Al_2O_3 impurity addition level

In this part of paper, we have totally focused on the changes in the basic crystallinity parameters of bulk $Bi_{2.1}Sr_{2.0}Ca_{1.1}Cu_{2.0}O_y$ superconductors with the different Al_2O_3 impurity addition level ($0.0 \leq x \leq 0.10$) to determine the main role of Al_2O_3 material on the crystal structure. Even, it has been noted that the conditions for the preparation procedure conditions or additions of new atoms in the crystal lattice have dramatically changed positively or negatively the basic crystallinity parameters of a material. In the current work, the Al_2O_3 impurity has exhibited the negative effects on the crystallinity parameters of Bi-2212 superconductors. Figure 1 has shown that the presence of Al_2O_3 impurity has extensively made the characteristic peak reflection intensities in the XRD diffractograms shift harshly towards to higher/lower angles. Similarly, the increase in the Al_2O_3 impurity in the crystal lattice of Bi-2212 system has triggered the formation of new impurity peaks, disappearances of peaks, and enhancement/degradation in the diffraction intensities. These variations related to the diffraction peaks have been explained by the changes in the basic crystallinity quality, phase analyses, average grain sizes, volume fractions, lattice cell parameters for the tetragonal crystal symmetry, grain boundary couplings, weak-interaction problems between the superconducting grains, grain alignment distributions and (mis)orientations, strength quality of connection between the grains, and crystal structure problems due to the introduction of Al_2O_3 impurity in the Bi-2212 crystal lattice.

Furthermore, Fig. 1 has clearly shown that in the crystal structure the un-added superconductor (given as black dashes in Fig. 1a) has obtained both low and high superconducting phases together at various 2θ angles. Likewise, the other bulk Bi/Al-1, Bi/Al-2, Bi/Al-3, Bi/Al-4, and Bi/Al-5 superconductors have exhibited the similar characteristic diffraction peaks (but at different 2θ angles and various diffraction peak intensities) in their XRD diffractograms. In more detail, the figure has shown that the characteristic peak intensities coincided with both the low and high phases have been observed to decrease monotonously depending on the increment in the Al_2O_3 impurity addition amount. In fact, some characteristic diffraction peaks have been noticed to wholly vanish with the increase in the Al_2O_3 impurity addition amount. This is because the Al_2O_3 impurity has led to the increase in the crystal structure problems (stress raisers, microscopic structural faults, weak-interaction problems between the superconducting grains, grain misorientations, internal omnipresent flaws/defects/distortions/porosity, partial melting, crystallinity quality problems, and grain boundary coupling problems) in the Bi-2212 crystal system, having already been discussed in previous papers.

3.2. Variation of low and high phase fractions of $Bi_{2.1}Sr_{2.0}Ca_{1.1}Cu_{2.0}O_y$ superconductors with Al_2O_3 impurity addition

We have also determined the effect of different Al_2O_3 impurity addition amount ($0.0 \leq x \leq 0.10$) on the variation of low and high phase fractions of $Bi_{2.1}Sr_{2.0}Ca_{1.1}Cu_{2.0}O_y$ superconductors utilizing from the characteristic XRD diffraction peaks. According to the experimental findings based on Fig. 1, it has been obvious that the enhancement of Al_2O_3 impurity addition amount has brought about the dramatic degradation of the peak reflection intensities related to the characteristic low and high superconducting phases. We have computed phase fraction values for the characteristic low and high superconducting phases and have numerically provided in Table 1. Numerical values have warned us that the characteristic high superconducting phases have been much more negatively affected rather than low ones. However, it can be said that both the characteristic low and especially high superconducting phases have been noted to decrease constantly depending on the Al_2O_3 impurity addition amount. This is exactly why the characteristic low superconducting phase seems to have increased relatively. As for the numerical values, the un-added Bi-2212 superconductor have had the characteristic low superconducting phase value of 76.6% and characteristic high superconducting phase value of 23.4%. With the increase in the Al_2O_3 impurity addition amount, the phase volume fraction value for the characteristic high superconducting phase has been noted to degrade systematically, and in fact for the maximum addition level the minimum characteristic high superconducting phase

has been observed. On this basis, the solid Bi/Al-1 superconductor has possessed the characteristic high superconducting phase value of 21.3%. The other materials have obtained the relative lower high superconducting phase volume fraction values. The smallest value of 14.2% has been observed for the solid Bi/Al-5 superconductor. On the other hand, the characteristic low superconducting phase values have been found to be in a range of 76.6%-85.8%. In this context, the maximum characteristic low superconducting phase value of 85.8% has been found to belong to the Bi/Al-5 superconductor. Shortly, it has been found that the un-added bulk Bi-2212 superconductor has presented the highest superconducting parameters while the maximum aluminum oxide impurity added Bi-2212 superconductor has exhibited the lowest superconducting features. These facts have already been verified by Ref. (Öz, Yıldırım, and Terzioğlu, 2022a; Öz, Yıldırım, and Terzioğlu, 2022b). We have also tried to bring out the role of aluminum oxide impurity addition amount on the low and high superconducting phase fractions with the use of Fig. 2. It has been clear that the increase in the aluminum oxide impurity addition amount has remarkably damaged the characteristic high superconducting phase values.

Table 1. Effect of different Al_2O_3 impurity addition amounts on low and high characteristic superconducting phase fractions of Bi-2212 superconductors.

Ceramics	***Phase volume fraction (≈%)***	
	2212	***2223***
Un-added	76.6	23.4
Bi/Al-1	78.7	21.3
Bi/Al-2	81.9	18.1
Bi/Al-3	82.8	17.2
Bi/Al-4	84.0	16.0
Bi/Al-5	85.8	14.2

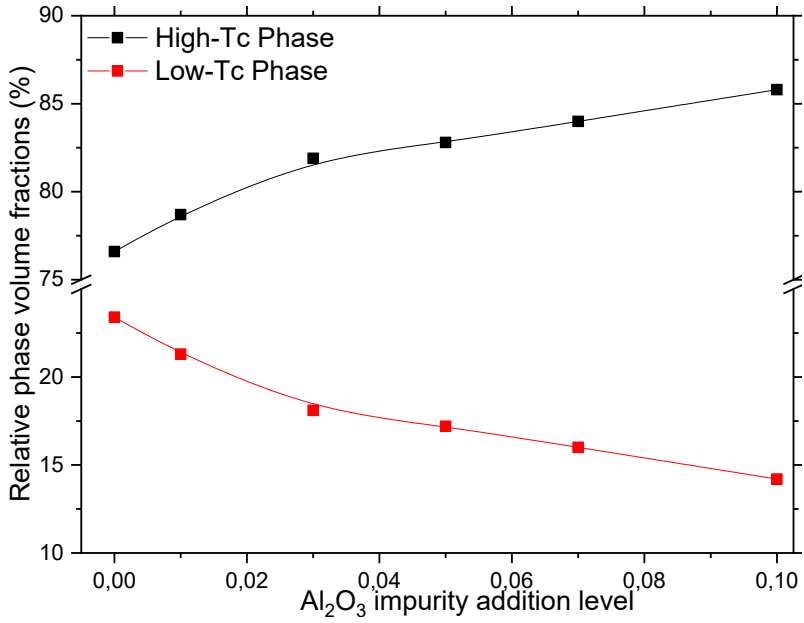

Fig. 2 Change in phase characteristic low and high superconducting phases with different Al_2O_3 impurity addition amounts for $Bi_{2.1}Sr_{2.0}Ca_{1.1}Cu_{2.0}O_y$ superconductors

3.3. Role of different Al_2O_3 impurity addition amounts on lattice cell parameters of $Bi_{2.1}Sr_{2.0}Ca_{1.1}Cu_{2.0}O_y$ superconductors

In this part of book chapter, we have thoroughly focused on the variation of the lattice cell constant parameters (*a* and *c*) for tetragonal crystal symmetry of $Bi_{2.1}Sr_{2.0}Ca_{1.1}Cu_{2.0}O_y$ superconductors by using the standard computation formulas provided in Ref. (Ulgen, Turgay, Terzioglu, Yildirim, and Oz, 2018). All the *a* and *c* lattice cell constant parameters calculated have been depicted in Table 2. One can see from the table that there has appeared reverse proportion between the *a* and *c* lattice cell constants parameters depending on the aluminum impurity addition amount. In more detail, the increase in the Al_2O_3 impurity addition level in the Bi-2212 crystal lattice has triggered the enhancement in the *a*-axis length from 5.40 Å (for the un-added Bi-2212 superconductor) to the value of 5.47 Å (for the Bi/Al-5 superconductor). On the other hand, the increase in the bulk Al_2O_3 impurity addition amount has led to the decrease in the *c* lattice cell constant parameters from 32.25 Å (for the un-added Bi-2212 superconductor) to 30.63 Å (for the Bi/Al-5 superconductor).

Table 2. Effect of different Al_2O_3 impurity addition levels on *a* and *c* lattice cell parameters and average grain size values of Bi-2212 superconductors.

Materials	*a (Å)*	*c (Å)*	*Average grain size (nm)*
Pure	5.40	32.25	49.53
Eu-1	5.41	32.02	47.41
Eu-2	5.43	31.66	44.22
Eu-3	5.44	31.20	42.16
Eu-4	5.45	30.96	40.85
Eu-5	5.47	30.63	38.68

3.4. Influence of various aluminum impurity addition amounts on average grain size value of $Bi_{2.1}Sr_{2.0}Ca_{1.1}Cu_{2.0}O_y$ superconductors

In the last part of chapter, we have been interested in the variation of average grain size parameters (deduced from the characteristic XRD diffraction peaks) of $Bi_{2.1}Sr_{2.0}Ca_{1.1}Cu_{2.0}O_y$ superconductors with the aluminum impurity addition level by using the Scherrer–Warren approach (Cullity and Stock, 2014; Ulgen, Terzioglu, and Yildirim 2022). The average grain size parameters calculated for the pure and aluminum oxide added Bi-2212 superconductors have been embedded in Table 2. According to the table, the average grain size values have been found to decrease systematically as the Al_2O_3 impurity addition level has increased in the Bi-2212 superconductors. Accordingly, the un-added has had the average grain size value of 49.53 nm that has been the maximum value. Conversely, the minimum average grain size value of 38.68 nm has been observed for the bulk Bi/Al-5 superconductor. The experimental findings have shown that the presence of aluminum oxide impurity in the Bi-2212 crystal structure has damaged seriously the basic crystallinity quality, phase analyses, average grain sizes, volume fractions, lattice cell parameters for the tetragonal crystal symmetry, grain boundary couplings, weak-interaction problems between the superconducting grains, grain alignment distributions and (mis)orientations, strength quality of connection between the grains, and crystal structure problems.

4. CONCLUSION

This study has studied on the variation of basic crystallinity quality, phase analyses, average grain sizes, volume fractions, lattice cell parameters for the tetragonal crystal symmetry, grain boundary couplings, weak-interaction problems between the superconducting grains, grain alignment distributions and (mis)orientations, strength quality of connection between the grains, and crystal structure problems of $Bi_{2.1}Sr_{2.0}Ca_{1.1}Cu_{2.0}O_y$ superconductors with the aluminum oxide

impurity addition level by using the XRD measurements conducted at 2θ angles between 4°-60° in the atmospheric air conditions. The experimental and theoretical computations have shown that the increase in the Al_2O_3 impurity addition level has resulted in the remarkable degradation in the basic crystal structures of Bi-2212 superconductors up to the highest addition level of x=0.10 as a result of the increase of the non-recoverable structural problems, intra/inter-grain boundary couplings, microvoids, strains, and impurity scatterings in the crystal system. Moreover, it has been noted that the increase in the aluminum oxide addition level has seriously suppressed the general superconducting parameters including the formation of cooper-pair probabilities, charge carrier concentrations, and super-electrons.

REFERENCES

1. Batlogg, B. (1998). Cuprate superconductors: science beyond high Tc. Solid state communications, 107(11), 639-647. Kleiner, R., & Huebener, R. P. (2004). Superconductivity: fundamentals and applications. Wiley-VCH.
2. Chen, M., Paul, W., Lakner, M., Donzel, L., Hoidis, M., Unter-naehrer, P., Weder, R., Mendik, M., 6.4 MVA resitive fault cur-rent limiter based on Bi-2212 superconductor, Physica C 372, 1657–1663, 2002.
3. Cullity, B. D. (1956). Elements of X-ray Diffraction. Addison-Wesley Publishing.
4. Erdem, U., Zalaoglu, Y., Ulgen, A. T., Turgay, T., & Yildirim, G. (2021). Role of trivalent Bi/Tm partial substitution on active operable slip systems in Bi-2212 crystal structure. Cryogenics, 113, 103212.
5. Ginzburg, V. L., & Andryushin, E. A. (2004). Superconductivity (Revised Edition). World Scientific.
6. Guner, S. B., Zalaoglu, Y., Turgay, T., Ozyurt, O., Ulgen, A. T., Dogruer, M., & Yildirim, G. (2019). A detailed research for determination of Bi/Ga partial substitution effect in Bi-2212 superconducting matrix on crucial characteristic features. Journal of Alloys and Compounds, 772, 388-398.
7. Kleiner, R., & Buckel, W. (2016). Superconductivity: an introduction. John Wiley & Sons.
8. Kuczkowski, A., & Kusz, B. (1998). High-Tc superconductor-polymer composites: YB2Cu3O7− x-polyester polymer and YBa2Cu3O7− x-Teflon. *Synthetic metals*, *94*(1), 145-148.
9. Meissner, W., & Ochsenfeld, R. (1933). Ein neuer effekt bei eintritt der supraleitfähigkeit. Naturwissenschaften, 21(44), 787-788.
10. Nagaya, S., Hirano, N., Naruse, M., Watanabe, T., & Tamada, T. (2012). Development of a high-efficiency conduction cooling technology for SMES coils. IEEE transactions on applied superconductivity, 23(3), 5602804-5602804.
11. Onnes, H. K. (1991). Further Experiments with Liquid Helium. D. On the Change of the Electrical Resistance of Pure Metals at very low Temperatures, etc. V. The Disappearance of the resistance of mercury. In Through Measurement to Knowledge (pp. 264-266). Springer, Dordrecht.
12. Öz, M., Yıldırım, G., Terzioğlu, C., 2022, Effect of aluminum oxide on main superconducting features of $Bi_{2.1}Sr_{2.0}Ca_{1.1}Cu_{2.0}O_y$ ceramics, International Conference on Engineering Technologies, 125, Konya.
13. Öz, M., Yıldırım, G., Terzioğlu, C., 2022, Influence of aluminum oxide on main electrical resistivity features of Bi-2212 ceramic compounds, International Conference on Engineering Technologies, 120, Konya.
14. Parinov, I. A. (2013). Microstructure and properties of high-temperature superconductors. Springer Science & Business Media.

15. Runde, M. (1995). Application of high-T/sub c/superconductors in aluminum electrolysis plants. IEEE Transactions on Applied Superconductivity, 5(2), 813-816.
16. Takayama-Muromachi, E. (1998). High-pressure synthesis of homologous series of high critical temperature (T c) superconductors. Chemistry of materials, 10(10), 2686-2698.
17. Ulgen, A. T., Turgay, T., Terzioglu, C., Yildirim, G., & Oz, M. (2018). Role of Bi/Tm substitution in Bi-2212 system on crystal structure quality, pair wave function and polaronic states. Journal of Alloys and Compounds, 764, 755-766.
18. Ulgen, A.T., Terzioglu, C., Yildirim, G., 2022, Change of Basic Electrical Conductivity and Superconducting Features of Bi-2212 Superconducting Ceramics with Europium Addition, International Research in Engineering Sciences II, Eğitim Yayınevi, 23-42.
19. Xu, H. H., Cheng, L., Yan, S. B., Yu, D. J., Guo, L. S., & Yao, X. (2012). Recycling failed bulk YBCO superconductors using the NdBCO/YBCO/MgO film-seeded top-seeded melt growth method. Journal of applied physics, 111(10), 103910.
20. Xu, X., Kim, J. H., Dou, S. X., Choi, S., Lee, J. H., Park, H. W., ... & Tomsic, M. (2009). A correlation between transport current density and grain connectivity in MgB 2/Fe wire made from ball-milled boron. Journal of Applied Physics, 105(10), 103913. [19] Coombs, T.A., A finite element model of magnetization of superconducting bulks using a solid-state flux pump, IEEE T. Appl. Supercond. 21 (2011) 3581–3586.
21. Yamauchi, H., & Karppinen, M. (2000). Application of high-pressure techniques: stabilization and oxidation-state control of novel superconductive and related multi-layered copper oxides. Superconductor Science and Technology, 13(4), R33.
22. Yildirim, G. (2013). Beginning point of metal to insulator transition for Bi-2223 superconducting matrix doped with Eu nanoparticles. Journal of alloys and compounds, 578, 526-535.
23. Zalaoglu, Y., Turgay, T., Ulgen, A. T., Erdem, U., Turkoz, M. B., & Yildirim, G. (2020). A novel research on the subject of the load-independent microhardness performances of Sr/Ti partial displacement in Bi-2212 ceramics. Journal of Materials Science: Materials in Electronics, 31(24), 22239-22251.

Investigation of the Behaviors of Ti and Pt Biomaterials in Proton Therapy Using Geant4 Simulation

Dr. Fatih EKİNCİ

Ministry of Youth and Sports, ORCID: 0000-0002-1011-1105

1- Introduction

Cranioplasty is the process of replacing the missing piece of bone in the skull for some reason or surgically placing another suitable material there. The history of cranioplasty applications dates back to very old years [1]. The ideal cranioplasty material should be non-heat-resistant, resistant to biomechanical processes, easy to use, compatible with tissues, not causing complications, and easily sterilizable [1]. There may be different events that can lead to the formation of bone defects in the skull. One of these is the removal of tumor tissue and skull bone together, followed by therapy during the surgery of a brain tumor that also covers the skull bone [2-3].

The rationale for the clinical use of proton therapy is that higher doses can be given to the tumor and better preservation of healthy tissue compared to photon-utilizing radiotherapy. The doses given in Radiotherapy using Photons are usually at limited energies to prevent harmful effects on healthy tissue. However, higher doses provide higher tumor control [5]. The transfer of a large part of the dose to the tumor is greater for protons and heavy ions than for photons. Because of the high compatibility and calibration achievable with proton therapy, treating tumors very close to critical tissues has resulted in better results [6]. Unlike other heavily charged particles, protons create less nuclear fission reactions in the environment they interact with, so less secondary particles emerge. The secondary particles formed vary according to the mass and charge of the incoming bullet particle. Due to the long range of these secondary particles, a small increase in dose may occur and cause a change in the radiation field. These events form a tail behind the Bragg peak. This tail is undesirable as it irradiates healthy surrounding tissues [7,8]. Although the contribution of protons to produce neutrons as secondary particles is as low as 1%, C, O etc. This contribution is higher for heavily charged particles [9]. The dose given to healthy tissues at risk close to the tumor is low in protontherapy. The use of protons in head and nervous system tumors has the potential to reduce the likelihood of spinal cord toxicity [10].

Monte Carlo-based Geant4 is a completely new simulation program [11, 12]. Geant4 is software that can simulate particles passing through and interacting with matter. Geant4; The project, which started as GEneration ANd Tracking in the 1970s, evolved into GEometry ANd Tracking in the 2000s [11, 12]. In the developing process, Geant3 was developed at CERN between 1982-1994, and later written in Fortran code, Geant3 reached its current version as Geant4 with updates [11]. It is a program that simulates physical events that occur when elementary particles pass through different geometric targets with a wide energy range [11, 12]. It was originally designed for high energy physics experiments.

Geant4 is a very difficult and complex system both in installation and software phase [12]. First, a detector must be constructed from materials and geometric shapes with the detector definition and response part defined [11, 12]. This placed detector is exposed to the electromagnetic field, at the same time it is necessary to identify the particles passing through the detector for the detector [11, 12]. In this sense, the Geant4 simulation program has a large library containing a large number of particles and their properties [11, 12].

2- Material and Method

In this study, Bragg curves in various energy ranges were calculated for the implanted (Titanium (Ti) and Platinum (Pt)) head and water phantom with the help of the Geant4 computer-based simulation program for Proton Therapy. By comparing the Bragg curves found, it was determined which energy range should be preferred at different depths. The same procedures were repeated for the most preferred Ti and Pt implants with a thickness of 1 and 1.5 cm in front of the brain and water. The phantom used in this study is presented in Figure 1. Ti and Pt biomaterials are given as adherents of the phantom. Thus, their use as a replacement for cortical bone was investigated.

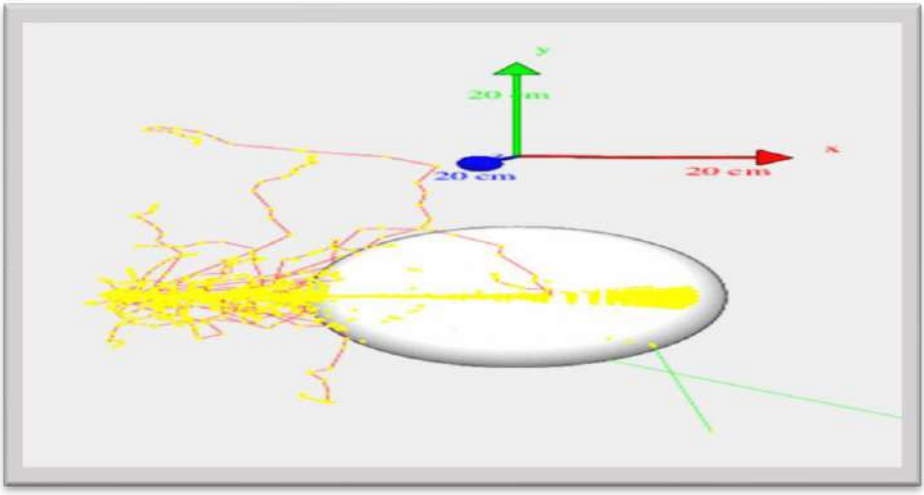

Figure 1. The phantom geometry of the cross-section is constructed. The biomaterials were placed at the contact point of the proton beam to the phantom.

Calculations with Geant4 were simulated using water for proton therapy and a wide energy range for implants of different thicknesses (Ti and Pt) for brain simulation from the Geant4 library. In the simulation, the water phantom and the

brain tissue phantom are simulated as a sphere with a radius of 15 cm. The detector is simulated as an ion chamber with a cube-shaped extinguishing gas Ar with a side length of 1 cm. A proton beam with 10^5 particles was used in the calculations. As the number of particles increases, the optimum particle number is chosen because the computation time increases. The gap cut or step size (range cut) is calculated for 0.01 cm (0.1 mm). Because, as the step size gets shorter, the calculations increase in 10 times, taking into account the time situation, the optimum step size is determined and calculations are made.

3- Results

In the phantom formed from water and brain tissue, 1 and 1.5 cm thick Pt (G4_Pt) biomaterial with atomic radius 1.83 Å, atomic volume 9.1 cm^3/mol density 21.45 g/cm^3 and ionization energy (I) 790 eV were used instead of cortical bone. Compared to the Bragg peak of the proton beam passing through a target with a greater density than water and brain tissue, the input dose was significantly increased. This reduced the range of the Bragg peak. Since the energy required to ionize Pt is 9 eV for the first, 18 eV for the second, its ionizing property is more. The proton beam formed close dose/range values in water and brain tissue as seen in Figure 2-3 and Table 1-2. The effect of Pt thickness on the Bragg peak was compared.

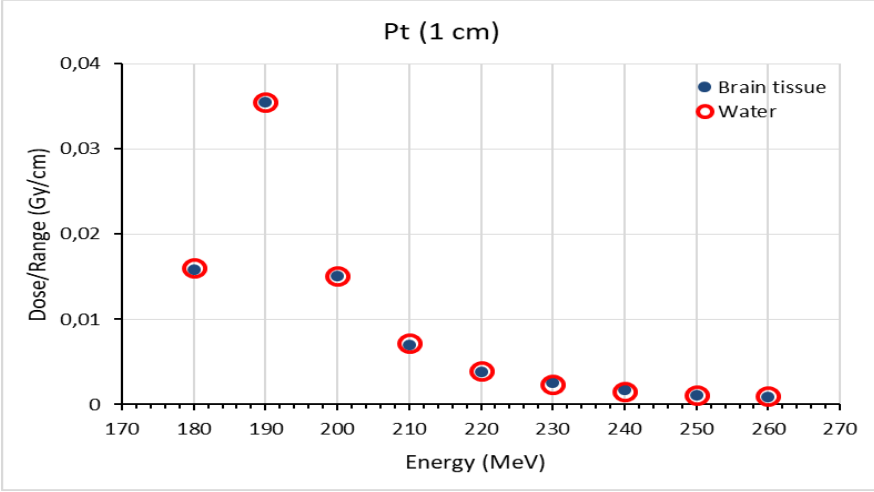

Figure 2. Comparison of the use of 1 cm thick Pt biomaterial instead of cortical bone in phantoms composed of water and brain tissue.

Table 1. Comparison of Bragg peaks for water and brain phantoms with Pt implants 1 cm thick with Geant4

Energy (MeV)	[a]Water Phantom (cm)	[b]Brain tissue Phantom (cm)	% Fark (| a-b | ×100/a)
180	1.68	1.70	1.19
190	2.31	2.31	0
200	4.25	4.25	0
210	6.50	6.62	1.23
220	8.79	8.87	1.36
230	11.14	10.83	2.78
240	13.38	13.12	1.94
250	15.94	15.86	0.5
260	18.70	18.16	2.88

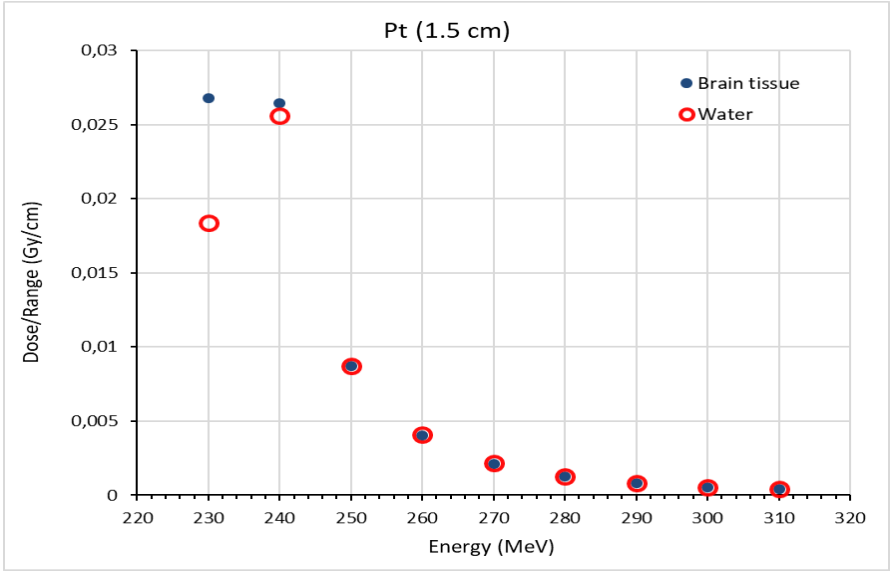

Figure 3. Comparison of the use of 1.5 cm thick Pt biomaterial instead of cortical bone in phantoms composed of water and brain tissue

Table 2. Comparison of Bragg peaks for water and brain phantoms with Pt implants 1.5 cm thick with Geant4

Energy (MeV)	[a]Water Phantom (cm)	[b]Brain tissue Phantom (cm)	% Fark (| a-b | ×100/a)
240	2.80	2.70	3.57
250	5.32	5.32	0
260	7.71	7.66	0.51
270	10.93	10.38	5.03
280	13.05	13.05	0
290	15.71	15.70	0.06
300	18.80	18.70	0.53
310	21.23	20.97	1.22

In the phantom created from water and brain tissue, it was simulated that there is a 1 and 1.5 cm thick Ti (G4_Ti) implant with an atomic radius of 2 Å, an Atomic Volume of 10.64 cm^3/mol, a density of 4.54 g/cm^3, and an I of 233 eV. A significant increase in the input dose was observed compared to the Bragg peak of the proton beam passing through a target with a high density compared to water. The dose/range and bragg peak range comparisons of Ti biomaterials are given in Figure 4-5 and Table 3-4. Since the energy required to ionize Ti is 6.82 for the first, 13.58 for the second and 27.49 eV for the third, it needs more energetic proton beams to ionize than water. However, Bragg peaks are not low despite the input dose like platinum, as it needs lower energy than Pl. Because the density of Pt is about 4.6 times that of Ti and its ionization potential is 34 times.

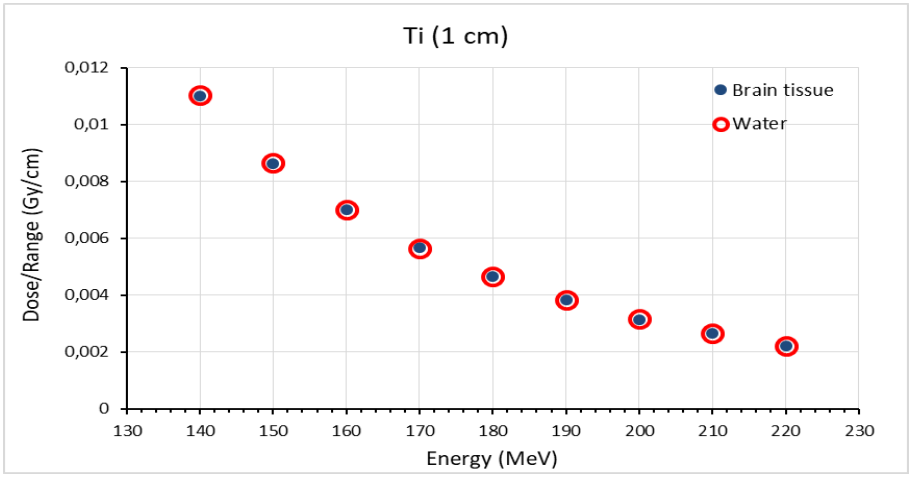

Figure 4. Comparison of the use of 1 cm thick Ti biomaterial instead of cortical bone in phantoms composed of water and brain tissue

Table 3. Comparison of Bragg peaks for water and brain phantoms with 1 cm thick Ti implants with Geant4

Energy (MeV)	**[a]Water Phantom (cm)**	**[b]Brain tissue Phantom (cm)**	**% Fark (| a-b | ×100/a)**
140	7.73	7.76	0.38
150	9.60	9.62	0.20
160	11.43	11.45	0.17
170	13.46	13.41	0.37
180	15.46	15.43	0.19
190	17.58	17.58	0
200	19.81	19.86	0.25
210	22.00	22.00	0
220	24.42	24.44	0.081

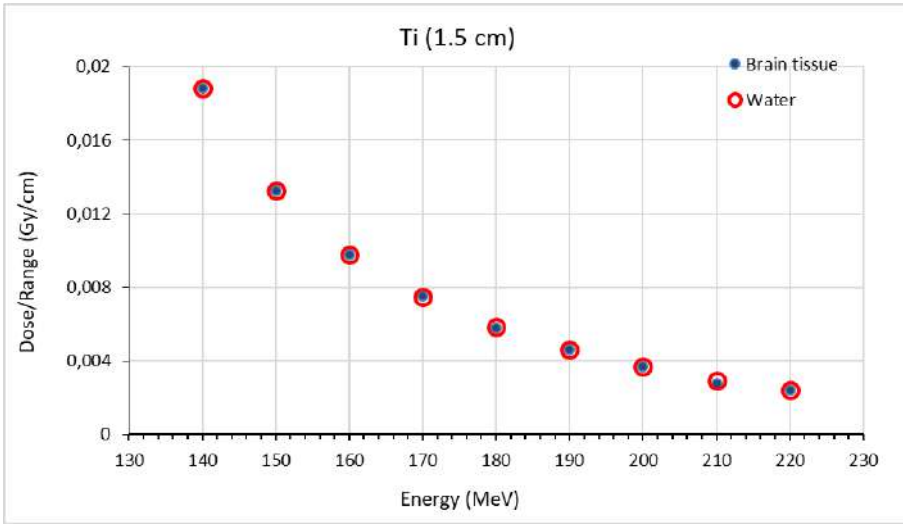

Figure 5. Comparison of the use of 1.5 cm thick Ti biomaterial instead of cortical bone in phantoms composed of water and brain tissue

Table 4. Comparison of Geant4 and Bragg peaks for water and brain phantoms with 1.5 cm thick Ti implants

Energy (MeV)	[a]Water Phantom (cm)	[b]Brain tissue Phantom (cm)	% Fark (| a-b | ×100/a)
140	4.61	4.61	0
150	6.38	6.38	0
160	8.27	8.28	0.12
170	10.22	10.19	0.29
180	12.23	12.28	0.40
190	14.40	14.35	0.34
200	16.55	16.58	0.18
210	18.93	19.16	1.21
220	21.23	21.10	0.61

Examining the graphs obtained with the Geant4, it appeared that there was an average of 3.16% difference in water and brain results without implants, with a difference of about 0.44 cm at 130 MeV energy for the Bragg peak. In the results

of implanted water and brain; For Pt 1.5 cm, 0.61 cm difference at 230 MeV energy average 3.8%, for Pt 1 cm 0.54 cm difference and average 2.5%, for Ti 1.5 cm 0.23 cm difference at 210 MeV energy and average 0.36% and for Ti 1 cm at 200 MeV energy 0.05 cm difference and mean deviation of 0.18% were observed. It can be said more clearly that the biggest reason for the difference and mean deviations for the implanted and implanted water phantom and brain is the effects of inhomogeneity. Water phantoms (1 g/cm^3) have homogeneous structures. However, not all parts of the human brain have the same density and thickness. It consists of structures such as sinus cavities (air spaces), skull bones (1.85 g/cm^3), hard connective tissues such as dura mater, brain parenchyma, vascular structures, adipose tissue (0.92 g/cm^3) and cerebral fluid (1.007 g/cm^3) in the brain. So it is not homogeneous. For this purpose, comparisons were made with the spherical G4_WATER (1 g/cm^3 and 75 eV) water phantom and G4_BRAIN_ICRP (1.03 g/cm^3 and 73.3 eV) human brain phantom. The reason for using human tissue equivalent brain phantoms or water phantoms is because the real human brain cannot be used to study Bragg curves.

In the calculations using biomaterials (Pt and Ti), it was seen that the higher input dose compared to the simulations without implants was due to the higher density (Pt= 21 g/cm^3 and Ti= 4.5 g/cm^3). For this, Ti biomaterial with low density and high radiation permeability and Pt biomaterial with high density and low radiation permeability were chosen. It can be preferred as a suitable metal in cranioplasty applications compared to Pt biomaterial, as it is lighter due to the density of Ti metal and better transmits radiation. As can be seen from the implanted graphs, the Bragg curves of the Ti implant were more smooth and expected than the Pt. It is understood that it is a more cost-effective implant because it requires less energy proton beam for Ti in the treatment of brain tumors of equal depth. The good radiation permeability of the Ti biomaterial has resulted in less proton beam energy used. Considering its chemical properties, biocompatibility and radiation properties, it is understood that it is preferred as an implant material in cranioplasty applications. The results obtained with the Geant4 simulation program show that the differences between water and brain tissue phantoms are not significant and are within the acceptable limits (<5%) in the medical field. Considering small differences as the effects of inhomogeneity, considering these differences means an increase in the quality of patient treatment.

4- Discussion

In this study, Bragg curves obtained using the human brain and spherical water phantom for the Proton Therapy device in the Geant4 (10.2) computer code were

compared with each other. A proton therapy device was designed in the study with the Geant4 simulation program. Simulations are not guaranteed to produce an optimum solution. Since it is a trial and error method, different variations should be tried. Each simulation model is unique. There are practical conveniences that ignore analytical solutions. Errors in both modeling and analysis of the findings may lead to incorrect results [13, 14]. For this reason, proton beams with different particle numbers in different energy ranges were used. The proton beam was sent to the target using the Pencil Beam Scanning method. Thus, scattering was prevented. The bundle thickness was determined as 1 cm. Modeling in our program was done by considering both the spherical water phantom and the human brain. When a charged particle enters the medium, it transfers its energy to the medium, approximately inversely proportional to the square of its velocity [15]. For this reason, as the particle slows down, the probability of ionization of the atoms in the environment increases and the maximum dose is transferred to the depth where the ionization events are maximum [16]. It was seen from the graphs that this was the reason why the input dose was lower than the Bragg peak and the input dose was higher as the energy decreased. The decrease in the energy of the particle as it travels through the medium can change the range, position, size, and shape of the Bragg peak. These effects can deflect the accuracy of the Bragg peak range by 1%. It is necessary to calculate this effect, since the density of the medium will change the stopping power of each particle [15]. Considering similar studies, different biomaterials as well as Ti-doped (NiTi and Ti_6Al_4V) biomaterials were used instead of cortical bone [17]. Results close to this study were found. Studies have shown that the importance of biomaterials has increased recently [17-19]. In particular, heavy ion treatment [20-22] on different phantoms using biomaterials is important for the discovery of new biomaterials [17, 19].

Reference

1- Aydin, S., Kucukyuruk, B., Abuzayed, B., Aydin, S. ve Sanus, G. Z. (2011). Cranioplasty: Review of materials and techniques. Journal of Neurosciences in Rural Practise, 2(2), 162-167.

2- Edwards, B.N. ve Gold, B.R. (1992). Analysis of surface cleanliness of three commercial dental implants. Biomaterials,13,775–780.

3- Brånemark, P.I., Hansson, B.O., Adell, R., Breine, U., Lindström, J., Hallén, O. (1977) Osseointegrated titanium implants in the treatment of the edentulous jaw. Scand J Plast Reconstr Surg, 11, 1–175.

4- Albrektsson, T., Brånemark, P. I., Hansson, H. A. ve Lindström, J. (1981). Osseointegrated titanium implants: requirements for ensuring a long-lasting, direct bone-to-implant anchorage in man. Acta Orthopaedica Scandinavica, 52(2), 155-170.

5- Niemierko, A., Urie, M., and Goitein, M. (1992). Optimization of 3D Radiation Therapy with both Physical and Biological End Points and Constraints, International Journal of Radiation Oncology, Biology, Physics, 23, 99-108.

6- Stephen J. Dowdell. (2011). Pencil beam scanning proton therapy: the significance of secondary particles, Doctor Thesis, University of Wollongong Centre for Medical Radiation Physics Faculty of Engineering, 1-173.

7- Brons, S. ve ark. (2009). The role of nuclear reactions in Monte Carlo calculations of absorbed and biological effective dose distributions in hadron therapy. 12th International Conference on Nuclear Reaction Mechanisms, 15 - 19 Jun, Villa Monastero, Varenna, Italy.

8- Ekinci F., Bostanci E., Dagli O. and Guzel M.S.(2021). Analysis of Bragg Curve Parameters and Lateral Straggle for Proton and Carbon Beam. Communications Faculty of Sciences University of Ankara Series A2-A3 Physical Sciences and Engineering, 2021, 63, 1, 32–41. DOI: 10.33769/aupse.864475

9- Pshenichnov, I., Mishustin, I. ve Greiner, W. (2005). Neutrons form fragmentation of light nuclei in tissue-like media: a study with Geant4 toolkit. Phys. Med. Biol., vol. 50, 5493-5507.

10- Cozzi, L., Fogliata, A., Lomax, A., and Bolsi, A. (2001). A treatment planning comparison of 3D conformal therapy, intensity modulated photon therapy and proton therapy for treatment of advanced head and neck tumors, Radiother Oncol, 61(3), 287-97.

11- Geant4. (2016). URL: http://www.geant4.org/geant4/ . Last access date: 20.04.2016.

12- Geant4Cern. (2016). URL: http://geant4.cern.ch. Last access date: 20.04.2016.

13- Lux, I., Koblinger, L. (1991). Monte Carlo Particle Transport Methods, Neutron and Photon Calculations, CRC Pres, boc raton.

14- Foster, D.G., Artur. (1982). Avarege Neutronic Properties of “Prompt” Fission Poducts, Los Alamos National Laboraty Report LA-9168-MS.

15- Lomax, A.J. (2009). Charged Particle theraphy The Physics of interaction, Cancer j, 15(4):285-91.

16- Brown, A., Suit, H. (2004). The centenary of the discovery of the Bragg Peak, Radiother. oncol.,73(3):265-8.

17- Ekinci, F., Bölükdemir, M.H. (2019). The Effect of the Second Peak formed in Biomaterials used in a Slab Head Phantom on the Proton Bragg Peak. Journal of Polytechnıc, 23, 1, 129-136 DOI: 10.2339/politeknik.523001

18- Ekinci Fatih. (2019). Investigation of the interaction of proton and carbon bundles with tissue equivalent targets. Doctor Thesis, Gazi Üniversitesi, Fen Bilimleri Enstitüsü, Türkiye.

19- Ekinci F., (2022), Investigation of tissue equivalence of phantom biomaterials in 4He heavy ion therapy. Radiation Effects and Defects in Solids. https://doi.org/10.1080/10420150.2022.2153251

20- Senirkentli G.B., Ekinci F., Bostanci E., Güzel M.S., Dağli Ö., Karim A.M. and Mishra A. (2021). Therapy for Mandibula Plate Phantom. Healthcare 2021, 9, 167. https://doi.org/10.3390/healthcare9020167

21- Ekinci F., Bostanci E., Guzel M.S., Dagli O. (2022). Effect of different embolization materials on proton beam stereotactic radiosurgery Arteriovenous Malformation dose distributions using the Monte Carlo simulation code. Journal of Radiation Research and Applied Sciences. Volume 15, Issue 3, September 2022, Pages 191-197. https://doi.org/10.1016/j.jrras.2022.05.011

22- Ekinci F., Bostanci E., Guzel M.S., Dagli O. (2022). Analysing the effect of a cranium thickness on a Bragg peak range in the proton therapy: a TRIM and GEANT4 based study. St. Petersburg State Polytechnical University Journal. Physics and Mathematics, vol. 15, no. 2, pp. 64–78. DOI 10.18721/JPM.15207.

On Higher Dimensional Groups

Ummahan EGE ARSLAN[1]
İ.Ilker AKCA[2]

1;2Department of Mathematics and Computer Science,
Faculty of Science, Eskişehir Osmangazi University, Eskişehir, Türkiye

Introduction

There are several approaches to generalize groups to higher dimensions. Crossed modules and 1-cat-groups are the same as 2-group formulations, namely a two-dimensional generalisation of the concept of group.

Crossed modules take place initially Whitehead's work (Whitehead,1949) as a model for 2-types. There he investigated the algebraic structure of relative homotopy groups. Since then, they have appeared in several mathematical contexts, including the theory of group presentations, algebraic K-theory, homological algebra, and also group representation. It is well known that categorical equivalences are important in terms of facilitating the solution of problems in different fields. Equivalent categories can be seen as various viewpoints on the same issue. One of the many categories equivalent to the category of crossed modules, perhaps the most useful is the category of 1-cat-group. The ability to flexibly transition between crossed modules and cat groups allows that representation theory for 2-groups may be described in crossed module language, (Barker, 2003).

There are also many different algebraic models, known as the 3-types in higher dimensions groups. Some of them are crossed squares of groups, 2-cat-groups, 2-crossed modules (Conduché, 1984), braided, regular crossed modules and (2-truncated) simplicial groups (Brown and Gilbert, 1989), quadratic modules (Baues, 1991). But we will only deal with crossed squares of groups and 2-cat-groups of these. Although the concept of crossed squares of groups was not connected to that of 2-cat-groups when it was initially given by Loday and Walery (Loday and Walery,1981), Loday mentioned that there is an equivalence of categories between the category of 2-cat-groups and that of crossed squares (Loday,1982).

In this work, we will explain this equivalence in detail. We will recall the definitions we will need in this study.

2-Dimensional Groups: Crossed Modules and 1-cat-groups

Definition 1 *A crossed module denoted by (G,N,∂) is a group morphism $\partial : G \to N$ with an action of N on G satisfying*

$$\partial(n \cdot g) = n\partial(g)n^{-1} \text{ and } \partial(g) \cdot g' = gg'g^{-1}$$

for all $g, g' \in G, n \in N$. A morphism of crossed modules from (G,N,∂) to (G',N',∂') is a pair of group morphisms, $\phi : G \to G, \psi : N \to N'$ such that $\phi(n \cdot g) = \psi(n) \cdot \phi(g)$. We thus get a category XMod of crossed modules.

Definition 2 *A 1-cat-group is a group G together with a subgroup N and two endomorphisms $s, b : G \to N$ satisfying the following conditions:*

(i) $s \mid_N = b \mid_N = id_N$

(ii) $[Kers, Kerb] = 1$

This 1-cat-group is denoted by $(G;N)$.

Proposition 3 *For any 1-cat-group* $(G;N)$:

i) $st = t, ts = s$

ii) $t^2 = t, s^2 = s$.

Proof. i) For $g \in N$, we have $s(t(g)) = s(g) = t(g)$, for $g \in G \backslash N$, we get $t(g) \in N$ and $s(t(g)) = t(g)$. Similarly $ts = s$.

ii) As $st = t$ and $ts = s$, we have $t^2 = t(st) = (ts)t = st = t$. ■

Proposition 4 *There is an equivalence of categories between the category of 1-cat-groups and that of crossed modules.*

Proof. See (Porter, 2011 and Brown etc. 2011). ■

3-Dimensional Groups: Crossed Squares and 2-Cat-Groups

Definition 5 *A 2-cat-group is a group that has two independent 1-cat-group structures on it. More explicitly, we can give the following definition.*

A 2-cat-group is a group G together with two subgroups N_1, N_2 *such that* $(G;N_1)$ *and* $(G;N_2)$ *are 1-cat-groups and following equations are valid:*

$$s_i s_j = s_j s_i, t_i t_j = t_j t_i, s_i t_j = t_j s_i$$

$i, j = 1,2, i \neq j$.

Definition 6 *A crossed square as defined in [10] (see also [23]) is a commutative diagram of groups*

$$\begin{array}{ccc} P & \xrightarrow{\lambda} & Q \\ {\scriptstyle \lambda'}\downarrow & & \downarrow{\scriptstyle \mu} \\ R & \xrightarrow[\mu']{} & S \end{array}$$

together with actions of S on P,Q and R. There are thus associative actions of R on P and Q, via μ', *and of Q on P and R via* μ *and a function* $h : Q \times R \longrightarrow P$, *such that the following axioms are satisfied:*

i) The maps $\lambda, \lambda^{'}, \mu, \mu'$ *and* $\mu' \lambda^{'} = \mu\lambda$ *are crossed modules,*

ii) The maps $\lambda, \lambda^{'}$ *are S-equivariant*,

iii) $q \cdot (q' \cdot p) h(q,r) = h(q,r)(q' \cdot (q \cdot p))$,

iv) $h(qq^{'}, r) = (q \cdot h(q', r)) h(q,r)$,

v) $h(q, rr^{'}) = h(q,r)\left(r \cdot h(q, r^{'})\right)$,

vi) $s \cdot h(q,r) = h(s \cdot q, s \cdot r)$,

vii) $\lambda^{'} h(q,r) = (q \cdot r) r^{-1}$,

viii) $\lambda h(q,r) = q\left(r \cdot q^{-1}\right)$,

ix) $h(q, \lambda^{'} p) = (q \cdot p) p^{-1}$,

x) $h(\lambda p, r) = p\left(r \cdot p^{-1}\right)$,

for all $r, r^{'} \in R, q, q^{'} \in Q, s \in S, p \in P$ *where* $q \cdot p, q \cdot r, r \cdot q^{-1}, r \cdot p^{-1}$ *denote* $\mu(q) \cdot p, \mu(q) \cdot r, \mu'(r) \cdot q^{-1}, \mu'(r) \cdot p^{-1}$,*respectively.*

One can easily get the category of crossed squares of groups and it is denoted by $\mathbf{Crs}^2$.

Proposition 7 *There is an equivalence of categories between the category of 2-cat-groups and that of crossed squares.*

Proof. We will give the construction of a 2-cat-group from a crossed square in detail. Since λ' and μ are crossed module there are semi-direct products $P \rtimes R$ and $Q \rtimes S$. It is defined an group action of $Q \rtimes S$ on $P \rtimes R$ by ■

$$\begin{array}{rccc} \lhd\colon (Q \rtimes S) \times (P \rtimes M') & \longrightarrow & P \rtimes R \\ ((q,s),(p,r)) & \longmapsto & (q \cdot (s \cdot p) h(q, s \cdot r), s \cdot r) \end{array}$$

$G = (P \rtimes R) \rtimes (Q \rtimes S)$ is a group with following operation

$$(p_1, r_1, q_1, s_1) \circledast (p_2, r_2, q_2, s_2) = ((p_1, r_1) * [(q_1, s_1) \lhd (p_2, r_2)], (q_1, s_1) * (q_2, s_2)).$$

The inverse of the element (p, r, q, s) in G is

$$\left(\left(s^{-1} \cdot q^{-1}\right) \cdot \left(s^{-1} \cdot \left(r^{-1} \cdot p^{-1}\right) h\left(s^{-1} \cdot q^{-1}, s^{-1} \cdot r^{-1}\right), s^{-1} \cdot r^{-1}, s^{-1} \cdot q^{-1}, s^{-1}\right).$$

Really, if $(p, r, q, p) \circledast (x, y, z, t) = (1, 1, 1, 1)$ then

$$(p, r) * [(q, p) \lhd (x, y)] = (1, 1) \text{ and } (q, p) * (z, t) = (1, 1).$$

Thus we get

$$\begin{array}{ll} (x, y) & = (q, p)^{-1} \lhd (p, r)^{-1} = \left(\left(p^{-1} \cdot q^{-1}\right), p^{-1}\right) \lhd \left(\left(r^{-1} \cdot l^{-1}\right), r^{-1}\right) \\ & = \left(\left(p^{-1} \cdot q^{-1}\right) \cdot \left(p^{-1} \cdot \left(r^{-1} \cdot l^{-1}\right)\right) h\left(p^{-1} \cdot q^{-1}, p^{-1} \cdot r^{-1}\right), p^{-1} \cdot r^{-1}\right) \end{array}$$

and

$$(z, t) = (q, p)^{-1} = \left(p^{-1} \cdot q, p^{-1}\right).$$

Also, it is satisfied that

$$(x, y, z, t) \circledast (p, r, q, p) = (1, 1, 1, 1)$$

by the conditions of crossed square.

It is well-known that $N_1 = Q \rtimes S$ is a semi-direct group. b_1 and s_1 defined as follows:

$$\begin{array}{rccc} b_1: & G & \longrightarrow & N_1 \\ & (p, r, q, s) & \longmapsto & (\lambda(p)(\mu'(r) \cdot q), \mu'(r) s) \end{array}$$

$$\begin{array}{rccc} s_1: & G & \longrightarrow & N_1 \\ & (p, r, q, s) & \longmapsto & (q, s) \end{array}$$

We will show that b_1 and s_1 are group homomorphisms.

We have the below equations:

$$
\begin{aligned}
&b_1((p_1,r_1,q_1,s_1)\circledast(p_2,r_2,q_2,s_2))\\
&=b_1\left((p_1,r_1)*[(q_1,s_1)\lhd(p_2,r_2)],(q_1,s_1)*(q_2,s_2)\right)\\
&=b_1\left((p_1,r_1)*[q_1\cdot(s_1\cdot p_2)h(q_1,s_1\cdot r_2),s_1\cdot r_2],q_1(s_1\cdot q_2),s_1s_2\right)\\
&=b_1\left(p_1\left(r_1\cdot[q_1\cdot(s_1\cdot p_2)h(q_1,s_1\cdot r_2)]\right),r_1(s_1\cdot r_2),q_1(s_1\cdot q_2),s_1s_2\right)\\
&=\left(\lambda\left(p_1\left(r_1\cdot[q_1\cdot(s_1\cdot p_2)h(q_1,s_1\cdot r_2)]\right)\right)\mu'(r_1(s_1\cdot r_2))\cdot q_1(s_1\cdot q_2),\right.\\
&\left.\mu'(r_1(s_1\cdot r_2))s_1s_2\right)
\end{aligned}
$$

So we get

$$
\begin{aligned}
&\lambda\left(p_1\left(r_1\cdot[q_1\cdot(s_1\cdot p_2)h(q_1,s_1\cdot r_2)]\right)\right)\mu'(r_1(s_1\cdot r_2))\cdot q_1(s_1\cdot q_2)\\
&=\lambda(p_1)\lambda(r_1\cdot(q_1\cdot(s_1\cdot p_2))))\lambda(r_1\cdot h(q_1,s_1\cdot r_2))\mu'(r_1(s_1\cdot r_2))\cdot(q_1(s_1\cdot q_2))\\
&=\lambda(p_1)(\mu'(r_1)\cdot\lambda(q_1\cdot(s_1\cdot p_2))(\mu'(r_1)\cdot\lambda h(q_1,p_1\cdot r_2))\\
&\quad\mu'(r_1(p_1\cdot r_2))\cdot(q_1(p_1\cdot q_2))\\
&=\lambda(p_1)(\mu'(r_1)\cdot(q_1\lambda(s_1\cdot p_2)q_1^{-1})[\mu'(r_1)\cdot\left(r_1\left(\mu'(s_1\cdot r_2)\cdot q_1^{-1}\right)\right)]\\
&\quad\mu'(r_1(s_1\cdot r_2))\cdot(q_1(s_1\cdot q_2))\\
&=\lambda(p_1)(\mu'(r_1)\cdot q_1)(\mu'(r_1)\cdot\lambda(s_1\cdot p_2))\left(\mu'(r_1)\cdot q_1^{-1}\right)(\mu'(r_1)\cdot r_1)\\
&\quad\left[[\mu'(r_1)\mu'(s_1\cdot r_2)]\cdot q_1^{-1}\right](\mu'(r_1(s_1\cdot r_2))\cdot q_1)\mu'(r_1(s_1\cdot r_2))\cdot(s_1\cdot q_2)\\
&=\lambda(p_1)(\mu'(r_1)\cdot q_1)(\mu'(r_1)\cdot\lambda(s_1\cdot p_2))(\mu'(r_1(s_1\cdot r_2))s_1)\cdot q_2\\
&=\lambda(p_1)(\mu'(r_1)\cdot q_1)(\mu'(r_1)\cdot\lambda(s_1\cdot p_2))(\mu'(r_1)\mu'(s_1\cdot r_2)s_1)\cdot q_2\\
&=\lambda(p_1)(\mu'(r_1)\cdot q_1)(\mu'(r_1)\cdot\lambda(s_1\cdot p_2))(\mu'\left(r_1\right)s_1\mu'(r_2)s_1^{-1}s_1)\cdot q_2
\end{aligned}
$$

and also have

$$
\begin{aligned}
\mu'(r_1(s_1\cdot r_2))s_1s_2&=\mu'(r_1)\mu(s_1\cdot r_2)s_1s_2\\
&=\mu'(r_1)s_1\mu(r_2)s_1^{-1}s_1s_2\\
&=\mu'(r_1)s_1\mu(r_2)s_2
\end{aligned}
$$

as the first and second component respectively. On the other hand,

$$
\begin{aligned}
&b_1((p_1,r_1,q_1,s_1))\circledast b_1((p_2,r_2,q_2,s_2))\\
&=(\lambda(p_1)(\mu'(r_1)\cdot q_1),\mu'(r_1)s_1)*(\lambda(p_2)(\mu'(r_2)\cdot q_2),\mu'(r_2)s_2)\\
&=(\lambda(p_1)(\mu'(r_1)\cdot q_1))[\mu'(r_1)s_1\cdot(\lambda(p_2)(\mu'(r_2)\cdot q_2))],\mu'(r_1)s_1\mu'(r_2)s_2)\\
&=(\lambda(p_1)(\mu'(r_1)\cdot q_1))[\mu'(r_1)\cdot(s_1\cdot(\lambda(p_2)(\mu'(r_2)\cdot q_2)))],\mu'(r_1)s_1\mu'(r_2)s_2)\\
&=(\lambda(p_1)(\mu'(r_1)\cdot q_1))[\mu'(r_1)\cdot((\lambda(s_1\cdot p_2)(s_1\cdot(\mu'(r_2)\cdot q_2))))],\\
&\mu'(r_1)s_1\mu'(r_2)s_2)\\
&=(\lambda(p_1)(\mu'(r_1)\cdot q_1))[\mu'(r_1)\cdot((\lambda(s_1\cdot p_2)][\mu'(r_1)\cdot(s_1\cdot(\mu'(r_2)\cdot q_2))))],\\
&\mu'(r_1)s_1\mu'(r_2)s_2)\\
&=(\lambda(p_1)(\mu'(r_1)\cdot q_1))[\mu'(r_1)\cdot((\lambda(s_1\cdot p_2)][\mu'(r_1)\cdot(s_1\cdot(\mu'(r_2)\cdot q_2))))],\\
&\mu'(r_1)s_1\mu'(r_2)s_2)\\
&=(\lambda(p_1)(\mu'(r_1)\cdot q_1))[\mu'(r_1)\cdot\lambda(s_1\cdot p_2)][(\mu'(r_1)p_1\mu'(r_2))\cdot q_2],\\
&\mu'(r_1)s_1\mu'(r_2)s_2).
\end{aligned}
$$

Thus, we see that b_1 is a group homomorphism.

Since

$$b_1((1,1,q,p))=\left(\lambda(1)\left(\mu'(1)\cdot q\right),\mu'(1)p\right)=(q,s)=Id((q,s))$$

and

$$s_1((1,1,q,p))=(q,s)=Id((q,s)),$$

it is verified the first condition of definition of 1-cat-group. By definitions of b_1 and s_1, we have

$$\begin{aligned} Kerb_1 &= \{(p,r,q,s) \in G \mid b_1((p,r,q,s)) = (\lambda(p)(\mu'(r)\cdot q), \mu'(r)s) = (1,1)\} \\ &= \{(p,r,q,s) \in G \mid s = \mu'\left(r^{-1}\right), \lambda(p) = \mu'(r)\cdot q^{-1}\} \\ Kers_1 &= \{(p,r,q,s) \in G \mid s_1((p,r,q,s)) = (q,s) = (1,1)\} \\ &= \{(p,r,1,1) \mid p \in P, r \in R\}. \end{aligned}$$

If we regard to sets $Kerb_1$ and $Kers_1$, we get

$$s \cdot \overline{r} = \mu'\left(r^{-1}\right) \cdot \overline{r} = r^{-1}\overline{r}r$$

and

$$q = \mu'(r^{-1}) \cdot \lambda(p^{-1}) = s \cdot \lambda(p^{-1}).$$

We can see that commutator condition for 1-cat-group is satisfied by following equations:

$$\begin{aligned} (\overline{p},\overline{r},1,1) \circledast (p,r,q,s) &= ((\overline{p},\overline{r}) * (1,1) \lhd (p,r), (1,1) * (q,s)) \\ &= ((\overline{p},\overline{r}) * 1 \cdot (1\cdot p)h(1,1\cdot r), 1\cdot r, 1(1\cdot q), 1s) \\ &= ((\overline{p},\overline{r}) * (p,r), (q,s)) \\ &= (\overline{p}(\overline{r}\cdot p), \overline{r}r, q, s) \end{aligned}$$

and

$$\begin{aligned} (p,r,q,s) \circledast (\overline{p},\overline{r},1,1) &= ((p,r) * [(q,s) \lhd (\overline{p},\overline{r})], (q,s) * (1,1)) \\ &= ((p,r) * ((q\cdot(s\cdot\overline{p})h(q,s\cdot\overline{r}), s\cdot\overline{r}), q, s) \\ &= p(r\cdot[(q\cdot(s\cdot\overline{p})h(q,s\cdot\overline{r})], r(s\cdot\overline{r}), q, s) \\ &= p(r\cdot(q\cdot(s\cdot\overline{p}))(r\cdot h(q,s\cdot\overline{r})), r(s\cdot\overline{r}), q, s) \\ &\overset{(**)}{=} p\left(r\cdot[(q\cdot(s\cdot\overline{p}))]\right)p^{-1}(\overline{r}\cdot p), r\left(r^{-1}\overline{r}r\right), q, s). \end{aligned}$$

$(**)$

$$\begin{aligned} r\cdot h(q,s\cdot\overline{r}) &= \mu'(r)\cdot h\left(s\cdot\lambda(p^{-1}), s\cdot\overline{r'}\right) \\ &= s^{-1}\cdot\left(s\cdot h\left(\lambda(p^{-1}),\overline{r}\right)\right) \\ &= h\left(\lambda(p^{-1}),\overline{r}\right) = p^{-1}(\overline{r}\cdot p) \end{aligned}$$

$$h(q,p\cdot\overline{r}) = h\left(q,\mu'\left(r^{-1}\right)\cdot\overline{r}\right) = h\left(q,r^{-1}(\overline{r}r)\right) = h\left(q,r^{-1}\right)\left(r^{-1}\cdot h(q,\overline{r}r)\right).$$

Thus

$$\begin{aligned} \overline{p} = pp^{-1}\overline{p}pp^{-1} &= p\left(\lambda(p^{-1})\cdot\overline{p}\right)p^{-1} = p\left(\mu\left(\lambda(p^{-1})\right)\cdot\overline{p}\right)p^{-1} \\ &= p\left(\mu\left(\mu'(r)\cdot q\right)\cdot\overline{p}\right)p^{-1} \\ &= p\left[\left(\mu'(r)\mu(q)\mu'(r^{-1})\right)\cdot\overline{p}\right]p^{-1} \\ &= p\left(\mu'(r)\cdot(\mu(q)\mu'(r^{-1}))\cdot\overline{p}\right)p^{-1} \\ &= p\left(\mu'(r)\cdot(q\cdot(p\cdot\overline{p}))\right)p^{-1} = p(r\cdot(q\cdot(s\cdot\overline{p})))p^{-1} \end{aligned}$$

for all $(\overline{p},\overline{r},1,1) \in Kers_1, (p,r,q,s) \in Kerb_1$. So we have the equation

$$(\overline{p},\overline{r},1,1) \circledast (p,r,q,s) = (p,r,q,s) \circledast (\overline{p},\overline{r},1,1).$$

Thus $(G;N_1)$ is a 1-cat-group.

On the other hand, since $G=(P\rtimes R)\rtimes(Q\rtimes S)$ is isomorphic to $(P\rtimes Q)\rtimes(R\rtimes S)$, we get a 1-cat-group $((P\rtimes Q)\rtimes(R\rtimes S);R\rtimes S)$. Thus we get obtained a 2-cat-group.

Let $(G;N_1\cap N_2)$ be a 2-cat-group. Take $P=\mathrm{Ker}s_1\cap\mathrm{Ker}s_2$, $Q=N_1\cap\mathrm{Ker}s_2$, $R=\mathrm{Ker}s_1\cap N_2$, $S=N_1\cap N_2$.

$\lambda:\mathrm{Ker}s_1\cap\mathrm{Ker}s_2\longrightarrow N_1\cap\mathrm{Ker}s_2$ is well defined by $\lambda(x)=b_1\mid_P(x)$, since for $x\in Kers_1\cap Kers_2$,

$$s_2(b_1\mid_P(x))=b_1\mid_P(s_2(x))=b_1\mid_P(1)=1$$

and $x\in Kers_1\cap Kers_2\subseteq G$, we get $\lambda(x)=b_1\mid_P(x)\in Kers_2$ and $\lambda(x)=b_1\mid_P(x)\in N_1$,respectively.

λ is a crossed module with conjuge action of $N_1\cap Kers_2$ on $Kers_1\cap Kers_2$. The action

$$\begin{array}{ccc} N_1\cap Kers_2\times Kers_1\cap Kers_2 & \longrightarrow & Kers_1\cap Kers_2 \\ (n,g) & \longmapsto & n\cdot g=ngn^{-1} \end{array}$$

is well defined because of

$$s_1\left(ngn^{-1}\right)=s_1(n)s_1(g)s_1(n)^{-1}=s_1(n)1s_1(n)^{-1}=1$$

and

$$s_2\left(ngn^{-1}\right)=s_2(n)s_2(g)s_2(n)^{-1}=111=1.$$

It is seen that the conditions of crossed modules are satisfied by following equations.

$$\lambda(n\cdot g)=b_1\mid_P\left(ngn^{-1}\right)=b_1(n)b_1(g)b_1(n)^{-1}=nb_1(g)n^{-1}\ (\because b_1\mid_N=Id_N)$$

$$\begin{aligned} \lambda(g)\cdot g'=\lambda(g)g'\lambda(g)^{-1} &= b_1(g)g'b_1(g)^{-1}\left(gg^{-1}\right) \\ &= b_1(g)g'\left(b_1(g)^{-1}g\right)g^{-1} \\ &\overset{(*)}{=} b_1(g)\left(b_1(g)^{-1}g\right)g'g^{-1} \\ &= gg'g^{-1} \end{aligned}$$

Since $b_1\left(b_1(g)^{-1}g\right)=b_1\left(b_1(g)^{-1}\right)b_1(g)=b_1(g)^{-1}b_1(g)=1$,we have $b_1(g)^{-1}g\in\mathrm{Ker}b_1$. Also $b_1(g)^{-1}g\in\mathrm{Ker}b_1$ and $g'\in\mathrm{Ker}s_1$ commute, that is

$$g'\left(b_1(g)^{-1}g\right)\overset{(*)}{=}\left(b_1(g)^{-1}g\right)g'$$

for $n\in N_1\cap Kers_2, g\in Kers_1\cap Kers_2$.

It is showed that λ',μ' and μ are also crossed modules by similar idea, so we will just check that they are well defined.

$\lambda':\mathrm{Ker}s_1\cap\mathrm{Ker}s_2\longrightarrow\mathrm{Ker}s_1\cap N_2$ is well defined by $\lambda'(x)=b_2\mid_P(x)$, it is clear that $\lambda'(x)=b_2\mid_P(x)\in N_2$ and $b_2\mid_P(x)\in\mathrm{Ker}s_2$, because of

$$s_1b_2(x)=b_2s_1(x)=b_2(1)=1,$$

for $x \in Kers_1 \cap Kers_2$.

Furthermore $\mu' = b_1 \mid_R$:Kers$_1 \cap N_2 \longrightarrow N_1 \cap N_2$ and $\mu = b_2 \mid_Q$: $N_1 \cap$Kers$_2 \longrightarrow N_1 \cap N_2$ are well defined, since $b_2(b_1(x)) \in N_2$, $b_1(b_2(x)) \in N_1$ and $b_1(b_2(x)) = b_2(b_1(x))$ for $x \in$Kers$_1 \cap N_2 \subseteq G$ and $x \in N_1 \cap$Kers$_2 \subseteq G$.

$h : Q \rtimes R \longrightarrow P, h(q,r) = qrq^{-1}r^{-1}$ is well defined since

$$s_1\left(qrq^{-1}r^{-1}\right) = s_1(q)\, s_1(r)\, s_1(r)^{-1} = s_1(q)\, 1 s_1(q)^{-1}\, 1 = 1$$

and

$$s_2\left(qrq^{-1}r^{-1}\right) = s_2(q)\, s_2(r)\, s_2(q)^{-1}\, s_2(r)^{-1} = 1 s_2(r)\, 1 s_2(r)^{-1} = 1.$$

It is satisfied $\mu'\lambda' = \mu\lambda$ by $b_2 b_1 = b_1 b_2$.

As a result, we have the following crossed square with regard to the functions and group actions given above:

$$\begin{array}{ccc} Kers_1 \cap Kers_2 & \xrightarrow{\lambda} & N_1 \cap Kers_2 \\ {\scriptstyle \lambda'}\downarrow & & \downarrow{\scriptstyle \mu} \\ Kers_1 \cap N_2 & \xrightarrow[\mu']{} & N_1 \cap N_2 \end{array}$$

Kaynaklar

1. Barker, M.,2003. Representations of Crossed Modules and Cat1-Groups, PhD Thesis, University of Wales,Bangor.

2. Baues, H. J.,1991. Combinatorial homotopy and 4-dimensional complexes, *Berlin,etc.: Walter de Gruyter*.

3. Brown,R., Higgins,P.J., Sivera R.,2011. Nonabelian Algebraic Topology: Filtered Spaces, Crossed Complexes, Cubical Homotopy Groupoids *EMS Tracts in Mathematics, vol. 15, European Mathematical Society.*

4. Brown,R.,Gilbert, N.D., 1989, Algebraic models of 3-types and automorphism structures for crossed modules, *Proc. Lond. Math. Soc.* (3), 59, 51-73.

5. Conduché,D. 1984. Modules croisés généralisés de longueur 2,*J. Pure Appl. Algebra*, 34:155–178.

6. Guin-Walery, D., Loday, J. L.,1981. Obstructions l'excision en K-th©orie algbrique, *in Evanston Conference on Algebraic K-theory, Lecture Notes in Maths., Springer*, 854, 179-216.

7. Loday,J.-L.,1982. Spaces with finitely many nontrivial homotopy groups, *Journal of Pure and Applied Algebra*, 24, 179-202 (1982).

8. Porter,T., 2011. Homotopy Quantum Field Theories meets the Crossed Menagerie: an introduction to HQFTs and their relationship with things simplicial and with lots of crossed gadgetry, Lecture Notes.

9. Whitehead, J.H.C.,1949. Combinatorial Homotopy II, *Bulletin American Mathematical Society,* 55, 453-496.

Comparison of Magnetic Flux Density Distribution of Different Multi-Surface PMG Arrangements for Superconducting Maglev Systems

Ufuk Kemal Ozturk[1], Murat Abdioglu[1,2]

[1]Electromagnetic Guidance and Acceleration Research Group (EMGA), Department of Physics, Faculty of Science, Karadeniz Technical University, 61080, Trabzon, Türkiye.
[2]Department of Mathematics and Science Education, Faculty of Education, Bayburt University, 69000, Bayburt, Türkiye.

1. Overview of the Maglev Train Technology

People's need for faster, safe, and ecologically friendly transportation systems has been increasing in the developing world. The aircrafts are the most popular and fastest transportation vehicles, but CO_2 emissions alone from flights within Europe have increased 28% since 2013 and if it goes on like this, aviation emissions are expected to double or triple by 2050 (Transport & Environment, 2022). Therefore, the aircrafts cannot be accepted as an eco-friendly solution. One can offer electric cars to overcome this problem. However, these vehicles are not fast and safe enough in addition to the fact that not eco-friendly enough contrary to popular belief. Of course, those don't emit CO_2 directly but need electricity. According to the annual report of the United States Environmental Protection Agency (United States Environmental Protection Agency, 2022), the electric production is responsible for 25 % of the greenhouse gas emissions in 2020 (Figure 1). Therefore, one can see that the electric cars are not a sufficient solution for the problem mentioned above. Similarly, the conventional metal wheel electric trains also don't completely meet the mentioned needing. On the other hand, the trains can carry lots of passengers and/or cargo at once and can be accepted as more efficient than the electric cars. Therefore, the most effective solution is to increase the energy efficiency of the electric trains.

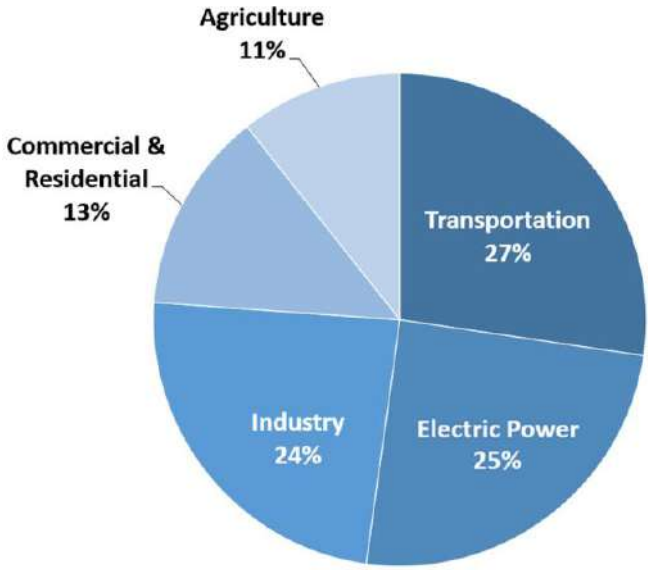

Figure 1. Sources of U.S. Greenhouse gas emissions in 2020 (United States Environmental Protection Agency, 2022).

Maglev trains are a very promising solution for the near future due to many advantages over conventional metal wheel-rail trains (Lee, Kim, & Lee, 2006):

a) Lower maintenance costs due to the elimination of wear between the wheel and the rail.

b) Maglev trains are not likely to derail as they move steadily on the guidance way.

c) Since there is no wheel, vibration and noises are eliminated.

d) They accelerate and decelerate very quickly.

e) They are less affected by weather conditions as they move on the guidance way without contact.

Maglev systems are classified into two, as electromagnetic Maglev (EML) and electrodynamic Maglev (EDL). Superconducting or normal conducting coils or permanent magnets are used in the EDL systems as magnetic field source. Today, non-superconductor-based Maglev trains are used in daily life in various countries such as Japan and China (Figure 2). However, studies all over the world are being conducted to make superconducting Maglev systems usable in everyday life due to their advantages, such as having more working gaps, less complexity, and lower system weights.

Figure 2. Non-superconducting, Transrapid Maglev train (Pirti, Yücel, & Ocalan, 2016).

Studies on Maglev systems gained momentum after the development of the first man-loaded superconducting Maglev vehicle by the researchers of Southwest Jiaotong University (Wang et al., 2002). Although studies on Maglev systems are being carried out by various research groups in many countries of the

world, studies on real-size Maglev systems are being conducted in China (Deng, et al., 2016), Brazil (Sotelo et al., 2013) and Germany (Schultz et al., 2005). The studies are increasing day by day the potential usage of Maglev systems in daily life, however the carrying capacity and movement stability are not yet at the required level. In addition, the fabrication cost of the system must be decreased by optimizing the superconductors used in the wagons and the permanent magnets used in the magnetic guidance way. In order to increase the carrying capacity, the vertical magnetic levitation force (F_y), the lateral magnetic guidance force (F_x) and related vertical (k_y) and the lateral (k_x) magnetic stiffness values between the superconducting materials in the Maglev system and the magnetic field distribution of the permanent magnetic guideway (PMG) should be increased.

The magnetic force performance of maglev systems can be increased in three ways. The first way is to improve the electromagnetic properties of the superconducting materials used in wagons (Abdioglu et al., 2022; Güner, 2020; Ozturk et al., 2012). The second way is optimizing the PMG in magnetic rail, which is used as a magnetic field source in the system (Ozturk, Abdioglu, et al., 2015) and the third way is to use additional magnets with superconductors in the wagon, which are called hybrid Maglev systems (Abdioglu, Kabaer, Ozturk, Erdem, & Celik, 2017; Abdioglu, Ozturk, Gedikli, Ekici, & Cansiz, 2015; Ozturk, Kabaer, & Abdioglu, 2015).

Two types of PMG configurations are generally used as magnetic field sources in the performed studies in literature. One of which is called conventional PMG (Liu, Wang, Wang, Wang, & Li, 2009), consisting of two opposite magnets and steel or iron used to concentrate the magnetic flux between these magnets. Another type of conventional PMGs is the one in which an upward or downward PM is used as a flux concentrator between opposite polarity PMs. The second type of PMG is called "Halbach" (Halbach, 1985), and in this PMG, five (or seven) magnets are arranged in a special magnetic orientation so that the magnetic field is concentrated on the top of the PMG.

Optimization of the magnetic guidance way is an important parameter for Maglev systems. Deng et al. conducted an experimental study (Z. Deng, Qian, et al., 2016) investigating the dynamic and static force performance between normal PMG (conventional PMG) or Halbach PMG and a three-seeded YBCO superconductor. In the study, the levitation force obtained with the Halbach PMG array and the decrease in this force depending on time were higher than the values obtained with the normal PMG array. The high temperature superconductor (HTS) arrangement in the system also affects the magnetic levitation force. In the study, it was also seen that the natural frequency magnetic stiffness values

obtained with Halbah PMG were higher than the values obtained with normal PMG. In the study, it was concluded that the Halbach PMG array has excellent performance in terms of both levitation and dynamic response characteristics.

The MagLev-Cobra research group in Brazil explained the properties of the full-size Maglev system fabricated in 2015 (Sotelo et al., 2015). The prototype, consisting of four 1.5 m long wagons, was tested between two buildings 200 m apart at the "Federal University of Rio de Janeiro" (Figure 3). The Maglev module can turn 50 m radius bends and climb ramps with 15% inclination. Six force sensors in the system can simultaneously measure the force and moment in three axes. A magnetic levitation force of 2000 N was obtained between each cryostat in the passenger compartment and the PMG. Due to the flux creep in the superconductors, it was observed that at the end of the one-day operating period of the Maglev system, there was a 35% decrease in the magnetic levitation force and this decrease was logarithmic with respect to time.

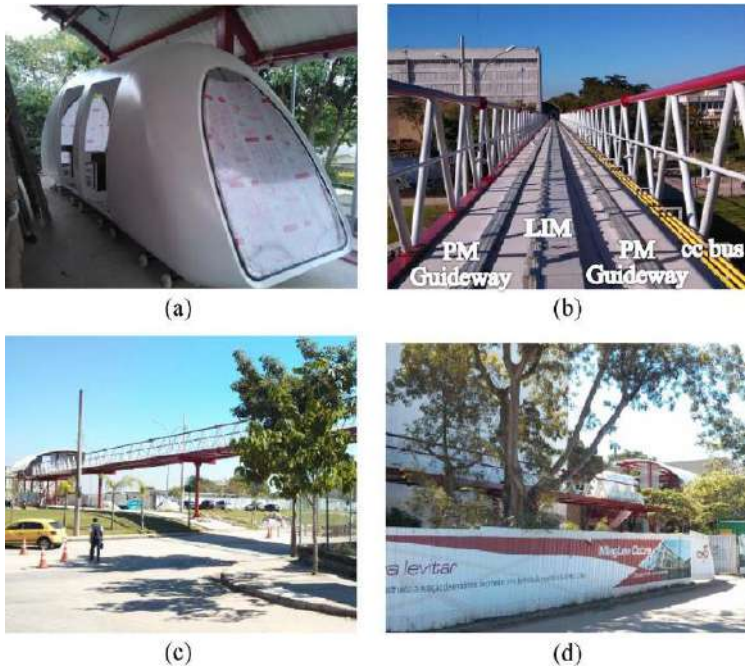

Figure 3. (a) Maglev vehicle; (b) Magnetic guideway and linear motor stator; (c-d) street view of the two stations and the road (Sotelo et al., 2015).

The research group in China explained the features of the Maglev test system (Z. Deng, Zhang, et al., 2016), which named "Super-Maglev" (Figure 4), consisting of a 45 m long runway (Figure 4b). The Maglev vehicle in the specified system has a length of 2.2 m and a width of 1.1 m, and has the capacity to carry

a single passenger at a working height of 10-20 mm. The magnetic guideway is 45 m long, in the form of a race-track with a curvature radius of 6 m, and a linear motor can accelerate the vehicle to 50 km/h maximum speed. During the movement of the vehicle, the working gap between the Maglev vehicle and the rail, levitation force, vehicle speed, acceleration, lateral balance, position, and total movement distance can be recorded in real time.

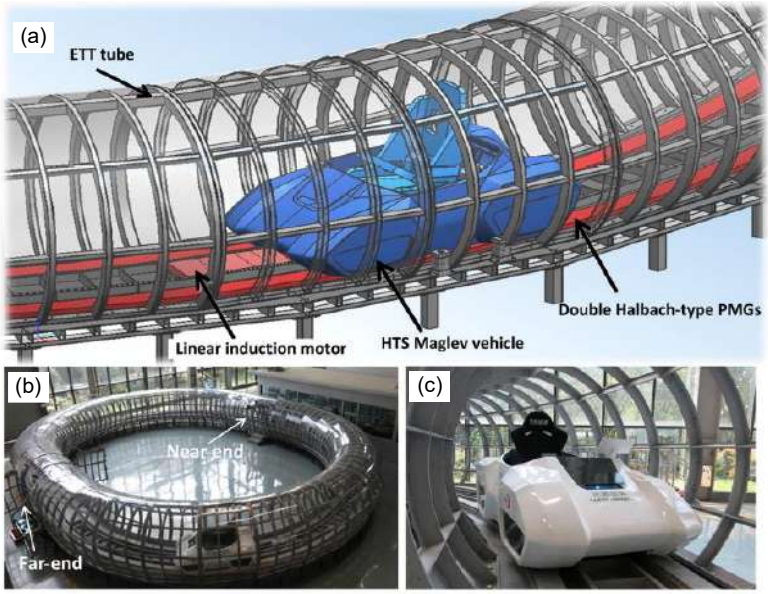

Figure 4. "Super-Maglev", HTS Maglev-ETT system developed in China; (a) design consisting of four main parts: HTS Maglev vehicle, ETT tube, Halbach PMG and linear induction motor, (b) panoramic view of the "Super-Maglev" and (c) HTS Maglev vehicle's close-up view while moving in the tube (Zigang Deng et al., 2017).

2. Magnetic Force Measurement System

The loading capacity, movement stability and the magnetic stiffness parameters of Maglev vehicles are determined via magnetic force measurement systems in laboratory scale. In our study, experimental studies on the levitation and guidance forces and also magnetic stiffness between the HTS and PMG units are conducted via the triaxial magnetic force measurement system, designed and fabricated by us (Figure 5). Three step motors are responsible for the movement of this system in three-axis. The superconductors are placed in the LN_2 vessel and cooled down to the superconducting transition temperature by adding LN_2 to the vessel for about 20 minutes. The force data on the HTS unit is collected via Tri-

Axial Load Cell (FUTEK MTA400) which can measure the force in x, y, and z axes up to 1110 N, 2220 N and 1110 N, respectively with the sensitivity of 0.5 N, 1 N and 0.5 N. We have given the technical properties of the measurement system in the previous studies (Abdioglu et al., 2015; Ozturk, Abdioglu, & Karaahmet, 2020). The positions in the vertical and lateral axis are measured via Baumer Laser sensors and the data collecting, and the control of the system is conducted by a PLC (programmable logic controller) programmed control unit. In the levitation force measurements, we have used YBCO HTSs with three-seed and 65 mm × 34 mm ×14 mm dimensions fabricated by ATZ GmbH company. The PMs in the PMGs have 40 mm × 30 mm × 30 mm dimensions and 0.53 T surface magnetic flux density.

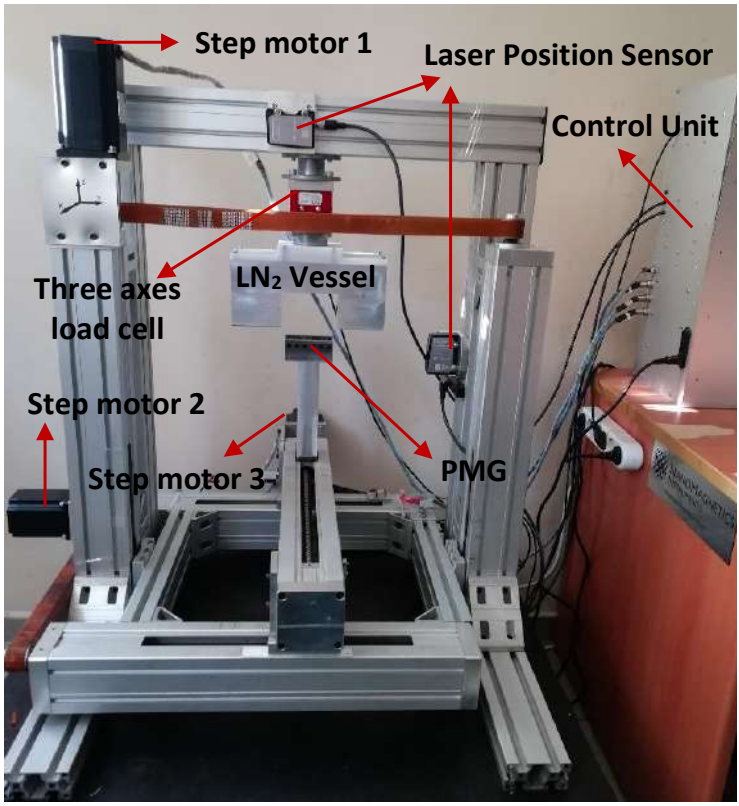

Figure 5. Three-axis magnetic levitation force measurement system

3. Magnetic Flux Density Distributions of Different PMG Configurations

As mentioned above, the magnetic flux density distribution is an important parameter to enhance the magnetic force performance and, therefore, the man or load carrying capacity and stable moving of Maglev systems. In addition to optimizing PMG's magnetic flux density distribution, we have designed HTS-PMG arrangements as multi-surface (Abdioglu et al., 2021; Ozturk, Badia-Majos, Abdioglu, Dilek, & Gedikli, 2021) as different from the studies in literature. This new structure allows us to enhance the magnetic force properties of the Maglev system by utilizing from the surfaces of the PMGs as much as possible. Figure 6 shows the schematic illustration of different multi-surface HTS-PMG configurations. Conf-1 includes four PM allowing four HTS, Conf-2 includes six PM allowing six HTS, whereas Conf-2 includes five PM allowing six HTS. Therefore, the HTS/PMG ratios are 1, 1 and 6/5 respectively for Conf-1, Conf-2 and Conf-3. The bigger HTS/PMG ratio provides bigger carrying capacity and moving stability in Maglev vehicles in addition to decreasing the total fabrication cost of the PMG.

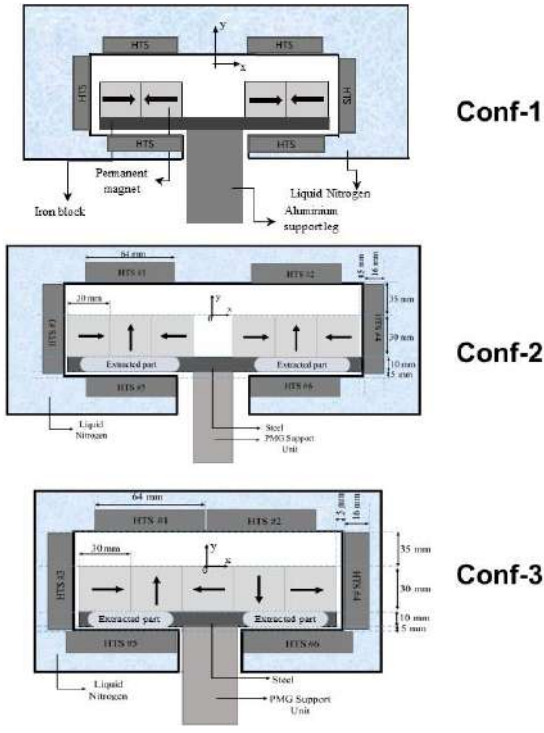

Figure 6. Schematic illustration of different multi-surface HTS-PMG configurations

Figure 7 shows the photo of different multi-surface HTS-PMG configurations. The HTS containers (cryostats) are made from non-magnetic aluminium material so as to not effecting the magnetic flux density distribution of the magnetic field source and resultant magnetic field in the medium. Soft ferromagnetic steel material is used as PMG container to fix the PMs together for aimed magnetic pole configuration and to shape the magnetic flux of the PMG.

Figure 7. Photo of different multi-surface HTS-PMG configurations

The magnetic flux density distributions of the PMG configurations from 5 mm above the top surface of the PMGs are calculated by numerical analysis (as magnetostatic solution) based on the finite element method (FEM) in COMSOL

Multiphysics 3.5a. The normalized magnetic flux density distributions of different HTS-PMG configurations schematized in Figure 6 are shown in Figure 8. The maximum values of normalized magnetic flux density (B_{norm}) of Conf-1, Conf-2 and Conf-3 are obtained as 0.69 T, 0.78 T and 0.89 T, respectively. This means that the maximum B_{norm} value of the Conf-3 is bigger than that of the Conf-1 and Conf-2 as 29 % and 14 %. One can see from Figure 8 that the Conf-3 has bigger magnetic flux density and magnetic flux density gradient than the other configurations.

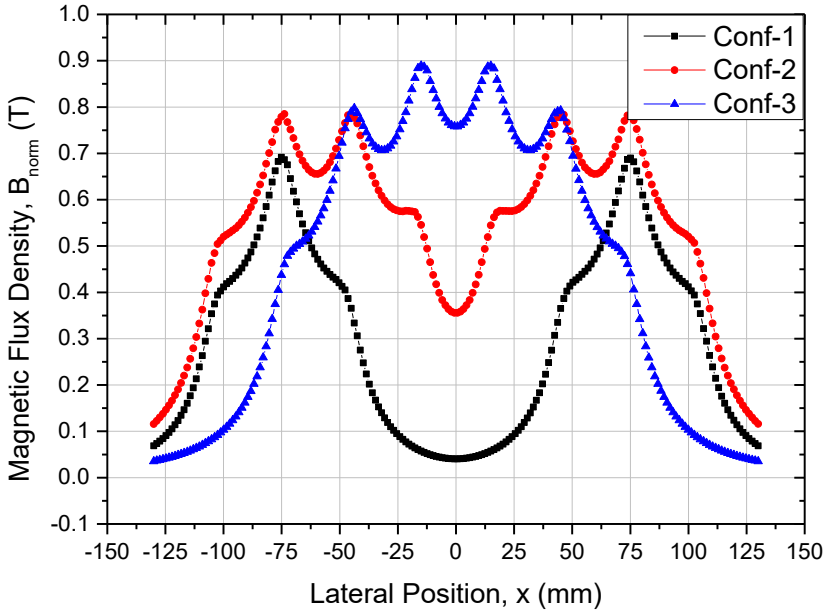

Figure 8. The normalized magnetic flux density (B_{norm}) distributions of different multi-surface HTS-PMG configurations.

4. Conclusions

Magnetic levitation force comparison of HTS-PMG configurations with multi-surface is given in Figure 9. The experimental studies on the levitation force were conducted via triaxial magnetic levitation force measurement system (Abdioglu et al., 2015; Ozturk et al., 2020) in our laboratory. The field cooling height (FCH) of FCH 20-30 is used in the measurements. FCH 20-30 means that the gap between the top surface of the PMG and the bottom surface of the upper HTSs is fixed at 20 mm before the cooling (Figure 6). In addition, the gap between the top surface of the lower HTSs and the bottom surface of the PMG unit (with steel part) is fixed at 20 mm. The distance is set as 35-15 (distance between the upper surface of the PMG and bottom of the upper HTSs is 35 mm which is a different measurement method given in (Ozturk et al., 2021)) after completely cooling of the HTSs by adding liquid nitrogen into the HTS container. Finally, the levitation force measurements are conducted

depending on the vertical gap between the upper surface of the PMG and bottom of the upper HTSs of 35 mm to 5 mm and again to initial gap of 35 mm. As shown in Figure 9, the levitation force curves, and maximum values of Conf-2 and Conf-3 are nearly same. On the other hand, the maximum values of Conf-2 and Conf-3 are nearly two times bigger than that of the Conf-1. The magnetic levitation force depends on the magnetic field distribution in the medium and magnetization degree of the HTS given as:

$$F_y = m\frac{dH}{dy}$$

Where, m and dH/dy indicates magnetization of the HTS and magnetic field gradient of the PMG, respectively. The bigger magnetic levitation force with bigger magnetic flux density indicates the importance of the PMG configurations in engineering applications as Maglev systems. In addition, although the levitation force of Conf-2 and Conf-3 are nearly same, six and five PMs are used in Conf-2 and Conf-3 respectively as can be seen in Figure 6 and Figure 7. The nearly same levitation force by using less number of PM in Conf-3 indicates the cost-effective property of Conf-3 for thousands of kilometres PMG rails in real applications.

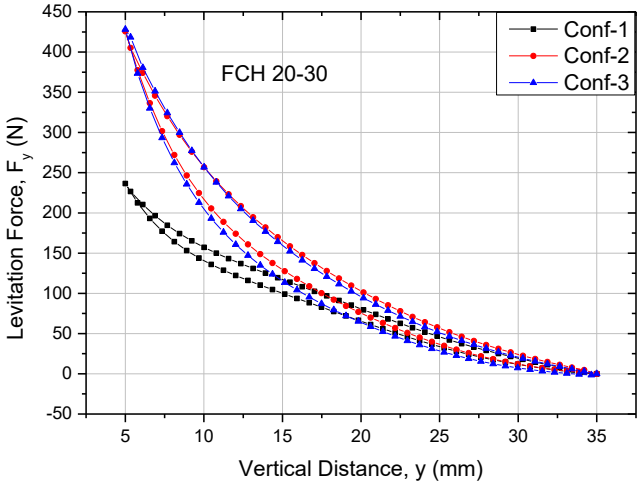

Figure 9. Magnetic levitation force comparison of HTS-PMG configurations with multi-surface arrangement

Acknowledgment

This work was supported by the Scientific and Technological Research Council of Turkey (TUBITAK–Turkey), with project number 118F426.

References

1. Abdioglu, M., Guner, S. B., Ozturk, K., Yang, C., Chen, I., & Celik, S. (2022). Magnetic levitation force and trapped field properties of multiseeded YBCO with triangular arrangement of seeds. *International Journal of Applied Ceramic Technology*, *19*(1), 459–466. https://doi.org/10.1111/ijac.13884
2. Abdioglu, M., Kabaer, M., Ozturk, K., Erdem, O., & Celik, S. (2017). Lateral Position Effect of Auxiliary Permanent Magnets on the Magnetic Force Properties of Cylindrical YBCO. *Journal of Superconductivity and Novel Magnetism*, *30*(10), 2933–2938. https://doi.org/10.1007/s10948-016-3685-x
3. Abdioglu, M., Ozturk, K., Ekici, M., Savaskan, B., Celik, S., & Cansiz, A. (2021). Design and Experimental Studies on Superconducting Maglev Systems With Multisurface HTS–PMG Arrangements. *IEEE Transactions on Applied Superconductivity*, *31*(6), 1–7. https://doi.org/10.1109/TASC.2021.3085243
4. Abdioglu, M., Ozturk, K., Gedikli, H., Ekici, M., & Cansiz, A. (2015). Levitation and guidance force efficiencies of bulk YBCO for different permanent magnetic guideways. *Journal of Alloys and Compounds*, *630*, 260–265. https://doi.org/10.1016/j.jallcom.2015.01.044
5. Deng, Z., Qian, N., Che, T., Jin, L., Si, S., Zhang, Y., & Zheng, J. (2016). Comprehensive comparison of the levitation performance of bulk YBaCuO arrays above two different types of magnetic guideways. *Journal of Magnetism and Magnetic Materials*, *420*, 171–176. https://doi.org/10.1016/j.jmmm.2016.07.033
6. Deng, Z., Zhang, W., Zheng, J., Ren, Y., Jiang, D., Zheng, X., . . . Deng, C. (2016). A High-Temperature Superconducting Maglev Ring Test Line Developed in Chengdu, China. *IEEE Transactions on Applied Superconductivity*, *26*(6), 1–8. https://doi.org/10.1109/TASC.2016.2555921
7. Deng, Z., Zhang, W., Zheng, J., Wang, B., Ren, Y., Zheng, X., & Zhang, J. (2017). A High-Temperature Superconducting Maglev-Evacuated Tube Transport (HTS Maglev-ETT) Test System. *IEEE Transactions on Applied Superconductivity*, *27*(6), 1–8. https://doi.org/10.1109/TASC.2017.2716842
8. Güner, S. B. (2020). Effects of silver doping on magnetic levitation performance of MgB2 superconductors. *Cryogenics*, *108*, 103061. https://doi.org/10.1016/j.cryogenics.2020.103061

9. Halbach, K. (1985). Application of permanent magnets in accelerators and electron storage rings (invited). *Journal of Applied Physics*, *57*(8), 3605–3608. https://doi.org/10.1063/1.335021
10. Lee, H.-W., Kim, K.-C., & Lee, J. (2006). Review of maglev train technologies. *IEEE Transactions on Magnetics*, *42*(7), 1917–1925. https://doi.org/10.1109/TMAG.2006.875842
11. Liu, L., Wang, J., Wang, S., Wang, L., & Li, J. (2009). Flux Concentrator Optimization of PMG for High-Temperature Superconducting Maglev Vehicle System. *Journal of Low Temperature Physics*, *157*(1-2), 67–72. https://doi.org/10.1007/s10909-009-9926-7
12. Ozturk, K., Abdioglu, M., & Karaahmet, Z. (2020). Magnetic force and stiffness performances of Maglev system based on multi–surface arrangements with three-seeded bulk YBaCuO superconductors. *Physica C: Superconductivity and Its Applications*, *578*, 1353739. https://doi.org/10.1016/j.physc.2020.1353739
13. Ozturk, K., Abdioglu, M., Sahin, E., Celik, S., Gedikli, H., & Savaskan, B. (2015). The Effect of Magnetic Field Distribution and Pole Array on the Vertical Levitation Force Properties of HTS Maglev Systems. *IEEE Transactions on Applied Superconductivity*, *25*(4), 1–7. https://doi.org/10.1109/TASC.2015.2417679
14. Ozturk, K., Akbulut, S., Kutuk, S., Bolat, S., Celik, S., & Basoglu, M. (2012). Comparative study of critical current density, pinning force and levitation force behavior in Yb211 doped-Sm123 bulk superconductors. *Journal of Alloys and Compounds*, *516*, 167–171. https://doi.org/10.1016/j.jallcom.2011.12.021
15. Ozturk, K., Badia-Majos, A., Abdioglu, M., Dilek, D. B., & Gedikli, H. (2021). Experimental and Numerical Investigation of Levitation Force Parameters of Novel Multisurface Halbach HTS–PMG Arrangement for Superconducting Maglev System. *IEEE Transactions on Applied Superconductivity*, *31*(7), 1–12. https://doi.org/10.1109/TASC.2021.3106816
16. Ozturk, K., Kabaer, M., & Abdioglu, M. (2015). Effect of onboard PM position on the magnetic force and stiffness performance of multi-seeded YBCO. *Journal of Alloys and Compounds*, *644*, 267–273. https://doi.org/10.1016/j.jallcom.2015.04.169
17. Pirti, A., Yücel, M. A., & Ocalan, T. (2016). Transrapid and the transition curve as sinusoid. *Tehnicki Vjesnik - Technical Gazette*, *23*(1). https://doi.org/10.17559/TV-20140217144435

18. Schultz, L., deHaas, O., Verges, P., Beyer, C., Rohlig, S., Olsen, H., . . . Funk, U. (2005). Superconductively Levitated Transport System—The SupraTrans Project. *IEEE Transactions on Appiled Superconductivity*, *15*(2), 2301–2305. https://doi.org/10.1109/TASC.2005.849636
19. Sotelo, G. G., Andrade, R. de, Dias, D. H. N., Ferreira, A. C., Costa, F., Machado, O. J., . . . Stephan, R. M. (2013). Tests With One Module of the Brazilian Maglev-Cobra Vehicle. *IEEE Transactions on Applied Superconductivity*, *23*(3), 3601204. https://doi.org/10.1109/TASC.2013.2237875
20. Sotelo, G. G., Oliveira, R. A. H. de, Costa, F. S., Dias, D. H. N., Andrade, R. de, & Stephan, R. M. (2015). A Full Scale Superconducting Magnetic Levitation (MagLev) Vehicle Operational Line. *IEEE Transactions on Applied Superconductivity*, *25*(3), 1–5. https://doi.org/10.1109/TASC.2014.2371432
21. Transport & Environment (2022). https://www.transportenvironment.org/challenges/planes/airplane-pollution/.
22. United States Environmental Protection Agency (2022). https://www.epa.gov/ghgemissions/inventory-us-greenhouse-gas-emissions-and-sinks.
23. Wang, J., Wang, S., Zheng, Y., Huang, H., Luo, F., Xu, Z., . . . et al (2002). The first man-loading high temperature superconducting Maglev test vehicle in the world. *Physica C: Superconductivity*, *378-381*, 809–814.

Tail Bifurcation in the Common Wall Lizard (*Podarcis muralis* Laurenti, 1768) and the European Glass Lizard (*Pseudopus apodus* Pallas, 1775)

Sema SARIKURT[1], Ufuk BÜLBÜL[2]

[1] Res. Assist., Karadeniz Technical University, ssarikurt@ktu.edu.tr
[2] Prof. Dr., Karadeniz Technical University, ufukb@ktu.edu.tr

INTRODUCTION

Lizards are known for their self-defense behavior of deliberately throwing their own tails (Vitt et al. 1977; Lozito and Tuan 2017). Caudal autotomy may occur as a result of escaping from predators, during mating, or as a result of intraspecific struggle, especially between males (Arnold 1984). In addition, this phenomenon is observed in lizards with extreme stress, for example, when individuals are startled or touched (Rose 1962; Thanou and Kornilios 2019). The loss of a tail containing fat reserves and the associated costs of replenishing a new one can have a negative impact on mobility, foraging, interspecies interactions, predator escape, growth, immune response, parasite burden and reproductive output, and survival (Lin et al. 2006; Maginnis 2006; Bateman and Flemming 2009; Argaez et al. 2018; Stark 2022).

Lizards use caudal autotomy as a strategy against their predators (Clause and Capaldi 2006). Certain sections along the tail, either on the vertebrae (intravertebral) or between the vertebrae (intervertebral), called fracture planes, allow the tail to fracture and subsequently rupture (Arnold 1984). After successful autotomy, the lizard regenerates its tail within a few weeks (Clause and Capaldi 2006).

Lizards leave tail and may increase their locomotor performance. They can escape more efficiently (Brown et al. 1995). Tail bifurcation and related malformations occur in species that exhibit tail autotomy (some salamanders and lizards) and are relatively common (Smith 1946). During the regeneration process following caudal autotomy, some morphological abnormalities may appear, such as bi, tri, or polyfurcation of the tail (Pelegrin and Leão 2016; Badiane 2017). These anomalies are usually associated with a failure in the process of tail regeneration following caudal autotomy, as opposed to congenital malformations arising during development (Conzendy et al. 2013).

The detachment of a part of the tail of the lizards not only occurs to escape predation, but also it can be the result of intraspecific aggression during mating and territorial fights (Iverson et al. 2004; Koleška et al. 2017). The ability to regenerate the tail of lizards shows that it is an important organ (for storing nutrients, maintaining balance, and in overcoming obstacles during locomotion) as explained by Iverson et al. (2004).

The common wall lizard *Podarcis muralis* (Laurenti 1768) is a widespread, mainly, European lacertid species. It is located from northern Spain to France, Luxembourg, southern Belgium, west- southeastern Czech Republic, central Germany, central Hungary, central Slovakia, most of the Balkans, and northwestern Anatolia part of Turkey (Pola and Koleška 2017). In Turkey, it is

distributed along Thrace, Northwest Anatolia, and around Ankara (Baran et al. 2021).

The species lives in dry and rocky areas. Body length can be up to 20 cm. Females are larger than males. The tail length can be 2.5 times the body length (Baran et al. 2021). *Podarcis muralis* is classified as Least Concern (LC) according to the IUCN Red List of the Threatened Species.

The European glass lizard, *Pseudopus apodus* (Pallas 1775) lives in Asia Minor, Central Asia, Southeast Europe, and the Balkans up to the Eastern Adriatic coast (Jandzik et al. 2018). It occurs in Eastern, Northern, Western, and Southern Anatolian regions and Thrace in Turkey (Baran et al. 2021). The body is cylindrical, legless and snake-like. *P. apodus* can be 120 cm or more in length. The head is covered with plates; there is a longitudinal recess on the sides of the body (Arnold 2002). This species lives on shrubbery, scrub, and stony slopes with plenty of vegetation. It hides under the bush, under stones, and in rodent nests (Baran et al. 2021). *Pseudopus apodus* is classified as Least Concern (LC) according to the IUCN Red List of the Threatened Species.

RESULT

In this study, we report the tail bifurcation of two lizard species in Turkey.

On May 18, 2020, tail bifurcation was observed in a female specimen of *Podarcis muralis* (Figures 1 and 2) during field research Yığılca district of Düzce Province in Turkey (GPS Data, N: PS Data, N: 40° 57' 46.4'' and E: 31°26' 31.4'', 342 m a.s.l). The specimen was caught by hand and anesthetized with a MS-222 solution. Sex was identified by the absence/presence of palpable hemipenis pockets. After measurements, the lizard was released back into its habitat. SVL (snout-vent length, tip of snout to anal cleft) and TL (tail length, anal cleft to the tip of tail) of *Podarcis muralis* were measured using a digital caliper with an accuracy of 0.01mm. SVL and TL were 59.93 mm and 105.11 mm, respectively. Bifurcation from the base of the tail occurred at 101.20 mm. The regenerated tail was 7.00 mm in length.

Figure 1. Tail bifurcation in a male specimen of female *Podarcis muralis*.

Figure 2. A close view of tail bifurcation in *Podarcis muralis*.

Apart from our findings, tail bifurcation was also reported in males and females of *Podarcis muralis* (Pola and Koleška 2017; Sorlin et al. 2019).

Pola and Koleška (2017) presented tail bifurcation in *P. muralis* from the Liguria, Italy. Length of the specimen was 160 mm long and more than half the length was formed by the tail, with the forked tail being shorter than the original tail in their sample.

In addition, Sorlin et al. (2019) observed tail bifurcation in a female of *Podarcis muralis* (SVL = 64.7 mm; tail length = 84.8 mm) and pronounced tail

split in a male individual SVL = 55.02 mm; tail length = 101.69 mm) of the species during fieldwork in the French Pyrenees.

Beside tail bifurcation, tail trifurcation was also recorded for *Podarcis muralis* by Badiane (2017). They observed the first bifurcation occurred approximately 1 cm away from the cloaca in the male individual captured in the Cres municipality on the island of Cres, Croatia. The second bifurcation was approximately 1 cm at the end of one of the two caudal arms.

All these findings show that individuals of the *Podarcis muralis* species are more likely to be exposed to adverse effects that cause tail autotomy (bifurcation or trifurcation) in their natural habitats.

Moreover, tail bifurcation can also be seen in other species of the genus *Podarcis*. Brock et al. (2014) observed tail bifurcation in adult individuals of *Podarcis erhardiii* on the Gaiduronissi Islet of Greece.

Our study presents the first record of tail bifurcation for *Pseudopus apodus*. During the field research on 25 February 2021, tail bifurcation was observed in a male specimen of *Pseudopus apodus* (Figures 3 and 4) captured from Çınarlı neighborhood, Sarıçam district, Adana Province of Turkey (GPS Data, N: 37° 04' 10.1'' and E: 35°23' 55.2'', 152 m a.s.l). The specimen was caught by hand and anesthetized with an MS-222 solution. Sex was identified by the absence/presence of palpable hemipenis pockets. SVL and TL were 162.90 mm and 195.46 mm, respectively. Bifurcation from the base of the tail occurred at 183.99 mm. The length of the regenerated tail was 2.82 mm.

Figure 3. Tail bifurcation in a male specimen of male *Pseudopus apodus*.

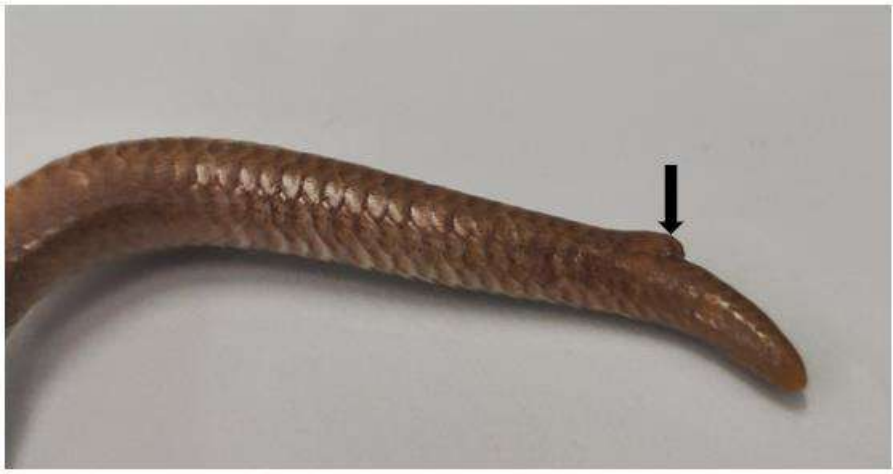

Figure 4. A close view of tail bifurcation in *Pseudopus apodus*.

Espasandín (2017) observed tail bifurcation in the slow worm, *Anguis fragilis* (Linnaeus 1758), from Spain. He found bifurcation in an adult male individual and SVL was 196 mm in this lizard. TL was 97 mm and the length of the regenerated tail was 9.34 mm. Our studied female individual of *Pseudopus apodus* had 162.90 mm of SVL. TL was 195.46 mm and bifurcation from the base of the tail occurred at 183.99 mm. The length of the regenerated tail was 2.82 mm. It is understood from these results that the bifurcated tail was shorter in *Pseudopus apodus* than in *Anguis fragilis*.

In Turkey, tail bifurcation in lizards was only reported by Bülbül and Sarıkurt (2022). They observed tail bifurcation in males belonged to *Darevskia clarkorum* (Darevsky and Vedmederja 1977) and *Darevskia rudis* (Bedriaga 1886). The SVL and TL of male *D. clarkorum*, were 55.37 mm and 66.43 mm, respectively. Tail bifurcation from the base of the tail occurred at 42.82 mm. The regenerated tail was 8.45 mm. SVL and TL were 83.56 mm and 128.93 mm, respectively in the specimen of *D. rudis*. Bifurcation from the base of the tail occurred at 33.38 mm. The length of the regenerated tail was 46.77 mm.

Other researches related to tail bifurcation were also performed in the different lacertids. Dudek and Ekner-Grzyb (2014) found individuals of two lizard species with forked tails in their work in central Poland. Their first observation was related to the common lizard *Zootoca vivipara* (Jacquin 1787). The second observation was performed on an adult female sand lizard *Lacerta agilis* (Linnaeus 1758). In addition, Kolenda et al. (2017) recorded tail bifurcation of the species *Lacerta agilis* and *Zootaxa vipera* in Poland.

Hoefer and Robinson (2020) reported the first observation of tail bifurcation in the Anolis family and species *Anolis sagrei* (Duméril and Bibron 1837). They found a two-tailed *A. sagrei* in South Eleuthera, Bahamas.

Ramadanovic and Zimic (2019) found an interesting individual of *Lacerta agilis* with a distinct color morph, malformation, and forked-tail in Kupres Polje (Eastern Bosnia and Herzegovina). The lizard had 62 mm length (SVL) and the length of tail was 67 mm. Length of the bifurcated tail was 35 mm.

Miles et al. (2020) caught an individual of *Plestiodon skiltonianus* (Tanner 1958) in Lander County, northeast of Austin, Nevada, USA.

In 2016, a study was performed by Jablonski related to the Desert lidless skink, *Ablepharus deserti* (Strauch 1868). He observed tail bifurcation in an adult female of *A. deserti* from Jalal-Abad, Kyrgyzstan. The tail is bifurcated with a new segment of the same length (~18 mm) as the original tail. The individual measured a total length of 90 mm (SVL 46 mm), with a tail of 44 mm.

Lozano and Patiño-Siro (2020) observed tail bifurcation in an adult female of the Green Iguana, *Iguana iguana* (Linnaeus 1758) in central Colombia. The tail bifurcation in this female started approximately 45 cm after the cloaca. The longest tail measured 29 cm and they noted a secondary regeneration of this tail at 14.5 cm. The shorter tail was reported to be 13 cm.

Vergilov and Natchev (2017) reported the first record of tail bifurcations in the snake-eyed skink *Ablepharus kitaibelii* (Bibron and Bory 1833) from Pastrina ridge (northwest Bulgaria).

Stark et al. (2018), an adult *Acanthodactylus aegyptius* (Baha El Din 2007) in southern Israel. This lizard (36.6 mm SVL; 45.2 tail length) had an original tail forked at the rear. The forked part of the tail begins 27 mm behind the cloaca, with the original tail tip being six mm longer than the regenerated one.

Rai (2021) observed a forked-tail Tokay Gecko (*Gekko gecko*, Linnaeus 1758) from Pandau, Nepal.

In conclusion, our study provided the first observation of tail bifurcation in *Pseudopus apodus* and an additional record of tail bifurcation in *Podarcis muralis* from Turkey. As more field observations are made, the possibility of tail bifurcation or trifurcation in different lizard species will increase.

REFERENCES

1. Argaez V., Solano-Zavalet I. and Zúñiga-Vega J.J. 2018. Another potential cost of tail autotomy: tail loss may result in high ectoparasite loads in *Sceloporus* lizards. Amphibia-Reptilia, 39: 191-202.
2. Arnold E.N. 1984. Evolutionary aspects of tail shedding in lizards and their relatives. Journal of Natural History, 18(1): 127-169.
3. Arnold E.N. 2002. Reptiles and Amphibians of Europe. 2nd edition. Princeton University Press, Princeton.
4. Badiane A. 2017. Trifurcation caudale chez le lézard des murailles *Podarcis muralis* (Laurenti, 1768) (Squamata: Lacertidae). Bulletin de la Société Herpétologique de France, 163:106-107.
5. Bateman P.W. and Fleming P.A. 2009. To cut a long tail short: a review of lizard caudal autotomy studies carried out over the last 20 years. Journal of Zoology, 277: 1-14.
6. Baran İ., Avcı A., Kumlutaş Y., Olgun K. and Ilgaz Ç. 2021. Türkiye Amfibi ve Sürüngenleri. Palme Yayınevi, Ankara (in Turkish).
7. Brown R.M., Douglas H.T. and Daniel H.G. 1995. Effect of caudal autotomy on locomotor performance of wall lizards (*Podarcis muralis*). Journal of Herpetology, 29(1): 98-105.
8. Brock K., Donihue C. and Pafilis P. 2014. New records of frugivory and ovophagy in *Podarcis* (Lacertidae) lizards from East Mediterranean Islands. North-Western Journal of Zoology, 10: 223-225.
9. Bülbül U. and Sarıkurt S. 2022. First observation of tail Bifurcation in the Clark's Lizard, *Darevskia clarkorum* (Darevsky & Vedmederja, 1977) and the Spiny-tailed lizard, *Darevskia rudis* (Bedriaga, 1886) (Squamata: Lacertidae). Commagene Journal of Biology, 6 (1): 119-121.
10. Clause A.R. and Capaldi E.A. 2006. Caudal autotomy and regeneration in lizards. Journal of Experimental Zoology Part A: Comparative Experimental Biology, 305(12): 965-973.
11. Conzendy P., Silva-Campos S.P., Mol-Lanna F., Cysneiros-Gomes de Amorim J.D. and Maria de Sousa B. 2013. *Ophiodes striatus* (Striped Worm Lizard). Bifurcated tail. Herpetological Review, 44: 145-146.
12. Dudek K. and Ekner-Grzyb A. 2014. Field observation of two-tailed sand lizard *Lacerta agilis* Linnaeus, 1758 and a common lizard *Zootoca vivipara* (Jacquin, 1787) in Poland. Natura Sloveniae, 16(1): 65-66.
13. Espasandín I. 2017. Cola bífida en *Anguis fragilis* (Linnaeus, 1758). Boletín de la Asociación Herpetológica Española, 28(2): 11-12.

14. Hoefer S. and Robinson N.J. 2020. Tail bifurcation in a brown anole, *Anolis sagrei* (Duméril & Bibron, 1837). Herpetology Notes, 13: 333-335.
15. Iverson J.B., Smith G.R. and Pieper L. 2004. Factors affecting long-term growth of the Allen Cays rock iguana in the Bahamas. In: Alberts A.C., Carter R.L., Hayes W.K. and Martins E.P. (eds) Iguanas: Biology and conservation. University of California Press, Berkeley, USA, 176–192.
16. Jablonski D. 2016. Tail bifurcation in a desert lidless skink (*Ablepharus deserti*) from Kyrgyzstan. Reptiles & Amphibians, 23(3): 171-172.
17. Jandzik D., Jablonski D., Zinenko O., Kukushkin O.V., Moravec J. and Gvoždík V. 2018. Pleistocene extinctions and recent expansions in an anguid lizard of the genus *Pseudopus*. Zoologica Scripta, 47(1): 21-32.
18. Kolenda K., Wieczorek M., Najbar A., Najbar B. and Skawiński T. 2017. Limb malformation and tail bifurcation in sand lizards (*Lacerta agilis*) and common lizards (*Zootaca vivipara*) from Poland. Herpetology Notes, 10: 713-716.
19. Koleška D., Kulma M. and Vrabec V. 2017. *Teira dugesii* (Madeiran wall lizard). Tail bifurcation. Herpetological Review, 48(2): 440-441.
20. Lin Z., Qu Y. and Ji X. 2006. Energetic and locomotor costs of tail loss in the Chinese Skink, *Eumeces chinensis*. Comparative Biochemistry and Physiology, 143(A): 508-513.
21. Lozano J.A. and Patiño-Siro D. 2020. Regenerate tail bifurcation in the Green Iguana (*Iguana iguana* Linnaeus, 1758). Herpetology Notes, 13: 483-484.
22. Lozito T.P. and Tuan R.S. 2017. Lizard tail regeneration as an instructive model of enhanced healing capabilities in an adult amniote. Connective Tissue Research, 58: 145-154.
23. Maginnis T.L. 2006. The costs of autotomy and regeneration in animals: a review and framework for future research. Behavioral Ecology, 17: 857-872.
24. Miles D.C., Danser C.L. and Shoemaker K.T. 2020. Tail bifurcation in *Plestiodon skiltonianus*. Herpetology Notes, 13: 343-345.
25. Pelegrin N. and Muniz Leão S. 2016. Injured Salvator merianae (Teiidae) regenerates six tails in central Argentina. Cuadernos de Herpetología, 30(1): 21-23.
26. Pola L. and Koleška D. 2017. Tail bifurcation in Common Wall lizard (*Podarcis muralis* Laurenti, 1768) from Liguria, Italy. 9th Workshop on Biodiversity, July 8-9 2017, Proceedings of the 9th Workshop on Biodiversity pp. 93-97, Jevany, Czech Republic.

27. Ramadanović D. and Zimić A. 2019. Record of a *Lacerta agilis* Linnaeus, 1758 with erythronotus colour morph and tail bifurcation. Herpetology Notes, 12: 779-781.
28. Rai T. P. 2021. Tail Bifurcation in a Tokay Gecko, *Gekko gecko* (Linnaeus 1758), with notes on the natural history of the species in Ilam, Nepal. Reptiles & Amphibians, 28(2): 312-313.
29. Rose W. 1962. The reptiles and amphibians of southern Africa. Maskew Miller Ltd, Cape Town.
30. Smith H.M. 1946. Handbook of Lizards of the United States and Canada. Cornell University Press, Ithaca, New York.
31. Sorlin M.V., Gangloff E., Kouyoumdjian L., Cordero G., Darnet E. and Aubret F. 2019. *Podarcis muralis* (Common wall lizard). Tail bifurcation. Herpetological Review, 50(2): 377-378.
32. Stark G., David D., Lewin A. and Meiri S. 2018. Natural history notes: *Acanthodactylus aegyptius* (Egyptian fringed-fingered lizard). Tail bifurcation. Herpetological Review, 49(2): 324-325.
33. Stark T. 2022. Caudal autophagy in captive *Cyclodomorphus gerrardii* (Squamata: Scincidae). Herpetology Notes, 15: 629-631.
34. Thanou E. and Kornilios P. 2019. Self-cannibalism in the Aegean wall-lizard, *Podarcis erhardii*. Herpetological Bulletin, 147: 26-27.
35. Vergilov V. and Natchev N. 2017. First record of tail bifurcations in the snake-eyed skink, *Ablepharus kitaibelii* Bibron & Bory de Saint-Vincent, 1833 from Pastrina hill (Northwestern Bulgaria). Arxius de Miscellània Zoològica, 15: 224-228.
36. Vitt L.J., Congdon J.D. and Dickson N.A. 1977. Adaptive strategies and energetics of tail autonomy in lizards. Ecology, 58(2): 326-337.

Generalizations of Lucas Type Polynomials

Asst. Prof. Dr.Yasemin TAŞYURDU

Erzincan Binali Yıldırım University,
Faculty of Arts and Sciences, Department of
Mathematics, Erzincan, Turkey
ytasyurdu@erzincan.edu.tr,
ORCID: https://orcid.org/0000-0002-9011-8269

1. Introduction

Large classes of polynomials appeared in many fields of mathematics and science can be defined by generalizing numbers. Such polynomials called Fibonacci type and Lucas type polynomials are emerged as the generalizations of numbers defined by the Fibonacci type and the Lucas type recurrence relations. Fibonacci and Lucas polynomials, the most famous special polynomials in the literature, are generalizations of the Fibonacci numbers, $f_n = f_{n-1} + f_{n-2}$ with $f_0 = 0, f_1 = 1$, and the Lucas numbers, $\ell_n = \ell_{n-1} + \ell_{n-2}$ with $\ell_0 = 2,\ \ell_1 = 1$ for $n \geq 2$, respectively (Horadam, A. F. 1961).

The Fibonacci polynomials are presented by the recurrence relation $f_n(x) = xf_{n-1}(x) + f_{n-2}(x)$ with initial terms $f_0(x) = 0,\ f_1(x) = 1$ for $n \geq 2$. Generalized identities and periods of these polynomials are obtained by many authors (Hoggatt Jr., V. E. & Bicknell, M. 1973, Gültekin, İ. & Taşyurdu, Y. 2013, Taşyurdu, Y. & Deveci, Ö. 2017). Similarly, the Lucas polynomials are presented by the recurrence relation

$$\ell_n(x) = x\ell_{n-1}(x) + \ell_{n-2}(x)$$

with initial terms $\ell_0(x) = 2$ and $\ell_1(x) = x$ for $n \geq 2$. Koshy has also collected almost every study in the literature on the Fibonacci type and the Lucas type numbers and polynomials and their generalizations and presented to readers as two wonderful books (Koshy, T. 2017).

The most interesting applications of these numbers and polynomials have been on their generalizations. For instance, bivariate Lucas polynomials are introduced as

$$\ell_n(x,y) = x\ell_{n-1}(x,y) + y\ell_{n-2}(x,y)$$

with initial terms $\ell_0(x,y) = 2,\ \ell_1(x,y) = x$ for $x, y \neq 0,\ x^2 + 4y \neq 0,\ n \geq 2$ and generalized identities of these polynomials are obtained (Catalani, M. 2004, Panwar, Y. K., Gupta V. K. & Bhandari, J. 2020). For $n \geq 2$, the $h(x)$-Lucas polynomials as another generalization of the Lucas polynomials are defined by recurrence relation

$$\ell_{h,n}(x) = h(x)\ell_{h,n-1}(x) + \ell_{h,n-2}(x)$$

with initial terms $\ell_{h,0}(x) = 2,\ \ell_{h,1}(x) = h(x)$ where $h(x)$ be a polynomial with real coefficients (Nalli A. & Haukkanen, P. 2009).

A new generalization of the Lucas numbers and polynomials called generalized Lucas polynomials is introduced by using different initial terms in the generalization methods from the above-cited studies. Let $|p_0| = 1$ or 2 and $p_1(x), d(x) = \alpha p_1(x)$ and $g(x)$ be fixed nonzero polynomials in $\mathbb{Q}[x]$ with α an integer of the form $2/p_0$. For $n \geq 2$, the generalized Lucas polynomial sequences, $\{\mathcal{L}_n(x)\}_{n\in\mathbb{N}}$ are defined by the recurrence relation

$$\mathcal{L}_n(x) = d(x)\mathcal{L}_{n-1}(x) + g(x)\mathcal{L}_{n-2}(x) \tag{1}$$

with initial terms $\mathcal{L}_0(x) = p_0$ and $\mathcal{L}_1(x) = p_1(x)$. It is clearly that we obtain classical Lucas polynomial for $p_0 = 2, p_1(x) = x, d(x) = x$ and $g(x) = 1$, and $\mathcal{L}_n(1) = \ell_n$ for $p_0 = 2, p_1(x) = d(x) = g(x) = 1$ where ℓ_n is the nth classical Lucas number. Binet formulas for the generalized Lucas polynomial sequences are given by

$$\mathcal{L}_n(x) = \frac{\sigma^n(x) + \rho^n(x)}{\alpha}$$

where $\sigma(x)$ and $\rho(x)$ are the roots of the quadratic equation $t^2 - d(x)t - g(x) = 0$ of equation (1). More information on the generalized Fibonacci type and Lucas type polynomials can be seen in (Florez, R. Higuita, R. A. & Mukherjee, A. 2014, 2018, Florez, R., McAnally, N. & Mukherjee, A. 2018).

In other generalizations called bi-periodic numbers and polynomials, nonzero real numbers are taken into account in recurrence relations of the Fibonacci type and the Lucas type numbers and polynomials. For $n \geq 2$, using the recurrence relations of the Fibonacci and the Lucas numbers, bi-periodic Fibonacci numbers are defined by

$$f_n = \begin{cases} af_{n-1} + f_{n-2}, & \text{if } n \text{ is even} \\ bf_{n-1} + f_{n-2}, & \text{if } n \text{ is odd} \end{cases}$$

with initial terms $f_0 = 0,\ f_1 = 1$ (Edson, M. & Yayenie, O. 2009), and bi-periodic Lucas numbers are defined by

$$l_n = \begin{cases} bl_{n-1} + l_{n-2}, & \text{if } n \text{ is even} \\ al_{n-1} + l_{n-2}, & \text{if } n \text{ is odd} \end{cases}$$

with initial terms $l_0 = 2,\ l_1 = a$ where a and b are any two nonzero real numbers (Bilgici, G. 2014).

For $n \geq 2$, using the recurrence relations of the Fibonacci and the Lucas polynomials, bi-periodic Fibonacci polynomials are defined by

$$q_n(x) = \begin{cases} axq_{n-1}(x) + q_{n-2}(x), & \text{if } n \text{ is even} \\ bxq_{n-1}(x) + q_{n-2}(x), & \text{if } n \text{ is odd} \end{cases}$$

with initial terms $q_0(x) = 0$, $q_1(x) = 1$, bi-periodic Lucas polynomials are defined by

$$l_n(x) = \begin{cases} bxl_{n-1}(x) + l_{n-2}(x), & \text{if } n \text{ is even} \\ axl_{n-1}(x) + l_{n-2}(x), & \text{if } n \text{ is odd} \end{cases}$$

with initial terms $l_0(x) = 2$, $l_1(x) = ax$ where a and b are any two nonzero real numbers. Also, some identities related to these bi-periodic polynomials are given (Yılmaz, Y., Çoşkun, A. & Taşkara, N. 2017).

In this study, we introduce new generalizations of the Lucas and the Lucas type polynomials, the bi-periodic Lucas and the bi-periodic Lucas type polynomials, which we shall call bi-periodic generalized Lucas polynomials using recurrence relations of the generalized Lucas polynomials. It is derived generating functions, general formulas and well-known identities for these polynomials. We also give special cases of the bi-periodic generalized Lucas polynomials and generalize all the results.

2. Bi-Periodic Generalized Lucas Polynomials

In this section, bi-periodic generalized Lucas polynomials, which are generalizations of the Lucas and the Lucas type polynomials including Pell-Lucas, Pell-Lucas-prime, Jacobsthal-Lucas, Fermat-Lucas, Chebyshev first kind, Morgan-Voyce second kind and Vieta-Lucas polynomials, are defined. Generating functions, Binet formulas, some basic properties as well as the Catalan's identity and Cassini's identity for these polynomials are obtained.

Definition 2.1. For any two nonzero real numbers a and b, the nth bi-periodic generalized Lucas polynomial is defined by the recurrence relation

$$\mathbb{L}_n(x) = \begin{cases} bd(x)\mathbb{L}_{n-1}(x) + g(x)\mathbb{L}_{n-2}(x), & \text{if } n \text{ is even} \\ ad(x)\mathbb{L}_{n-1}(x) + g(x)\mathbb{L}_{n-2}(x), & \text{if } n \text{ is odd} \end{cases} \tag{2}$$

for $n \geq 2$ and initial terms $\mathbb{L}_0(x) = p_0$, $\mathbb{L}_1(x) = ap_1(x)$ where $|p_0| = 1$ or 2 and $p_1(x)$, $d(x) = \alpha p_1(x)$ and $g(x)$ are fixed nonzero polynomials in $\mathbb{Q}[x]$

with α an integer of the form $2/p_0$. The sequences of the bi-periodic generalized Lucas polynomials are denoted by $\{\mathbb{L}_n(x)\}_{n\epsilon\mathbb{N}}$.

The sequences of the bi-periodic Lucas polynomials are as follows

$$\{\mathbb{L}_n(x)\}_{n\epsilon\mathbb{N}} = \{p_0, ap_1(x), abd(x)p_1(x) + g(x)p_0, a^2bd^2(x)p_1(x)$$
$$+ad(x)g(x)p_0 + ag(x)p_1(x), a^2b^2d^3(x)p_1(x) + abd^2(x)g(x)p_0$$
$$+2abd(x)g(x)p_1(x) + g^2(x)p_0, a^3b^2d^4(x)p_1(x)$$
$$+5a^2bd^2(x)g(x)p_1(x) + 2ad(x)g^2(x)p_0 + ag^2(x)p_1(x), \dots\}$$

Note that $p_0 = 2$, $p_1(x) = x$, $d(x) = x$ and $g(x) = 1$, we get the bi-periodic Lucas polynomial $\mathbb{L}_n(x) = L_n(x)$. Special cases of the bi-periodic generalized Lucas polynomials are given in the Table 1.

Table 1: Special cases of the polynomials $\mathbb{L}_n(x)$

Bi-Periodic Generalized Lucas Polynomials	$\mathbb{L}_n(x)$	p_0	$p_1(x)$	$d(x)$	$g(x)$
Bi-periodic Lucas polynomials	$L_n(x)$	2	x	x	1
Bi-periodic $h(x)$-Lucas polynomials	$L_{h,n}(x)$	2	$h(x)$	$h(x)$	1
Bi-periodic Lucas polynomials with two variables	$L_n(x,y)$	2	x	x	y
Bi-periodic Pell-Lucas polynomials	$Q_n(x)$	2	$2x$	$2x$	1
Bi-periodic Pell-Lucas-prime polynomials	$Q'_n(x)$	1	x	$2x$	1
Bi-periodic Jacobsthal-Lucas polynomials	$j_n(x)$	2	1	1	$2x$
Bi-periodic Fermat-Lucas polynomials	$\vartheta_n(x)$	2	$3x$	$3x$	-2
Bi-periodic Chebyshev first kind polynomials	$T_n(x)$	1	x	$2x$	-1
Bi-periodic Morgan-Voyce second kind polynomials	$C_n(x)$	2	$x+2$	$x+2$	-1
Bi-periodic Vieta-Lucas polynomials	$v_n(x)$	2	x	x	-1

Since the all results obtained in the study are provided for all the bi-periodic generalized Lucas polynomials, the values given in Table 1 can be used in the relevant theorems or corollaries for any bi-periodic polynomials.

Alternative recurrence relations can be given for the bi-periodic generalized Lucas polynomials where $\xi(n) = n - 2\left\lfloor \frac{n}{2} \right\rfloor$ is the parity function, i.e.,

$$\xi(n) = \begin{cases} 0, & if\ n \text{ is even} \\ 1, & \text{if } n \text{ is odd} \end{cases}.$$

Also using this parity function, we obtain the following equalities for proofs in this study:

$$1 - \xi(n) + \left\lfloor \frac{n+1}{2} \right\rfloor = \left\lfloor \frac{n+2}{2} \right\rfloor$$

$$\xi(n+1) + \left\lfloor \frac{n+1}{2} \right\rfloor = \left\lfloor \frac{n+2}{2} \right\rfloor$$

$$\xi(n+r) + \left\lfloor \frac{n-r}{2} \right\rfloor + \left\lfloor \frac{n+r}{2} \right\rfloor = n$$

$$\xi(n+r) - \left\lfloor \frac{n-r+1}{2} \right\rfloor - \left\lfloor \frac{n+r+1}{2} \right\rfloor = -n$$

$$\xi(n) - 2\left\lfloor \frac{n+1}{2} \right\rfloor = -n.$$

For any two nonzero real numbers a and b, the nth bi-periodic generalized Lucas polynomial is given by

$$\mathbb{L}_n(x) = a^{\xi(n)} b^{1-\xi(n)} d(x) \mathbb{L}_{n-1}(x) + g(x) \mathbb{L}_{n-2}(x) \qquad (3)$$

for $n \geq 2$ and initial terms $\mathbb{L}_0(x) = p_0$, $\mathbb{L}_1(x) = a p_1(x)$ where $|p_0| = 1$ or 2 and $p_1(x)$, $d(x) = \alpha p_1(x)$ and $g(x)$ are fixed nonzero polynomials in $\mathbb{Q}[x]$ with α an integer of the form $2/p_0$. Then the quadratic equation of the bi-periodic generalized Lucas polynomials is

$$t^2 - d(x)abt - g(x)ab = 0$$

and their roots are $\sigma(x) = \frac{d(x)ab + \sqrt{d^2(x)a^2b^2 + 4g(x)ab}}{2}$ and $\mathfrak{d}(x) = \frac{d(x)ab - \sqrt{d^2(x)a^2b^2 + 4g(x)ab}}{2}$. Also, the roots $\sigma(x)$ and $\mathfrak{d}(x)$ provide the following relations

$$\mathfrak{o}(x) + \mathfrak{d}(x) = d(x)ab$$

$$\mathfrak{o}(x) - \mathfrak{d}(x) = \sqrt{d^2(x)a^2b^2 + 4g(x)ab}$$

$$\mathfrak{o}(x)\mathfrak{d}(x) = -g(x)ab$$

$$d(x)\mathfrak{o}(x) + g(x) = \frac{\mathfrak{o}^2(x)}{ab}$$

$$d(x)\mathfrak{d}(x) + g(x) = \frac{\mathfrak{d}^2(x)}{ab}.$$

2.1. Generating Functions and Binet Formulas of Polynomials $\mathbb{L}_n(x)$

In this section, we obtain the generating functions and the Binet formulas for the sequences of the bi-periodic generalized Lucas polynomials, $\{\mathbb{L}_n(x)\}_{n\epsilon\mathbb{N}}$.

Let the generating functions of the sequences $\{\mathbb{L}_n(x)\}_{n\epsilon\mathbb{N}}$ be $G_n(x,t)$ such that

$$G_n(x,t) = \sum_{n=0}^{\infty} \mathbb{L}_n(x)t^n \tag{4}$$

where $\mathbb{L}_n(x)$ is the nth bi-periodic generalized Lucas polynomial. Some identities for the even and odd subscript terms in the sequences of the bi-periodic generalized Lucas polynomials are given in the following lemma used to obtain these functions.

Lemma 2.2. The sequences of the bi-periodic generalized Lucas polynomials, $\{\mathbb{L}_n(x)\}_{n\epsilon\mathbb{N}}$ satisfy the following identities

i. $\mathbb{L}_{2n}(x) = \big(abd^2(x) + 2g(x)\big)\mathbb{L}_{2n-2}(x) - g^2(x)\mathbb{L}_{2n-4}(x)$

ii. $\mathbb{L}_{2n+1}(x) = \big(abd^2(x) + 2g(x)\big)\mathbb{L}_{2n-1}(x) - g^2(x)\mathbb{L}_{2n-3}(x).$

Proof. Using the equation (2), we have

i. $\mathbb{L}_{2n}(x) = bd(x)\mathbb{L}_{2n-1}(x) + g(x)\mathbb{L}_{2n-2}(x)$

$= bd(x)\big(ad(x)\mathbb{L}_{2n-2}(x) + g(x)\mathbb{L}_{2n-3}(x)\big) + g(x)\mathbb{L}_{2n-2}(x)$

$= \big(abd^2(x) + g(x)\big)\mathbb{L}_{2n-2}(x) + bd(x)g(x)\mathbb{L}_{2n-3}(x)$

$$= \left(abd^2(x) + g(x)\right)\mathbb{L}_{2n-2}(x) + g(x)\mathbb{L}_{2n-2}(x) - g^2(x)\mathbb{L}_{2n-4}(x)$$
$$= \left(abd^2(x) + 2g(x)\right)\mathbb{L}_{2n-2}(x) - g^2(x)\mathbb{L}_{2n-4}(x)$$

ii. $\mathbb{L}_{2n+1}(x) = ad(x)\mathbb{L}_{2n}(x) + g(x)\mathbb{L}_{2n-1}(x)$
$$= ad(x)\left(bd(x)\mathbb{L}_{2n-1}(x) + g(x)\mathbb{L}_{2n-2}(x)\right) + g(x)\mathbb{L}_{2n-1}(x)$$
$$= \left(abd^2(x) + g(x)\right)\mathbb{L}_{2n-1}(x) + ad(x)g(x)\mathbb{L}_{2n-2}(x)$$
$$= \left(abd^2(x) + g(x)\right)\mathbb{L}_{2n-1}(x) + g(x)\mathbb{L}_{2n-1}(x) - g^2(x)\mathbb{L}_{2n-3}(x)$$
$$= \left(abd^2(x) + 2g(x)\right)\mathbb{L}_{2n-1}(x) - g^2(x)\mathbb{L}_{2n-3}(x)$$

and theorem is proved.

Using the Lemma 2.2, the generating functions for the sequences of the bi-periodic generalized Lucas polynomials are given in the following Theorem.

Theorem 2.3. The generating functions for the sequences of the bi-periodic generalized Lucas polynomials are

$$G_n(x,t) = \frac{p_0 + ap_1(x)t - (abd(x)p_1(x) + g(x)p_0)t^2 + \left(ag(x)p_1(x)\right)t^3}{1 - \left(abd^2(x) + 2g(x)\right)t^2 + g^2(x)t^4}.$$

Proof. Using equation (4), we get

$$G_n(x,t) = \sum_{n=0}^{\infty} \mathbb{L}_n(x)t^n$$
$$= \mathbb{L}_0(x) + \mathbb{L}_1(x)t + \mathbb{L}_2(x)t^2 + \cdots + \mathbb{L}_n(x)t^n + \cdots$$

Let generating functions $G_n(x,t)$ be the sum of the even subscript and odd subscript terms separately. Then

$$G_n(x,t) = G_n^{\mathrm{C}}(x,t) + G_n^{T}(x,t) \tag{5}$$

where $G_n^{\mathrm{C}}(x,t)$ is the sum of the even subscript terms and $G_n^{T}(x,t)$ is the sum of the odd subscript terms. Therefore,

$$G_n^{\mathrm{C}}(x,t) = \mathbb{L}_0(x) + \mathbb{L}_2(x)t^2 + \sum_{i=2}^{\infty} \mathbb{L}_{2i}(x)t^{2i}. \tag{6}$$

If both sides of equation (6) are multiplied by $-\left(abd^2(x)+2g(x)\right)t^2$ and $g^2(x)t^4$, then we get

$$-\left(abd^2(x)+2g(x)\right)t^2G_n^{\mathbb{C}}(x,t)=-\left(abd^2(x)+2g(x)\right)\sum_{i=0}^{\infty}\mathbb{L}_{2i}(x)t^{2i+2} \qquad (7)$$

and

$$g^2(x)t^4G_n^{\mathbb{C}}(x,t)=g^2(x)\sum_{i=0}^{\infty}\mathbb{L}_{2i}(x)t^{2i+4}. \qquad (8)$$

From the equations (6), (7) and (8), we obtain

$$\begin{aligned}
&\left(1-\left(abd^2(x)+2g(x)\right)t^2+g^2(x)t^4\right)G_n^{\mathbb{C}}(x,t)\\
&=\mathbb{L}_0(x)+\mathbb{L}_2(x)t^2+\sum_{i=2}^{\infty}\mathbb{L}_{2i}(x)t^{2i}-\left(abd^2(x)+2g(x)\right)\mathbb{L}_0(x)\,t^2\\
&\quad-\left(abd^2(x)+2g(x)\right)\sum_{i=1}^{\infty}\mathbb{L}_{2i}(x)t^{2i+2}+g^2(x)\sum_{i=0}^{\infty}\mathbb{L}_{2i}(x)t^{2i+4}\\
&=p_0+(abd(x)p_1(x)+g(x)p_0)t^2+\sum_{i=2}^{\infty}\mathbb{L}_{2i}(x)t^{2i}\\
&\quad-\left(abd^2(x)+2g(x)\right)p_0\,t^2-\left(abd^2(x)+2g(x)\right)\sum_{i=2}^{\infty}\mathbb{L}_{2i-2}(x)t^{2i}\\
&\quad+g^2(x)\sum_{i=2}^{\infty}\mathbb{L}_{2i-4}(x)t^{2i}\\
&=p_0-(abd(x)p_1(x)+g(x)p_0)t^2\\
&\quad+\sum_{i=2}^{\infty}(\mathbb{L}_{2i}(x)-\left(abd^2(x)+2g(x)\right)\mathbb{L}_{2i-2}(x)+g^2(x)\mathbb{L}_{2i-4}(x)\right)t^{2i}.
\end{aligned}$$

Using Lemma 2.2, i., the generating functions for even subscript terms in the sequences of the bi-periodic generalized Lucas polynomials are obtained as

$$G_n^C(x,t) = \frac{p_0 - (abd(x)p_1(x) + g(x)p_0)t^2}{1 - \big(abd^2(x) + 2g(x)\big)t^2 + g^2(x)t^4}.$$

Now let consider the sum of the odd subscript terms in the generating functions. Therefore,

$$G_n^T(x,t) = \mathbb{L}_1(x)t + \mathbb{L}_3(x)t^3 + \sum_{i=2}^{\infty} \mathbb{L}_{2i+1}(x)t^{2i+1}. \tag{9}$$

If both sides of equation (9) are multiplied by $-\big(abd^2(x) + 2g(x)\big)t^2$ and $g^2(x)t^4$, then we get

$$-\big(abd^2(x) + 2g(x)\big)t^2 G_n^T(x,t) = -\big(abd^2(x) + 2g(x)\big)\sum_{i=0}^{\infty} \mathbb{L}_{2i+1}(x)t^{2i+3} \tag{10}$$

and

$$g^2(x)t^4 G_n^T(x,t) = g^2(x)\sum_{i=0}^{\infty} \mathbb{L}_{2i+1}(x)t^{2i+5}. \tag{11}$$

From the equations (9), (10) and (11), we obtain

$$\begin{aligned}
&\big(1 - \big(abd^2(x) + 2g(x)\big)t^2 + g^2(x)t^4\big)G_n^T(x,t) \\
&= \mathbb{L}_1(x)t + \mathbb{L}_3(x)t^3 + \sum_{i=2}^{\infty} \mathbb{L}_{2i+1}(x)t^{2i+1} - \big(abd^2(x) + 2g(x)\big)\mathbb{L}_1(x)t^3 \\
&\quad -\big(abd^2(x) + 2g(x)\big)\sum_{i=1}^{\infty} \mathbb{L}_{2i+1}(x)t^{2i+3} + g^2(x)\sum_{i=0}^{\infty} \mathbb{L}_{2i+1}(x)t^{2i+5} \\
&= ap_1(x) + \big(a^2bd^2(x)p_1(x) + ad(x)g(x)p_0 + ag(x)p_1(x)\big)t^3 \\
&\quad + \sum_{i=2}^{\infty} \mathbb{L}_{2i+1}(x)t^{2i+1} - \big(abd^2(x) + 2g(x)\big)ap_1(x)t^3 \\
&\quad -\big(abd^2(x) + 2g(x)\big)\sum_{i=2}^{\infty} \mathbb{L}_{2i-1}(x)t^{2i+1} + g^2(x)\sum_{i=2}^{\infty} \mathbb{L}_{2i-3}(x)t^{2i+1}
\end{aligned}$$

$$= ap_1(x)t + \left(a^2bd^2(x)p_1(x) + 3ag(x)p_1(x)\right)t^3$$

$$-\left(abd^2(x) + 2g(x)\right)ap_1(x)t^3$$

$$+\sum_{i=2}^{\infty}(\mathbb{L}_{2i+1}(x) - \left(abd^2(x) + 2g(x)\right)\mathbb{L}_{2i-1}(x)+g^2(x)\mathbb{L}_{2i-3}(x)\Big)t^{2i+1}.$$

Using Lemma 2.2, ii., the generating functions for odd subscript terms in the sequences of the bi-periodic generalized Lucas polynomials are obtained as

$$G_n^T(x,t) = \frac{ap_1(x)t + \left(ag(x)p_1(x)\right)t^3}{1 - \left(abd^2(x) + 2g(x)\right)t^2 + g^2(x)t^4}.$$

From equation (5), the generating functions for the sequences of the bi-periodic generalized Lucas polynomials are

$$G_n(x,t) = \frac{p_0 + ap_1(x)t - (abd(x)p_1(x) + g(x)p_0)t^2 + \left(ag(x)p_1(x)\right)t^3}{1 - \left(abd^2(x) + 2g(x)\right)t^2 + g^2(x)t^4}$$

and theorem is proved.

Now we give Binet formulas that allow us to calculate the nth terms of sequences $\{\mathbb{L}_n(x)\}_{n\epsilon\mathbb{N}}$ in the following theorem.

Theorem 2.4. The Binet formula for the nth bi-periodic generalized Lucas polynomial is given by

$$\mathbb{L}_n(x) = \left(\frac{a^{\xi(n)}}{(ab)^{\left\lfloor\frac{n+1}{2}\right\rfloor}}\right)\frac{\mathcal{o}^n(x) + \mathfrak{d}^n(x)}{\alpha}$$

where $\xi(n) = n - 2\left[\frac{n}{2}\right]$ and $\mathcal{o}(x) = \frac{d(x)ab+\sqrt{d^2(x)a^2b^2+4g(x)ab}}{2}$, $\mathfrak{d}(x) = \frac{d(x)ab-\sqrt{d^2(x)a^2b^2+4g(x)ab}}{2}$.

Proof. By induction method on n. The result is clearly true for $n = 0,1$. Suppose that result is true for $n \in \mathbb{N}$, namely

$$\mathbb{L}_n(x) = \left(\frac{a^{\xi(n)}}{(ab)^{\left\lfloor\frac{n+1}{2}\right\rfloor}}\right)\frac{\mathcal{o}^n(x) + \mathfrak{d}^n(x)}{\alpha}.$$

Using equation (3) and the hypothesis of induction, we shall show that result is true for $n+1$. Then, we have

$$\mathbb{L}_{n+1}(x) = a^{\xi(n+1)}b^{1-\xi(n+1)}d(x)\mathbb{L}_n(x) + g(x)\mathbb{L}_{n-1}(x)$$

$$= a^{\xi(n+1)}b^{1-\xi(n+1)}d(x)\left(\left(\frac{a^{\xi(n)}}{(ab)^{\left\lfloor\frac{n+1}{2}\right\rfloor}}\right)\frac{\mathscr{o}^n(x)+\mathfrak{d}^n(x)}{\alpha}\right)$$

$$+g(x)\left(\left(\frac{a^{\xi(n-1)}}{(ab)^{\left\lfloor\frac{n}{2}\right\rfloor}}\right)\frac{\mathscr{o}^{n-1}(x)+\mathfrak{d}^{n-1}(x)}{\alpha}\right)$$

$$= \frac{a^{\xi(n+1)}\mathscr{o}^{n-1}(x)}{\alpha}\left(\frac{a^{\xi(n)}b^{1-\xi(n+1)}d(x)\mathscr{o}(x)}{(ab)^{\left\lfloor\frac{n+1}{2}\right\rfloor}}+\frac{a^{\xi(n-1)}g(x)}{a^{\xi(n+1)}(ab)^{\left\lfloor\frac{n}{2}\right\rfloor}}\right)$$

$$+\frac{a^{\xi(n+1)}\mathfrak{d}^{n-1}(x)}{\alpha}\left(\frac{a^{\xi(n)}b^{1-\xi(n+1)}d(x)\mathfrak{d}(x)}{(ab)^{\left\lfloor\frac{n+1}{2}\right\rfloor}}+\frac{a^{\xi(n-1)}g(x)}{a^{\xi(n+1)}(ab)^{\left\lfloor\frac{n}{2}\right\rfloor}}\right)$$

$$= \frac{a^{\xi(n+1)}\mathscr{o}^{n-1}(x)}{\alpha}\left(\frac{abd(x)\mathscr{o}(x)}{a^{1-\xi(n)}b^{\xi(n+1)}(ab)^{\left\lfloor\frac{n+1}{2}\right\rfloor}}+\frac{abg(x)}{(ab)^{\left\lfloor\frac{n}{2}\right\rfloor+1}}\right)$$

$$+\frac{a^{\xi(n+1)}\mathfrak{d}^{n-1}(x)}{\alpha}\left(\frac{abd(x)\mathfrak{d}(x)}{a^{1-\xi(n)}b^{\xi(n+1)}(ab)^{\left\lfloor\frac{n+1}{2}\right\rfloor}}+\frac{abg(x)}{(ab)^{\left\lfloor\frac{n}{2}\right\rfloor+1}}\right)$$

$$= \frac{a^{\xi(n+1)}\mathscr{o}^{n-1}(x)}{\alpha}\left(\frac{ab\big(d(x)\mathscr{o}(x)+g(x)\big)}{(ab)^{\left\lfloor\frac{n+2}{2}\right\rfloor}}\right)$$

$$+\frac{a^{\xi(n+1)}\mathfrak{d}^{n-1}(x)}{\alpha}\left(\frac{ab(d(x)\mathfrak{d}(x)+g(x))}{(ab)^{\left\lfloor\frac{n+2}{2}\right\rfloor}}\right)$$

$$= \frac{a^{\xi(n+1)}\mathscr{o}^{n-1}(x)}{\alpha}\left(\frac{\mathscr{o}^2(x)}{(ab)^{\left\lfloor\frac{n+2}{2}\right\rfloor}}\right)+\frac{a^{\xi(n+1)}\mathfrak{d}^{n-1}(x)}{\alpha}\left(\frac{\mathfrak{d}^2(x)}{(ab)^{\left\lfloor\frac{n+2}{2}\right\rfloor}}\right)$$

$$= \left(\frac{a^{\xi(n+1)}}{(ab)^{\left\lfloor \frac{n+2}{2} \right\rfloor}} \right) \frac{\mathfrak{o}^n(x) + \mathfrak{d}^n(x)}{\alpha}$$

where $d(x)\mathfrak{o}(x) + g(x) = \frac{\mathfrak{o}^2(x)}{ab}$ and $d(x)\mathfrak{d}(x) + g(x) = \frac{\mathfrak{d}^2(x)}{ab}$. Thus, the proof is completed.

2.2. Identities for Polynomials $\mathbb{L}_n(x)$

Theorem 2.5. Negative subscript terms in the sequences of the bi-periodic generalized Lucas polynomials are given by

$$\mathbb{L}_{-n}(x) = \big(-g(x)\big)^{-n} \mathbb{L}_n(x).$$

Proof. Using Binet formula for the nth bi-periodic generalized Lucas polynomial given in Theorem 2.4, we have

$$\mathbb{L}_{-n}(x) = \left(\frac{a^{\xi(-n)}}{(ab)^{\left\lfloor \frac{-n+1}{2} \right\rfloor}} \right) \frac{\mathfrak{o}^{-n}(x) + \mathfrak{d}^{-n}(x)}{\alpha}$$

$$= \left(\frac{a^{\xi(-n)}}{(ab)^{\left\lfloor \frac{-n+1}{2} \right\rfloor}} \right) \frac{\mathfrak{o}^n(x) + \mathfrak{d}^n(x)}{(-g(x)ab)^n \alpha}$$

$$= \big(-g(x)\big)^{-n} \left(\frac{a^{\xi(n)}}{(ab)^{\left\lfloor \frac{n+1}{2} \right\rfloor}} \right) \frac{\mathfrak{o}^n(x) + \mathfrak{d}^n(x)}{\alpha}$$

$$= \big(-g(x)\big)^{-n} \mathbb{L}_n(x)$$

where $\mathfrak{o}(x)\mathfrak{d}(x) = -g(x)ab$. Thus, the proof is completed.

Theorem 2.6. The limit of the ratio of consecutive terms in the sequences of the bi-periodic generalized Lucas polynomials is

i. $\lim_{n\to\infty} \frac{\mathbb{L}_{2n+1}(x)}{\mathbb{L}_{2n}(x)} = \frac{\mathfrak{o}(x)}{b}$

ii. $\lim_{n\to\infty} \frac{\mathbb{L}_{2n}(x)}{\mathbb{L}_{2n-1}(x)} = \frac{\mathfrak{o}(x)}{a}$

where $\mathbb{L}_n(x)$ is the nth bi-periodic generalized Lucas polynomial.

Proof. Using Binet formula for the nth bi-periodic generalized Lucas polynomial given in Theorem 2.4, we have

i.
$$\lim_{n\to\infty}\frac{\mathbb{L}_{2n+1}(x)}{\mathbb{L}_{2n}(x)}=\lim_{n\to\infty}\frac{\left(\frac{a^{\xi(2n+1)}}{(ab)^{\left\lfloor\frac{2n+2}{2}\right\rfloor}}\right)\left(\frac{\sigma^{2n+1}(x)+\mathfrak{d}^{2n+1}(x)}{\alpha}\right)}{\left(\frac{a^{\xi(2n)}}{(ab)^{\left\lfloor\frac{2n+1}{2}\right\rfloor}}\right)\left(\frac{\sigma^{2n}(x)+\mathfrak{d}^{2n}(x)}{\alpha}\right)}$$
$$=\lim_{n\to\infty}\frac{\frac{a}{(ab)^{n+1}}\left(\sigma^{2n+1}(x)+\mathfrak{d}^{2n+1}(x)\right)}{\frac{1}{(ab)^{n}}\left(\sigma^{2n}(x)+\mathfrak{d}^{2n}(x)\right)}$$
$$=\lim_{n\to\infty}\frac{1}{b}\frac{\sigma^{2n+1}(x)\left(1+\left(\frac{\mathfrak{d}(x)}{\sigma(x)}\right)^{2n+1}\right)}{\sigma^{2n}(x)\left(1+\left(\frac{\mathfrak{d}(x)}{\sigma(x)}\right)^{2n}\right)}$$
$$=\frac{\sigma(x)}{b}$$

and

ii.
$$\lim_{n\to\infty}\frac{\mathbb{L}_{2n}(x)}{\mathbb{L}_{2n-1}(x)}=\lim_{n\to\infty}\frac{\left(\frac{a^{\xi(2n)}}{(ab)^{\left\lfloor\frac{2n+1}{2}\right\rfloor}}\right)\left(\frac{\sigma^{2n}(x)+\mathfrak{d}^{2n}(x)}{\alpha}\right)}{\left(\frac{a^{\xi(2n-1)}}{(ab)^{\left\lfloor\frac{2n}{2}\right\rfloor}}\right)\left(\frac{\sigma^{2n-1}(x)+\mathfrak{d}^{2n-1}(x)}{\alpha}\right)}$$
$$=\lim_{n\to\infty}\frac{\frac{1}{(ab)^{n}}\left(\sigma^{2n}(x)+\mathfrak{d}^{2n}(x)\right)}{\frac{a}{(ab)^{n}}\left(\sigma^{2n-1}(x)+\mathfrak{d}^{2n-1}(x)\right)}$$
$$=\lim_{n\to\infty}\frac{1}{a}\frac{\sigma^{2n}(x)\left(1+\left(\frac{\mathfrak{d}(x)}{\sigma(x)}\right)^{2n}\right)}{\sigma^{2n-1}(x)\left(1+\left(\frac{\mathfrak{d}(x)}{\sigma(x)}\right)^{2n-1}\right)}$$
$$=\frac{\sigma(x)}{a}$$

where $|\mathfrak{d}(x)|<\sigma(x)$ and $\lim_{n\to\infty}\left(\frac{\mathfrak{d}(x)}{\sigma(x)}\right)^{n}=0$. This completes the proof.

Now we present some basic identities for the bi-periodic generalized Lucas polynomials, such as Catalan's identity and Cassini's identity.

Theorem 2.7. (Catalan's Identity) Let n and r be nonnegative integers. For $n \geq r$, we have

$$a^{1-\xi(n+r)}b^{1+\xi(n+r)}\mathbb{L}_{n-r}(x)\mathbb{L}_{n+r}(x) - a^{1-\xi(n)}b^{1+\xi(n)}\mathbb{L}_n{}^2(x) = \left(-g(x)\right)^{n-r}(ab)^{1-r}\left(\frac{\sigma^r(x)-\mathfrak{d}^r(x)}{\alpha}\right)^2$$

where $\mathbb{L}_n(x)$ is the nth bi-periodic generalized Lucas polynomial.

Proof. Using Binet formula for the nth bi-periodic generalized Lucas polynomial given in Theorem 2.4, we have

$$\begin{aligned}
&a^{1-\xi(n+r)}b^{1+\xi(n+r)}\mathbb{L}_{n-r}(x)\mathbb{L}_{n+r}(x) - a^{1-\xi(n)}b^{1+\xi(n)}\mathbb{L}_n{}^2(x)\\
&= a^{1-\xi(n+r)}b^{1+\xi(n+r)}\left(\frac{a^{\xi(n-r)}}{(ab)^{\left\lfloor\frac{n-r+1}{2}\right\rfloor}}\right)\left(\frac{a^{\xi(n+r)}}{(ab)^{\left\lfloor\frac{n+r+1}{2}\right\rfloor}}\right)\\
&\qquad\left(\frac{\sigma^{n-r}(x)+\mathfrak{d}^{n-r}(x)}{\alpha}\right)\left(\frac{\sigma^{n+r}(x)+\mathfrak{d}^{n+r}(x)}{\alpha}\right)\\
&\quad -a^{1-\xi(n)}b^{1+\xi(n)}\left(\frac{a^{\xi(n)}}{(ab)^{\left\lfloor\frac{n+1}{2}\right\rfloor}}\right)\left(\frac{a^{\xi(n)}}{(ab)^{\left\lfloor\frac{n+1}{2}\right\rfloor}}\right)\\
&\qquad\left(\frac{\sigma^{n}(x)+\mathfrak{d}^{n}(x)}{\alpha}\right)\left(\frac{\sigma^{n}(x)+\mathfrak{d}^{n}(x)}{\alpha}\right)\\
&= a^{1-\xi(n+r)}b^{1+\xi(n+r)}\left(\frac{1}{a^{\left\lfloor\frac{n-r}{2}\right\rfloor}b^{\left\lfloor\frac{n-r+1}{2}\right\rfloor}}\right)\left(\frac{1}{a^{\left\lfloor\frac{n+r}{2}\right\rfloor}b^{\left\lfloor\frac{n+r+1}{2}\right\rfloor}}\right)\\
&\qquad\left(\frac{\sigma^{2n}(x)+\sigma^{n-r}(x)\mathfrak{d}^{n+r}(x)+\mathfrak{d}^{n-r}(x)\sigma^{n+r}(x)+\mathfrak{d}^{2n}(x)}{\alpha^2}\right)\\
&\quad -a^{1-\xi(n)}b^{1+\xi(n)}\left(\frac{1}{a^{2\left\lfloor\frac{n}{2}\right\rfloor}b^{2\left\lfloor\frac{n+1}{2}\right\rfloor}}\right)\left(\frac{\sigma^{2n}(x)+2\sigma^{n}(x)\mathfrak{d}^{n}(x)+\mathfrak{d}^{2n}(x)}{\alpha^2}\right)
\end{aligned}$$

$$= a^{1-\xi(n+r)-\left\lfloor\frac{n-r}{2}\right\rfloor-\left\lfloor\frac{n+r}{2}\right\rfloor} b^{1+\xi(n+r)-\left\lfloor\frac{n-r+1}{2}\right\rfloor-\left\lfloor\frac{n+r+1}{2}\right\rfloor}$$

$$\left(\frac{\mathcal{o}^{2n}(x)+\mathcal{o}^{n-r}(x)\mathfrak{d}^{n+r}(x)+\mathfrak{d}^{n-r}(x)\mathcal{o}^{n+r}(x)+\mathfrak{d}^{2n}(x)}{\alpha^2}\right)$$

$$-a^{1-\xi(n)-2\left\lfloor\frac{n}{2}\right\rfloor} b^{1+\xi(n)-2\left\lfloor\frac{n+1}{2}\right\rfloor}\left(\frac{\mathcal{o}^{2n}(x)+2\big(\mathcal{o}(x)\mathfrak{d}(x)\big)^n+\mathfrak{d}^{2n}(x)}{\alpha^2}\right)$$

$$= (ab)^{1-n}\left(\frac{\mathcal{o}^{n-r}(x)\mathfrak{d}^{n+r}(x)+\mathfrak{d}^{n-r}(x)\mathcal{o}^{n+r}(x)-2\big(\mathcal{o}(x)\mathfrak{d}(x)\big)^n}{\alpha^2}\right)$$

$$= (ab)^{1-n}\big(\mathcal{o}(x)\mathfrak{d}(x)\big)^n\left(\frac{\mathcal{o}^{2r}(x)+\mathfrak{d}^{2r}(x)-2\big(\mathcal{o}(x)\mathfrak{d}(x)\big)^r}{\alpha^2\big(\mathcal{o}(x)\mathfrak{d}(x)\big)^r}\right)$$

$$= (ab)^{1-n}(-g(x)ab)^n\frac{\big(\mathcal{o}^r(x)-\mathfrak{d}^r(x)\big)^2}{\alpha^2(-g(x)ab)^r}$$

$$= \big(-g(x)\big)^{n-r}(ab)^{1-r}\left(\frac{\mathcal{o}^r(x)-\mathfrak{d}^r(x)}{\alpha}\right)^2$$

where $\mathcal{o}(x)\mathfrak{d}(x) = -g(x)ab$. This completes the proof.

Theorem 2.8. (Cassini's Identity) Let n be nonnegative integer. Then, we have

$$a^{1-\xi(n+1)}b^{1+\xi(n+1)}\mathbb{L}_{n-1}(x)\mathbb{L}_{n+1}(x) - a^{1-\xi(n)}b^{1+\xi(n)}{\mathbb{L}_n}^2(x)$$

$$= \big(-g(x)\big)^{n-1}\left(\frac{d^2(x)a^2b^2+4g(x)ab}{\alpha^2}\right).$$

Proof. The proof can be seen in an obvious way by taking $r = 1$ in the Catalan's identity.

3. Conclusion and Suggestion

The Fibonacci and the Lucas numbers have many generalizations, applications and interpretations presented in different ways. The most interesting applications of these numbers have been on their generalizations. In this paper, the biperiodic generalized Lucas polynomials, which generalize well-known Lucas polynomials, the $h(x)$-Lucas polynomials, the Lucas polynomials with two

variable, the Pell-Lucas polynomials, the Pell-Lucas-prime polynomials, the Jacobsthal-Lucas polynomials, the Fermat-Lucas polynomials, the Chebyshev first kind polynomials, the Morgan-Voyce second kind polynomials, the Vieta-Lucas polynomials, are defined. Also, the bi-periodic Lucas polynomials, the bi-periodic $h(x)$-Lucas polynomials, the bi-periodic Lucas polynomials with two variable, the bi-periodic Pell-Lucas polynomials, the bi-periodic Pell-Lucas-prime polynomials, the bi-periodic Jacobsthal-Lucas polynomials, the bi-periodic Fermat-Lucas polynomials, the bi-periodic Chebyshev firts kind polynomials, the bi-periodic Morgan-Voyce second kind polynomials, the bi-periodic Vieta-Lucas polynomials are presented. Binet formulas that allow us to calculate the nth terms of these polynomial sequences and some properties of their consecutive terms are given. Also generating functions, Catalan's identity and Cassini's identity are obtained.

It would be interesting to study these polynomials in matrix theory. More general formulas that allow us to calculate the nth terms of these polynomial sequences and sums formulas can be explored.

Acknowledgments

The author would like to thank the editors and the anonymous referees for their contributions.

4. References

[1] Horadam, A. F. 1961 A Generalized Fibonacci sequence, The American Mathematical Monthly, 68(5). 455-459.

[2] Hoggatt Jr., V. E. & Bicknell, M. 1973 Generalized Fibonacci polynomials and Zeckendorf 's theorem, The Fibonacci Quarterly, 11(4), 399–419.

[3] Gültekin, İ. & Taşyurdu, Y. 2013 On period of the sequence of Fibonacci polynomials modulo m, Discrete Dynamics in Nature and Society vol. (2013), 3p.

[4] Taşyurdu, T. & Deveci, Ö. 2017 The Fibonacci polynomials in rings, Ars Combinatoria, 133, 355-366.

[5] Koshy, T. 2017 Fibonacci and Lucas numbers with applications, 1, 2nd Edition, Wiley-Interscience Publications, New York, 704p.

[6] Catalani, M. 2004 Some formulae for bivariate Fibonacci and Lucas polynomials, 1-9. Site: https://doi.org/10.48550/arXiv.math/0406323

[7] Panwar, Y. K., Gupta V. K. & Bhandari, J. 2020 Generalized identities of bivariate Fibonacci and bivariate Lucas polynomials, Journal of Amasya University the Institute of Sciences and Technology, 1(2), 146-154.

[8] Nalli A. & Haukkanen, P. 2009 On generalized Fibonacci and Lucas polynomials, Chaos, Solitons and Fractals, 45(5), 3179-3186.

[9] Florez, R. Higuita, R. A. & Mukherjee, A. 2014 Alternating sums in the Hosoya polynomial triangle, J. Integer Seq. 17, Article 14.9.5

[10] Florez, R., Higuita, R. A. & Mukherjee, A. 2018 Characterization of the strong divisibility property for generalized Fibonacci polynomials, Integers 18, Article number A1.

[11] Florez, R., McAnally, N. & Mukherjee, A. 2018 Identities for the generalized Fibonacci polynomial, Integers 18B, Article number A12.

[12] Edson, M. & Yayenie, O. 2009 A New Generalization of Fibonacci sequence & extended Binet's formula, Integers, 9, 639–654.

[13] Bilgici, G. 2014 Two Generalizations of Lucas Sequence, Applied Mathematics and Computation, 245, 526–538.

[14] Yılmaz, Y., Çoşkun, A. & Taşkara, N. 2017 On properties of bi-periodic Fibonacci and Lucas polynomials, AIP Conference Proceedings 1863, 310002.

Heat Shock Protein 90 Inhibitors and Combination Therapy Approach in Cancer

Özlem KAPLAN[1] and Nazan GÖKŞEN TOSUN[2]

[1]Alanya Alaadddin Keykubat University, Rafet Kayış Faculty of Engineering, Genetics and Bioengineering Department, Antalya, Turkey (ozlem.kaplan@istanbul.edu.tr), ORCID: 0000-0002-3052-4556
[2]Tokat Gaziosmanpaşa University, Tokat Vocational School of Health Sciences, Department of Medical Services and Techniques, Tokat, Turkey (nazan.goksen@gop.edu.tr) ORCID: 0000-0001-5269-1067

1. Introduction

Heat shock proteins (HSPs) are molecular chaperones that enable proteins to fold and mature properly. The response of cells to stress factors such as heat shock, hypoxia, chemical factors, and acidosis increases the expression of HSPs (Hu et al., 2022). The HSP family is classified based on molecular weight. This family's most well-known members are HSP27, HSP60, HSP70, and HSP90. Members of this family interact with each other through a signaling network (J. Wu et al., 2017). HSP90 regulates the folding of newly synthesized proteins, correcting misfolded proteins, and avoiding misfolded protein aggregation. Thus, the activation of proteins has an essential role in late-stage maturation and stability (Schopf, Biebl, and Buchner, 2017). HSP90-protein interactions are critical for tumor proliferation, survival, and migration (Hu et al., 2022). More than 400 proteins that interact with HSP90 have been discovered (Workman, 2004). Many of these proteins are oncogenic proteins, which are the main drivers of the emergence and development of cancers. These proteins participate in a wide range of vital biological activities such as signal transduction, DNA damage repair, chromatin remodeling, cell proliferation, and hormone receptor activation. Many malignant activities, such as tumor development, invasion, adhesion, angiogenesis, and metastasis have been related to the HSP90 protein in the literature (Magwenyane et al., 2022; J. Wu et al., 2017; Žáčková et al., 2013; Zuehlke and Johnson, 2010). For all these reasons, HSP90 is an excellent therapeutic target in cancer, and inhibiting it can disrupt tumor proteins and pathways (Jhaveri et al., 2014). The HSP90 family contains four isoforms that are found in distinct parts of the cell. TRAP1 in the mitochondria endoplasmic reticulum (ER) and GRP94 in the ER, HSP90β and HSP90α are found in the nucleus and cytoplasm, respectively. (Li and Buchner, 2013; Li, Soroka, and Buchner, 2012). All isoforms have sequence homology at their N-terminal, and the ATP binding sites at their N-terminal were investigated as targets for HSP90 inhibition (Soga, Akinaga, and Shiotsu, 2013). Many HSP90 inhibitors have been developed and are currently being evaluated in clinical trials. However, HSP90 inhibitor did not give effective results as monotherapy. In addition to the development of tumor resistance in monotherapy, toxicity was the main factor limiting the effectiveness of the therapy (Chatterjee and Burns, 2017). A possible technique is to combine HSP90 inhibitors with other anticancer treatments to overcome this limitation of monotherapy. Several studies have demonstrated that using HSP90 inhibitors in combination with other anticancer treatments has a synergistic impact (Ren, Li, Zhang, and Yang, 2022). In this section, we summarize the function of HSP90 in cancer, the use of HSP90 inhibitors and the combination of these inhibitors with other treatment strategies.

2. Structural properties of HSP90 protein

HSP90 which has a molecular weight of 90 kDa is a chaperone protein found in all species except Archaea. The HSP90 protein is homodimer, and a homodimer has 3 domains: N-terminal, Middle, and C-terminal (Figure 1) (Meyer et al., 2003; So″ti, Vermes, Haystead, and Csermely, 2003). The N-terminal domain forms the main ATPase domain of HSP90. The N-terminal domain has a supercharged binding domain, which is like gyrase, histidine kinase, and topoisomerase (Bickel and Gohlke, 2019; Prodromou, Roe, Piper, and Pearl, 1997). The middle domain performs the ATPase activity responsible for hydrolyzing adenosine triphosphate (ATP) (Meyer et al., 2003). The C-terminal is responsible for the dimer formation of HSP90. The C terminus also contains the motif Met-Glu-Glu-Val-Asp, which is the interaction domain of co-chaperones with HSP90 (Blundell, Pal, Roe, Pearl, and Prodromou, 2017).

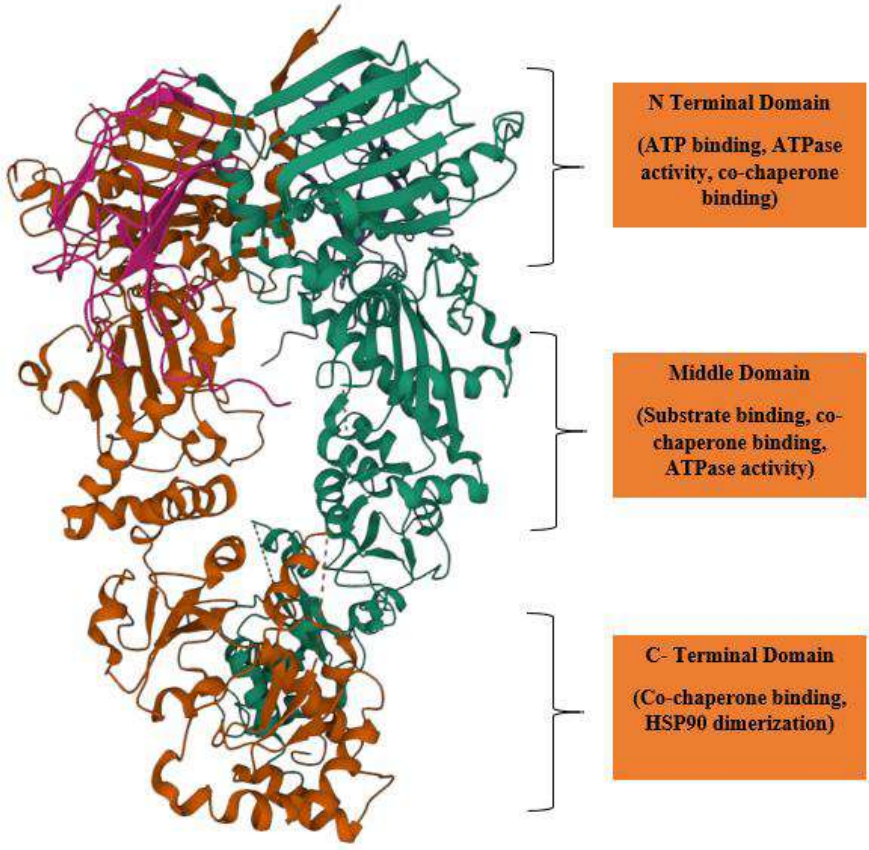

Figure 1. Crystal structure of the HSP90 protein (PDB ID: 2CG9)

HSP90's activity in folding target proteins is an ATP-dependent process and relies on dynamic conformational changes. This process is based on a complex mechanism regulated by multiple co-chaperones. Dimerization is required for HSP90 to function effectively in cancer cells (Hoter, El-Sabban, and Naim, 2018). The N-terminal domain of the HSP90 remains open, creating dimers across the C-terminal domain. Unfolded proteins are loaded into the middle domain of HSP90 in an open conformation, and ATP interaction causes dimerization of the N-terminal domain. ATP hydrolysis causes HSP90 to become more twisted and closed, and ADP is released from HSP90, causing the conformation to revert to its open state. Proteins are folded and released in their native conformations by repeating this cycle (Hoter et al., 2018). HSP90 folds and activates approximately 10% of the proteins in the human proteome. HSP90 has various roles in cell survival derived from chaperone function due to its broad involvement in protein activity and stability (Hartl, Bracher, and Hayer-Hartl, 2011). When cells are exposed to the HSP90 inhibitor, it leads to degradation of oncogenic proteins through the proteasome and oncogenic proteins are unable to function (Magwenyane et al., 2022).

3. HSP90 inhibitors in cancer treatment

Inhibition of the HSP90 protein is important in the prevention of cancer development and for this purpose, many HSP90 inhibitors have been defined in recent years. The well-known HSP90 inhibitors were summarized in Table 1. Geldanamycin is the first natural product-based HSP90 inhibitor, and it has shown anti-cancer efficacy in different cancer cell lines. Unfortunately, geldanamycin showed poor bioavailability, hepatotoxicity, low chemical stability, and solubility in further studies (Neckers and Workman, 2012). Researchers synthesized geldanamycin derivatives to ameliorate these negative properties (Khandelwal, Crowley, and Blagg, 2016). Among the modified geldanamycin derivatives, 17-DMAG and 17-AAG exhibited excellent inhibitory properties due to their high solubility. 17-DMAG and 17-AAG have also entered clinical trials for further evaluation (Rastelli, Tian, Wang, Myles, and Liu, 2005; Schulte and Neckers, 1998). Afterward, another 17-AAG analogue, gamitrinib-TPP, a geldanamycin mitochondrial matrix inhibitor was designed by Kang et al. Gamitrinib-TPP has a mitochondrial targeting moiety and suppressed tumor growth due to its "mitochondriotoxic" mechanism of action (Kang et al., 2009).

Radicicol is a resorcinol lactone antibiotic and showed a better affinity for HSP90 compared to geldanamycin. However, due to its electrophilic nature, radicicol is rapidly converted to an inactive form and is not suitable for testing in clinical trials. Therefore, Soga et al. synthesized KF25706, which is more

metabolically stable and exhibits *in vivo* anti-cancer activity (Soga et al., 1999). Radicicol-derived Ganetespib (STA-9090) has been shown to have better tumor penetration than 17-AAG, as well as milder side effects than 17-AAG and is currently being clinically evaluated in phase I-III studies (Jhaveri, Taldone, Modi, and Chiosis, 2012; Shimamura et al., 2012; Ying et al., 2012). Cheung et al. performed compound screen and found CCT018159, a resorcinol-containing compound that showed inhibitory activity of HSP90 (Cheung et al., 2005). AUY922 synthesized based on CCT018159 is being evaluated in phase II studies in clinical trials. KW-2478 is a resorcinol derivative molecule that has entered the clinical stage and has been clinically tested in patients with B-cell malignancies and multiple refractory myelomas (Cavenagh et al., 2017). Similarly, the solid metastatic tumors were treated with another resorcinol derivative molecule AT13387 due to its anti-HSP90 properties (Smyth et al., 2012). Both geldanamycin and radicicol derivatives destroy cancer cells significantly, but their potential for use is limited due to their toxicity and insufficient *in vivo* efficacy. Therefore, researchers have developed new HSP90 inhibitors by setting forth of the structural properties of geldanamycin and radicicol (Neckers and Workman, 2012). Radanamycin was the first chimeric HSP90 inhibitor (Roe et al., 1999), and later analogues of radanamycin; radamide, resorcinol, and radester were produced (Shen and Blagg, 2005). Comparing these three compounds in terms of HSP90 binding affinity and anti-proliferative activity, it was observed that they all exhibited enhanced effects.

Chiosis et al. designed small molecule inhibitors for HSP90 inhibition that bind to the N-terminal ATP binding site (Chiosis et al., 2001). PU3, the first purine-based HSP90 inhibitor, was synthesized to inhibit HSP90 by binding to its N-terminal ATP binding site. (Chiosis, Lucas, Shtil, Huezo, and Rosen, 2002). Subsequently, purine-based analogues continued to be developed and BIIB021 was one of the most promising HSP90 inhibitors among all analogues. Comparing the activity of BIIB021 in healthy cells and tumor cells, it was executed to have high selectivity for tumors. (Lundgren et al., 2009). In addition, by adding a phosphate ester to this anoline, BIIB028 was developed, and these two analogues entered clinical trials (Dickson et al., 2013)

A Phase I clinical trial of the MPC-3100 in 2011. MPC-0767 molecule was designed and produced as an HSP90 inhibitor with better water solubility than MPC-3100 (S.-H. Kim et al., 2015). Preliminary animal investigations revealed that this prodrug had comparable pharmacokinetics and effectiveness, including tumor regressions, to MPC-3100. In 2010, Debio 0932, Phase I data were presented in solid tumors and lymphoma with no significant efficacy (Isambert et al., 2012).

Table 1. HSP90 inhibitors

Inhibitor	Clinical Stage	Drug Combination	Reference
17- AAG	Phase I/II/III	Cytarabine, irinotecan, sorafenib, tosylate, docetaxel, bortezomib, gemcitabine, everolimus	(Schulte and Neckers, 1998)
17- DMAG	Phase I	Trastuzumab	(Kaur et al., 2004; Zhao and Cao, 2014)
AT13387	Phase I/II	Abiraterone acetate, crizotinib, imatinib, prednisone, onalespib	(Woodhead et al., 2010)
BIIB028	Phase I/II/III	onalespib, bortezomib, cetuximab	(Hong et al., 2013)
BIIB021	Phase I/II	Exemestane, trastuzumab	(Lundgren et al., 2009)
CCT018159	-	-	(Smith et al., 2006)
Debio 0932	Phase I/II	-	(Isambert et al., 2012)
Gamitrinib TPP	Phase I	-	(Kang et al., 2009; Wei et al., 2022)
DN401	-	-	(Park et al., 2020)
Geldanamycin	Phase I/II	docetaxel, irinotecan hydrochloride	(M. S. Wu, Lien, Shen, Yang, and Chen, 2013)
IPI-504	Phase I/II/III	docetaxel, irinotecan, imatinib, sorafenib, bortezomib, cytarabine mesylate, everolimus, gemcitabine	(Patterson, Palombella, Fritz, and Normant, 2008)
KW-2478	Phase I/II	Bortezomib	(Yong et al., 2016)
Macbecin	-	-	(Martin et al., 2008)
MPC-3100	Phase I	-	(S.-H. Kim et al., 2015)
NVP-AUY992	-	-	(Jeong, Oh, Kwon, and Seo, 2017)
NVP-BEP800	-	-	(Stingl et al., 2010)
PU3	Phase I	-	(Taldone and Chiosis, 2009)
Radamide	-	-	(Kyle Hadden, Lubbers, and J. Blagg, 2006)

Table 1. HSP90 inhibitors (continued)

Inhibitor	Clinical Stage	Drug Combination	Reference
SNX-2112	-	-	(Chandarlapaty et al., 2008)
TAS-116	Phase I	-	(Doi et al., 2019)
XL888	Phase I	-	(Bussenius et al., 2012)
STA-9090	Phase I/II	Docetaxel, crizotinib, sirolimus, capecitabine, bortezomib, fulvestrant, dexamethasone, carboplatin	(Shah et al., 2018)
Radanamycin	-	-	(Kyle Hadden et al., 2006)
Radester	-	-	(Y. J. Kim, Lee, Myung, Kim, and Lee, 2012)
Radicicol	-	-	(Y. J. Kim et al., 2012)

4. HSP90 inhibition and combination therapy

Cancer cells increase their ability to survive against developed therapeutic molecules through chromosomal rearrangements and rapidly occurring reactive mutations. As tumors develop by developing resistance to these molecules, the efficacy of anticancer therapy eventually decreases. The most prevalent and difficult phenomena in clinical treatment is resistance to radiation and chemotherapy, the two main anticancer treatments. As described in the previous sections, although HSP90 inhibitors show great promise as anticancer drugs, they did not provide the desired effect when used as monotherapy. As a result, HSP90 inhibitors developed since their discovery have not received FDA approval for monotherapy in cancer. Therefore, using HSP90 inhibitors in combined therapies may provide important results in increasing the effectiveness of treatment. Numerous research has been studied to investigate the effects of combining HSP inhibitors with other agents, and the results have shown that they have additive or synergistic benefits. HSP90 inhibitors may have an indirect anticancer effect by blocking tumor survival pathways associated with resistance mechanisms. Moreover, combination therapies always allow the use of lower doses than monotherapy, thus preventing toxic side effects. In this section, we focused on describing the various studies and results on combination therapies of HSP90 inhibitors.

a. Combined therapy with chemotherapy

The effects of combinations of HSP90 inhibitors with taxanes targeting microtubules in cancer chemotherapy on cancer cells have been demonstrated by various studies. These combinations have been shown to have a synergistic effect in targeting tumors. Therapy of paclitaxel in combination with 17-AAG showed that the cytotoxic effect of paclitaxel was increased 5-22-fold compared to treatment of paclitaxel alone. (Nguyen et al., 2001). Solit et al. found 17-AAG made breast cancer cells more sensitive to Taxol (Solit, Basso, Olshen, Scher, and Rosen, 2003). In addition, ganetespib combined with docetaxel is a combination that has gone into phase II studies. The patients diagnosed with advanced lung adenocarcinoma, following the diagnosis after 6 months, the patients have been treated with this combination therapy and significantly prolonged survival rates have been carried out by this study (Ramalingam et al., 2015). Based on these findings, a phase III study was conducted on lung cancer patients. In patients with advanced lung adenocarcinoma, combined therapy of ganetespib and docetaxel has been reported to have synergistic effects, but not improve survival (Pillai et al., 2020).

Cisplatin, a well-known chemotherapeutic agent used to treat various types of cancer, interacts with DNA bases, and causes apoptosis. In studies, 17-AAG has shown synergistic anticancer activity with cisplatin (Bagatell, Beliakoff, David, Marron, and Whitesell, 2005). Here it is proposed that 17-AAG sensitizes cells to cisplatin by inducing depletion of the antiapoptotic protein IGF1R and AKT.

As a triple combined therapy approach, ganetespib, pemetrexed, and cisplatin chemotherapeutic drugs have been used together for treatment in patients with malignant pleural mesothelioma and effective results have been obtained. Antifolate and platinum drugs have been used in combination in the first-line treatment of malignant pleural mesothelioma. Reversing antifolate resistance, Ganetespib disrupts the HSP90 client thymidylate synthase (Fennell et al., 2020). Following SNX-5422 treatment, combined therapy consisting of, carboplatin, SNX-5422, and paclitaxel demonstrated significant tolerance and antitumor activity against non-small cell lung cancer (Gutierrez et al., 2021). 5-Fluorouracil (5-FU) known as a nucleotide analog that targets the enzyme thymidylate synthase. The colorectal xenograft model was treated with 5FU and ganetespib as a combined therapy approach. It was reported to induce cell cycle arrest by downregulating thymidylate synthase expression with a synergistic effect. Besides, ganetespib showed a significant effect in inhibiting PI3K/Akt and ERK signaling pathways involved in proliferation and treatment resistance (Nagaraju, Alese, Landry, Diaz, and El-Rayes, 2014).

b. Combined therapy with radiotherapy

An HSP90 inhibitor plays a key role in the DNA damage response by promoting the degradation of kinases involved in the DNA damage response and can abolish cell cycle checkpoints S and G2/M (Trepel, Mollapour, Giaccone, and Neckers, 2010). Thanks to this role of HSP90 inhibitors, tumor cells can be selectively radiosensitizer. Approaches using HSP90 inhibitors to resolve the radiation resistance of tumor cells have long been promising. In head and neck squamous cell carcinoma xenografts, BIIB021 and 17-AAG, the HSP90 inhibitors, exhibited anticancer effects. In addition, combining BIIB021 and radiotherapy resulted in slower growth of xenografts (Yin et al., 2010). Kinzel et al. demonstrated that the combined use of the HSP90 inhibitor NW457 and radiotherapy produced a synergistic effect and inhibited tumor growth in colorectal cancer (Kinzel et al., 2016). Mehta et al. demonstrated that the Hsp90 inhibitor AT13387 can sensitize to radiotherapy in pancreatic cancer cells and head and neck squamous cell carcinoma (Mehta et al., 2020).

c. Combined therapy with immunotherapy

Immunotherapy has received great interest as a treatment strategy for many types of human cancer. In recent years, some studies have suggested that a therapeutic approach combining immunotherapy and HSP90 inhibitors may be effective. Proia and Kaufmann demonstrated that concomitant use of the HSP90 inhibitor ganetespib and the anti-PD-L1 antibody enhanced antitumor efficacy in mice with melanoma tumors and colon carcinoma (Proia and Kaufmann, 2015). Ganetespib ameliorates tumor cytotoxicity to these cells via T-cell mediated, and this effect may be clarified by the upregulation of interferon response genes induced by ganetespib (Mbofung et al., 2017). In another work, the combination of HSP90 inhibitor with XL888 and PD-1 blockade demonstrated a successful effect in pancreatic ductal adenocarcinoma models. XL-888 reduces IF-6 expression in these cells and increases the efficiency of anti-PD-1 blocking by directly inhibiting cell growth (Zhang et al., 2021).

d. Combined therapy with other HSP Inhibitors

Monotherapy with an HSP90 inhibitor causes especially increased expression of other HSPs and resistance to HSP90 inhibitors. When HSP90 is inhibited, other members of the HSP family, including HSP27 and HSP70, are up-regulated, effectively reversing the effects of HSP90 inhibition (Lee, Hong, Chang, and Chang, 2012). Previous studies have reported that the HSP90 inhibitor 17-AAG causes up-regulation of HSP27 and increases resistance by modulating glutathione (GSH) (McCollum, TenEyck, Sauer, Toft, and Erlichman, 2006). In

addition, studies with 17AAG revealed that overexpression of HSP70 can inhibit apoptosis (Guo et al., 2005). Therefore, simultaneous inhibition of HSP90 as well as other HSPs may be beneficial in solving this problem. Lee et al. simultaneously inhibited HSP90 and HSP27 in breast cancer stem-like cells with the use of Geldanamycin and Hsp27-specific siRNA. The results demonstrated the synergistic effect of HSP90 and HSP27 inhibition in these cells (Lee et al., 2012). Lamoureux et al. used a combination of OGX-427, an HSP27 inhibitor, with the Hsp90 inhibitor PF-04929113, and found that it enhanced anticancer effects in castration-resistant prostate cancer xenografts (Lamoureux et al., 2014). Gou et al. showed that KNK437, an HSP70 inhibitor, significantly increased the antileukemia activity of 17-AAG (Guo et al., 2005). All these studies recommended that HSP90 inhibitors may be used in combination with other HSP inhibitors as a new strategy against HSP90 inhibitor resistance.

5. Conclusions

Recently, many HSP90 inhibitors have been discovered and tested in many *in vitro/in vivo,* and clinical studies. Clinical and preclinical investigations demonstrated that, in contrast to HSP90 inhibitor monotherapy, combining HSP90 inhibitors with other treatments, such as chemotherapies, immunotherapy, targeted medicines, and radiotherapy, can increase efficacy. This chapter describes HSP90 inhibitors for cancer therapy and their use in combined therapy. These approaches represent forward-looking strategies for future cancer treatments.

6. References

1. Bagatell, R., Beliakoff, J., David, C. L., Marron, M. T., and Whitesell, L. (2005). Hsp90 inhibitors deplete key anti-apoptotic proteins in pediatric solid tumor cells and demonstrate synergistic anticancer activity with cisplatin. *International Journal of Cancer, 113*(2), 179-188. doi:https://doi.org/10.1002/ijc.20611
2. Bickel, D., and Gohlke, H. (2019). C-terminal modulators of heat shock protein of 90 kDa (HSP90): State of development and modes of action. *Bioorganic and medicinal chemistry, 27*(21), 115080. doi:https://doi.org/10.1016/j.bmc.2019.115080
3. Blundell, K. L. I. M., Pal, M., Roe, S. M., Pearl, L. H., and Prodromou, C. (2017). The structure of FKBP38 in complex with the MEEVD tetratricopeptide binding-motif of Hsp90. *PLOS ONE, 12*(3), e0173543. doi:10.1371/journal.pone.0173543
4. Bussenius, J., Blazey, C. M., Aay, N., Anand, N. K., Arcalas, A., Baik, T., . . . Rice, K. D. (2012). Discovery of XL888: A novel tropane-derived small molecule inhibitor of HSP90. *Bioorganic and Medicinal Chemistry Letters, 22*(17), 5396-5404. doi:https://doi.org/10.1016/j.bmcl.2012.07.052
5. Cavenagh, J., Oakervee, H., Baetiong-Caguioa, P., Davies, F., Gharibo, M., Rabin, N., . . . Yong, K. (2017). A phase I/II study of KW-2478, an Hsp90 inhibitor, in combination with bortezomib in patients with relapsed/refractory multiple myeloma. *Br J Cancer, 117*(9), 1295-1302. doi:10.1038/bjc.2017.302
6. Chandarlapaty, S., Sawai, A., Ye, Q., Scott, A., Silinski, M., Huang, K., . . . Solit, D. B. (2008). SNX2112, a Synthetic Heat Shock Protein 90 Inhibitor, Has Potent Antitumor Activity against HER Kinase–Dependent Cancers. *Clinical Cancer Research, 14*(1), 240-248. doi:10.1158/1078-0432.Ccr-07-1667
7. Chatterjee, S., and Burns, T. F. (2017). Targeting Heat Shock Proteins in Cancer: A Promising Therapeutic Approach. *International Journal of Molecular Sciences, 18*(9), 1978. Retrieved from https://www.mdpi.com/1422-0067/18/9/1978
8. Cheung, K. M., Matthews, T. P., James, K., Rowlands, M. G., Boxall, K. J., Sharp, S. Y., . . . Workman, P. (2005). The identification, synthesis, protein crystal structure and in vitro biochemical evaluation of a new 3,4-diarylpyrazole class of Hsp90 inhibitors. *Bioorg Med Chem Lett, 15*(14), 3338-3343. doi:10.1016/j.bmcl.2005.05.046

9. Chiosis, G., Lucas, B., Shtil, A., Huezo, H., and Rosen, N. (2002). Development of a purine-scaffold novel class of Hsp90 binders that inhibit the proliferation of cancer cells and induce the degradation of Her2 tyrosine kinase. *Bioorg Med Chem, 10*(11), 3555-3564. doi:10.1016/s0968-0896(02)00253-5
10. Chiosis, G., Timaul, M. N., Lucas, B., Munster, P. N., Zheng, F. F., Sepp-Lorenzino, L., and Rosen, N. (2001). A small molecule designed to bind to the adenine nucleotide pocket of Hsp90 causes Her2 degradation and the growth arrest and differentiation of breast cancer cells. *Chem Biol, 8*(3), 289-299. doi:10.1016/s1074-5521(01)00015-1
11. Dickson, M. A., Okuno, S. H., Keohan, M. L., Maki, R. G., D'Adamo, D. R., Akhurst, T. J., . . . Schwartz, G. K. (2013). Phase II study of the HSP90-inhibitor BIIB021 in gastrointestinal stromal tumors. *Annals of Oncology, 24*(1), 252-257. doi:https://doi.org/10.1093/annonc/mds275
12. Doi, T., Kurokawa, Y., Sawaki, A., Komatsu, Y., Ozaka, M., Takahashi, T., . . . Nishida, T. (2019). Efficacy and safety of TAS-116, an oral inhibitor of heat shock protein 90, in patients with metastatic or unresectable gastrointestinal stromal tumour refractory to imatinib, sunitinib and regorafenib: a phase II, single-arm trial. *European Journal of Cancer, 121*, 29-39. doi:https://doi.org/10.1016/j.ejca.2019.08.009
13. Fennell, D. A., Danson, S., Woll, P. J., Forster, M., Talbot, D., Child, J., . . . Wheeler, G. M. (2020). Ganetespib in Combination with Pemetrexed–Platinum Chemotherapy in Patients with Pleural Mesothelioma (MESO-02): A Phase Ib Trial. *Clinical Cancer Research, 26*(18), 4748-4755. doi:10.1158/1078-0432.Ccr-20-1306
14. Guo, F., Rocha, K., Bali, P., Pranpat, M., Fiskus, W., Boyapalle, S., . . . Bhalla, K. (2005). Abrogation of Heat Shock Protein 70 Induction as a Strategy to Increase Antileukemia Activity of Heat Shock Protein 90 Inhibitor 17-Allylamino-Demethoxy Geldanamycin. *Cancer Research, 65*(22), 10536-10544. doi:10.1158/0008-5472.Can-05-1799
15. Gutierrez, M., Guo, R., Giaccone, G., Liu, S. V., Hao, Z., Hilton, C., . . . Drilon, A. (2021). Phase 1 multicenter study of the HSP90 inhibitor SNX-5422 plus carboplatin and paclitaxel in patients with lung cancers. *Lung Cancer, 162*, 23-28. doi:https://doi.org/10.1016/j.lungcan.2021.10.001
16. Hartl, F. U., Bracher, A., and Hayer-Hartl, M. (2011). Molecular chaperones in protein folding and proteostasis. *Nature, 475*(7356), 324-332. doi:10.1038/nature10317
17. Hong, D., Said, R., Falchook, G., Naing, A., Moulder, S., Tsimberidou, A.-M., . . . Rosen, L. S. (2013). Phase I Study of BIIB028, a Selective Heat

Shock Protein 90 Inhibitor, in Patients with Refractory Metastatic or Locally Advanced Solid Tumors. *Clinical Cancer Research, 19*(17), 4824-4831. doi:10.1158/1078-0432.Ccr-13-0477

18. Hoter, A., El-Sabban, M. E., and Naim, H. Y. (2018). The HSP90 Family: Structure, Regulation, Function, and Implications in Health and Disease. *Int J Mol Sci, 19*(9). doi:10.3390/ijms19092560
19. Hu, C., Yang, J., Qi, Z., Wu, H., Wang, B., Zou, F., . . . Liu, Q. (2022). Heat shock proteins: Biological functions, pathological roles, and therapeutic opportunities. *MedComm (2020), 3*(3), e161. doi:10.1002/mco2.161
20. Isambert, N., Hollebecque, A., Berge, Y., Ingen, H. v., Brienza, S., Destaillats, A., . . . Delord, J.-P. (2012). A phase I study of Debio 0932, an oral HSP90 inhibitor, in patients with solid tumors. *Journal of Clinical Oncology, 30*(15_suppl), 3026-3026. doi:10.1200/jco.2012.30.15_suppl.3026
21. Jeong, J. H., Oh, Y. J., Kwon, T. K., and Seo, Y. H. (2017). Chalcone-templated Hsp90 inhibitors and their effects on gefitinib resistance in non-small cell lung cancer (NSCLC). *Archives of Pharmacal Research, 40*(1), 96-105. doi:10.1007/s12272-016-0848-z
22. Jhaveri, K., Ochiana, S. O., Dunphy, M. P., Gerecitano, J. F., Corben, A. D., Peter, R. I., . . . Chiosis, G. (2014). Heat shock protein 90 inhibitors in the treatment of cancer: current status and future directions. *Expert Opin Investig Drugs, 23*(5), 611-628. doi:10.1517/13543784.2014.902442
23. Jhaveri, K., Taldone, T., Modi, S., and Chiosis, G. (2012). Advances in the clinical development of heat shock protein 90 (Hsp90) inhibitors in cancers. *Biochim Biophys Acta, 1823*(3), 742-755. doi:10.1016/j.bbamcr.2011.10.008
24. Kang, B. H., Plescia, J., Song, H. Y., Meli, M., Colombo, G., Beebe, K., . . . Altieri, D. C. (2009). Combinatorial drug design targeting multiple cancer signaling networks controlled by mitochondrial Hsp90. *J Clin Invest, 119*(3), 454-464. doi:10.1172/jci37613
25. Kaur, G., Belotti, D., Burger, A. M., Fisher-Nielson, K., Borsotti, P., Riccardi, E., . . . Giavazzi, R. (2004). Antiangiogenic Properties of 17-(Dimethylaminoethylamino)-17-Demethoxygeldanamycin: An Orally Bioavailable Heat Shock Protein 90 Modulator. *Clinical Cancer Research, 10*(14), 4813-4821. doi:10.1158/1078-0432.Ccr-03-0795
26. Khandelwal, A., Crowley, V. M., and Blagg, B. S. J. (2016). Natural Product Inspired N-Terminal Hsp90 Inhibitors: From Bench to Bedside? *Med Res Rev, 36*(1), 92-118. doi:10.1002/med.21351

27. Kim, S.-H., Tangallapally, R., Kim, I. C., Trovato, R., Parker, D., Patton, J. S., . . . Yager, K. M. (2015). Discovery of an l-alanine ester prodrug of the Hsp90 inhibitor, MPC-3100. *Bioorganic and Medicinal Chemistry Letters, 25*(22), 5254-5257. doi:https://doi.org/10.1016/j.bmcl.2015.09.053
28. Kim, Y. J., Lee, S. A., Myung, S. C., Kim, W., and Lee, C. S. (2012). Radicicol, an inhibitor of Hsp90, enhances TRAIL-induced apoptosis in human epithelial ovarian carcinoma cells by promoting activation of apoptosis-related proteins. *Molecular and Cellular Biochemistry, 359*(1), 33-43. doi:10.1007/s11010-011-0997-9
29. Kinzel, L., Ernst, A., Orth, M., Albrecht, V., Hennel, R., Brix, N., . . . Lauber, K. (2016). A novel HSP90 inhibitor with reduced hepatotoxicity synergizes with radiotherapy to induce apoptosis, abrogate clonogenic survival, and improve tumor control in models of colorectal cancer. *Oncotarget, 7*(28). Retrieved from https://www.oncotarget.com/article/9774/text/
30. Kyle Hadden, M., Lubbers, J. D., and J. Blagg, S. B. (2006). Geldanamycin, Radicicol, and Chimeric Inhibitors of the Hsp90 Nterminal ATP Binding Site. *Current Topics in Medicinal Chemistry, 6*(11), 1173-1182. doi:http://dx.doi.org/10.2174/156802606777812031
31. Lamoureux, F., Thomas, C., Yin, M.-J., Fazli, L., Zoubeidi, A., and Gleave, M. E. (2014). Suppression of Heat Shock Protein 27 Using OGX-427 Induces Endoplasmic Reticulum Stress and Potentiates Heat Shock Protein 90 Inhibitors to Delay Castrate-resistant Prostate Cancer. *European Urology, 66*(1), 145-155. doi:https://doi.org/10.1016/j.eururo.2013.12.019
32. Lee, C.-H., Hong, H.-M., Chang, Y.-Y., and Chang, W.-W. (2012). Inhibition of heat shock protein (Hsp) 27 potentiates the suppressive effect of Hsp90 inhibitors in targeting breast cancer stem-like cells. *Biochimie, 94*(6), 1382-1389. doi:https://doi.org/10.1016/j.biochi.2012.02.034
33. Li, J., and Buchner, J. (2013). Structure, function and regulation of the hsp90 machinery. *Biomed J, 36*(3), 106-117. doi:10.4103/2319-4170.113230
34. Li, J., Soroka, J., and Buchner, J. (2012). The Hsp90 chaperone machinery: conformational dynamics and regulation by co-chaperones. *Biochim Biophys Acta, 1823*(3), 624-635. doi:10.1016/j.bbamcr.2011.09.003
35. Lundgren, K., Zhang, H., Brekken, J., Huser, N., Powell, R. E., Timple, N., . . . Burrows, F. J. (2009). BIIB021, an orally available, fully synthetic

small-molecule inhibitor of the heat shock protein Hsp90. *Mol Cancer Ther, 8*(4), 921-929. doi:10.1158/1535-7163.Mct-08-0758

36. Magwenyane, A. M., Ugbaja, S. C., Amoako, D. G., Somboro, A. M., Khan, R. B., and Kumalo, H. M. (2022). Heat Shock Protein 90 (HSP90) Inhibitors as Anticancer Medicines: A Review on the Computer-Aided Drug Discovery Approaches over the Past Five Years. *Comput Math Methods Med, 2022*, 2147763. doi:10.1155/2022/2147763
37. Martin, C. J., Gaisser, S., Challis, I. R., Carletti, I., Wilkinson, B., Gregory, M., . . . Zhang, M.-Q. (2008). Molecular Characterization of Macbecin as an Hsp90 Inhibitor. *Journal of Medicinal Chemistry, 51*(9), 2853-2857. doi:10.1021/jm701558c
38. Mbofung, R. M., McKenzie, J. A., Malu, S., Zhang, M., Peng, W., Liu, C., . . . Hwu, P. (2017). HSP90 inhibition enhances cancer immunotherapy by upregulating interferon response genes. *Nature Communications, 8*(1), 451. doi:10.1038/s41467-017-00449-z
39. McCollum, A. K., TenEyck, C. J., Sauer, B. M., Toft, D. O., and Erlichman, C. (2006). Up-regulation of Heat Shock Protein 27 Induces Resistance to 17-Allylamino-Demethoxygeldanamycin through a Glutathione-Mediated Mechanism. *Cancer Research, 66*(22), 10967-10975. doi:10.1158/0008-5472.Can-06-1629
40. Mehta, R. K., Pal, S., Kondapi, K., Sitto, M., Dewar, C., Devasia, T., . . . Nyati, M. K. (2020). Low-Dose Hsp90 Inhibitor Selectively Radiosensitizes HNSCC and Pancreatic Xenografts. *Clinical Cancer Research, 26*(19), 5246-5257. doi:10.1158/1078-0432.Ccr-19-3102
41. Meyer, P., Prodromou, C., Hu, B., Vaughan, C., Roe, S. M., Panaretou, B., . . . Pearl, L. H. (2003). Structural and Functional Analysis of the Middle Segment of Hsp90: Implications for ATP Hydrolysis and Client Protein and Co-chaperone Interactions. *Molecular Cell, 11*(3), 647-658. doi:https://doi.org/10.1016/S1097-2765(03)00065-0
42. Nagaraju, G. P., Alese, O. B., Landry, J., Diaz, R., and El-Rayes, B. F. (2014). HSP90 inhibition downregulates thymidylate synthase and sensitizes colorectal cancer cell lines to the effect of 5FU-based chemotherapy. *Oncotarget, 5*(20). Retrieved from https://www.oncotarget.com/article/2484/text/
43. Neckers, L., and Workman, P. (2012). Hsp90 molecular chaperone inhibitors: are we there yet? *Clin Cancer Res, 18*(1), 64-76. doi:10.1158/1078-0432.Ccr-11-1000
44. Nguyen, D. M., Lorang, D., Chen, G. A., Stewart, J. H., Tabibi, E., and Schrump, D. S. (2001). Enhancement of paclitaxel-mediated cytotoxicity

in lung cancer cells by 17-allylamino geldanamycin: in vitro and in vivo analysis. *The Annals of Thoracic Surgery, 72*(2), 371-379. doi:https://doi.org/10.1016/S0003-4975(01)02787-4

45. Park, H.-K., Yoon, N. G., Lee, J.-E., Hu, S., Yoon, S., Kim, S. Y., . . . Kang, B. H. (2020). Unleashing the full potential of Hsp90 inhibitors as cancer therapeutics through simultaneous inactivation of Hsp90, Grp94, and TRAP1. *Experimental and Molecular Medicine, 52*(1), 79-91. doi:10.1038/s12276-019-0360-x
46. Patterson, J., Palombella, V. J., Fritz, C., and Normant, E. (2008). IPI-504, a novel and soluble HSP-90 inhibitor, blocks the unfolded protein response in multiple myeloma cells. *Cancer Chemother Pharmacol, 61*(6), 923-932. doi:10.1007/s00280-007-0546-0
47. Pillai, R. N., Fennell, D. A., Kovcin, V., Ciuleanu, T.-E., Ramlau, R., Kowalski, D., . . . Ramalingam, S. S. (2020). Randomized Phase III Study of Ganetespib, a Heat Shock Protein 90 Inhibitor, With Docetaxel Versus Docetaxel in Advanced Non–Small-Cell Lung Cancer (GALAXY-2). *Journal of Clinical Oncology, 38*(6), 613-622. doi:10.1200/jco.19.00816
48. Prodromou, C., Roe, S. M., Piper, P. W., and Pearl, L. H. (1997). A molecular clamp in the crystal structure of the N-terminal domain of the yeast Hsp90 chaperone. *Nature Structural Biology, 4*(6), 477-482. doi:10.1038/nsb0697-477
49. Proia, D. A., and Kaufmann, G. F. (2015). Targeting Heat-Shock Protein 90 (HSP90) as a Complementary Strategy to Immune Checkpoint Blockade for Cancer Therapy. *Cancer Immunology Research, 3*(6), 583-589. doi:10.1158/2326-6066.Cir-15-0057
50. Ramalingam, S., Goss, G., Rosell, R., Schmid-Bindert, G., Zaric, B., Andric, Z., . . . Fennell, D. (2015). A randomized phase II study of ganetespib, a heat shock protein 90 inhibitor, in combination with docetaxel in second-line therapy of advanced non-small cell lung cancer (GALAXY-1). *Annals of Oncology, 26*(8), 1741-1748. doi:https://doi.org/10.1093/annonc/mdv220
51. Rastelli, G., Tian, Z. Q., Wang, Z., Myles, D., and Liu, Y. (2005). Structure-based design of 7-carbamate analogs of geldanamycin. *Bioorg Med Chem Lett, 15*(22), 5016-5021. doi:10.1016/j.bmcl.2005.08.013
52. Ren, X., Li, T., Zhang, W., and Yang, X. (2022). Targeting Heat-Shock Protein 90 in Cancer: An Update on Combination Therapy. *Cells, 11*(16), 2556. Retrieved from https://www.mdpi.com/2073-4409/11/16/2556
53. Roe, S. M., Prodromou, C., O'Brien, R., Ladbury, J. E., Piper, P. W., and Pearl, L. H. (1999). Structural Basis for Inhibition of the Hsp90 Molecular

Chaperone by the Antitumor Antibiotics Radicicol and Geldanamycin. *Journal of Medicinal Chemistry, 42*(2), 260-266. doi:10.1021/jm980403y

54. Schopf, F. H., Biebl, M. M., and Buchner, J. (2017). The HSP90 chaperone machinery. *Nature Reviews Molecular Cell Biology, 18*(6), 345-360. doi:10.1038/nrm.2017.20
55. Schulte, T. W., and Neckers, L. M. (1998). The benzoquinone ansamycin 17-allylamino-17-demethoxygeldanamycin binds to HSP90 and shares important biologic activities with geldanamycin. *Cancer Chemotherapy and Pharmacology, 42*(4), 273-279. doi:10.1007/s002800050817
56. Shah, S., Luke, J. J., Jane, H. A., Chen, T., Giobbie-Hurder, A., Ibrahim, N., . . . Hodi, F. S. (2018). Results from phase II trial of HSP90 inhibitor, STA-9090 (ganetespib), in metastatic uveal melanoma. *Melanoma Research, 28*(6). Retrieved from https://journals.lww.com/melanomaresearch/Fulltext/2018/12000/Results_from_phase_II_trial_of_HSP90_inhibitor,.16.aspx
57. Shen, G., and Blagg, B. S. J. (2005). Radester, a Novel Inhibitor of the Hsp90 Protein Folding Machinery. *Organic Letters, 7*(11), 2157-2160. doi:10.1021/ol050580a
58. Shimamura, T., Perera, S. A., Foley, K. P., Sang, J., Rodig, S. J., Inoue, T., . . . Shapiro, G. I. (2012). Ganetespib (STA-9090), a nongeldanamycin HSP90 inhibitor, has potent antitumor activity in in vitro and in vivo models of non-small cell lung cancer. *Clin Cancer Res, 18*(18), 4973-4985. doi:10.1158/1078-0432.Ccr-11-2967
59. Smith, N. F., Hayes, A., James, K., Nutley, B. P., McDonald, E., Henley, A., . . . Workman, P. (2006). Preclinical pharmacokinetics and metabolism of a novel diaryl pyrazole resorcinol series of heat shock protein 90 inhibitors. *Mol Cancer Ther, 5*(6), 1628-1637. doi:10.1158/1535-7163.Mct-06-0041
60. Smyth, T., Van Looy, T., Curry, J. E., Rodriguez-Lopez, A. M., Wozniak, A., Zhu, M., . . . Wallis, N. G. (2012). The HSP90 Inhibitor, AT13387, Is Effective against Imatinib-Sensitive and -Resistant Gastrointestinal Stromal Tumor Models. *Molecular Cancer Therapeutics, 11*(8), 1799-1808. doi:10.1158/1535-7163.Mct-11-1046
61. So″ti, C., Vermes, Á., Haystead, T. A. J., and Csermely, P. (2003). Comparative analysis of the ATP-binding sites of Hsp90 by nucleotide affinity cleavage: a distinct nucleotide specificity of the C-terminal ATP-binding site. *European Journal of Biochemistry, 270*(11), 2421-2428. doi:https://doi.org/10.1046/j.1432-1033.2003.03610.x

62. Soga, S., Akinaga, S., and Shiotsu, Y. (2013). Hsp90 inhibitors as anti-cancer agents, from basic discoveries to clinical development. *Curr Pharm Des, 19*(3), 366-376. doi:10.2174/138161213804143617
63. Soga, S., Neckers, L. M., Schulte, T. W., Shiotsu, Y., Akasaka, K., Narumi, H., . . . Akinaga, S. (1999). KF25706, a novel oxime derivative of radicicol, exhibits in vivo antitumor activity via selective depletion of Hsp90 binding signaling molecules. *Cancer Res, 59*(12), 2931-2938.
64. Solit, D. B., Basso, A. D., Olshen, A. B., Scher, H. I., and Rosen, N. (2003). Inhibition of heat shock protein 90 function down-regulates Akt kinase and sensitizes tumors to Taxol. *Cancer Res, 63*(9), 2139-2144.
65. Stingl, L., Stühmer, T., Chatterjee, M., Jensen, M. R., Flentje, M., and Djuzenova, C. S. (2010). Novel HSP90 inhibitors, NVP-AUY922 and NVP-BEP800, radiosensitize tumour cells through cell-cycle impairment, increased DNA damage and repair protraction. *British Journal of Cancer, 102*(11), 1578-1591. doi:10.1038/sj.bjc.6605683
66. Taldone, T., and Chiosis, G. (2009). Purine-Scaffold Hsp90 Inhibitors. *Current Topics in Medicinal Chemistry, 9*(15), 1436-1446. doi:http://dx.doi.org/10.2174/156802609789895737
67. Trepel, J., Mollapour, M., Giaccone, G., and Neckers, L. (2010). Targeting the dynamic HSP90 complex in cancer. *Nature Reviews Cancer, 10*(8), 537-549. doi:10.1038/nrc2887
68. Wei, S., Yin, D., Yu, S., Lin, X., Savani, M. R., Du, K., . . . Ashley, D. M. (2022). Antitumor Activity of a Mitochondrial-Targeted HSP90 Inhibitor in Gliomas. *Clin Cancer Res, 28*(10), 2180-2195. doi:10.1158/1078-0432.Ccr-21-0833
69. Woodhead, A. J., Angove, H., Carr, M. G., Chessari, G., Congreve, M., Coyle, J. E., . . . Woolford, A. J. A. (2010). Discovery of (2,4-Dihydroxy-5-isopropylphenyl)-[5-(4-methylpiperazin-1-ylmethyl)-1,3-dihydroisoindol-2-yl]methanone (AT13387), a Novel Inhibitor of the Molecular Chaperone Hsp90 by Fragment Based Drug Design. *Journal of Medicinal Chemistry, 53*(16), 5956-5969. doi:10.1021/jm100060b
70. Workman, P. (2004). Combinatorial attack on multistep oncogenesis by inhibiting the Hsp90 molecular chaperone. *Cancer Lett, 206*(2), 149-157. doi:10.1016/j.canlet.2003.08.032
71. Wu, J., Liu, T., Rios, Z., Mei, Q., Lin, X., and Cao, S. (2017). Heat Shock Proteins and Cancer. *Trends in Pharmacological Sciences, 38*(3), 226-256. doi:https://doi.org/10.1016/j.tips.2016.11.009
72. Wu, M. S., Lien, G. S., Shen, S. C., Yang, L. Y., and Chen, Y. C. (2013). HSP90 Inhibitors, Geldanamycin, and Radicicol, Enhance Fisetin-Induced

Cytotoxicity via Induction of Apoptosis in Human Colonic Cancer Cells. *Evid Based Complement Alternat Med, 2013*, 987612. doi:10.1155/2013/987612

73. Yin, X., Zhang, H., Lundgren, K., Wilson, L., Burrows, F., and Shores, C. G. (2010). BIIB021, a novel Hsp90 inhibitor, sensitizes head and neck squamous cell carcinoma to radiotherapy. *International Journal of Cancer, 126*(5), 1216-1225. doi:https://doi.org/10.1002/ijc.24815
74. Ying, W., Du, Z., Sun, L., Foley, K. P., Proia, D. A., Blackman, R. K., . . . Koya, K. (2012). Ganetespib, a unique triazolone-containing Hsp90 inhibitor, exhibits potent antitumor activity and a superior safety profile for cancer therapy. *Mol Cancer Ther, 11*(2), 475-484. doi:10.1158/1535-7163.Mct-11-0755
75. Yong, K., Cavet, J., Johnson, P., Morgan, G., Williams, C., Nakashima, D., . . . Cavenagh, J. (2016). Phase I study of KW-2478, a novel Hsp90 inhibitor, in patients with B-cell malignancies. *Br J Cancer, 114*(1), 7-13. doi:10.1038/bjc.2015.422
76. Žáčková, M., Moučková, D., Lopotová, T., Ondráčková, Z., Klamová, H., and Moravcová, J. (2013). Hsp90 — a potential prognostic marker in CML. *Blood Cells, Molecules, and Diseases, 50*(3), 184-189. doi:https://doi.org/10.1016/j.bcmd.2012.11.002
77. Zhang, Y., Ware, M. B., Zaidi, M. Y., Ruggieri, A. N., Olson, B. M., Komar, H., . . . Lesinski, G. B. (2021). Heat Shock Protein-90 Inhibition Alters Activation of Pancreatic Stellate Cells and Enhances the Efficacy of PD-1 Blockade in Pancreatic Cancer. *Molecular Cancer Therapeutics, 20*(1), 150-160. doi:10.1158/1535-7163.Mct-19-0911
78. Zhao, L., and Cao, F. (2014). [Effects of 17-DMAG on non-small cell lung cancer cell lines A549 and H1975 being resistant to EGFR-TKI]. *Zhongguo Fei Ai Za Zhi, 17*(11), 778-782. doi:10.3779/j.issn.1009-3419.2014.11.02
79. Zuehlke, A., and Johnson, J. L. (2010). Hsp90 and co-chaperones twist the functions of diverse client proteins. *Biopolymers, 93*(3), 211-217. doi:10.1002/bip.21292

A Comparative Study: Carbon Nanotube/Polypyrrole (CNT/PPy) Composites Synthesized By Electrochemical And Plasma Polymerization Methods

Barış BALIKÇI[1], Prof. Dr. Songül ŞEN GÜRSOY[2*]

[1]Burdur Mehmet Akif Ersoy University,
Institute of Applied and Natural Sciences, Department of Chemistry,
TR-15030 Burdur, Turkey

[2]Burdur Mehmet Akif Ersoy University,*
Faculty of Arts and Sciences, Department of Chemistry,
TR-15030 Burdur, Turkey
ORCID: 0000-0002-9506-9822

Introduction

Polymers, known as insulators, are macromolecules composed of small structural units linked together by covalent bonds. However, towards the end of the 1970s, a new class of polymers called conductive polymers emerged [1]. In 2000, MacDiarmid, Heeger, and Shirakawa were awarded the Nobel Prize in chemistry for their research on conductive polymers. Conductive polymers have attracted a lot of attention due to their easy processing and cheapness compared to metals. Among conductive polymers, polypyrrole (PPy) attracts a lot of attention due to its superior properties such as good redox properties [2], easy chemical and electrochemical synthesis. Composite materials combine the best properties of two or more materials to create useful functionality. In particular, nanocomposites with large surface areas have better properties than many properties of the same material with normal particle size. Carbon nanotubes (CNTs) were discovered in the 1990s. For more than 20 years, carbon nanotubes have combined very well with functional polymers due to their superior properties such as high conductivity values, chemical stability, low density and light weight, as well as large surface areas. The electrical, morphological, thermal, chemical, mechanical and optical properties of these materials are excellent [3]. These composites are potential materials for the development of supercapasitors [4] biologic sensors [5] and flexible light-emitting diodes [6].

Among the PPy composites, CNT/PPy have a great place due to their interesting properties by combining the properties of these two materials with a synergetic effect. However, the strong van der Walls interactions between CNTs cause some limitations in application areas because hydrophobic CNTs form crystal structures by packing among themselves. In addition, weak polymer interactions with CNTs reduce the performance of the composite as it will cause weak interfacial bonding and agglomeration. In addition, most of the work on the preparation of CNT/PPy composites has focused on wet chemical vehicles. Disadvantages of these methods can be listed as the dispersion of the CNTs in any liquid medium, the fact that the coating process does not occur uniformly throughout the composite, and the CNTs stick together and precipitate during the synthesis. In order to overcome these problems, plasma polymerization is recommended in some studies. However, the influence of surfactant on the properties of conducting polymers has been investigated in our some studies. These studies showed that the structural, morphological, thermal and conductivity properties of conducting polymers was affected by surfactant types [7, 8].

In this study, the effects of different types of surfactants on the properties of PPy/CNT composites prepared by chemical and plasma polymerization were

investigated. It has been predicted that surfactants can enhance the interaction between ppy and cnts and promote the individual presence of CNTs. Althought, CNT/PPy composites have been synthesized by chemical and plasma polymerization for different purposes in some studies [9, 10] no comparative study was found in the literature by performing chemical and plasma polymerization of this composite at the same time.

1. Material and Methods

1.1. Chemicals

Pyrrole (Aldrich) was purified by distillation at reduced pressure before used. Lithium perchlorate ($LiClO_4$, Sigma-Aldrich), ethanole (Sigma-Aldrich), sulphyric acide were used for the synthesis of composite. MWCNT was purchased from NANOCYL S. A. (NC7000). TTAB (Fluka, Germany), NADBS (Fluka, Germany) and polyethylene oxide (10) iso-octylphenyl ether (Tween 20) (Merck, Germany) were used as received. All other compounds were analytical reagent grade.

1.2. Apparatus

CNT/PPy composites were synthesized by using two different methods. Electrochemical polymerization was performed with three electrode system (CompactStat, Ivium Technologies, Netherlands). Indium tin oxide (ITO), Ag/AgCl and Pt wire were used as working, reference and auxiliary electrode, respectively. Plasma polymerization of polymers was made with (PlazmaTek, Isparta) plasma polymerization system. FTIR spectra were performed between 400 cm^{-1} and 4000 cm^{-1} with a 4 cm^{-1} resolution on a Perkin Elmer Frontier (Beaconsfield, Beuckinghamshire, HP91QA, England). For SEM analysis, JEOL SEM-7100-EDX (Zaventem, Belgium) model scanning electron microscope was used. The conductivity was measured using the four-probe technique with a PCIDAS6014 current source, a voltmeter and a temperature controller. Dry powders were pressed into pellets using a steel die having a diameter of 13 mm in a hydraulic press at 700 MPa. Thermal degradation and mass losses of polymers were monitored with a Perkin Elmer Diamond TG/DTA model thermal analyzer at a temperature range of 25-900 ºC and at a heating rate of 10ºC/min in N_2 atmosphere. The modification of CNTs was achived in 96% H_2SO_4:70% HNO_3 (3:1) mixture for 2 hours in ultrasonic bath. After that CNTs were washed with distiled water. CNTs were dried in a vacuum oven at 60°C.

2.3. Electrochemical synthesis of polymers

Pyrrole (2.5 mmol) and $LiClO_4$ (2.5 mmol) were dissolved in 25 mL of 0.1 M H_2SO_4. 100 mg CNT was added monomer solution and the mixture was sonicated in ultrasonic bath for 10 minutes. The monomer, pyrrole, was polymerized onto CNT by cyclic voltametric method in the range of -0.1-1.5 V with 50 cycle at room temperature. The same procedures were repeated by adding TTAB, NaDBSA, Tween-20 surfactants to the initial solution. The molar ratio of monomer to surfactant was chosen as 5.

2.4. Plasma synthesis of polymers

100 mg of CNT was mixed in 5 mL of ethanol for 10 minutes in an ultrasonic bath. The prepared solution was evenly spread over the coverslips (5 pieces) with a pipette. The plasma is produced at low pressure (0.30 Torr) with 13.56 MHz frequency at a power of 40 W for 20 minutes in presence of pyrrole vapour for obtaining uniform coating of pyrrole on the surface of CNT. The same procedures were repeated in the initial solution using TTAB, NaDBSA, Tween-20 surfactants.

3. Results and Discussion

3.1. FTIR Results

The FTIR spectra of polymers and CNT were shown in Fig. 1a, b. The FTIR spectra of electrochemically synthesized polymers includes more sharp bands than that of the plasma polymerized ones. Additionally, characteristic polypyrrole peaks were available for both methods. The characteristic peaks of polypyrrole shifted when the different kinds of surfactants were joined the polymer structure. The FT-IR spectrum of the CNTs shows an intense band at around 1633 cm^{-1} attributed to C=O stretching from the carboxylic acid incorporated into the CNT structure after functionalization in acid medium [11]. The peak at 1538 cm^{-1} in the spectrum of CNT/PPy-TTAB is more clear than than that of CNT/PPy-NaDBS and CNT/PPy-Tween 20 (Fig1a). However, the spectra of plasma polymerized polymers look alike each other with some shifts. The characteristic bands were seen between 1430 and 1485 cm^{-1} attributed to the pyrrole ring and conjugated C–N stretching mode. The bands between 1275 and 1293 cm^{-1} in the spectra of polymers due to the C–H or C–N in-plane deformation modes. The peaks at around 1172-1186 cm^{-1} shows the breathing vibration of the pyrrole ring. The band belongs to the C–H and N–H in-plane deformation vibrations at about 1040 cm^{-1} was present in all samples. Although characteristic peaks were observed in all polymers synthesized by both methods, the skeletal vibrations are affected by doping of the polymer [12]. In addition,

the FTIR spectra of polymers synthesized by plasma polymerization contain weaker bands compared to those synthesized electrochemically. It can be concluded that the reason for this is that the CNT surface is coated with PPy in a much thinner layer in plasma polymerization. This is also supported by the SEM results. SEM images of plasma polymerized polymers are more similar to CNT morphologically. This indicates that the PPy coating is thin in plasma polymerization.

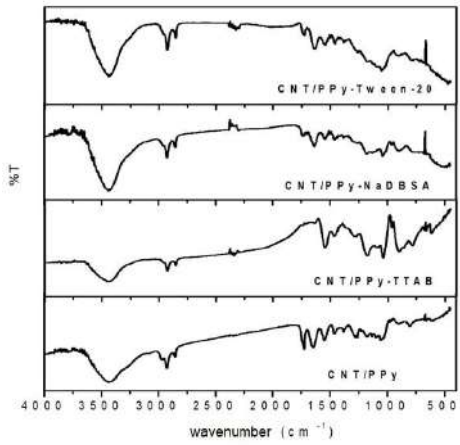

(a)

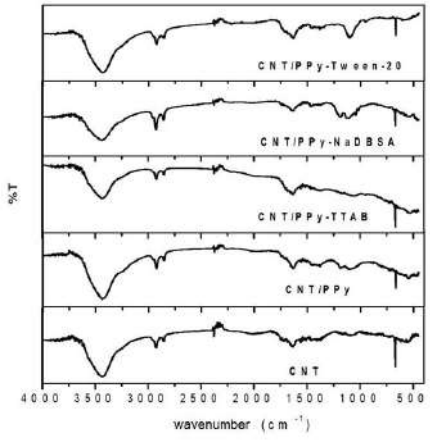

(b)

Figure 1. FTIR spectra of polymers (a) electrochemical polymerization (b) plasma polymerization and CNT

3.2. TGA Results

Fig. 2 shows the TGA curves of CNT/PPy and CNT/PPy-NaDBS composites prepared by two different methods. Among composites synthesized in presence of surfactants only the CNT/PPy-NaDBS composite was examined due to its high yield amount. Table 1 exhibites T_i, initial degradation temperature; T_m, maximum degradation temperature, and T_f, final degradation temperature of CNT/PPy and CNT/PPy-NaDBS composite. Plasma polymerized CNT/PPy exhibits one-step decomposition when CNT/PPy-NaDBS composite exhibits three step decomposition. Amount of residue was (in wt.%) at 900 ºC higher for CNT/PPy than composite prepared in the presence of surfactant in plasma polymerization. However, the initial decomposition temperature of composite was higher that that of CNT/PPy. The presence of surfactant increased the thermal stability due to increased interaction between CNT and polypyrrole.

In contrast to plasma polymerization, the use of surfactant in electrochemically synthesized polymers increased the residual value at 900 ºC, while lowering the initial decomposition temperature. The initial degradation temperature of the composite prepared electrochemically without surfactant, CNT/PPy, was 240 ºC. The composite prepared with surfactant (CNT/PPy-NaDBS) showed lower initial decomposition temperature (225 ºC). Besides it shows higher residue value (%60) than CNT/PPy (%45) at 900 ºC. As a result thermal behaviours of composites were changing according to the polymerization method and presence of surfactant.

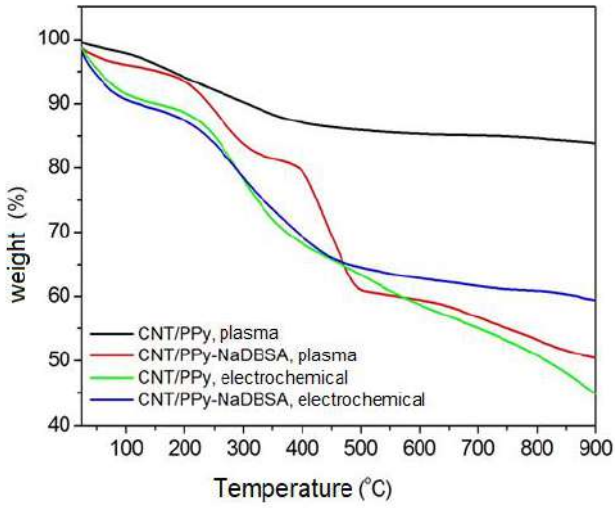

Figure 2. TGA thermographs of polymers

Table 1. Thermal degradation temperatures of CNT/PPy composites prepared in presence of surfactant with different synthesis methods.

Polymer	T_i	T_m	T_f	% residue at 900 °C
CNT/PPy, plasma	140	280	420	70
CNT/PPy-NaDBSA, plasma	195	248	300	52
	400	445	490	
	635	738	840	
CNT/PPy, electrochemical	240	300	360	45
	475	638	800	
CNT/PPy-NaDBSA, electrochemical	225	333	440	60

3.3. SEM and Conductivity Results

Fig. 3 (a-i) presents the SEM images of the composites and CNT. The morphologies of composites synthesized by electrochemistry are different from those of composites synthesized by plasma technique. It is seen that the presence of surfactants also effect the morphologies of composites as reported earlier [13]. Electrochemically synthesized composites showed more flat and smooth morphology (Fig 3a-d) than the plasma polymerized composites. The morphologies differs from each other as the surfactant changes in composite structure. When the conductivity values of the polymers are compared, it is seen that the conductivity of the surfactant-used composites synthesized by the plasma method has increased significantly. However, the conductivity of CNT has been calculated as 8.2044×10^{-6} S cm^{-1}. The conductivity values of polymers are given in Table 2. The conductivity values of CNT composites synthesized without surfactant are close to each other. Composite morphology in plasma polymerization is very similar to CNT. This can be explained by the ability of very thin polymer coating, which is one of the most important features of plasma polymerization. If the layers of the polymer films have thin layer surface morphology, electron hopping consisting easily on the chain and between the chains. Thin layer of PPy could shorten the electron transition of the system and decrease the contact resistance which can effectively reforming the charge transfer capacity between the polypyrrole and CNT [14, 15].

The highest conductivity value (9.767×10^{-3} Scm^{-1}) was belongs to CNT/PPy-NaDBSA composite synthesized by plasma polymerization. The morphology of this composite is more compact and smooth than the other polymers also (Fig. 3h). Moreover, the influences of the thickness of coating-polymer on the electrical properties of the CNT/PPy composites have been studied before in a study. The results showed that the polymer thickness improves the properties of carbon based device [9].

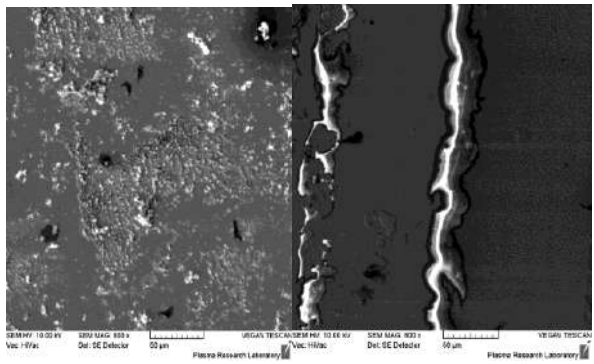

(a) **(b)**

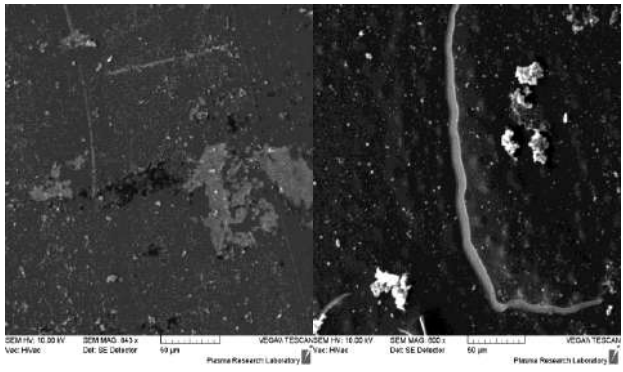

(c) **(d)**

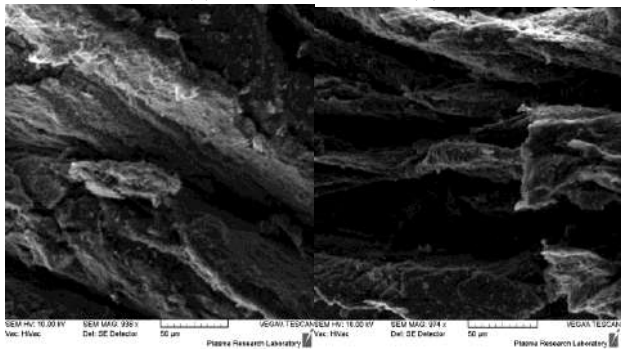

(e) **(f)**

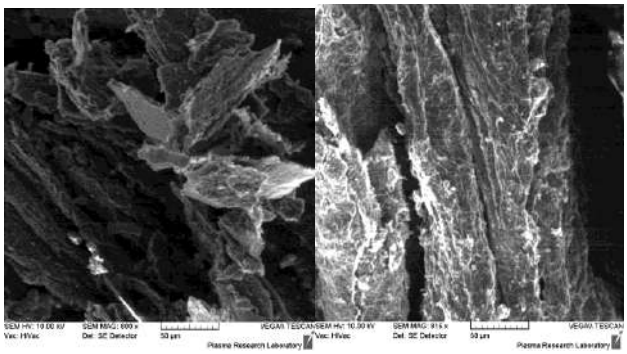

(g) (h)

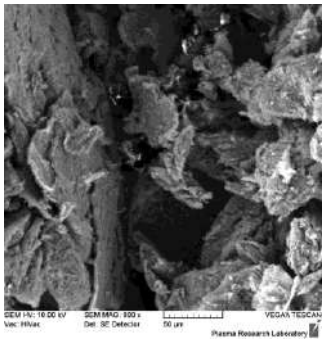

(i)

Figure 3. SEM images of electrochemically synthesized polymers; (a) CNT/PPy, (b) CNT/ PPy-NaDBSA, (c) CNT/PPy-TTAB (d) CNT/PPy-Tween-20, plasma polymerized polymers; (e) CNT/PPy, (f) CNT/ PPy-NaDBSA, (g) CNT/PPy-TTAB, (h) CNT/PPy-Tween-20 and (i) CNT

Table 2. Conductivity values of polymers

Polymer	**Conductivity (S cm^{-1}) (electrochemical)**	**Conductivity (S cm^{-1}) (plasma)**
CNT/PPy	8.5167 $x10^{-6}$	7.7146 $x10^{-6}$
CNT/PPy-NaDBSA	2.0346 $x10^{-5}$	9.767 $x10^{-3}$
CNT/PPy-TTAB	5.9826 $x10^{-6}$	7.2044 $x10^{-6}$
CNT/PPy-Tween 20	6.9833 $x10^{-7}$	1.5072 $x10^{-3}$

Conclusions

In this study, CNT/PPy composites were synthesized by electrochemical and plasma polymerization methods in the presence of three different types of surfactants. Composites were synthesized onto ITO electrode as working electrode by the CV method in electrochemical polymerization method. The plasma is produced at low pressure in presence of pyrrole vapour for obtaining uniform coating of pyrrole on the surface of CNT. FTIR results showed that the

CNT surface is coated with PPy with a much thinner layer in plasma polymerization than that of electrochemical polymerization. Thermal behaviours of composites were changing according to the polymerization method and presence of surfactant. SEM and conductivity results supported that the conductivity of the surfactant-used composites synthesized by the plasma method has increased significantly.

Acknowledgments

This work was supported by Scientific and Technological Research Council of Turkey, 2209-A "University Students Domestic Research Projects Support Program" (Project number 1919B011402196).

References

[1] MacDiarmid, A. G. Heeger, A. J. (1980). Organic metals and semiconductors: The chemistry of polyacetylene, (CH)*x*, and its derivatives. *Synthetic Metals*, *1 (2)*, 101-118. https://doi.org/10.1016/0379-6779(80)90002-8.

[2] Suematsu, S. Oura, Y. Tsujimoto, H. Kanno, H. Naoi, K. (2000). Conducting polymer films of cross-linked structure and their QCM analysis. *Electrochimica Acta, 45,* 3813-3821. https://doi.org/10.1016/S0013-4686(00)00466-7

[3] Romero, J. G. V. Luengo, C. A. Huber, J. G. and Rosolen, J. M. (2002). Synthesis of single-wall nanotubes by pyrolysis of graphite in Helium atmosphere, *Qu´ımica Nova, 25, 1*, 59-61. https://doi.org/10.1590/S0100-40422002000100011.

[4] Canobre, S. C. Xavier, F. F. S. Fagundes, W. S. de Freitas, A. C. and Amaral, F. A. (2015). Performance of the Chemical and Electrochemical Composites of PPy/CNT as Electrodes in Type I Supercapacitors, *Journal of Nanomaterials*, *16 (1),* 160-173. https://doi.org/10.1155/2015/560164.

[5] Ferreira, P. A. B. Araujo, M. C. M. Prado, C. M. de Lima, R. A. Rodríguez, B. A. G. Dutra. R. F. (2020). An ultrasensitive Cystatin C renal failure immunosensor based on a PPy/CNT electrochemical capacitor grafted on interdigitated electrode. *Colloids and Surfaces B: Biointerfaces, 189,* 110834. https://doi.org/10.1016/j.colsurfb.2020.110834.

[6] Kim, M. Kim,Y. C. (2014). Single wall carbon nanotube/poly(3,4-ethylenedioxythiophene) nanocomposite film as a transparent electrode for flexible organic light-emitting diodes, *Synthetic Metals, (198),* 31-35. https://doi.org/10.1016/j.synthmet.2014.09.033.

[7] Sen Gursoy, S. Cogal, S. Uygun Oksuz, A. (2014). Influence of surfactants on properties of electrochemically synthesized pyrrole/1-dimethylaminopyrrole copolymer, *Iran Polym J, 23*, 783-792. https://doi.org/10.1007/s13726-014-0274-3.

[8] Uygun, A. Yavuz, A. G. Sen, S. Omastová, M. (2009). Polythiophene/SiO_2 nanocomposites prepared in the presence of surfactants and their application to glucose biosensing, *Synthetic Metals, 159 (19-20),* 2022-2028. https://doi.org/10.1016/j.synthmet.2009.07.009

[9] Zhang, B. Xu, Y. Zheng, Y. Dai, L. Zhang, M. Yang, J. Chen, Y. Chen X. Zhou, J. (2011). A Facile Synthesis of Polypyrrole/Carbon Nanotube Composites with Ultrathin, Uniform and Thickness-Tunable Polypyrrole Shells, *Nanoscale Research Letters, 6*, 431-440.

https://doi.org/10.1186/1556-276X-6-431.
[10] Yavuz, H. Girard, G. Bai, J. (2016). Dielectric barrier discharge assisted continuous plasma polypyrrole deposition fort he surface modification of carbon nanotube-grafted carbon fibers, *Thin Solid Films, 616,* 220-227. https://doi.org/10.1016/j.tsf.2016.08.028
[11] Jeykumari, D. R. S. Ramaprabhu, S. Narayanan, S. S. (2007). A thionine functionalizedmultiwalled carbon nanotube modified electrode for the determination of hydrogen peroxide. *Carbon, 45 (6),* 1340-1353. https://doi.org/10.1016/j.carbon.2007.01.006.
[12] Maia, G. Ticianelli, E.A. Nart, F.C. (1994). FTIR Investigation of the polypyrrole oxidation in Na_2SO_4 and $NaNO_3$ aqueous solutions. *Zeitschrift Phys Chem, 186,* 245-257. https://doi.org/10.1524/zpch.1994.186.Part_2.245.
[13] Xue, H.G. Shen, Z.Q. Li, Y.F. (2001). Polyaniline–polyisoprene composite film based glucose biosensor with high permselectivity. *Synthetic Metals, 124,* 345–349. https://doi.org/10.1016/S0379-6779(01)00381-2.
[14] Ma, Y. Cheung, W. Wei, D. Bogozi, A. Chiu, P. Wang, L. Pontoriero, F. Mendelsohn, R. He, H. (2008). Improved Conductivity of Carbon Nanotube Networks by In Situ Polymerization of a Thin Skin of Conducting Polymer. *Acsnano, 2,* 1197-1204. https://doi.org/10.1021/nn800201n.
[15] Li, L. Qin, Z. Liang, X. Fan, Q. Lu, Y. Wu, W. Zhu, M. (2009). Facile Fabrication of Uniform Core-Shell Structured Carbon Nanotube-Polyaniline Nanocomposites. *J Phys Chem C 113,* 5502-5507. https://doi.org/10.1021/jp808582f.

Fundamental Analytical Methods and Case Studies Used in Archaeological Studies: The Basis of Archaeometry

Dr. Gülin GENCOGLU KORKMAZ [1, 2]

[1]Heidelberg University, Institute of Earth Sciences
Konya Technical University Faculty of Engineering and Natural Science
[2]Geological Engineering Department2
ORCID: 0000-0003-0185-2806

INTRODUCTION

Archaeology is an important science that enlights on the history of humanity when, especially, it is studied together with many sciences such as chemistry, physics, biology, geology, geochronology, geography, geomorphology.

Geochemical analytical methods are necessary in order to determine what archeological artifacts, finds, and cultural heritage items are made of, identify their origins, and the time period they belong to. As a result of the rapid scientific and technological advances precipitated by the Second World War, several analytical techniques were deployed in archaeological studies, including X-ray analysis and electron microscopy, neutron activation analysis, and mass spectrometry (Pollard, Batt, Stern, Young, & Young, 2007). In order to characterize the material of the ceramics from which the pottery is made, to identify the rocks used in the restoration works to identify the rocks used in the construction of the artifact, and to determine their origins, the most important thing is petrographical analysis under a polarizing microscope. With a petrographical analysis, the binder-aggregate ratios of mortars and plasters, the types and properties of the aggregates they contain can be determined, and suggestions can be developed on possible source areas. Moreover the properties of the rock, mineralogicalcompositions, textural properties and alteration and weatheringtypes could be determined, and suggestions can be made for the type of stone to be used in the building. After that, the analytical method can be determined based on the mineralogy-petrography of the material, the scope, and the aim of the study.

There are several comprehensive publications regarding archaeometric studies in the literature. In this study, the most common geochemical techniques such as XRF, XRD, ICP-MS, LIBS, FT-IR and RAMAN which were utilized in archaeological studies and some case studies will be presented (Table 1).

Table 1 Some of the analytical techniques commonly utilized in archaeological studies modified from Ricci (2017).

Abbreviation	Name	Principle	Sample Preparation	Portable - Labratory
XRF	**X-ray Fluorescence**	Elemental quantitative and qualitative analysis can be performed. It uses high energy X-ray beam to excite the sample and measures the wavelength and energy of the characteristic radiations emitted from the atoms when they are coming back to the fundamental state. It is used for chemical analysis for the surface of ceramic glaze and body	In the labratory you can make pellet samples (<65 micron sized powder samples) In-situ analyses dont require any sample preparation process	Portable for in-situ measurements Labratory and in-situ
XRD	**X-ray Diffraction**	Qualitative and semi-quantitative analysis of the mineralogical composition. It is based constructive interference of monochromatic Xrays and a crystalline sample. One of the most useful technique to study the crystal stru cture and atomic spacing of the clay minerals.	10-100 mg of homogenous powdered samples	Labratory
FT-IR	**Fourier-Transform Infrared Spectroscopy**	It is an absorption technique which can be used to identify chemical compounds and it provides information about the chemical bonding in both inorganic and organic materials.	A few mg samples adequate	Labratory
Raman	**Raman Spectroscopy**	It is an absorption technique, as FT-IR, for molecular identification based on inelastic scattering of monochromatic light. It allows to identify organic and inorganic materials and in the ceramic material studies it is used to detect minerals.	There is no sample preparation process. It is not a destructive technique.	Labratory and in-situ

LIBS	**Laser-Induced Breakdown Spectroscopy**	It is a practical atomic emission spectroscopy method which is used highly energetic laser pulses to provoke optical sample excitation, offers an appealing means of discriminating different materials, their sources, volcanic ant archaelogical centers in real-time.	There is no sample preparation process. It is not a destructive technique. If you want to make more detail study and get more trace elemnts (even light elements) you can prepare pellet samples	Labratory , in-situ also remote
LA-ICP-MS	**Laser Ablation-Inductively Coupled Plasma Mass Spectrometer**	A type of mass spectrometer that uses induction coupled plasma to ionize the sample. It atomizes the sample and creates atomic and small polyatomic ions that are then detected.	You can make the analyses on the carbon coated thin sections	Labratory

XRD & XRF (XRF, micro-XRF, P-XRF)

One of the most commonly used techniques on the archaeological studies has been XRF. With the advancement of technology, micro-XRF and portable XRF devices have been developed. Portable X-Ray spectroscopy (p-XRF) is a technique utilized to detect and measure the chemical contents of the objects in excavation sites, museums and private collections, as it allows on-site analysis, is non-destructive and could make quick measurements (Şimşek et al., 2014).

Tolun and Ay (2017) found ancient granite quarries in the Troas and Mysia Regions and Western Anatolia in their archeometry studies. Major and trace element chemistry was determined by XRF method and mineralogical petrographic examinations were examined under optical microscope (OM). As a result of this study, they determined that at least two different granite types were used in the Agora of Smyrna and the Ancient City of Tlos.

The lack of detailed petrographic and mineralogical analysis and description of the natural geological building materials used in archaeological structures, the failure to use the correct rock or material during the restoration of such important structures, and the restoration of the building in different rocks instead of the rocks used in ancient times may cause the archaeological structure to turn into a building image outside of its primitive nature.

In order to restore historical buildings correctly, documenting and recording the current state of the building and defining the building materials by making archeometric analyzes during the pre-restoration project preparation phase are the

substantial parameters. Recently, archaeometric studies regarding building materials are widely used to solve different problems on archaeological artifacts of different sizes and types (metal, glass, ceramics, stone, mortar, plaster) and building materials. Aydın, Tetiker, and Tanrıkulu (2019) conducted a comprehensive study in the Şanlıurfa-Hacı Yadigâr Mosque. In this study, analyzes were made on mortar, plaster, and stone samples taken from the mosque using optical petrographic, XRD, and P-XRF Methods. In the non-destructive sampling areas, only P-XRF analyzes were made.

Optical microscope, XRD and micro-XRF methods were used in archaeometric studies for Early Roman ceramics in the Tarsus region (Akyol, Tekkök, Kadıoğlu, & Demirci, 2007). Thin sections of the obtained ceramic pieces were taken to show all layers from the outside to the inside, and petrographic examinations were made under an optical microscope. Thin sections were also prepared and studied for clay, (soil) sediment and stone samples. XRD analysis was performed to determine the mineral phases in soil and clay samples. Point Micro-XRF analysis, which is one of the non-destructive methods, was applied to determine the coloring matter in the glaze. Consequently, material characterization was made and sources were tried to be determined, the content and source of paint materials were determined, and the presence of local or non-local ateliers was determined with geochemical methods.

Ceramics composed of variety of clay minerals have a long history and are found in almost all societies. They do not deteriorate easily, and are often found in large quantities in archeological excavations. Clay minerals' structures present in could be detected by XRD (Fig.1) and have frequently been used as a reference for the thermal treatment of ceramic objects since the distinct crystallographic phases of minerals be exposed to variations in clay bounding up with the firing temperature (Mangueira, Toledo, Teixeira, & Franco, 2011)

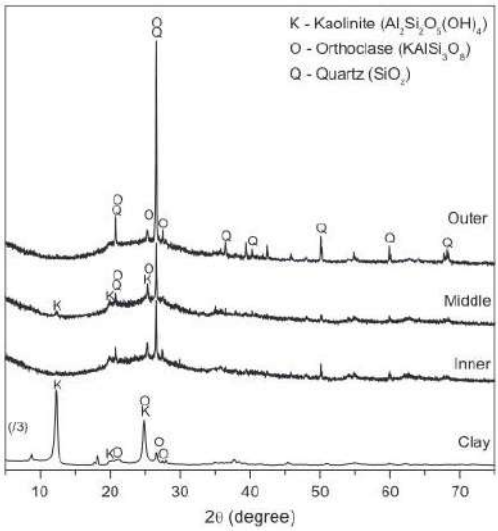

Fig. 1. X-Ray diffractograms of the outer, middle, and inner layers of the ceramic sample and the clay (Mangueira et al., 2011).

In their study, Dirican, Atakuman, Biler, and Erdoğu present the first data of archaeometric studies carried out to determine the raw material sources and production techniques of pottery (ceramic), stone ax and chisel, marble, obsidian and some other stone findings unearthed in Gökçeada Uğurlu Höyük. For this purpose, after petrographic studies to determine the mineralogical and chemical properties of the raw material used in the production of the findings, XRD and P-XRF methods are applied.

In this study, although the source of ilmenite and smectites, which are the materials of pottery ceramics, was found on Gökçeada, the central source of the serpentinites determined in the structure of some materials could not be found around Gökçeada. However, the fact that the source of the obsidians was determined as Göllüdag and Nenezi Dağ in Central Anatolia makes this study interesting and clearly reveals the importance of geochemical analyzes in archaeological studies.

LIBS & LA-ICP-MS

LIBS is a very fast, sensitive and successful technique for qualitatively and quantitatively determining the elements in a given sample, and it was first applied in this field in 1963, right after the discovery of lasers (Miziolek, Palleschi, & Schechter, 2006). By using LIBS method, major, trace and even some rare earth elements (Na, Li) within the sample can be detected easily and fastly. Along with that, more detailed trace element contents can be determined with micro-LIBS

device. LIBS has recently been used frequently in geology studies because it does not require any sample preparation, can be applied on solid samples, and has advantages such as fast analysis and fast results (i.e. (Gençoğlu Korkmaz, Gündoğdu, Kılıç, & Kurt, 2021). LIBS can also be used with XRF or RAMAN to give more effective results. Recently, the Raman method is frequently preferred with LIBS in studies such as mineral determination, identification and classification of minerals, since no damage is caused to the samples to be analyzed and analyzes are carried out in an easy and practical way without sample preparation (Akçe & Kadıoğlu, 2020; Bazalgette Courrèges-Lacoste, Ahlers, & Pérez, 2007; Koralay & Kadioglu, 2015; Lu et al., 2015; Sharma, Misra, Lucey, Wiens, & Clegg, 2007; Yunfeng, Ying, Jingwen, Zhongchen, & Ying, 2015).

LIBS is a widespread (Awasthi, Kumar, Rai, & Rai, 2016; Harmon et al., 2018; Muhammed Shameem et al., 2020; Remus et al., 2010; Remus et al., 2012) and easy technique for analysis and characterization of the composition of a broad variety of objects of cultural heritage containing sculpture, painted artworks, polychromes, icons, pottery, and glass, metal, and stone artifacts. Remus et al. (2012) tested whether the localities of obsidians taken from two different obsidian centers in California could be distinguished and to what extent sub-sources could be identified in each of these centers in their study on obsidians using the LIBS method (Fig. 2). Classification of samples was performed using PLSDA, a common chemometric technique to perform statistical regression on high-dimensional data. Separation of samples from Coso Volcanic Field, Bodie Hills, and other large obsidian fields in north-central California has been demonstrated to be possible with greater than 90% accuracy using both spectral bands. Since obsidian is a high silica rhyolitic volcanic glass and almost every obsidian has a similar composition, it was preferred to determine the detection limits of trace elements with the LIBS method in order to be geochemically distinctive, thus determining the obsidian sources and sub-sources.

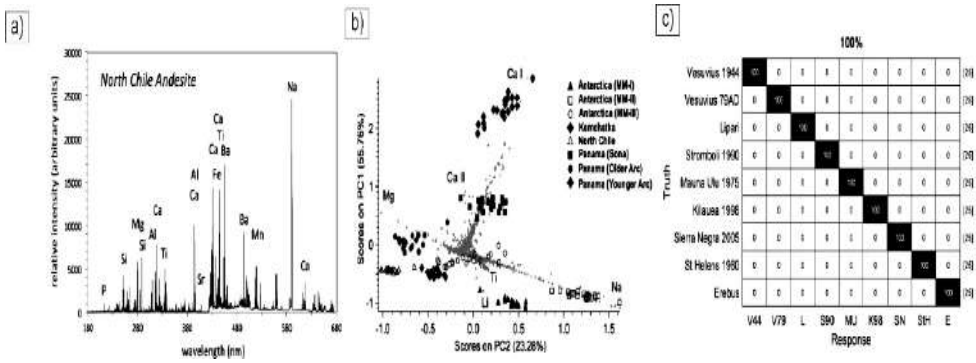

Fig. 2. a) Al, Mg, Si, Ba, Ca, Ti, Fe, P spectra obtained as a result of LIBS analysis on obsidians, b) PCA distributions and discrimination diagram and c) PLSDA diagram Remus et al. (2012) modified.

Restoration of archaeological metal objects includes a complex and multistep process that contains the object's analysis, strengthening its surface and internal structure, corrosion stabilization, preservation, reconstruction of components, and replenishment of losses. Cleaning of abrasive layers has a critical role due to the possibility of removing contaminations, suggesting the shape of the object being restored and its technological and decorative features. Recent studies have recommended several methods for cleaning metal objects (Craddock, 2009; Scott, 1994). Laser cleaning is a promising approach, which can solve some complicated restoration tasks as the cleaning of objects with inlays. Fs lasers present pioneering cleaning facilities to reveal the information about the investigation of some historical materials such as coins (Abdel-Kareem, Al-Zahrani, Khedr, & Harith, 2016), parchment papers (Walczak & Heald, 2008), wood or soil based cultural heritage objects (Kaminska et al., 2005). It has been presented that copper-zinc alloy coin determines optimal conditions for removal of acorroded layer. Korkmaz et al. (2022) utilized a historical coin, which was made of copper-zinc alloys was used for ablation process to investigate the effectiveness of 800nm wavelength for cleaning surface corroded layers (Fig. 3). Hence, a series of experiments were performed using laser power values ranging from 10-500 mW per pulse and several repetitive applications were executed to reach desired results. Experimental studies reveal that the best method applied on archaeological artifacts is mechanical cleaning without using chemicals. At the same time, it has the advantage of minimizing the risk of any layer or corrosion formation on the work because it is a recyclable work. For this reason, it is one of the most successful techniques among conservation methods, as it offers the opportunity to analyze again in the future.

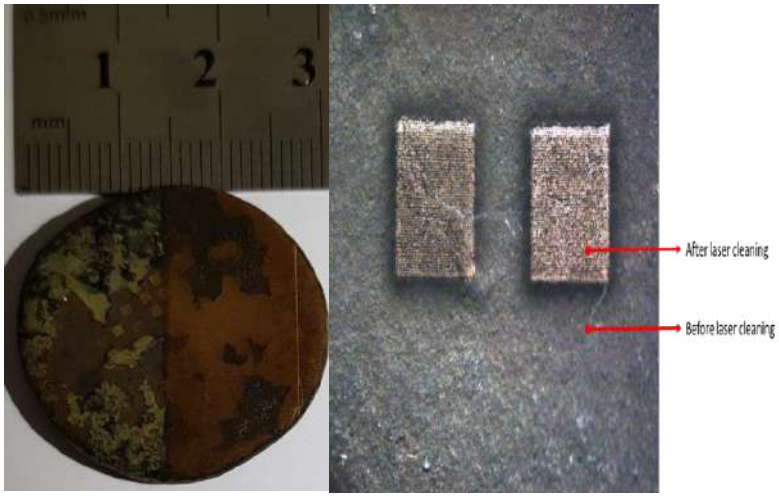

Fig. 3. Before and after photos of cleaning the surface of a historical coin collected in Konya region with Fs-LIBS (Korkmaz et al., 2022)

It is commonly known that obsidian (volcanic glass) was used in the construction of many tools in archaeological periods. Erturac et al. (2012) performed some geochemical analysis (for 8 major oxides and 30 minor elements) using the LA-ICP-MS method of 200 samples taken from various levels of each obsidian outcrop in their study from the Göllüdağ Volcanic Complex (Central Anatolia).

Obsidians, which can be found in 10-50 cm dimensions and do not contain devitrification products such as lithophytic and spherulite (McPhie, 1993), and therefore observed as outcrops suitable for chipping, are defined as obsidian sources (OBS). Prehistoric obsidian workshops (chipping centers) are observed in many OBS environments around Göllüdağ (Balkan-Atlı et al., 2010). In this study, obsidians were classified as a result of spatial geochemical analyzes, their sources were determined and their relationships were revealed. This study clearly reveals that trade routes in the past could be determined by identifying and correlating material sources with detailed spatial analyzes of the materials and minerals with LA-ICP-MS.

Galiová et al. (2010) have analyzed the dentin of a prehistoric bear (Ursus arctos) tooth by both LIBS and LA-ICP-MS (Fig. 4). From an archaeological point of view, it has been possible to reconstruct the etiology of the brown bear fossil, ie nutrition, health and migration, based on the measurements made. The Sr=Ca and Sr=Ba profiles in the sample showed seasonal fluctuations, proving that this bear migrated between the location of the hibernaculum and the location

of the fossils. Combined with results from other techniques (i.e., study of cementation increases), it was concluded that this bear specimen most likely hunted before hibernating while foraging and migrating near a human settlement (where fossils were found). This study demonstrated that LIBS and LA-ICP-MS can be successfully applied as direct or complementary techniques in spatially resolved microchemical analysis of fossil specimens.

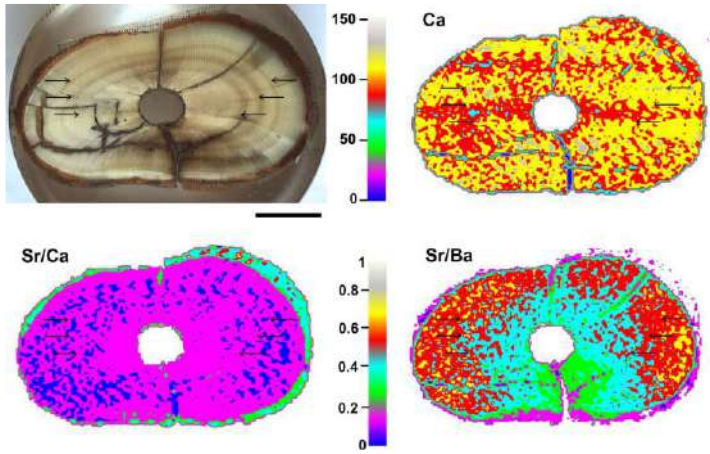

Fig. 4. Element mappings by using LA-ICP-MS and LIBS modified from Galiová et al. (2010)

FT-IR & RAMAN

FT-IR is an absorption technique which can be used to identify chemical compounds and it provides information about the chemical bonding in both inorganic and organic materials. Raman is an absorption technique, as FT-IR, for molecular identification based on inelastic scattering of monochromatic light. It allows to identify organic and inorganic materials and in the ceramic material studies it is used to detect minerals (Ricci, 2017).

Point analysis, line length analysis, and mapping could be done with Confocal Raman spectroscopy (CRS). Generally, point analysis is applied in mineralogical determinations. Eroğlu, Bilgen, Yetiş, Kadıoğlu, and Deniz (2021) conducted a coprehensive study on Determination of Construction Materials of Karabuk Ovacik Çukur Mosque and in their study, the pigment structures used in the wall paintings of the building were determined. In addition, the FT-IR analysis technique was used to determine the binder that allows the material used in the paint samples to adhere to the surface. The analyzes of the pigment and possible binders in the paint samples taken from the south and west walls were generated. Moreover, FT-IR and CRS analyzes were applied to the red, yellow, blue, green,

brown, and black paint layer samples taken. In this study, data on aggregate binder ratios in mortar-plaster and gypsum, lime and cement contents in binders were obtained in detail. Rock types and building materials were characterized. In paints, pigments of natural and artificial origin and different types of organic binders (protein, oil and resin) are used; It is determined that modern paints are preferred in the decorations on the cement-based walls of the recent period.

CONCLUSIONS

Analytical techniques applied in archaeometric studies can be divided different subgroups in accordance with sample preparation process (the sampling strategy/non-destructive and destructive techniques), characterization and identification of the materials, conservation and preservation of the cultural assests, technology and techniques used.

Considering the economic costs, an analytical method suitable for the purpose should be chosen, and a significant light should be enlighted on the history, together with developing techniques and technologies, by conducting studies in collaboration with other important sciences such as biology, chemistry and geology.

References

1. Abdel-Kareem, O., Al-Zahrani, A., Khedr, A., & Harith, M. A. (2016). Evaluatıng The Use Of Laser In Analysıs And Cleanıng Of The Islamıc Marıne Archaeologıcal Coıns Excavated From The Red Sea. *International journal of conservation science, 7*(2).
2. Akçe, M. A., & Kadıoğlu, Y. K. (2020). Raman Spektroskopisinin İlkeleri ve Mineral Tanımlamalarında Kullanılması. *Nevşehir Bilim ve Teknoloji Dergisi, 9*(2), 99-115.
3. Akyol, A. A., Tekkök, B., Kadıoğlu, Y. K., & Demirci, Ş. (2007). Tarsus-Gözlükule Erken Roma Dönemi Seramikleri Arkeometrik Çalışmaları. *ARKEOMETRİ SONUÇLARI TOPLANTISI*, 99.
4. Awasthi, S., Kumar, R., Rai, G. K., & Rai, A. K. (2016). Study of archaeological coins of different dynasties using libs coupled with multivariate analysis. *Optics and Lasers in Engineering, 79*, 29-38. doi:https://doi.org/10.1016/j.optlaseng.2015.11.005
5. Aydın, M., Tetiker, S., & Tanrıkulu, H. (2019). Şanlıurfa-Hacı Yadigâr Camii restorasyon amaçlı yapı malzemelerinin arkeometrik özelliklerinin incelenmesi.
6. Balkan-Atlı, N., Kuhn, S. L., Astruc, L., Kayacan, N., Dinçer, B., & Çakan, G. (2010). Göllü Dağ Survey 2009. *Anatolia Antiqua. Eski Anadolu, 18*(1), 191-202.
7. Bazalgette Courrèges-Lacoste, G., Ahlers, B., & Pérez, F. R. (2007). Combined Raman spectrometer/laser-induced breakdown spectrometer for the next ESA mission to Mars. *Spectrochimica Acta Part A: Molecular and Biomolecular Spectroscopy, 68*(4), 1023-1028. doi:https://doi.org/10.1016/j.saa.2007.03.026
8. Craddock, P. (2009). *Scientific investigation of copies, fakes and forgeries*: Routledge.
9. Dirican, M., Atakuman, Ç., Biler, C. N., & Erdoğu, B. Uğurlu Höyük-Gökçeada'da Bulunan Neolitik Ve Kalkolitik Dönem Seramik Ve Taş Buluntuları Üzerinde İlk Arkeometrik Gözlemler.
10. Eroğlu, M., Bilgen, M., Yetiş, E., Kadıoğlu, Y. K., & Deniz, K. (2021). Karabük Ovacık Çukur Camisi Yapı Malzemelerinin Arkeometrik Analizleri. *Art-Sanat Dergisi*(16), 151-179.
11. Erturac, M. K., Astruc, L., Balkan-Atli, N., Gratuze, B., Mouralis, D., Kuzucuoğlu, C., & Dinçer, B. (2012). *Göllüdağ Volkanik Kompleksi İçerisindeki Obsidiyen Kaynaklarının Özellikleri*.
12. Galiová, M., Kaiser, J., Fortes, F. J., Novotný, K., Malina, R., Prokeš, L., . . . Svoboda, J. (2010). Multielemental analysis of prehistoric animal teeth

by laser-induced breakdown spectroscopy and laser ablation inductively coupled plasma mass spectrometry. *Applied optics, 49*(13), C191-C199.
13. Gençoğlu Korkmaz, G., Gündoğdu, Y., Kılıç, H. Ş., & Kurt, H. (2021, 10-12 April). *Determınatıon Of The Element Contents Of The Geologıcal Rock Samples Wıth The Help Of Cf-Lıbs.* Paper presented at the II.Internatıonal Hazar Scıentıfıc Researchesconference, Khazar University, Baku, Azerbaijan.
14. Harmon, R. S., Throckmorton, C. S., Hark, R. R., Gottfried, J. L., Wörner, G., Harpp, K., & Collins, L. (2018). Discriminating volcanic centers with handheld laser-induced breakdown spectroscopy (LIBS). *Journal of Archaeological Science, 98*, 112-127. doi:https://doi.org/10.1016/j.jas.2018.07.009
15. Koralay, T., & Kadioglu, Y. K. (2015). The origin and determination of silica types in the silica occurrences from Altintas region (Usak-Western Anatolia) using multianalytical techniques. *Spectrochim Acta A Mol Biomol Spectrosc, 137*, 516-526. doi:10.1016/j.saa.2014.08.027
16. Korkmaz, G. G., Gündoğdu, Y., İlker, I., KIZIL, A., Gezgin, S. Y., & Kilic, H. Ş. (2022). Femtosecond Laser Cleaning of Archaeological Cultural Assets. *Journal of International Environmental Application and Science, 17*(2), 75-84.
17. Lu, Y., Li, Y., Li, Y., Wang, Y., Wang, S., Bao, Z., & Zheng, R. (2015). Micro spatial analysis of seashell surface using laser-induced breakdown spectroscopy and Raman spectroscopy. *Spectrochimica Acta Part B: Atomic Spectroscopy, 110*, 63-69. doi:https://doi.org/10.1016/j.sab.2015.05.012
18. Mangueira, G. M., Toledo, R., Teixeira, S., & Franco, R. W. A. (2011). A study of the firing temperature of archeological pottery by X-ray diffraction and electron paramagnetic resonance. *Journal of Physics and Chemistry of Solids, 72*(2), 90-96. doi:https://doi.org/10.1016/j.jpcs.2010.11.005
19. McPhie, J. (1993). *Volcanic textures: a guide to the interpretation of textures in volcanic rocks*.
20. Miziolek, A. W., Palleschi, V., & Schechter, I. (2006). *Laser induced breakdown spectroscopy*: Cambridge university press.
21. Muhammed Shameem, K. M., Dhanada, V. S., Harikrishnan, S., George, S. D., Kartha, V. B., Santhosh, C., & Unnikrishnan, V. K. (2020). Echelle LIBS-Raman system: A versatile tool for mineralogical and archaeological applications. *Talanta, 208*, 120482. doi:https://doi.org/10.1016/j.talanta.2019.120482

22. Pollard, A. M., Batt, C. M., Stern, B., Young, S. M., & Young, S. (2007). *Analytical chemistry in archaeology*: Cambridge University Press.
23. Remus, J., Gottfried, J., Harmon, R., Draucker, A., Baron, D., & Yohe, R. (2010). Archaeological Applications of Laser-induced Breakdown Spectroscopy: An Example from the Coso Volcanic Field, California, Using Advanced Statistical Signal Processing Analysis. *Applied Optics - APPL OPT, 49*. doi:10.1364/AO.49.00C120
24. Remus, J., Harmon, R., Hark, R., Haverstock, G., Baron, D., Potter, I., . . . East, L. (2012). Advanced signal processing analysis of laser-induced breakdown spectroscopy data for the discrimination of obsidian sources. *Applied optics, 51*, B65-73. doi:10.1364/AO.51.000B65
25. Ricci, G. (2017). Archaeometric studies of historical ceramic materials.
26. Scott, D. A. (1994). An examination of the patina and corrosion morphology of some Roman bronzes. *Journal of the American Institute for Conservation, 33*(1), 1-23.
27. Sharma, S. K., Misra, A. K., Lucey, P. G., Wiens, R. C., & Clegg, S. M. (2007). Combined remote LIBS and Raman spectroscopy at 8.6m of sulfur-containing minerals, and minerals coated with hematite or covered with basaltic dust. *Spectrochimica Acta Part A: Molecular and Biomolecular Spectroscopy, 68*(4), 1036-1045. doi:https://doi.org/10.1016/j.saa.2007.06.046
28. Şimşek, G., Casadio, F., Colomban, P., Bellot-Gurlet, L., Faber, K., Zelleke, G., . . . Moinet, E. (2014). On-site identification of early Böttger red stoneware made at Meissen using portable XRF: 1, Body Analysis. *Journal of American Ceramic Society, 97*(9), 2745-2754.
29. Tolun, M., & Ay, V. (2017). Troas Granit Sütunlarının Batı Anadolu Kıyılarındaki Dağılımı Üzerine Arkeometrik Bir Yaklaşım. *ARKEOLOJİ VE SANAT*, 119-130.
30. Walczak, C. E., & Heald, R. (2008). Mechanisms of mitotic spindle assembly and function. *International review of cytology, 265*, 111-158.
31. Yunfeng, B., Ying, Z., Jingwen, Y., Zhongchen, W., & Ying, L. (2015). Classification and discrimination of minerals using laser induced breakdown spectroscopy and Raman spectroscopy. *Plasma Science and Technology, 17*(11), 923.